

Stony Brook University



OFFICIAL COPY

The official electronic file of this thesis or dissertation is maintained by the University Libraries on behalf of The Graduate School at Stony Brook University.

© All Rights Reserved by Author.

**Synthetic, Medicinal, and Computational Studies on Novel Anticancer, Antitubercular, and
Anti-nociceptive Agents**

A Dissertation Presented

by

Longfei Wei

to

The Graduate School

in Partial Fulfillment of the

Requirements

for the Degree of

Doctor of Philosophy

in

Chemistry

Stony Brook University

August 2016

Copyright by
Longfei Wei
2016

Stony Brook University

The Graduate School

Longfei Wei

We, the dissertation committee for the above candidate for the
Doctor of Philosophy degree, hereby recommend
acceptance of this dissertation.

**Iwao Ojima - Dissertation Advisor
Distinguished Professor, Department of Chemistry**

**Jonathan G. Rudick - Chairperson of Defense
Assistant Professor, Department of Chemistry**

**Peter J. Tonge - Third Member
Professor, Department of Chemistry**

**Ramesh C. Gupta – Outside Member
Vice President, Chem-Master International Inc.**

This dissertation is accepted by the Graduate School

Nancy Goroff

Interim Dean of the Graduate School

Abstract of the Dissertation

**Synthetic, Medicinal, and Computational Studies on Novel Anticancer, Antitubercular, and
Anti-nociceptive Agents**

by

Longfei Wei

Doctor of Philosophy

in

Chemistry

Stony Brook University

2016

Multidrug resistance is a major obstacle to effective cancer chemotherapy. New-generation taxoids SB-T-1214 and SB-T-1216 have shown two to three orders of magnitude higher potency than those of paclitaxel and docetaxel against multidrug-resistant cancer cell lines. A structure-activity relationship (SAR) study has been conducted in order to test which moiety of the new-generation taxoids account for the high potency against multidrug resistant cancer cell lines.

In order to selectively deliver new-generation taxoids into tumor cells, tumor-targeted drug delivery systems with a smart methyl-branched disulfide linker have been developed in the Ojima laboratory. The metabolic stability of this disulfide linker has been assessed in various solvent systems including biologically relevant cell culture media and human blood plasma *via* real-time kinetic analysis by ^{19}F NMR.

Polyamidoamine (PAMAM) dendrimers are attractive anticancer drug delivery vehicles, because of their well-defined architectures and biocompatible properties. Novel PAMAM dendrimer-based tumor-targeting multifunctional conjugates have been designed, synthesized, and characterized. Biological evaluations of these conjugates against various cancer cell lines have been conducted *via* MTT cytotoxicity assays, confocal fluorescence microscopy (CFM) imaging, and flow cytometry analysis.

Potential binding sites of novel benzimidazole inhibitors with FtsZ proteins have been identified *via* molecular docking, homology modeling, and protein alignment for antitubercular drug discovery. Novel mechanism of action has been proposed based on the docking results.

A pharmacophore-guided docking strategy has been developed for designing novel FABP inhibitors as anti-nociceptive and anti-inflammatory agents. Newly designed analogs have better binding energy scores and smaller cLogP values.

Dedication Page

This thesis is dedicated to my grandmother, who passed away last year and could not witness my success now.

Table of Contents

List of Figures.....	xiii
List of Schemes.....	xxiv
List of Tables.....	xxix
List of Abbreviations.....	xxx
Acknowledgements.....	xxxv
Vita.....	xxxvii

Chapter 1

Design, Synthesis, and Biological Evaluation of New-Generation Taxoids

Chapter Contents

§ 1.1 Introduction.....	2
§ 1.1.1 Cancer and Cancer Statistics.....	2
§ 1.1.2 Paclitaxel and Taxanes.....	4
§ 1.1.3 Semi-synthesis of Taxanes via the β -Lactam Synthone Method.....	6
§ 1.1.4 Asymmetric Synthesis of β -Lactam.....	8
§ 1.1.5 Structure-Activity Relationship (SAR) Study on Taxanes.....	14
§ 1.1.6 Multidrug Resistance (MDR).....	17
§ 1.1.7 New-Generation Taxoids.....	18
§ 1.2 Synthesis and Biological Evaluation of New-Generation Taxoids.....	20
§ 1.2.1 Synthesis of Eantiopure β -Lactam.....	20
§ 1.2.2 Synthesis of New-Generation Taxoids SB-T-1214 and SB-T-1216.....	25
§ 1.2.3 Synthesis of New-Generation Taxoid SB-T-1211.....	29
§ 1.2.4 Synthesis of New-Generation Taxoid 10-Ac-docetaxel.....	32
§ 1.2.5 Synthesis of New-Generation Taxoid SB-T-0035.....	34
§ 1.2.6 Biological Evaluation of New-Generation Taxoids.....	37
§ 1.3 Summary.....	44
§ 1.4 Experimental.....	44
§ 1.5 References.....	66

Chapter 2

Metabolic Stability Assessment of Self-Immolative Disulfide Linkers in Tumor-Targeted Drug Delivery Systems via ^{19}F NMR

Chapter Contents

§ 2.1 Introduction.....	74
§ 2.1.1 Tumor-Targeted Drug Delivery Systems (TTDDS)	74
§ 2.1.2 Self-Immolative Disulfide Linker	77
§ 2.1.3 Drug Release Study of the Self-Immolative Disulfide Linker Systems via ^{19}F NMR	81
§ 2.2 Metabolic Stability Assessment of Tumor-Targeted Drug Delivery Systems via ^{19}F NMR	84
§ 2.2.1 Synthesis of Methyl-Branched Self-Immolative Disulfide Linker	84
§ 2.2.2 Effects of Solvent Systems and Drug Formulations on the Fluorine Signal Chemical Shifts of Designed Probes	86
§ 2.2.3 Metabolic Stability Assessment of Tumor-Targeted Drug Delivery Systems via Time-Resolved ^{19}F NMR	91
§ 2.3 Summary	95
§ 2.4 Experimental	95
§ 2.5 References.....	103

Chapter 3

PAMAM Dendrimer-based Tumor-Targeted Drug Delivery Systems

Chapter Contents

§ 3.1 Introduction.....	108
§ 3.1.1 Nanocarrier-based Drug Delivery	108
§ 3.1.2 Dendrimer.....	111
§ 3.1.3 Applications of Dendrimer in Anticancer Drug Delivery.....	115
§ 3.1.4 Enhanced Permeability and Retention (EPR) Effect.....	118
§ 3.1.5 Biotin as Tumor-Targeting Module	119
§ 3.1.6 Multivalent Binding Effect.....	120
§ 3.1.7 Theranostics	122
§ 3.2 PAMAM Dendrimer-based Tumor-Targeting Taxoid/FITC Conjugates.....	125
§ 3.2.1 Rational Design.....	125
§ 3.2.2 Synthesis of Biotin-PEGylated-G1/G3 PAMAM Dendrimers	127
§ 3.2.3 Synthesis of SB-T-1214-Linker-PEG-Azide and FITC-PEG-Azide Click Ready Probes	133
§ 3.2.4 Construct of Final Dendrimer Conjugates	135
§ 3.2.5 Biological Evaluation of PAMAM Dendrimer-based Tumor-Targeting Taxoid/FITC Conjugates.....	162
§ 3.3 Asymmetric Bow-Tie Dendrimer-based (ABTD) Tumor-Targeted Drug Delivery Systems	172
§ 3.3.1 Rational Design.....	172
§ 3.3.2 Synthesis of ABTD Conjugates	175
§ 3.4 Tri-branched PAMAM Dendrimer-based Tumor-Targeting Theranostic Conjugates	185
§ 3.4.1 Rational Design.....	185

§ 3.4.2 Towards Synthesis of a Tri-branched PAMAM Dendrimer-based Tumor-Targeting Theranostic Conjugate bearing MRI Contrast Agent.....	187
§ 3.4.3 Towards Synthesis of Second-Generation Versatile Tri-branched PAMAM Dendrimer- based Tumor-Targeting Theranostic Conjugates-Route 1	194
§ 3.4.4 Towards Synthesis of Second-Generation Versatile Tri-branched PAMAM Dendrimer- based Tumor-Targeting Theranostic Conjugates-Route 2	199
§ 3.5 Summary	206
§ 3.6 Experimental	206
§ 3.7 References.....	230

Chapter 4

Identification of Potential Binding Sites of Novel Benzimidazole Inhibitors with FtsZ Proteins via Molecular Modeling for Antitubercular Drug Discovery

Chapter Contents

§ 4.1 Introduction.....	237
§ 4.1.1 FtsZ as the Target for Antitubercular Drug Discovery	237
§ 4.1.2 Crystal Structures of FtsZ Proteins	238
§ 4.1.3 Novel Benzimidazole Inhibitors Targeting FtsZ Proteins.....	241
§ 4.2 Identification of Potential Binding Sites of Novel Benzimidazole Inhibitors with FtsZ Proteins via Molecular Modeling.....	243
§ 4.2.1 Docking Study of Benzimidazole Inhibitors into <i>Mtb</i> FtsZ Head-to-Head Lateral Dimer Crystal Structures	243
§ 4.2.2 Docking Study of Benzimidazole Inhibitors into <i>Mj</i> FtsZ Head-to-Tail Longitudinal Dimer Crystal Structure	245
§ 4.2.3 Construction of <i>Mtb</i> FtsZ Head-to-Tail Longitudinal Dimer Models via Homology Modeling/Protein Alignment.....	246
§ 4.2.4 Docking Study of Benzimidazole Inhibitors into <i>Mtb</i> FtsZ Head-to-Tail Longitudinal Dimer Models.....	249
§ 4.2.5 Docking Study of Benzimidazole Inhibitors into <i>Mtb</i> FtsZ Head-to-Tail Curved Longitudinal Trimer Crystal Structure	257
§ 4.2.6 Proposed Mechanism of Action	261
§ 4.3 Summary	262
§ 4.4 References.....	262

Chapter 5

Design of Novel Fatty Acid Binding Protein (FABP) Inhibitors via Molecular Modeling for Anti-nociceptive and Anti-inflammatory Drug Discovery

Chapter Contents

§ 5.1 Introduction.....	266
§ 5.1.1 Fatty acid-binding proteins (FABPs)	266
§ 5.1.2 Known FABP Inhibitors	268
§ 5.1.3 Discovery and Development of SB-FI-26 as Lead FABP Inhibitor	270
§ 5.1.4 Co-crystal Structure of FABP5 with SB-FI-26.....	272
§ 5.2 Design of Novel SB-FI-26 Analogs as Potential FABP Inhibitors.....	274
§ 5.2.1 Validation of a Pharmacophore-guided Docking Strategy	274
§ 5.2.2 Computational Structural-based Design of New SB-FI-26 Analogs	278
§ 5.3 Summary	281
§ 5.4 References.....	281

List of Figures

Chapter 1

Figure 1.1 The hallmarks of cancer.....	2
Figure 1.2 Ten leading cancer types for the estimated new cancer cases and deaths by sex, United States, 2016.....	3
Figure 1.3 Chemical structure of paclitaxel (Taxol®).....	4
Figure 1.4 The mechanism of action of paclitaxel.....	5
Figure 1.5 Chemical structures of docetaxel (left) and cabazitaxel (right).....	5
Figure 1.6 Chemical structure of 10-deacetyl-baccatin III (10-DAB III).....	6
Figure 1.7 Greene-Potier's protocol for semi-synthesis of paclitaxel.....	7
Figure 1.8 Ojima-Holton's protocol for semi-synthesis of paclitaxel.....	8
Figure 1.9 Ojima's protocol for semi-synthesis of docetaxel.....	8
Figure 1.10 Pathways for the formation of <i>cis</i> - and <i>trans</i> - β -lactam.....	10
Figure 1.11 Suggested model for the relative stereoselectivity in Staudinger reaction.....	11
Figure 1.12 Mechanism for lithium chiral ester enolate-imine cyclocondensation reaction.....	12
Figure 1.13 MM2 calculations on <i>E</i> - and <i>Z</i> -enolates by MACROMODEL.....	13
Figure 1.14 Summary of key structure-activity relationships (SAR) of taxanes.....	14
Figure 1.15 Chemical structure of a C-4 derivative of paclitaxel in clinical trial.....	15
Figure 1.16 Chemical structure of a C-7 derivative of paclitaxel in clinical trial.....	16
Figure 1.17 Chemical structure of a C-14 derivative of docetaxel in clinical trial.....	17
Figure 1.18 Model of anticancer drug transport by P-glycoprotein.....	18
Figure 1.19 Designed new-generation taxoids.....	20

Figure 1.20 Biological evaluation of new generation taxoids against SK-BR-3 sensitive cell line (set 1).....	38
Figure 1.21 Biological evaluation of new generation taxoids against SK-BR-3 sensitive cell line (set 2).....	39
Figure 1.22 Biological evaluation of new generation taxoids against SK-BR-3 resistant cell line (set 1).....	40
Figure 1.23 Biological evaluation of new generation taxoids against SK-BR-3 resistant cell line (set 2).....	40
Figure 1.24 Biological evaluation of new generation taxoids against MCF-7 sensitive cell line (set 1).....	41
Figure 1.25 Biological evaluation of new generation taxoids against MCF-7 sensitive cell line (set 2).....	42
Figure 1.26 Biological evaluation of new generation taxoids against MCF-7 resistant cell line (set 1).....	43
Figure 1.27 Biological evaluation of new generation taxoids against MCF-7 resistant cell line (set 2).....	43

Chapter 2

Figure 2.1 Chemical structure of imatinib (Gleevec®).....	74
Figure 2.2 A typical tumor-targeting drug conjugate.....	75
Figure 2.3 Receptor-mediated endocytosis of tumor-targeting drug conjugates.....	76
Figure 2.4 Targeting modules (TTM) employed in tumor-targeted drug delivery systems (TTDDS).....	77
Figure 2.5 Linker systems employed in tumor-targeted drug delivery systems (TTDDS).....	78
Figure 2.6 Chemical structures of mAb-SB-T-12136 monoclonal antibody (mAb) drug conjugate, SB-T-12136-SH , and SB-T-1213	79
Figure 2.7 Second-generation mechanism-based self-immolative disulfide linkers.....	80
Figure 2.8 Validation of the drug release of a second-generation mechanism-based self-immolative disulfide linker <i>in vitro</i> with the biotin-linker-coumarin conjugate.....	81

Figure 2.9 A model system for the mechanism-based drug release using cysteine as the trigger for thiolactonization.....	82
Figure 2.10 Time-resolved ¹⁹ F NMR spectra for the disulfide linker cleavage and thiolactonization process of probe 1 (2.5 mM) in 30% DMSO in D ₂ O beginning at 1 h after the addition of 6 equiv. of GSH at 25 °C with 15 min intervals.....	83
Figure 2.11 Designed probe 2 for metabolic stability assessment in biologically relevant media by ¹ F NMR.....	83
Figure 2.12 Chemical structure of probe BLT-S-F₆ and taxoid SB-T-12822-5	86
Figure 2.13 Chemical structure of solutol HS 15.....	86
Figure 2.14 Chemical structure of polysorbate 80.....	86
Figure 2.15 ¹⁹ F NMR spectra (512 scans) showing individual chemical shifts of 200 μM BLT-S-F₆ , SB-T-12822-5 , and a 1:1 mixture of the two compounds in D ₂ O-ethanol (v/v = 60/40).....	87
Figure 2.16 ¹⁹ F NMR spectra (>268 scans) showing individual chemical shifts of 200 μM BLT-S-F₆ , SB-T-12822-5 , and a 1:1 mixture of the two compounds in D ₂ O-ethanol-solutol HS 15 (v/v/v = 84/8/8).....	88
Figure 2.17 ¹⁹ F NMR spectra (512 scans) showing individual chemical shifts of 200 μM BLT-S-F₆ and SB-T-12822-5 in D ₂ O-ethanol-polysorbate 80 (v/v/v = 96/2/2), and a 1:1 mixture of the two compounds in D ₂ O-ethanol-polysorbate 80 (v/v/v = 94/4/2).....	89
Figure 2.18 ¹⁹ F NMR spectra (1024 scans) showing individual chemical shifts of 200 μM BLT-S-F₆ and SB-T-12822-5 in blood plasma-D ₂ O-ethanol-polysorbate 80 (v/v/v/v = 86/10/2/2), and a 1:1 mixture of the two compounds in human blood plasma-D ₂ O-ethanol-polysorbate 80 (v/v/v/v = 84/10/4/2).....	90
Figure 2.19 ¹⁹ F NMR spectra (512 scans) showing individual chemical shifts of 200 μM BLT-S-F₆ and SB-T-12822-5 in RPMI 1640-D ₂ O-ethanol-polysorbate 80 (v/v/v/v = 86/10/2/2), and a 1:1 mixture of the two compounds in RPMI 1640 cell culture media-D ₂ O-ethanol-polysorbate 80 (v/v/v/v = 84/10/4/2).....	91
Figure 2.20 ¹⁹ F NMR spectra for the drug release of BLT-S-F₆ (200 μM) in 86% blood plasma, 10% D ₂ O, 2% ethanol, and 2% polysorbate 80 without addition of GSH at 0 h, 24 h and 48 h at 37 °C (2048 scans/spectrum).....	92
Figure 2.21 Time-resolved ¹⁹ F NMR spectra for the drug release of BLT-S-F₆ (200 μM) in 86% blood plasma, 10% D ₂ O, 2% ethanol, and 2% polysorbate 80 at 30 min after the addition of 100 equiv. of GSH with 1 h intervals for 13 h at 37 °C (1024 scans/spectrum).....	93

Figure 2.22 Time-resolved ^{19}F NMR spectra for the drug release of **BLT-S-F₆** (200 μM) in 86% RPMI-1640 cell culture media, 10% D_2O , 2% ethanol, and 2% polysorbate 80 at 30 min after the addition of 100 equiv. of GSH with 1 h intervals for 12 h at 37 °C (1024 scans/spectrum).....94

Figure 2.23 ^{19}F NMR spectra for the drug release of **BLT-S-F₆** (200 μM) in 96% D_2O , 2% ethanol, and 2% polysorbate 80 with addition of 100 equiv. of GSH at 0 h, 17 h, 40 h, 72 h, 120 h and 168 h at 37 °C (>512 scans/spectrum).....95

Chapter 3

Figure 3.1 Examples of nanocarriers for anticancer drug delivery.....109

Figure 3.2 Examples of polymer-anticancer drug conjugates.....111

Figure 3.3 Graphical representations of dendrimers from core to generation 4.....112

Figure 3.4 Schematic representations of divergent method and convergent method for synthesizing dendrimers.....112

Figure 3.5 Schematic representation of polyester dendrimers-poly(ethylene oxide) “bow-tie” hybrids with tunable molecular weight and architecture.....113

Figure 3.6 Schematic representation of a well-defined polyamide-based hyperbranched multifunctional dendrimer platform.....114

Figure 3.7 Schematic representation of “diblock” PAMAM cystamine core dendrimer-based conjugate for synthesis of bioactive nanoparticles.....114

Figure 3.8 Dendrimers as multi-purpose nanodevices for anticancer drug delivery and diagnostic imaging.....115

Figure 3.9 Schematic representation of generation 5 (G5) PAMAM dendrimer surface-functionalized with FITC, FA and MTX.....116

Figure 3.10 A quantitative assessment of ligand distribution of the multifunctional dendrimer conjugate.....117

Figure 3.11 Bifunctional dendrimer conjugates of folic acid and methotrexate with defined ratio.....117

Figure 3.12 Schematic representation of enhanced permeability and retention (EPR) effect...118

Figure 3.13 Chemical structure of D-(+)-biotin119

Figure 3.14 Quantitative assessments of multivalent interactions between folate-binding protein (FBP) and G5 dendrimer-based nanodevices using surface plasmon resonance (SPR).....	121
Figure 3.15 Qualitative assessments of multivalent interactions between folate receptors (FAR) and G5 dendrimer-based nanodevices using flow cytometry.....	121
Figure 3.16 Schematic representation of the concept of theranostic.....	122
Figure 3.17 Platinum (II)-gadolinium (III) complexes as potential theranostic agents for cancer treatment.....	123
Figure 3.18 Theranostic vitamin-linker-taxoid conjugates bearing FITC for in vitro imaging or ¹⁸ F for in vivo imaging.....	124
Figure 3.19 Theranostic vitamin-linker-taxoid conjugates bearing chelated radiotracer for potential <i>in vivo</i> PET/SPECT/MRI imaging.....	124
Figure 3.20 Chemical structure of PAMAM dendrimers with a cleavable cystamine core and amine surface.....	125
Figure 3.21 Designed PAMAM dendrimer-based biotin-linker-taxoid conjugates.....	126
Figure 3.22 Designed PAMAM dendrimer-based biotin-FITC conjugates.....	126
Figure 3.23 MALDI-TOF spectrum of biotin PEGylated G1 PAMAM dendrimer.....	130
Figure 3.24 ESI-MS spectrum of biotin PEGylated G1 PAMAM dendrimer before dialysis....	131
Figure 3.25 ESI-MS spectrum of biotin PEGylated G1 PAMAM dendrimer after dialysis....	131
Figure 3.26 MALDI-TOF spectrum of biotin PEGylated G3 PAMAM dendrimer.....	133
Figure 3.27 MALDI-TOF spectrum of biotin PEGylated G1 alkyne conjugate 3-19	137
Figure 3.28 ESI-MS spectrum of biotin PEGylated G1 alkyne conjugate 3-19	138
Figure 3.29 LC-MS spectrum of biotin PEGylated G1 alkyne conjugate 3-19	139
Figure 3.30 Expanded LC-MS spectrum of biotin PEGylated G1 alkyne conjugate 3-19	140
Figure 3.31 Extracted mass spectra from TIC in LC-MS analysis of biotin PEGylated G1 alkyne conjugate 3-19	141
Figure 3.32 Deconvolution of Extracted mass spectra from TIC in LC-MS analysis of biotin PEGylated G1 alkyne conjugate 3-19	142

Figure 3.33 Integration of peak area from TIC and UV-215 in LC-MS analysis of biotin PEGylated G1 alkyne conjugate 3-19	143
Figure 3.34 MALDI-TOF spectrum of biotin-G1-FITC conjugate 3-20	144
Figure 3.35 ESI-MS spectrum of biotin-G1-FITC conjugate 3-20	145
Figure 3.36 LC-MS spectrum of biotin-G1-FITC conjugate 3-20	146
Figure 3.37 Expanded LC-MS spectrum of biotin-G1-FITC conjugate 3-20	147
Figure 3.38 Extracted mass spectra from TIC in LC-MS analysis of biotin-G1-FITC conjugate 3-20	148
Figure 3.39 Deconvolution of extracted mass spectra from TIC in LC-MS analysis of biotin-G1-FITC conjugate 3-20	148
Figure 3.40 MALDI-TOF spectrum of biotin-G1-SB-T-1214 conjugate 3-21	150
Figure 3.41 ESI-MS spectrum of biotin-G1-SB-T-1214 conjugate 3-21	150
Figure 3.42 LC-MS spectrum of biotin-G1-SB-T-1214 conjugate 3-21	151
Figure 3.43 Expanded LC-MS spectrum of biotin-G1-SB-T-1214 conjugate 3-21	152
Figure 3.44 Extracted mass spectra from TIC in LC-MS analysis of biotin-G1-SB-T-1214 conjugate 3-21	153
Figure 3.45 Deconvolution of extracted mass spectra from TIC in LC-MS analysis of biotin-G1-SB-T-1214 conjugate 3-21	154
Figure 3.46 Integration of peak area from TIC and UV-215 in LC-MS analysis of biotin-G1-SB-T-1214 conjugate 3-21	155
Figure 3.47 MALDI-TOF spectrum of biotin PEGylated G3 alkyne conjugate 3-22	156
Figure 3.48 ESI-MS spectrum of biotin PEGylated G3 alkyne conjugate 3-22	156
Figure 3.49 MALDI-TOF spectrum of biotin-G3-FITC conjugate 3-23	157
Figure 3.50 ESI-MS spectrum of biotin-G3-FITC conjugate 3-23	157
Figure 3.51 HR-MS deconvolution spectrum of biotin-G3-FITC conjugate 3-23	158
Figure 3.52 MALDI-TOF spectrum of biotin-G3-SB-T-1214 conjugate 3-24	159
Figure 3.53 ESI-MS spectrum of biotin-G3-SB-T-1214 conjugate 3-24	159

Figure 3.54 Confocal fluorescence microscopy (CFM) images of ID8 cell line after incubation with 5 μ M Biotin-PEG-FITC at 37 $^{\circ}$ C for 1 h.....	162
Figure 3.55 Confocal fluorescence microscopy (CFM) images of HCT116 cell line after incubation with 10 μ M Biotin-PEG-FITC at 37 $^{\circ}$ C for 24 h.....	163
Figure 3.56 Confocal fluorescence microscopy (CFM) images of MCF7 cell line after incubation with 10 μ M Biotin-PEG-FITC at 37 $^{\circ}$ C for 24 h.....	163
Figure 3.57 Confocal fluorescence microscopy (CFM) images of ID8 cell line after incubation with 5 μ M Biotin-G1-FITC conjugate at 37 $^{\circ}$ C for 1 h.....	164
Figure 3.58 Confocal fluorescence microscopy (CFM) images of HCT116 cell line after incubation with 10 μ M Biotin-G1-FITC conjugate at 37 $^{\circ}$ C for 24 h.....	164
Figure 3.59 Confocal fluorescence microscopy (CFM) images of MCF7 cell line after incubation with 10 μ M Biotin-G1-FITC conjugate at 37 $^{\circ}$ C for 24 h.....	165
Figure 3.60 Confocal fluorescence microscopy (CFM) images of ID8 cell line after incubation with 5 μ M Biotin-G3-FITC conjugate at 37 $^{\circ}$ C for 1 h.....	165
Figure 3.61 Confocal fluorescence microscopy (CFM) images of HCT116 cell line after incubation with 10 μ M Biotin-G3-FITC conjugate at 37 $^{\circ}$ C for 24 h.....	166
Figure 3.62 Confocal fluorescence microscopy (CFM) images of MCF7 cell line after incubation with 10 μ M Biotin-G3-FITC conjugate at 37 $^{\circ}$ C for 24 h.....	166
Figure 3.63 Flow cytometry analysis of ID8 cell line after incubation with 5 μ M Biotin-PEG-FITC, Biotin-G1-FITC or Biotin-G3-FITC conjugates at 37 $^{\circ}$ C for 1 h.....	167
Figure 3.64 Flow cytometry analysis of HCT116 and MCF7 cell lines after incubation with 10 μ M Biotin-PEG-FITC at 37 $^{\circ}$ C at different time intervals.....	168
Figure 3.65 Flow cytometry analysis of HCT116 and MCF7 cell lines after incubation with 10 μ M Biotin-G1-FITC conjugate at 37 $^{\circ}$ C at different time intervals.....	168
Figure 3.66 Flow cytometry analysis of HCT116 and MCF7 cell lines after incubation with 10 μ M Biotin-G3-FITC conjugate at 37 $^{\circ}$ C at different time intervals.....	169
Figure 3.67 Flow cytometry analysis of HCT 116 cell line after incubation with 10 μ M Biotin-PEG-FITC, Biotin-G1-FITC or Biotin-G3-FITC conjugates at 37 $^{\circ}$ C at different time intervals.....	169
Figure 3.68 Flow cytometry analysis of MCF7 cell line after incubation with 10 μ M Biotin-PEG-FITC, Biotin-G1-FITC or Biotin-G3-FITC conjugates at 37 $^{\circ}$ C at different time intervals.....	170

Figure 3.69 Schematic representation of asymmetric bow-tie dendrimer-based (ABTD) tumor-targeted drug delivery systems.	172
Figure 3.70 Synthetic strategy for constructing asymmetric bow-tie dendrimer-based (ABTD) tumor-targeted drug delivery systems.....	173
Figure 3.71 Chemical structures of designed asymmetric bow-tie dendrimer-based (ABTD) tumor-targeted drug delivery systems.....	174
Figure 3.72 Designed ABTD conjugates.....	175
Figure 3.73 MALDI-TOF spectrum of alkyne PEGylated G1 PAMAM dendrimer 3-28	177
Figure 3.74 ESI-MS spectrum of alkyne PEGylated G1 PAMAM dendrimer 3-28	177
Figure 3.75 Schematic representation of biotin-G3-G1-alkyne.....	178
Figure 3.76 ESI-MS MS spectrum of biotin-G3-G1-alkyne.....	180
Figure 3.77 Deconvolution MS spectrum of biotin-G3-G1-alkyne.....	180
Figure 3.78 HPLC spectra of biotin-G3-G1-alkyne.....	181
Figure 3.79 HPLC spectra of SB-T-1214-linker-PEG-azide.....	181
Figure 3.80 GPC analysis of ABTD1 and biotin-G3-G1-alkyne.....	183
Figure 3.81 GPC analysis of ABTD3 and biotin-G3-G1-alkyne.....	184
Figure 3.82 Designed tri-branched PAMAM dendrimer-based theranostic conjugate bearing tumor-targeting modules, cytotoxic warheads and MRI contrast agent.....	185
Figure 3.83 Designed tri-branched PAMAM dendrimer-based theranostic conjugates bearing tumor-targeting modules, cytotoxic warheads and fluorescent probe for <i>in vitro</i> internalization study, or DOTA radionuclide chelator for <i>in vivo</i> PET/SPECT imaging.....	186
Figure 3.84 Designed tri-branched PAMAM dendrimer-based theranostic conjugates bearing single taxoid warhead.....	187
Figure 3.85 MALDI-TOF spectrum of compound 3-39	191
Figure 3.86 MALDI-TOF spectrum of compound 3-40	192
Figure 3.87 MALDI-TOF spectrum of conjugate 3-41	194
Figure 3.88 Designed tri-branched PAMAM dendrimer platform bearing four taxoids.....	194
Figure 3.89 Designed tri-branched PAMAM dendrimer platform bearing single taxoid.....	194

Figure 3.90 ESI-MS spectrum of Boc protected G1 PAMAM dendrimer 3-48	197
Figure 3.91 MALDI-TOF spectrum of conjugate 3-49	198
Figure 3.92 ESI-MS spectrum of conjugate 3-49 after dialysis.....	199
Figure 3.93 ESI-MS spectrum of conjugate 3-58 after dialysis.....	202
Figure 3.94 MALDI-TOF spectrum of conjugate 3-60	205
Figure 3.95 ESI-MS spectrum of conjugate 3-60	205

Chapter 4

Figure 4.1 Mechanism of FtsZ inhibition.....	237
Figure 4.2 First reported crystal structure of FtsZ protein from <i>M. jannaschii</i>	238
Figure 4.3 <i>Mtb</i> FtsZ lateral dimer crystal structure in complex with GTP-gamma-S	239
Figure 4.4 <i>Mtb</i> FtsZ curved trimer head-to-tail crystal structure in complex with GDP.....	240
Figure 4.5 Hinge-opening mechanism for the straight-to-curved conformational change at the longitudinal interface induced by GTP hydrolysis.....	240
Figure 4.6 Schematic representation of membrane deformation due the force produced by hydrolysis-induced FtsZ bending.....	241
Figure 4.7 Early lead compounds from optimization of hit benzimidazoles.....	242
Figure 4.8 Dose-dependent inhibition of FtsZ polymerization by SB-P17G-C2.....	243
Figure 4.9 Chemical structures of selected benzimidazole inhibitors used in the initial docking study.....	244
Figure 4.10 Potential binding sites of selected benzimidazole inhibitors in the initial docking study against 1RLU by AutoDock.....	245
Figure 4.11 Potential binding sites of selected benzimidazole inhibitors in the initial docking study against 1W5A by AutoDock.....	246
Figure 4.12 Homology model of head-to-tail <i>Mtb</i> FtsZ dimer (purple) based on template <i>Mj</i> FtsZ structure 1W5A (cyan).....	247
Figure 4.13 Protein alignment of <i>Mtb</i> FtsZ and <i>Mj</i> FtsZ.....	248

Figure 4.14 Zoom-in GTPase site of aligned <i>MtbFtsZ</i> and <i>MjFtsZ</i> structures.....	248
Figure 4.15 <i>MtbFtsZ</i> head-to-tail dimer model in complex with GTP γ S generated by protein alignment.....	249
Figure 4.16 Chemical structures of SB-P17G-A38 (SBZ013251) and SB-P17G-A42 (SBZ013221).....	249
Figure 4.17 Docked pose of SB-P17G-A38 (SBZ013251) with <i>MtbFtsZ</i> head-to-tail dimer model with GTP γ S bound.....	250
Figure 4.18 2D interaction diagram of SB-P17G-A38 (SBZ013251) with <i>MtbFtsZ</i> head-to-tail dimer model with GTP γ S bound.....	251
Figure 4.19 Docked pose of SB-P17G-A42 (SBZ013221) with <i>MtbFtsZ</i> head-to-tail dimer model with GTP γ S bound.....	252
Figure 4.20 2D interaction diagram of SB-P17G-A42 (SBZ013221) with <i>MtbFtsZ</i> head-to-tail dimer model with GTP γ S bound.....	253
Figure 4.21 Docked pose of SB-P17G-A38 (SBZ013251) with <i>MtbFtsZ</i> head-to-tail dimer model with GDP bound.....	254
Figure 4.22 2D interaction diagram of SB-P17G-A38 (SBZ013251) with <i>MtbFtsZ</i> head-to-tail dimer model with GDP bound.....	255
Figure 4.23 Docked pose of SB-P17G-A38 (SBZ013251) with <i>MtbFtsZ</i> head-to-tail dimer model with citrate bound.....	256
Figure 4.24 2D interaction diagram of SB-P17G-A38 (SBZ013251) with <i>MtbFtsZ</i> head-to-tail dimer model with citrate bound.....	257
Figure 4.25 Docked pose of SB-P17G-A38 with <i>MtbFtsZ</i> curved head-to-tail crystal structure with GDP bound (GDP site).....	258
Figure 4.26 2D interaction diagram of SB-P17G-A38 with <i>MtbFtsZ</i> curved head-to-tail crystal structure with GDP bound (GDP site).....	259
Figure 4.27 Docked pose of SB-P17G-A38 with <i>MtbFtsZ</i> curved head-to-tail crystal structure with GDP bound (T7 loop site).....	260
Figure 4.28 2D interaction diagram of SB-P17G-A38 with <i>MtbFtsZ</i> curved head-to-tail crystal structure with GDP bound (T7 loop site).....	261
Figure 4.29 Proposed mechanism of action for benzimidazole inhibitors.....	262

Chapter 5

Figure 5.1 Crystal structure of oleic acid (OLA) bound to human B-FABP.....	268
Figure 5.2 Representative chemical structures of known inhibitors of FABPs in development.....	268
Figure 5.3 Crystal structure of BMS309403 bound to human A-FABP.....	269
Figure 5.4 Schematic representation of anadamide inactivation FABP drug target.....	270
Figure 5.5 Initial hit compounds from virtual screening using footprint similarity method.....	271
Figure 5.6 Fluorescence displacement assay for purchased 48 top scoring compounds.....	272
Figure 5.7 Crystal structure of FABP5 in complex with SB-FI-26.....	273
Figure 5.8 2D Interaction diagram of SB-FI-26 with FABP5.....	274
Figure 5.9 Two hydrogen bonds acceptor pharmacophores are used as a filter in the MOE docking protocol.....	275
Figure 5.10 Docked poses of SB-FI-26 (magenta) compared with co-crystal structure (green) using rigid-receptor method. Rmsd: 0.7266 Å.....	276
Figure 5.11 Docked poses of SB-FI-26 (magenta) compared with co-crystal structure (green) using induced-fit method. Rmsd: 1.1140 Å.....	276
Figure 5.12 Overlay of designed analog (magenta, compound 41) with SB-FI-26 (green).....	279
Figure 5.13 Overlay of designed analog (magenta, compound 44) with SB-FI-26 (green).....	280
Figure 5.14 Chemical structures, binding energies, and calculated cLogP values for new analogs of SB-FI-26.....	280
Figure 5.15 Overlay of designed analog (magenta) with SB-FI-26 (green).....	281

List of Schemes

Chapter 1

Scheme 1.1 Benzyl protection of glycolic acid.....	20
Scheme 1.2 TIPS protection of benzyl glycolate 1-1	21
Scheme 1.3 Benzyl deprotection by hydrogenolysis.....	21
Scheme 1.4 Synthesis of activated ester 1-4 via EDC coupling.....	21
Scheme 1.5 Synthesis of diol 1-5 via Sharpless asymmetric dihydroxylation.....	21
Scheme 1.6 Synthesis of Whitesell's chiral auxiliary 1-6 by selectively reduction of diol 1-5	22
Scheme 1.7 Synthesis of key intermediate chiral ester 1-7	22
Scheme 1.8 Synthesis of imine 1-8 by condensation reaction.....	23
Scheme 1.9 Synthesis of enantiopure β -lactam 1-9 by chiral ester enolate-imine cyclocondensation.....	23
Scheme 1.10 Cerium ammonium nitrate (CAN) deprotection of <i>p</i> -methoxyphenyl (PMP) group.....	24
Scheme 1.11 <i>t</i> -Boc protection of β -lactam 1-10	24
Scheme 1.12 Enzymatic resolution of racemic β -lactam intermediate.....	25
Scheme 1.13 Hydrolysis of enantiopure β -lactam (+) 1-12	25
Scheme 1.14 TIPS protection of enantiopure β -lactam (+) 1-13	25
Scheme 1.15 TES protection of C-7 position in 10-DAB III.....	26
Scheme 1.16 Acylation of C-10 position in 1-14 with cyclopropanecarbonyl chloride.....	26
Scheme 1.17 Ojima-Holton coupling to generate 1-16	27
Scheme 1.18 HF/pyridine deprotection to generate new-generation taxoid SB-T-1214	27
Scheme 1.19 Acylation of C-10 position in 1-14 with <i>N,N</i> -dimethylcarbamoyl chloride.....	28
Scheme 1.20 Ojima-Holton coupling to generate 1-19	28

Scheme 1.21 HF/pyridine deprotection to generate new-generation taxoid SB-T-1216	29
Scheme 1.22 DiTroc protection of 10-DAB III.....	30
Scheme 1.23 Ojima-Holton coupling to generate 1-22	30
Scheme 1.24 Deprotection of Troc groups by Zinc dust.....	31
Scheme 1.25 HF/pyridine deprotection to generate SB-T-1211 in the first synthetic route.....	31
Scheme 1.26 Ojima-Holton coupling to generate 1-25	31
Scheme 1.27 Selective removal C-10 acetyl group by hydrazine monohydrate.....	32
Scheme 1.28 HF/pyridine deprotection to generate SB-T-1211 in the second synthetic route...	32
Scheme 1.29 TIPS protection to generate β -lactam 1-27	33
Scheme 1.30 CAN deprotection to generate β -lactam 1-28	33
Scheme 1.31 Boc protection to generate β -lactam 1-29	33
Scheme 1.32 Ojima-Holton coupling to generate 1-30	34
Scheme 1.33 HF/pyridine deprotection to generate 10-Ac-docetaxel	34
Scheme 1.34 Benzoyl protection to generate β -lactam 1-32	35
Scheme 1.35 Ojima-Holton coupling to generate 1-33	36
Scheme 1.36 HF/pyridine deprotection to generate SB-T-0035	37

Chapter 2

Scheme 2.1 Oxidation of 2-mercaptopyridine.....	84
Scheme 2.2 Synthesis of intermediate 2-2	84
Scheme 2.3 First disulfide exchange and TIPS protection.....	85
Scheme 2.4 Synthesis of thiolactone 2-5	85
Scheme 2.5 Hydrolysis of thiolactone 2-5	85
Scheme 2.6 Synthesis of methyl-branched disulfide linker 2-7 via a second thiol-disulfide exchange.....	85

Chapter 3

Scheme 3.1 Mono protection of triethylene glycol.....	127
Scheme 3.2 Conversion of hydroxyl group in 3-1 to azide group.....	127
Scheme 3.3 Staudinger reduction of azide to amine.....	127
Scheme 3.4 Synthesis of biotin-OSu activated ester 3-4	128
Scheme 3.5 Synthesis of biotin-PEG- <i>tert</i> -butyl ester 3-5	128
Scheme 3.6 TFA deprotection of biotin-PEG- <i>tert</i> -butyl ester 3-5	128
Scheme 3.7 Synthesis of biotin-PEG-Osu activated ester 3-7	129
Scheme 3.8 Synthesis of biotin PEGylated G1 PAMAM dendrimer 3-8	130
Scheme 3.9 Synthesis of biotin PEGylated G3 PAMAM dendrimer 3-9	132
Scheme 3.10 Synthesis of SB-T-1214-linker conjugate 3-10	133
Scheme 3.11 Removal of the TIPS protecting group in 3-10	134
Scheme 3.12 Synthesis of diazide 3-12	134
Scheme 3.13 Mono-reduction of diazide 3-12	134
Scheme 3.14 Synthesis of SB-T-1214-linker-PEG-azide click ready probe 3-14	135
Scheme 3.15 Synthesis of FITC-PEG-azide click ready probe 3-15	135
Scheme 3.16 Synthesis of 6-maleimidocaproic acid 3-16	135
Scheme 3.16 Synthesis of mixed anhydride 3-17	136
Scheme 3.18 Synthesis of maleimido-alkyne spacer 3-18	136
Scheme 3.19 Synthesis of biotin PEGylated G1 alkyne conjugate 3-19	137
Scheme 3.20 Synthesis of biotin-G1-FITC conjugate via CuAAC.....	144
Scheme 3.21 Synthesis of biotin-G1-SB-T-1214 conjugate 3-21 via CuAAC.....	149
Scheme 3.22 Synthesis of biotin PEGylated G3 alkyne conjugate 3-22	155
Scheme 3.23 Synthesis of biotin-G3-FITC conjugate 3-23 via CuAAC.....	157

Scheme 3.24 Synthesis of biotin-G3-SB-T-1214 conjugate 3-24 via CuAAC	160
Scheme 3.25 Synthesis of amide 3-25	175
Scheme 3.26 TFA deprotection of 3-25	176
Scheme 3.27 Synthesis of activated ester 3-27	176
Scheme 3.28 Synthesis of alkyne PEGylated G1 PAMAM dendrimer 3-28	176
Scheme 3.29 Synthesis of bismaleimide crosslinker 3-29	178
Scheme 3.30 Construct of biotin-G3-G1-alkyne.....	179
Scheme 3.31 Synthesis of ABTD1 via CuAAC.....	182
Scheme 3.32 Synthesis of ABTD3 via CuAAC.....	184
Scheme 3.33 Synthesis of diazide 3-33	188
Scheme 3.34 Synthesis of mono-Boc-1,4-diaminobutane 3-34	188
Scheme 3.35 Synthesis of tri-branched intermediate 3-35	188
Scheme 3.36 Synthesis of tri-branched spacer 3-36	189
Scheme 3.37 TFA deprotection of 3-36	189
Scheme 3.38 Attachment of DOTA chelator onto tri-branched spacer 3-37	190
Scheme 3.39 TFA deprotection of 3-38	190
Scheme 3.40 Chelation of tri-branched spacer 3-39 with Gd (III).....	192
Scheme 3.41 Conjugation of alkyne PEGylated half G1 dendron onto tri-branched spacer.....	193
Scheme 3.42 Synthesis of mono-azide 3-42	195
Scheme 3.43 Synthesis of mono-Boc-PEG-diamine 3-43	195
Scheme 3.44 Synthesis of triazine intermediate 3-44	195
Scheme 3.45 TFA deprotection of 3-44	196
Scheme 3.46 Synthesis of activated ester 3-46	196
Scheme 3.47 Synthesis of tri-branched spacer 3-47	196
Scheme 3.48 Synthesis Boc protected G1 PAMAM dendrimer 3-48	197

Scheme 3.49 Synthesis of conjugate 3-49	198
Scheme 3.50 Synthesis of 3-50	199
Scheme 3.51 Synthesis of 3-51	200
Scheme 3.52 Synthesis of Ns protected Boc-PEG-diamine.....	200
Scheme 5.53 TFA deprotection of 3-52	200
Scheme 3.54 Synthesis of tri-branched intermediate 3-54	200
Scheme 3.55 Removal of Ns group by thiolphenol.....	201
Scheme 3.56 Synthesis of intermediate 3-56	201
Scheme 3.57 TFA deprotection of 3-56	201
Scheme 3.58 Synthesis of conjugate 3-58	202
Scheme 3.59 Attempts towards conjugate 3-59	203
Scheme 3.60 Attempts towards conjugate 3-60	204

List of Tables

Chapter 1

Table 1.1 Structure and cytotoxicity (IC_{50} , nM) of selected new-generation taxoids against various cancer cell lines.....	19
---	----

Chapter 3

Table 3.1 Selected examples of nanocarrier-based drugs on the market.....	108
Table 3.2 The relative expression levels of vitamin receptors in cancer cells.....	119
Table 3.3 Cytotoxicity (IC_{50} , nM) of SB-T-1214, BLT-s, Biotin-G1-SB-T-1214, and Biotin-G3-SB-T-1214 against MCF7 and ID8 cell lines.....	171

Chapter 5

Table 5.1 Family members of fatty acid-binding proteins (FABPs).....	266
Table 5.2 Binding affinities for known inhibitors of FABPs in development.....	269
Table 5.3 Comparison of pharmacophore-based docking energy scores by MOE with experimental K_i values.....	277
Table 5.4 Docking results of new SB-FI-26 analogs.....	278

List of Abbreviations

10-DAB III	10-deacetyl-baccatin III
ABC	ATP-binding cassette
ABTD	asymmetric bow-tie dendrimer-based
Ac	acetyl
AD	asymmetric dihydroxylation
AEA	arachidonoyl ethanolamide, anandamide
ATP	adenosine triphosphate
BLT	biotin-linker-taxoid
BMS	Bristol-Myers Squibb
BR	biotin receptor
C	carbon
CAN	ceric ammonium nitrate
CB	cannabinoid
CFM	confocal fluorescence microscopy
CML	chronic myelogenous leukemia
CNS	central nervous system
CuAAC	copper (I)-catalyzed alkyne-azide cycloaddition
DCM	dichloromethane
DHB	2, 5-dihydroxybenzoic acid
DIC	<i>N,N'</i> -diisopropylcarbodiimide
DIPEA	<i>N,N</i> -diisopropylethylamine
DMAP	4-dimethylaminopyridine

DMF	dimethylformamide
DMSO	dimethyl sulfoxide
DOTA	1,4,7,10-tetraazacyclododecane-1,4,7,10-tetraacetic acid
DPBS	Dulbecco's phosphate-buffered saline
DPC	di-2-pyridyl carbonate
EDC	1-ethyl-3-(3-dimethylaminopropyl)carbodiimide
EE	ethoxyethyl
ee	enantiomeric excess
EGFR	epidermal growth factor receptor
EPR	enhanced permeability and retention
ESI	electrospray ionization
F	fluorine
FA	folic acid
FAAH	fatty acid amide hydrolase
FABP	fatty acid-binding protein
FAR	folate receptor
FBP	folate-binding protein
FBS	fetal bovine serum
FDA	Food and Drug Administration
FITC	fluorescein isothiocyanate
FPS	footprint similarity
FtsZ	filamentous temperature-sensitive protein Z
GDP	guanosine diphosphate
GPC	gel permeation chromatography
GSH	glutathione

GTP	guanosine triphosphate
H	hydrogen
HF	hydrogen fluoride
HPLC	high performance liquid chromatography
HPMA	<i>N</i> -(2-hydroxypropyl)methacrylamide
IR	infrared spectroscopy
LC	liquid chromatography
<i>m</i> -	<i>meta</i> -
mAb	monoclonal antibody
MALDI	matrix-assisted laser desorption/ionization
MDR	multidrug resistance
MDS	methylsulfonyl
<i>Mj</i>	<i>Methanocaldococcus jannaschii</i>
MOA	mechanism of action
MOE	molecular operating environment
MRI	magnetic resonance imaging
MRP1	multidrug resistance associated-protein 1
MS	mass spectrometry
<i>Mtb</i>	<i>Mycobacterium tuberculosis</i>
MTT	3-(4,5-dimethylthiazol-2-yl)-2,5-diphenyltetrazolium bromide
MTX	methotrexate
Mw	molecular weight
N	nitrogen
NBD	nucleotide-binding domain
NCI	National Cancer Institute

NHS	<i>N</i> -hydroxysuccinimide
NIR	near-infrared
NMR	nuclear magnetic resonance
NSCLC	non-small cell lung cancer
O	oxygen
OLA	oleic acid
<i>p</i> -	<i>para</i> -
PAMAM	poly(amidoamine)
PDB	Protein Data Bank
PEG	polyethylene glycol
PET	positron emission tomography
Pgp	P-glycoprotein
PMA	phosphomolybdic acid
PMP	<i>p</i> -methoxyphenyl
PUFA	polyunsaturated fatty acid
Rmsd	root-mean-square deviation
RPMI	Roswell Park Memorial Institute
Rt	retention time
S	sulfur
SAR	structure-activity relationship
SET	single electron transfer
SPECT	single photon emission computed tomography
SPR	surface plasmon resonance
SWNT	single-walled carbon nanotube
<i>t</i> -Boc	<i>tert</i> -butoxycarbonyl

TB	tuberculosis
TCEP	tri(2-carboxyethyl)phosphine
TEA	triethylamine
TES	triethylsilyl
TESCl	chlorotriethylsilane
TFA	trifluoroacetic acid
TIC	total ion current
TIPS	triisopropylsilyl
TLC	thin layer chromatography
TOF	time of flight
Troc	2,2,2-trichloroethoxycarbonyl
TrocCl	2,2,2-trichloroethyl chloroformate
TTDDS	Tumor-Targeted Drug Delivery Systems
TTM	tumor-targeting module
UV	ultraviolet
VEGF	vascular endothelial growth factor
WHO	World Health Organization
β -LSM	β -lactam synthon method

Acknowledgments

First, I would like to express my heartfelt thanks to my dissertation advisor, Distinguished Professor Iwao Ojima. Thank you for welcoming me into your research group when I first visited Stony Brook University as an undergraduate student six years ago, and willing to guide me again after I joined the Chemistry Ph.D. Program a year later. You provided me the opportunity and encouragement to do multidisciplinary research in the field of drug discovery and development, including synthetic medicinal chemistry, drug delivery, computational modeling, and cell biology. Your training and guidance truly helped me to grow up in the world of scientific research, not only in terms of the core skills, but also the spirits to learn, to discover, and to solve challenge problems with great persistence. Thank you for keeping me passionate about doing research! And of course, I would like to thank you and Mrs. Yoko Ojima for the annual BBQ and Thanksgiving parties. I will miss the fun time!

I would also like to thank my dissertation committee members, Professor Jonathan Rudick and Professor Peter Tonge, for their inspiring discussions and advices. They have been very responsible and helpful during my Ph.D. study. I feel deeply fortunate to have them as my committee members. I would also like to extend my sincere gratitude to Dr. Ramesh Gupta for his willingness to be my outside committee member for my Ph.D. defense.

In addition, I would like to thank many chemistry faculty members for their education and help. I would like to thank Professor Robert Rizzo for training me in the field of computer-aided drug design and molecular modeling, which opened a new door for me and led me to experience another fantastic area of research. I would like to thank Professor Kathy Parker for her impressive organic synthesis and mechanism lectures, and also welcoming me to do rotation in her lab during my first graduate semester. I would like to thank Professor Dale Drucehammer for his physical organic chemistry lectures, and accepting me to do my second rotation during the winter of my first graduate year, as well as serving as third member for my first meeting. I would like to thank Professor Elizabeth Boon, Professor Nicole Sampson, Professor Peter Tonge, Professor Isaac Carrico, and Professor Erwin London for teaching me chemical biology courses in total three semesters. I learned different aspects of chemical biology, as well as writing research proposals in these courses, which I found to be very useful for my Ph.D. study.

Moreover, I would like to thank Dr. Mohammad Akhtar, Dr. Rong Chen, Dr. Zachary Katsamanis, and Professor Ming-Yu Ngai for their help when I served as teaching assistant in undergraduate and graduate level chemistry courses. I learned a lot from these teaching experiences!

I would like to further thank many members of the Chemistry Department and collaborators within Stony Brook University: Dr. Jim Marecek and Dr. Francis Picart for their help with NMR spectrometry, Dr. Béla Ruzsicska for his help with mass spectrometry, Dr. Galina Botchkina and Dr. Anne Savitt for their help in cell culture, Dr. Guo-Wei Tian for his help in confocal fluorescence microscopy, and Todd Rueb for his help in flow cytometry experiments.

It has been a memorable experience working with previous and current Ojima group members. I want specially thank Dr. Joshua Seitz, Dr. Edison Zuniga, and Dr. William Berger for being great mentors during my visit as an undergraduate. I would also like to thank Dr. Tao Wang in particular, for his help in the dendrimer-based drug delivery project. He paved the road in this project with his intelligence and tremendous time and efforts. In addition, I would like to thank all other Ojima group alumni and current group members. It was a great pleasure to work with all of you in this lab! I wish all of you best of the luck in your future! In addition, I want to thank Mrs. Patricia Marinaccio for always being supportive and helpful as a family member of the Ojima group, and Mrs. Roxanne Brockner for her help in chemical and lab supply ordering.

Most importantly, I would like to thank my family and friends for their continuous love, support, and encouragement in my life! Words cannot express all that you mean to me.

Vita

EDUCATION

Department of Chemistry, Stony Brook University, Stony Brook, NY

Ph.D. Candidate in Chemistry (Medicinal)

August 2011-present, expected August 2016

Advisor: Distinguished Professor **Iwao Ojima**

Chemical Biology Training Program

August 2011-June 2012

Visiting Student, International Academic Program

August 2010-December 2010

School of Chemistry and Chemical Engineering, Nanjing University, Nanjing, China

B.S. in Chemistry

September 2007-June 2011

AWARDS and HONORS

Chemistry Award for Excellence in Doctoral Research, 2016

Stony Brook University Department of Chemistry

The Chemical Computing Group Research Excellence Award in Medicinal Chemistry, 2016

American Chemical Society Division of Medicinal Chemistry and Chemical Computing Group

PEER-REVIEWED PUBLICATIONS

- Design, synthesis and application of fluorine-labeled taxoids as ^{19}F NMR probes for the metabolic stability assessment of tumor-targeted drug delivery systems. Seitz, J. D.; Vineberg, J. G.; **Wei, L.**; Khan, J. F.; Lichtenthal, B.; Lin, C.-F.; Ojima, I. *Journal of Fluorine Chemistry*, 2015, 171, 148-161.
- Strategic incorporation of fluorine in the drug discovery of new-generation antitubercular agents targeting bacterial cell division protein FtsZ. Ojima, I.; Awasthi, D.; **Wei, L.**; Haranahalli, K. *Journal of Fluorine Chemistry*, 2016, in press.
- Design, synthesis, and biological evaluations of novel asymmetric bow-tie PAMAM dendrimer-based conjugates for tumor-targeted drug delivery. Wang, T.; **Wei, L.**; Sun, Y.; Zhang, Y.; Teng, Y.-H. G.; Li, W.; Ruzsicska, B.; Ojima, I. To be submitted to *Journal of the American Chemical Society* shortly.
- Design, synthesis, and biological evaluations of novel PAMAM dendrimer-based tumor-targeting taxoid conjugates. **Wei, L.**; Wang, T.; Sun, Y.; Bahl, S.; Ojima, I. *Manuscript in preparation*.
- Computational structure-based design of fatty acid binding proteins (FABPs) inhibitors as anti-nociceptive and anti-inflammatory agents. **Wei, L.**; Tong, S.; Rebecchi, M. J.; Hsu, H.-C.; Kaczocha, M.; Li, H.; Rizzo, R. C.; Deutsch, D.; Ojima, I. *Manuscript in preparation*.

SELECTED PRESENTATIONS

- Computational structure-based design of fatty acid binding proteins (FABPs) inhibitors as anti-nociceptive and anti-inflammatory agents. **Wei, L.**; Tong, S.; Rebecchi, M. J.; Hsu, H.-C.; Kaczocha, M.; Li, H.; Rizzo, R. C.; Deutsch, D.; Ojima, I. Abstracts of Papers, 251th ACS National Meeting & Exposition, San Diego, CA, United States, **2016**, MEDI-181.

- Design, synthesis, and biological evaluations of novel PAMAM dendrimer-based tumor-targeting taxoid conjugates. **Wei, L.**; Wang, T.; Bahl, S.; Teng, Y.-H. G.; Ojima, I. Abstracts of Papers, 250th ACS National Meeting & Exposition, Boston, MA, United States, **2015**, MEDI-164.
- Design and synthesis of a novel tri-branched asymmetric bowtie PAMAM dendrimer-based drug conjugate as a cancer theranostic agent. **Wei, L.**; Wang, T.; Teng, Y.-H. G.; Ojima, I. Abstracts of Papers, 249th ACS National Meeting & Exposition, Denver, CO, United States, **2015**, MEDI-121.
- Computational and structural biology approaches to the identification of potential binding sites of novel benzimidazole inhibitors with Mtb-FtsZ for antitubercular drug discovery. **Wei, L.**; Lazo, E. O.; Awasthi, D.; Chowdhury, S. R.; Jakoncic, J.; Ojima, I. Abstracts of Papers, 247th ACS National Meeting & Exposition, Dallas, TX, United States, **2014**, MEDI-100.

MEMBERSHIPS

American Chemical Society

March 2014-present

New York Academy of Sciences

January 2016-present

Chapter 1

Design, Synthesis, and Biological Evaluation of New-Generation Taxoids

Chapter Contents

§ 1.1 Introduction.....	2
§ 1.1.1 Cancer and Cancer Statistics.....	2
§ 1.1.2 Paclitaxel and Taxanes.....	4
§ 1.1.3 Semi-synthesis of Taxanes via the β -Lactam Synthon Method.....	6
§ 1.1.4 Asymmetric Synthesis of β -Lactam.....	8
§ 1.1.5 Structure-Activity Relationship (SAR) Study on Taxanes.....	14
§ 1.1.6 Multidrug Resistance (MDR).....	17
§ 1.1.7 New-Generation Taxoids.....	18
§ 1.2 Synthesis and Biological Evaluation of New-Generation Taxoids.....	20
§ 1.2.1 Synthesis of Eantiopure β -Lactam.....	20
§ 1.2.2 Synthesis of New-Generation Taxoids SB-T-1214 and SB-T-1216.....	25
§ 1.2.3 Synthesis of New-Generation Taxoid SB-T-1211.....	29
§ 1.2.4 Synthesis of New-Generation Taxoid 10-Ac-docetaxel.....	32
§ 1.2.5 Synthesis of New-Generation Taxoid SB-T-0035.....	34
§ 1.2.6 Biological Evaluation of New-Generation Taxoids.....	37
§ 1.3 Summary.....	44
§ 1.4 Experimental.....	44
§ 1.5 References.....	66

§ 1.1 Introduction

§ 1.1.1 Cancer and Cancer Statistics

Cancer is a collection of diseases characterized by uncontrolled growth of abnormal cells, which are capable of invading surrounding tissues. As a genetic disease, cancer has the capabilities to sustain chronic proliferation by controlling of mitogenic signaling, circumvent tumor suppressor genes, resist apoptotic programmed cell death, divide with unlimited replicative potential, develop angiogenesis, and activate local invasion as well as distant metastasis (**Figure 1.1**).¹ In addition to these well-studied hallmarks of cancer, emerging attributes of cancer cells, such as reprogramming of cellular energy metabolism and evading elimination by immune cells, have been proposed to be important for the development of cancer as well.¹

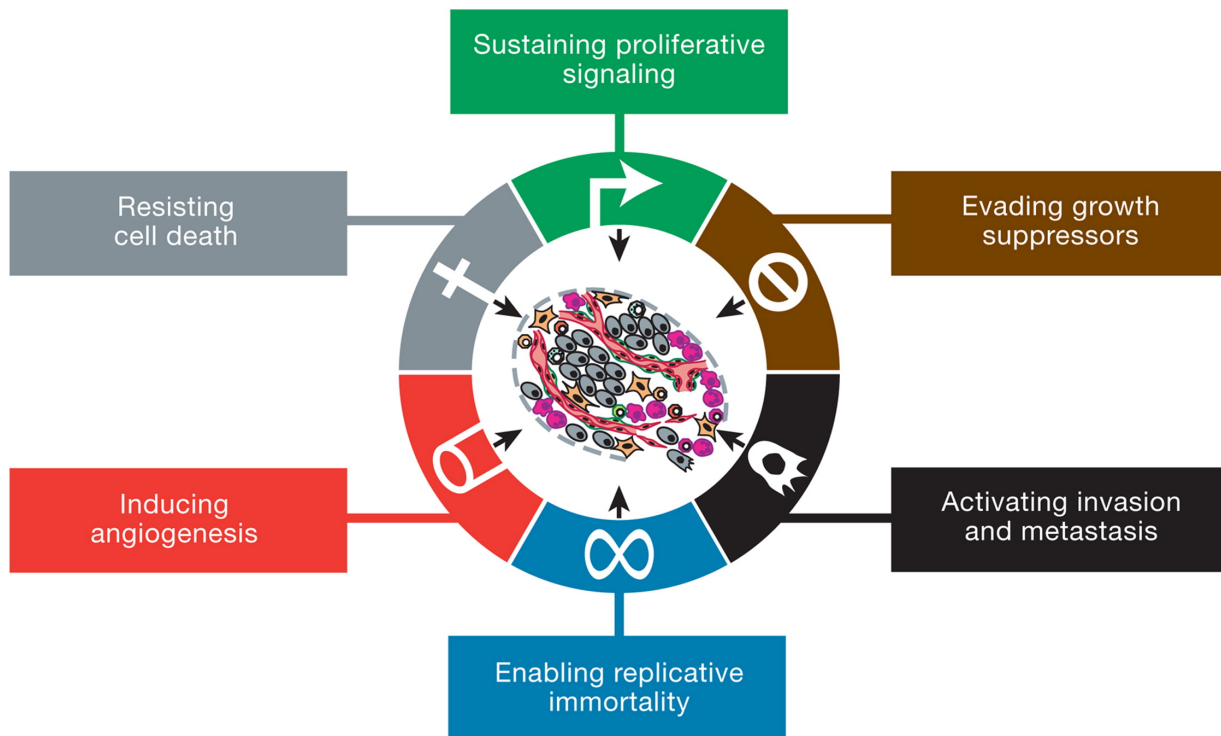


Figure 1.1 The hallmarks of cancer. Reprinted from *Cell*, 144, Hanahan, D.; Weinberg, R. A., Hallmarks of Cancer: The Next Generation, 646-674, Copyright (2011), with permission from Elsevier.

Cancer is the second leading cause of death in the United States, exceeded only by heart disease.² The lifetime risk of developing an invasive cancer is 42% for men and 38% for women.^{2,3} It is estimated in 2016, 1,685,210 new cancer cases and 595,690 cancer deaths are expected to occur in the United States.^{2,3} **Figure 1.2** shows the top 10 common cancer types for the estimated new cancer cases and deaths by sex in 2016. Prostate (21%), lung and bronchus (14%), and colorectal cancers (8%) account for 44% of the new cases in men; breast (29%), lung

and bronchus (13%), and colorectal cancers (8%) account for 50% of the new cases in women.² Lung and bronchus cancer is the leading cancer type for deaths in both men and women, accounting for 27% and 26% respectively.²

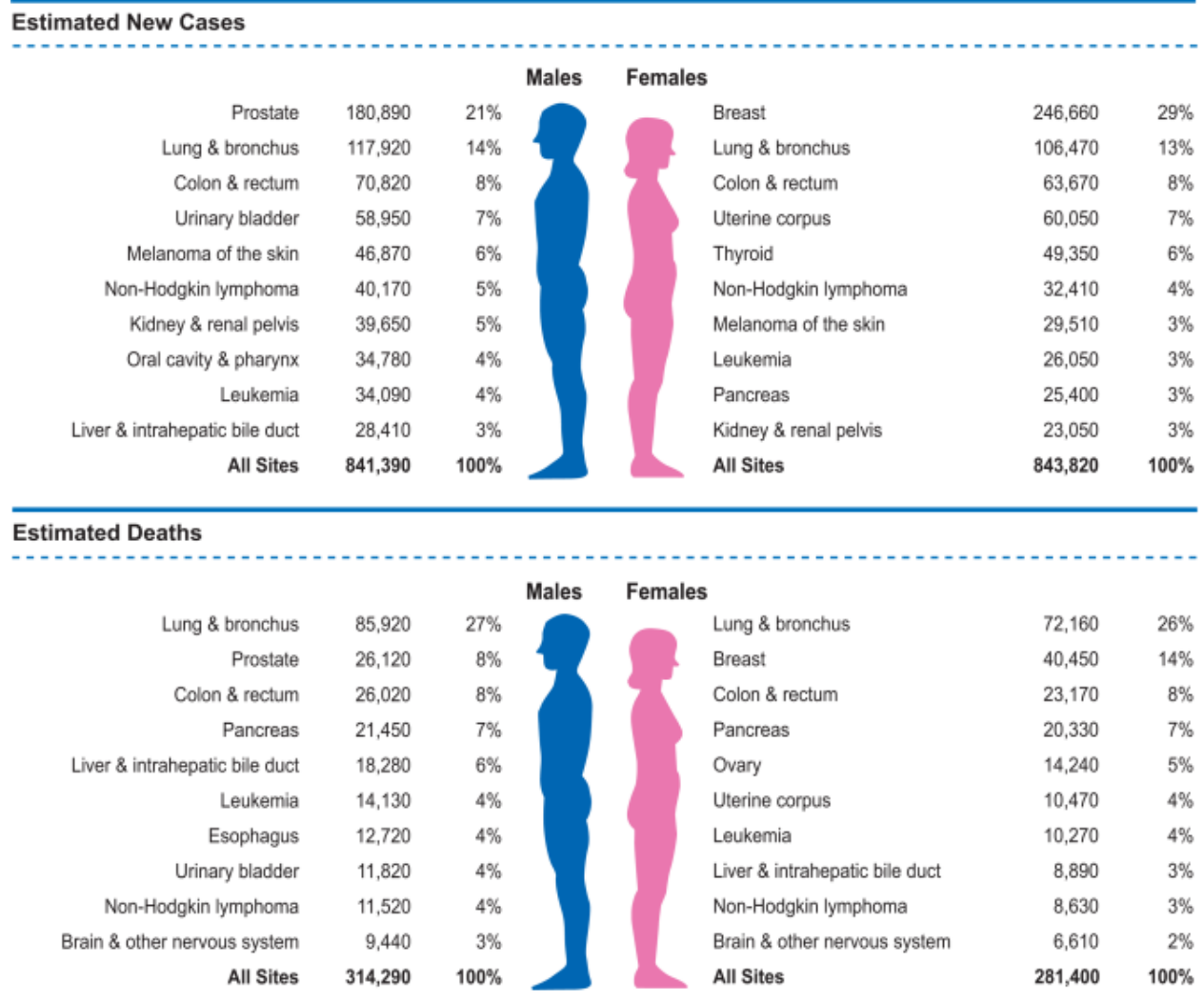


Figure 1.2 Ten leading cancer types for the estimated new cancer cases and deaths by sex, United States, 2016. Reproduced from Siegel, R. L.; Miller, K. D.; Jemal, A. Cancer Statistics, 2016. *Ca-Cancer J Clin* **2016**, *66*, 7-30, with permission from John Wiley & Sons.

Globally, according to the International Agency for Research on Cancer (IARC), it was estimated 14.1 million new cancer cases and 8.2 million deaths in 2012.⁴ Among different cancer types, lung cancer (1.82 million), breast cancer (1.67 million), and colorectal cancer (1.36 million) are most commonly diagnosed, and lung cancer (1.6 million) is also the leading cause of cancer deaths worldwide.⁴

§ 1.1.2 Paclitaxel and Taxanes

Cancer chemotherapy is one of the most common treatments for cancer. The goal of cancer chemotherapy is to stop the growth, invasion, and metastasis of cancer cells by using highly potent cytotoxic agents. Cancer chemotherapeutic agents could be classified into different categories based on different criteria. For example, chemotherapeutic drugs could be grouped as alkylating agents, antimetabolites, antibiotics, mitosis inhibitors, topoisomerases inhibitors and others based on the mechanism of action (MOA) in a classical classification manner.⁵

Paclitaxel is one of the most successful chemotherapeutic agents approved by the U.S. Food and Drug Administration (FDA). This diterpenoid natural product was first isolated from the bark of the pacific yew tree, *Taxus brevifolia*, by Dr. Monroe Wall and Dr. Mansukh Wani during a screening program initiated by National Cancer Institute (NCI) to find anticancer agents in plants in the 1960s.⁶ The chemical structure of paclitaxel was subsequently elucidated and reported in 1971.⁷ The chemical structure of paclitaxel consists of a tetracyclic baccatin III core, with an *N*-benzoylphenylisoserine side chain at the C-13 position (**Figure 1.3**). Paclitaxel was later developed by Bristol-Myers Squibb (BMS) under the trademark name Taxol®, and subsequently approved by FDA for the treatment of ovarian cancer (1992), breast cancer (1994), Kaposi's sarcoma (1997), and non-small cell lung cancer (NSCLC) (1998).⁸

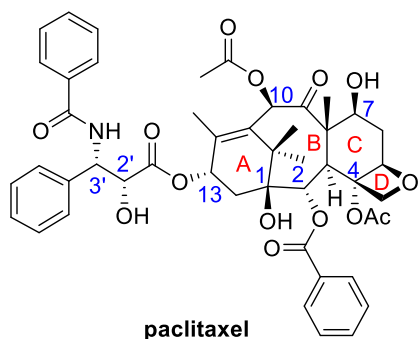


Figure 1.3 Chemical structure of paclitaxel (Taxol®)

The mechanism of action of paclitaxel was first discovered and reported by Dr. Susan Horwitz and her colleagues in 1979.^{9,10} Unlike other antimetabolic drugs such as vinblastine and vincristine, which inhibit microtubule assembly, paclitaxel is a microtubule-stabilizing agent.^{9,10} Microtubules, composed of α - and β -tubulin heterodimers, are highly dynamic filamentous protein polymers, and play an important role in mitosis and cell division. Paclitaxel binds to a pocket in the second globular domain of the β -tubulin subunit of the tubulin heterodimer, increasing the affinity for other surrounding tubulin molecules presumably by inducing a conformation change.¹¹ As a result, dynamics of the microtubule assembly is stabilized, and ability of chromosome to separate during mitosis is inhibited, eventually lead to apoptosis of cells.¹¹ The mechanism of action of paclitaxel is illustrated in **Figure 1.4**.¹²

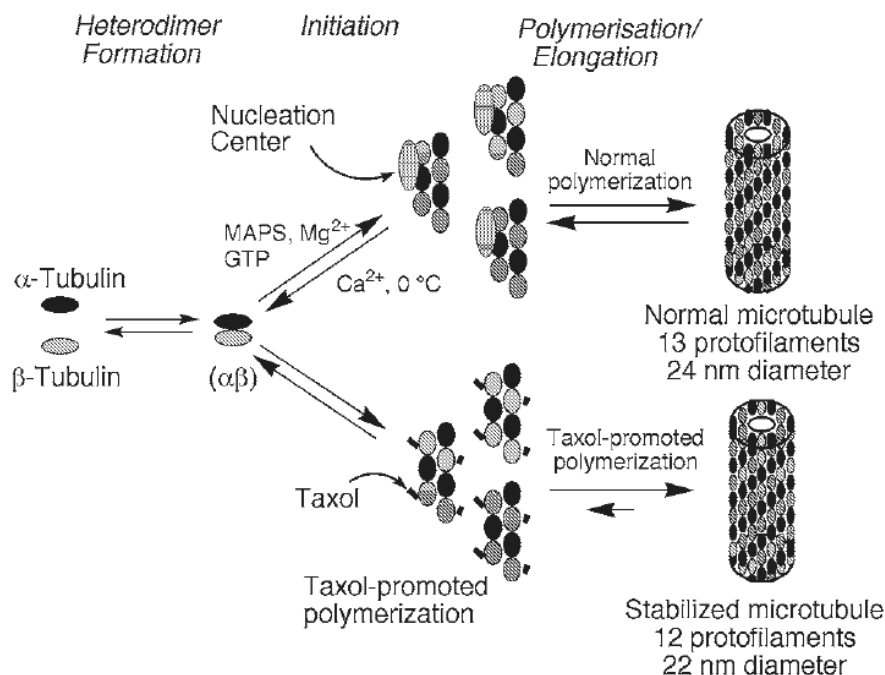


Figure 1.4 The mechanism of action of paclitaxel. Reproduced from Kingston, D. G. I. Taxol, a molecule for all seasons. *Chem Commun* **2001**, *10*, 867-880, with permission of The Royal Society of Chemistry.

In addition to paclitaxel, other taxanes were also developed to treat various types of cancer. Docetaxel (Taxotere®) is a semi-synthetic analogue of paclitaxel, and was approved by FDA for the treatment of non-small cell lung cancer (NSCLC) (1999), prostate cancer (2004), breast cancer (2004), head and neck cancer (2006), and gastric cancer (2006).¹³ Recently, cabazitaxel (Jevtana®), another taxane anticancer agent, was approved by FDA for the treatment of hormone-refractory metastatic prostate cancer (2010).¹⁴ The chemical structures of docetaxel and cabazitaxel are shown in **Figure 1.5**. A number of other taxane anticancer agents are currently under clinical investigations.

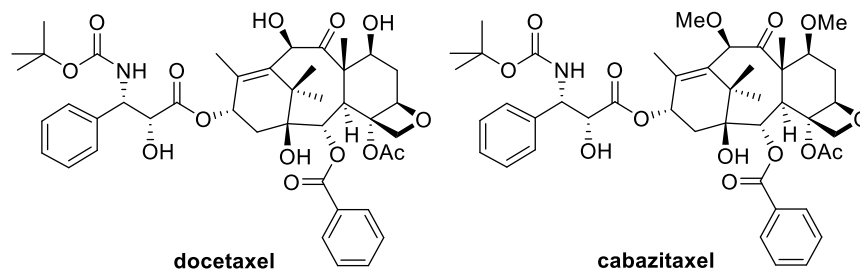


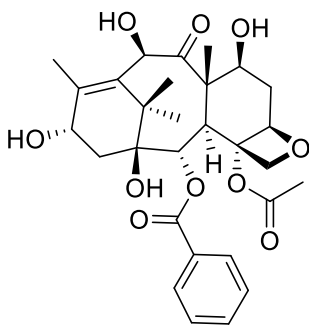
Figure 1.5 Chemical structures of docetaxel (left) and cabazitaxel (right)

§ 1.1.3 Semi-synthesis of Taxanes via the β -Lactam Synthone Method

After paclitaxel advanced into clinical studies in the 1980s, the supply of this natural product became a problem. The original supply from the extracts of the bark of pacific yew tree only produce paclitaxel in low yield, and this non-renewable process creates serious environmental concerns about the old-growth forests in the Pacific Northwest of the United States.^{12,15} In order to produce large-scale paclitaxel to meet the need of clinical studies, various methods were explored including bioproduction of paclitaxel by plant tissue culture, total synthesis of paclitaxel, as well as semi-synthesis of this natural product from renewable sources.^{12,15}

The total synthesis of paclitaxel is challenging because of this complex natural product contains 4 fused ring systems and 11 chiral centers. In spite of such difficulties, synthetic chemists have accomplished the total synthesis of paclitaxel over the years, first by Holton^{16,17} and Nicolaou¹⁸⁻²² simultaneously in 1994, and later by Danishefsky²³ (1996), Wender^{24,25} (1997), Kuwajima²⁶ (1998), Mukaiyama²⁷ (1999), Takahashi²⁸ (2006), as well as most recently by Sato-Chida^{29,30} and Nakada³¹ (2015) in two formal syntheses to a Takahashi intermediate. These synthetic efforts are intriguing and impressive in the field of organic synthesis. However, such methods could not meet the demands of large quantities of pure paclitaxel for clinical trials due to long steps and low yields.

On the other hand, semi-synthesis of paclitaxel via the β -lactam synthone method (β -LSM) first developed by Ojima³² and Holton³³ in 1992 from 10-deacetyl-baccatin III (10-DAB III) (**Figure 1.6**), a renewable source from the needles of European yew tree, is much more practical, and eventually became the commercial way for producing paclitaxel by Bristol-Myers Squibb (BMS).



10-deacetyl baccatin III (10-DAB III)

Figure 1.6 Chemical structure of 10-deacetyl-baccatin III (10-DAB III)

In 1981, Potier discovered that 10-deacetyl-baccatin III (10-DAB III) could be extracted from the needles of European yew tree (*Taxus bacata* L.) in high yield (~ 1 g/kg of fresh leaves at that time).³⁴ Although 10-DAB III is far less active than paclitaxel, this discovery eventually led to the semi-synthesis of paclitaxel commercialized. The isolation of this semi-synthesis

precursor was later developed by an Italian company called Indena S.p.A., to provide large quantities of 10-DAB III to BMS for conversion to paclitaxel.¹⁵

In 1988, Greene and Potier developed the first semi-synthesis route to paclitaxel from 7-*TES*-baccatin III by reacting the C-13 hydroxyl group with protected *N*-benzoylphenylisoserine side chain found in paclitaxel in the presence of di-2-pyridyl carbonate (DPC) and 4-dimethylaminopyridine (DMAP) (**Figure 1.7**).³⁵ This procedure, however, suffered from low conversion even if harsh conditions, long reaction time, as well as large excess of optically pure (2*R*,3*S*)-*N*-benzoyl-1-*O*-EE-3-phenylisoserine (EE = ethoxyethyl) were used.^{35,36} In addition, considerable epimerization at the C-2' hydroxyl group from the phenylisoserine moiety during coupling was observed.³⁶ Therefore, a more practical and efficient semi-synthesis method was needed to solve these problems.

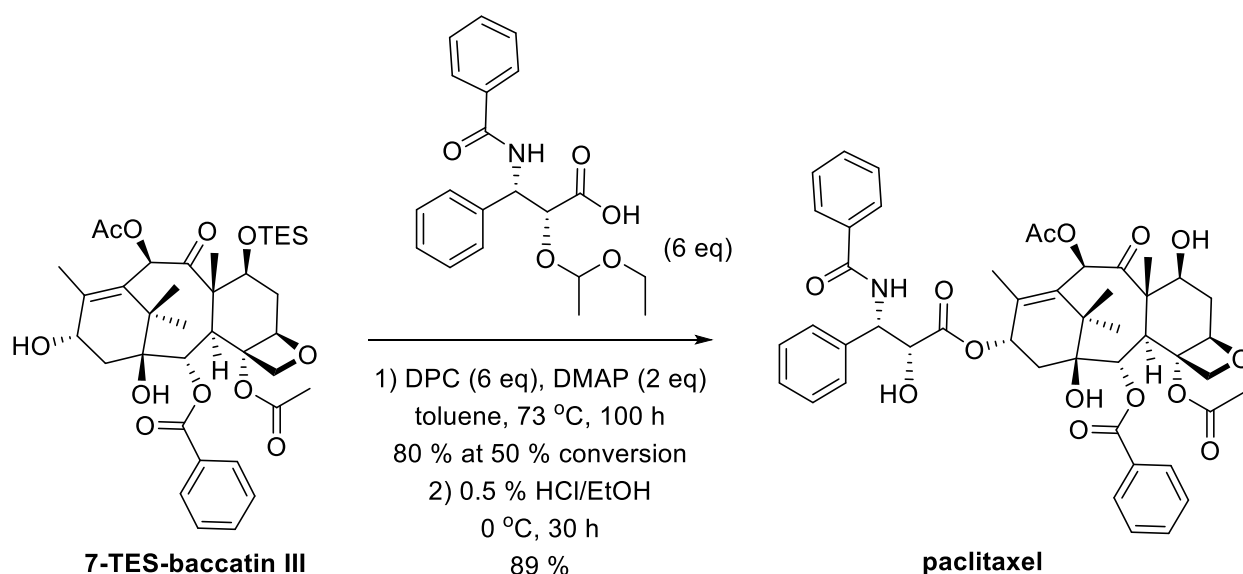


Figure 1.7 Greene-Potier's protocol for semi-synthesis of paclitaxel

Later, in a patent application, Holton used 7-*TES*-baccatin III to couple with five equivalents of enantiopure (3*R*,4*S*)-*N*-benzoyl-3-*O*-EE- β -lactam in the presence of DMAP and pyridine, followed by deprotection with aq. HCl to afford paclitaxel.³³ This protocol, however, is still inefficient because large excess of enantiopure β -lactam (5 eq) is required and long reaction time (> 12 h) is needed, and this β -lactam was obtained through tedious optical resolution at that time. Ojima developed a more efficient coupling condition by employing NaH or NaHMDS or LiHMDS as the base to generate 13-*O*-metalated derivatives of 7-*TES*-baccatin III to react with enantiopure β -lactam, and coupling product was obtained in excellent yield within 30 min with only slight excess of β -lactam (1.2 eq) (**Figure 1.8**).³² Moreover, enantiopure β -lactam was generated by a highly efficient chiral ester-enolate imine cyclocondensation reaction developed in the Ojima laboratory in 1990.^{37,38} Holton and his collaborators developed a similar process independently using 13-*O*-lithiated-7-*TES*-baccatin III to couple with enantiopure β -lactam for the synthesis of paclitaxel, and was adopted by BMS for commercial production.³⁶

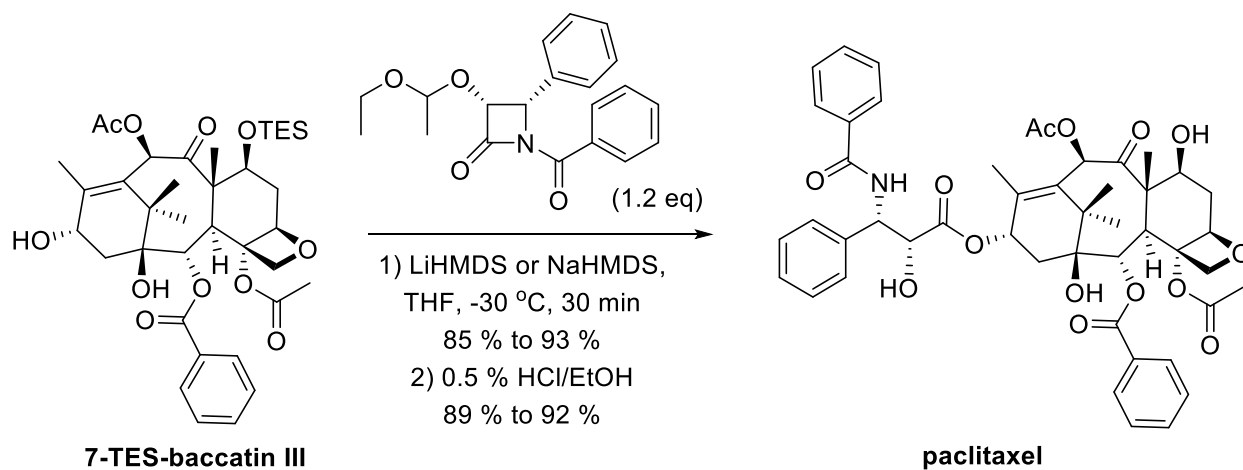


Figure 1.8 Ojima-Holton's protocol for semi-synthesis of paclitaxel

Semi-synthesis of docetaxel was achieved in a similar manner by reacting 7,10-diTroceacetyl baccatin III (Troc = 2,2,2-trichloroethoxycarbonyl) with (3*R*,4*S*)-*N*-tert-butoxycarbonyl-3-*O*-EE- β -lactam under NaHMDS as the base (**Figure 1.9**).^{39,40} It is worth to mention Holton's earlier protocol using DMAP and pyridine did not work in the semi-synthesis of docetaxel, due to the lack of reactivity of (3*R*,4*S*)-*N*-tert-butoxycarbonyl-3-*O*-EE- β -lactam, as the electron withdrawing ability of *tert*-butoxycarbonyl group is much weaker than benzoyl group.^{39,40}

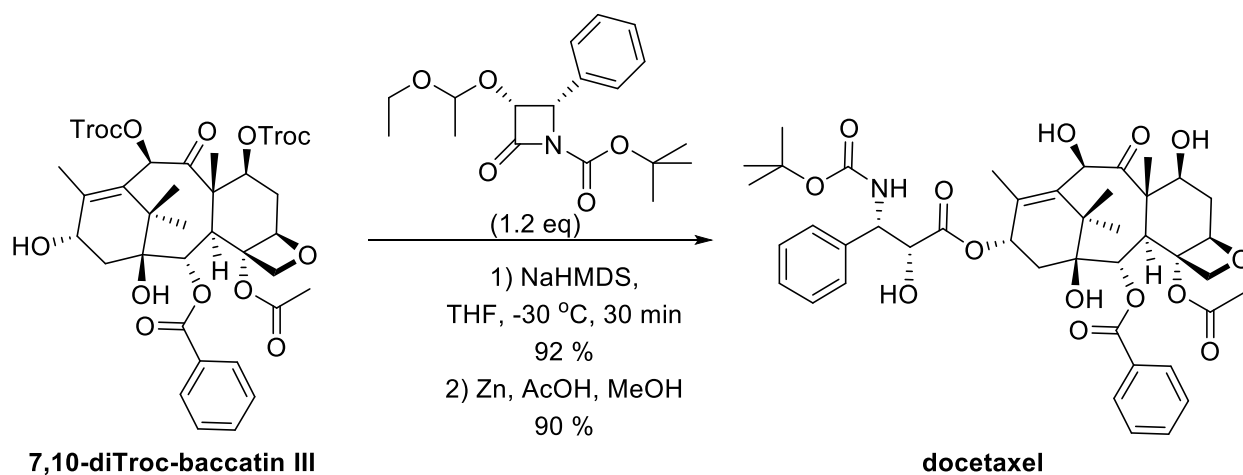


Figure 1.9 Ojima's protocol for semi-synthesis of docetaxel

The Ojima-Holton protocol for semi-synthesis of paclitaxel and docetaxel was later employed in the synthesis of numerous taxoids (taxol-like compounds), and made structure-activity relationship (SAR) study on taxoids feasible.³⁶

§ 1.1.4 Asymmetric Synthesis of β -Lactam

The β -lactam ring is the core structure of several famous antibiotics such as penicillins, cephalosporins, carbapenems, and monobactams. The first synthetic β -lactam was prepared by

Dr. Hermann Staudinger in 1907 by the reaction of an imine with a ketene through a [2+2] cycloaddition.^{41,42} However, the utility of β -lactams was not well recognized in medicinal chemistry until the antibiotic properties of the first semisynthetic penicillins were discovered in 1940s.⁴³

The synthesis of β -lactams has been extensively studied for a long time because of the existence of the naturally occurring β -lactam antibiotics, however, their potential as synthetic intermediates for synthesizing other types of compounds of biological interests has not been widely recognized until the development of the “ β -lactam synthon method” in the Ojima laboratory.⁴⁴ One important application of the “ β -lactam synthon method” is synthesis of paclitaxel, docetaxel and new taxoid antitumor agents through the Ojima-Holton coupling of baccatins with enantiopure β -lactams.⁴⁴

For asymmetric synthesis of β -lactams, two different methods were developed for the semi-synthesis of taxanes. The first route involves Staudinger’s ketene-imine [2+2] cycloaddition, followed by enzymatic resolution, and the second route utilizes chiral ester-enolate imine cyclocondensation reaction.

For Staudinger’s ketene-imine [2+2] cycloaddition, the most widely accepted mechanism is a stepwise mechanism rather than a concerted mechanism.^{45,46} The first step involves a nucleophilic attack of the nitrogen atom in the imine to the *sp*-hybridized carbon atom of the ketene to form a zwitterionic intermediate, and in the second step, a conrotatory electrocyclic ring closure occurs to give rise to the final β -lactam (**Figure 1.10**).^{45,46}

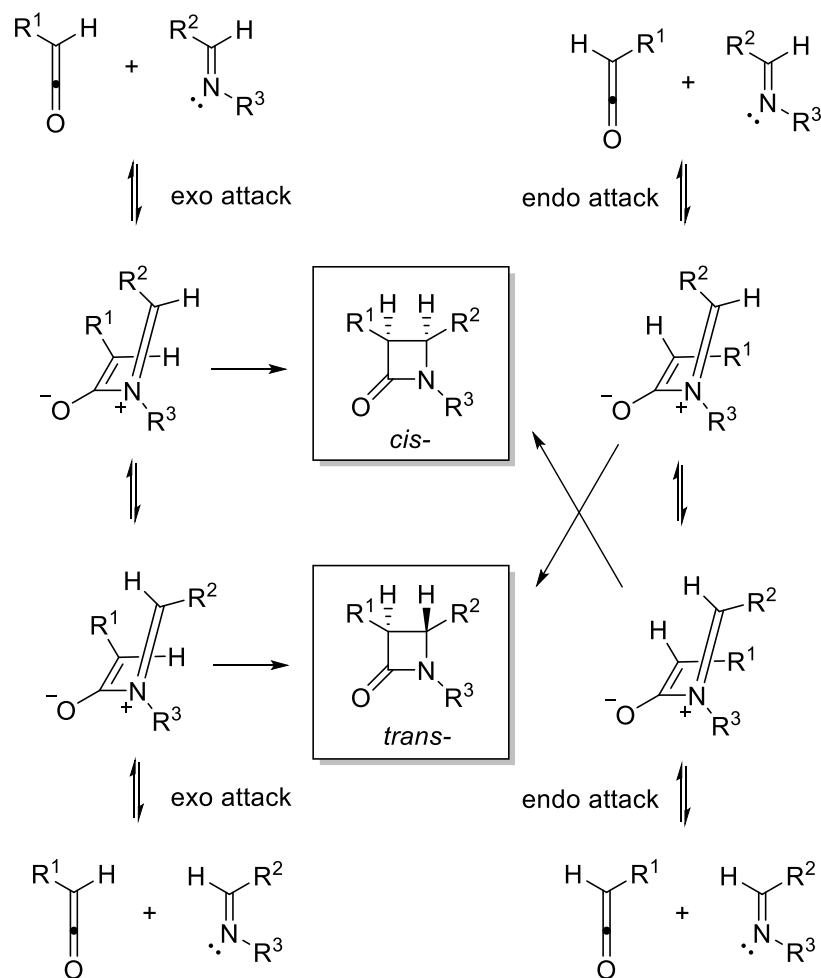


Figure 1.10 Pathways for the formation of *cis*- and *trans*-β-lactam. Adapted with permission from Jiao, L.; Liang, Y.; Xu, J. X. Origin of the relative stereoselectivity of the beta-lactam formation in the Staudinger reaction. *J Am Chem Soc* **2006**, *128*, 6060-6069. Copyright (2006) American Chemical Society.

The Staudinger [2+2] cycloaddition produces two stereocenters when a monosubstituted ketene and an acyclic imine are used in the reaction, so in principle the reaction could form *cis*-, *trans*-, or a mixture of *cis*- and *trans*- products. The relative stereoselectivity is determined by substituent effects, electronic effects, as well as reaction conditions.^{45,46} A suggested model is shown in **Figure 1.11**. When the isomerization of the zwitterionic intermediate is not possible, direct ring closure takes place, and the products are dominated by the substituent effects.⁴⁵ In this case, *E*-ketenes lead to *cis*-β-lactams, and *Z*-ketenes lead to *trans*-β-lactams. However, when isomerization of the zwitterionic intermediate happens, the electronic effects play a key role, and will influence the stereochemical outcome of this reaction.⁴⁵

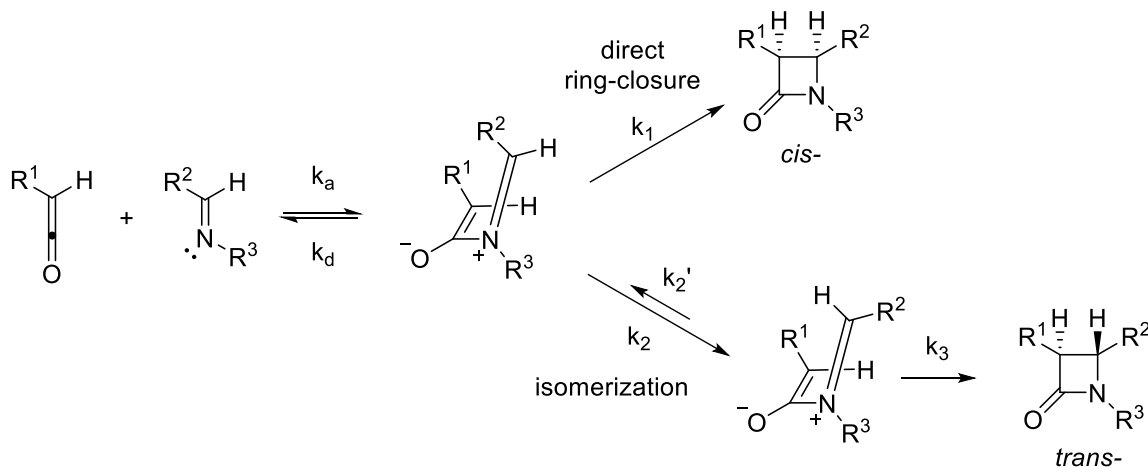


Figure 1.11 Suggested model for the relative stereoselectivity in Staudinger reaction. Adapted with permission from Jiao, L.; Liang, Y.; Xu, J. X. Origin of the relative stereoselectivity of the beta-lactam formation in the Staudinger reaction. *J Am Chem Soc* **2006**, *128*, 6060-6069. Copyright (2006) American Chemical Society.

In the semi-synthesis of taxanes, *cis*- β -lactams are needed from the Staudinger reaction. The (+)- and (-)-enantiomers could be separated by enzymatic kinetic resolution of the racemic *cis*- β -lactams.⁴⁷

The major drawback for the enzymatic kinetic resolution is the long reaction time, and theoretical yield for this step is only 50%. Therefore, an efficient lithium chiral ester enolate-imine cyclocondensation reaction was developed in the Ojima laboratory to generate highly enantiomerically pure β -lactams.^{32,37,38} As **Figure 1.12** shows, chiral enolate, which was generated by reacting a chiral ester with Lithium diisopropylamide (LDA), could attack the imine to form a six-membered ring transition state, and then form the uncyclized lithiated β -amino chiral ester.^{32,37,38} Subsequent ring closure give rise to the desired β -lactams in high enantiomeric excess (ee), and regenerate the chiral auxiliary.^{32,37,38}

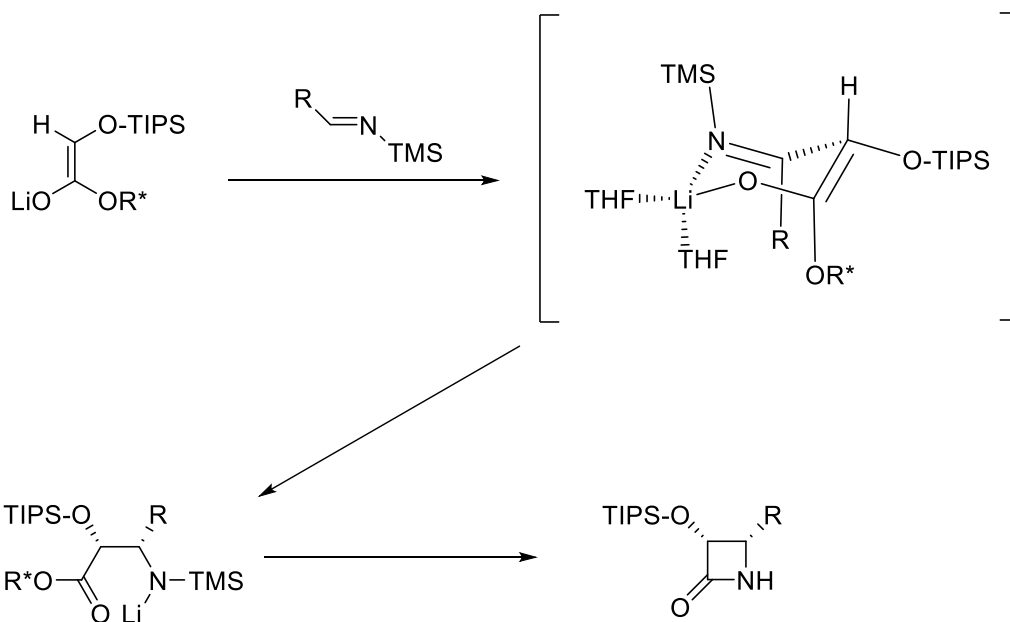
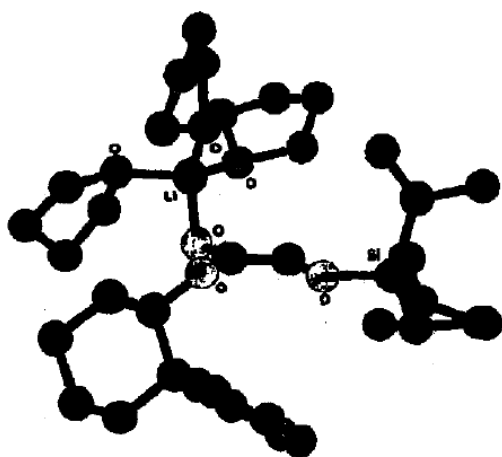
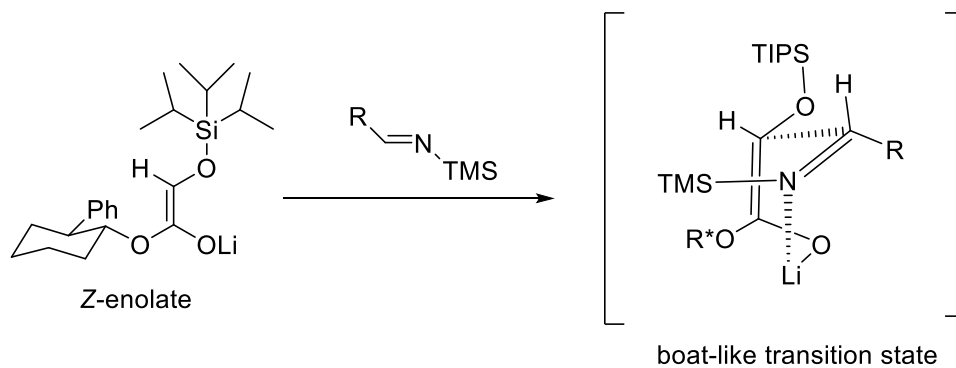
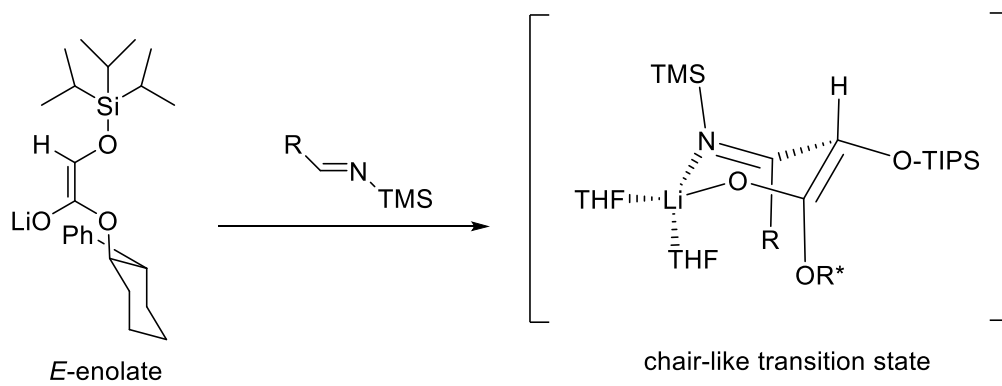


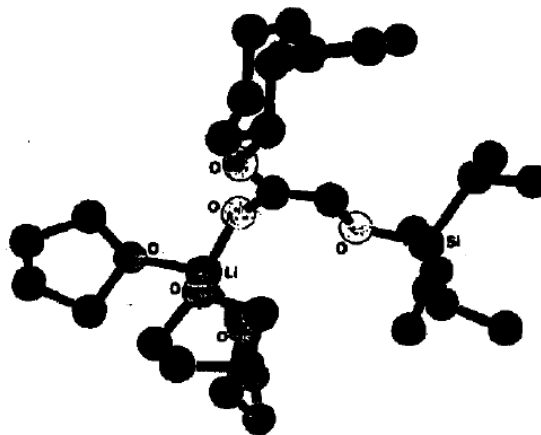
Figure 1.12 Mechanism for lithium chiral ester enolate-imine cyclocondensation reaction. Adapted from *Tetrahedron*, 48, Ojima, I.; Habus, I.; Zhao, M.; Zucco, M.; Park, Y. H.; Sun, C. M.; Brigaud, T. New and Efficient Approaches to the Semisynthesis of Taxol and Its C-13 Side-Chain Analogs by Means of Beta-Lactam Synthon Method, 6985-7012, Copyright (1992), with permission from Elsevier.

Both the chiral auxiliaries and *O*-protecting groups provide steric influence in the transition state of the lithium chiral ester enolate-imine cyclocondensation reaction. A screening of different chiral auxiliaries and *O*-protecting groups reveals that a combination of Whitesell's chiral auxiliary and triisopropylsilyl (TIPS) protecting group give the optimal yield (85% isolated yield) and enantioselectivity (> 96% ee) for the synthesis of 3-*O*-protected-4-substituted β -lactams.^{32,37,38}

The high enantioselectivity could be attributed to the favor of forming an *E*-enolate followed by a chair-like transition state, instead of a *Z*-enolate followed by a boat-like transition state.³² MM2 calculations of the two enolates using the MACROMODEL program also suggests the *E*-enolate is thermodynamically favored by 2.5 kcal/mol (**Figure 1.13**).³²



***E*-enolate, (-)-*E*-8e.3THF**



***Z*-enolate, (-)-*Z*-8e.3THF**

Figure 1.13 MM2 calculations on *E*- and *Z*-enolates by MACROMODEL. Adapted from *Tetrahedron*, 48, Ojima, I.; Habus, I.; Zhao, M.; Zucco, M.; Park, Y. H.; Sun, C. M.; Brigaud, T. New and Efficient Approaches to the Semisynthesis of Taxol and Its C-13 Side-Chain Analogs by Means of Beta-Lactam Synthon Method, 6985-7012, Copyright (1992), with permission from Elsevier.

§ 1.1.5 Structure-Activity Relationship (SAR) Study on Taxanes

Extensive structure-activity relationship (SAR) studies on taxanes were conducted in the laboratories of Potier, Kingston, Ojima, Bristol-Myers Squibb, and many others over the years. The key findings in the early SAR studies are summarized below.

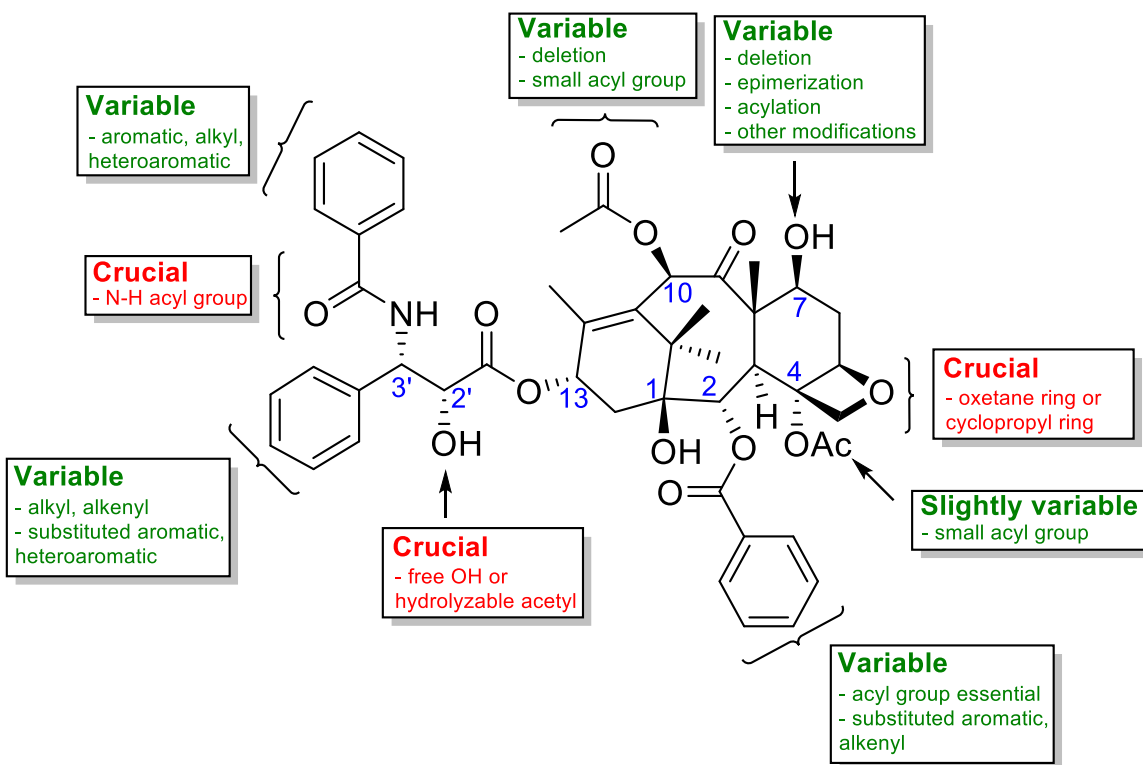


Figure 1.14 Summary of key structure-activity relationships (SAR) of taxanes

The C-13 side chain is absolutely necessary for the cytotoxicity. Compounds lacking the C-13 side chain, such as baccatin III or 10-deacetylbaccatin III (10-DAB III) are inactive.⁴⁸ However, modifications on the C-13 side chain are permitted, and could give rise to more active compounds. For example, docetaxel, which was initially prepared by Potier and his colleagues, has a *tert*-butoxycarbonyl (*t*-Boc) group on the C-3'N position of the C-13 side chain.⁴⁹ Phenyl group at C-3' position could also be replaced. A series of C-3' isobutyl and isobutenyl analogs with modifications at C-10 were prepared in the Ojima laboratory, and a number of them have shown exceptional activities against drug-resistant cancer cells.⁵⁰ Acylation at the C-2' hydroxyl group does not destroy the cytotoxicity, presumably because the acetyl group get hydrolyzed in living cells, as 2'-acetylpaclitaxel was not able to promote microtubule assembly in a tubulin-assembly study, in which hydrolysis is slow or nonexistent.⁴⁸

The benzoyloxy group at C-2 position is necessary for the cytotoxicity. 2-debenzoylpaclitaxel is not active.⁵¹ However, modifications on the C-2 benzoyl group are permitted. For example, replacement of benzoyl group with substituted benzoyl group give to a

number of analogs, which can be more cytotoxic or less cytotoxic than paclitaxel.⁵²⁻⁵⁴ Interestingly, the position of substituents on the benzene ring of the substituted benzoyl group plays a vital role for the activity. 2-*p*-azidobenzoylpaclitaxel is essentially inactive, while 2-*m*-azidobenzoylpaclitaxel is almost an order of magnitude more active than paclitaxel.^{52,53} A number of analogs with *meta*- substituents of the C-2 benzoyl group and modifications on the C-10 and C-3' positions developed in the Ojima laboratory have shown similar activity against both sensitive and resistant cancer cell lines.⁵⁴

The C-4 acetate group is necessary for the cytotoxicity. 4-Deacetylpaclitaxel and 4-deacetoxyaclarin are both much less active than paclitaxel.^{55,56} Some derivatives at C-4 are more active, for example, carbonate shown in **Figure 1.15** below is in clinical trial.⁵⁷

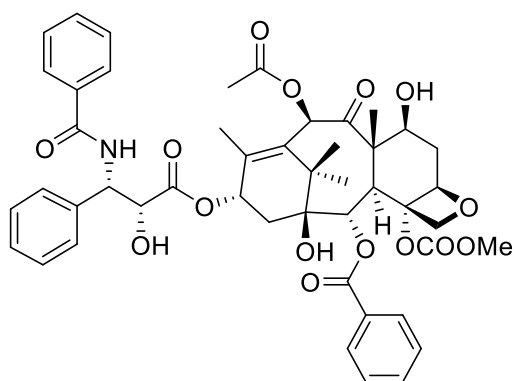


Figure 1.15 Chemical structure of a C-4 derivative of paclitaxel in clinical trial

The oxetane ring is required for the cytotoxicity. Opening of the oxetane ring eliminates the cytotoxicity.⁵⁸ Changing the oxetane ring to sulfetane ring significantly reduces the activity.⁵⁹ Changing the oxetane ring to cyclopropyl ring in a docetaxel analog, however, gives almost same activity as paclitaxel.⁶⁰

The hydroxyl group at C-7 position is not essential. Deoxygenation at C-7 gives 7-deacetoxyaclarin, which has similar cytotoxicity as paclitaxel.^{61,62} In addition, the C-7 hydroxyl can easily epimerize via a retro-adol mechanism.⁴⁹ The 7-*epi*-paclitaxel has essentially same activity as paclitaxel.⁴⁸ Modifications of C-7 hydroxy group could give some more potent analogs, for example, thiomethyl derivative was selected by BMS in clinical trials (**Figure 1.16**).¹²

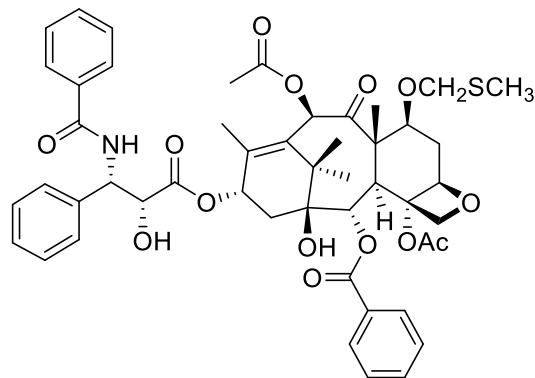


Figure 1.16 Chemical structure of a C-7 derivative of paclitaxel in clinical trial

The hydroxyl group at C-10 position is not essential. Deoxygenation at C-10 gives 10-deacetytaxepa, which has similar cytotoxicity as paclitaxel.⁶³ Re-acylation at C-10 gives a number of more cytotoxic analogs, and several developed in the Ojima laboratory have shown good cytotoxicity against resistant cell line MCF7-R.⁵⁰

Cabazitaxel (**Figure 1.5**), which has methoxy groups at both C-7 and C-10 positions as well as the same side chain as docetaxel, was developed by Sanofi-Aventis and approved by the US FDA for the treatment of hormone-refractory metastatic prostate cancer in 2010.¹⁴ Cabazitaxel showed activity against both docetaxel-sensitive and docetaxel-resistant cancers in preclinical testing and initial clinical trials, because of its poor affinity for P-glycoprotein.¹⁴ Subsequent clinical studies of cabazitaxel in combination with steroid prednisone were conducted against patients with hormone-refractory metastatic prostate cancer who had been previously treated with a regimen containing docetaxel, and significantly overall longer survival was achieved compared with previous standard treatment by using mitoxantrone.¹⁴

The C-11 – C-12 double bond in A-ring is not reactive. Hydrogenation of baccatin III gives a product that the C-2 benzoyl group reduced to cyclohexylcarbonyl group, leaving the double bond untouched.⁶⁴ Allylic bromination, followed by reacting with different nucleophiles gives C-18 analogs.⁶⁵ However, all of these analogs are not as cytotoxic as paclitaxel.⁶⁵

A number of C-14 analogs have been prepared in the Ojima laboratory from 14 β -hydroxy-10-DAB III, which has a carbonate group linking C-1 position and C-14 position.^{66,67} Most of these analogs have shown better activities than paclitaxel.⁶⁷ One of the derivatives, IDN5109, developed by Indena S.p.A. is under clinical trials as an oral active anticancer drug (**Figure 1.17**).⁶⁸

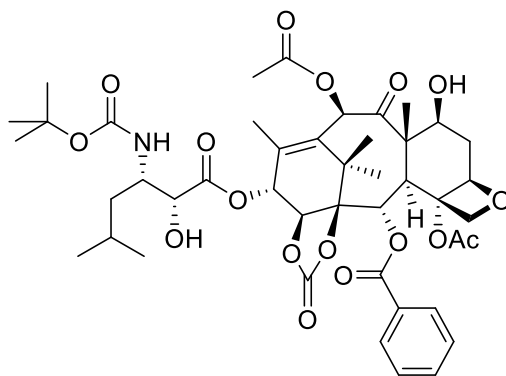


Figure 1.17 Chemical structure of a C-14 derivative of docetaxel in clinical trial

§ 1.1.6 Multidrug Resistance (MDR)

Despite the success of taxane class anticancer drugs, many cancers fail to respond to such chemotherapeutic agents by acquiring multidrug resistance (MDR). P-glycoprotein (Pgp, also known as ABCB1), multidrug resistance associated-protein 1 (MRP1, also known as ABCC1), and ABCG2 (BCRP) are the three common ATP-binding cassette (ABC) transporters that are responsible for MDR.⁶⁹ Among them, Pgp is the most prevalent ABC transporter, acting as an efflux pump to expel hydrophobic drugs including vinca alkaloids, anthracycline, epipodophyllotoxins, and taxanes out of cell membrane.⁷⁰ Pgp is a transmembrane protein that utilizes ATP hydrolysis as the energy source for its biological functions. **Figure 1.5** shows a model of anticancer drug transport by Pgp. First, anticancer drug (magenta) gets into membrane bilayer from outside of cell through partition and recognized by Pgp (cyan spheres), and then ATP (yellow) binds to the nucleotide-binding domain (NBD) of Pgp, causing a huge conformation change of Pgp to expel the hydrophobic drug out of the cell membrane.⁷¹

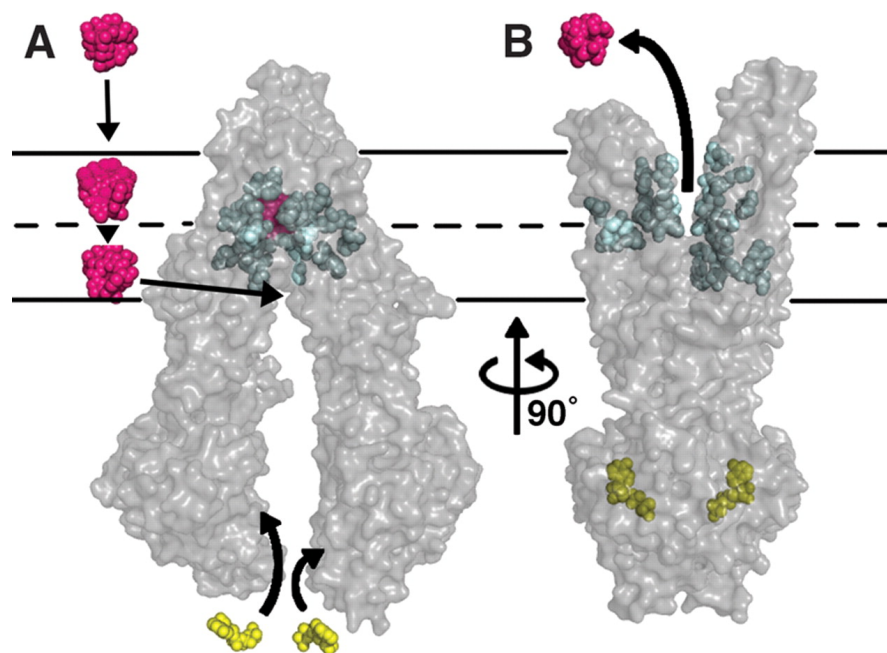


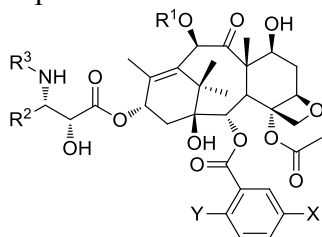
Figure 1.18 Model of anticancer drug transport by P-glycoprotein. From Aller, S. G.; Yu, J.; Ward, A.; Weng, Y.; Chittaboina, S.; Zhuo, R. P.; Harrell, P. M.; Trinh, Y. T.; Zhang, Q. H.; Urbatsch, I. L.; Chang, G. Structure of P-Glycoprotein Reveals a Molecular Basis for Poly-Specific Drug Binding. *Science* **2009**, 323, 1718-1722. Reprinted with permission from AAAS.

§ 1.1.7 New-Generation Taxoids

The Ojima laboratory has developed a series of highly potent new-generation taxoids based on extensive structure-activity relationship (SAR) study of taxoids throughout the years. Selected results are shown in **Table 1.1**.⁷²

The focus of the modifications on new-generation taxoids developed in the Ojima laboratory focused on C-2 benzoyl, C-10, and C-3' positions, and keep the C-3'N position with *t*-Boc group as found in docetaxel. As shown in **Table 1.1**, most of these new generation taxoids have shown one to two orders of magnitude higher potency than those of paclitaxel and docetaxel in sensitive cancer cell lines, as well as two to three orders of magnitude higher potency against multidrug-resistant cancer cell lines.⁷²

Table 1.1 Structure and cytotoxicity (IC₅₀, nM) of selected new-generation taxoids against various cancer cell lines. Adapted from Ojima, I.; Zuniga, E. S.; Berger, W. T.; Seitz, J. D. Tumor-targeting drug delivery of new-generation taxoids. *Future Med Chem* 2012, 4, 33-50, with permission from Future Science Ltd.



Taxoid	R ¹	R ²	R ³	X	Y
Paclitaxel	Ac	Ph	PhCO	H	H
Docetaxel	H	Ph	<i>t</i> -Boc	H	H
SB-T-1213	EtCO	<i>i</i> -butenyl	<i>t</i> -Boc	H	H
SB-T-1214	<i>c</i> -PrCO	<i>i</i> -butenyl	<i>t</i> -Boc	H	H
SB-T-1216	Me ₂ NCO	<i>i</i> -butenyl	<i>t</i> -Boc	H	H
SB-T-11033	EtCO	<i>i</i> -Bu	<i>t</i> -Boc	MeO	H
SB-T-121303	EtCO	<i>i</i> -butenyl	<i>t</i> -Boc	MeO	H
SB-T-121313	EtCO	<i>i</i> -butenyl	<i>t</i> -Boc	MeO	MeO
SB-T-121602	Me ₂ NCO	<i>i</i> -butenyl	<i>t</i> -Boc	Me	H

Taxoid	MCF7 ^a	NCI/ADR ^b	LCC6-MDR ^c	CFPAC-1 ^d	HT-29 ^e	DLD-1 ^f
Paclitaxel	1.7	550	346	68	12	300
Docetaxel	1.0	723	120	-	-	-
SB-T-1213	0.18	4.0	-	4.6	0.37	3.9
SB-T-1214	0.20	3.9	-	0.38	0.73	3.8
SB-T-1216	0.13	7.4	-	0.66	0.052	5.4
SB-T-11033	0.36	0.61	0.80	-	-	-
SB-T-121303	0.36	0.79	0.90	0.89	-	-
SB-T-121313	0.30	-	-	0.025	0.56	-
SB-T-121602	0.08	-	-	0.31	0.003	0.46

^a Human mammary cancer cell line (Pgp⁻); ^b Human ovarian cancer cell line (Pgp⁺); ^c *mdr1* transduced human breast cancer cell line (Pgp⁺); ^d Human pancreatic cancer cell line; ^e Human colon cancer cell line (Pgp⁻); ^f Human colon cancer cell line (Pgp⁺).

In order to test which moiety of the new-generation taxoids account for the high potency against multidrug resistant cancer cell lines, in collaboration with Professor Jan Kovar, four new-generation taxoids were designed, which are structural combinations of paclitaxel or docetaxel with new-generation taxoids **SB-T-1214** or **SB-T-1216** (**Figure 1.19**). The SAR study of these taxoids may provide useful information for the design of novel taxoids with better activities against multidrug resistant cancer cell lines.

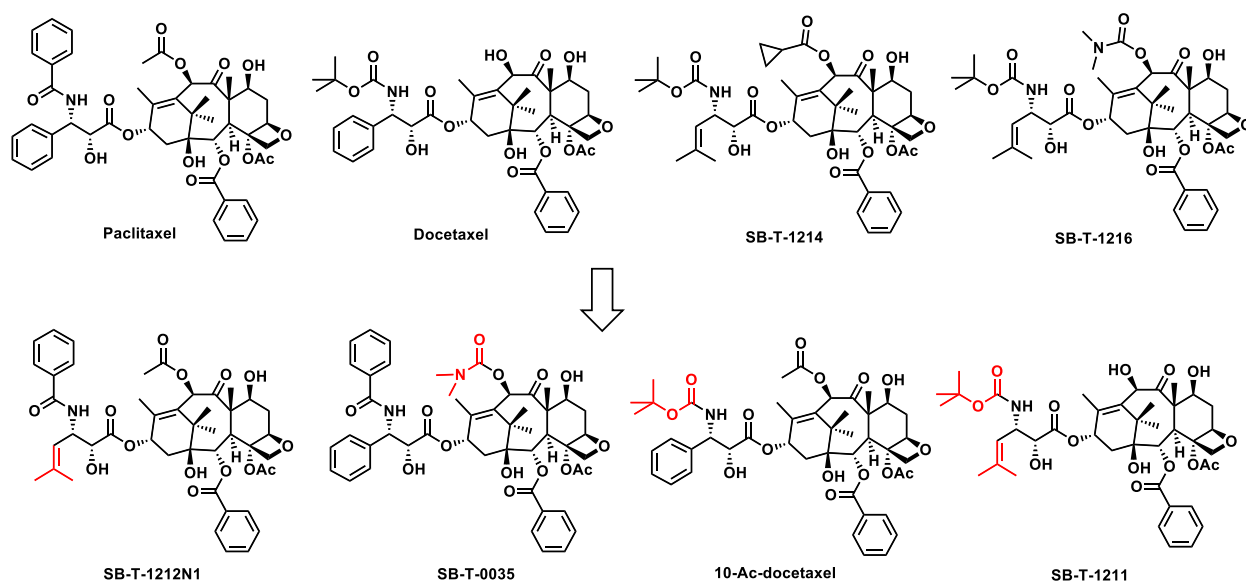


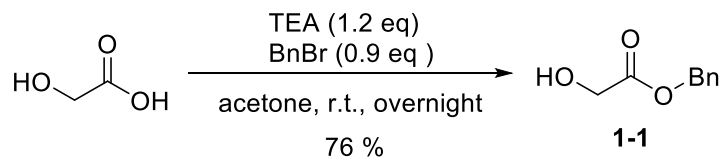
Figure 1.19 Designed new-generation taxoids

§ 1.2 Synthesis and Biological Evaluation of New-Generation Taxoids

§ 1.2.1 Synthesis of Eantiopure β -Lactam

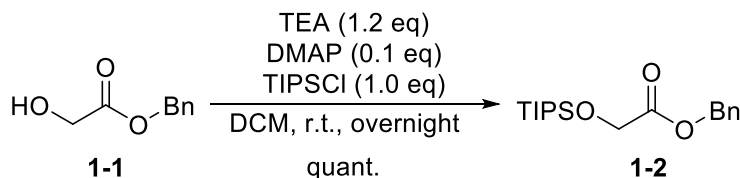
In order to make new-generation taxoids, enantiopure β -lactam is an important precursor, which could be prepared by two different routes. The first route involves synthesis of Whitesell's chiral auxiliary via Sharpless asymmetric dihydroxylation (AD), followed by chiral ester enolate-imine cyclocondensation.

The synthesis of the chiral ester begins with benzyl protection of the commercially available glycolic acid. Crude benzyl glycolate **1-1** was generated in 76% yield when using triethylamine (TEA) as the base (**Scheme 1.1**).



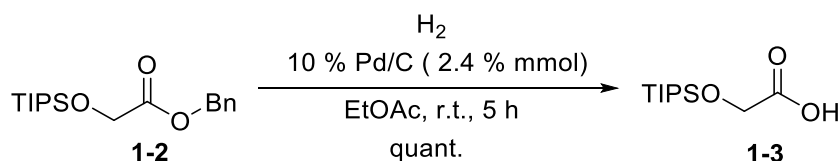
Scheme 1.1 Benzyl protection of glycolic acid

Benzyl glycolate **1-1** was then reacted with triisopropylsilyl chloride (TIPSCl) in the presence of TEA and catalytic amount of 4-dimethylaminopyridine (DMAP). TIPS-Protected benzyl glycolate **1-2** was then generated in quantitative yield (**Scheme 1.2**).



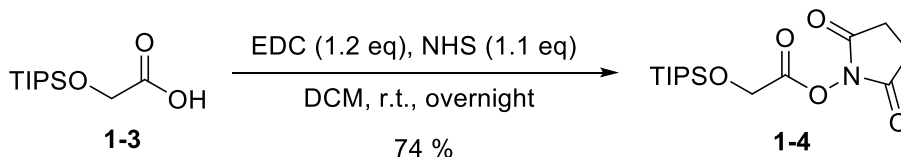
Scheme 1.2 TIPS protection of benzyl glycolate **1-1**

The benzyl group of TIPS-protected benzyl glycolate **1-2** was subsequently removed by hydrogenolysis under hydrogen gas in the presence of 10% Pd/C to afford crude product TIPS glycolic acid **1-3** in quantitative yield (**Scheme 1.3**). The crude product was directly used in the next step without further purification, because TIPS group is not very stable under acidic condition and may fall off if not used at once.



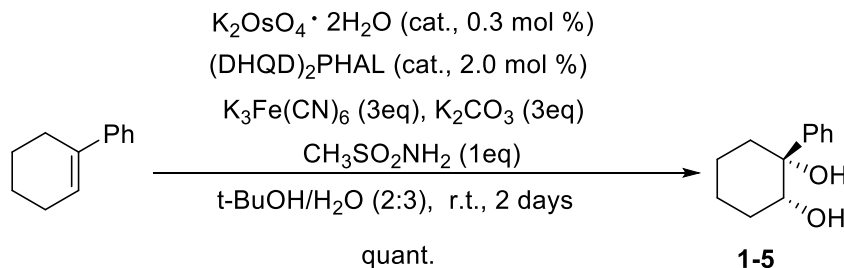
Scheme 1.3 Benzyl deprotection of **1-2** by hydrogenolysis

The free carboxylic acid group in TIPS glycolic acid **1-3** was then activated by *N*-hydroxysuccinimide (NHS) via 1-ethyl-3-(3-dimethylaminopropyl)carbodiimide (EDC) coupling to give activated ester **1-4** in 74% yield (**Scheme 1.4**).



Scheme 1.4 Synthesis of activated ester **1-4** via EDC coupling

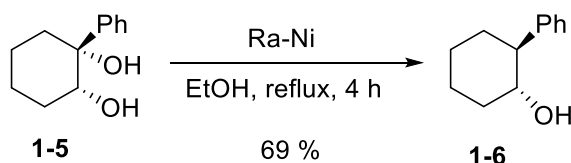
With activated ester **1-4** in hand, Whitesell's chiral auxiliary was prepared in order to react with activated ester to form the chiral ester. First, crude (+)-(1*R*,2*R*)-1-phenylcyclohexane-*cis*-1,2-diol **1-5** was obtained in quantitative yield via Sharpless asymmetric dihydroxylation (AD) reaction (**Scheme 1.5**).



Scheme 1.5 Synthesis of diol **1-5** via Sharpless asymmetric dihydroxylation

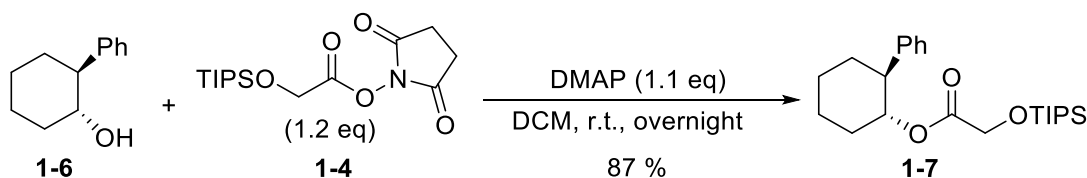
In this reaction, osmium tetroxide is a stereospecific oxidant that produces the diol from the alkene by a *syn*-addition. The reaction is carried out using three equivalents of potassium ferricyanide as oxidants and catalytic amount of osmium tetroxide. This oxidation reaction can be highly enantioselective in the presence of chiral ligands. (DHQD)₂PHAL, one of the most effective ligands, which will lead to a (*R,R*) configuration of the product, is used in this reaction. This ligand will not only induce high enantioselectivity, but also accelerate the reaction. The presence of organic sulfonamide methanesulfonamide will further make this reaction more effective by accelerating the hydrolysis of the osmate ester.

Whitesell's chiral auxiliary **1-6** was generated by selectively reduction of the crude diol **1-5** from the previous step with Raney nickel in 69% yield after recrystallization with pentane (**Scheme 1.6**). Raney nickel is extremely pyrophoric when dry, and therefore must be kept in wet ethanol all the time. Aqueous slurry of Raney nickel is transferred into the flask with the aid of ethanol in portions.



Scheme 1.6 Synthesis of Whitesell's chiral auxiliary **1-6** by selective reduction of diol **1-5**

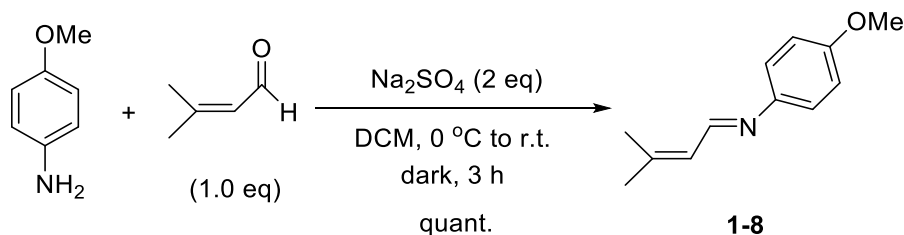
Key intermediate chiral ester **1-7** for making the β -lactams was obtained by reacting Whitesell's chiral auxiliary **1-6** with activated ester **1-4** in the presence of DMAP in toluene in 87% yield (**Scheme 1.7**). The reason for using toluene as the solvent is that the side product of this reaction *N*-hydroxysuccinimide (NHS) is not very soluble in toluene, and could be easily removed by filtration. Purity of the starting materials is very important for the completion of this reaction in short time, and will affect the yield of this reaction to large extent. The product need to be carefully purified by column chromatography and carefully dried on vacuum, as impurity or moisture in the chiral ester **1-7** may lead to the failure of next key step chiral ester enolate-imine cyclocondensation.



Scheme 1.7 Synthesis of key intermediate chiral ester **1-7**

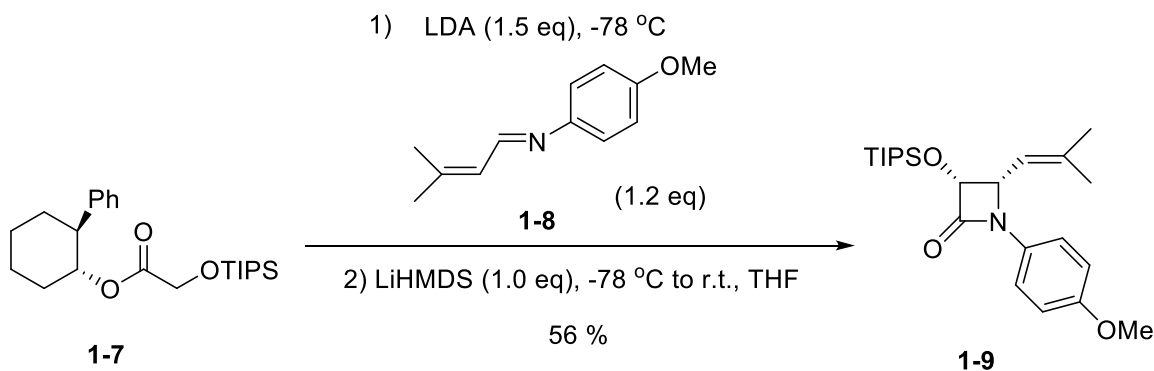
The crude imine **1-8** was generated in quantitative yield in the condensation reaction of recrystallized *p*-anisidine and 3-methyl-2-butenal (**Scheme 1.7**). This is a condensation reaction between an aldehyde with nitrogen nucleophile, and involves addition and elimination steps. The product of this reaction is an imine, which is also called Schiff base. The reaction is reversible

and the product is very reactive and unstable as it has a conjugated structure. Therefore, an excess of drying agent sodium sulfate is used to prevent the hydrolysis of the product. The condensation reaction must be done in the dark, as the product is prone to isomerization. The resulting material was used immediately without further purification to prevent the product going back to the starting material or performing isomerization.



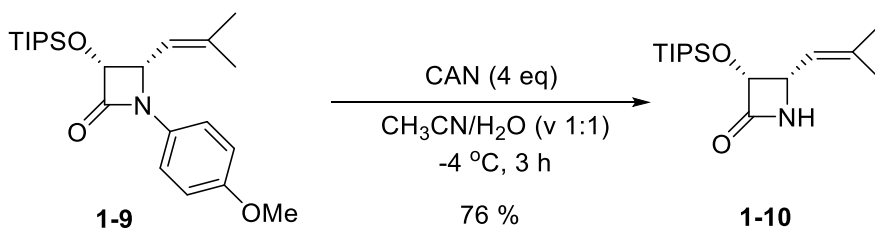
Scheme 1.8 Synthesis of imine **1-8** by condensation reaction

With the chiral ester **1-7** and imine **1-8** in hand, the chiral ester enolate-imine cyclocondensation reaction, previously developed in the Ojima laboratory, was performed, affording enantiopure β -lactam **1-9** in 56% yield (**Scheme 1.9**). The first two small-scale trials of this reaction failed because a small amount of water existed in the chiral ester, and this reaction is very water sensitive. The product was first purified by column chromatography, and then by recrystallization. The yield of this step is low because uncyclized product was also obtained, and the purification of the product was difficult.



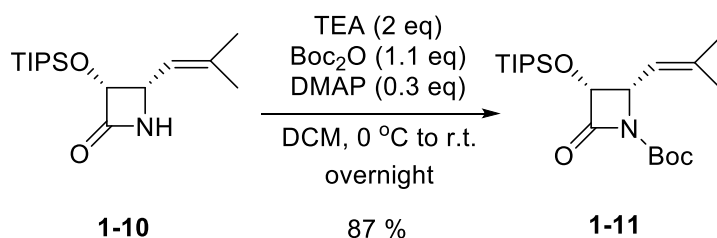
Scheme 1.9 Synthesis of enantiopure β -lactam **1-9** by chiral ester enolate-imine cyclocondensation

Further modification of the β -lactam, deprotection of the *p*-methoxyphenyl (PMP) moiety in the presence of ceric ammonium nitrate (CAN), gave rise to modified β -lactam **1-10** in 76% yield (**Scheme 1.10**). The mechanism for the removal of the PMP group involves two single electron transfers (SET). First, the PMP group donates a single electron to cerium (IV), forming a radical cation intermediate. After hydrolysis of the methoxy group by water, donation of a second electron to another CAN molecule will result in a quinone like radical, which will be then cleaved by a second water molecule, producing the product **1-10** with quinone and methanol as side products. Cold temperature is maintained to avoid side reactions.



Scheme 1.10 CAN deprotection of *p*-methoxyphenyl (PMP) group

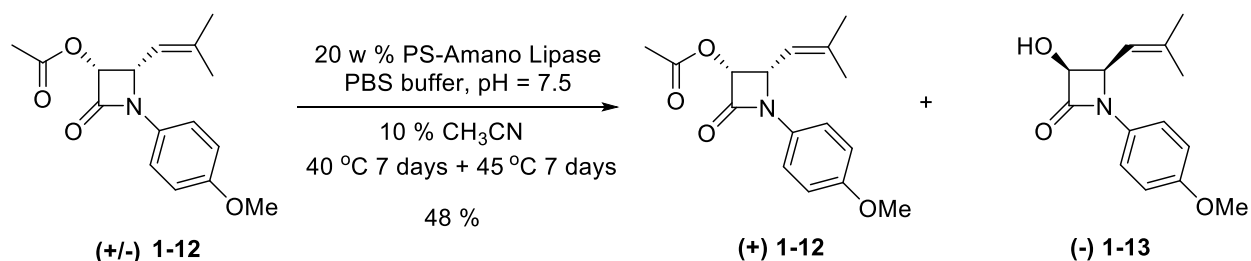
After CAN deprotection, the amine in β -lactam **1-10** was protected with *t*-Boc group to yield the desired enantiopure β -lactam **1-11** in 87% yield (**Scheme 1.11**). This protection is in order to have the proper *N*-substituted *t*-Boc group found in new-generation taxoids **SB-T-1214** and **SB-T-1216**. DMAP is used as the catalyst, and TEA is used to create the basic environment. The nucleophilic nitrogen in the β -lactam ring will attack *t*-Boc anhydride, forming the final desired enantiopure β -lactam **1-11**.



Scheme 1.11 *t*-Boc protection of β -lactam **1-10**

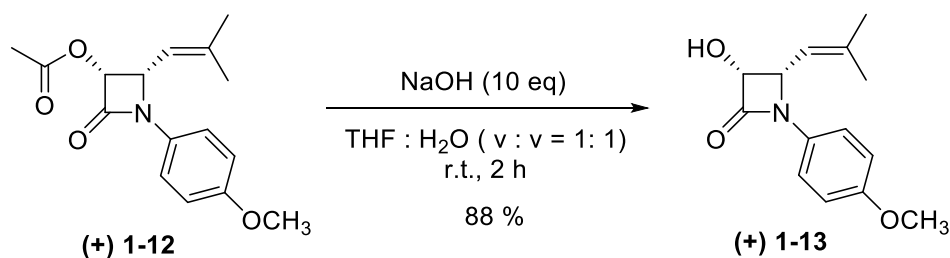
The second route for preparing enantiopure β -lactam **1-11** involves Staudinger [2+2] cycloaddition to afford racemic β -lactam intermediate, followed by enzymatic resolution to separate the two enantiomers.

The racemic β -lactam intermediate (+/-) **1-12** was reacted with 20w% PS-Amano Lipase to give the desired enantiomer (+) **1-12** in 48% yield, and undesired enantiomer was hydrolyzed by the enzyme to give (-) **1-13** (**Scheme 1.12**). This reaction was monitored by ^1H NMR. The ratio of (+) **1-12** and (-) **1-13** should be 1:1 if the reaction went completion. After 7 days, the NMR result indicates the ratio of (+) **1-12** and (-) **1-13** is around 10:7, so the temperature was raised from 40 $^\circ\text{C}$ to 45 $^\circ\text{C}$. After another 7 days, the NMR result indicates the ratio of (+) **1-12** and (-) **1-13** is 1:1. (+) **1-12** and (-) **1-13** was then separated by column chromatography to give (+) **1-12** in 48% yield. The theoretical yield for this reaction is 50%, which is a major drawback of this synthetic route.



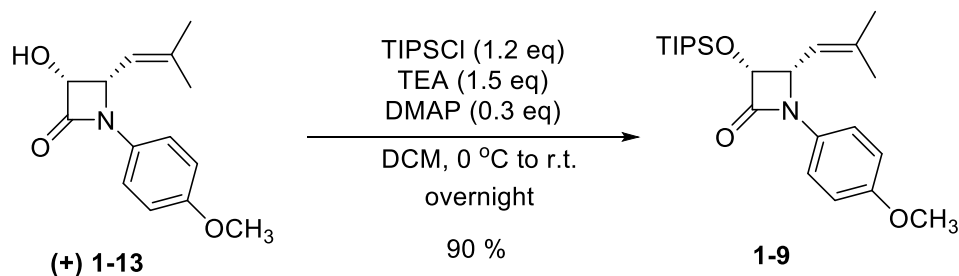
Scheme 1.12 Enzymatic resolution of racemic β -lactam intermediate

The enantiopure β -lactam (+) **1-12** was then hydrolyzed by sodium hydroxide to give (+) **1-13** in 88% yield (**Scheme 1.13**). The enantiomeric excess (ee) of β -lactam (+) **1-13** was confirmed by chiral HPLC, together with β -lactam (-) **1-13** obtained in the previous enzymatic resolution step, and the result indicates the ee of β -lactam (+) **1-13** is 100%.



Scheme 1.13 Hydrolysis of enantiopure β -lactam (+) **1-12**

Enantiopure β -lactam (+) **1-13** was then reacted with triisopropylsilyl chloride (TIPSCl) in the presence of TEA and DMAP to give β -lactam intermediate **1-9** in 90% yield (**Scheme 1.14**). β -Lactam intermediate **1-9** was also generated in the first synthetic route, and could undergo same modifications to afford desired final β -lactam **1-11** through CAN deprotection and *t*-Boc protection as mentioned above.

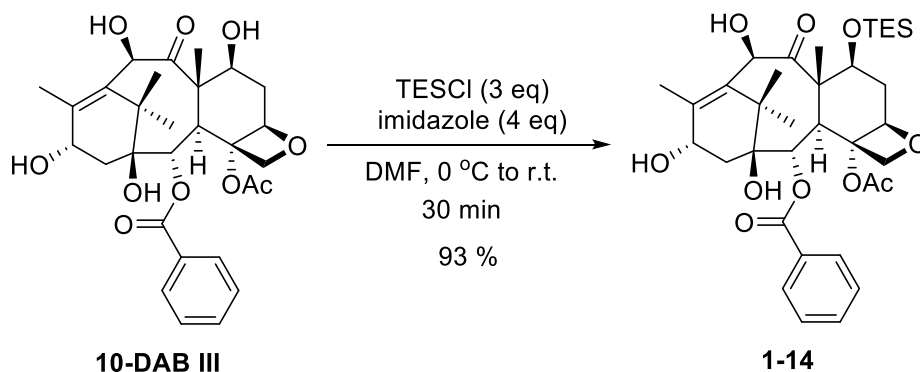


Scheme 1.14 TIPS protection of enantiopure β -lactam (+) **1-13**

§ 1.2.2 Synthesis of New-Generation Taxoids SB-T-1214 and SB-T-1216

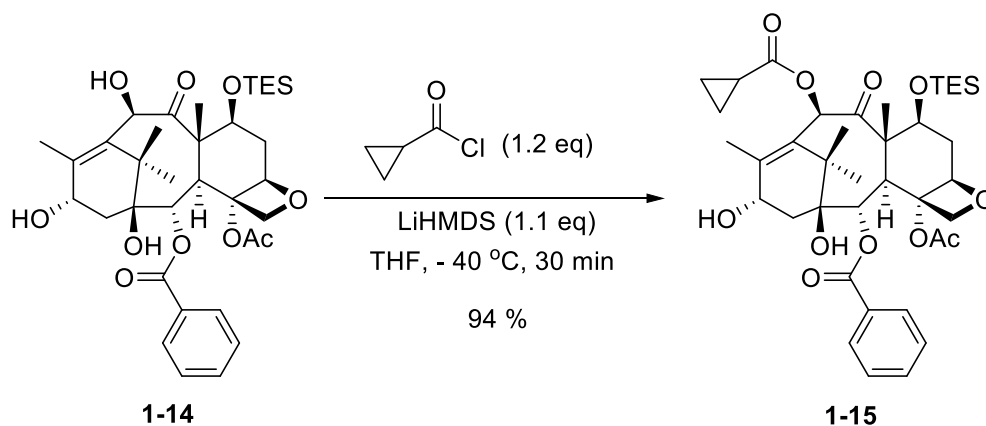
The synthesis of new-generation taxoids **SB-T-1214** and **SB-T-1216** begins with triethylsilyl (TES) protection of the C-7 alcohol of 10-DAB III in order to selectively acylate the

C-10 position in the following step (**Scheme 1.15**). The structure of 10-deacetylbaccatin III contains four alcohols at C-1, C-7, C-10 and C-13, among which C-7 alcohol is the most acidic one and could be selectively protected with chlorotriethylsilane (TESCl). The C-1 hydroxyl is sterically hindered by the benzoyl group at C-2 position, and does not compete with the C-7 alcohol. This was confirmed by the experiments that acylation of 10-DAB III under different conditions gave C-7, C-10, and C-13 acylated products, leaving C-1 hydroxyl group untouched.⁷³ The mono-TES protection of C-7 hydroxyl was carefully monitored by thin-layer chromatography (TLC) so that multiple protections do not occur at C-10 and C-13 positions. The reaction was done within 30 min, and desired 7-TES-10-DAB III **1-14** was obtained in 93% yield.



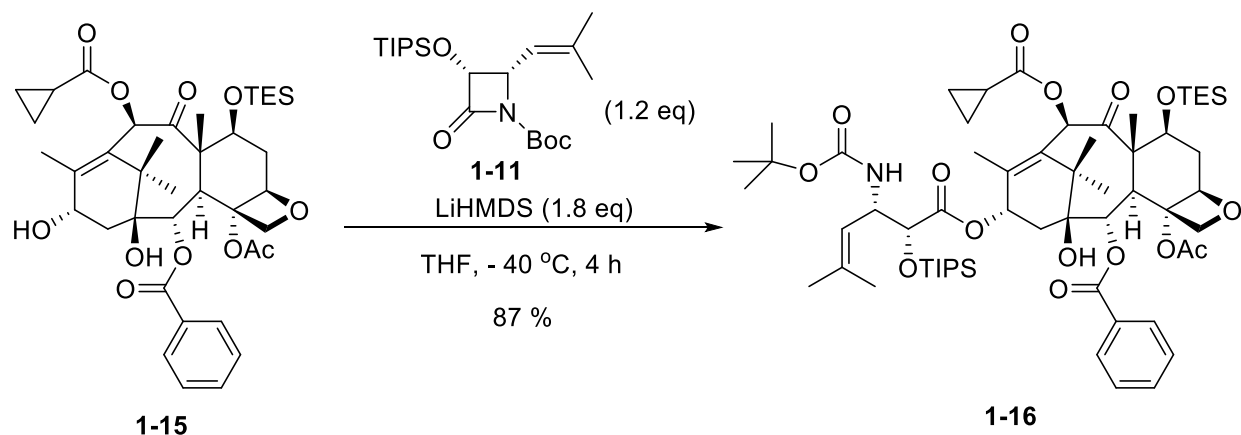
Scheme 1.15 TES protection of C-7 position in 10-DAB III

After the C-7 alcohol of 10-DAB III was selectively protected, the C-10 alcohol becomes most reactive on the baccatin core, and was selectively acylated with cyclopropanecarbonyl chloride in the presence of LiHMDS (**Scheme 1.16**). This reaction was carefully monitored by TLC so that multiple acylations do not occur. The reaction was done within 30 min at -40 °C, and desired product **1-15** was obtained in 94% yield.



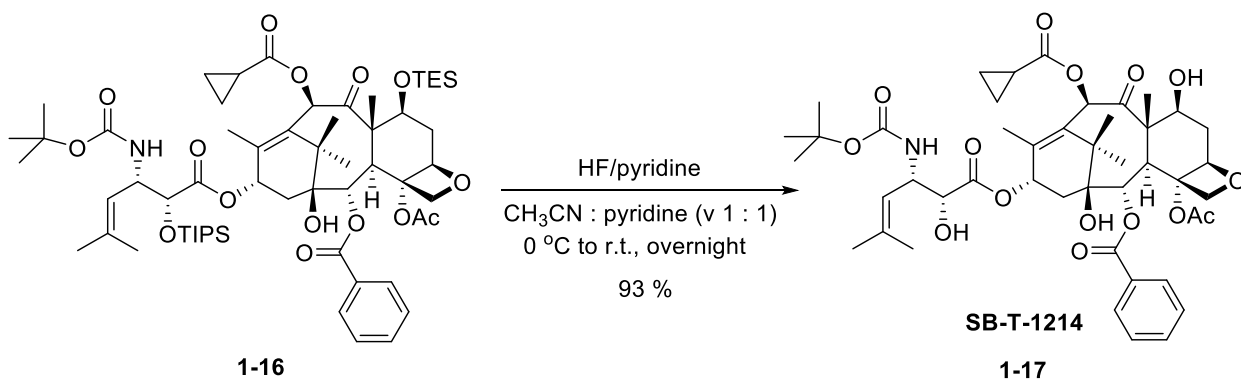
Scheme 1.16 Acylation of C-10 position in **1-14** with cyclopropanecarbonyl chloride

The C-10 modified baccatin core **1-15** was then used to react with the enantiopure β -lactam **1-11** via the Ojima-Holton coupling protocol. The C-13 hydroxyl group is deprotonated by LiHMDS, and acts as a nucleophile to attack the carbonyl carbon of the β -lactam ring, the β -lactam ring is opened and stereochemistry is maintained (**Scheme 1.17**). The desired product **1-16** was obtained in 87% yield.



Scheme 1.17 Ojima-Holton coupling to generate **1-16**

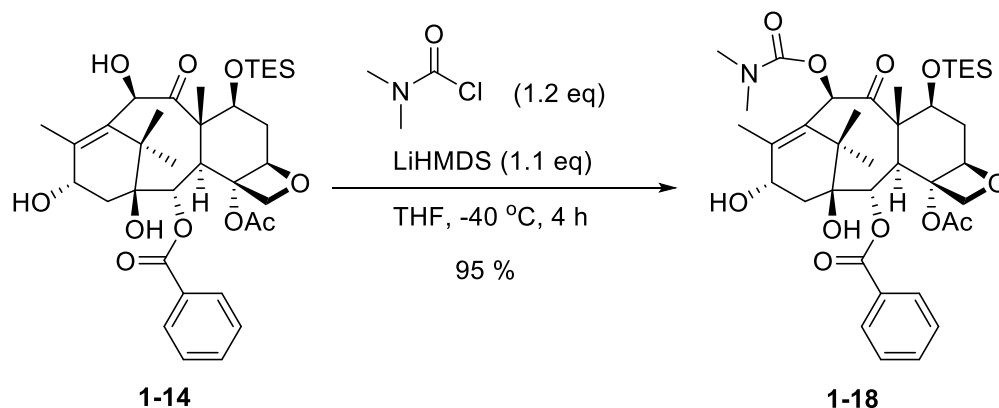
New-generation taxoid **SB-T-1214** was finally generated by deprotection of the C-7 TES protecting group and the C-2' TIPS protecting group with HF/pyridine at the same time (**Scheme 1.18**). Desired taxoid **SB-T-1214** was obtained in 93% yield. After recrystallization with ethyl acetate, purity of the new-generation taxoid **SB-T-1214** was confirmed by HPLC as 97.5%.



Scheme 1.18 HF/pyridine deprotection to generate new-generation taxoid **SB-T-1214**

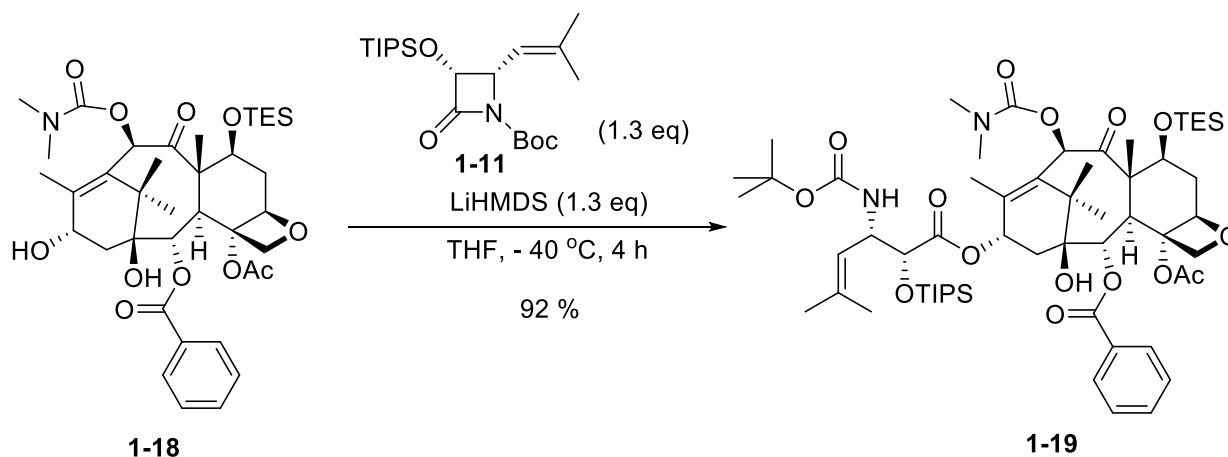
The chemical structures of new-generation taxoid **SB-T-1214** and **SB-T-1216** are the same except the C-10 position, in **SB-T-1214** C-10 position is acylated with cyclopropanecarbonyl group, whereas in **SB-T-1216** C-10 position is acylated with *N,N*-dimethylcarbamoyl group. For the synthesis of new-generation taxoid **SB-T-1216**, after the C-7 alcohol of 10-DAB III is selectively protected, the C-10 position was selectively acylated with *N,N*-dimethylcarbamoyl chloride in the presence of LiHMDS (**Scheme 1.19**). The difference between these two acylation reactions is that, compared to acylation with cyclopropanecarbonyl chloride, the R_f value of the

C-10 *N,N*-dimethylcarbamoyl acylated product **1-18** is very similar to the R_f value of the starting material 7-TES-10-DAB III **1-14**. Also, this reaction is slower compared to acylation of 7-TES-10-DAB III **1-14** with cyclopropanecarbonyl chloride. Therefore, this reaction need to be carefully monitored by TLC and mass spectrometry to make sure all the starting material converts to product. The reaction was finished within 4 hour at -40 °C, and desired product **1-18** was obtained in 95% yield.



Scheme 1.19 Acylation of C-10 position in **1-14** with *N,N*-dimethylcarbamoyl chloride

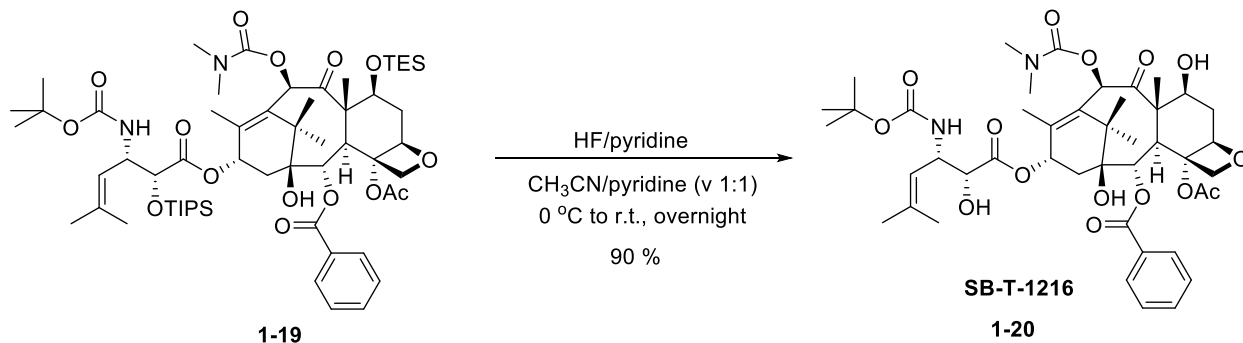
The C-10 modified baccatin core **1-18** was then used to react with the enantiopure β -lactam **1-11** via the Ojima-Holton coupling protocol (**Scheme 1.20**). The desired product **1-19** was obtained in 92% yield.



Scheme 1.20 Ojima-Holton coupling to generate **1-19**

New-generation taxoid **SB-T-1216** was finally generated by deprotection of the C-7 TES protecting group and the C-2' TIPS protecting group with HF/pyridine at the same time (**Scheme**

1.21). Desired taxoid **SB-T-1216** was obtained in 90% yield. After recrystallization with ethyl acetate, purity of the new-generation taxoid SB-T-1216 was confirmed by HPLC as 98%.

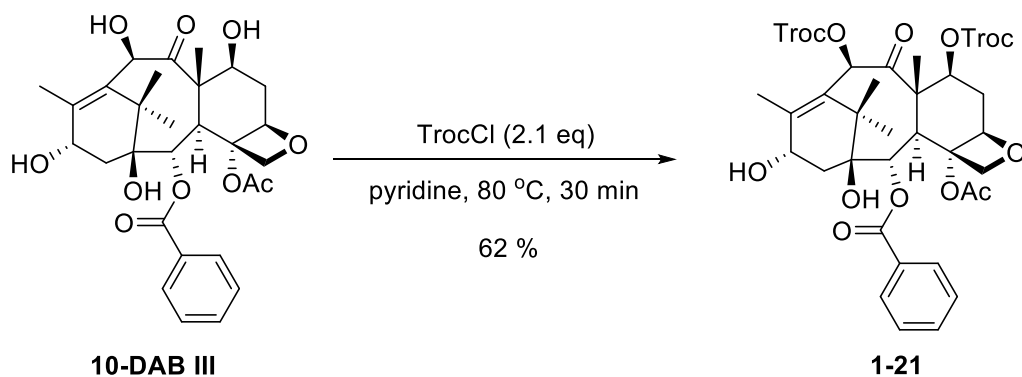


Scheme 1.21 HF/pyridine deprotection to generate new-generation taxoid **SB-T-1216**

§ 1.2.3 Synthesis of New-Generation Taxoid **SB-T-1211**

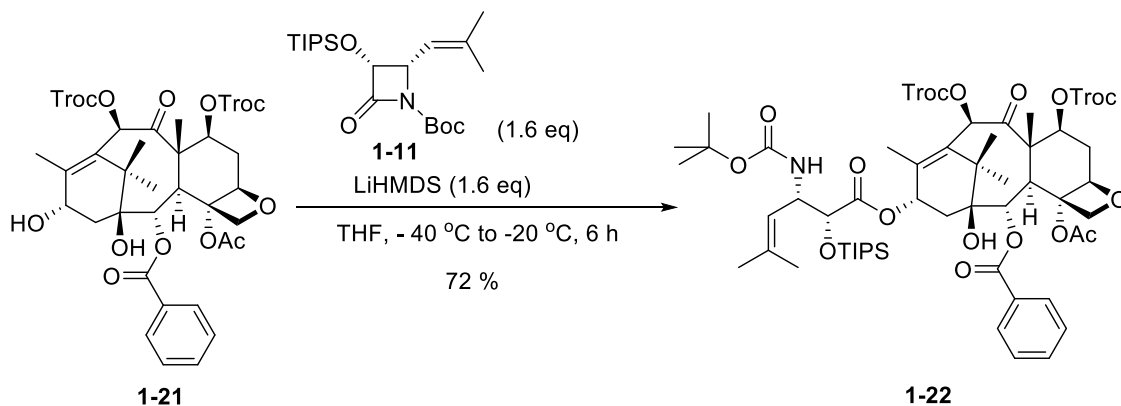
For the synthesis of new generation taxoid **SB-T-1211**, two different synthetic routes were employed. In the first route, C-7 and C-10 positions of 10-DAB III was selectively protected by TrocCl, followed by Ojima-Holton coupling of the free C-13 hydroxy group with the enantiopure β-lactam, then removal of the two Troc protecting groups by zinc dust and TIPS protecting group by HF/pyridine gave final taxoid **SB-T-1211**. However, after deprotection, the purity of the final compound after two column chromatography purifications is still less than 90%, and HPLC analysis shows a major impure peak, which is hard to remove. Recrystallizations under various conditions were also tried and were not successful. This impurity is presumably coming from the zinc dust deprotection step. In addition, the yields for preparing **SB-T-1211** in the first synthetic route were not very good. Thus, a second synthetic route was investigated. In the second route, 7-TES-baccatin III **1-14** was used to couple with the enantiopure β-lactam via Ojima-Holton protocol, then the acetyl group on the C-10 position of baccatin core was selectively removed by hydrazine monohydrate, followed by deprotection of the TES and TIPS groups by HF/pyridine to gave final taxoid **SB-T-1211** in decent yield and purity.

In the first synthetic route, in order to selectively protect the C-7 and C-10 positions of the baccatin core, 10-DAB III was treated with 2.1 eq of 2,2,2-trichloroethyl chloroformate (TrocCl) in the presence of pyridine to give 7,10-diTroc-10-deacetylbaccatin III **1-21** in 62% yield (**Scheme 1.22**). Side product 7,10,13-triTroc-10-deacetylbaccatin III was also isolated in 27% yield under this condition. It is possible to reduce the amount of side product by shorten the reaction time, use lower temperature, or use less amount of TrocCl.



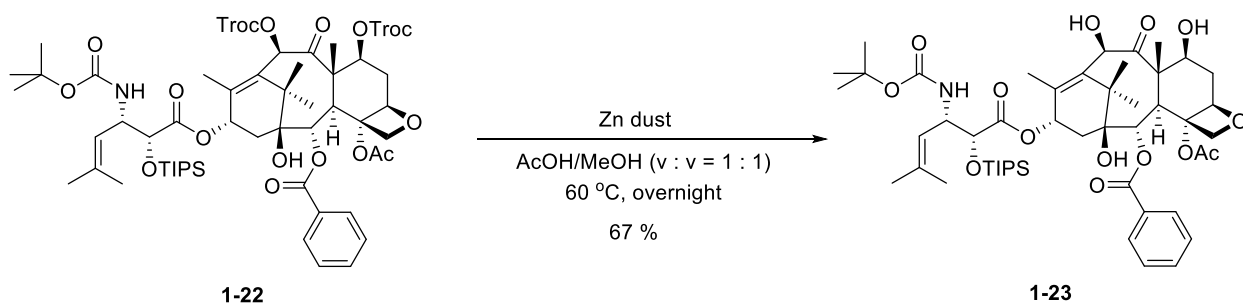
Scheme 1.22 DiTroc protection of 10-DAB III

7,10-DiTroc-10-deacetylbaccatin III **1-21** was then used to couple with eantiopure β -lactam **1-11** via the Ojima-Holton coupling protocol (**Scheme 1.23**). Compared with previous two coupling reactions for synthesizing **SB-T-1214** and **SB-T-1216**, however, this reaction could not go completion even with prolonged reaction time (up to 6 h), large excess of the base and β -lactam (1.6 eq of each), and increased temperature (up to $-20\text{ }^{\circ}\text{C}$). Desired taxoid **1-22** was isolated in 72% yield, and unreacted starting material 7,10-diTroc-10-deacetylbaccatin III **1-21** was recovered (conversion 74%, conversion yield 97%).



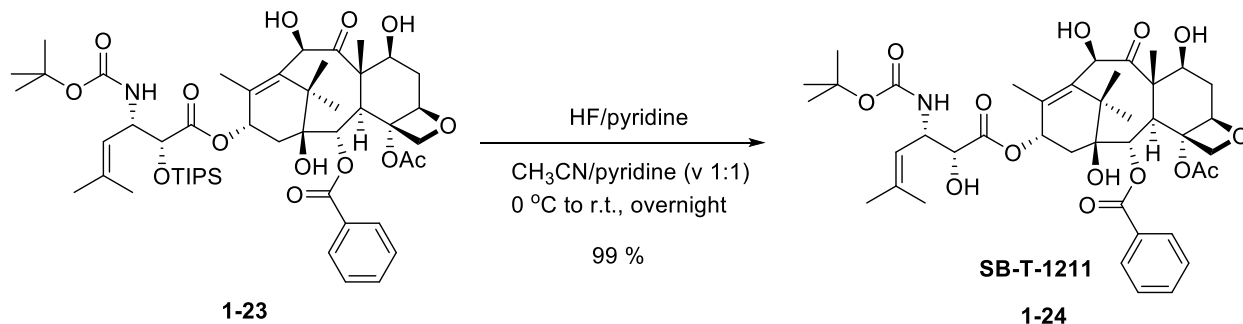
Scheme 1.23 Ojima-Holton coupling to generate **1-22**

After Ojima-Holton coupling to attach the C-13 side chain, Zn dust was employed to remove both of the Troc protecting groups at C-7 and C-10 positions. This reaction was quite messy, and after careful purification by column chromatography, desired product **1-23** was obtained in 67% yield (**Scheme 1.24**).



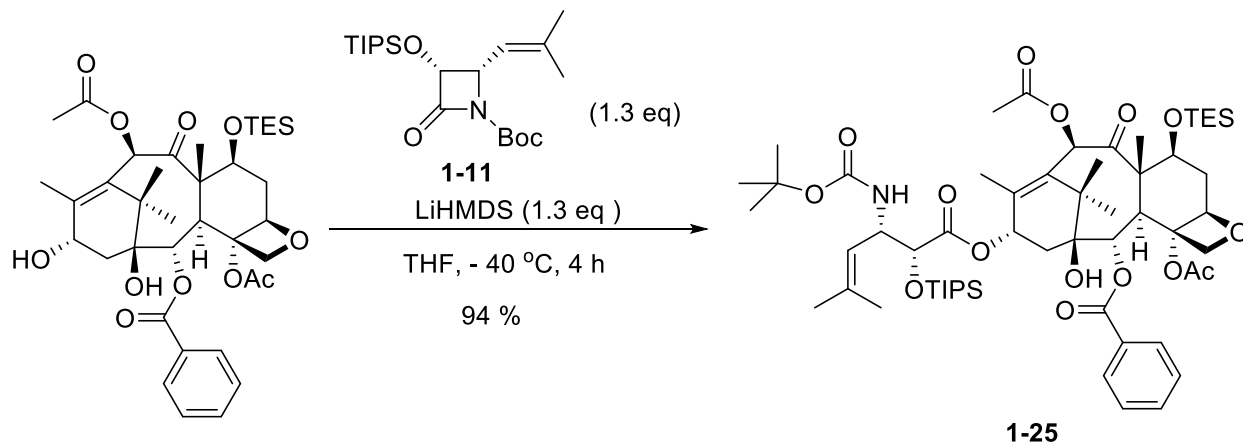
Scheme 1.24 Deprotection of Troc groups by Zinc dust

Finally, removal of the TIPS protecting group by HF/pyridine gave new-generation taxoid **SB-T-1211** in 99% yield (**Scheme 1.25**). However, there is a major impurity (more polar than desired product, ~10%) showed in HPLC analysis, and this impurity could not be removed by column chromatography. Recrystallizations under various conditions were also not successful.



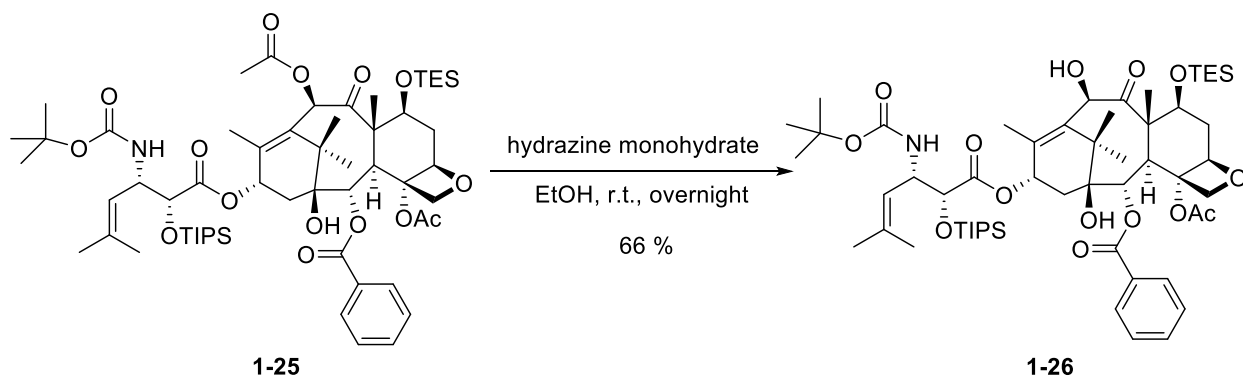
Scheme 1.25 HF/pyridine deprotection to generate **SB-T-1211** in the first synthetic route

In order to synthesize **SB-T-1211** with high purity and improve the yield, a second route was investigated. First, 7-triethylsilylbaccatin III was used to couple with the enantiopure β -lactam **1-11** via the Ojima-Holton protocol. This coupling reaction proceeded very smoothly, and desired product **1-25** was isolated in 94% yield (**Scheme 1.26**).



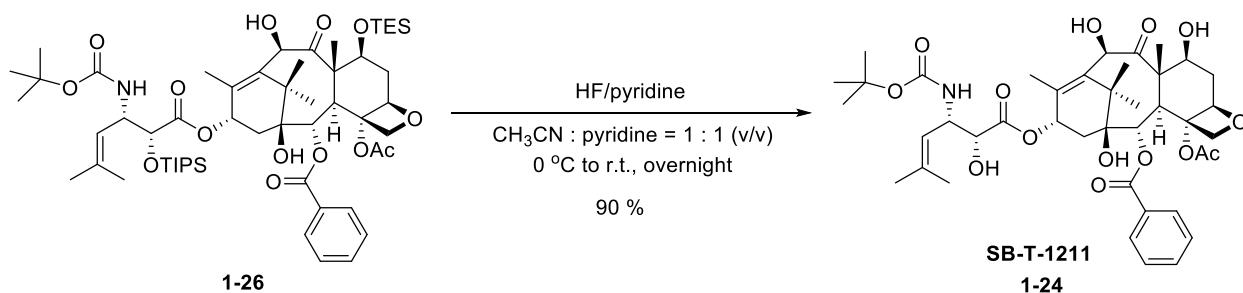
Scheme 1.26 Ojima-Holton coupling to generate **1-25**

Then acetyl group on the C-10 position of the baccatin core was subsequently selectively removed by hydrazine monohydrate at room temperature, affording desired product **1-26** in 66% yield (**Scheme 1.27**).



Scheme 1.27 Selective removal C-10 acetyl group by hydrazine monohydrate

Finally, deprotection of the C-7 TES protecting group and C-2' TIPS protecting group by HF/pyridine gave new-generation taxoid **SB-T-1211** in 90% yield (**Scheme 1.28**). Purity of the new-generation taxoid **SB-T-1211** synthesized in the second route was confirmed by HPLC as 97%. This synthetic route proved to be more efficient than the first one, and the reactions during the synthesis are cleaner and the purifications are thus much easier.

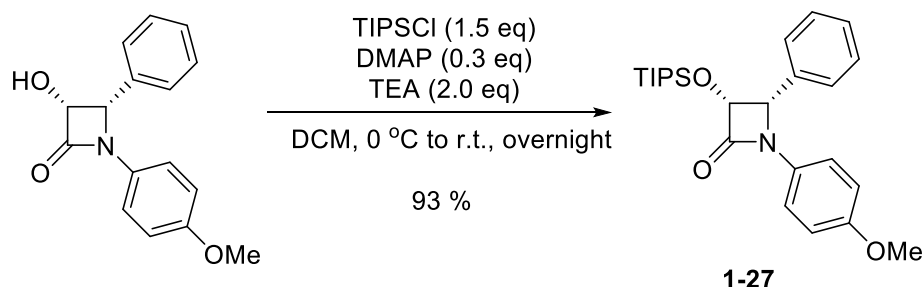


Scheme 1.28 HF/pyridine deprotection to generate **SB-T-1211** in the second synthetic route

§ 1.2.4 Synthesis of New-Generation Taxoid 10-Ac-docetaxel

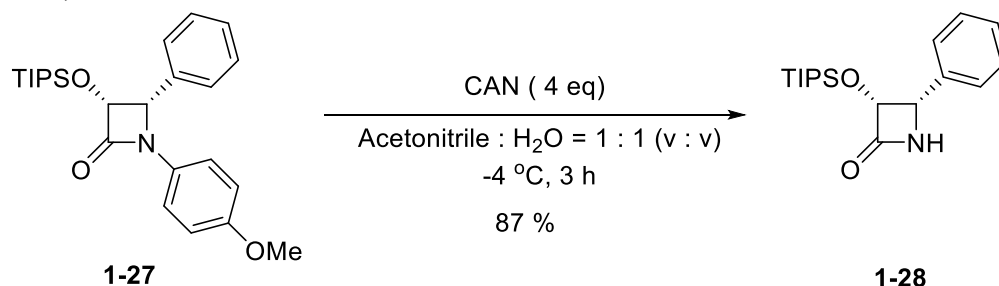
The structure difference between **10-Ac-docetaxel** and paclitaxel is the C-3'N position, *t*-Boc group found in docetaxel as well as new-generation taxoids **SB-T-1214** and **SB-T-1216** is used instead of benzoyl group found in paclitaxel. For the synthesis of 10-Ac-docetaxel, a different β -lactam (*3R,4S*)-*N*-*tert*-butoxycarbonyl-3-*O*-TIPS-4-phenyl- β -lactam is used to couple with 7-TES-baccatin III under Ojima-Holton coupling protocol, followed by deprotections to yield **10-Ac-docetaxel**.

In order to prepare the required (3*R*,4*S*)-*N*-*tert*-butoxycarbonyl-3-*O*-TIPS-4-phenyl- β -lactam, first, enantiopure β -lactam intermediate (3*R*,4*S*)-*N*-4-methoxyphenyl-3-hydroxyl-4-phenyl- β -lactam was reacted with TIPSCl in the presence of TEA and catalytic amount of DMAP to generate the TIPS protected β -lactam **1-27** in 93% yield (**Scheme 1.29**).



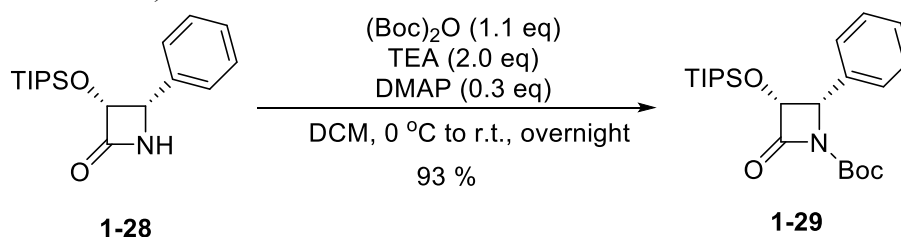
Scheme 1.29 TIPS protection to generate β -lactam **1-27**

Further modification of β -lactam **1-27**, deprotection of the *p*-methoxyphenyl (PMP) moiety in the presence of ceric ammonium nitrate (CAN), gave rise to β -lactam **1-28** in 87% yield (**Scheme 1.30**).



Scheme 1.30 CAN deprotection to generate β -lactam **1-28**

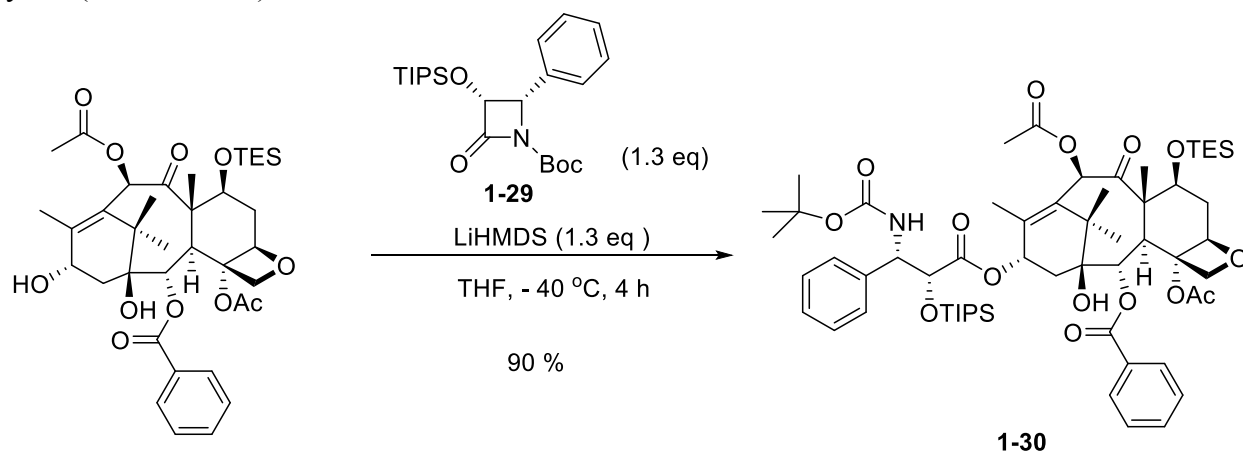
After CAN deprotection, the amine in β -lactam **1-28** was then protected with *t*-Boc group by reacting with Boc anhydride in the presence of TEA and catalytic amount of DMAP to afford final enantiopure β -lactam (3*R*,4*S*)-*N*-*tert*-butoxycarbonyl-3-*O*-TIPS-4-phenyl- β -lactam **1-29** in 93% yield (**Scheme 1.31**).



Scheme 1.31 Boc protection to generate β -lactam **1-29**

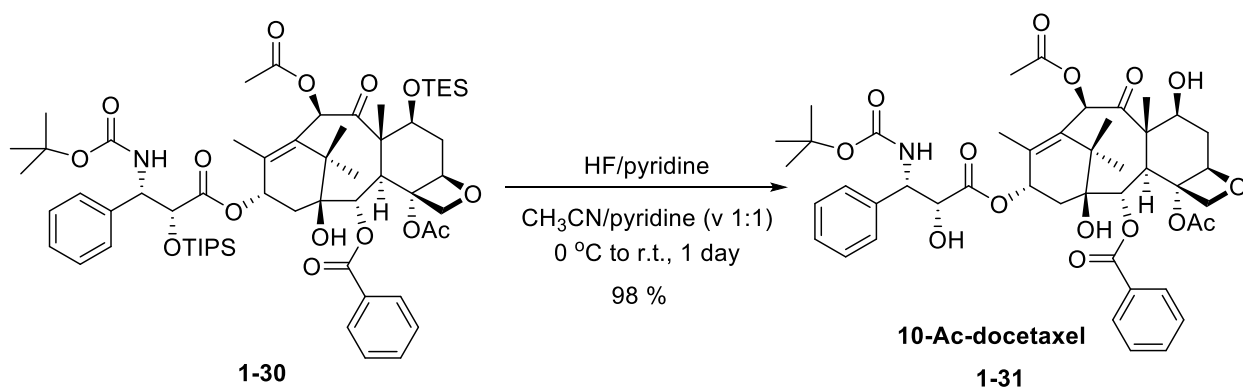
The 7-triethylsilylbaccatin III was subsequently used to react with the enantiopure β -lactam **1-29** via the Ojima-Holton coupling protocol. The C-13 hydroxyl group is deprotonated by

LiHMDS, and acts as a nucleophile to attack the carbonyl carbon of the β -lactam ring, the β -lactam ring is opened and stereochemistry is maintained. The product **1-30** was obtained in 90% yield (**Scheme 1.32**).



Scheme 1.32 Ojima-Holton coupling to generate **1-30**

New-generation taxoid 10-Ac-docetaxel **1-31** was then generated by deprotection of the C-7 TES protecting group and the C-2' TIPS protecting group with HF/pyridine at the same time (**Scheme 1.33**). Desired product was obtained in 98% yield. Purity of the new-generation taxoid 10-Ac-docetaxel **1-31** was checked by HPLC as 97%.



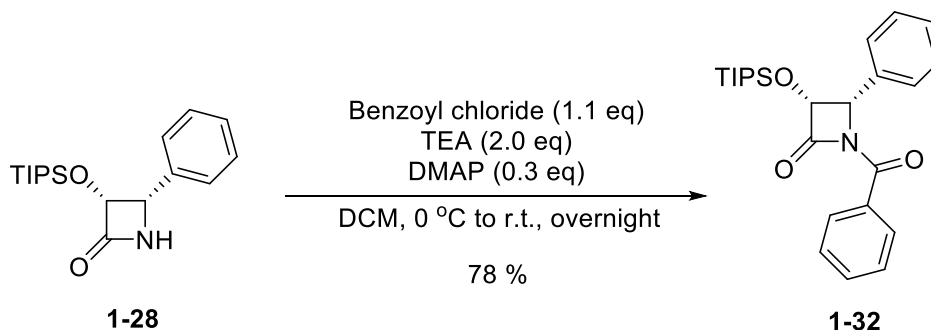
Scheme 1.33 HF/pyridine deprotection to generate **10-Ac-docetaxel**

§ 1.2.5 Synthesis of New-Generation Taxoid SB-T-0035

The structure difference between **SB-T-0035** and paclitaxel is the C-10 position, *N,N*-dimethylcarbamoyl group found in **SB-T-1216** is used instead of acetyl group found in paclitaxel. For the synthesis of **SB-T-0035**, a different β -lactam (3*R*,4*S*)-*N*-benzoyl-3-*O*-TIPS-4-phenyl- β -lactam is used to couple with 7-TES-10-*N,N*-dimethylcarbamoyl-baccatin III **1-18** under Ojima-Holton coupling protocol, followed by deprotections to yield **SB-T-0035**.

The same β -lactam intermediate **1-28** used in the previous synthesis for preparing **10-Ac-docetaxel** was protected with benzoyl group by reacting with benzoyl chloride in the presence of

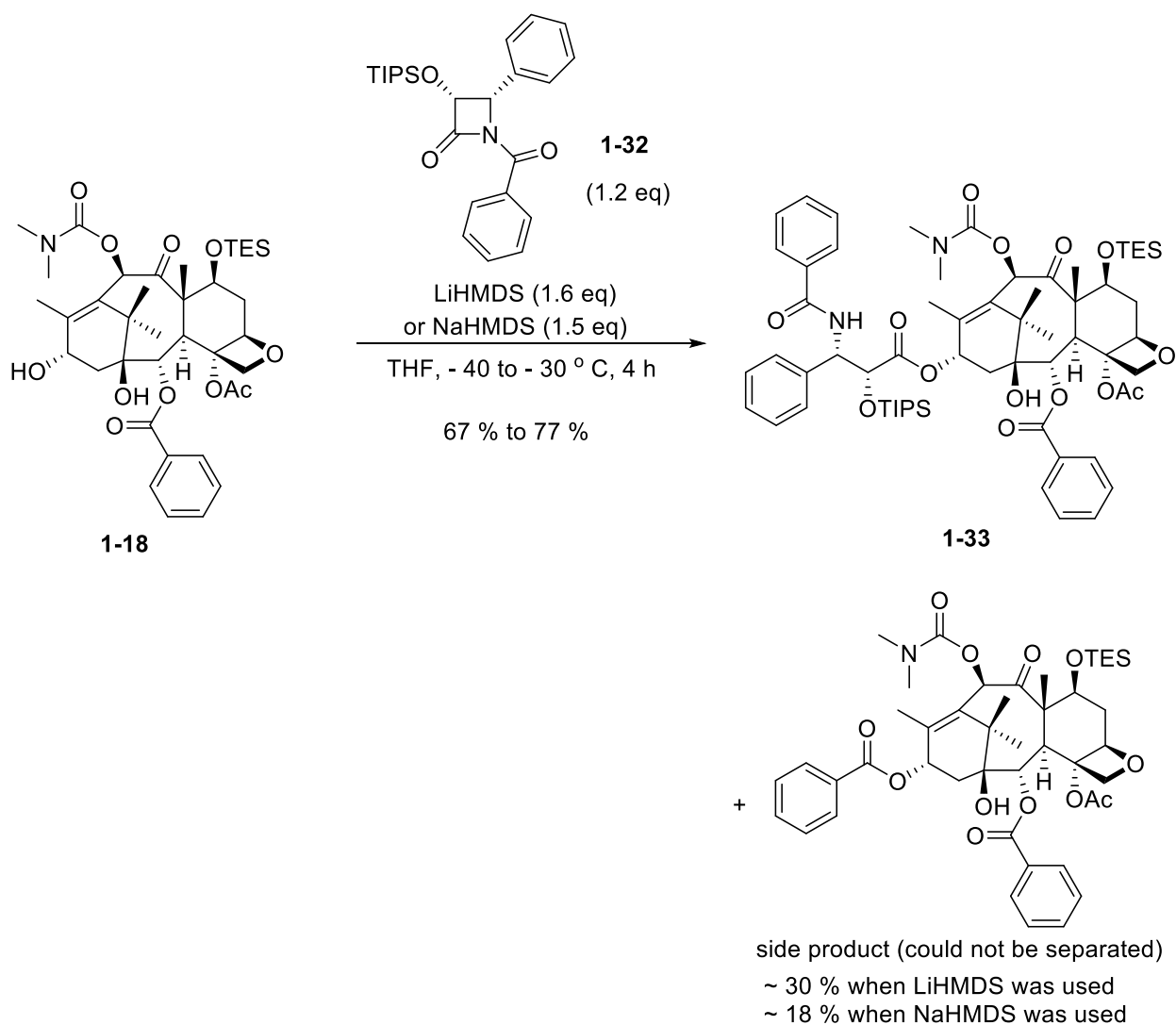
TEA and catalytic amount of DMAP to afford final enantiopure β -lactam (3*R*,4*S*)-*N*-benzoyl-3-*O*-TIPS-4-phenyl- β -lactam **1-32** in 78% yield (**Scheme 1.34**). The yield for this step is not so good compared with Boc protection, because the purity of benzoyl chloride reagent used in this step is not very good even if after fresh distillation.



Scheme 1.34 Benzoyl protection to generate β -lactam **1-32**

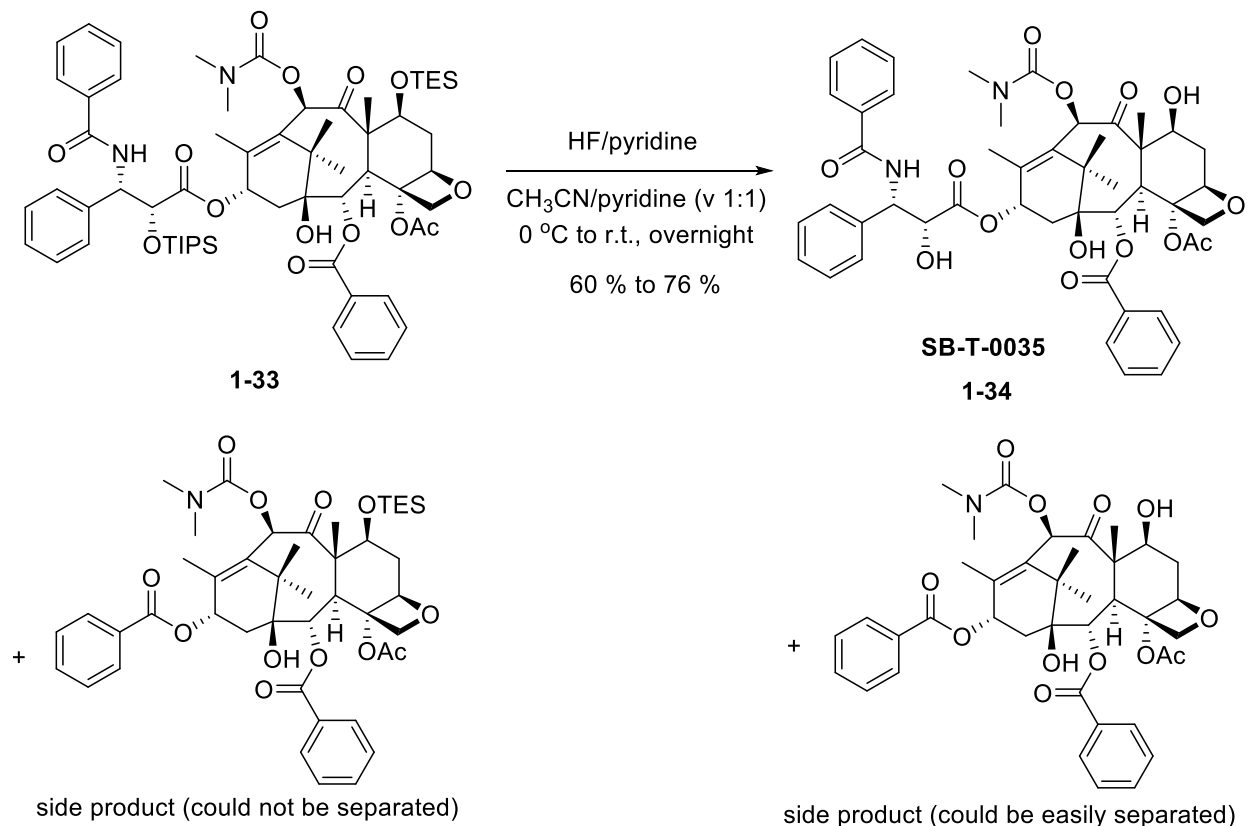
The C-10 modified baccatin core 7-TES-10-*N,N*-dimethylcarbamoyl-baccatin III **1-18** was then used to react with the enantiopure β -lactam **1-32** via the Ojima-Holton coupling protocol (**Scheme 1.35**). Initial trial of this coupling reaction with LiHMDS as the base under -40 °C gave low conversion (67% isolated yield), and generated significant amount of side product 13-benzoyl-10-*N,N*-dimethylcarbamoyl-7-TES-baccatin III (~ 30% in the product based on the integration of ^1H NMR), as the C-13 hydroxyl group after deprotonation could either attack the carbonyl carbon of the β -lactam ring, or the carbonyl carbon of the benzoyl group.

It is also worth to mention that this side product has the exact same R_f value as the product (silica TLC, developing solvents hexanes : ethyl acetate = 3 : 1), and could not be separated by flash column chromatography at this stage. However, after the next HF/pyridine deprotection step, the side product could be easily removed from desired product by column chromatography, since the side product is much more nonpolar than the desired product after deprotection in the next step. The coupling condition was eventually optimized to using NaHMDS as the base and -30 °C as the reaction temperature, which gave better conversion (77% isolated yield), as well as less amount of undesired side product 13-benzoyl-10-*N,N*-dimethylcarbamoyl-7-TES-baccatin III (~ 18% in the product based on the integration of ^1H NMR).



Scheme 1.35 Ojima-Holton coupling to generate **1-33**

Then the silyl protecting groups in mixture **1-33** were deprotected by HF/pyridine (**Scheme 1.36**). After deprotection, side product 13-benzoyl-10-*N,N*-dimethylcarbamoyl-baccatin III becomes much more nonpolar than desired product **SB-T-0035**, and could be easily separated by flash column chromatography. Desired product new-generation taxoid was obtained in 60% yield when LiHMDS was used as the base in the previous coupling step, or 76% yield when NaHMDS was used as the base. Purity of the new-generation taxoid **SB-T-0035** was confirmed by HPLC as 97%.



Scheme 1.36 HF/pyridine deprotection to generate **SB-T-0035**

§ 1.2.6 Biological Evaluation of New-Generation Taxoids

After new generation taxoids were synthesized, they were sent out to our collaborator Professor Jan Kovar at Charles University in Czech Republic for biological testing. In a previous study conducted by Professor Jan Kovar's group, paclitaxel and docetaxel showed IC_{50} of 1.0 nM and 0.5 nM respectively against a sensitive melanoma cell line MDA-MB-435, and IC_{50} of 1000 nM and 300 nM respectively against a resistant ovarian cancer cell line NCI/ADR-RES.⁷⁴ In sharp contrast, new generation taxoid **SB-T-1216** showed IC_{50} of 0.2 nM against sensitive MDA-MB-435 cell line, and IC_{50} of 3.0 nM against resistant NCI/ADR-RES cell line.⁷⁴ It is expected that new generation taxoids, **SB-T-1212N1**, **SB-T-0035**, **10-Ac-docetaxel**, and **SB-T-1211** (**Figure 1.19**), which have modifications at C-10, C-3', and C-3'N positions by combining the structures of paclitaxel, docetaxel, and **SB-T-1216**, would have different cytotoxicity against sensitive and resistant cancer cell lines and may indicate which part of the modification could contribute to the high potency of **SB-T-1216** against resistant cancers.

Figure 1.20 to **Figure 1.27** showed the preliminary biological evaluation results of these new-generation taxoids together with paclitaxel and docetaxel against human breast cancer cell lines SK-BR-3-sensitive, SK-BR-3-resistant, MCF-7-sensitive, MCF-7-resistant cancer cell

lines. These cell lines were selected for systematic comparison of the cytotoxicity of each taxoid against sensitive and resistant strains.

In SK-BR-3-sensitive cell line (set 1, **Figure 1.20**), all taxoids showed good efficacy. At low concentration (3 nM) of the drugs, **SB-T-1216** is the most cytotoxic one, but at higher concentrations (> 30 nM), all other taxoids showed similar activities including paclitaxel, docetaxel, and **SB-T-1211**. In the second set of experiments for this cell line (**Figure 1.21**), **SB-T-1212N1** showed the best activity at 10 nM among all the taxoids, and can almost completely kill all the cancer cells at 30 nM, indicating the importance of the isobutenyl group at the C-3' position of the C-13 side chain. Interestingly, **SB-T-0035** also showed excellent activity at 30 nM, but only moderate activity at 10 nM.

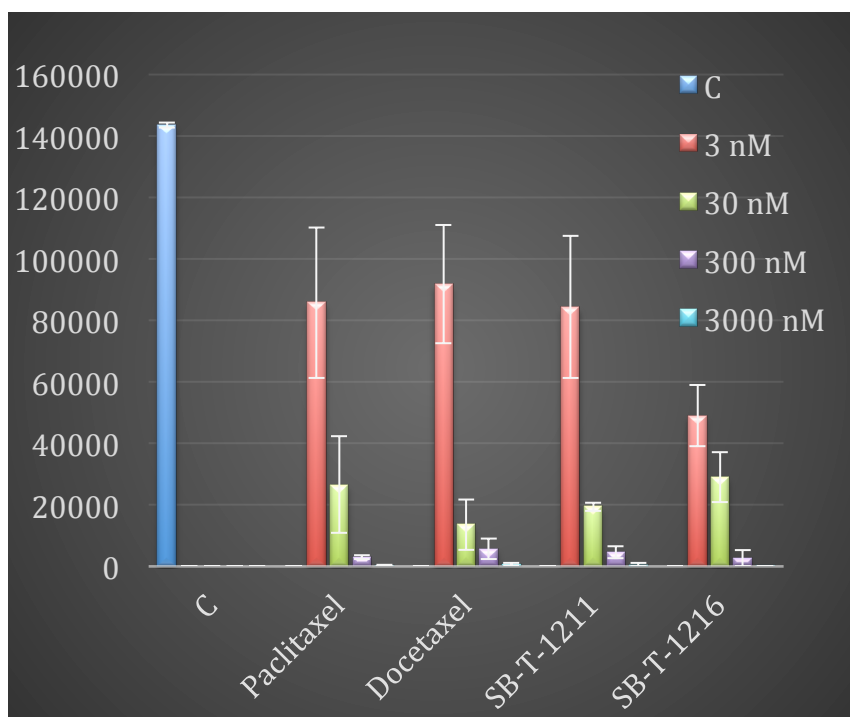


Figure 1.20 Biological evaluation of new generation taxoids against SK-BR-3-sensitive cell line (set 1)

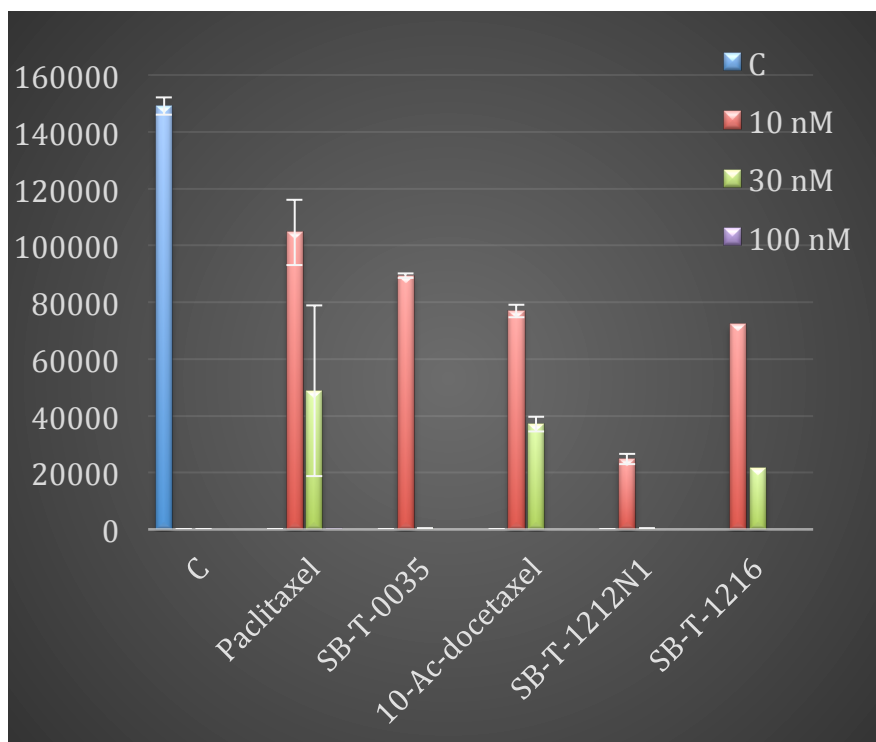


Figure 1.21 Biological evaluation of new generation taxoids against SK-BR-3-sensitive cell line (set 2)

In SK-BR-3-resistant cancer cell line (**Figure 1.22** and **Figure 1.23**), paclitaxel is essentially inactive, even at a very high concentration (300 nM). **SB-T-0035**, which is the only other taxoid has the same side chain as paclitaxel with a modification at C-10 position, behaved better than paclitaxel but worse than other taxoids, showing C-10 modification could help overcome drug-resistance to some extent, which is in agreement with the previous findings in Ojima laboratory during extensive SAR studies.⁵⁰ Interestingly, docetaxel showed much better activity than paclitaxel in this case. **10-Ac-Docetaxel** showed even better potency. These results indicate *t*-Boc group at C-3'N position of the side chain could help to overcome drug-resistance. **SB-T-1212N1** also showed excellent activity in this cell line, suggesting the importance of isobutenyl group at the C-3' position of the C-13 side chain may play a role in overcoming drug-resistant as well.

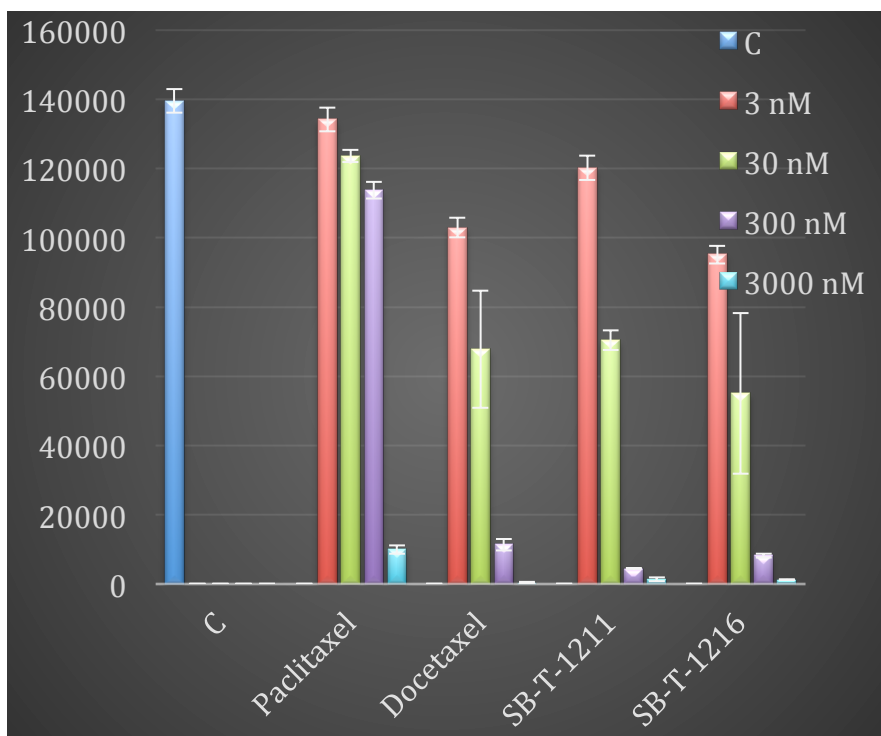


Figure 1.22 Biological evaluation of new generation taxoids against SK-BR-3-resistant cell line (set 1)

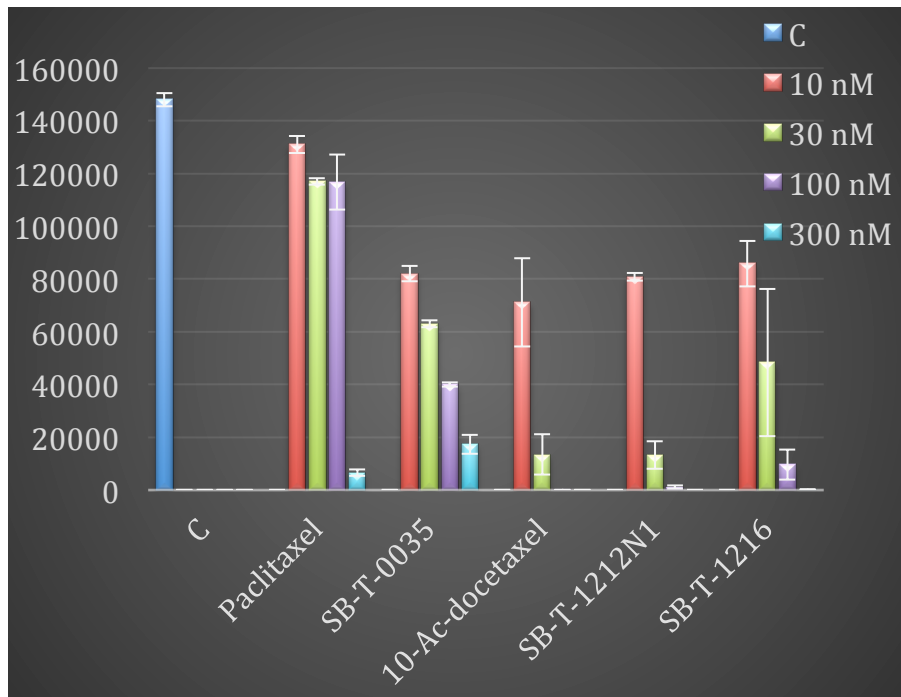


Figure 1.23 Biological evaluation of new generation taxoids against SK-BR-3-resistant cell line (set 2)

In MCF-7-sensitive cancer cell line (**Figure 1.24** and **Figure 1.25**), all taxoids showed good efficacy, including paclitaxel and docetaxel. **SB-T-1216** was found to have the best potency at 3 nM, but not as good as other taxoids at 30 nM, and this trend was also observed in SK-BR-3-sensitive cell line.

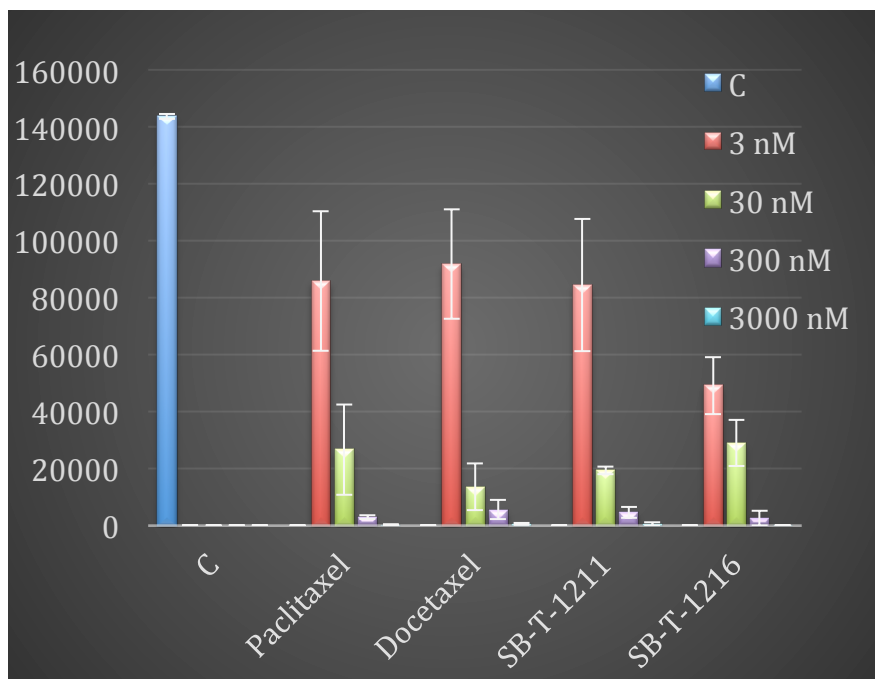


Figure 1.24 Biological evaluation of new generation taxoids against MCF-7-sensitive cell line (set 1)

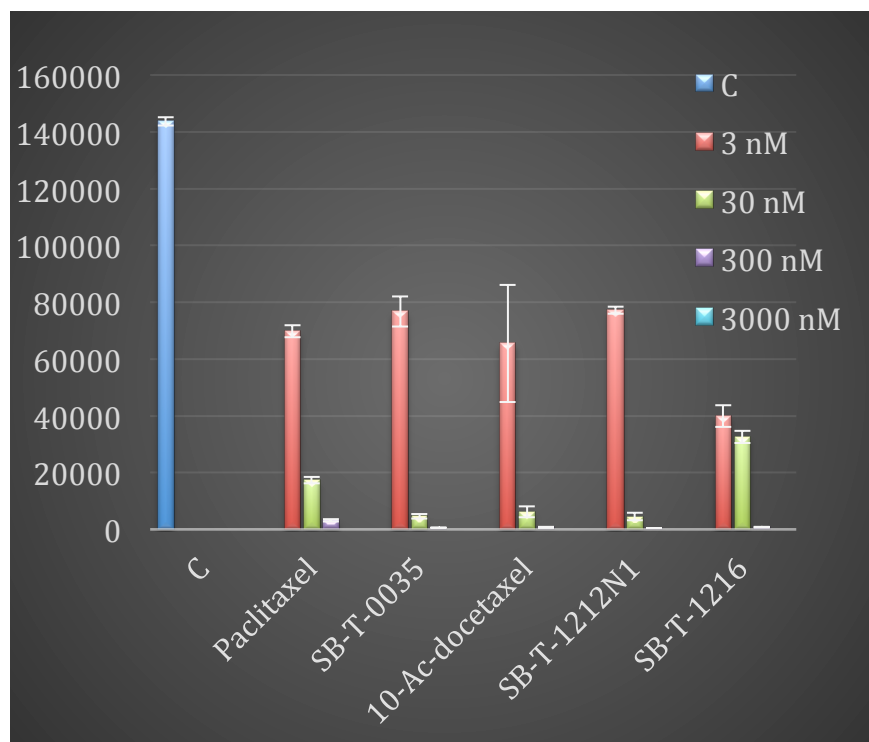


Figure 1.25 Biological evaluation of new generation taxoids against MCF-7-sensitive cell line (set 2)

In MCF-7-resistant cell line (**Figure 1.26** and **Figure 1.27**), paclitaxel was again inactive, and **SB-T-0035** showed potency between paclitaxel and other taxoids, which was observed for SK-BR-3-resistant cell line as well. **SB-T-1216** showed the best potency at 30 nM among all the taxoids. These results again suggest that C-10 modification do help overcome drug-resistant to some extent, but most likely the combination of C-10 modification and C-13 side chain modifications give the most potent taxoids to overcome drug-resistance, presumably because all these positions have close interactions with the drug efflux pump P-glycoprotein.

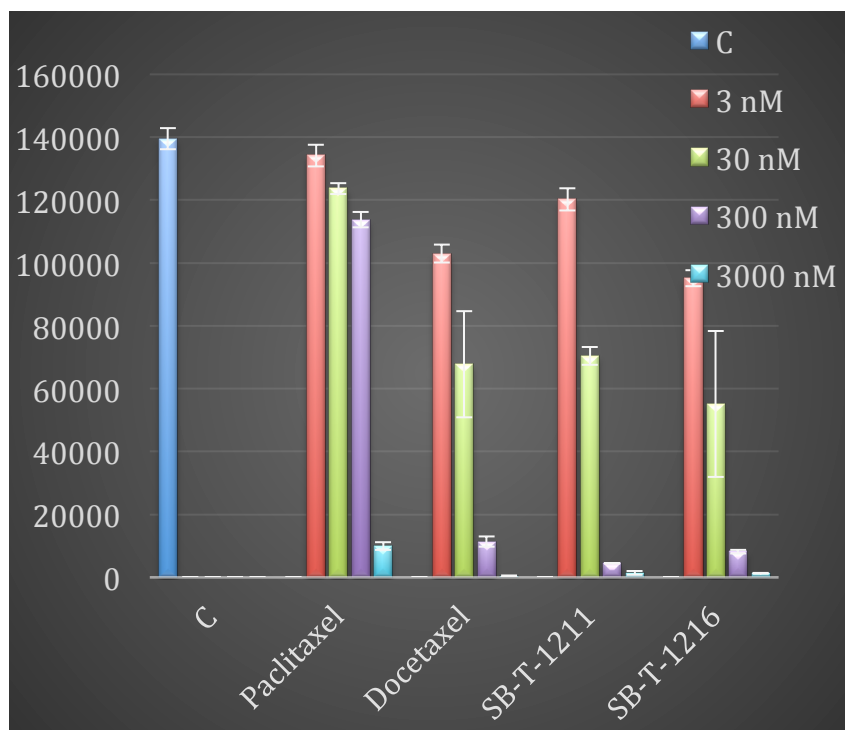


Figure 1.26 Biological evaluation of new generation taxoids against MCF-7 resistant cell line (set 1)

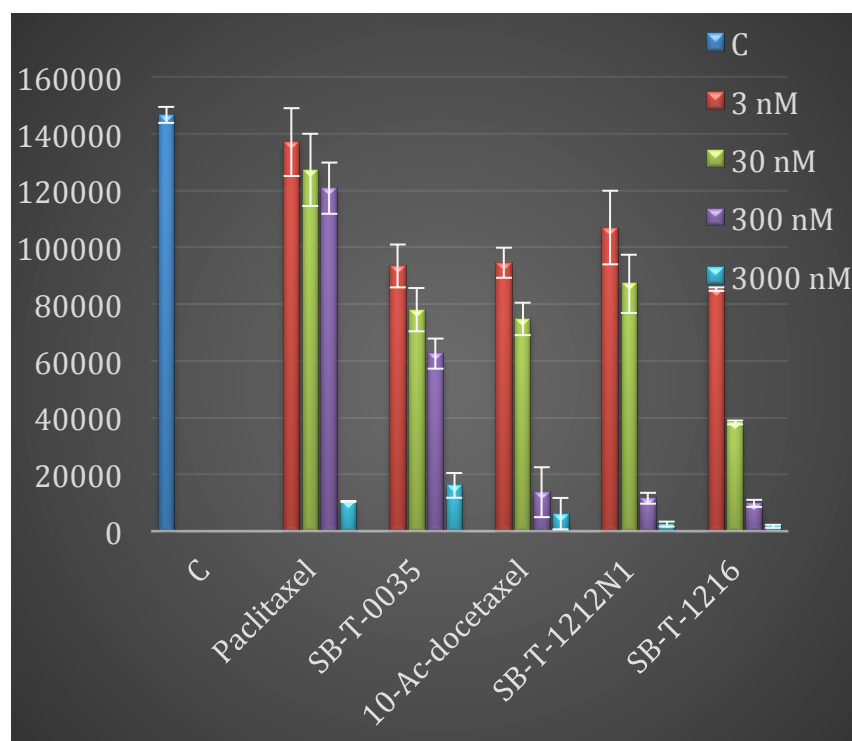


Figure 1.27 Biological evaluation of new generation taxoids against MCF-7 resistant cell line (set 2)

§ 1.3 Summary

New-generation taxoids **SB-T-1214**, **SB-T-1216**, **SB-T-1211**, **10-Ac-docetaxel**, and **SB-T-0035** have been synthesized in good yield and high purity via β -Lactam Synthon Method. These taxoids have been evaluated against both drug-sensitive and drug-resistant cancer cell lines in comparison with paclitaxel and docetaxel. The biological evaluation results suggest combination of *t*-Boc group on the C-3'N-position, 2-methyl-1-propenyl group on the C-3'-position, together with C-10 modification could contribute to the high potency of new-generation taxoids against multi-drug resistant cell lines overexpressing P-glycoprotein.

§ 1.4 Experimental

Caution

Taxoids have been classified as highly potent cytotoxic agents. Thus, all taxoids and structurally related compounds and derivatives must be considered as mutagens and potential reproductive hazards for both males and females. Appropriate precautions (i.e. use of gloves, goggles, lab coat and fume hood) must be taken while handling these compounds.

General Methods

^1H NMR and ^{13}C NMR spectra were measured on a Varian 300 spectrometer or a Bruker 400 MHz, 500 MHz, or 700 MHz NMR spectrometer. Melting points were measured on a Thomas-Hoover capillary melting point apparatus and are uncorrected. Optical rotations were measured on Perkin-Elmer Model 241 polarimeter. TLC analyses were performed on Sorbent Technologies aluminum-backed Silica G TLC plates (Sorbent Technologies, 200 μm , 20 cm \times 20 cm), and were visualized with UV light and stained with sulfuric acid-EtOH, 10% phosphomolybdic acid (PMA)-EtOH, 10% vanillin-EtOH with 1% sulfuric acid, ninhydrin-butanol with 10% AcOH, or DACA stain. Column chromatography was carried out on silica gel 60 (Merck; 230-400 mesh ASTM). Chemical purity was determined with a Shimadzu L-2010A HPLC HT series HPLC assembly, using a Kinetex PFP column (4.6 mm \times 100 mm, 2.6 μm) column, using $\text{CH}_3\text{CN}/\text{water}$ as the solvent system with a flow rate of 1 mL/min.

Materials

All chemicals were purchased from Sigma Aldrich, Fisher Scientific or VWR International and used as received or purified before use by standard methods. Dichloromethane and methanol were dried before use by distillation over calcium hydride under nitrogen. Ether and tetrahydrofuran were dried before use by distillation over sodium-benzophenone under nitrogen. 10-Deacetylbaaccatin III (10-DAB III) was obtained from Indena, S.p.A, Italy. Reaction flasks were dried in a 100 $^\circ\text{C}$ oven and allowed to cool to room temperature in a desiccator over calcium sulfate and assembled under an inert nitrogen gas atmosphere.

Experimental Procedures

Benzyl 2-hydroxyacetate (benzyl glycolate) (**1-1**)⁷⁵

To a 250-mL round-bottom flask 2-hydroxyacetic acid (glycolic acid) (7.34 g, 96.5 mmol) was dissolved in 100 mL acetone. To the mixture, triethylamine (10.6 g, 105 mmol) was added slowly within 20 min. The reaction mixture was allowed to stir at room temperature for 30 min. After that, benzyl bromide (15.0 g, 87.7 mmol) was added dropwise within 30 min. White precipitate came out immediately. After stirring at room temperature overnight, the white precipitate was removed by vacuum filtration. The filtrate was mixed with water (100 mL), and the mixture was extracted with ethyl acetate (3 x 100 mL). The combined organic layer was washed with brine (3 x 60 mL), and dried over anhydrous MgSO₄. The MgSO₄ was subsequently removed by vacuum filtration, and the filtrate was concentrated in vacuo to give benzyl 2-hydroxyacetate (benzyl glycolate) **1-1** (11.1 g, 66.8 mmol) as pale yellow oil in 76% crude yield. ¹H NMR (400 MHz, CDCl₃): δ 4.20 (s, 2H), 5.23 (s, 2H), 7.36 (m, 5H). All data are in agreement with literature values.⁷⁵

Benzyl 2-(triisopropylsiloxy)acetate (**1-2**)⁷⁶

To a solution of benzyl 2-hydroxyacetate (benzyl glycolate) **1-1** (11.1 g, 66.8 mmol) in DCM (100 mL) in a 250-mL round-bottom flask, was added 4-dimethylaminopyridine (DMAP) (816 mg, 6.68 mmol) and followed by adding triethylamine (8.12 g, 80.2 mmol) dropwise. After that, triisopropylsilyl chloride (12.9 g, 66.8 mmol) was added dropwise. White precipitate came out slowly. The reaction mixture was allowed to stir at room temperature overnight. The white precipitate was removed by vacuum filtration. The filtrate was mixed with water (50 mL), and the mixture was extracted with ethyl acetate (3 x 50 mL). The combined organic layer was washed with brine (3 x 50 mL), and dried over anhydrous MgSO₄. The MgSO₄ was subsequently removed by vacuum filtration, and the filtrate was concentrated in vacuo to give crude benzyl 2-(triisopropylsilyloxy)acetate **1-2** as pale yellow oil. The crude was further purified by column chromatography on silica gel (gradient eluent: hexanes/ethyl acetate from 10/1 to 3/1) to give benzyl 2-(triisopropylsiloxy)acetate **1-2** as pale yellow oil (21.5 g, 66.7 mmol) in quantitative yield. ¹H NMR (400 MHz, CDCl₃): δ 1.08 (m, 21H), 4.36 (s, 2H), 5.18 (s, 2H), 7.34 (m, 5H). ¹³C NMR (100 MHz, CDCl₃): δ 12.1, 18.0, 62.3, 66.6, 128.5, 128.6, 128.7, 135.8, 171.6. All data are in agreement with literature values.⁷⁶

2-(Triisopropylsiloxy)acetic acid (**1-3**)⁷⁶

Ethyl acetate was dried over anhydrous MgSO₄, and the MgSO₄ was subsequently removed by vacuum filtration to give dry ethyl acetate. To a 500-mL round-bottom flask, was added benzyl 2-(triisopropylsiloxy)acetate **1-2** (19.5 g, 60.4 mmol) in 200 mL dry ethyl acetate. The flask was evacuated and flushed with nitrogen gas three times and 10% Pd/C (1.62 g, 1.52 mmol) was then added. The flask was evacuated and flushed with nitrogen gas three times again. After that the flask was evacuated and flushed with hydrogen gas three times, kept filled with hydrogen gas,

and was allowed to stir at room temperature for 5 h. Hydrogen gas was consumed quickly at first, and then was consumed slowly. The reaction was monitored by TLC. Upon completion, the reaction mixture was filtered with the aid of Celite to remove the catalyst, and washed with dry ethyl acetate. The filtrate was concentrated in vacuo to give crude 2-(triisopropylsiloxy)acetic acid **1-3** (15.0 g, 64.5 mmol) as pale yellow oil (over 100%, contain solvent ethyl acetate). The crude product was used in next step immediately without further purification. ¹H NMR (400 MHz, CDCl₃): δ 1.13 (m, 21H), 4.29 (s, 2H). All data are in agreement with literature values.⁷⁶

2,5-Dioxopyrrolidin-1-yl 2-(triisopropylsiloxy)acetate (1-4)

To a solution of crude 2-((triisopropylsilyl)oxy)acetic acid (15.0 g, 64.5 mmol) in 100 mL DCM in a 250-mL round-bottom flask, was added 1-ethyl-3-(3-dimethylaminopropyl)carbodiimide hydrochloride (EDCHCl) (13.9 g, 72.5 mmol) and *N*-hydroxysuccinimide (NHS) (7.65 g, 66.5 mmol). The reaction mixture was allowed to stir at room temperature overnight. The reaction was monitored by TLC. Upon completion, the reaction mixture was quenched with saturated ammonium chloride solution in water (50 mL), and extracted with DCM (3 x 50 mL). The combined organic layer was washed with brine (3 x 50 mL), and dried over anhydrous MgSO₄. The MgSO₄ was subsequently removed by vacuum filtration, and the filtrate was concentrated in vacuo to give crude 2,5-dioxopyrrolidin-1-yl 2-(triisopropylsiloxy)acetate **1-4** as pale yellow solid. The crude product was further purified by recrystallization with hexanes to give 2,5-dioxopyrrolidin-1-yl 2-(triisopropylsiloxy)acetate **1-4** (13.6 g, 41.4 mmol) as white solid in 69% yield over two steps. ¹H NMR (400 MHz, CDCl₃): δ 1.13 (m, 21H), 2.87 (s, 4H), 4.67 (s, 2H).

(+)-(1*R*,2*R*)-1-Phenylcyclohexane-*cis*-1,2-diol (1-5)⁷⁷

To a 250-mL round-bottom flask was added the following reagents in the order into water (80 mL) when stirring has already started: potassium ferricyanide (62.4 g, 190 mmol), anhydrous potassium carbonate (26.2 g, 190 mmol), methanesulfonamide (6.01 g, 63.2 mmol), potassium osmate dihydrate (70.0 mg, 0.190 mmol), (DHQD)₂PHAL (985 mg, 1.26 mmol), 1-phenylcyclohexene (10.1 g, 63.8 mmol), and *tert*-butyl alcohol (54 mL). The slurry was stirred vigorously for 2 days. The reaction was monitored by TLC. Upon completion, the reaction mixture was treated with ethyl acetate with stirring to dissolve the product. The organic layer was collected, washed with 2M KOH with vigorous shaking to remove methanesulfonamide, and dried over anhydrous MgSO₄. The MgSO₄ was subsequently removed by vacuum filtration, and the filtrate was concentrated in vacuo to give crude (+)-(1*R*,2*R*)-1-phenylcyclohexane-*cis*-1,2-diol **1-5** (12.2 g, 63.5 mmol) as white solid in quantitative yield. ¹H NMR (400 MHz, CDCl₃): δ 1.46 (m, 2H), 1.71 (m, 3H), 1.85 (m, 3H), 4.01 (m, 1H), 7.27 (m, 1H), 7.39 (m, 2H), 7.52 (m, 2H). All data are in agreement with literature values.⁷⁷

(-)-(1*R*,2*S*)-*trans*-2-Phenyl-1-cyclohexanol (1-6)⁷⁷

Slurry of activated W-2 Raney nickel in wet ethanol was prepared (~180 mL settled Ra-Ni), and was added to a 1000-mL 3-necked round-bottom flask with the aid of anhydrous ethanol in

portions. Crude (+)-(1*R*,2*R*)-1-phenylcyclohexane-*cis*-1,2-diol **1-5** (12.2 g, 63.5 mmol) from the previous step in 60 mL anhydrous ethanol was then added. The reaction mixture was stirred vigorously by a mechanical stirring bar, and refluxed for 4 h. The reaction was monitored by TLC. Upon the reaction is completed, the reaction mixture was allowed to cool to room temperature and transferred with anhydrous ethanol and filtered. The Raney nickel sludge was transferred with water to a specific waste container. The filtrate was concentrated and extracted with ethyl acetate (3 x 100 mL) and washed with brine (3 x 50 mL). The combined organic layer was dried over anhydrous MgSO₄. The MgSO₄ was subsequently removed by vacuum filtration, and the filtrate was concentrated in vacuo to give crude (-)-(1*R*,2*S*)-*trans*-2-phenyl-1-cyclohexanol **1-6** (9.93g, 56.4 mmol) as pale yellow solid in 89% yield. The crude product was further purified by recrystallization with pentane to give (-)-(1*R*,2*S*)-*trans*-2-phenyl-1-cyclohexanol **1-6** (7.72 g, 43.8 mmol) as white solid in 69% yield. ¹H NMR (400 MHz, CDCl₃): δ 1.40 (m, 4H), 1.76 (m, 1H), 1.1.86 (m, 2H), 2.12 (m, 1H), 2.42 (m, 1H), 3.68 (m, 1H), 7.24 (m, 3H), 7.35 (m, 2H). All data are in agreement with literature values.⁷⁷

(1*R*,2*S*)-*trans*-2-Phenylcyclohexyl-1-triisopropylsiloxyacetate (1-7, chiral ester)³²

To a solution of (-)-(1*R*,2*S*)-*trans*-2-phenyl-1-cyclohexanol **1-6** (6.07 g, 34.5 mmol) and DMAP (6.32 g, 51.8 mmol) dissolved in toluene (100 mL) in a 250-mL round-bottom flask, was added 2,5-dioxopyrrolidin-1-yl 2-((triisopropylsilyl)oxy)acetate **1-4** (13.6 g, 41.4 mmol). The reaction was stirred at room temperature under inert condition for 24 hours and monitored by TLC. Upon completion, the reaction was quenched with saturated ammonium chloride solution in water (50 mL), and extracted with ethyl acetate (3 x 100 mL). The combined organic layer was washed with brine (3 x 50 mL), and dried over anhydrous MgSO₄. The MgSO₄ was subsequently removed by vacuum filtration, and the filtrate was concentrated in vacuo to give crude (1*R*,2*S*)-*trans*-2-phenylcyclohexyl-1-triisopropylsiloxyacetate **1-7** as pale yellow oil. The crude product was further purified by column chromatography on silica gel (gradient eluent: hexanes/ethyl acetate from 100/1 to 40/1) to give (1*R*,2*S*)-*trans*-2-phenylcyclohexyl-1-triisopropylsiloxyacetate **1-7** as colorless oil (11.7 g, 30.0 mmol) in 87% yield. ¹H NMR (400 MHz, CDCl₃): δ 1.02 (m, 21H), 1.38 (m, 4H), 1.76 (m, 3H), 2.15 (m, 1H), 2.65 (m, 1H), 3.90 (d, J = 16.6 Hz, 1H), 4.07 (d, J = 16.6 Hz, 1H), 5.09 (m, 1H), 7.22 (m, 5H). ESI-MS: 391.3 [M+H]⁺. All data are in agreement with literature values.³²

(*E*)-4-Methoxy-*N*-(3-methylbut-2-en-1-ylidene)aniline (1-8)⁶⁷

To a solution of recrystallized *p*-anisidine (1.85 g, 15.0 mmol) and anhydrous Na₂SO₄ (4.26 g, 30.0 mmol) in DCM (75 mL) in a 250-mL round-bottom flask cooled to 0 °C by an ice bath, was added 3-methylbut-2-enal (1.26 g, 15.0 mmol) dropwise. The reaction mixture was allowed to stir at room temperature under inert atmosphere in dark for 3 h. The reaction was monitored via TLC. Upon completion, the reaction mixture was filtered to remove sodium sulfate. The filtrate was evaporated in vacuo at room temperature in dark to give crude (*E*)-4-methoxy-*N*-(3-methylbut-2-en-1-ylidene)aniline **1-8** (2.83 g, 15.0 mmol) as pale yellow oil in quantitative yield,

which was then used immediately in the subsequent step without further purification. ¹H NMR (400 MHz, CDCl₃): δ 1.96 (s, 3H), 2.01 (s, 3H), 3.81 (s, 3H), 5.29 (s, 1H), 6.88 (m, 2H), 7.11 (m, 2H), 8.38 (d, J = 9.6 Hz, 1H). All data are in agreement with literature values.⁶⁷

(3*R*,4*S*)-1-(4-Methoxyphenyl)-4-(2-methylprop-1-en-1-yl)-3-(triisopropylsiloxy)azetidin-2-one (1-9)⁶⁷

To a dry 100-mL round-bottom flask under inert condition, was added dry THF (15 mL), and cooled to -78 °C by an acetone/dry ice bath. LDA (2.0 M solution in THF/heptane/ethyl benzene) (3.95 mL, 7.90 mmol) was then added dropwise. To the mixture, a solution of chiral ester (1*R*,2*S*)-*trans*-2-phenylcyclohexyl-triisopropylsilyl-oxyacetate **1-7** (2.00 g, 5.13 mmol) in dry THF (15 mL) was added slowly within 1 h. The reaction mixture was allowed to stir at -78 °C for another 1 h. A solution of crude imine (*E*)-4-methoxy-*N*-(3-methylbut-2-en-1-ylidene)aniline **1-8** (1.19 g, 6.31 mmol) in dry THF (15 mL) was then added very slowly within 3 h. The reaction mixture was allowed to stir at -78 °C for another 3 h. LiHMDS (1.0 M solution in methyl *tert*-butyl ether) (5.13 mL) was then added dropwise. The reaction mixture was stirred for another 1 h, and then allowed to slowly warm up to room temperature overnight. Upon the reaction is completed, the reaction mixture was quenched with saturated NH₄Cl solution in water (30 mL), and extracted with ethyl acetate (3 x 50 mL). The combined organic layer was washed with brine (3 x 50 mL), and dried over anhydrous MgSO₄. The MgSO₄ was subsequently removed by vacuum filtration, and the filtrate was concentrated in vacuo to give crude **1-9** as yellow oil. The crude product was further carefully purified by column chromatography on silica gel (gradient eluent: hexanes/ethyl acetate from 50/1 to 4/1) to give (3*R*,4*S*)-1-(4-methoxyphenyl)-4-(2-methylprop-1-en-1-yl)-3-(triisopropylsiloxy)azetidin-2-one **1-9** as pale yellow solid (1.16 g, 2.87 mmol) in 56% yield. ¹H NMR (400 MHz, CDCl₃): δ 1.06 (m, 21H), 1.79 (d, J = 1.2 Hz, 3H), 1.84 (d, J = 1.2 Hz, 3H), 3.77 (s, 3H), 4.80 (dd, J = 10.0 Hz, 5.0 Hz, 1H), 5.05 (d, J = 5.0 Hz, 1H), 5.33 (m, 1H), 6.82 (m, 2H), 7.32 (m, 2H). All data are in agreement with literature values.⁶⁷

(3*R*,4*S*)-4-(2-Methylprop-1-en-1-yl)-3-(triisopropylsiloxy)azetidin-2-one (1-10)⁶⁷

To a 100-mL round-bottom flask (3*R*,4*S*)-1-(4-methoxyphenyl)-4-(2-methylprop-1-en-1-yl)-3-(triisopropylsiloxy)azetidin-2-one **1-9** (450 mg, 1.11 mmol) was dissolved in acetonitrile (30 mL) and cooled to -4 °C by a salt ice bath. To this solution was added a solution of cerium ammonium nitrate (CAN) (2.44g, 4.46 mmol) dissolved in H₂O (30 mL) dropwise via an addition funnel within 1 h. The reaction temperature of -4 °C was maintained throughout the reaction. The reaction was monitored via TLC. Upon completion, the reaction mixture was quenched with saturated aqueous Na₂SO₃ solution (30 mL). The mixture was extracted with ethyl acetate (3 x 80 mL). The combined organic layer was washed with brine (3 x 50 mL), and dried over anhydrous MgSO₄. The MgSO₄ was subsequently removed by vacuum filtration, and the filtrate was concentrated in vacuo to give crude **1-10** as brown oil. The crude product was further purified by column chromatography on silica gel (gradient eluent: hexanes/ethyl acetate

from 10/1 to 1/1) to give (3*R*,4*S*)-4-(2-methylprop-1-en-1-yl)-3-(triisopropylsiloxy)azetidin-2-one **1-10** as pale yellow solid (251 mg, 0.845 mmol) in 76% yield. ¹H NMR (400 MHz, CDCl₃): δ 1.03 (m, 21H), 1.69 (d, *J* = 1.6 Hz, 3H), 1.76 (d, *J* = 1.4 Hz, 3H), 4.44 (dd, *J* = 9.6 Hz, 4.8 Hz, 1H), 5.00 (dd, *J* = 4.7 Hz, 2.3 Hz, 1H), 5.32 (m, 1H), 5.79 (br. s, 1H). All data are in agreement with literature values.⁶⁷

(3*R*,4*S*)-1-*tert*-Butoxycarbonyl-3-triisopropylsilyloxy-4-(2-methyl-1-propenyl)azetidin-2-one (1-11)⁶⁷

To (3*R*,4*S*)-4-(2-methylprop-1-en-1-yl)-3-(triisopropylsiloxy)azetidin-2-one **1-10** (250 mg, 0.842 mmol) dissolved in 5 mL DCM in a 25-mL round-bottom flask, was added DMAP (31 mg, 0.25 mmol) and triethylamine (170 mg, 1.68 mmol). The reaction mixture was cooled to 0 °C under inert conditions, and was added di-*tert*-butyl dicarbonate (202 mg, 0.93 mmol). The reaction was allowed to stir at room temperature overnight and monitored via TLC. Upon the reaction was completed, the reaction mixture was quenched with saturated NH₄Cl solution in water. The mixture was extracted with ethyl acetate (3 x 15 mL). The combined organic layer was washed with brine (3 x 15 mL), and dried over anhydrous MgSO₄. The MgSO₄ was subsequently removed by vacuum filtration, and the filtrate was concentrated in vacuo to give crude **1-11** as pale yellow oil. The crude product was further purified by column chromatography on silica gel (gradient eluent: hexanes/ethyl acetate from 50/1 to 10/1) to give (3*R*,4*S*)-1-*tert*-butoxycarbonyl-3-triisopropylsilyloxy-4-(2-methyl-1-propenyl)azetidin-2-one **1-11** as colorless oil (290 mg, 0.730 mmol) in 87% yield. ¹H NMR (400 MHz, CDCl₃): δ 1.02 (m, 21H), 1.48 (s, 9H), 1.76 (d, *J* = 1.2 Hz, 3H), 1.79 (d, *J* = 1.2 Hz, 3H), 4.75 (dd, *J* = 9.9 Hz, 5.7 Hz, 4H), 4.96 (d, *J* = 5.7 Hz, 1H), 5.26 (m, 1H). ¹³C NMR (100 MHz, CDCl₃): δ 12.03, 17.74, 18.47, 26.30, 28.26, 57.03, 118.64, 139.85, 148.56, 166.79. All data are in agreement with literature values.⁶⁷

Enzymatic resolution of β-lactam ((+)-1-12)⁷⁸

To racemic β-lactam (±)-1-(4-methoxyphenyl)-3-acetoxy-4-(2-methylprop-1-enyl)azetidin-2-one (1.90 g, 6.57 mmol) dissolved in CH₃CN (33 mL) in a 1000-mL three-neck round-bottom flask, was added 330 mL of PBS buffer (pH 7.5). The mixture was heated up to 40 °C in an oil bath, and PS Amano lipase (0.381 g) was then added into the mixture. The reaction mixture was stirred vigorously with a mechanical stirrer and the temperature was maintained at 40 °C. The reaction was monitored by ¹H NMR. After 7 days, the ¹H NMR result indicates the ratio of (+)-1-(4-methoxyphenyl)-3-acetoxy-4-(2-methylprop-1-enyl)azetidin-2-one **(+)-1-12** and (-)-1-(4-methoxyphenyl)-3-hydroxy-4-(2-methylprop-1-enyl)azetidin-2-one **(-)-1-13** is around 10:7, so the temperature was raised from 40 °C to 45 °C. After another 7 days, the ¹H NMR result indicates the ratio of **(+)-1-12** and **(-)-1-13** is 1:1. The residual lipase was filtered over Celite and washed with DCM. The filtrate was extracted using DCM (3 x 200 mL). The organic layers were washed three times with brine, and dried over anhydrous MgSO₄. The MgSO₄ was subsequently removed by vacuum filtration, and the filtrate was concentrated in vacuo. The resulting crude was purified via column chromatography on silica gel (gradient eluent:

hexanes/ethyl acetate from 10/1 to 1/1) to yield (+)-1-(4-methoxyphenyl)-3-acetoxy-4-(2-methylprop-1-enyl)azetidin-2-one **(+)-1-12** as a white solid (904 mg, 3.13 mmol) in 48% yield with 100% ee, and (-)-1-(4-methoxyphenyl)-3-hydroxy-4-(2-methylprop-1-enyl)azetidin-2-one **(-)-1-13** as a pale yellow solid. To measure optical purity, to (+)-1-(4-methoxyphenyl)-3-acetoxy-4-(2-methylprop-1-enyl)azetidin-2-one **(+)-1-12** (9 mg, 0.031 mmol) dissolved in THF (0.5 mL), cooled to 0 °C, was added NaOH (12 mg, 0.30 mmol) in distilled water (0.5 mL). After 2 h, the reaction was quenched with 1 mL saturated NH₄Cl in water and extracted with DCM (4 x 10 mL). The organic layers were collected, dried over MgSO₄. The MgSO₄ was subsequently removed by vacuum filtration, and the filtrate was concentrated in vacuo to yield (+)-1-(4-methoxyphenyl)-3-hydroxy-4-(2-methylprop-1-enyl)azetidin-2-one **(+)-1-13** as a pale yellow solid. The (+) and (-) enantiomers of 1-(4-methoxyphenyl)-3-hydroxy-4-(2-methylprop-1-enyl)azetidin-2-one were dissolved in isopropanol and analyzed for optical purity using HPLC (column: Chiracel OD-H; method: isocratic program; flow rate: 0.6 mL/min; eluent: 90%/10% hexanes/isopropanol). The retention time of (-)-1-(4-methoxyphenyl)-3-hydroxy-4-(2-methylprop-1-enyl)azetidin-2-one **(-)-1-13** is 20 min, and the retention time of (+)-1-(4-methoxyphenyl)-3-hydroxy-4-(2-methylprop-1-enyl)azetidin-2-one **(+)-1-13** is 26 min. (+)-1-(4-methoxyphenyl)-3-acetoxy-4-(2-methylprop-1-enyl)azetidin-2-one **(+)-1-12** ¹H NMR (500 MHz, CDCl₃): δ 1.79 (s, 3H), 1.82 (s, 3H), 2.11 (s, 3H), 3.78 (s, 3H), 4.96 (dd, J = 9.4 Hz, 4.8 Hz, 1H), 5.13 (d, J = 9.4 Hz, 1H), 5.80 (d, J = 4.8 Hz, 1H), 6.85 (d, J = 8.9 Hz, 2H), 7.31 (J = 8.9 Hz, 2H). (-)-1-(4-methoxyphenyl)-3-hydroxy-4-(2-methylprop-1-enyl)azetidin-2-one **(-)-1-13** ¹H NMR (500 MHz, CDCl₃): δ 1.85 (s, 3H), 1.86 (s, 3H), 3.12 (d, J = 7.6 Hz, 1H), 3.78 (s, 3H), 4.89 (dd, J = 8.9 Hz, 5.1 Hz, 1H), 5.03 (dd, J = 7.6 Hz, 5.1 Hz, 1H), 5.29 (m, 1H), 6.84 (m, 2H), 7.31 (m, 2H). All data are in agreement with literature values.⁷⁸

(+)-1-(4-Methoxyphenyl)-3-hydroxy-4-(2-methylprop-1-enyl)azetidin-2-one ((+)-1-13)⁷⁹

To (+)-1-(4-methoxyphenyl)-3-acetoxy-4-(2-methylprop-1-enyl)azetidin-2-one **(+)-1-12** (100 mg, 0.346 mmol; 794 mg, 2.75 mmol) dissolved in THF (3 mL; 24 mL), cooled to 0 °C, was added NaOH (138 mg, 3.46 mmol; 1.10 g, 27.5 mmol) dissolved in distilled water (3 mL; 24 mL). After 2 h, the reaction was quenched with 10 mL saturated NH₄Cl and the mixture was extracted with CH₂Cl₂ (4 x 30 mL). The organic layers were collected, and dried over MgSO₄. The MgSO₄ was subsequently removed by vacuum filtration, and the filtrate was concentrated in vacuo. The resulting crude was combined and purified via column chromatography on silica gel (gradient eluent: hexanes/ethyl acetate from 10/1 to 1/1) to yield (+)-1-(4-methoxyphenyl)-3-hydroxy-4-(2-methylprop-1-enyl)azetidin-2-one **(+)-1-13** as a white solid (671 mg, 2.71 mmol) in 88% combined yield. ¹H NMR (500 MHz, CDCl₃) δ 1.860 (s, 3H), 1.862 (s, 3H), 2.66 (d, J = 7.7 Hz, 1H), 3.78 (s, 3H), 4.89 (dd, J = 8.8 Hz, 5.1 Hz, 1H), 5.02 (dd, J = 7.7 Hz, 5.1 Hz, 1H), 5.26 (m, 1H), 6.85 (m, 2H), 7.31 (m, 2H). All data are in agreement with literature values.⁷⁹

(+)-1-(4-Methoxyphenyl)-3-triisopropylsiloxy-4-(2-methylprop-1-enyl)azetidin-2-one (1-9)⁷⁹

To a solution of (+)-1-(4-methoxyphenyl)-3-hydroxyl-4-(2-methylprop-1-enyl)azetidin-2-one (**1-13**) (671 mg, 2.71 mmol) and DMAP (114 mg, 0.934 mmol) dissolved in DCM (30 mL) cooled to 0 °C, was added TEA (476 mg, 4.70 mmol) followed by the dropwise addition of chlorotriisopropylsilane (713 mg, 3.70 mmol). The reaction mixture was stirred at room temperature and the reaction was monitored via TLC. After overnight, the reaction was quenched with saturated NH₄Cl (20 mL) and the mixture was extracted with ethyl acetate (3 x 50 mL). The organic layer was washed three times with brine, and dried over anhydrous MgSO₄. The MgSO₄ was subsequently removed by vacuum filtration, and the filtrate was concentrated in vacuo. The resulting crude was purified via column chromatography on silica gel (gradient eluent: hexanes/ethyl acetate from 10/1 to 4/1) to yield (+)-1-(4-methoxyphenyl)-3-triisopropylsiloxy-4-(2-methylprop-1-enyl)azetidin-2-one **1-9** as a white solid (990 mg, 2.45 mmol) in 90% yield. ¹H NMR (500 MHz, CDCl₃) δ 1.13 (m, 21H), 1.847 (s, 3H), 1.849 (s, 3H), 3.77 (s, 3H), 4.80 (dd, J = 10.0 Hz, 5.0 Hz, 1H), 5.06 (d, J = 5.0 Hz, 1H), 5.32 (m, 1H), 6.84 (m, 2H), 7.31 (m, 2H). All data are in agreement with literature values.⁷⁹

10-Deacetyl-7-triethylsilylbaccatin III (**1-14**)²⁷

To a 25-mL round-bottom flask was added 10-DAB III (500 mg, 0.917 mmol) and imidazole (272 mg, 4.00 mmol). The flask was purged with nitrogen gas and 10 mL anhydrous DMF was added. The mixture was dissolved and cooled to 0 °C in an ice bath. Then chlorotriethylsilane (0.5 mL, 2.98 mmol) was added dropwise. The reaction was monitored by TLC (hexanes/ethyl acetate = 1/1, stain with 5% sulfuric acid in ethanol). Upon completion after 30 min, the reaction was quenched with 5 mL saturated ammonium chloride solution in H₂O and diluted with 20 mL H₂O. The aqueous layer was extracted with ethyl acetate (3 x 20 mL). The combined organic layer was washed with brine (3 x 20 mL), and dried over anhydrous MgSO₄. The MgSO₄ was subsequently removed by vacuum filtration, and the filtrate was concentrated in vacuo to give crude product **1-14** as colorless oil. The crude product was further purified by column chromatography on silica gel (gradient eluent: hexanes/ethyl acetate from 4/1 to 1/1) to give 10-deacetyl-7-triethylsilylbaccatin III **1-14** as white solid (562 mg, 0.853 mmol) in 93% yield. ¹H NMR (400 MHz, CDCl₃): δ 0.55 (m, 6H, Si(CH₂CH₃)₃), 0.94 (t, J = 8.0 Hz, 9H, Si(CH₂CH₃)₃), 1.08 (s, 6H, 16-Me, 17-Me), 1.55 (s, 1H, 1-OH), 1.73 (s, 3H, 19-Me), 1.90 (m, 1H, 6-H), 2.01 (d, J = 5.0 Hz, 1H, 13-OH), 2.08 (s, 3H, 18-Me), 2.26 (m, 2H, 14-CH₂), 2.28 (s, 3H, OAc), 2.47 (m, 1H, 6-H), 3.95 (d, J = 6.8 Hz, 1H, 3-H), 4.16 (d, J = 8.3 Hz, 1H, 20-H), 4.25 (d, J = 2.1 Hz, 1H, 10-OH), 4.31 (d, J = 8.3 Hz, 1H, 20-H), 4.41 (dd, J = 10.6 Hz, 6.7 Hz, 1H, 7-H), 4.87 (m, 1H, 13-H), 4.95 (dd, J = 9.5 Hz, 1.8 Hz, 1H, 5-H), 5.17 (d, J = 2.1 Hz, 1H, 10-H), 5.60 (d, J = 7.0 Hz, 1H, 2-H), 7.47 (t, J = 7.8 Hz, 2H, Bz), 7.60 (m, 1H, Bz), 8.10 (m, 2H, Bz). ¹³C NMR (100 MHz, CDCl₃): δ 5.2, 6.8, 9.9, 15.2, 19.5, 22.6, 26.9, 37.3, 38.6, 42.7, 47.0, 58.0, 68.0, 73.0, 74.7, 74.8, 76.6, 78.8, 80.8, 84.3, 128.6, 129.4, 130.1, 133.6, 135.2, 141.7, 167.1, 170.8, 210.3. All data are consistent with the reported values.²⁷

10-Cyclopropanecarbonyl-10-deacetyl-7-triethylsilylbaccatin III (**1-15**)⁵⁰

To a 50-mL round-bottom flask was added 10-deacetyl-7-triethylsilylbaccatin III **1-14** (536 mg, 0.813 mmol). The flask was purged with nitrogen gas and 16 mL freshly distilled anhydrous THF was added. The starting material was dissolved and cooled to -40 °C in an acetone/dry ice bath by adding small amount of dry ice into acetone, and monitored using a thermometer. LiHMDS (0.90 mL, 0.90 mmol) was added dropwise, and then cyclopropanecarbonyl chloride (94 μ L, 0.976 mmol) was added dropwise. The reaction was monitored by TLC (DCM/MeOH = 20/1, stain with 5% sulfuric acid in ethanol). Upon completion after 30 min, the reaction was quenched with 10 mL saturated ammonium chloride solution and then diluted with 20 mL H₂O. The aqueous layer was extracted with ethyl acetate (3 x 50 mL). The combined organic layer was washed with brine (3 x 50 mL), and dried over anhydrous MgSO₄. The MgSO₄ was subsequently removed by vacuum filtration, and the filtrate was concentrated in vacuo to give crude product as white solid. The crude product was further purified by column chromatography on silica gel (gradient eluent: hexanes/ethyl acetate from 10/1 to 1/1) to give 10-cyclopropanecarbonyl-10-deacetyl-7-triethylsilylbaccatin III **1-15** as white solid (556 mg, 0.765 mmol) in 94% yield. ¹H NMR (400 MHz, CDCl₃): δ 0.56 (m, 6H, Si(CH₂CH₃)₃), 0.92 (t, J = 7.9 Hz, 9H, Si(CH₂CH₃)₃), 1.01 (m, 2H, cyclopropane), 1.05 (s, 3H, 17-Me), 1.16 (m, 2H, cyclopropane), 1.20 (s, 3H, 16-Me), 1.61 (br. s, 1H, 1-OH), 1.68 (s, 3H, 19-Me), 1.76 (m, 1H, cyclopropane), 1.87 (m, 1H, 6-H), 2.19 (s, 3H, 18-Me), 2.27 (m, 2H, 14-CH₂), 2.28 (s, 3H, OAc), 2.52 (m, 1H, 6-H), 3.88 (d, J = 7.0 Hz, 1H, 3-H), 4.15 (d, J = 8.3 Hz, 1H, 20-H), 4.30 (d, J = 8.3 Hz, 1H, 20-H), 4.48 (dd, J = 10.5 Hz, 6.7 Hz, 1H, 7-H), 4.84 (t, J = 7.8 Hz, 1H, 13-H), 4.96 (d, J = 8.2 Hz, 1H, 5-H), 5.64 (d, J = 7.0 Hz, 1H, 2-H), 6.46 (s, 1H, 10-H), 7.47 (t, J = 7.7 Hz, 2H, Bz), 7.60 (t, J = 7.7 Hz, 1H, Bz), 8.10 (d, J = 7.3 Hz, 2H, Bz). ¹³C NMR (100 MHz, CDCl₃): δ 5.3, 6.8, 8.6, 8.7, 10.0, 13.0, 14.9, 20.2, 22.7, 26.8, 37.3, 38.2, 42.8, 47.3, 68.0, 72.4, 74.7, 75.5, 76.5, 78.8, 80.9, 84.3, 128.6, 129.4, 130.1, 132.8, 133.6, 143.8, 167.1, 170.7, 173.2, 202.3. All data are consisted with the reported values.⁵⁰

10-Cyclopropanecarbonyl-3'-dephenyl-3'-(2-methyl-2-propenyl)-7-triethylsilyl-2'-triisopropylsilyldocetaxel (1-16)⁵⁰

To a 50-mL round-bottom flask was added 10-cyclopropanecarbonyl-10-deacetyl-7-triethylsilylbaccatin III **1-15** (375 mg, 0.516 mmol). The flask was purged with nitrogen gas and 20 mL freshly distilled anhydrous THF was added. The starting material was dissolved and cooled to -40 °C in an acetone/dry ice bath by adding small amount of dry ice into acetone, and monitored using a thermometer. LiHMDS (0.68 mL, 0.68 mmol) was added dropwise, and then enantiopure β -lactam (3*R*,4*S*)-1-*tert*-butoxycarbonyl-3-triisopropylsilyloxy-4-(2-methyl-1-propenyl)azetid-2-one **1-11** (246 mg, 0.620 mmol) in 6 mL anhydrous THF was added dropwise. The reaction was monitored by TLC (hexanes /ethyl acetate = 3/1, stain with 5% sulfuric acid in ethanol). After two hour, there is still starting material left in in the reaction mixture, so another 0.5 eq. LiHMDS (0.26 mL, 0.26 mmol) was added to the reaction mixture. Upon completion after 4 hour, the reaction was quenched with 10 mL saturated ammonium chloride solution and then diluted with 20 mL H₂O. The aqueous layer was extracted with ethyl

acetate (3 x 50 mL). The combined organic layer was washed with brine (3 x 50 mL), and dried over anhydrous MgSO₄. The MgSO₄ was subsequently removed by vacuum filtration, and the filtrate was concentrated in vacuo to give crude product as pale yellow solid. The crude product was further purified by column chromatography on silica gel (gradient eluent: hexanes/ethyl acetate from 10/1 to 3/1) to give 10-cyclopropanecarbonyl-10-deacetyl-3'-dephenyl-3'-(2-methyl-2-propenyl)-7-triethylsilylbaccatin III **1-16** as white solid (506 mg, 0.450 mmol) in 87% yield. Unreacted 10-cyclopropanecarbonyl-10-deacetyl-7-triethylsilylbaccatin III **1-15** (31 mg, 0.043 mmol, 8%) and excess β-lactam **1-11** (36 mg, 0.091 mmol) were also obtained from column chromatography. Conversion is 92% based on the amount of isolated unreacted starting material **1-15**. ¹H NMR (400 MHz, CDCl₃): δ 0.56 (m, 6H, Si(CH₂CH₃)₃), 0.92 (m, 9H, Si(CH₂CH₃)₃), 1.01 (m, 2H, cyclopropane), 1.04 (m, 21H, TIPS), 1.16 (m, 2H, cyclopropane), 1.19 (s, 3H, 17-Me), 1.23 (s, 3H, 16-Me), 1.34 (s, 9H, t-Bu), 1.61 (br. s, 1H, 1-OH), 1.68 (s, 3H, 19-Me), 1.73 (m, 1H, cyclopropane), 1.75 (s, 3H, isobutenyl), 1.79 (s, 3H, isobutenyl), 1.87 (m, 1H, 6-H), 2.00 (s, 3H, 18-Me), 2.36 (s, 3H, OAc), 2.38 (m, 2H, 14-CH₂), 2.52 (m, 1H, 6-H), 3.84 (d, J = 7.0 Hz, 1H, 3-H), 4.20 (d, J = 8.3 Hz, 1H, 20-H), 4.30 (d, J = 8.3 Hz, 1H, 20-H), 4.43 (d, J = 2.8 Hz, 1H, 2'-H), 4.46 (dd, J = 10.5 Hz, 6.7 Hz, 1H, 7-H), 4.80 (m, 2H, 3'-H, 3'-N-H), 4.93 (d, J = 7.8 Hz, 1H, 5-H), 5.34 (d, J = 8.6 Hz, isobutenyl), 5.69 (d, J = 7.2 Hz, 1H, 2-H), 6.09 (t, J = 8.3 Hz, 1H, 13-H), 6.48 (s, 1H, 10-H), 7.46 (t, J = 7.8 Hz, 2H, Bz), 7.60 (t, J = 7.4 Hz, 1H, Bz), 8.10 (d, J = 7.1 Hz, 2H, Bz). All data are consistent with the reported values.⁵⁰

10-Cyclopropanecarbonyl-3'-dephenyl-3'-(2-methyl-2-propenyl)docetaxel (1-17, SB-T-1214)⁵⁰

To a 50-mL round-bottom flask was added 10-cyclopropanecarbonyl-10-deacetyl-3'-dephenyl-3'-(2-methyl-2-propenyl)-7-triethylsilylbaccatin III **1-16** (496 mg, 0.441 mmol). The flask was purged with nitrogen gas. Then 11 mL acetonitrile and 11 mL pyridine were added. The starting material was dissolved and cooled to 0 °C in an ice bath. 5.0 mL HF/pyridine was then added dropwise. The reaction mixture was allowed to warm up to room temperature gradually. The reaction was monitored by TLC (hexanes/ ethyl acetate = 1/1, stain with 5% sulfuric acid in ethanol). Upon completion after overnight, the reaction was quenched with 10 mL 0.2 M citric acid in water (3.8%). The aqueous layer was extracted with ethyl acetate (3 x 30 mL). The combined organic layer was washed with saturated copper sulfate (3 x 30 mL) to remove pyridine, and then washed with water (3 x 30 mL) and brine (3 x 30 mL), and dried over anhydrous MgSO₄. The MgSO₄ was subsequently removed by vacuum filtration, and the filtrate was concentrated in vacuo to give crude product as white solid. The crude product was further purified by column chromatography on silica gel (gradient eluent: hexanes/ethyl acetate from 10/1 to 1/1) to give 10-cyclopropanecarbonyl-3'-dephenyl-3'-(2-methyl-2-propenyl)docetaxel **1-17 (SB-T-1214)** as white solid (351 mg, 0.411 mmol) in 93% yield. The product was further purified by recrystallization with ethyl acetate to give desired product **SB-T-1214** (298 mg, 0.349 mmol) as white crystal in high purity (97.5% by HPLC). ¹H NMR (400 MHz, CDCl₃): δ 1.00 (m, 2H, cyclopropane), 1.14 (m, 2H, cyclopropane), 1.16 (s, 3H, 17-Me), 1.27 (s, 3H, 16-

Me), 1.36 (s, 9H, t-Bu), 1.65 (s, 1H, 1-OH), 1.67 (s, 3H, 19-Me), 1.77 (br. s, 6H, isobutenyl), 1.80 (m, 1H, cyclopropane), 1.84 (m, 1H, 6-H), 1.90 (s, 3H, 18-Me), 2.36 (s, 3H, OAc), 2.48 (m, 2H, 14-CH₂), 2.52 (m, 1H, 6-H), 3.44 (m, 1H, 7-OH), 3.81 (d, J = 7.0 Hz, 1H, 3-H), 4.18 (d, J = 8.4 Hz, 1H, 20-H), 4.22 (m, 1H, 2'-H), 4.30 (d, J = 8.4 Hz, 1H, 20-H), 4.41 (m, 1H, 7-H), 4.75 (m, 2H, 3'-H, 3'-N-H), 4.96 (d, J = 7.8 Hz, 1H, 5-H), 5.31 (m, 1H, 4'-H), 5.66 (d, J = 7.0 Hz, 1H, 2-H), 6.18 (t, J = 8.2 Hz, 1H, 13-H), 6.30 (s, 1H, 10-H), 7.48 (t, J = 7.8 Hz, 2H, Bz), 7.61 (t, J = 7.4 Hz, 1H, Bz), 8.10 (d, J = 7.2 Hz, 2H, Bz). ¹³C NMR (100 MHz, CDCl₃): δ 9.2, 9.4, 9.5, 13.0, 15.0, 18.6, 22.0, 22.4, 25.7, 26.7, 28.2, 35.5, 35.6, 43.2, 45.6, 51.6, 58.6, 72.3, 72.4, 75.1, 75.4, 76.5, 77.0, 77.2, 79.2, 80.0, 81.1, 84.5, 120.6, 128.7, 129.3, 130.2, 132.9, 133.7, 138.0, 142.7, 155.5, 167.0, 170.1, 175.2, 203.9. Melting point: 159-160 °C. α_D = -85° (CHCl₃, c = 0.26). All data are consistent with the reported values except α_D. (It was reported α_D = -160° in the literature, however, α_D was measured multiple times including previous **SB-T-1214** sample, and all gave similar results, so the reported value should be wrong. No melting point was given in the reference.⁵⁰

10- *N,N*-Dimethylcarbamoyl -10-deacetyl-7-triethylsilylbaccatin III (**1-18**)⁵⁰

To a 25-mL round-bottom flask was added 10-deacetyl-7-triethylsilylbaccatin III **1-14** (305 mg, 0.455 mmol). The flask was purged with nitrogen gas and 9 mL freshly distilled anhydrous THF was added. The starting material was dissolved and cooled to -40 °C in an acetone/dry ice bath by adding small amount of dry ice into acetone, and monitored using a thermometer. LiHMDS (0.59 mL, 0.59 mmol) was added dropwise, and then *N,N*-dimethylcarbamoyl chloride (54 μL, 0.592 mmol) was added dropwise. The reaction was monitored by TLC (DCM/MeOH = 20/1, stain with 5% sulfuric acid in ethanol). Upon completion after 4 hour, the reaction was quenched with 5 mL saturated ammonium chloride solution and then diluted with 10 mL H₂O. The aqueous layer was extracted with ethyl acetate (3 x 30 mL). The combined organic layer was washed with brine (3 x 30 mL), and dried over anhydrous MgSO₄. The MgSO₄ was subsequently removed by vacuum filtration, and the filtrate was concentrated in vacuo to give crude product as white solid. The crude product was further purified by column chromatography on silica gel (gradient eluent: hexanes/ethyl acetate from 10/1 to 1/1) to give 10-*N,N*-dimethylcarbamoyl-10-deacetyl-7-triethylsilylbaccatin III **1-18** as white solid (320 mg, 0.438 mmol) in 95% yield. ¹H NMR (400 MHz, CDCl₃): δ 0.58 (m, 6H, Si(CH₂CH₃)₃), 0.92 (t, J = 8.0 Hz, 9H, Si(CH₂CH₃)₃), 1.08 (s, 3H, 17-Me), 1.20 (s, 3H, 16-Me), 1.60 (s, 1H, 1-OH), 1.68 (s, 3H, 19-Me), 1.87 (m, 1H, 6-H), 2.24 (s, 3H, 18-Me), 2.27 (m, 2H, 14-CH₂), 2.28 (s, 3H, OAc), 2.52 (m, 1H, 6-H), 2.94 (s, 3H, CON(CH₃)₂), 3.08 (s, 3H, CON(CH₃)₂), 3.90 (d, J = 7.0 Hz, 1H, 3-H), 4.15 (d, J = 8.2 Hz, 1H, 20-H), 4.30 (d, J = 8.2 Hz, 1H, 20-H), 4.48 (dd, J = 10.4 Hz, 6.7 Hz, 1H, 7-H), 4.84 (m, 1H, 13-H), 4.96 (d, J = 8.1 Hz, 1H, 5-H), 5.64 (d, J = 7.0 Hz, 1H, 2-H), 6.39 (s, 1H, 10-H), 7.47 (t, J = 8.0 Hz, 2H, Bz), 7.60 (t, J = 7.5 Hz, 1H, Bz), 8.10 (d, J = 7.2 Hz, 2H, Bz). ¹³C NMR (100 MHz, CDCl₃): δ 5.4, 6.9, 10.1, 15.0, 20.4, 22.9, 27.0, 37.4, 38.4, 42.9, 47.4, 58.6, 68.2, 72.5, 74.9, 76.8, 79.0, 81.1, 84.4, 128.7, 129.6, 130.3, 133.4, 133.7, 143.7, 155.5, 167.3, 170.9, 203.4. ESI-MS: 730.3 [M+H]⁺. All data are consistent with literature values.⁵⁰

10-*N,N*-Dimethylcarbamoyl -3'-dephenyl-3'-(2-methyl-2-propenyl)-7-triethylsilyl-2'-triisopropylsilyldocetaxel (1-19)⁵⁰

To a 25-mL round-bottom flask was added 10-*N,N*-dimethylcarbamoyl-10-deacetyl-7-triethylsilylbaccatin III **1-18** (150 mg, 0.205 mmol). The flask was purged with nitrogen gas and 6 mL freshly distilled anhydrous THF was added. The starting material was dissolved and cooled to -40 °C in an acetone/dry ice bath by adding small amount of dry ice into acetone, and monitored using a thermometer. LiHMDS (0.27 mL, 0.27 mmol) was added dropwise, and then enantiopure β -lactam (3*R,4S*)-1-*tert*-butoxycarbonyl-3-triisopropylsilyloxy-4-(2-methyl-1-propenyl)azetid-2-one **1-11** (106 mg, 0.267 mmol) in 2 mL anhydrous THF was added dropwise. The reaction was monitored by TLC (hexanes /ethyl acetate = 3/1, stain with 5% sulfuric acid in ethanol). Upon completion after 4 hour, the reaction was quenched with 5 mL saturated ammonium chloride solution and then diluted with 10 mL H₂O. The aqueous layer was extracted with ethyl acetate (3 x 20 mL). The combined organic layer was washed with brine (3 x 20 mL), and dried over anhydrous MgSO₄. The MgSO₄ was subsequently removed by vacuum filtration, and the filtrate was concentrated in vacuo to give crude product as pale yellow solid. The crude product was further purified by column chromatography on silica gel (gradient eluent: hexanes/ethyl acetate from 10/1 to 3/1) to give 10-*N,N*-dimethylcarbamoyl-10-deacetyl-3'-dephenyl-3'-(2-methyl-2-propenyl)-7-triethylsilylbaccatin III (**1-19**) as white solid (214 mg, 0.190 mmol) in 92% yield. ¹H NMR (400 MHz, CDCl₃): δ 0.58 (m, 6H, Si(CH₂CH₃)₃), 0.92 (m, 9H, Si(CH₂CH₃)₃), 1.10 (m, 21H, TIPS), 1.19 (s, 3H, 17-Me), 1.23 (s, 3H, 16-Me), 1.34 (s, 9H, *t*-Bu), 1.68 (s, 3H, 19-Me), 1.75 (s, 3H, isobutenyl), 1.79 (s, 3H, isobutenyl), 1.88 (m, 1H, 6-H), 2.05 (s, 3H, 18-Me), 2.36 (s, 3H, OAc), 2.38 (m, 1H, 14-CH₂), 2.52 (m, 1H, 6-H), 2.94 (s, 3H, CON(CH₃)₂), 3.06 (s, 3H, CON(CH₃)₂), 3.86 (d, *J* = 6.7 Hz, 1H, 3-H), 4.20 (d, *J* = 8.4 Hz, 1H, 20-H), 4.30 (d, *J* = 8.4 Hz, 1H, 20-H), 4.43 (d, *J* = 2.8 Hz, 1H, 2'-H), 4.46 (dd, *J* = 10.4 Hz, 6.5 Hz, 1H, 7-H), 4.78 (m, 2H, 3'-H, 3'-N-H), 4.94 (d, *J* = 8.4 Hz, 1H, 5-H), 5.34 (d, *J* = 8.6 Hz, isobutenyl), 5.69 (d, *J* = 7.0 Hz, 1H, 2-H), 6.10 (t, *J* = 8.3 Hz, 1H, 13-H), 6.49 (s, 1H, 10-H), 7.46 (t, *J* = 7.8 Hz, 2H, Bz), 7.60 (t, *J* = 7.6 Hz, 1H, Bz), 8.10 (d, *J* = 7.4 Hz, 2H, Bz). All data are consisted with the reported values.⁵⁰

10-*N,N*-Dimethylcarbamoyl -3'-dephenyl-3'-(2-methyl-2-propenyl)docetaxel (1-20, SB-T-1216)⁵⁰

To a 25-mL round-bottom flask was added 10-*N,N*-dimethylcarbamoyl-10-deacetyl-3'-dephenyl-3'-(2-methyl-2-propenyl)-7-triethylsilylbaccatin III **1-19** (210 mg, 0.186 mmol). The flask was purged with nitrogen gas. Then 3 mL acetonitrile and 3 mL pyridine were added. The starting material was dissolved and cooled to 0 °C in an ice bath. 3.0 mL HF/pyridine was then added dropwise. The reaction mixture was allowed to warm up to room temperature gradually. The reaction was monitored by TLC (hexanes/ ethyl acetate = 1/1, stain with 5% sulfuric acid in ethanol). Upon completion after overnight, the reaction was quenched with 10 mL 0.2 M citric acid in water (3.8%). The aqueous layer was extracted with ethyl acetate (3 x 15 mL). The combined organic layer was washed with saturated copper sulfate (3 x 20 mL) to remove

pyridine, and then washed with water (3 x 15 mL) and brine (3 x 15 mL), and dried over anhydrous MgSO₄. The MgSO₄ was subsequently removed by vacuum filtration, and the filtrate was concentrated in vacuo to give crude product as white solid. The crude product was further purified by column chromatography on silica gel (gradient eluent: hexanes/ethyl acetate from 10/1 to 1/1) to give 10-*N,N*-dimethylcarbamoyl -3'-dephenyl-3'-(2-methyl-2-propenyl)docetaxel **1-20 (SB-T-1216)** as white solid (143 mg, 0.167 mmol) in 90% yield. The product was further purified by recrystallization with ethyl acetate to give desired product **SB-T-1216** (112 mg, 0.131 mmol) as white crystal in high purity (98% by HPLC). ¹H NMR (500 MHz, CDCl₃): δ 1.16 (s, 3H, 17-Me), 1.25 (s, 3H, 16-Me), 1.35 (s, 9H, t-Bu), 1.67 (s, 3H, 19-Me), 1.77 (s, 6H, isobutenyl), 1.86 (m, 1H, 6-H), 1.92 (s, 3H, 18-Me), 2.36 (s, 3H, OAc), 2.38 (m, 2H, 14-CH₂), 2.56 (m, 1H, 6-H), 2.96 (s, 3H, CON(CH₃)₂), 3.04 (s, 3H, CON(CH₃)₂), 3.81 (d, J = 6.7 Hz, 1H, 3-H), 4.18 (d, J = 8.4 Hz, 1H, 20-H), 4.22 (m, 1H, 2'-H), 4.30 (d, J = 8.4 Hz, 1H, 20-H), 4.45 (m, 1H, 7-H), 4.75 (m, 2H, 3'-H, 3'-N-H), 4.98 (d, J = 8.3 Hz, 1H, 5-H), 5.31 (m, 1H, 4'-H), 5.66 (d, J = 7.1 Hz, 1H, 2-H), 6.18 (t, J = 8.5 Hz, 1H, 13-H), 6.26 (s, 1H, 10-H), 7.48 (t, J = 7.5 Hz, 2H, Bz), 7.61 (t, J = 7.0 Hz, 1H, Bz), 8.10 (d, J = 7.9 Hz, 2H, Bz). ESI-MS: 857.3 [M+H]⁺. All data are consisted with the reported values.⁵⁰

7,10-DiTroc-10-deacetylbaaccatin III (1-21)⁷³

To a 25-mL round-bottom flask was added 10-DAB III (300 mg, 0.551 mmol). The flask was purged with nitrogen gas and 5 mL pyridine was added. The starting material was dissolved. Then 2,2,2-trichloroethyl chloroformate (160 μL, 1.16 mmol) was added dropwise. Then reaction mixture was heated up to 80 °C in an oil bath. The reaction was monitored by TLC (hexanes/ethyl acetate = 1/1, stain with 5% sulfuric acid in ethanol). Upon completion after 30 min, the reaction was quenched with 5 mL saturated ammonium chloride solution and then diluted with 10 mL H₂O. The aqueous layer was extracted with ethyl acetate (3 x 20 mL). The combined organic layer was washed with brine (3 x 20 mL), and dried over anhydrous MgSO₄. The MgSO₄ was subsequently removed by vacuum filtration, and the filtrate was concentrated in vacuo to give crude product. The crude product was further purified by column chromatography on silica gel (gradient eluent: hexanes/ethyl acetate from 10/1 to 1/1) to give 7,10-diTroc-10-deacetylbaaccatin III **1-21** as white solid (304 mg, 0.340 mmol) in 62% yield and side product 7,10,13-triTroc-10-deacetylbaaccatin III as white solid (160 mg, 0.150 mmol) in 27% yield. Product: ¹H NMR (400 MHz, CDCl₃): δ 1.12 (s, 3H, 17-Me), 1.16 (s, 3H, 16-Me), 1.85 (s, 3H, 19-Me), 2.04 (m, 1H, 6-H), 2.11 (d, J = 5.1 Hz, 1H, 13-OH), 2.14 (s, 3H, 18-Me), 2.27 (m, 2H, 14-CH₂), 2.32 (s, 3H, OAc), 2.64 (m, 1H, 6-H), 3.98 (d, J = 6.9 Hz, 1H, 3-H), 4.16 (d, J = 8.7 Hz, 1H, 20-H), 4.31 (d, J = 8.2 Hz, 1H, 20-H), 4.60 (d, J = 11.8 Hz, 1H, Troc), 4.74 (d, J = 11.8 Hz, 1H, Troc), 4.80 (d, J = 11.8 Hz, 1H, Troc), 4.88 (m, 1H, 13-H), 4.90 (d, J = 11.8 Hz, 1H, Troc), 4.98 (d, J = 8.0 Hz, 1H, 5-H), 5.58 (dd, J = 10.6 Hz, 7.2 Hz, 1H, 7-H), 5.64 (d, J = 7.0 Hz, 1H, 2-H), 6.27 (s, 1H, 10-H), 7.48 (t, J = 7.6 Hz, 2H, Bz), 7.62 (m, 1H, Bz), 8.10 (m, 2H, Bz). ¹³C NMR (100 MHz, CDCl₃): δ 10.8, 15.5, 20.2, 22.7, 26.7, 33.4, 38.5, 42.8, 47.5, 56.5, 68.1, 74.3, 76.4, 78.8, 79.9, 80.6, 83.9, 94.4, 94.4, 128.8, 129.3, 130.2, 131.1, 133.9, 146.6, 153.4,

153.4, 167.1, 171.0, 201.3. ESI-MS: 912.0 $[M+NH_4]^+$. Side product: 1H NMR (400 MHz, $CDCl_3$): δ 1.19 (s, 3H, 17-Me), 1.21 (s, 3H, 16-Me), 1.85 (s, 3H, 19-Me), 2.04 (m, 1H, 6-H), 2.11 (s, 3H, 18-Me), 2.38 (m, 2H, 14- CH_2), 2.41 (s, 3H, OAc), 2.64 (m, 1H, 6-H), 3.98 (d, J = 6.9 Hz, 1H, 3-H), 4.13 (d, J = 8.8 Hz, 1H, 20-H), 4.34 (d, J = 8.4 Hz, 1H, 20-H), 4.60 (d, J = 11.8 Hz, 1H, Troc), 4.74 (d, J = 11.8 Hz, 1H, Troc), 4.80 (d, J = 11.8 Hz, 1H, Troc), 4.86 (s, 2 H, 13-Troc), 4.90 (d, J = 11.8 Hz, 1H, Troc), 4.98 (d, J = 8.2 Hz, 1H, 5-H), 5.60 (dd, J = 10.6 Hz, 7.2 Hz, 1H, 7-H), 5.67 (d, J = 7.0 Hz, 1H, 2-H), 6.01 (t, J = 7.6 Hz, 1H, 13-H), 6.28 (s, 1H, 10-H), 7.48 (t, J = 7.6 Hz, 2H, Bz), 7.62 (m, 1H, Bz), 8.10 (m, 2H, Bz). ESI-MS: 1087.9 $[M+NH_4]^+$. All data are consisted with the reported values.⁷³

7,10-DiTroc-3'-dephenyl-3'-(2-methyl-2-propenyl)-2'-triisopropylsilyldocetaxel (1-22)

To a 50-mL round-bottom flask was added 7,10-diTroc-10-deacetylbaaccatin III **1-21** (296 mg, 0.331 mmol). The flask was purged with nitrogen gas and 12 mL freshly distilled anhydrous THF was added. The starting material was dissolved and cooled to -40 °C in an acetone/dry ice bath by adding small amount of dry ice into acetone, and monitored using a thermometer. LiHMDS (0.43 mL, 0.43 mmol) was added dropwise, and then enantiopure β -lactam (3*R*,4*S*)-1-*tert*-butoxycarbonyl-3-triisopropylsilyloxy-4-(2-methyl-1-propenyl)azetid-2-one **1-11** (171 mg, 0.430 mmol) in 3 mL anhydrous THF was added dropwise. The reaction was monitored by TLC (hexanes/ethyl acetate = 3/1, stain with 5% sulfuric acid in ethanol). After 4 hours, there is still starting material left in the reaction mixture, so another 0.3 eq. LiHMDS (0.10 mL, 0.10 mmol) and β -lactam (3*R*,4*S*)-1-*tert*-butoxycarbonyl-3-triisopropylsilyloxy-4-(2-methyl-1-propenyl)azetid-2-one **1-11** (40 mg, 0.10 mmol) was added to the reaction mixture. After another 2 hours, the reaction still did not go completion and was quenched with 5 mL saturated ammonium chloride solution and then diluted with 10 mL H_2O . The aqueous layer was extracted with ethyl acetate (3 x 30 mL). The combined organic layer was washed with brine (3 x 30 mL), and dried over anhydrous $MgSO_4$. The $MgSO_4$ was subsequently removed by vacuum filtration, and the filtrate was concentrated in vacuo to give crude product as pale yellow solid. The crude product was further purified by column chromatography on silica gel (gradient eluent: hexanes/ethyl acetate from 10/1 to 1/1) to give 7,10-diTroc-3'-dephenyl-3'-(2-methyl-2-propenyl)-2'-triisopropylsilyldocetaxel **1-22** as white solid (308 mg, 0.239 mmol) in 72% yield. Unreacted 7,10-diTroc-10-deacetylbaaccatin III **1-21** (78 mg, 0.087 mmol) was recovered from column chromatography. Conversion is 74% based on the amount of starting material **1-21** recovered. 1H NMR (400 MHz, $CDCl_3$): δ 1.11 (m, 21H, TIPS), 1.19 (s, 3H, 17-Me), 1.24 (s, 3H, 16-Me), 1.34 (s, 9H, *t*-Bu), 1.71 (s, 1H, 1-OH), 1.76 (s, 3H, 19-Me), 1.80 (s, 3H, isobutenyl), 1.85 (s, 3H, isobutenyl), 2.01 (s, 3H, 18-Me), 2.08 (m, 1H, 6-H), 2.37 (s, 3H, OAc), 2.41 (m, 2H, 14- CH_2), 2.63 (m, 1H, 6-H), 3.95 (d, J = 7.0 Hz, 1H, 3-H), 4.21 (d, J = 8.5 Hz, 1H, 20-H), 4.33 (d, J = 8.5 Hz, 1H, 20-H), 4.44 (d, J = 2.5 Hz, 1H, 2'-H), 4.60 (d, J = 11.8 Hz, 1H, Troc), 4.74 (d, J = 11.8 Hz, 1H, Troc), 4.80 (d, J = 11.8 Hz, 1H, Troc), 4.84 (m, 2H, 3'-H, 3'-N-H), 4.92 (d, J = 11.8 Hz, 1H, Troc), 4.96 (d, J = 8.1 Hz, 1H, 5-H), 5.32 (d, J = 8.7 Hz, 1H, isobutenyl), 5.58 (dd, J = 10.8 Hz, 7.1 Hz, 1H, 7-H), 5.70 (d, J = 7.0 Hz, 1H, 2-H), 6.11 (t, J = 8.9 Hz, 1H, 13-H), 6.25

(s, 1H, 10-H), 7.47 (t, J = 7.9 Hz, 2H, Bz), 7.62 (d, J = 7.4 Hz, 1H, Bz), 8.10 (d, J = 7.2 Hz, 2H, Bz). ESI-MS: 1314.3 [M+H]⁺.

3'-Dephenyl-3'-(2-methyl-2-propenyl)-2'-triisopropylsilyldocetaxel (1-23)

To a 50-mL round-bottom flask was added 7,10-diTroc-3'-dephenyl-3'-(2-methyl-2-propenyl)-2'-triisopropylsilyldocetaxel **1-22** (295 mg, 0.229 mmol), and followed by adding 5 mL acetic acid and 5 mL methanol. The starting material was dissolved. Then Zinc dust (600 mg) was added in small portions. The reaction was monitored by TLC (hexanes/ethyl acetate = 2/1, stain with 5% sulfuric acid in ethanol). After 2 hours, the reaction did not go completion, and another 600 mg Zinc dust was added to the reaction mixture. After another 2 hours, the reaction still did not go completion and another 600 mg Zinc dust was added to the reaction mixture, and the reaction mixture was allowed to stir overnight. Upon completion after overnight (TLC was messy and showed a major polar spot and a couple of relatively nonpolar spots), the reaction was quenched with 5 mL saturated ammonium chloride solution and then diluted with 10 mL H₂O. The aqueous layer was extracted with ethyl acetate (3 x 30 mL). The combined organic layer was washed with brine (3 x 30 mL), and dried over anhydrous MgSO₄. The MgSO₄ was subsequently removed by vacuum filtration, and the filtrate was concentrated in vacuo to give crude product as pale yellow solid. The crude product was further purified by column chromatography on silica gel (gradient eluent: hexanes/ethyl acetate from 10/1 to 1/1) to give 3'-dephenyl-3'-(2-methyl-2-propenyl)-2'-triisopropylsilyldocetaxel **1-23** as white solid (145 mg, 0.154 mmol) in 67% yield. ¹H NMR (400 MHz, CDCl₃): δ 1.11 (m, 24H, TIPS, 17-Me), 1.23 (s, 3H, 16-Me), 1.34 (s, 9H, t-Bu), 1.75 (s, 6H, isobutenyl), 1.80 (s, 3H, 19-Me), 1.86 (m, 1H, 6-H), 1.93 (s, 3H, 18-Me), 2.33 (m, 2H, 14-CH₂), 2.36 (s, 3H, OAc), 2.60 (m, 1H, 6-H), 3.95 (d, J = 7.0 Hz, 1H, 3-H), 4.16 (d, J = 1.7 Hz, 1H, 10-OH), 4.24 (m, 2H, 7-H, 20-H), 4.33 (d, J = 8.4 Hz, 1H, 20-H), 4.42 (d, J = 3.0 Hz, 1H, 2'-H), 4.76 (m, 1H, 3'-N-H), 4.83 (m, 1H, 3'-H), 4.96 (dd, J = 9.7 Hz, J = 2.2 Hz, 1H, 5-H), 5.20 (d, J = 1.7 Hz, 1H, 10-H), 5.32 (d, J = 8.6 Hz, 1H, 4'-H), 5.68 (d, J = 7.3 Hz, 1H, 2-H), 6.14 (t, J = 8.4 Hz, 1H, 13-H), 7.46 (t, J = 8.0 Hz, 2H, Bz), 7.623 (m, 1H, Bz), 8.10 (d, J = 7.1 Hz, 2H, Bz). ESI-MS: 945.2 [M+H]⁺.

3'-Dephenyl-3'-(2-methyl-2-propenyl)-docetaxel (1-24, SB-T-1211) (Procedure 1)

To a 25-mL round-bottom flask was added 3'-dephenyl-3'-(2-methyl-2-propenyl)-2'-triisopropylsilyldocetaxel **1-23** (144 mg, 0.153 mmol). The flask was purged with nitrogen gas. Then 3 mL acetonitrile and 3 mL pyridine were added. The starting material was dissolved and cooled to 0 °C in an ice bath. 2.0 mL HF/pyridine was then added dropwise. The reaction mixture was allowed to warm up to room temperature gradually. The reaction was monitored by TLC (hexanes/ethyl acetate = 1/2, stain with 5% sulfuric acid in ethanol). Upon completion after overnight, the reaction was quenched with 5 mL 0.2 M citric acid in water (3.8%). The aqueous layer was extracted with ethyl acetate (3 x 20 mL). The combined organic layer was washed with saturated copper sulfate (3 x 20 mL) to remove pyridine, and then washed with water (3 x 20 mL) and brine (3 x 20 mL), and dried over anhydrous MgSO₄. The MgSO₄ was subsequently

removed by vacuum filtration, and the filtrate was concentrated in vacuo to give crude product as white solid. The crude product was further purified by column chromatography on silica gel (gradient eluent: hexanes/ethyl acetate from 5/1 to 1/2) to give 3'-dephenyl-3'-(2-methyl-2-propenyl)-docetaxel **1-24** (**SB-T-1211**) as white solid (119 mg, 0.151 mmol) in 99% yield. ¹H NMR (400 MHz, CDCl₃): δ 1.16 (s, 3H, 17-Me), 1.25 (s, 3H, 16-Me), 1.38 (s, 9H, t-Bu), 1.78 (s, 9H, 19-Me&isobutenyl), 1.86 (m, 1H, 6-H), 1.90 (s, 3H, 18-Me), 2.36 (m, 2H, 14-CH₂), 2.38 (s, 3H, OAc), 2.61 (m, 1H, 6-H), 3.43 (br. s, 1H, 7-OH), 3.96 (d, J = 7.2 Hz, 1H, 3-H), 4.24 (m, 4H, 7-H, 10-OH, 20-H, 2'-H), 4.33 (d, J = 8.4 Hz, 1H, 20-H), 4.76 (m, 1H, 3'-N-H), 4.82 (d, J = 8.6 Hz, 1H, 3'-H), 4.98 (d, J = 8.3 Hz, 1H, 5-H), 5.24 (d, J = 1.4 Hz, 1H, 10-H), 5.34 (d, J = 8.5 Hz, 1H, 4'-H), 5.70 (d, J = 7.0 Hz, 1H, 2-H), 6.19 (t, J = 8.0 Hz, 1H, 13-H), 7.50 (t, J = 7.9 Hz, 2H, Bz), 7.63 (t, J = 7.4 Hz, 1H, Bz), 8.12 (d, J = 7.2 Hz, 2H, Bz). ¹³C NMR (100 MHz, CDCl₃): δ 9.9, 14.5, 18.6, 20.6, 22.4, 25.7, 26.3, 28.3, 35.9, 37.0, 43.1, 46.5, 57.6, 72.0, 72.3, 73.8, 74.6, 74.9, 76.7, 78.9, 78.0, 81.0, 84.1, 128.7, 129.2, 130.1, 133.7, 135.8, 137.9, 138.8, 167.0, 170.2, 211.5. ESI-MS: 786.3 [M+H]⁺.

10-Acetyl-3'-dephenyl-3'-(2-methyl-2-propenyl)-7-triethylsilyl-2'-triisopropylsilyldocetaxel (1-25)

To a 50-mL round-bottom flask was added 7-triethylsilylbaccatin III (250 mg, 0.357 mmol). The flask was purged with nitrogen gas and 15 mL freshly distilled anhydrous THF was added. The starting material was dissolved and cooled to -40 °C in an acetone/dry ice bath by adding small amount of dry ice into acetone, and monitored using a thermometer. LiHMDS (0.46 mL, 0.46 mmol) was added dropwise, and then enantiopure β-lactam (3*R*,4*S*)-1-*tert*-butoxycarbonyl-3-triisopropylsilyloxy-4-(2-methyl-1-propenyl)azetidin-2-one **1-11** (184 mg, 0.46 mmol) in 5 mL anhydrous THF was added dropwise. The reaction was monitored by TLC (hexanes/ethyl acetate = 3/1, stain with 5% sulfuric acid in ethanol). Upon completion after 4 hours, the reaction was quenched with 10 mL saturated ammonium chloride solution and then diluted with 20 mL H₂O. The aqueous layer was extracted with ethyl acetate (3 x 50 mL). The combined organic layer was washed with brine (3 x 50 mL), and dried over anhydrous MgSO₄. The MgSO₄ was subsequently removed by vacuum filtration, and the filtrate was concentrated in vacuo to give crude product as pale yellow solid. The crude product was further purified by column chromatography on silica gel (gradient eluent: hexanes/ethyl acetate from 10/1 to 3/1) to give 10-acetyl-3'-dephenyl-3'-(2-methyl-2-propenyl)-7-triethylsilyl-2'-triisopropylsilyldocetaxel **1-25** as white solid (368 mg, 0.335 mmol) in 94% yield. ¹H NMR (400 MHz, CDCl₃): δ 0.56 (m, 6H, Si(CH₂CH₃)₃), 0.92 (m, 9H, Si(CH₂CH₃)₃), 1.11 (m, 21H, TIPS), 1.19 (s, 3H, 17-Me), 1.23 (s, 3H, 16-Me), 1.34 (s, 9H, t-Bu), 1.64 (br. s, 1H, 1-OH), 1.69 (s, 3H, 19-Me), 1.75 (s, 3H, isobutenyl), 1.79 (s, 3H, isobutenyl), 1.87 (m, 1H, 6-H), 2.00 (s, 3H, 18-Me), 2.17 (s, 3H, 10-OAc), 2.36 (s, 3H, 4-OAc), 2.38 (m, 2H, 14-CH₂), 2.52 (m, 1H, 6-H), 3.84 (d, J = 6.9 Hz, 1H, 3-H), 4.20 (d, J = 8.4 Hz, 1H, 20-H), 4.30 (d, J = 8.4 Hz, 1H, 20-H), 4.43 (d, J = 2.9 Hz, 1H, 2'-H), 4.48 (dd, J = 10.6 Hz, 6.6 Hz, 1H, 7-H), 4.80 (m, 2H, 3'-H, 3'-N-H), 4.93 (d, J = 7.9 Hz, 1H, 5-H), 5.34 (d, J = 8.6 Hz, isobutenyl), 5.69 (d, J = 7.0 Hz, 1H, 2-H), 6.09 (t, J = 8.5 Hz, 1H, 13-H), 6.47 (s, 1H, 10-H), 7.46

(t, J = 7.9 Hz, 2H, Bz), 7.60 (t, J = 7.5 Hz, 1H, Bz), 8.10 (d, J = 7.1 Hz, 2H, Bz). ESI-MS: 1098.6 [M+H]⁺.

3'-Dephenyl-3'-(2-methyl-2-propenyl)-7-triethylsilyl-2'-triisopropylsilyldocetaxel (1-26)

To a 25-mL round-bottom flask was added 10-acetyl-3'-dephenyl-3'-(2-methyl-2-propenyl)-7-triethylsilyl-2'-triisopropylsilyldocetaxel **1-25** (200 mg, 0.182 mmol). The flask was purged with nitrogen gas and 4 mL anhydrous EtOH was added. The starting material was dissolved. Hydrazine monohydrate (2 mL) was then added dropwise. The reaction was monitored by ESI-MS, because the product has similar R_f value as the starting material. Upon completion after 4 hours, the reaction was quenched with 10 mL saturated ammonium chloride solution and then diluted with 20 mL H₂O. The aqueous layer was extracted with ethyl acetate (3 x 50 mL). The combined organic layer was washed with brine (3 x 50 mL), and dried over anhydrous MgSO₄. The MgSO₄ was subsequently removed by vacuum filtration, and the filtrate was concentrated in vacuo to give crude product as pale yellow solid. The crude product was further purified by column chromatography on silica gel (gradient eluent: hexanes/ethyl acetate from 10/1 to 3/1) to give 3'-dephenyl-3'-(2-methyl-2-propenyl)-7-triethylsilyl-2'-triisopropylsilyldocetaxel **1-26** as white solid (128 mg, 0.121 mmol) in 66% yield. ¹H NMR (400 MHz, CDCl₃): δ 0.56 (m, 6H, Si(CH₂CH₃)₃), 0.92 (m, 9H, Si(CH₂CH₃)₃), 1.12 (m, 21H, TIPS), 1.22 (s, 3H, 17-Me), 1.26 (s, 3H, 16-Me), 1.34 (s, 9H, t-Bu), 1.57 (s, 1H, 1-OH), 1.74 (s, 3H, 19-Me), 1.75 (s, 3H, isobutenyl), 1.79 (s, 3H, isobutenyl), 1.94 (m, 1H, 6-H), 1.93 (s, 3H, 18-Me), 2.38 (s, 3H, 4-OAc), 2.40 (m, 2H, 14-CH₂), 2.46 (m, 1H, 6-H), 3.90 (d, J = 7.2 Hz, 1H, 3-H), 4.20 (d, J = 8.4 Hz, 1H, 20-H), 4.24 (d, J = 1.8 Hz, 10-OH), 4.30 (d, J = 8.4 Hz, 1H, 20-H), 4.39 (dd, J = 10.6 Hz, 6.6 Hz, 1H, 7-H), 4.43 (d, J = 3.1 Hz, 1H, 2'-H), 4.80 (m, 2H, 3'-H, 3'-N-H), 4.93 (d, J = 8.1 Hz, 1H, 5-H), 5.12 (d, J = 1.8 Hz, 10-H), 5.34 (d, J = 8.3 Hz, isobutenyl), 5.65 (d, J = 7.4 Hz, 1H, 2-H), 6.16 (t, J = 8.9 Hz, 1H, 13-H), 7.46 (t, J = 7.8 Hz, 2H, Bz), 7.60 (t, J = 7.7 Hz, 1H, Bz), 8.10 (d, J = 7.2 Hz, 2H, Bz). ESI-MS: 1056.6 [M+H]⁺.

3'-Dephenyl-3'-(2-methyl-2-propenyl)-docetaxel (1-24, SB-T-1211) (Procedure 2)

To a 25-mL round-bottom flask was added 3'-dephenyl-3'-(2-methyl-2-propenyl)-7-triethylsilyl-2'-triisopropylsilyldocetaxel **1-26** (123 mg, 0.1116 mmol). The flask was purged with nitrogen gas. Then 2 mL acetonitrile and 2 mL pyridine were added. The starting material was dissolved and cooled to 0 °C in an ice bath. 1.0 mL HF/pyridine was then added dropwise. The reaction mixture was allowed to warm up to room temperature gradually. The reaction was monitored by TLC (hexanes/ethyl acetate = 1/1, stain with 5% sulfuric acid in ethanol). Upon completion after overnight, the reaction was quenched with 5 mL 0.2 M citric acid in water (3.8%). The aqueous layer was extracted with ethyl acetate (3 x 20 mL). The combined organic layer was washed with saturated copper sulfate (3 x 20 mL) to remove pyridine, and then washed with water (3 x 20 mL) and brine (3 x 20 mL), and dried over anhydrous MgSO₄. The MgSO₄ was subsequently removed by vacuum filtration, and the filtrate was concentrated in vacuo to give crude product as white solid. The crude product was further purified by column chromatography on silica gel

(gradient eluent: hexanes/ethyl acetate from 5/1 to 1/2) to give 3'-dephenyl-3'-(2-methyl-2-propenyl)-docetaxel **1-24** (**SB-T-1211**) as white solid (82 mg, 0.104 mmol) in 90% yield. ¹H NMR (400 MHz, CDCl₃): δ 1.16 (s, 3H, 17-Me), 1.25 (s, 3H, 16-Me), 1.38 (s, 9H, t-Bu), 1.78 (s, 9H, 19-Me&isobutenyl), 1.86 (m, 1H, 6-H), 1.90 (s, 3H, 18-Me), 2.36 (m, 2H, 14-CH₂), 2.38 (s, 3H, OAc), 2.61 (m, 1H, 6-H), 3.43 (br. s, 1H, 7-OH), 3.96 (d, J = 7.2 Hz, 1H, 3-H), 4.24 (m, 4H, 7-H, 10-OH, 20-H, 2'-H), 4.33 (d, J = 8.4 Hz, 1H, 20-H), 4.76 (m, 1H, 3'-N-H), 4.82 (d, J = 8.6 Hz, 1H, 3'-H), 4.98 (d, J = 8.3 Hz, 1H, 5-H), 5.24 (d, J = 1.4 Hz, 1H, 10-H), 5.34 (d, J = 8.5 Hz, 1H, 4'-H), 5.70 (d, J = 7.0 Hz, 1H, 2-H), 6.19 (t, J = 8.0 Hz, 1H, 13-H), 7.50 (t, J = 7.9 Hz, 2H, Bz), 7.63 (t, J = 7.4 Hz, 1H, Bz), 8.12 (d, J = 7.2 Hz, 2H, Bz). ¹³C NMR (100 MHz, CDCl₃): δ 9.9, 14.5, 18.6, 20.6, 22.4, 25.7, 26.3, 28.3, 35.9, 37.0, 43.1, 46.5, 57.6, 72.0, 72.3, 73.8, 74.6, 74.9, 76.7, 78.9, 78.0, 81.0, 84.1, 128.7, 129.2, 130.1, 133.7, 135.8, 137.9, 138.8, 167.0, 170.2, 211.5. ESI-MS: 786.3 [M+H]⁺.

(+)-(3*R*,4*S*)-1-(4-Methoxyphenyl)-3-triisopropylsilyloxy-4-phenyl-azetidin-2-one (1-27)³²

To a 250-mL round-bottom flask, enantiopure β-lactam (+)-(3*R*,4*S*)-1-(4-methoxyphenyl)-3-hydroxy-4-phenyl-azetidin-2-one ($\alpha_D = +213^\circ$, CHCl₃, c = 0.30) (816 mg, 3.03 mmol) was added, followed by adding 70 mL DCM. DMAP (111 mg, 0.909 mmol) and TEA (613 mg, 6.06 mmol) were then added to the reaction mixture and cooled to 0 °C. TIPSCl (876 mg, 4.55 mmol) was then added dropwise. The reaction mixture was allowed to slowly warm up to room temperature and stirred overnight. The reaction was monitored by TLC. Upon completion, the reaction mixture was quenched with saturated ammonium chloride solution in water (30 mL), and extracted with ethyl acetate (3 x 50 mL). The combined organic layer was washed with brine (3 x 50 mL), and dried over anhydrous MgSO₄. The MgSO₄ was subsequently removed by vacuum filtration, and the filtrate was concentrated in vacuo to give crude **1-27** as pale yellow solid. The crude product was further purified by column chromatography on silica gel (gradient eluent: hexanes/ethyl acetate from 50/1 to 10/1) to give (+)-(3*R*,4*S*)-1-(4-methoxyphenyl)-3-triisopropylsilyloxy-4-phenyl-azetidin-2-one **1-27** as white solid (1.20 g, 2.82 mmol) in 93% yield. ¹H NMR (400 MHz, CDCl₃): δ 0.95 (m, 21H), 3.73 (s, 3H), 5.14 (d, J = 5.0 Hz, 1H), 5.23 (d, J = 5.0 Hz, 1H), 6.78 (m, 2H), 7.27 (m, 2H), 7.32 (m, 5H). ¹³C NMR (100 MHz, CDCl₃): δ 11.7, 17.4, 17.5, 55.4, 63.3, 77.8, 114.3, 118.7, 128.2, 128.3, 128.4, 131.0, 134.1, 156.1, 165.7. ESI-MS: 426.2 [M+H]⁺. Melting point: 100-102 °C. $\alpha_D = +98^\circ$ (CHCl₃, c = 0.50). All data are consisted with the reported values.³²

(+)-(3*R*,4*S*)-3-Triisopropylsilyloxy-4-phenyl-azetidin-2-one (1-28)³²

To a 250-mL round-bottom flask (+)-(3*R*,4*S*)-1-(4-methoxyphenyl)-3-triisopropylsilyloxy-4-phenyl-azetidin-2-one **1-27** (600 mg, 1.41 mmol) was dissolved in acetonitrile (40 mL) and cooled to -4 °C by a salt ice bath. To this solution was added a solution of cerium ammonium nitrate (CAN) (3.09g, 5.64 mmol) dissolved in H₂O (40 mL) dropwise via an addition funnel within 1 h. The reaction temperature of -4 °C was maintained throughout the reaction. The reaction was monitored via TLC. Upon completion after 3 h, the reaction mixture was quenched

with saturated aqueous Na₂SO₃. The aqueous layer was extracted with ethyl acetate (3 x 50 mL). The combined organic layer was washed with brine (3 x 50 mL), and dried over anhydrous MgSO₄. The MgSO₄ was subsequently removed by vacuum filtration, and the filtrate was concentrated in vacuo to give crude product as brown oil. The crude product was further purified by column chromatography on silica gel (gradient eluent: hexanes/ethyl acetate from 10/1 to 3/1) to give (+)-(3*R*,4*S*)-3-triisopropylsilyloxy-4-phenyl-azetidin-2-one **1-28** as white solid (332 mg, 1.04 mmol) in 74% yield. ¹H NMR (400 MHz, CDCl₃): δ 0.92 (m, 21H), 4.80 (d, J = 4.7 Hz, 1H), 5.17 (dd, J = 4.7 Hz, 2.6 Hz, 1H), 6.13 (br. s, 1H), 7.32 (m, 5H). ¹³C NMR (100 MHz, CDCl₃): δ 11.7, 17.4, 17.5, 59.6, 79.9, 128.0, 128.2, 128.2, 136.3, 169.9. ESI-MS: 320.2 [M+H]⁺. Melting point: 78-79 °C. α_D = +56° (CHCl₃, c = 0.27). All data are in agreement with literature values.³²

(+)-(3*R*,4*S*)-1-*tert*-Butoxycarbonyl-3-triisopropylsilyloxy-4-phenyl-azetidin-2-one (1-29)⁸⁰

To (+)-(3*R*,4*S*)-3-triisopropylsilyloxy-4-phenyl-azetidin-2-one **1-28** (100 mg, 0.313 mmol) dissolved in 3 mL DCM, was added DMAP (12 mg, 0.098 mmol) and triethylamine (65 mg, 0.64 mmol). The reaction mixture was cooled to 0 °C under inert conditions, and was added di-*tert*-butyl dicarbonate (82 mg, 0.38 mmol) in 2 mL DCM dropwise. The reaction was allowed to stir at room temperature overnight and monitored via TLC. Upon the reaction was completed, the reaction mixture was quenched with saturated NH₄Cl solution in water, and extracted with ethyl acetate (3 x 15 mL). The combined organic layer was washed with brine (3 x 15 mL), and dried over anhydrous MgSO₄. The MgSO₄ was subsequently removed by vacuum filtration, and the filtrate was concentrated in vacuo to give crude product as pale yellow oil. The crude product was further purified by column chromatography on silica gel (gradient eluent: hexanes/ethyl acetate from 20/1 to 5/1) to give (+)-(3*R*,4*S*)-1-*tert*-butoxycarbonyl-3-triisopropylsilyloxy-4-phenyl-azetidin-2-one **1-29** (126 mg, 0.300 mmol) as white solid in 96% yield. ¹H NMR (400 MHz, CDCl₃): δ 0.92 (m, 21H), 1.41 (s, 9H), 5.06 (d, J = 5.7 Hz, 1H), 5.15 (d, J=5.7 Hz, 1H), 7.32 (m, 5H). ¹³C NMR (100 MHz, CDCl₃): δ 11.6, 17.3, 17.4, 27.9, 62.4, 77.6, 83.4, 128.0, 128.1, 128.3, 133.9, 148.0, 166.4. ESI-MS: 437.3 [M+NH₄]⁺. Melting point: 59-60 °C. α_D = +85° (CHCl₃, c = 0.92).

7-Triethylsilyloxy-2'-triisopropylsilyloxy-3'-*N*-debenzoyl-3'-*N*-*tert*-butoxycarbonylpaclitaxel (1-30)

To a 25-mL round-bottom flask was added 7-triethylsilylbaccatin III (150 mg, 0.214 mmol) and (+)-(3*R*,4*S*)-1-*tert*-butoxycarbonyl-3-triisopropylsilyloxy-4-phenyl-azetidin-2-one **1-29** (117 mg, 0.278 mmol). The flask was purged with nitrogen gas and 8 mL freshly distilled anhydrous THF was added. The starting material was dissolved and cooled to -40 °C in an acetone/dry ice bath by adding small amount of dry ice into acetone, and monitored using a thermometer. LiHMDS (0.28 mL, 0.28 mmol) was added dropwise. The reaction was monitored by TLC (hexanes/ethyl acetate = 3/1, stain with 5% sulfuric acid in ethanol). Upon completion after 4 hours, the reaction was quenched with 5 mL saturated ammonium chloride solution and diluted with 5 mL H₂O. The

aqueous layer was extracted with ethyl acetate (3 x 30 mL). The combined organic layer was washed with brine (3 x 30 mL), and dried over anhydrous MgSO₄. The MgSO₄ was subsequently removed by vacuum filtration, and the filtrate was concentrated in vacuo to give crude product as pale yellow solid. The crude product was further purified by column chromatography on silica gel (gradient eluent: hexanes/ethyl acetate from 10/1 to 3/1) to give 7-triethylsilyloxy-2'-triisopropylsilyloxy-3'-*N*-debenzoyl-3'-*N*-*tert*-butoxycarbonylpaclitaxel **1-30** as a white solid (216 mg, 0.193 mmol) in 90% yield. ¹H NMR (400 MHz, CDCl₃): δ 0.59 (m, 6H, TES), 0.92 (m, 30H, TES&TIPS), 1.25 (s, 6H, C-16, C-17), 1.29 (s, 9H, tBu), 1.63 (s, 1H, 1-OH), 1.70 (s, 3H, C-19), 1.90 (m, 1H, C-6), 2.04 (s, 3H, C-18), 2.18 (s, 3H, OAc at C-10), 2.23 (m, 1H, C-14), 2.35 (m, 1H, C-14), 2.54 (s, 3H, OAc at C-4), 2.56 (m, 1H, C-6), 3.85 (d, J = 6.9 Hz, 1H, C-3), 4.18 (d, J = 8.5 Hz, 1H, C-20), 4.30 (d, J = 8.5 Hz, 1H, C-20), 4.49 (dd, J = 10.6 Hz, J = 6.7 Hz, 1H, C-7), 4.80 (br. s, 1H, C-2'), 4.95 (d, J = 8.2 Hz, 1H, C-5), 5.31 (m, 1H, C-3'), 5.39 (m, 1H, NH), 5.70 (d, J = 7.1 Hz, 1H, C-2), 6.26 (br. t, J = 7.8 Hz, 1H, C-13), 6.47 (s, 1H, C-10), 7.29 (m, 3H, Ph), 7.34 (m, 2H, Ph), 7.48 (t, J = 7.8 Hz, 2H, OBz), 7.68 (t, J = 7.3 Hz, 1H, OBz), 8.12 (d, J = 7.2 Hz, 1H, OBz). ESI-MS: 1120.4 [M+H]⁺.

3'-*N*-Debenzoyl-3'-*N*-*tert*-butoxycarbonylpaclitaxel (1-31, 10-Ac-docetaxel)⁸⁰

To a 25-mL round-bottom flask was added 7-triethylsilyloxy-2'-triisopropylsilyloxy-3'-*N*-debenzoyl-3'-*N*-*tert*-butoxycarbonylpaclitaxel **1-30** (211 mg, 0.188 mmol). The flask was purged with nitrogen gas. 4 mL acetonitrile and 4 mL pyridine were then added into the flask. The starting material was dissolved and cooled to 0 °C in an ice bath. 2 mL HF/pyridine was then added dropwise. The reaction mixture was allowed to warm up to room temperature gradually. The reaction was monitored by TLC (hexanes/ethyl acetate = 1/1, stain with 5% sulfuric acid in ethanol). Upon completion after overnight, the reaction was quenched with 5 mL 0.2 M citric acid in water (3.8%). The aqueous layer was extracted with ethyl acetate (3 x 30 mL). The combined organic layer was washed with saturated copper sulfate (3 x 30 mL) to remove pyridine, and then washed with water (3 x 30 mL) and brine (3 x 30 mL), and dried over anhydrous MgSO₄. The MgSO₄ was subsequently removed by vacuum filtration, and the filtrate was concentrated in vacuo to give crude product as white solid. The crude product was further purified by column chromatography on silica gel (gradient eluent: hexanes/ethyl acetate from 10/1 to 1/1) to give 3'-*N*-debenzoyl-3'-*N*-*tert*-butoxycarbonylpaclitaxel **1-31 (10-Ac-docetaxel)** as white solid (149 mg, 0.175 mmol) in 93% yield. ¹H NMR (400 MHz, CDCl₃): δ 1.15 (s, 3H, C-17), 1.27 (s, 3H, C-16), 1.34 (s, 9H, tBu), 1.68 (s, 3H, C-19), 1.85 (s, 3H, C-18), 1.88 (m, 1H, C-6), 2.25 (s, 3H, OAc at C-10), 2.28 (m, 2H, C-14), 2.38 (s, 3H, OAc at C-4), 2.46 (br. s, 1H, OH), 2.55 (m, 1H, C-6), 3.30 (br. s, 1H, OH), 3.80 (d, J = 7.0 Hz, 1H, C-3), 4.16 (d, J = 8.4, 1H, C-20), 4.29 (d, J = 8.4, 1H, C-20), 4.42 (dd, J = 10.2 Hz, J = 7.2 Hz, 1H, C-7), 4.62 (br. s, 1H, C-2'), 4.95 (dd, J = 9.5 Hz, J = 2.0 Hz, 1H, C-5), 5.26 (m, 1H, C-3'), 5.35 (d, J = 9.3 Hz, 1H, NH), 5.67 (d, J = 7.0 Hz, 1H, C-2), 6.24 (br. t, J = 8.8 Hz, 1H, C-13), 6.29 (s, 1H, C-10), 7.34 (m, 5H, Ph), 7.50 (t, J = 7.8 Hz, 2H, OBz), 7.62 (m, 1H, OBz), 8.10 (d, J = 7.2 Hz, 1H, OBz). ESI-MS: 850.3 [M+H]⁺.

(+)-(3*R*,4*S*)-1-Benzoyl-3-triisopropylsilyloxy-4-phenyl-azetidin-2-one (1-32)⁸⁰

To (+)-(3*R*,4*S*)-3-triisopropylsilyloxy-4-phenyl-azetidin-2-one (100 mg, 0.313 mmol) dissolved in DCM (5 mL), was added DMAP (12 mg, 0.098 mmol) and triethylamine (65 mg, 0.64 mmol). The reaction mixture was cooled to 0 °C under inert conditions, and was added benzoyl chloride (53 mg, 0.38 mmol) in 2 mL DCM dropwise. The reaction was allowed to stir at room temperature overnight and monitored via TLC. Upon the reaction was completed, the reaction mixture was quenched with saturated NH₄Cl solution in water, and extracted with ethyl acetate (3 x 15 mL). The combined organic layer was washed with brine (3 x 15 mL), and dried over anhydrous MgSO₄. The MgSO₄ was subsequently removed by vacuum filtration, and the filtrate was concentrated in vacuo to give crude product as pale yellow oil. The crude product was further purified by column chromatography on silica gel (gradient eluent: hexanes/ethyl acetate from 10/1 to 3/1) to give (+)-(3*R*,4*S*)-1-benzoyl-3-triisopropylsilyloxy-4-phenyl-azetidin-2-one **1-32** as sticky colorless oil in 84% yield. ¹H NMR (400 MHz, CDCl₃): δ 0.92 (m, 21H), 5.25 (d, J = 6.2 Hz, 1H), 5.43 (d, J = 6.2 Hz, 1H), 7.32 (m, 5H), 7.48 (m, 2H), 7.59 (m, 1H), 8.03 (m, 2H). ¹³C NMR (100 MHz, CDCl₃): δ 11.7, 17.4, 17.5, 61.2, 76.6, 128.2, 128.2, 128.4, 129.9, 132.1, 133.3, 133.8, 165.5, 166.3. ESI-MS: 424.2 [M+H]⁺. α_D = +169° (CHCl₃, c = 0.87).

7-Triethylsilyloxy-10-*N,N*-dimethylcarbamoyl-10-deacetyl-2'-triisopropylsilyloxy-paclitaxel (1-33)

To a 50-mL round-bottom flask was added 10-*N,N*-dimethylcarbamoyl-10-deacetyl-7-triethylsilylbaccatin III **1-18** (180 mg, 0.247 mmol) and (+)-(3*R*,4*S*)-1-benzoyl-3-triisopropylsilyloxy-4-phenyl-azetidin-2-one **1-32** (126 mg, 0.296 mmol). The flask was purged with nitrogen gas and 8 mL freshly distilled anhydrous THF was added. The starting material was dissolved and cooled to -30 °C in an acetone/dry ice bath by adding small amount of dry ice into acetone, and monitored by a thermometer. NaHMDS (0.37 mL, 0.37 mmol) was added dropwise. The reaction was monitored by TLC (hexanes/ethyl acetate = 3/1, stain with 5% sulfuric acid in ethanol). After 4 hours, the reaction was quenched with 5 mL saturated ammonium chloride solution and diluted with 5 mL H₂O. The aqueous layer was extracted with ethyl acetate (3 x 30 mL). The combined organic layer was washed with brine (3 x 30 mL), and dried over anhydrous MgSO₄. The MgSO₄ was subsequently removed by vacuum filtration, and the filtrate was concentrated in vacuo to give crude product as pale yellow oil. The crude product was further purified by column chromatography on silica gel (gradient eluent: hexanes/ethyl acetate from 10/1 to 3/1) to give a mixture of product 7-triethylsilyloxy-10-*N,N*-dimethylcarbamoyl-10-deacetyl-2'-triisopropylsilyloxy-paclitaxel **1-33** and side product 13-benzoyl-10-*N,N*-dimethylcarbamoyl-10-deacetyl-7-triethylsilylbaccatin III **1-35** as white solid (216 mg) in 77% yield. Mixture of product and side product: ¹H NMR (400 MHz, CDCl₃): δ 0.62 (m, 6H, Si(CH₂CH₃)₃), 0.92 (m, 22H, Si(CH₂CH₃)₃ & TIPS), 1.25 (m, 6H, C-17 & C-16), 1.72 (s, 3H, C-19), 1.90 (s, 3H, C-18), 1.92 (m, 1H, C-6), 2.10 (br. s 2H, OH), 2.23 (m, 1H, C-14), 2.34 (s, 1H, OH), 2.39 (m, 1H, C-14), 2.55 (s, 3H, OAc at C-10), 2.59 (m, 1H, C-6), 2.94 (s, 3H, CON(CH₃)₂), 3.09 (two s, 3H, CON(CH₃)₂), 3.90 (two d, J = 6.8 Hz, 1H, C-3), 4.22 (m, 2H,

C-20), 4.53 (m, 1H, C-7), 4.95 (m, 1H, C-5), 5.71 (d, J = 6.9 Hz, 1H, C-2), 6.0 (m, C-13), 6.43 (two s, 1H, C-10), 7.12 (d, J = 8.8 Hz, 1H), 7.46 (m, 10H), 7.75 (d, J = 7.3 Hz, 1H), 8.04 (d, J = 7.8 Hz, 1H), 8.16 (m, 2H).

10-*N,N*-Dimethylcarbamoyl-10-deacetylpaclitaxel (**1-34**, SB-T-0035)⁸⁰

To a 25-mL round-bottom flask was added 7-triethylsilyloxy-10-*N,N*-dimethylcarbamoyl-10-deacetyl-2'-triisopropylsilyloxy-paclitaxel **1-33** (110 mg). The flask was purged with nitrogen gas. 3 mL acetonitrile and 3 mL pyridine were then added into the flask. The starting material was dissolved and cooled to 0 °C in an ice bath. 2 mL HF/pyridine was then added dropwise. The reaction mixture was allowed to warm up to room temperature gradually. The reaction was monitored by TLC (hexanes/ethyl acetate = 1/1, stain with 5% sulfuric acid in ethanol). Upon completion after overnight, the reaction was quenched with 5 mL 0.2 M citric acid in water (3.8%). The aqueous layer was extracted with ethyl acetate (3 x 30 mL). The combined organic layer was washed with saturated copper sulfate (3 x 30 mL) to remove pyridine, and then washed with water (3 x 30 mL) and brine (3 x 30 mL), and dried over anhydrous MgSO₄. The MgSO₄ was subsequently removed by vacuum filtration, and the filtrate was concentrated in vacuo to give crude product as white solid. The crude product was further purified by column chromatography on silica gel (gradient eluent: hexanes/ethyl acetate from 10/1 to 1/1) to give product 10-*N,N*-dimethylcarbamoyl-10-deacetylpaclitaxel **1-34** (SB-T-0035) as white solid (62 mg, 0.0702 mmol) in 76% yield and side product 13-benzoyl-10-*N,N*-dimethylcarbamoyl-10-deacetyl-baccatin III **1-35** as white solid. Product: ¹H NMR (400 MHz, CDCl₃): δ 1.15 (s, 3H, C-17), 1.23 (s, 3H, C-16), 1.67 (s, 3H, C-19), 1.81 (s, 3H, C-18), 1.90 (m, 1H, C-6), 2.30 (m, 2H, C-14), 2.38 (s, 3H, OAc at C-10), 2.53 (m, 1H, C-6), 2.96 (s, 3H, CON(CH₃)₂), 3.04 (s, 3H, CON(CH₃)₂), 3.17 (br. s, 1H, OH), 3.55 (br. s, 1H, OH), 3.79 (d, J = 6.9 Hz, 1H, C-3), 4.19 (d, J = 8.3 Hz, 1H, C-20), 4.29 (d, J = 8.3 Hz, 1H, C-20), 4.43 (dd, J = 10.8 Hz, J = 6.7 Hz, 1H, C-7), 4.79 (d, J = 2.6 Hz, 1H, C2'-H), 4.97 (d, J = 7.8 Hz, 1H, C-5), 5.66 (d, J = 7.0 Hz, 1H, C-2), 5.79 (dd, J = 9.0 Hz, J = 2.5 Hz, 1H, C-3'), 6.24 (m, 2H, C-13 & C10), 6.99 (d, J = 8.8 Hz, 1H, C3'-NH), 7.36 (m, 5H, Ph), 7.50 (m, 5H, C2-OBz & C3'-N-OBz), 7.61 (m, 1H, C2-OBz), 7.74 (d, J = 7.2 Hz, 2 H, C3'-N-OBz), J = 8.12 (d, J = 7.2 Hz, 2H, C2-OBz). ESI-MS: 883.3 [M+H]⁺. Side product: ¹H NMR (400 MHz, CDCl₃): δ 1.22 (s, 3H, C-17), 1.32 (s, 3H, C-16), 1.73 (s, 3H, C-19), 1.92 (m, 1H, C-6), 1.96 (s, 3H, C-18), 2.21 (s, 3H, OAc at C-10), 2.27 (m, 1H, C-14), 2.36 (m, 1H, C-14), 2.60 (m, 1H, C-6), 3.00 (s, 3H, CON(CH₃)₂), 3.09 (s, 3H, CON(CH₃)₂), 3.26 (d, J = 3.6 Hz, 1H, OH), 3.93 (d, J = 6.8 Hz, 1H, C-3), 4.20 (d, J = 8.4 Hz, 1H, C-20), 4.29 (d, J = 8.4 Hz, 1H, C-20), 4.55 (m, 1H, C-7), 5.00 (d, J = 7.7 Hz, 1H, C-5), 5.71 (d, J = 6.8 Hz, 1H, C-2), 6.26 (t, J = 8.4 Hz, 1H, C-13), 6.37 (s, 1H, C-10), 7.46 (t, J = 8.0 Hz, 1H, C2-OBz), 7.60 (m, 3H, C13-OBz), 7.68 (m, 1 H, C2-OBz), J = 8.05 (d, J = 7.1 Hz, 2H, C2-OBz), 8.18 (d, J = 7.1 Hz, 2H, C13-OBz). ESI-MS: 720.2 [M+H]⁺. All data are consisted with literature values.⁸⁰

§ 1.5 References

- (1) Hanahan, D.; Weinberg, R. A. Hallmarks of Cancer: The Next Generation. *Cell* **2011**, *144*, 646-674.
- (2) Siegel, R. L.; Miller, K. D.; Jemal, A. Cancer Statistics, 2016. *Ca-Cancer J Clin* **2016**, *66*, 7-30.
- (3) American Cancer Society. Cancer Facts & Figures 2016. 2016.
- (4) Ferlay, J.; Soerjomataram, I.; Dikshit, R.; Eser, S.; Mathers, C.; Rebelo, M.; Parkin, D. M.; Forman, D.; Bray, F. Cancer incidence and mortality worldwide: Sources, methods and major patterns in GLOBOCAN 2012. *Int J Cancer* **2015**, *136*, E359-E386.
- (5) Espinosa, E.; Zamora, P.; Feliu, J.; Baron, M. G. Classification of anticancer drugs - a new system based on therapeutic targets. *Cancer Treat Rev* **2003**, *29*, 515-523.
- (6) Wall, M. E.; Wani, M. C. Camptothecin and Taxol - Discovery to Clinic - 13th Bruce-F-Cain-Memorial-Award-Lecture. *Cancer Res* **1995**, *55*, 753-760.
- (7) Wani, M. C.; Taylor, H. L.; Wall, M. E.; Coggon, P.; Mcphail, A. T. Plant Antitumor Agents .6. Isolation and Structure of Taxol, a Novel Antileukemic and Antitumor Agent from *Taxus-Brevifolia*. *J Am Chem Soc* **1971**, *93*, 2325-2327.
- (8) Rowinsky, E. K.; Donehower, R. C. Paclitaxel (Taxol) *New Engl J Med* **1995**, *332*, 1004-1014.
- (9) Schiff, P. B.; Fant, J.; Horwitz, S. B. Promotion of Microtubule Assembly In vitro by Taxol. *Nature* **1979**, *277*, 665-667.
- (10) Schiff, P. B.; Horwitz, S. B. Taxol Stabilizes Microtubules in Mouse Fibroblast Cells. *P Natl Acad Sci-Biol* **1980**, *77*, 1561-1565.
- (11) Jordan, M. A.; Wilson, L. Microtubules as a target for anticancer drugs. *Nat Rev Cancer* **2004**, *4*, 253-265.
- (12) Kingston, D. G. I. Taxol, a molecule for all seasons. *Chem Commun* **2001**, *10*, 867-880.
- (13) National Cancer Institute. FDA approval for docetaxel. <http://www.cancer.gov/about-cancer/treatment/drugs/fda-docetaxel - Anchor-Hea-39459>.
- (14) Galsky, M. D.; Dritselis, A.; Kirkpatrick, P.; Oh, W. K. Cabazitaxel. *Nat Rev Drug Discov* **2010**, *9*, 677-678.

- (15) Cragg, G. M.; Schepartz, S. A.; Suffness, M.; Grever, M. R. The Taxol Supply Crisis - New Nci Policies for Handling the Large-Scale Production of Novel Natural Product Anticancer and Anti-Hiv Agents. *J Nat Prod* **1993**, *56*, 1657-1668.
- (16) Holton, R. A.; Somoza, C.; Kim, H. B.; Liang, F.; Biediger, R. J.; Boatman, P. D.; Shindo, M.; Smith, C. C.; Kim, S. C.; Nadizadeh, H.; Suzuki, Y.; Tao, C. L.; Vu, P.; Tang, S. H.; Zhang, P. S.; Murthi, K. K.; Gentile, L. N.; Liu, J. H. First Total Synthesis of Taxol .1. Functionalization of the B-Ring. *J Am Chem Soc* **1994**, *116*, 1597-1598.
- (17) Holton, R. A.; Kim, H. B.; Somoza, C.; Liang, F.; Biediger, R. J.; Boatman, P. D.; Shindo, M.; Smith, C. C.; Kim, S. C.; Nadizadeh, H.; Suzuki, Y.; Tao, C. L.; Vu, P.; Tang, S. H.; Zhang, P. S.; Murthi, K. K.; Gentile, L. N.; Liu, J. H. First Total Synthesis of Taxol .2. Completion of the C-Ring and D-Ring. *J Am Chem Soc* **1994**, *116*, 1599-1600.
- (18) Nicolaou, K. C.; Yang, Z.; Liu, J. J.; Ueno, H.; Nantermet, P. G.; Guy, R. K.; Claiborne, C. F.; Renaud, J.; Couladouros, E. A.; Paulvannan, K.; Sorensen, E. J. Total Synthesis of Taxol. *Nature* **1994**, *367*, 630-634.
- (19) Nicolaou, K. C.; Nantermet, P. G.; Ueno, H.; Guy, R. K.; Couladouros, E. A.; Sorensen, E. J. Total Synthesis of Taxol .1. Retrosynthesis, Degradation, and Reconstitution. *J Am Chem Soc* **1995**, *117*, 624-633.
- (20) Nicolaou, K. C.; Liu, J. J.; Yang, Z.; Ueno, H.; Sorensen, E. J.; Claiborne, C. F.; Guy, R. K.; Hwang, C. K.; Nakada, M.; Nantermet, P. G. Total Synthesis of Taxol .2. Construction of a-Ring and C-Ring Intermediates and Initial Attempts to Construct the Abc Ring-System. *J Am Chem Soc* **1995**, *117*, 634-644.
- (21) Nicolaou, K. C.; Yang, Z.; Liu, J. J.; Nantermet, P. G.; Claiborne, C. F.; Renaud, J.; Guy, R. K.; Shibayama, K. Total Synthesis of Taxol .3. Formation of Taxols Abc Ring Skeleton. *J Am Chem Soc* **1995**, *117*, 645-652.
- (22) Nicolaou, K. C.; Ueno, H.; Liu, J. J.; Nantermet, P. G.; Yang, Z.; Renaud, J.; Paulvannan, K.; Chadha, R. Total Synthesis of Taxol .4. The Final Stages and Completion of the Synthesis. *J Am Chem Soc* **1995**, *117*, 653-659.
- (23) Danishefsky, S. J.; Masters, J. J.; Young, W. B.; Link, J. T.; Snyder, L. B.; Magee, T. V.; Jung, D. K.; Isaacs, R. C. A.; Bornmann, W. G.; Alaimo, C. A.; Coburn, C. A.; DiGrandi, M. J. Total synthesis of baccatin III and taxol. *J Am Chem Soc* **1996**, *118*, 2843-2859.
- (24) Wender, P. A.; Badham, N. F.; Conway, S. P.; Floreancig, P. E.; Glass, T. E.; Granicher, C.; Houze, J. B.; Janichen, J.; Lee, D. S.; Marquess, D. G.; McGrane, P. L.; Meng, W.; Mucciario, T. P.; Muhlebach, M.; Natchus, M. G.; Paulsen, H.; Rawlins, D. B.; Satkofsky, J.; Shuker, A. J.; Sutton, J. C.; Taylor, R. E.; Tomooka, K. The pinene path to taxanes .5. Stereocontrolled synthesis of a versatile taxane precursor. *J Am Chem Soc* **1997**, *119*, 2755-2756.

- (25) Wender, P. A.; Badham, N. F.; Conway, S. P.; Floreancig, P. E.; Glass, T. E.; Houze, J. B.; Krauss, N. E.; Lee, D. S.; Marquess, D. G.; McGrane, P. L.; Meng, W.; Natchus, M. G.; Shuker, A. J.; Sutton, J. C.; Taylor, R. E. The pinene path to taxanes .6. A concise stereocontrolled synthesis of taxol. *J Am Chem Soc* **1997**, *119*, 2757-2758.
- (26) Morihira, K.; Hara, R.; Kawahara, S.; Nishimori, T.; Nakamura, N.; Kusama, H.; Kuwajima, I. Enantioselective total synthesis of taxol. *J Am Chem Soc* **1998**, *120*, 12980-12981.
- (27) Mukaiyama, T.; Shiina, I.; Iwadare, H.; Saitoh, M.; Nishimura, T.; Ohkawa, N.; Sakoh, H.; Nishimura, K.; Tani, Y.; Hasegawa, M.; Yamada, K.; Saitoh, K. Asymmetric total synthesis of Taxol (R). *Chem-Eur J* **1999**, *5*, 121-161.
- (28) Doi, T.; Fuse, S.; Miyamoto, S.; Nakai, K.; Sasuga, D.; Takahashi, T. A formal total synthesis of taxol aided by an automated synthesizer. *Chem-Asian J* **2006**, *1*, 370-383.
- (29) Fukaya, K.; Tanaka, Y.; Sato, A. C.; Kodama, K.; Yamazaki, H.; Ishimoto, T.; Nozaki, Y.; Iwaki, Y. M.; Yuki, Y.; Umei, K.; Sugai, T.; Yamaguchi, Y.; Watanabe, A.; Oishi, T.; Sato, T.; Chida, N. Synthesis of Paclitaxel. 1. Synthesis of the ABC Ring of Paclitaxel by SmI₂-Mediated Cyclization. *Org Lett* **2015**, *17*, 2570-2573.
- (30) Fukaya, K.; Kodama, K.; Tanaka, Y.; Yamazaki, H.; Sugai, T.; Yamaguchi, Y.; Watanabe, A.; Oishi, T.; Sato, T.; Chida, N. Synthesis of Paclitaxel. 2. Construction of the ABCD Ring and Formal Synthesis. *Org Lett* **2015**, *17*, 2574-2577.
- (31) Hirai, S.; Utsugi, M.; Iwamoto, M.; Nakada, M. Formal Total Synthesis of (-)-Taxol through Pd-Catalyzed Eight-Membered Carbocyclic Ring Formation. *Chem-Eur J* **2015**, *21*, 355-359.
- (32) Ojima, I.; Habus, I.; Zhao, M.; Zucco, M.; Park, Y. H.; Sun, C. M.; Brigaud, T. New and Efficient Approaches to the Semisynthesis of Taxol and Its C-13 Side-Chain Analogs by Means of Beta-Lactam Synthon Method. *Tetrahedron* **1992**, *48*, 6985-7012.
- (33) Holton, R. A. Method for preparation of taxol. Eur. Pat. Appl. EP 400971, May 30, 1990.
- (34) Chauviere, G.; Guenard, D.; Picot, F.; Senilh, V.; Potier, P. Structural-Analysis and Biochemical-Study of Isolated Products of the Yew - *Taxus-Baccata* L (Taxaceae). *Cr Acad Sci li* **1981**, *293*, 501-503.
- (35) Denis, J. N.; Greene, A. E.; Guenard, D.; Guerittevoegelein, F.; Mangatal, L.; Potier, P. A Highly Efficient, Practical Approach to Natural Taxol. *J Am Chem Soc* **1988**, *110*, 5917-5919.
- (36) Ojima, I., Kuduk, S. D., Chakravarty, S. Recent advances in the medicinal chemistry of taxoids anticancer agents. *Adv Med Chem* **1999**, *4*, 69-124.

- (37) Ojima, I.; Habus, I. Asymmetric-Synthesis of Beta-Lactams by Chiral Ester Enolate - Imine Condensation. *Tetrahedron Lett* **1990**, *31*, 4289-4292.
- (38) Ojima, I.; Habus, I.; Zhao, M. Z.; Georg, G. I.; Jayasinghe, L. R. Efficient and Practical Asymmetric-Synthesis of the Taxol C-13 Side-Chain, N-Benzoyl-(2r,3s)-3-Phenylisoserine, and Its Analogs Via Chiral 3-Hydroxy-4-Aryl-Beta-Lactams through Chiral Ester Enolate-Imine Cyclocondensation. *J Org Chem* **1991**, *56*, 1681-1683.
- (39) Ojima, I.; Sun, C. M.; Zucco, M.; Park, Y. H.; Duclos, O.; Kuduk, S. A Highly Efficient Route to Taxotere by the Beta-Lactam Synthone Method. *Tetrahedron Lett* **1993**, *34*, 4149-4152.
- (40) Ojima, I.; Zucco, M.; Duclos, O.; Kuduk, S. D.; Sun, C. M.; Park, Y. H. N-Acyl-3-Hydroxy-Beta-Lactams as Key Intermediates for Taxotere and Its Analogs. *Bioorg Med Chem Lett* **1993**, *3*, 2479-2482.
- (41) Staudinger, H. Announcements from the chemical institute at Strasbourg University in Alsace, France - Ketene. *Liebigs Ann Chem* **1907**, *356*, 51-123.
- (42) Tidwell, T. T. Hugo (ugo) Schiff, Schiff bases, and a century of beta-lactam synthesis. *Angew Chem Int Edit* **2008**, *47*, 1016-1020.
- (43) Sheehan, J. C.: The enchanted ring: the untold story of penicillin. The MIT Press., 1984.
- (44) Ojima, I. Recent Advances in the Beta-Lactam Synthone Method. *Acc Chem Res* **1995**, *28*, 383-389.
- (45) Jiao, L.; Liang, Y.; Xu, J. X. Origin of the relative stereoselectivity of the beta-lactam formation in the Staudinger reaction. *J Am Chem Soc* **2006**, *128*, 6060-6069.
- (46) Cossio, F. P.; Arrieta, A.; Sierra, M. A. The mechanism of the ketene-imine (Staudinger) reaction in its centennial: Still an unsolved problem? *Acc Chem Res* **2008**, *41*, 925-936.
- (47) Brieva, R.; Crich, J. Z.; Sih, C. J. Chemoenzymatic Synthesis of the C-13 Side-Chain of Taxol - Optically-Active 3-Hydroxy-4-Phenyl Beta-Lactam Derivatives. *J Org Chem* **1993**, *58*, 1068-1075.
- (48) Kingston, D. G. I.; Samaranyake, G.; Ivey, C. A. The Chemistry of Taxol, a Clinically Useful Anticancer Agent. *J Nat Prod* **1990**, *53*, 1-12.
- (49) Guenard, D.; Guerittevoegelein, F.; Potier, P. Taxol and Taxotere - Discovery, Chemistry, and Structure-Activity-Relationships. *Acc Chem Res* **1993**, *26*, 160-167.

- (50) Ojima, I.; Slater, J. C.; Michaud, E.; Kuduk, S. D.; Bounaud, P. Y.; Vrignaud, P.; Bissery, M. C.; Veith, J. M.; Pera, P.; Bernacki, R. J. Syntheses and structure-activity relationships of the second-generation antitumor taxoids: Exceptional activity against drug-resistant cancer cells. *J Med Chem* **1996**, *39*, 3889-3896.
- (51) Chen, S. H.; Wei, J. M.; Farina, V. Taxol Structure-Activity-Relationships - Synthesis and Biological Evaluation of 2-Deoxytaxol. *Tetrahedron Lett* **1993**, *34*, 3205-3206.
- (52) Chaudhary, A. G.; Gharpure, M. M.; Rimoldi, J. M.; Chordia, M. D.; Gunatilaka, A. A. L.; Kingston, D. G. I.; Grover, S.; Lin, C. M.; Hamel, E. Unexpectedly Facile Hydrolysis of the 2-Benzoate Group of Taxol and Syntheses of Analogs with Increased Activities. *J Am Chem Soc* **1994**, *116*, 4097-4098.
- (53) Kingston, D. G. I.; Chaudhary, A. G.; Chordia, M. D.; Gharpure, M.; Gunatilaka, A. A. L.; Higgs, P. I.; Rimoldi, J. M.; Samala, L.; Jagtap, P. G.; Giannakakou, P.; Jiang, Y. Q.; Lin, C. M.; Hamel, E.; Long, B. H.; Fairchild, C. R.; Johnston, K. A. Synthesis and biological evaluation of 2-acyl analogues of paclitaxel (Taxol). *J Med Chem* **1998**, *41*, 3715-3726.
- (54) Ojima, I.; Wang, T.; Miller, M. L.; Lin, S. N.; Borella, C. P.; Geng, X. D.; Pera, P.; Bernacki, R. J. Synthesis and structure-activity relationships of new second-generation taxoids. *Bioorg Med Chem Lett* **1999**, *9*, 3423-3428.
- (55) Chordia, M. D.; Chaudhary, A. G.; Kingston, D. G. I.; Jiang, Y. Q.; Hamel, E. Synthesis and Biological Evaluation of 4-Deacetoxytaxol. *Tetrahedron Lett* **1994**, *35*, 6843-6846.
- (56) Neidigh, K. A.; Gharpure, M. M.; Rimoldi, J. M.; Kingston, D. G. I.; Jiang, Y. Q.; Hamel, E. Synthesis and Biological Evaluation of 4-Deacetylpaclitaxel. *Tetrahedron Lett* **1994**, *35*, 6839-6842.
- (57) Chen, S. H.; Wei, J. M.; Long, B. H.; Fairchild, C. A.; Carboni, J.; Mamber, S. W.; Rose, W. C.; Johnston, K.; Casazza, A. M.; Kadow, J. F.; Farina, V.; Vyas, D. M.; Doyle, T. W. Novel C-4 Paclitaxel (Taxol(R)) Analogs - Potent Antitumor Agents. *Bioorg Med Chem Lett* **1995**, *5*, 2741-2746.
- (58) Samaranayake, G.; Magri, N. F.; Jitrangsri, C.; Kingston, D. G. I. Modified Taxols .5. Reaction of Taxol with Electrophilic Reagents and Preparation of a Rearranged Taxol Derivative with Tubulin Assembly Activity. *J Org Chem* **1991**, *56*, 5114-5119.
- (59) Gunatilaka, A. A. L.; Ramdayal, F. D.; Sarragiotto, M. H.; Kingston, D. G. I.; Sackett, D. L.; Hamel, E. Synthesis and biological evaluation of novel paclitaxel (Taxol) D-ring modified analogues. *J Org Chem* **1999**, *64*, 2694-2703.

- (60) Dubois, J.; Thoret, S.; Gueritte, F.; Guenard, D. Synthesis of 5(20)deoxydocetaxel, a new active docetaxel analogue. *Tetrahedron Lett* **2000**, *41*, 3331-3334.
- (61) Chaudhary, A. G.; Rimoldi, J. M.; Kingston, D. G. I. Modified Taxols .10. Preparation of 7-Deoxytaxol, a Highly Bioactive Taxol Derivative, and Interconversion of Taxol and 7-Epi-Taxol. *J Org Chem* **1993**, *58*, 3798-3799.
- (62) Chen, S. H.; Huang, S.; Kant, J.; Fairchild, C.; Wei, J. M.; Farina, V. Synthesis of 7-Deoxytaxol and 7,10-Dideoxytaxol Via Radical Intermediates. *J Org Chem* **1993**, *58*, 5028-5029.
- (63) Chaudhary, A. G.; Kingston, D. G. I. Synthesis of 10-Deacetoxytaxol and 10-Deoxytaxotere. *Tetrahedron Lett* **1993**, *34*, 4921-4924.
- (64) Samaranayake, G.; Neidigh, K. A.; Kingston, D. G. I. Modified Taxols .8. Deacylation and Reacylation of Baccatin-Iii. *J Nat Prod* **1993**, *56*, 884-898.
- (65) Uoto, K.; Mitsui, I.; Terasawa, H.; Soga, T. First synthesis and cytotoxic activity of novel docetaxel analogs modified at the C18-position. *Bioorg Med Chem Lett* **1997**, *7*, 2991-2996.
- (66) Ojima, I.; Park, Y. H.; Sun, C. M.; Fenoglio, I.; Appendino, G.; Pera, P.; Bernacki, R. J. Structure-Activity-Relationships of New Taxoids Derived from 14-Beta-Hydroxy-10-Deacetylbaaccatin-Iii. *J Med Chem* **1994**, *37*, 1408-1410.
- (67) Ojima, I.; Slater, J. C.; Kuduk, S. D.; Takeuchi, C. S.; Gimi, R. H.; Sun, C. M.; Park, Y. H.; Pera, P.; Veith, J. M.; Bernacki, R. J. Syntheses and structure-activity relationships of taxoids derived from 14 beta-hydroxy-10-deacetylbaaccatin III. *J Med Chem* **1997**, *40*, 267-278.
- (68) Nicoletti, M. I.; Colombo, T.; Rossi, C.; Monardo, C.; Stura, S.; Zucchetti, M.; Riva, A.; Morazzoni, P.; Donati, M. B.; Bombardelli, E.; D'Incalci, M.; Giavazzi, R. IDN5109, a taxane with oral bioavailability and potent antitumor activity. *Cancer Res* **2000**, *60*, 842-846.
- (69) Sharom, F. J. ABC multidrug transporters: structure, function and role in chemoresistance. *Pharmacogenomics* **2008**, *9*, 105-127.
- (70) Szakacs, G.; Paterson, J. K.; Ludwig, J. A.; Booth-Genthe, C.; Gottesman, M. M. Targeting multidrug resistance in cancer. *Nat Rev Drug Discov* **2006**, *5*, 219-234.
- (71) Aller, S. G.; Yu, J.; Ward, A.; Weng, Y.; Chittaboina, S.; Zhuo, R. P.; Harrell, P. M.; Trinh, Y. T.; Zhang, Q. H.; Urbatsch, I. L.; Chang, G. Structure of P-Glycoprotein Reveals a Molecular Basis for Poly-Specific Drug Binding. *Science* **2009**, *323*, 1718-1722.

- (72) Ojima, I.; Zuniga, E. S.; Berger, W. T.; Seitz, J. D. Tumor-targeting drug delivery of new-generation taxoids. *Future Med Chem* **2012**, *4*, 33-50.
- (73) Gueritte-Voegelein, F.; Senilh, V.; David, B.; Guenard, D.; Potier, P. Chemical studies of 10-deacetyl baccatin III. Hemisynthesis of taxol derivatives. *Tetrahedron* **1986**, *42*, 4451-4460.
- (74) Ehrlichova, M.; Vaclavikova, R.; Ojima, I.; Pepe, A.; Kuznetsova, L. V.; Chen, J.; Truksa, J.; Kovar, J.; Gut, I. Transport and cytotoxicity of paclitaxel, docetaxel, and novel taxanes in human breast cancer cells. *Naunyn Schmiedebergs Arch Pharmacol* **2005**, *372*, 95-105.
- (75) Macrae, M. X.; Blake, S.; Mayer, M.; Yang, J. Nanoscale Ionic Diodes with Tunable and Switchable Rectifying Behavior. *J Am Chem Soc* **2010**, *132*, 1766-+.
- (76) Yu, H. W.; Ballard, C. E.; Boyle, P. D.; Wang, B. H. An inexpensive carbohydrate derivative used as a chiral auxiliary in the synthesis of alpha-hydroxy carboxylic acids. *Tetrahedron* **2002**, *58*, 7663-7679.
- (77) Gonzalez, J.; Aurigemma, C.; Truesdale, L. Synthesis of (+)-(1S,2R)- and (-)-(1R,2S)-trans-2-phenylcyclohexanol via Sharpless asymmetric dihydroxylation (AD). *Org Synth* **2003**, *79*, 93-102.
- (78) Kuznetsova, L. V.; Pepe, A.; Ungureanu, I. M.; Pera, P.; Bernacki, R. J.; Ojima, I. Syntheses and structure-activity relationships of novel 3'-difluoromethyl and 3'-trifluoromethyl-taxoids. *J Fluorine Chem* **2008**, *129*, 817-828.
- (79) Kuznetsova, L.; Ungureanu, I. M.; Pepe, A.; Zanardi, I.; Wu, X.; Ojima, I. Trifluoromethyl- and difluoromethyl- β -lactams as useful building blocks for the synthesis of fluorinated amino acids, dipeptides, and fluoro-taxoids. *J Fluorine Chem* **2004**, *125*, 487-500.
- (80) Ojima, I.; Fumero-Oderda, C. L.; Kuduk, S. D.; Ma, Z.; Kirikae, F.; Kirikae, T. Structure-activity relationship study of taxoids for their ability to activate murine macrophages as well as inhibit the growth of macrophage-like cells. *Bioorg Med Chem* **2003**, *11*, 2867-2888.

Chapter 2

Metabolic Stability Assessment of Self-Immolative Disulfide Linkers in Tumor-Targeted Drug Delivery Systems via ^{19}F NMR

Chapter Contents

§ 2.1 Introduction.....	74
§ 2.1.1 Tumor-Targeted Drug Delivery Systems (TTDDS)	74
§ 2.1.2 Self-Immolative Disulfide Linker	77
§ 2.1.3 Drug Release Study of the Self-Immolative Disulfide Linker Systems via ^{19}F NMR	81
§ 2.2 Metabolic Stability Assessment of Tumor-Targeted Drug Delivery Systems via ^{19}F NMR	84
§ 2.2.1 Synthesis of Methyl-Branched Self-Immolative Disulfide Linker	84
§ 2.2.2 Effects of Solvent Systems and Drug Formulations on the Fluorine Signal Chemical Shifts of Designed Probes	86
§ 2.2.3 Metabolic Stability Assessment of Tumor-Targeted Drug Delivery Systems via Time-Resolved ^{19}F NMR	91
§ 2.3 Summary	95
§ 2.4 Experimental	95
§ 2.5 References.....	103

§ 2.1 Introduction

§ 2.1.1 Tumor-Targeted Drug Delivery Systems (TTDDS)

The therapeutic concept of drug targeting was founded on Paul Ehrlich's vision of "the magic bullet" that he proclaimed at the beginning of the 20th century.¹ Because of severe side effects could be potentially caused by traditional non-targeted therapeutic agents, chemotherapy has switched into the era of "targeted therapy" recently.² Targeted cancer therapies block the growth and spread of cancer by interfering with specific molecular targets that are associated with cancer.³ In 1996, Druker and his colleagues identified imatinib (Gleevec®) as a selective inhibitor of the Bcr-Abl tyrosine kinase for the treatment of chronic myelogenous leukemia (CML) (**Figure 2.1**).⁴ Bevacizumab (Avastin®) is a humanized monoclonal antibody that targets vascular endothelial growth factor (VEGF), a key regulator of tumor angiogenesis, and has recently been approved by the US Food and Drug Administration (FDA) for the treatment of metastatic colorectal cancer.^{5,6} Imatinib (Gleevec®) and bevacizumab (Avastin®) are just two examples among the many targeted cancer therapies that have been approved by the US FDA, and there are growing interests on targeted cancer therapies.

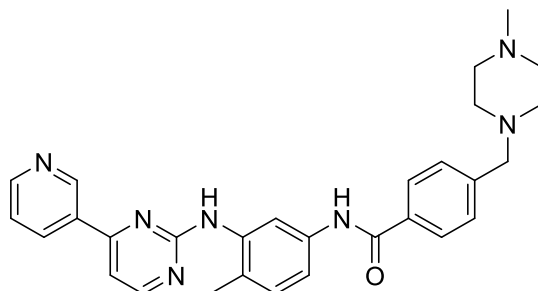


Figure 2.1 Chemical structure of imatinib (Gleevec®)

However, currently there are still limitations of targeted cancer therapies. One problem is that targeted cancer therapies are only limited to certain types of cancer. For example, imatinib is specifically used for the treatment of chronic myelogenous leukemia (CML). Another limitation is that some patients may develop multidrug resistance (MDR), making such chemotherapeutic drugs ineffective. Therefore, there is great need for conquering such limitations.

The Ojima laboratory has been working on the discovery and development of tumor-targeted drug delivery systems (TTDDS), in which novel "guided molecular missiles" have been generated in the fight against cancer. Typically, such tumor-targeting drug conjugates consist of a tumor-targeting module (TTM) connected to a cytotoxic warhead directly or through a suitable "smart" linker (**Figure 2.2**).⁷⁻¹⁰ The tumor-targeting module (TTM) should have strong affinity for tumor-specific receptor, thus could guide the conjugates specifically towards tumor cells targeting the overexpressed receptors. The warhead could be linked to the TTM directly by covalent bond, such as hydrolyzable ester bond or amide bond. However, the cytotoxic warhead may not be efficiently released to its active form (amide bond linker) or the linker maybe too

labile during blood circulation (ester bond linker). Therefore, a suitable cleavable linker is preferred to connect the tumor-targeting module (TTM) and cytotoxic warhead. Ideally, such linker should be stable during blood circulation to keep the pro-drug inactive, and could readily be cleaved to release the active drug once the tumor-targeting conjugates got internalized into tumor cells.¹⁰

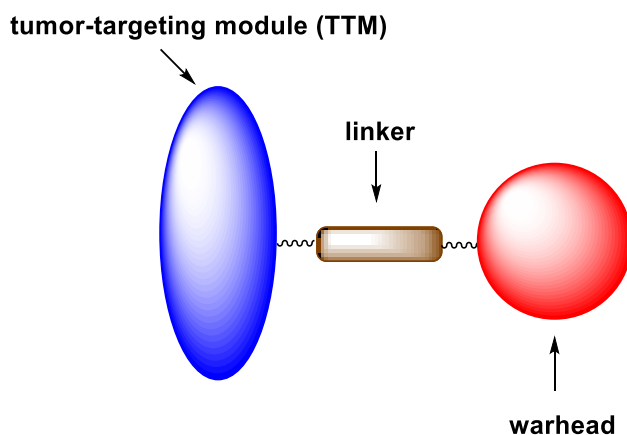


Figure 2.2 A typical tumor-targeting drug conjugate. Adapted with permission from Ojima, I. Guided molecular missiles for tumor-targeting chemotherapy-case studies using the second-generation taxoids as warheads. *Acc Chem Res* **2008**, *41*, 108-119. Copyright (2008) American Chemical Society.

As shown in **Figure 2.3**, the tumor-targeting drug conjugates could be recognized by the overexpressed tumor-specific receptors on the surface of cell membranes, get internalized through a receptor-mediated endocytosis process, and the disulfide linker could be cleaved by taking advantage of the fact that the concentration of glutathione is more than 1000 times higher in tumor cells than in blood plasma, thus eventually release the drug in its active form to its target protein.^{8,10}

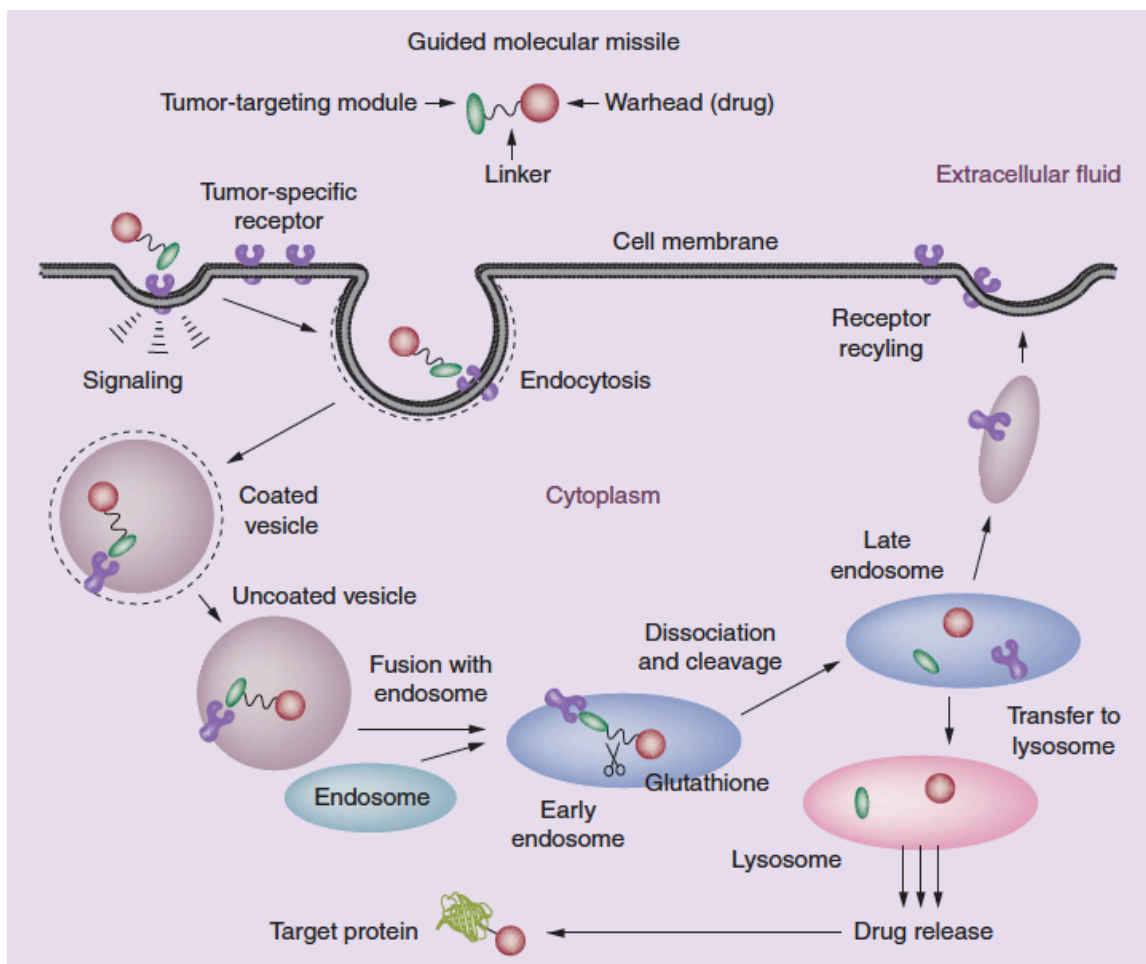


Figure 2.3 Receptor-mediated endocytosis of tumor-targeting drug conjugates. Reprinted from Ojima, I.; Zuniga, E. S.; Berger, W. T.; Seitz, J. D. Tumor-targeting drug delivery of new-generation taxoids. *Future Med Chem* 2012, 4, 33-50, with permission from Future Science Ltd.

Monoclonal antibodies (mAb)^{11,12}, polyunsaturated fatty acids (PUFAs)¹³, folic acid¹⁴, biotin¹⁵⁻¹⁸, and hyaluronic acid have been employed as tumor-targeting modules (TTM) (**Figure 2.4**), and new-generation taxoids have been used as cytotoxic anticancer agents to construct the tumor-targeting drug conjugates. In addition, functionalized single-walled carbon nanotubes (SWNTs) have been designed as vehicles for tumor-targeted drug delivery, making mass delivery of cytotoxic warheads possible to maximize the efficacy.¹⁵ More recently, tumor-targeting drug conjugates bearing dual tumor-targeting modules (TTM) or dual-cytotoxic drugs have been synthesized for enhanced tumor-targeting efficacy and anti-tumor activity, respectively.^{17,18}

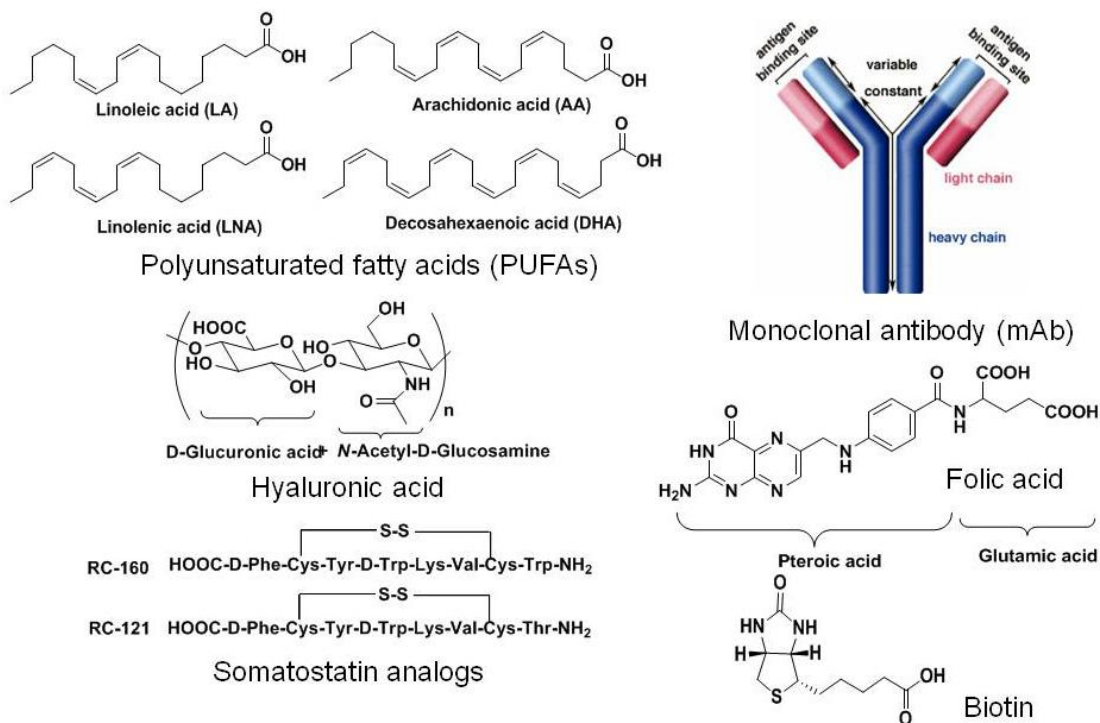


Figure 2.4 Targeting modules (TTM) employed in tumor-targeted drug delivery systems (TTDDS). Adapted from *Bioorg Med Chem*, 13, Jaracz, S.; Chen, J.; Kuznetsova, L. V.; Ojima, L. Recent advances in tumor-targeting anticancer drug conjugates, 5043-5054, Copyright (2005), with permission from Elsevier.

§ 2.1.2 Self-Immolative Disulfide Linker

Various types of linker systems could be used to connect the tumor-targeting module (TTM) and warhead including acid labile linker, proteolytic linker, disulfide linker, and hydrolytic linker (**Figure 2.5**).¹⁹

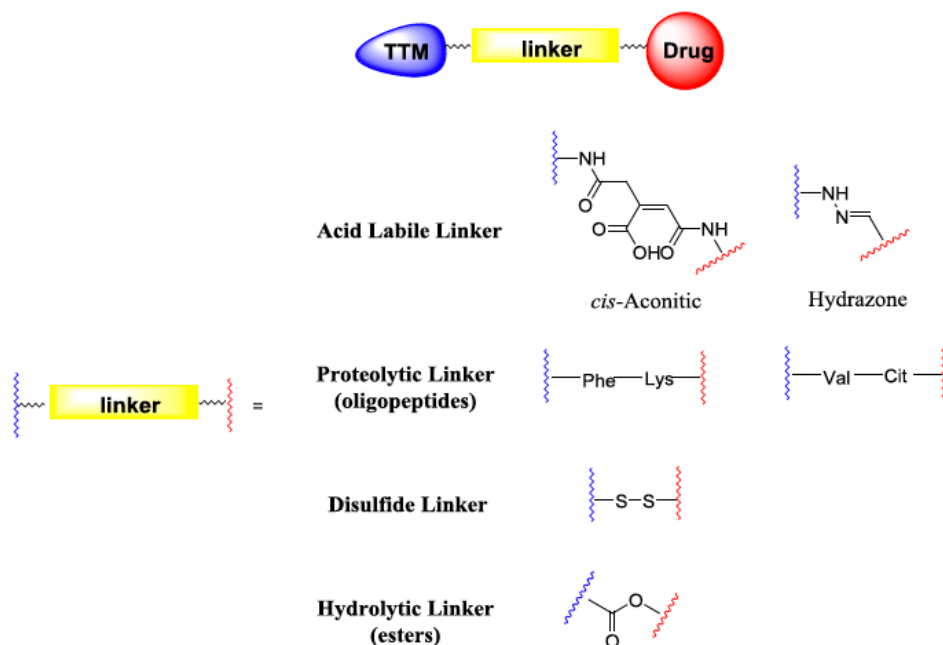


Figure 2.5 Linker systems employed in tumor-targeted drug delivery systems (TTDDS). Adapted from Chen, J.; Jaracz, S.; Zhao, X.; Chen, S.; Ojima, I. Antibody-cytotoxic agent conjugates for cancer therapy. *Expert Opin Drug Deliv* **2005**, 2, 873-890, with permission from Taylor & Francis.

The focus of the linker system in the Ojima laboratory is the disulfide linker, which could be cleaved inside the tumor cells through disulfide exchange by reacting with an intracellular thiol such as thioredoxin or glutathione, taking advantage of the fact that the concentration of such thiol is much higher in tumor tissues (2-8 mM) than circulating human blood plasma (1-2 μM).²⁰

A first-generation self-immolative disulfide linker was employed in the **mAb-SB-T-12136** monoclonal antibody (mAb) drug conjugates (**Figure 2.6**).^{7,11} The 10-methyldisulfanyl (MDS)-alkanoyl analog of new-generation taxoid **SB-T-1213** was connected to monoclonal antibodies (mAbs) KS61 and KS77.^{7,11} These immunoconjugates was designed to target the human epidermal growth factor receptors (EGFR), which are overexpressed in several human head, neck, lung, and breast cancers.^{7,11} In the *in vivo* tumor growth inhibition assay, both of the mAb drug conjugates showed excellent antitumor activity against against human squamous cancer (A431) xenografts in SCID mice.^{7,11} The drawback for the first-generation self-immolative disulfide linker used in the mAb drug conjugates, however, is that the original taxoid warhead was not released because of the compromised modification at C-10 position of the taxoid in order to attach the disulfide linker, and the warhead taxoid released (**SB-T-12136-SH**) is 8 times less potent than the parent taxoid (**SB-T-1213**).^{7,11} Therefore, there was need to design new self-immolative disulfide linker systems to solve this problem.

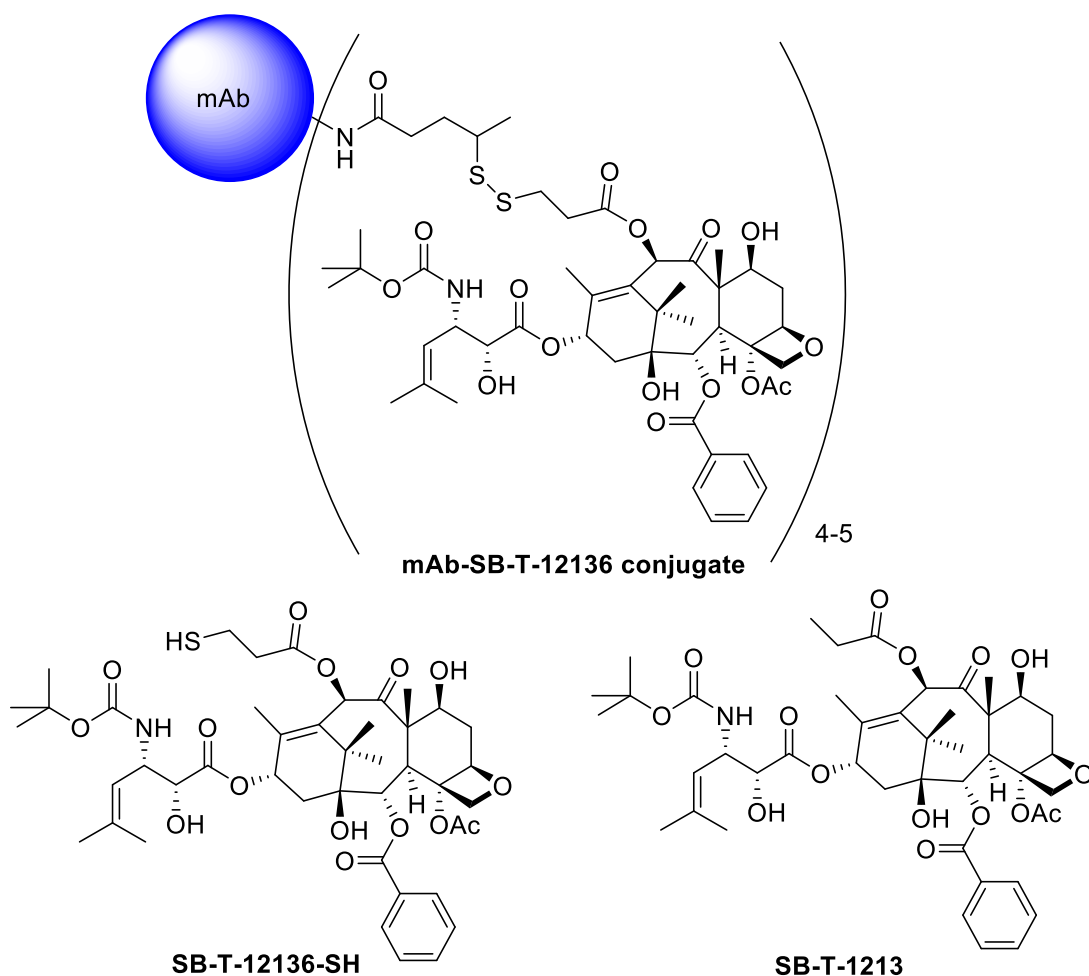


Figure 2.6 Chemical structures of **mAb-SB-T-12136** monoclonal antibody (mAb) drug conjugate, **SB-T-12136-SH**, and **SB-T-1213**. Adapted with permission from Ojima, I.; Geng, X. D.; Wu, X. Y.; Qu, C. X.; Borella, C. P.; Xie, H. S.; Wilhelm, S. D.; Leece, B. A.; Bartle, L. M.; Goldmacher, V. S.; Chari, R. V. J. Tumor-specific novel taxoid-monovalent antibody conjugates. *J Med Chem* **2002**, *45*, 5620-5623. Copyright (2002) American Chemical Society.

Second-generation mechanism-based self-immolative disulfide linkers were then designed, in which original taxoid warhead could be released by a cascade glutathione-triggered disulfide bond cleavage and subsequent thiolactonization process (**Figure 2.7**).^{8,16}

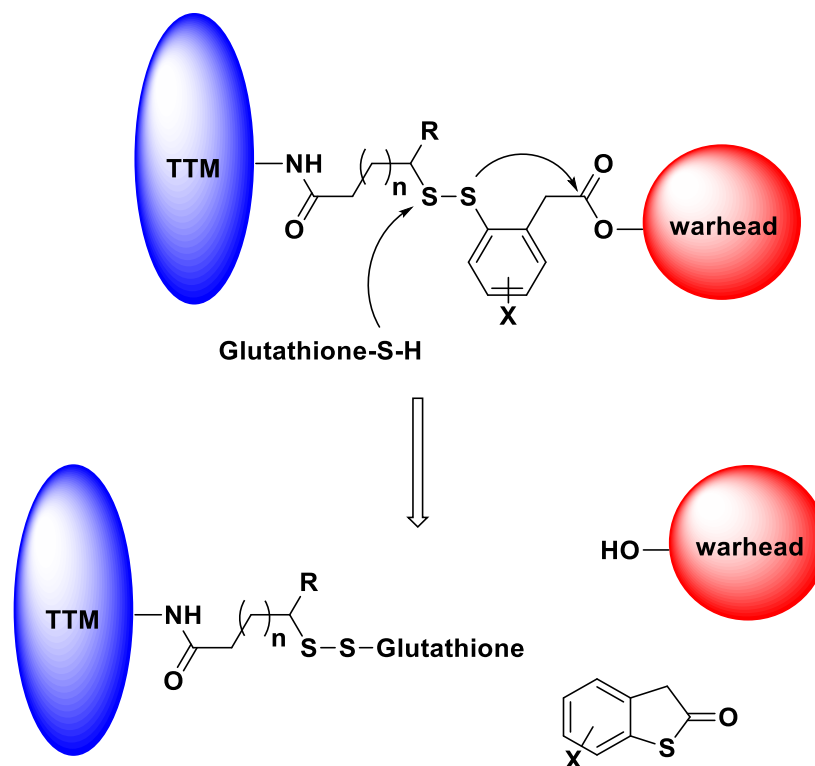


Figure 2.7 Second-generation mechanism-based self-immolative disulfide linkers. Adapted with permission from Ojima, I. Guided molecular missiles for tumor-targeting chemotherapy-case studies using the second-generation taxoids as warheads. *Acc Chem Res* **2008**, *41*, 108-119. Copyright (2008) American Chemical Society.

The linker cleavage and subsequent drug release of the second-generation mechanism-based self-immolative disulfide linker system was validated *in vitro* with a biotin-linker-coumarin probe (**Figure 2.8**).¹⁶ The probe itself is non-fluorescent, but after linker cleavage, fluorescent coumarin will be released. Epifluorescence image A of **Figure 2.8** shows blue fluorescence of released coumarin after incubation of biotin-linker-coumarin probe with GSH-OEt to trigger self-immolative linker cleavage in L1210FR cells, and epifluorescence image B of **Figure 2.8** shows no fluorescence signal observed after incubation of biotin-linker-coumarin probe without adding GSH-OEt.¹⁶

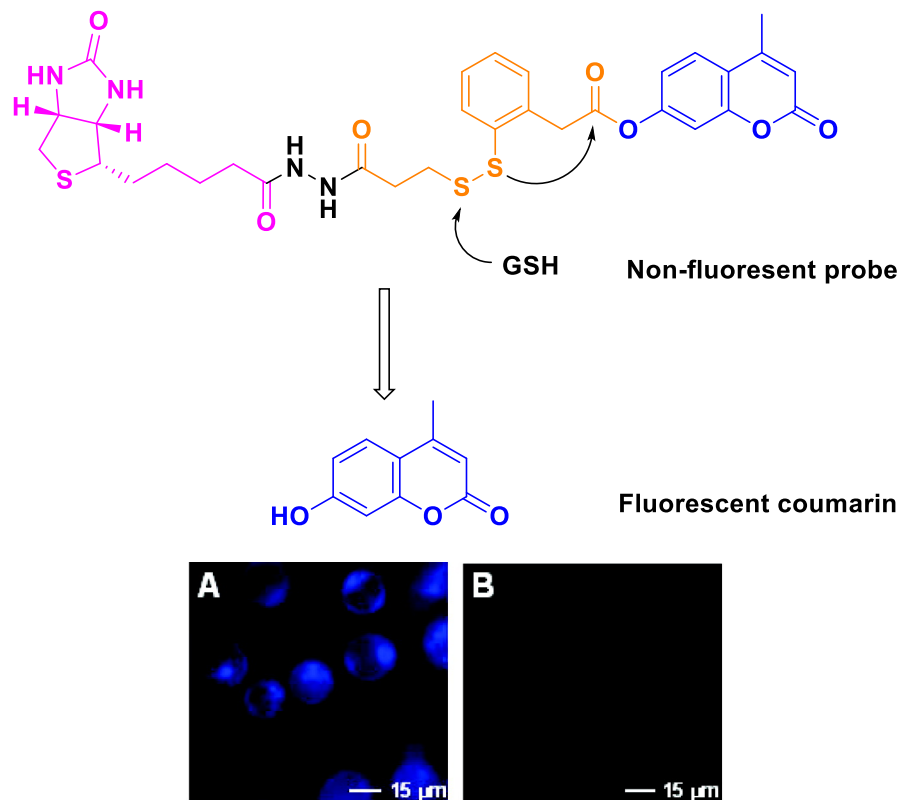


Figure 2.8 Validation of the drug release of a second-generation mechanism-based self-immolative disulfide linker *in vitro* with the biotin-linker-coumarin conjugate. Adapted with permission from Chen, S. Y.; Zhao, X. R.; Chen, J. Y.; Chen, J.; Kuznetsova, L.; Wong, S. S.; Ojima, I. Mechanism-Based Tumor-Targeting Drug Delivery System. Validation of Efficient Vitamin Receptor-Mediated Endocytosis and Drug Release. *Bioconjugate Chem* **2010**, *21*, 979-987. Copyright (2010) American Chemical Society.

§ 2.1.3 Drug Release Study of the Self-Immolative Disulfide Linker Systems via ^{19}F NMR

^{19}F NMR was used to study the linker cleavage and subsequent drug release of the second-generation mechanism-based self-immolative disulfide linker systems. Because of the absence of fluorine in natural substances, using ^{19}F NMR allows direct observation and monitoring of fluorinated compounds and their metabolites in biological systems without influence from the background signals.²¹

The disulfide linker cleavage study by ^{19}F NMR was first conducted in a model system shown below (**Figure 2.9**).^{8,22} This proof of concept experiment demonstrated mechanism-based drug release using cysteine as the trigger for thiolactonization, in which two different fluorine signals were monitored for chemical shift changes by time-resolved ^{19}F NMR.^{8,22}

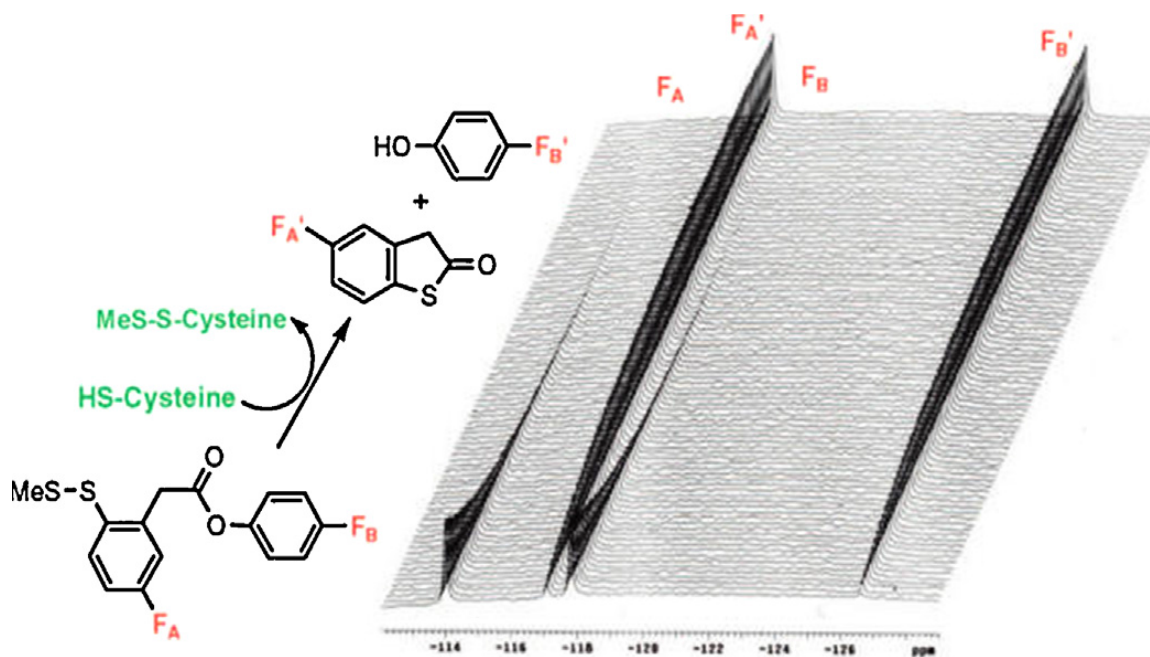


Figure 2.9 A model system for the mechanism-based drug release using cysteine as the trigger for thiolactonization. Adapted from Ojima, I. Use of fluorine in the medicinal chemistry and chemical biology of bioactive compounds - A case study on fluorinated taxane anticancer agents. *ChemBiochem* **2004**, *5*, 628-635, with permission from John Wiley & Sons.

Then, probe **1** was designed and synthesized by Dr. Joshua Seitz. Time-resolved ^{19}F NMR spectra for the disulfide linker cleavage and thiolactonization process of probe **1** (2.5 mM) in 30% DMSO in D_2O beginning at 1 h after the addition of 6 equiv. of GSH at 25 °C with 15 min intervals is shown below (**Figure 2.10**).²³ This ^{19}F NMR experiment indicates that the "self-immolation" of the disulfide linker proceeded in two steps, first generating the mechanistically anticipated thiolate **3-A** as detectable transient species/intermediate, and then releasing the drug through thiolactonization processes.²³ It also suggests that the introduction of a fluorine *para* to a disulfide linkage can stabilize the thiolate being formed, which may contribute to the fast disulfide exchange reaction as probe **1** was almost completely cleaved within one hour.²³ The thiolactonization process, however, was slow due to reduced nucleophilicity of the thiolate in the presence of *para* fluorine.²³

However, because of the poor solubility and low signal intensity of the probe **1**, it is not suitable for metabolic stability assessment in biologically relevant cell culture media or human blood plasma. An improved conjugate, probe **2**, was thus designed and subsequently evaluated by ^{19}F NMR for linker cleavage and drug release study (**Figure 2.11**).

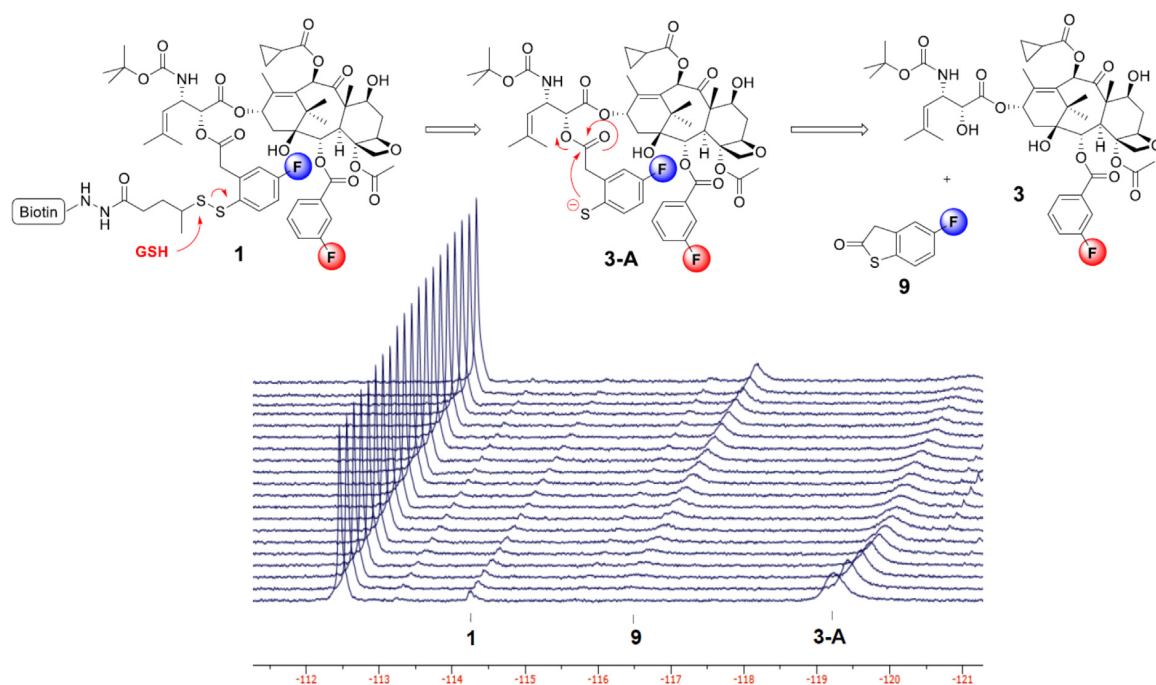


Figure 2.10 Time-resolved ^{19}F NMR spectra for the disulfide linker cleavage and thiolactonization process of probe **1** (2.5 mM) in 30% DMSO in D_2O beginning at 1 h after the addition of 6 equiv. of GSH at 25 °C with 15 min intervals. Reprinted from *J Fluorine Chem*, 171, Seitz, J. D.; Vineberg, J. G.; Wei, L. F.; Khan, J. F.; Lichtenthal, B.; Lin, C. F.; Ojima, I. Design, synthesis and application of fluorine-labeled taxoids as ^{19}F NMR probes for the metabolic stability assessment of tumor-targeted drug delivery systems, 148-161, Copyright (2015), with permission from Elsevier.

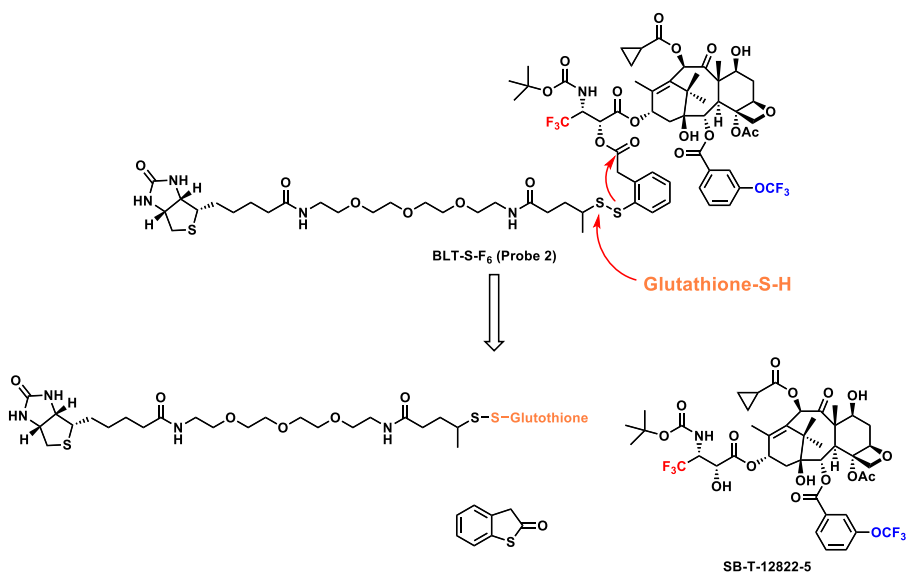
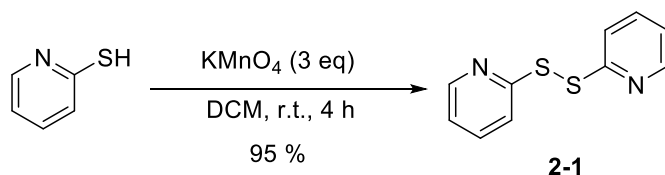


Figure 2.11 Designed probe **2** for metabolic stability assessment in biologically relevant media by ^{19}F NMR

§ 2.2 Metabolic Stability Assessment of Tumor-Targeted Drug Delivery Systems via ¹⁹F NMR

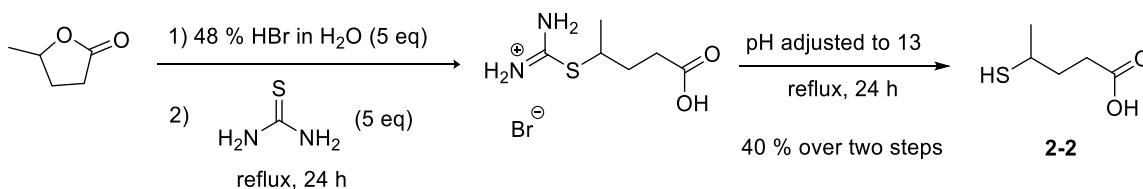
§ 2.2.1 Synthesis of Methyl-Branched Self-Immolative Disulfide Linker

The methyl-branched disulfide linker was synthesized via a route involving two thiol-disulfide exchange reactions. First, intermediate 2,2'-dipyridyl disulfide **2-1** was prepared by oxidation of 2-mercaptopyridine in the presence of potassium permanganate in 95% yield (Scheme 2.1).



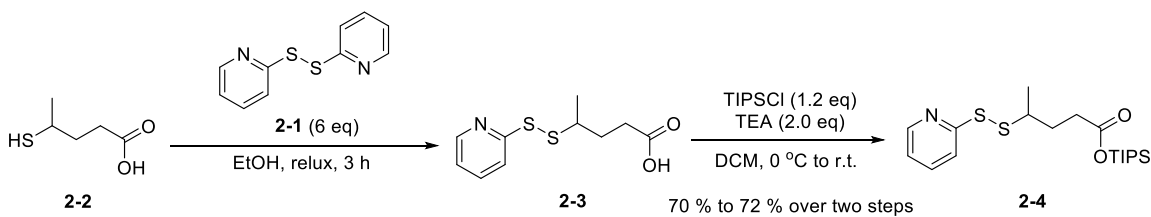
Scheme 2.1 Oxidation of 2-mercaptopyridine

For synthesizing another intermediate **2-2**, γ -valerolactone was activated by HBr under reflux conditions for the nucleophilic attack by thiourea. The resulting salt in aqueous layer was then directly hydrolyzed under basic conditions to yield desired **2-2** as a colorless oil in 40% yield for two steps (Scheme 2.2).



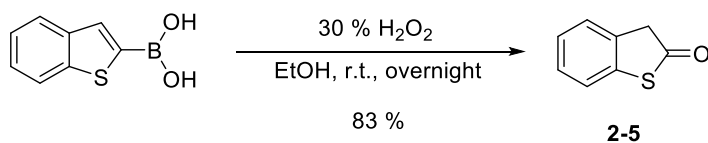
Scheme 2.2 Synthesis of intermediate **2-2**

With intermediates **2-1** and **2-2** in hand, the first thiol-disulfide exchange reaction was performed to afford **2-3**. Large excess of 2,2'-dipyridyl disulfide **2-1** was used to push the reaction to go to completion. It is not very easy to separate all the unreacted 2,2'-dipyridyl disulfide from desired product by column chromatography. In the first run, pure **2-3** was obtained after careful purification by two column chromatography, and then used in the subsequent TIPS protection reaction to give **2-4** in 72% yield over two steps. In the second run, **2-3** together with small amount of unreacted 2,2'-dipyridyl disulfide was obtained, and used in the subsequent TIPS protection reaction to give **2-4** in 70% yield over two steps, as unreacted **2-1** would not affect the TIPS protection step and could be easily separated after TIPS protection (Scheme 2.3).



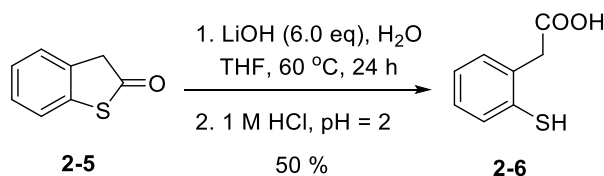
Scheme 2.3 First disulfide exchange and TIPS protection

Then, desired thiolactone **2-5** was obtained by oxidation of boronic acid moiety in the presence of hydrogen peroxide in 83% yield (**Scheme 2.4**).



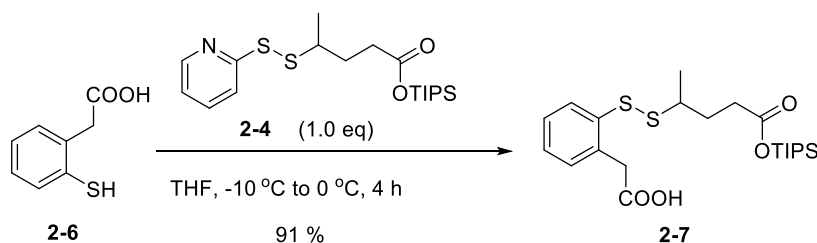
Scheme 2.4 Synthesis of thiolactone **2-5**

The thiolactone **2-5** was subsequently hydrolyzed by LiOH, and acidified with aqueous HCl to pH=2 (**Scheme 2.5**). Desired product **2-6** was obtained in 50% yield after purified by column chromatography. The yield of this step is low, due to some product dimerized in the presence of air. Once pure product was obtained, it was immediately stored under inert condition at -20 °C fridge to avoid dimerization.



Scheme 2.5 Hydrolysis of thiolactone **2-5**

The final step for making the methyl-branched disulfide linker involves a second thiol-disulfide exchange reaction between intermediates **2-4** and **2-6** (**Scheme 2.6**). High concentration of starting materials and low temperature between -10 °C to 0 °C was maintained during the reaction to afford desired methyl-branched disulfide linker **2-7** in 91% yield. The product is unstable and was immediately stored under inert condition at -20 °C fridge to avoid decomposition.



Scheme 2.6 Synthesis of methyl-branched disulfide linker **2-7** via a second thiol-disulfide exchange

§ 2.2.2 Effects of Solvent Systems and Drug Formulations on the Fluorine Signal Chemical Shifts of Designed Probes

Probe **BLT-S-F₆** and its corresponding taxoid **SB-T-12822-5** after linker cleavage and drug release were designed (**Figure 2.12**), and synthesized by Dr. Jacob Vineberg and Jonathan Khan in order to evaluate the metabolic stability of tumor-targeted drug delivery system *via* ¹⁹F NMR.

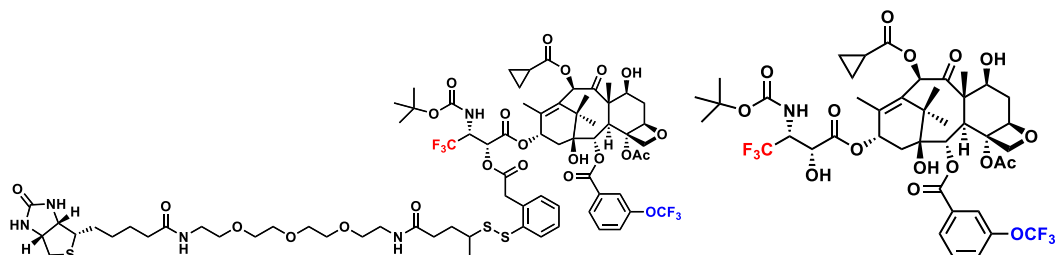


Figure 2.12 Chemical structures of probe **BLT-S-F₆** and taxoid **SB-T-12822-5**

Solutol HS 15 or polysorbate 80 was used as excipient to increase the solubility of **BLT-S-F₆** in biological related media. Solutol HS 15 is a combination of polyglycol mono- and di-esters of 12-hydroxystearic acid (lipophilic part), and about 30% free polyethylene glycol (hydrophilic part) (**Figure 2.13**). Polysorbate 80 is derived from oleic acid (lipophilic part) and polyethoxylated sorbitan (hydrophilic part) (**Figure 2.14**).

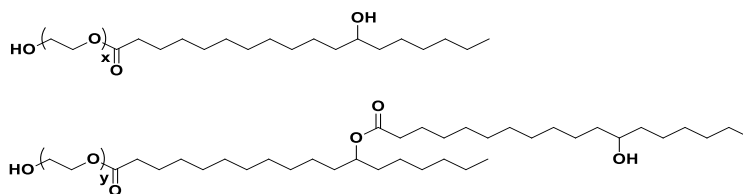


Figure 2.13 Chemical structure of solutol HS 15

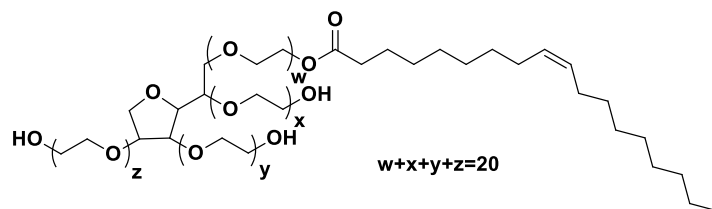


Figure 2.14 Chemical structure of polysorbate 80

The chemical shift differences of CF₃ and OCF₃ groups between **BLT-S-F₆** and its corresponding taxoid **SB-T-12822-5** in ¹⁹F NMR spectra were evaluated in various solvent systems. Without any excipient, ¹⁹F NMR spectra of **BLT-S-F₆**, **SB-T-12822-5** and a 1:1 mixture of the two compounds in D₂O-ethanol (v/v = 60/40) showed no significant chemical shift difference between **BLT-S-F₆** and its corresponding taxoid **SB-T-12822-5** in terms of both

CF₃ and OCF₃ groups (0.019 ppm chemical shift difference of OCF₃ group and 0.046 ppm chemical shift difference of CF₃ group) (**Figure 2.15**).

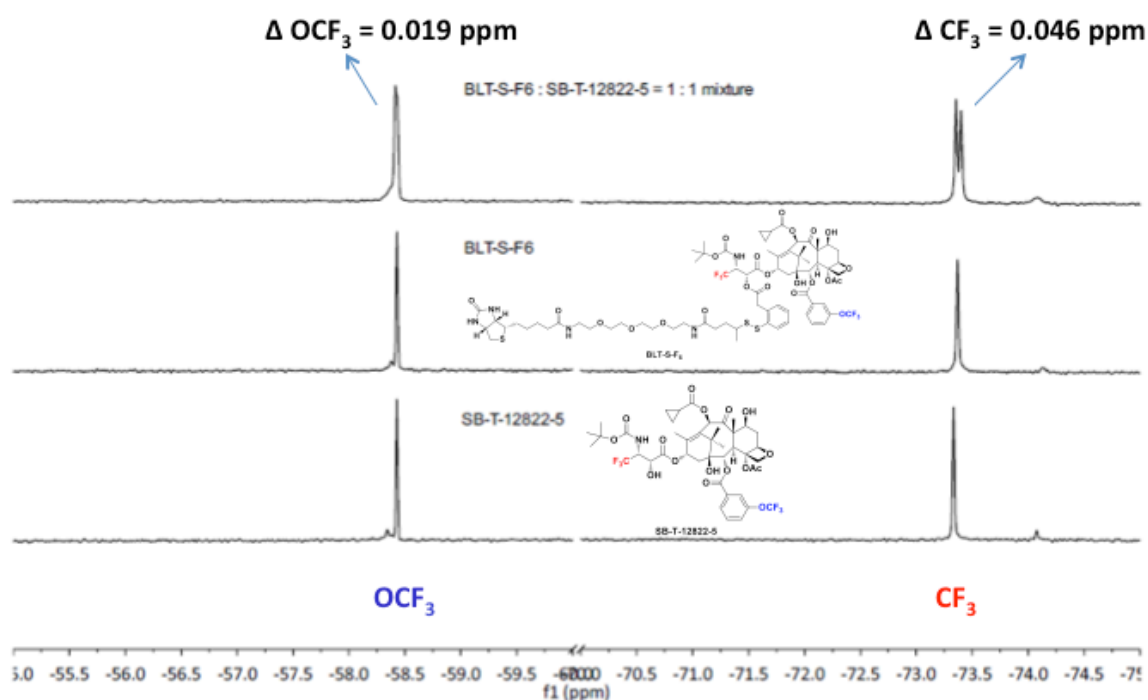


Figure 2.15 ¹⁹F NMR spectra (512 scans) showing individual chemical shifts of 200 μM **BLT-S-F₆**, **SB-T-12822-5**, and a 1:1 mixture of the two compounds in D₂O-ethanol (v/v = 60/40)

With solutol HS 15 as an excipient, it was found that using the solvent system of D₂O-ethanol-solutol HS 15 (v/v/v = 84/8/8) could solubilize the drug/drug conjugate at concentration of 200 μM effectively. However, ¹⁹F NMR spectra of **BLT-S-F₆**, **SB-T-12822-5** and a 1:1 mixture of the two compounds in D₂O-ethanol-solutol HS 15 (v/v/v = 84/8/8) showed no chemical shift difference between **BLT-S-F₆** and its corresponding taxoid **SB-T-12822-5** at all in terms of both CF₃ and OCF₃ groups (**Figure 2.16**). Thus, this solvent system cannot apply for linker cleavage study by ¹⁹F NMR.

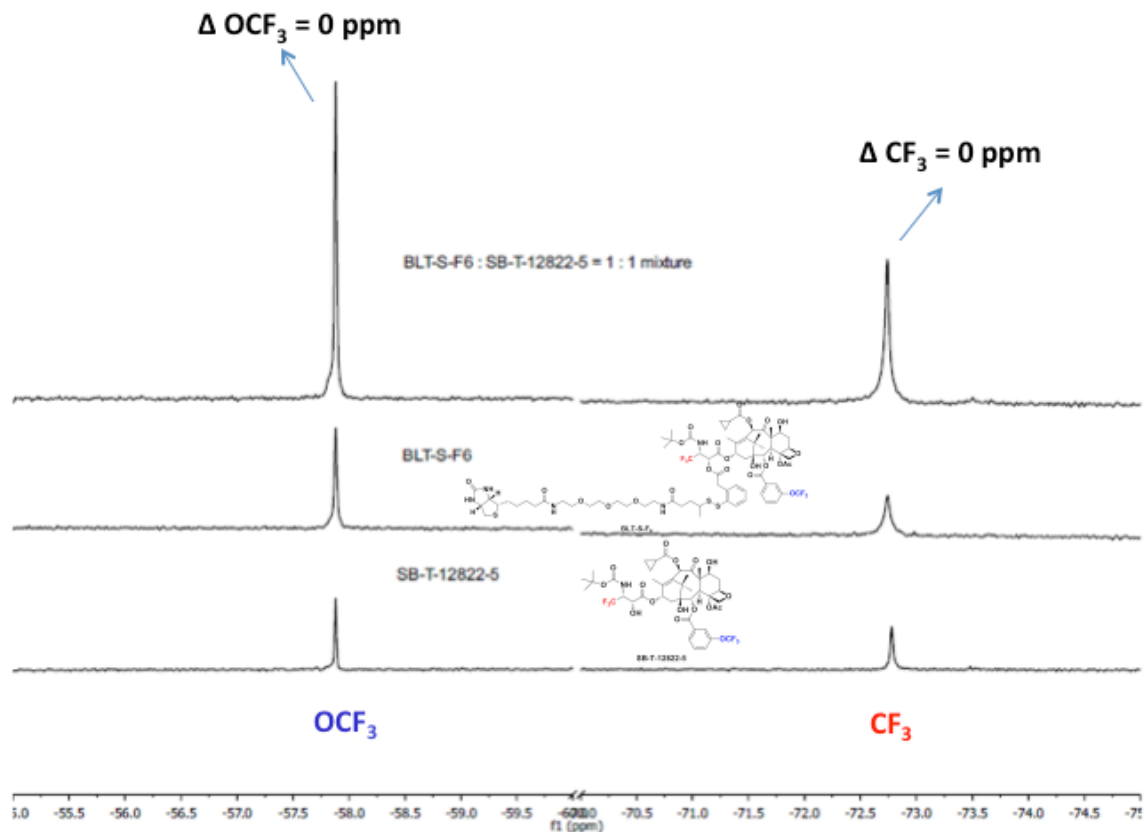


Figure 2.16 ^{19}F NMR spectra (>268 scans) showing individual chemical shifts of 200 μM **BLT-S-F₆**, **SB-T-12822-5**, and a 1:1 mixture of the two compounds in D_2O -ethanol-solutol HS 15 (v/v/v = 84/8/8)

With polysorbate 80 as an excipient, it was found that using the solvent system of D_2O -ethanol-polysorbate 80 (v/v/v = 96/2/2) could solubilize the drug/drug conjugate at concentration of 200 μM effectively. ^{19}F NMR spectra of **BLT-S-F₆** and **SB-T-12822-5** in D_2O -ethanol-polysorbate 80 (v/v/v = 96/2/2), and a 1:1 mixture of the two compounds in D_2O -ethanol-polysorbate 80 (v/v/v = 94/4/2) clearly showed no chemical shift difference between **BLT-S-F₆** and its corresponding taxoid **SB-T-12822-5** in terms of OCF_3 group, and 0.187 ppm chemical shift difference in terms of CF_3 group (**Figure 2.17**). This result demonstrated polysorbate 80 is a suitable excipient for the metabolic stability of tumor-targeted drug delivery system *via* ^{19}F NMR. OCF_3 group could be used as an internal standard since there is no chemical shift difference before or after the drug is released, and CF_3 group could be used as a reporter group to evaluate how much drug is released from the tumor-targeted drug conjugate.

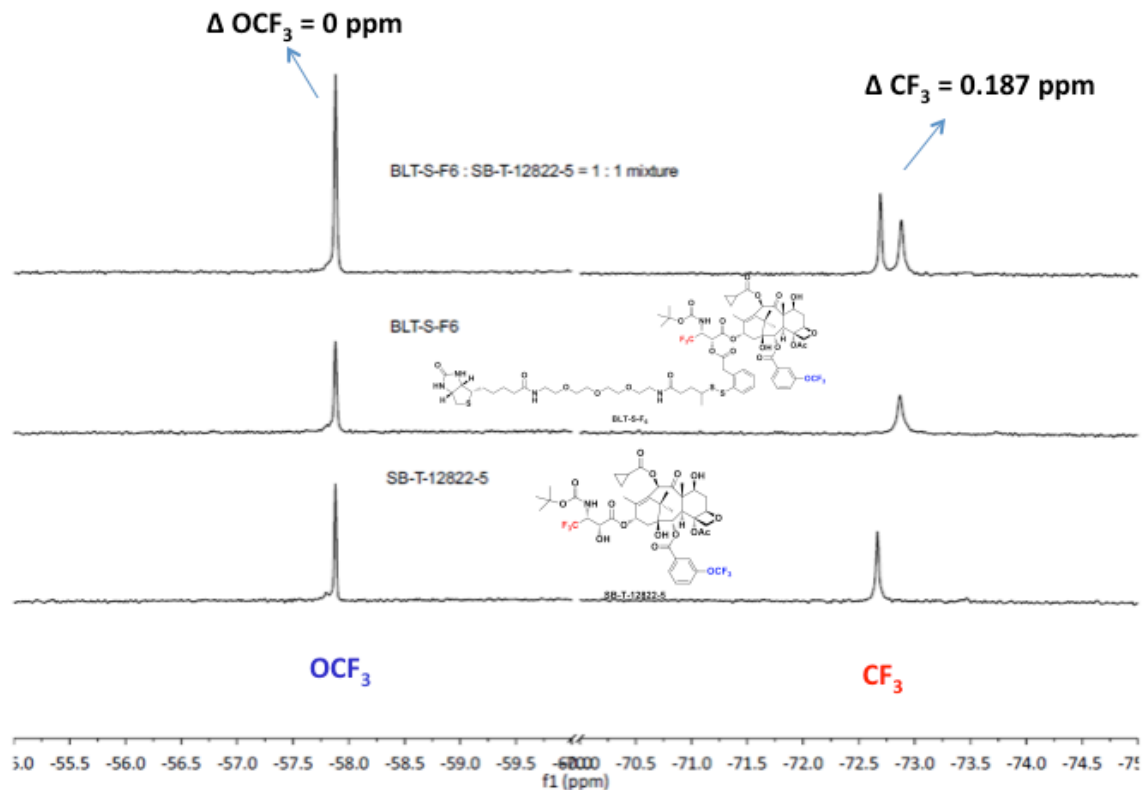


Figure 2.17 ^{19}F NMR spectra (512 scans) showing individual chemical shifts of 200 μM **BLT-S-F₆** and **SB-T-12822-5** in D_2O -ethanol-polysorbate 80 (v/v/v = 96/2/2), and a 1:1 mixture of the two compounds in D_2O -ethanol-polysorbate 80 (v/v/v = 94/4/2)

Further evaluation of chemical shift differences of CF_3 and OCF_3 groups between **BLT-S-F₆** and **SB-T-12822-5** with polysorbate 80 as an excipient in human blood plasma and cell culture media showed similar results as using D_2O -ethanol-polysorbate 80 (v/v/v = 94/4/2) solvent system.

^{19}F NMR spectra of **BLT-S-F₆** and **SB-T-12822-5** in blood plasma- D_2O -ethanol-polysorbate 80 (v/v/v/v = 86/10/2/2), and a 1:1 mixture of the two compounds in human blood plasma- D_2O -ethanol-polysorbate 80 (v/v/v/v = 84/10/4/2) clearly showed no chemical shift difference between **BLT-S-F₆** and its corresponding taxoid **SB-T-12822-5** in terms of OCF_3 group, and 0.210 ppm chemical shift difference in terms of CF_3 group (**Figure 2.18**).

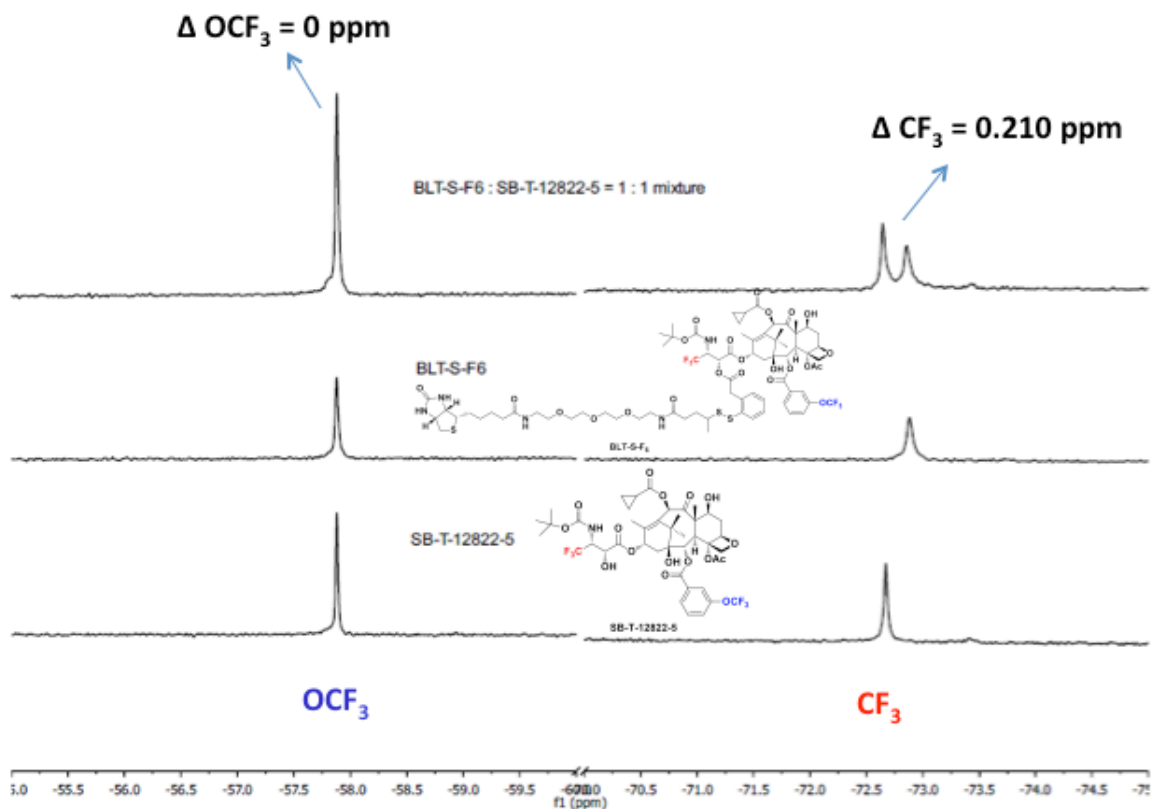


Figure 2.18 ^{19}F NMR spectra (1024 scans) showing individual chemical shifts of 200 μM **BLT-S-F₆** and **SB-T-12822-5** in blood plasma- D_2O -ethanol-polysorbate 80 (v/v/v/v = 86/10/2/2), and a 1:1 mixture of the two compounds in human blood plasma- D_2O -ethanol-polysorbate 80 (v/v/v/v = 84/10/4/2)

^{19}F NMR spectra of **BLT-S-F₆** and **SB-T-12822-5** in RPMI 1640- D_2O -ethanol-polysorbate 80 (v/v/v/v = 86/10/2/2), and a 1:1 mixture of the two compounds in RPMI 1640 cell culture media- D_2O -ethanol-polysorbate 80 (v/v/v/v = 84/10/4/2) clearly showed no chemical shift difference between **BLT-S-F₆** and its corresponding taxoid **SB-T-12822-5** in terms of OCF_3 group, and 0.206 ppm chemical shift difference in terms of CF_3 group (**Figure 2.19**).

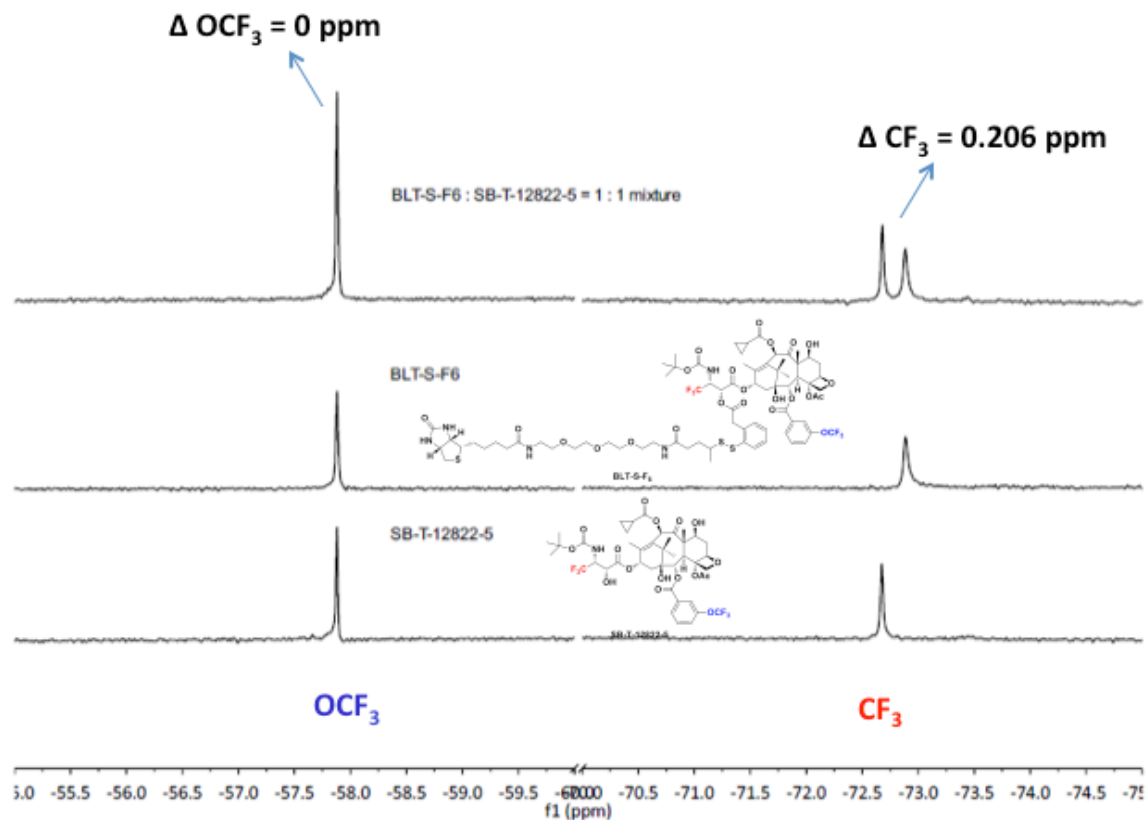


Figure 2.19 ^{19}F NMR spectra (512 scans) showing individual chemical shifts of 200 μM **BLT-S-F₆** and **SB-T-12822-5** in RPMI 1640- D_2O -ethanol-polysorbate 80 (v/v/v/v = 86/10/2/2), and a 1:1 mixture of the two compounds in RPMI 1640 cell culture media- D_2O -ethanol-polysorbate 80 (v/v/v/v = 84/10/4/2)

§ 2.2.3 Metabolic Stability Assessment of Tumor-Targeted Drug Delivery Systems via Time-Resolved ^{19}F NMR

Disulfide linker cleavage of **BLT-S-F₆** was subsequently evaluated in human blood plasma. ^{19}F NMR spectra for the drug release of BLT-S-F₆ (200 μM) in 86% blood plasma, 10% D_2O , 2% ethanol, and 2% polysorbate 80 without addition of GSH at 0 h, 24 h and 48 h at 37 °C showed less than 5% drug release within 24 h and less than 10% drug release within 48 h. This result demonstrated the tumor-targeted drug conjugate would be stable during blood circulation with minimal drug release before reach the tumor cells (**Figure 2.20**).

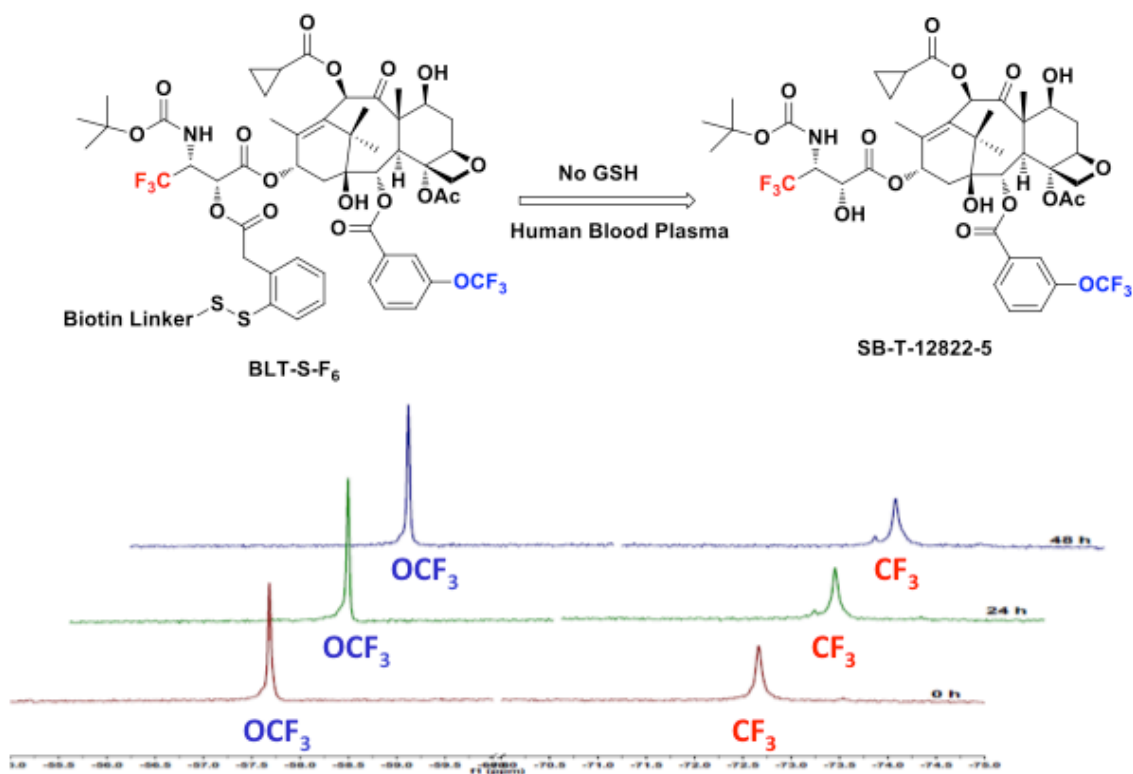


Figure 2.20 ^{19}F NMR spectra for the drug release of **BLT-S-F₆** (200 μM) in 86% blood plasma, 10% D_2O , 2% ethanol, and 2% polysorbate 80 without addition of GSH at 0 h, 24 h and 48 h at 37 $^\circ\text{C}$ (2048 scans/spectrum). Adapted from *J Fluorine Chem*, 171, Seitz, J. D.; Vineberg, J. G.; Wei, L. F.; Khan, J. F.; Lichtenthal, B.; Lin, C. F.; Ojima, I. Design, synthesis and application of fluorine-labeled taxoids as ^{19}F NMR probes for the metabolic stability assessment of tumor-targeted drug delivery systems, 148-161, Copyright (2015), with permission from Elsevier.

Time-resolved ^{19}F NMR spectra for the drug release of **BLT-S-F₆** (200 μM) in 86% blood plasma, 10% D_2O , 2% ethanol, and 2% polysorbate 80 at 30 min after the addition of 100 equiv. of GSH with 1 h intervals for 13 h at 37 $^\circ\text{C}$ showed drug was almost fully released after 13.5 h. By plotting the normalized integration values, the half-life of the disulfide linker was calculated to be approximately 3 h. This result demonstrated the tumor-targeted drug conjugate would be readily cleaved and release the free drug by the high concentration of glutathione inside the tumor cells once it got internalized via receptor mediated endocytosis (**Figure 2.21**).

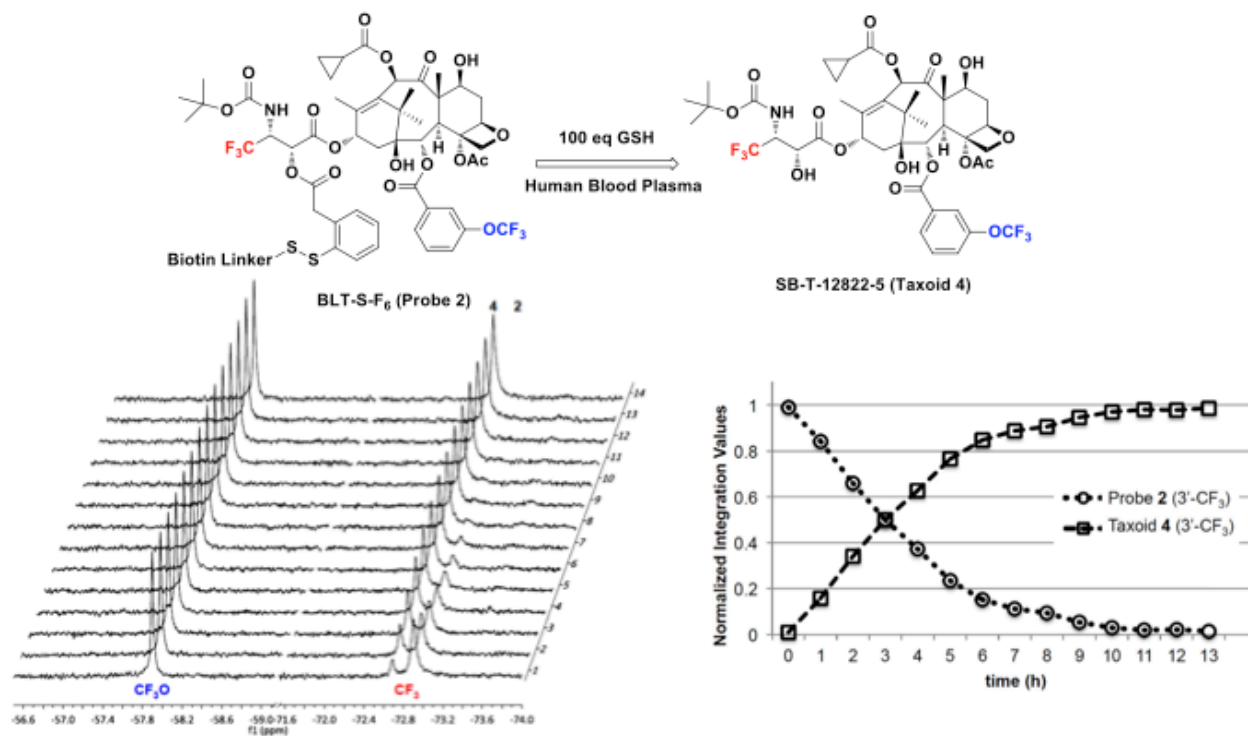


Figure 2.21 Time-resolved ^{19}F NMR spectra for the drug release of BLT-S-F₆ (200 μM) in 86% blood plasma, 10% D₂O, 2% ethanol, and 2% polysorbate 80 at 30 min after the addition of 100 equiv. of GSH with 1 h intervals for 13 h at 37 $^{\circ}\text{C}$ (1024 scans/spectrum). Adapted from *J Fluorine Chem*, 171, Seitz, J. D.; Vineberg, J. G.; Wei, L. F.; Khan, J. F.; Lichtenthal, B.; Lin, C. F.; Ojima, I. Design, synthesis and application of fluorine-labeled taxoids as ^{19}F NMR probes for the metabolic stability assessment of tumor-targeted drug delivery systems, 148-161, Copyright (2015), with permission from Elsevier.

Similarly, disulfide linker cleavage of BLT-S-F₆ was evaluated in RPMI cell culture media. Time-resolved ^{19}F NMR spectra for the drug release of BLT-S-F₆ (200 μM) in 86% RPMI-1640 cell culture media, 10% D₂O, 2% ethanol, and 2% polysorbate 80 at 30 min after the addition of 100 equiv. of GSH with 1 h intervals for 12 h at 37 $^{\circ}\text{C}$ demonstrated the disulfide linker cleavage is much slower in cell culture media than human blood plasma. More than 50% cleavage was observed after 12.5 h (**Figure 2.22**).

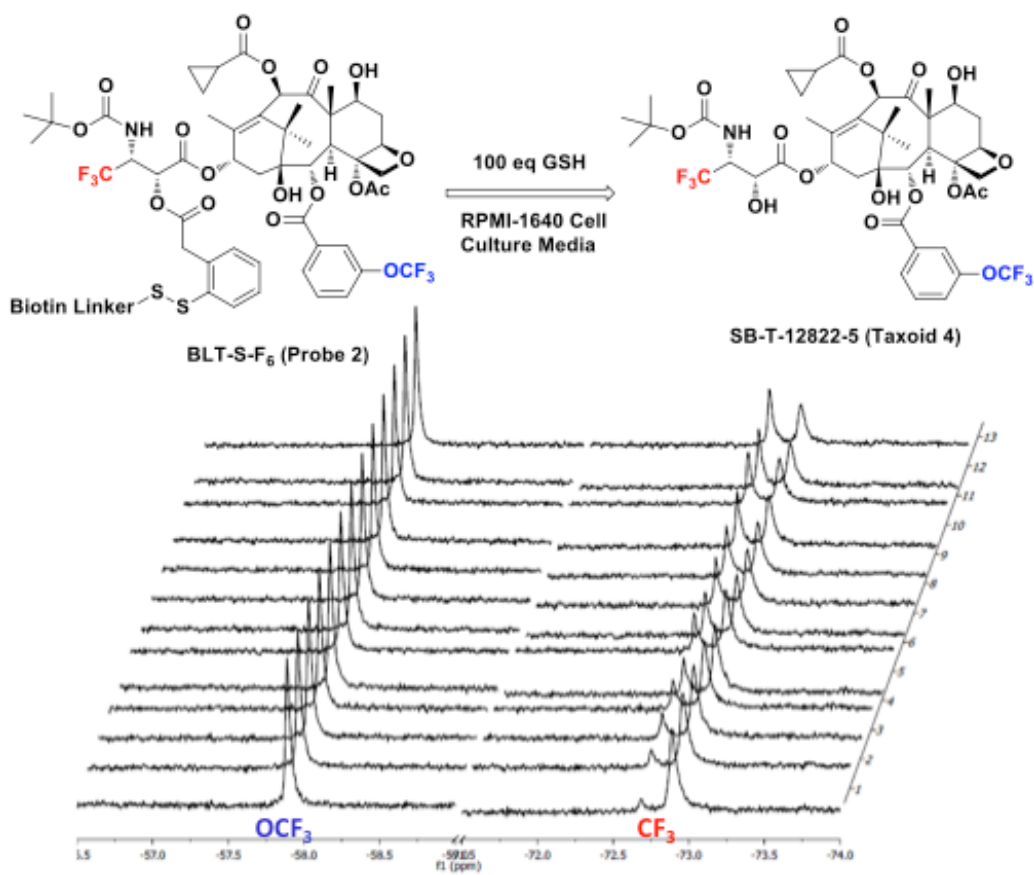


Figure 2.22 Time-resolved ^{19}F NMR spectra for the drug release of **BLT-S-F₆** (200 μM) in 86% RPMI-1640 cell culture media, 10% D_2O , 2% ethanol, and 2% polysorbate 80 at 30 min after the addition of 100 equiv. of GSH with 1 h intervals for 12 h at 37 $^\circ\text{C}$ (1024 scans/spectrum)

Also, disulfide linker cleavage of **BLT-S-F₆** was evaluated in D_2O . ^{19}F NMR spectra for the drug release of **BLT-S-F₆** (200 μM) in 96% D_2O , 2% ethanol, and 2% polysorbate 80 with addition of 100 equiv. of GSH at 0 h, 17 h, 40 h, 72 h, 120 h and 168 h at 37 $^\circ\text{C}$ showed the disulfide linker cleavage was significantly slower in D_2O . Around 50% of cleavage was achieved after 3 to 4 days (**Figure 2.23**). This is presumably because the presence of an excipient such as polysorbate 80 could significantly reduce the rate of disulfide linker cleavage by protecting the disulfide bond from exposure to GSH. However, in biological systems such as human blood plasma, there are many proteins and other substances that may interacting with the excipient, leading to the exposure of the disulfide bond to the attack of GSH, resulting in the smooth cleavage of the linker system.

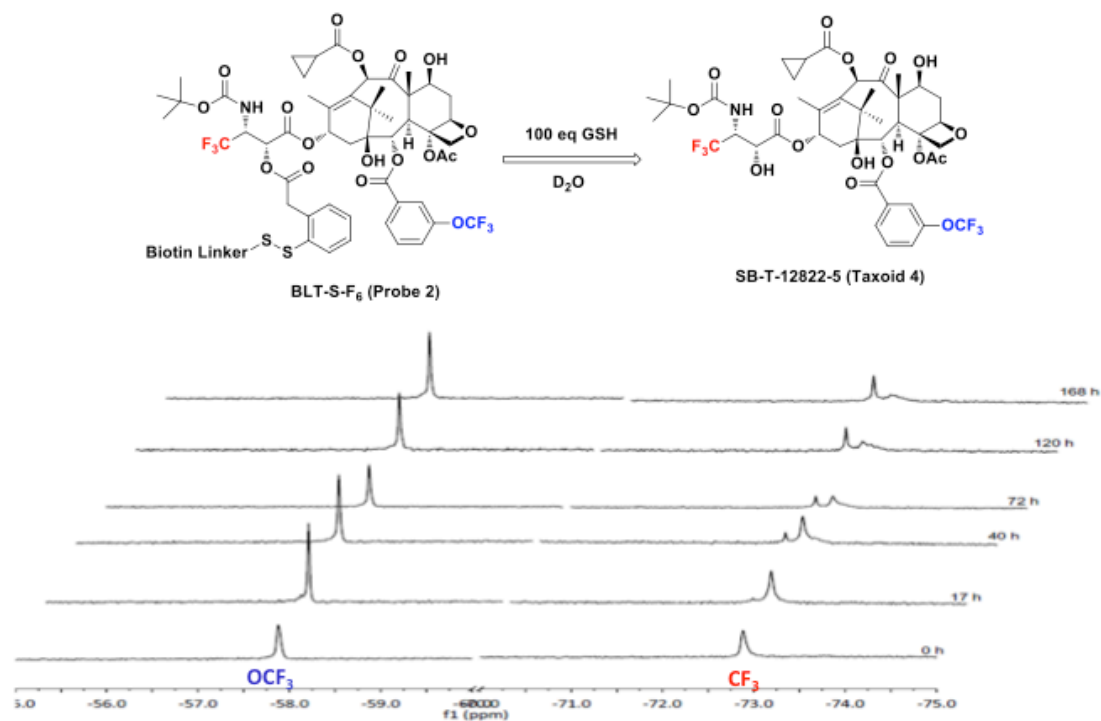


Figure 2.23 ^{19}F NMR spectra for the drug release of **BLT-S-F₆** (200 μM) in 96% D_2O , 2% ethanol, and 2% polysorbate 80 with addition of 100 equiv. of GSH at 0 h, 17 h, 40 h, 72 h, 120 h and 168 h at 37 $^\circ\text{C}$ (>512 scans/spectrum)

§ 2.3 Summary

The self-immolative methyl-branched disulfide linker in tumor-targeted drug delivery systems has been synthesized. The stability of the disulfide linker system has been assessed in different solvent systems including biological relevant human blood plasma and cell culture media via ^{19}F NMR. By using polysorbate 80 as an excipient to formulate biotin-linker-taxoid drug conjugate **BLT-S-F₆**, it has been shown that the disulfide linker system is stable in human blood plasma, and could release the taxoid warhead smoothly in the presence of 100 equiv. of supplemental GSH (20 mM), which is comparable to the level of GSH in tumors (2-8 mM).

§ 2.4 Experimental

Caution

Taxoids have been classified as highly potent cytotoxic agents. Thus, all taxoids and structurally related compounds and derivatives must be considered as mutagens and potential reproductive

hazards for both males and females. Appropriate precautions (i.e. use of gloves, goggles, lab coat and fume hood) must be taken while handling these compounds.

General Methods

^1H NMR and ^{13}C NMR spectra were measured on a Varian 300 spectrometer or a Bruker 400 MHz, 500 MHz, or 700 MHz NMR spectrometer. Melting points were measured on a Thomas-Hoover capillary melting point apparatus and are uncorrected. Optical rotations were measured on Perkin-Elmer Model 241 polarimeter. TLC analyses were performed on Sorbent Technologies aluminum-backed Silica G TLC plates (Sorbent Technologies, 200 μm , 20 cm \times 20 cm), and were visualized with UV light and stained with sulfuric acid-EtOH, 10% phosphomolybdic acid (PMA)-EtOH, 10% vanillin-EtOH with 1% sulfuric acid, ninhydrin-butanol with 10% AcOH, or DACA stain. Column chromatography was carried out on silica gel 60 (Merck; 230-400 mesh ASTM). Chemical purity was determined with a Shimadzu L-2010A HPLC HT series HPLC assembly, using a Kinetex PFP column (4.6 mm \times 100 mm, 2.6 μm) column, using $\text{CH}_3\text{CN}/\text{water}$ as the solvent system with a flow rate of 1 mL/min.

Materials

All chemicals were purchased from Sigma Aldrich, Fisher Scientific or VWR International and used as received or purified before use by standard methods. Dichloromethane and methanol were dried before use by distillation over calcium hydride under nitrogen. Ether and tetrahydrofuran were dried before use by distillation over sodium-benzophenone kept under nitrogen. 10-Deacetylbaicatin III was obtained from Indena, S.p.A, Italy. Reaction flasks were dried in a 100 $^\circ\text{C}$ oven and allowed to cool to room temperature in a desiccator over calcium sulfate and assembled under an inert nitrogen gas atmosphere.

Experimental Procedures

Chemical Synthesis

2,2'-Dipyridyl disulfide (**2-1**)²⁴

To a 1000-mL round-bottom flask, 2-mercaptopyridine (5.56 g, 50.0 mmol/ 6.00 g, 54.0 mmol) was dissolved in 500 mL DCM. Potassium permanganate (23.7 g, 150 mmol/ 24.0 g, 152 mmol) was then added in portions. The reaction mixture turned from yellow color to dark yellow/dark green color. The reaction was monitored by TLC (hexanes/ethyl acetate = 1/1, stain with vanillin). Upon completion after 4 h, the reaction mixture was filtered through Celite, and the filtrate was concentrated in vacuo to give crude product as yellow oil. The crude products from two runs were combined, and purified by column chromatography on silica gel (gradient eluent: hexanes/ethyl acetate from 20/1 to 4/1) to give 2,2'-dipyridyl disulfide **2-1** (10.7 g, 48.6 mmol) as colorless crystalline solid in 93% yield. ^1H NMR (400 MHz, CDCl_3): δ 7.11 (m, 2H), 7.62 (m, 4H), 8.47 (m, 2H). ESI m/z : 220.9 $[\text{M}+\text{H}]^+$. All data are in agreement with literature values.²⁴

4-Mercaptopentanoic acid (2-2)²⁵

To a solution of γ -valerolactone (2.10 g, 21.0 mmol/4.00 g, 40.0 mmol) dissolved in 48% HBr in water (12.0 mL, 105 mmol/23.0 mL, 200 mmol) in a 100-mL round-bottom flask was added thiourea (8.00 g, 105 mmol/15.2 g, 200 mmol). The mixture was allowed to heat up to reflux and stirred under reflux condition for 24 h. The reaction mixture was then allowed to cool to room temperature and diluted with water. The aqueous layer was washed with DCM (3 x 30 mL), and then washed with ethyl ether (3 x 30 mL). The aqueous layer containing the intermediate was collected, and the pH of the aqueous layer was adjusted to 14 with 5 M NaOH/12 M KOH. The solution turned pink color at pH=10 and then became colorless again. Large amount of white precipitate (thiourea) came out during basification, and was removed by vacuum filtration. The filtrate was then heat up to reflux and stirred under reflux condition for another 24 h. Upon completion, the reaction mixture was cooled to room temperature, and the pH was adjusted to 2 by 1 M HCl. The acidified solution was extracted with DCM (3 x 100 mL). The organic layers were collected, and dried over anhydrous MgSO₄. The MgSO₄ was subsequently removed by vacuum filtration, and the filtrate was concentrated in vacuo to give 4-mercaptopentanoic acid **2-2** (905 mg, 6.75 mmol/1.53 g, 11.4 mmol) as a pale yellow oil with a strong rotten egg smell in 32%/29% yield over two steps. ¹H NMR (400 MHz, CDCl₃): δ 1.36 (d, J = 6.8 Hz, 3H), 1.44 (d, J = 7.2 Hz, 1H), 1.76 (m, 1H), 1.97 (m, 1H), 2.52 (m, 2H), 2.96 (m, 1H), 11.4 (br. s, 1H). All data are in agreement with literature values.²⁵

4-(Pyridin-2-ylthio)pentanoic acid (2-3)²⁶

To a solution of 4-mercaptopentanoic acid **2-2** (840 mg, 6.27 mmol/960 mg, 7.18 mmol) in EtOH (20 mL/30 mL) in a 500-mL round-bottom flask was added 2,2'-dipyridyl disulfide (8.50 g, 37.6 mmol/9.50 g, 43.1 mmol) dissolved in EtOH (120 mL/150 mL) via an addition funnel. The reaction mixture was allowed to heat up to reflux and stirred under reflux condition for 3 h. The reaction was monitored by TLC. Upon completion, the reaction solvent was evaporated. The resulting crude was purified by column chromatography on silica gel (gradient eluent: hexanes/ethyl acetate from 10/1 to 3/1) to give 4-(pyridin-2-ylthio)pentanoic acid **2-3** (1.54 g, 6.34 mmol/2.33 g, 9.59 mmol) as pale yellow oil in > 100% yield (contains small amount of excess 2,2'-dipyridyl disulfide). ¹H NMR (400 MHz, CDCl₃): δ 1.34 (d, J = 6.8 Hz, 3H), 1.90 (m, 2H), 2.54 (m, 2H), 3.02 (m, 1H), 7.08 (m, 1H), 7.63 (m, 1H), 7.72 (m, 1H), 8.46 (m, 1H). All data are in agreement with literature values.²⁶

Triisopropylsilyl 4-(pyridin-2-ylthio)pentanoate (2-4)²⁶

To 4-(pyridin-2-ylthio)pentanoic acid **2-3** (1.52 g, 6.27 mmol/1.74 g, 7.16 mmol) (theoretical yield from previous step) in DCM (35 mL/40 mL) in a 100-mL round-bottom flask cooled to 0 °C in an ice bath was added triethylamine (1.80 mL, 12.5 mmol/2.00 mL, 14.3 mmol). Chlorotriisopropylsilane (1.60 mL, 7.52 mmol/1.84 mL, 8.60 mmol) was then added dropwise. The mixture was stirred at room temperature overnight and the reaction was monitored via TLC.

Upon completion, the reaction solvent was evaporated and the resulting crude was purified by column chromatography on silica gel (gradient eluent: hexanes/ethyl acetate from 50/1 to 10/1) to give triisopropylsilyl 4-(pyridin-2-ylthio)pentanoate **2-4** (1.81 g, 4.52 mmol/2.00 g, 5.01 mmol) as pale yellow oil in 72%/70% yield over two steps. ¹H NMR (400 MHz, CDCl₃): δ 1.05 (m, 21H), 1.34 (d, J = 6.8 Hz, 3H), 1.88 (m, 1H), 1.98 (m, 1H), 2.52 (m, 2H), 3.03 (m, 1H), 7.06 (m, 1H), 7.62 (m, 1H), 7.72 (m, 1H), 8.44 (m, 1H). All data are in agreement with literature values.²⁶

Benzo[b]thiophen-2(3H)-one (2-5)²⁷

To benzo[b]thiophen-2-ylboronic acid (1.08 g, 6.07 mmol) dissolved in 20 mL EtOH in a 100-mL round-bottom flask, was added 9 mL 30% hydrogen peroxide dropwise. The reaction mixture was allowed stir at room temperature overnight and the reaction was monitored via TLC. Upon completion after overnight, the mixture was diluted with water (~70 mL), and extracted with DCM (3 x 60 mL). The organic layers were combined, and dried over MgSO₄. The MgSO₄ was subsequently removed by vacuum filtration, and the filtrate was concentrated in vacuo to afford crude product as red oil. The resulting crude was further purified by column chromatography on silica gel (gradient eluent: hexanes/ethyl acetate from 50/1 to 10/1) to give benzo[b]thiophen-2(3H)-one **2-5** (759 mg, 5.06 mmol) as white solid in 83% yield. ¹H NMR (300 MHz, CDCl₃): δ 3.98 (s, 2H), 7.30 (m, 4H). All data are consisted with the reported values.²⁷

2-(2-Mercaptophenyl)acetic acid (2-6)¹⁶

To benzo[b]thiophen-2(3H)-one **2-5** (750 mg, 5.00 mmol) dissolved in 12 mL THF in a 100-mL round-bottom flask warmed to 60 °C, was added a solution of LiOH (1.26 g, 30.0 mmol) dissolved in 16 mL water dropwise via an addition funnel. The reaction mixture was allowed to stir overnight at 60 °C and the reaction was monitored via TLC. Upon reaction completion after overnight, the reaction mixture was cooled to room temperature and diluted with 6 mL water and 30 mL diethyl ether. The pH of the solution was adjusted to pH=2 by 1 M HCl. The aqueous layer was extracted with DCM (3 x 50 mL). The combined organic layer was washed with brine (3 x 50 mL), and dried over anhydrous MgSO₄. The MgSO₄ was subsequently removed by vacuum filtration, and the filtrate was concentrated in vacuo to afford crude product. The resulting crude was further purified by column chromatography on silica gel (gradient eluent: hexanes/ethyl acetate from 10/1 to 1/1) to give 2-(2-mercaptophenyl)acetic acid **2-6** (416 mg, 2.48 mmol) as yellow solid in 50% yield. ¹H NMR (400 MHz, CDCl₃): δ 3.49 (s, 1H), 3.82 (s, 2H), 7.18 (m, 2H), 7.23 (m, 1H), 7.40 (m, 1H). All data are consisted with the reported values.¹⁶

2-(2-((5-Oxo-5-((triisopropylsilyl)oxy)pentan-2-yl)disulfanyl)phenyl)acetic acid (2-7)²⁶

To a 10-mL round-bottom flask, 2-(2-mercaptophenyl)acetic acid **2-6** (92.0 mg, 0.548 mmol) and triisopropylsilyl 4-(pyridin-2-ylthio)pentanoate **2-4** (216 mg, 0.541 mmol) were added, the flask was purged with nitrogen gas and the mixture was cooled to -10 °C in an acetone/dry ice

bath by mixing acetone with small amount of dry ice. 2 mL anhydrous THF was then added into the flask and the reaction mixture was allowed to stir between -10 °C to 0 °C by keep adding small amount of dry ice into the acetone/dry ice bath. The reaction was monitored by TLC. Upon completion after 4 hour, the reaction solvent was evaporated in vacuo without heat and the resulting crude was purified immediately by column chromatography on silica gel (gradient eluent: hexanes/ethyl acetate from 10/1 to 3/1) to give 2-(2-((5-oxo-5-((triisopropylsilyl)oxy)pentan-2-yl)disulfanyl)phenyl)acetic acid **2-7** (226 mg, 0.496 mmol) as pale yellow sticky oil in 91% yield. The oil was stored in a vial purged with nitrogen in the fridge before use in subsequent step. ¹H NMR (400 MHz, CDCl₃): δ 1.05 (m, 21H), 1.26 (m, 3H), 1.78 (m, 1H), 2.00 (m, 1H), 2.42 (m, 2H), 2.90 (m, 1H), 3.88 (m, 2H), 7.21 (m, 2H), 7.31 (m, 1H), 7.80 (d, J = 8.1 Hz, 1H). All data are consisted with the reported values.²⁶

¹⁹F NMR Experiments:

¹⁹F NMR experiments were performed on a Bruker Nanobay 400 MHz NMR spectrometer operating at a ¹⁹F Larmor frequency of 376 MHz with a BBFO_{PLUS} 5 mm probe (¹H-¹⁹F) at 25 °C or 37 °C. ¹⁹F NMR spectra were recorded using a pulse sequence of proton decoupling with a spectral width of 15,040 Hz (40 ppm), an acquisition time of 0.8 s, and a relaxation delay of 1.0 s. The obtained spectra were analyzed with TOPSPIN 3.0 (Bruker).

Formulation studies on SB-T-12822-5 and BLT-S-F₆

Stock solutions of **SB-T-12822-5** and **BLT-S-F₆** were prepared by dissolving each compound in ethanol to final concentrations of [10 mM]. In each experiment, an aliquot of the prepared stock solution (10 μL) was diluted with various volumes of aqueous media (PBS, saline, human blood plasma, RPMI cell culture media, D₂O), 0-8% ethanol and/or excipient (solutol HS 15, polysorbate 80), and 10% D₂O (50 μL) to a final volume of 500 μL. Formulation studies with excipients were performed with 500 μL sample volume in NMR tubes with D₂O as the NMR reference solvent.

Time-resolved ¹⁹F NMR for BLT-S-F₆:

For linker stability studies in human blood plasma/RPMI cell culture media, supplemental glutathione (100 equivalents) was dissolved in [200 μM] solutions of **BLT-S-F₆** with 84% human blood plasma/RPMI cell culture media, 10% D₂O, 2% ethanol, 2% polysorbate 80 (total 500 μL). Time-resolved ¹⁹F NMR spectra representing disulfide bond cleavage and drug release were recorded in real-time in the NMR spectrometer at 37 °C beginning 30 min following GSH addition by measuring one spectrum every 1 h (1024 of scans/spectrum) over a 13 h period (total of 13 spectra). The rate of drug release was monitored by measuring the integration ratio of the C3'-CF₃ peaks of conjugate **BLT-S-F₆** and free taxoid **SB-T-12822-5**. The normalized integration ratios indicating drug release were plotted as a function of time.

Stock Solution:

5.1 mg **BLT-S-F₆** was dissolved in 312 μL EtOH to make a 10 mM **BLT-S-F₆** stock solution.

3.0 mg **SB-T-12822-5** was dissolved in 315 μL EtOH to make a 10 mM **SB-T-12822-5** stock solution.

EtOH-D₂O system:

1. 1:1 mixture

To a vial was added 10 μL **BLT-S-F₆** 10 mM stock solution, 10 μL **SB-T-12822-5** 10 mM stock solution and 180 μL EtOH. 300 μL D₂O was added to the mixture dropwise. Then the mixture solution was transferred to a NMR tube.

2. **BLT-S-F₆**

To a vial was added 10 μL **BLT-S-F₆** 10 mM stock solution and 190 μL EtOH. 300 μL D₂O was added to the mixture dropwise. Then the mixture solution was transferred to a NMR tube.

3. **SB-T-12822-5**

To a vial was added 10 μL **SB-T-12822-5** 10 mM stock solution and 190 μL EtOH. 300 μL D₂O was added to the mixture dropwise. Then the mixture solution was transferred to a NMR tube.

EtOH-Solutol-D₂O system:

1. 1:1 mixture

To a vial was added 10 μL **BLT-S-F₆** 10 mM stock solution, 10 μL **SB-T-12822-5** stock solution and 60 μL Solutol/EtOH (v/v = 2:/1) solution. 420 μL D₂O was added to the mixture dropwise. Then the mixture solution was transferred to a NMR tube.

2. **BLT-S-F₆**

To a vial was added 10 μL **BLT-S-F₆** 10 mM stock solution, 10 μL EtOH and 60 μL Solutol/EtOH (v/v = 2:/1) solution. 420 μL D₂O was added to the mixture dropwise. Then the mixture solution was transferred to a NMR tube.

3. **SB-T-12822-5**

To a vial was added 10 μL **SB-T-12822-5** 10 mM stock solution, 10 μL EtOH and 60 μL Solutol/EtOH (v/v = 2:/1) solution. 420 μL D₂O was added to the mixture dropwise. Then the mixture solution was transferred to a NMR tube.

EtOH-Polysorbate 80-D₂O system:

1. 1:1 mixture

To a vial was added 10 μL **BLT-S-F₆** 10 mM stock solution, 10 μL **SB-T-12822-5** stock solution and 10 μL polysorbate 80. 470 μL D₂O was added to the mixture dropwise. Then the mixture solution was transferred to a NMR tube.

2. **BLT-S-F₆**

To a vial was added 10 μL **BLT-S-F₆** 10 mM stock solution and 10 μL polysorbate 80. 480 μL D₂O was added to the mixture dropwise. Then the mixture solution was transferred to a NMR tube

3. **SB-T-12822-5**

To a vial was added 10 μL **SB-T-12822-5** 10 mM stock solution and 10 μL polysorbate 80. 480 μL D₂O was added to the mixture dropwise. Then the mixture solution was transferred to a NMR tube.

EtOH-Polysorbate 80-D₂O-GSH system:

To a vial was added 10 **BLT-S-F₆** 10 mM stock solution and 10 μL polysorbate 80. 3.1 mg GSH (100 eq) dissolved in 480 μL D₂O was added to the mixture dropwise. Then the mixture solution was transferred to a NMR tube. The NMR tube was kept in a 37 °C water bath during the reaction while not measuring NMR.

EtOH-Polysorbate 80-D₂O-Human Blood Plasma system:

1. 1:1 mixture

To a vial was added 10 μL **BLT-S-F₆** 10 mM stock solution, 10 μL **SB-T-12822-5** 10 mM stock solution and 10 μL polysorbate 80. 50 μL D₂O was added to the mixture dropwise. 420 μL human blood plasma was then added and mixed. Then the mixture solution was transferred to a NMR tube.

2. **BLT-S-F₆**

To a vial was added 10 μL **BLT-S-F₆** 10 mM stock solution and 10 μL polysorbate 80. 50 μL D₂O was added to the mixture dropwise. 430 μL human blood plasma was then added and mixed. Then the mixture solution was transferred to a NMR tube. The NMR tube was kept in a 37 °C water bath during the reaction while not measuring NMR.

3. **SB-T-12822-5**

To a vial was added 10 μL **SB-T-12822-5** 10 mM stock solution and 10 μL polysorbate 80. 50 μL D₂O was added to the mixture dropwise. 430 μL human blood plasma was then added and mixed. Then the mixture solution was transferred to a NMR tube.

EtOH-Polysorbate 80-D₂O-Human Blood Plasma-GSH system:

To a vial was added 10 μL **BLT-S-F₆** 10 mM stock solution and 10 μL polysorbate 80. 50 μL D₂O was added to the mixture dropwise. 3.1 mg GSH (100 eq) dissolved in 430 μL blood plasma was added and mixed. Then the mixture solution was transferred to a NMR tube. The NMR tube was kept in a 37 °C water bath during the reaction while not measuring NMR.

EtOH-Polysorbate 80-D₂O-Human Blood Plasma-GSH kinetic run:

To a vial was added 10 μL **BLT-S-F₆** 10 mM stock solution and 10 μL polysorbate 80. 50 μL D₂O was added to the mixture dropwise. 3.1 mg GSH (100 eq) dissolved in 430 μL human blood plasma was added and mixed. Then the mixture solution was transferred to a NMR tube. A quick acquisition was done before the kinetic run to make sure everything is okay. The first kinetic acquisition started 30 min after the sample was prepared. Each acquisition is 1024 scans (~31min) and then relaxed for 1722 seconds (one acquisition per hour). The NMR run was at 37 °C.

EtOH-Polysorbate 80-D₂O-RPMI cell culture medium system:

RPMI cell culture medium was pretreated with 10% FBS and 1% PenStrip.

1. 1:1 mixture

To a vial was added 10 μL **BLT-S-F₆** 10 mM stock solution, 10 μL **SB-T-12822-5** 10 mM stock solution and 10 μL polysorbate 80. 50 μL D₂O was added to the mixture dropwise. 420 μL RPMI medium was then added and mixed. Then the mixture solution was transferred to a NMR tube.

2. **BLT-S-F₆**

To a vial was added 10 μL **BLT-S-F₆** 10 mM stock solution and 10 μL polysorbate 80. 50 μL D₂O was added to the mixture dropwise. 430 μL RPMI medium was then added and mixed. Then the mixture solution was transferred to a NMR tube. The NMR tube was kept in a 37 °C water bath during the reaction while not measuring NMR.

3. **SB-T-12822-5**

To a vial was added 10 μL **SB-T-12822-5** 10 mM stock solution and 10 μL polysorbate 80. 50 μL D₂O was added to the mixture dropwise. 430 μL RPMI medium was then added and mixed. Then the mixture solution was transferred to a NMR tube.

EtOH-Polysorbate 80-D₂O-RPMI cell culture medium-GSH system:

To a vial was added 10 μL **BLT-S-F₆** 10 mM stock solution and 10 μL polysorbate 80. 50 μL D₂O was added to the mixture dropwise. 3.1 mg GSH (100 eq) dissolved in 430 μL RPMI medium (the color of medium changed from purple to yellow immediately when dissolving GSH) was added and mixed. Then the mixture solution was transferred to a NMR tube. The NMR tube was kept in a 37 °C water bath during the reaction while not measuring NMR.

§ 2.5 References

- (1) Strebhardt, K.; Ullrich, A. Paul Ehrlich's magic bullet concept: 100 years of progress. *Nat Rev Cancer* **2008**, *8*, 473-480.
- (2) DeVita, V. T., Jr.; Chu, E. A history of cancer chemotherapy. *Cancer Res* **2008**, *68*, 8643-8653.
- (3) National Cancer Institute. <http://www.cancer.gov/about-cancer/treatment/types/targeted-therapies/targeted-therapies-fact-sheet>.
- (4) Druker, B. J.; Tamura, S.; Buchdunger, E.; Ohno, S.; Segal, G. M.; Fanning, S.; Zimmermann, J.; Lydon, N. B. Effects of a selective inhibitor of the Abl tyrosine kinase on the growth of Bcr-Abl positive cells. *Nat Med* **1996**, *2*, 561-566.
- (5) Presta, L. G.; Chen, H.; O'Connor, S. J.; Chisholm, V.; Meng, Y. G.; Krummen, L.; Winkler, M.; Ferrara, N. Humanization of an anti-vascular endothelial growth factor monoclonal antibody for the therapy of solid tumors and other disorders. *Cancer Res* **1997**, *57*, 4593-4599.
- (6) Ferrara, N.; Hillan, K. J.; Gerber, H. P.; Novotny, W. Discovery and development of bevacizumab, an anti-VEGF antibody for treating cancer. *Nat Rev Drug Discov* **2004**, *3*, 391-400.
- (7) Jaracz, S.; Chen, J.; Kuznetsova, L. V.; Ojima, L. Recent advances in tumor-targeting anticancer drug conjugates. *Bioorg Med Chem* **2005**, *13*, 5043-5054.
- (8) Ojima, I. Guided molecular missiles for tumor-targeting chemotherapy-case studies using the second-generation taxoids as warheads. *Acc Chem Res* **2008**, *41*, 108-119.
- (9) Ojima, I. Tumor-targeting drug delivery of chemotherapeutic agents. *Pure Appl Chem* **2011**, *83*, 1685-1698.
- (10) Ojima, I.; Zuniga, E. S.; Berger, W. T.; Seitz, J. D. Tumor-targeting drug delivery of new-generation taxoids. *Future Med Chem* **2012**, *4*, 33-50.
- (11) Ojima, I.; Geng, X. D.; Wu, X. Y.; Qu, C. X.; Borella, C. P.; Xie, H. S.; Wilhelm, S. D.; Leece, B. A.; Bartle, L. M.; Goldmacher, V. S.; Chari, R. V. J. Tumor-specific novel taxoid-monoclonal antibody conjugates. *J Med Chem* **2002**, *45*, 5620-5623.
- (12) Wu, X.; Ojima, I. Tumor specific novel taxoid-monoclonal antibody conjugates. *Curr Med Chem* **2004**, *11*, 429-438.

- (13) Kuznetsova, L.; Chen, J.; Sun, L.; Wu, X. Y.; Pepe, A.; Veith, J. A.; Pera, P.; Bernacki, R. J.; Ojima, I. Syntheses and evaluation of novel fatty acid-second-generation taxoid conjugates as promising anticancer agents. *Bioorg Med Chem Lett* **2006**, *16*, 974-977.
- (14) Seitz, J. D.; Vineberg, J. G.; Herlihy, E.; Park, B.; Melief, E.; Ojima, I. Design, synthesis and biological evaluation of a highly-potent and cancer cell selective folate-taxoid conjugate. *Bioorg Med Chem* **2015**, *23*, 2187-2194.
- (15) Chen, J. Y.; Chen, S. Y.; Zhao, X. R.; Kuznetsova, L. V.; Wong, S. S.; Ojima, I. Functionalized Single-Walled Carbon Nanotubes as Rationally Designed Vehicles for Tumor-Targeted Drug Delivery. *J Am Chem Soc* **2008**, *130*, 16778-16785.
- (16) Chen, S. Y.; Zhao, X. R.; Chen, J. Y.; Chen, J.; Kuznetsova, L.; Wong, S. S.; Ojima, I. Mechanism-Based Tumor-Targeting Drug Delivery System. Validation of Efficient Vitamin Receptor-Mediated Endocytosis and Drug Release. *Bioconjugate Chem* **2010**, *21*, 979-987.
- (17) Vineberg, J. G.; Zuniga, E. S.; Kamath, A.; Chen, Y. J.; Seitz, J. D.; Ojima, I. Design, Synthesis, and Biological Evaluations of Tumor-Targeting Dual-Warhead Conjugates for a Taxoid-Camptothecin Combination Chemotherapy. *J Med Chem* **2014**, *57*, 5777-5791.
- (18) Vineberg, J. G.; Wang, T.; Zuniga, E. S.; Ojima, I. Design, Synthesis, and Biological Evaluation of Theranostic Vitamin-Linker-Taxoid Conjugates. *J Med Chem* **2015**, *58*, 2406-2416.
- (19) Chen, J.; Jaracz, S.; Zhao, X.; Chen, S.; Ojima, I. Antibody-cytotoxic agent conjugates for cancer therapy. *Expert Opin Drug Deliv* **2005**, *2*, 873-890.
- (20) Zheng, Z. B.; Zhu, G.; Tak, H.; Joseph, E.; Eiseman, J. L.; Creighton, D. J. N-(2-hydroxypropyl)methacrylamide copolymers of a glutathione (GSH)-activated glyoxalase i inhibitor and DNA alkylating agent: synthesis, reaction kinetics with GSH, and in vitro antitumor activities. *Bioconjugate Chem* **2005**, *16*, 598-607.
- (21) Wolf, W.; Albright, M. J.; Silver, M. S.; Weber, H.; Reichardt, U.; Sauer, R. Fluorine-19 NMR spectroscopic studies of the metabolism of 5-fluorouracil in the liver of patients undergoing chemotherapy. *Magn Reson Imaging* **1987**, *5*, 165-169.
- (22) Ojima, I. Use of fluorine in the medicinal chemistry and chemical biology of bioactive compounds - A case study on fluorinated taxane anticancer agents. *Chembiochem* **2004**, *5*, 628-635.
- (23) Seitz, J. D.; Vineberg, J. G.; Wei, L. F.; Khan, J. F.; Lichtenthal, B.; Lin, C. F.; Ojima, I. Design, synthesis and application of fluorine-labeled taxoids as F-19 NMR probes for

the metabolic stability assessment of tumor-targeted drug delivery systems. *J Fluorine Chem* **2015**, *171*, 148-161.

(24) Shaabani, A.; Tavasoli-Rad, F.; Lee, D. G. Potassium permanganate oxidation of organic compounds. *Synth Commun* **2005**, *35*, 571-580.

(25) Widdison, W. C.; Wilhelm, S. D.; Cavanagh, E. E.; Whiteman, K. R.; Leece, B. A.; Kovtun, Y.; Goldmacher, V. S.; Xie, H.; Steeves, R. M.; Lutz, R. J.; Zhao, R.; Wang, L.; Blaettler, W. A.; Chari, R. V. J. Semisynthetic Maytansine Analogs for the Targeted Treatment of Cancer. *J Med Chem* **2006**, *49*, 4392-4408.

(26) Banerjee, P. S.; Zuniga, E. S.; Ojima, I.; Carrico, I. S. Targeted and armed oncolytic adenovirus via chemoselective modification. *Bioorg Med Chem Lett* **2011**, *21*, 4985-4988.

(27) Bordwell, F. G.; Fried, H. E. Heterocyclic aromatic anions with $4n + 2$ π -electrons. *J Org Chem* **1991**, *56*, 4218-4223.

Chapter 3

PAMAM Dendrimer-based Tumor-Targeted Drug Delivery Systems

Chapter Contents

§ 3.1 Introduction.....	108
§ 3.1.1 Nanocarrier-based Drug Delivery.....	108
§ 3.1.2 Dendrimer.....	111
§ 3.1.3 Applications of Dendrimer in Anticancer Drug Delivery.....	115
§ 3.1.4 Enhanced Permeability and Retention (EPR) Effect.....	118
§ 3.1.5 Biotin as Tumor-Targeting Module	119
§ 3.1.6 Multivalent Binding Effect.....	120
§ 3.1.7 Theranostics	122
§ 3.2 PAMAM Dendrimer-based Tumor-Targeting Taxoid/FITC Conjugates.....	125
§ 3.2.1 Rational Design.....	125
§ 3.2.2 Synthesis of Biotin-PEGylated-G1/G3 PAMAM Dendrimers	127
§ 3.2.3 Synthesis of SB-T-1214-Linker-PEG-Azide and FITC-PEG-Azide Click Ready Probes.....	133
§ 3.2.4 Construct of Final Dendrimer Conjugates	135
§ 3.2.5 Biological Evaluation of PAMAM Dendrimer-based Tumor-Targeting Taxoid/FITC Conjugates.....	162
§ 3.3 Asymmetric Bow-Tie Dendrimer-based (ABTD) Tumor-Targeted Drug Delivery Systems.....	172
§ 3.3.1 Rational Design.....	172
§ 3.3.2 Synthesis of ABTD Conjugates	175
§ 3.4 Tri-branched PAMAM Dendrimer-based Tumor-Targeting Theranostic Conjugates.....	185
§ 3.4.1 Rational Design.....	185

§ 3.4.2 Towards Synthesis of a Tri-branched PAMAM Dendrimer-based Tumor-Targeting Theranostic Conjugate bearing MRI Contrast Agent	187
§ 3.4.3 Towards Synthesis of Second-Generation Versatile Tri-branched PAMAM Dendrimer-based Tumor-Targeting Theranostic Conjugates-Route 1.....	194
§ 3.4.4 Towards Synthesis of Second-Generation Versatile Tri-branched PAMAM Dendrimer-based Tumor-Targeting Theranostic Conjugates-Route 2.....	199
§ 3.5 Summary	206
§ 3.6 Experimental	206
§ 3.7 References.....	230

§ 3.1 Introduction

§ 3.1.1 Nanocarrier-based Drug Delivery

Nanocarriers are nanosized (diameter 1-100 nm) drug delivery vehicles, which can carry multiple drugs, imaging agents, and/or other functional groups.^{1,2} Nanocarrier-based drugs, such as polymer-protein conjugates and liposomes-carried drugs, first reached clinical trials in the mid- 1980s, and were subsequently marketed in the mid-1990s.^{1,2} **Table 3.1** shows selected examples of nanocarrier-based drugs on the market.¹ SMANCS, a conjugate of neocarzinostatin (an antitumor protein) and poly(styrene-comaleic acid), has a molecular size of about 90 kDa upon binding to albumin in plasma, and it is the first polymeric drug approved for clinical use employing the enhanced permeability and retention (EPR) effect.³ Other examples include Myocet (non-PEG coated liposome-encapsulated form of Doxorubicin), Doxil/Caelyx (PEG coated liposome-encapsulated form of Doxorubicin), Abraxane (albumin-bound Paclitaxel) and etc.¹

Table 3.1 Selected examples of nanocarrier-based drugs on the market. Reprinted by permission from Macmillan Publishers Ltd: Nature Nanotechnology, Peer, D.; Karp, J. M.; Hong, S.; FaroKHzad, O. C.; Margalit, R.; Langer, R. Nanocarriers as an emerging platform for cancer therapy. *Nat Nanotechnol* **2007**, 2, 751-760, copyright (2007).

Compound	Commercial name	Nanocarrier	Indications
Styrene maleic anhydride-neocarzinostatin (SMANCS)	Zinostatin/Stimalmer	Polymer-protein conjugate	Hepatocellular carcinoma
PEG-L-asparaginase	Oncaspar	Polymer-protein conjugate	Acute lymphoblastic leukemia
PEG-granulocyte colony-stimulating factor (G-CSF)	Neulasta/PEGfilgrastim	Polymer-protein conjugate	Prevention of chemotherapy-associated neutropenia
IL2 fused to diphtheria toxin	Ortak (Denilelukin diftiox)	Immunotoxin (fusion protein)	Cutaneous T-cell lymphoma
Anti-CD33 antibody conjugated to calicheamicin	Mylotarg	Chemo-immunoconjugate	Acute myelogenous leukemia
Anti-CD20 conjugated to yttrium-90 or indium-111	Zevalin	Radio-immunoconjugate	Relapsed or refractory, low-grade, follicular, or transformed non-Hodgkin's lymphoma
Anti-CD20 conjugated to iodine-131	Bexxar	Radio-immunoconjugate	Relapsed or refractory, low-grade, follicular, or transformed non-Hodgkin's lymphoma
Daunorubicin	DaunoXome	Liposomes	Kaposi's sarcoma
Doxorubicin	Myocet	Liposomes	Combinational therapy of recurrent breast cancer, ovarian cancer, Kaposi's sarcoma
Doxorubicin	Doxil/Caelyx	PEG-liposomes	Refractory Kaposi's sarcoma, recurrent breast cancer, ovarian cancer
Vincristine	OncotCS	Liposomes	Relapsed aggressive non-Hodgkin's lymphoma (NHL)
Paclitaxel	Abraxane	Albumin-bound paclitaxel nanoparticles	Metastatic breast cancer

Various types of nanocarriers have been employed in cancer detection and/or therapy, including immunoconjugates, polymer-drug conjugates, carbon nanotubes, dendrimers, gold nanoparticles, and lipid-based carriers such as liposomes and micelles (**Figure 3.1a**).¹ Functional groups, such as chemotherapeutic drugs or targeting modules, could be either attached to the surface of the nanocarrier through covalent bonds, or entrapped inside the nanocarriers (**Figure 3.1b**).¹

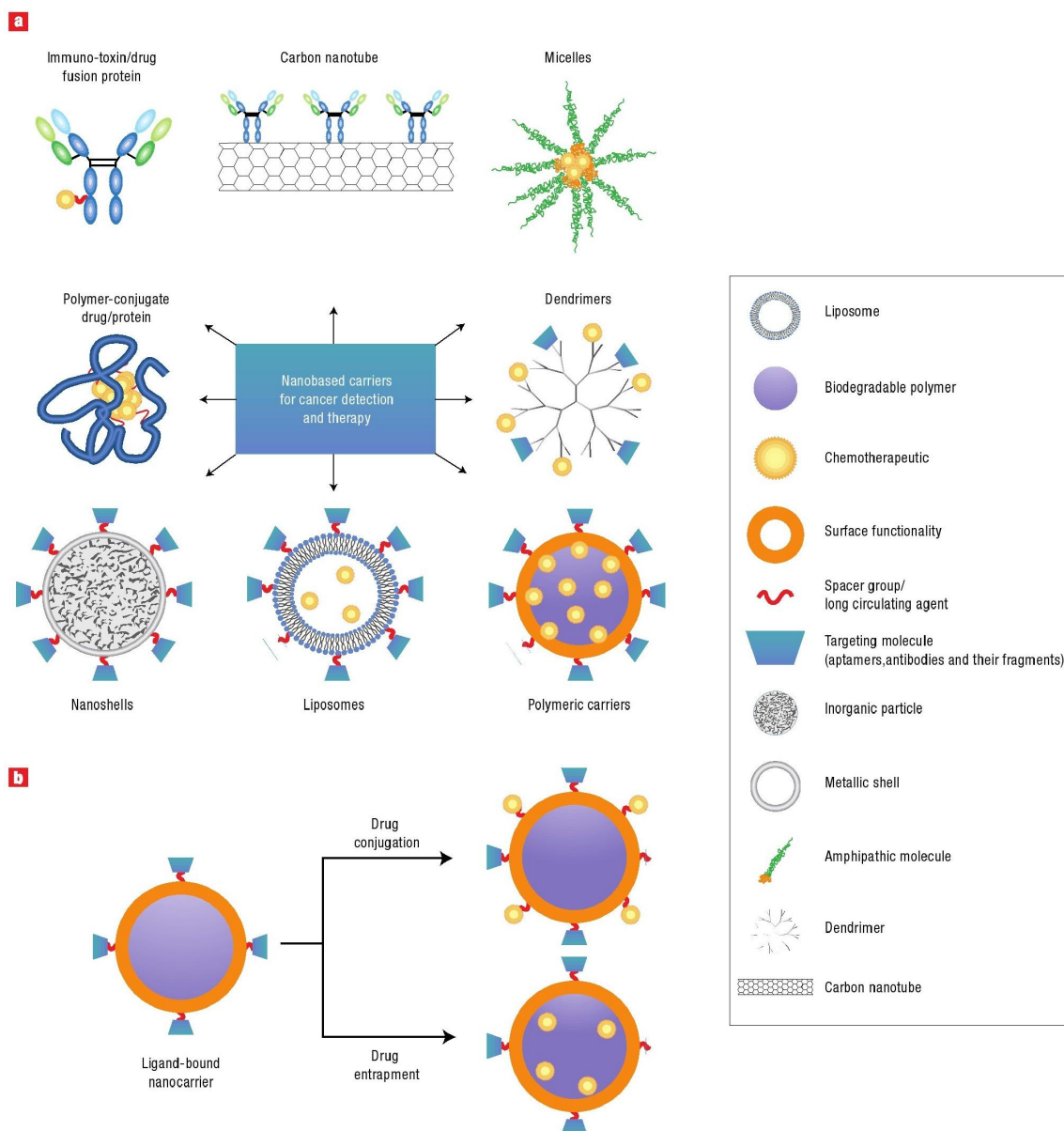


Figure 3.1 Examples of nanocarriers for anticancer drug delivery. Reprinted by permission from Macmillan Publishers Ltd: Nature Nanotechnology, Peer, D.; Karp, J. M.; Hong, S.; Farokhzad, O. C.; Margalit, R.; Langer, R. Nanocarriers as an emerging platform for cancer therapy. *Nat Nanotechnol* **2007**, 2, 751-760, copyright (2007).

Among different types of nanocarriers, polymer-anticancer drug conjugates have potential advantages in improved drug targeting to tumor, reduced drug toxicity, and overcoming the mechanism of drug resistance.² **Figure 3.2** shows selected examples of polymer-anticancer drug conjugates. (*N*-(2-hydroxypropyl) methacrylamide) HPMAC copolymer-Gly-Phe-Leu-Gly-doxorubicin conjugate (**Figure 3.2 top left**), which contains ~ 8 wt% doxorubicin drug loading, was developed by Duncan and her

colleagues in the 1980s.^{2,4} The preclinical evaluation of this polymer drug conjugate showed improved anti-tumor activity *in vivo* through the EPR-mediated tumor targeting.⁴ This polymer drug conjugate was subsequently evaluated in phase I and phase II clinical trials, and showed promising activities against non-small cell lung cancer (NSCLC) as the first synthetic polymer-drug conjugate advanced to clinical study.^{2,5,6} A multivalent receptor-targeted conjugate containing galactosamine to promote liver targeting (**Figure 3.2 bottom left**) was also developed in the same group to treat primarily liver cancer, which employed both active receptor-mediated targeting and passive size-mediated targeting.^{2,7,8} Polyglutamate-paclitaxel conjugate (**Figure 3.2 top right**) was first developed by Li and his colleagues, and is currently in phase III study under name Xyotax.⁹ This highly water-soluble conjugate contains ~37 wt% drug loading with an overall Mw of 49,000.⁹ Paclitaxel is slowly released by hydrolysis, but largely released through biodegradation of the glutamic acid polymer backbone by lysosomal chaperone B after endocytic uptake.¹⁰ Polymer combination therapy, in which different drugs could be attached to the polymer carrier simultaneously, is another attractive way of using polymer as drug delivery vehicle. For example, polymer drug conjugate containing both the aromatase inhibitor aminoglutethimide and doxorubicin was developed (**Figure 3.2 bottom right**).²

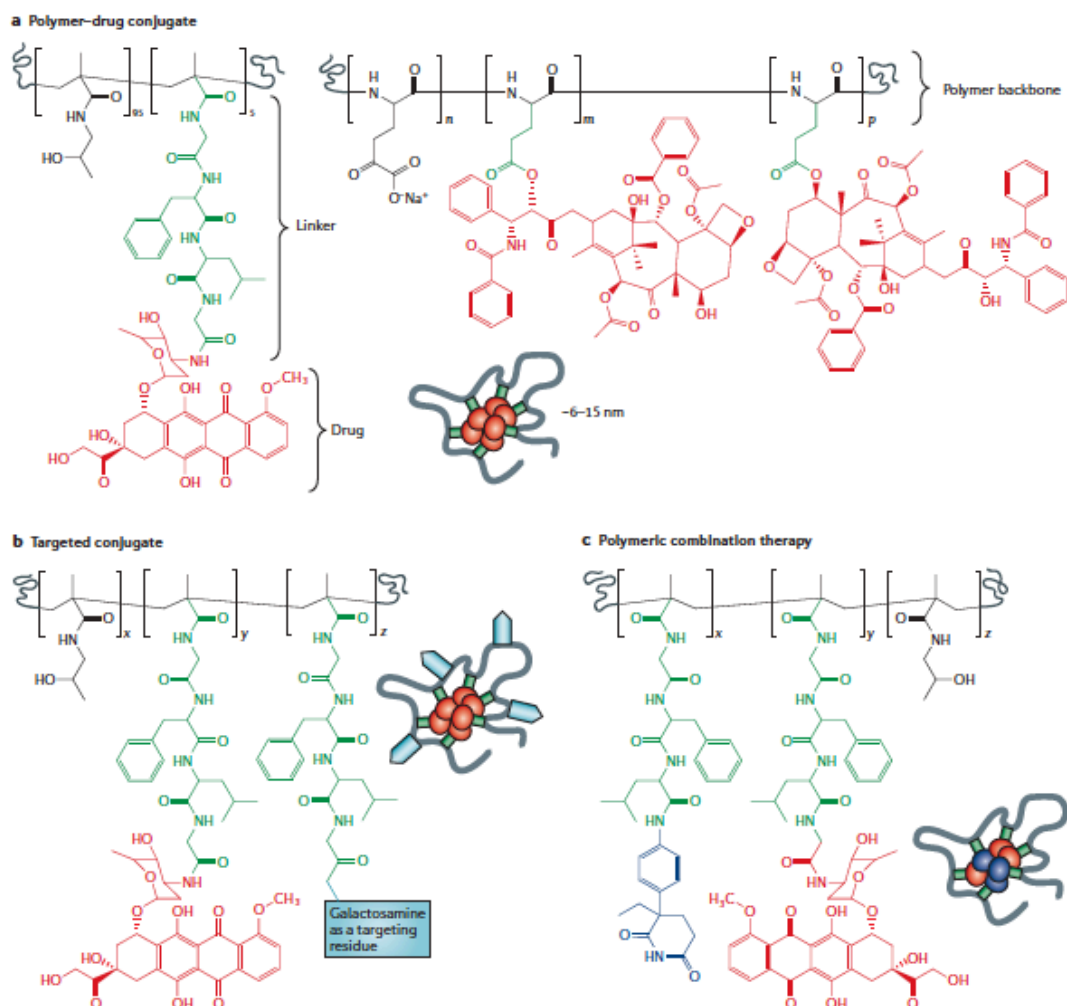


Figure 3.2 Examples of polymer-anticancer drug conjugates. Reprinted by permission from Macmillan Publishers Ltd: Nature Reviews Cancer, Duncan, R. Polymer conjugates as anticancer nanomedicines. *Nat Rev Cancer* **2006**, *6*, 688-701, copyright (2006).

§ 3.1.2 Dendrimer

Dendrimers are a class of macromolecules, which commonly have highly branched well-defined three-dimensional architectures.¹¹ The name dendrimer comes from the Greek word for tree (Dendron). As shown in **Figure 3.3**, dendrimers usually are constructed with three components, namely the core molecule, branches, and the surface molecules.¹² By increasing a distinct layer to a dendrimer will increase its generation, therefore, the property and shape of a dendrimer is mainly determined by the types and amount of branches used to grow the dendrimer. The diameter of a dendrimer increases linearly while the number of surface groups increases exponentially, resulting in flexible and open shapes for low generation dendrimers, and more dense three-dimensional shapes for higher generation dendrimers.¹¹

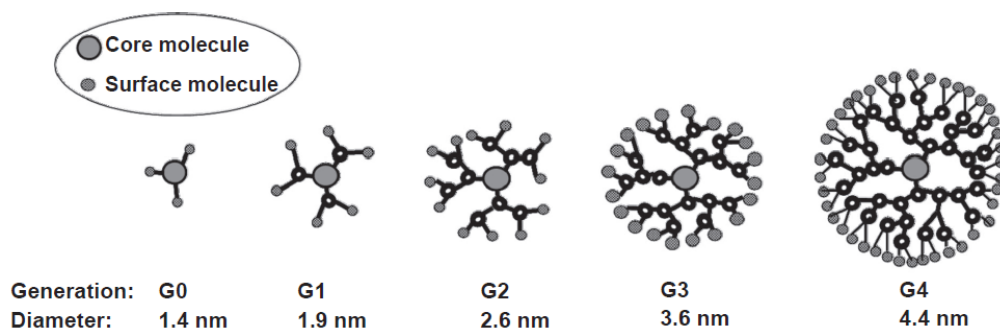


Figure 3.3 Graphical representations of dendrimers from core to generation 4. Reprinted from Bharali, D. J.; Khalil, M.; Gurbuz, M.; Simone, T. M.; Mousa, S. A. *Int J Nanomed* **2009**, *4*, 1-7, with permission from Dove Press.

The divergent method and the convergent method are the two main strategies for synthesizing dendrimers. Schematic representations of the two methods are shown in **Figure 3.4**.¹¹ In the divergent method, dendrimers grow branches or generations from a core molecule outward to its surface. In the mid-1980s, Tomalia et al. first synthesized a poly(amidoamine) (PAMAM) type dendrimer using this strategy.¹³ The convergent method, on the contrary, builds dendrimers from outside in, and was first introduced by Hawker and Fréchet in 1990.¹⁴

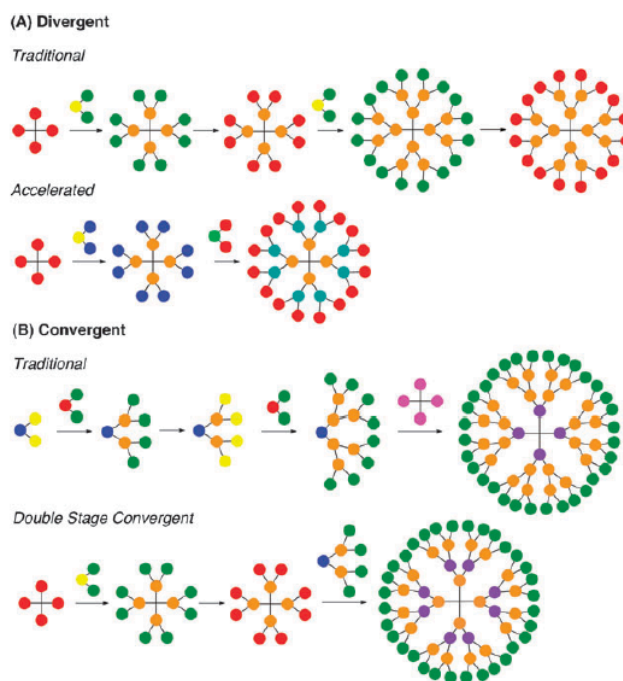


Figure 3.4 Schematic representations of divergent method and convergent method for synthesizing dendrimers. Reproduced from Mintzer, M. A.; Grinstaff, M. W. Biomedical applications of dendrimers: a tutorial. *Chem Soc Rev* **2011**, *40*, 173-190, with permission of The Royal Society of Chemistry.

In 2002, Gillies and Fréchet reported a novel “bow-tie” shape polyester dendritic scaffold, in which one dendron has hydroxyl functionality and could be used for drug or radiolabel attachment, while the other dendron is conjugated to multiple poly(ethylene oxide) chains for improving the solubility.¹⁵ Molecular weight and architecture could be controlled by changing the generation of the dendron and number of poly(ethylene oxide) chains attached (**Figure 3.5**).¹⁵

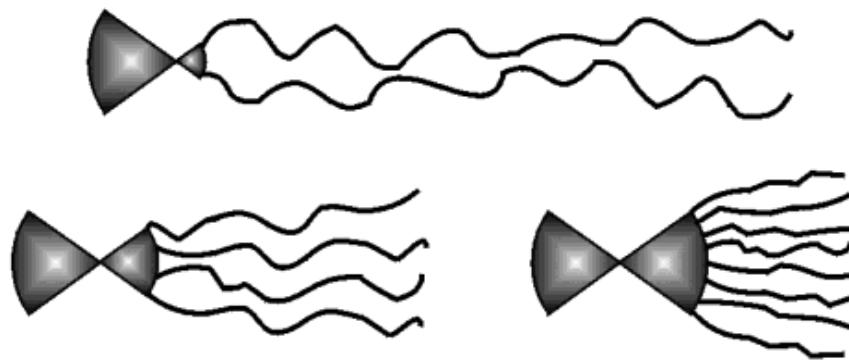


Figure 3.5 Schematic representation of polyester dendrimers-poly(ethylene oxide) “bow-tie” hybrids with tunable molecular weight and architecture. Reprinted with permission from Gillies, E. R.; Fréchet, J. M. J. Designing macromolecules for therapeutic applications: Polyester dendrimer-poly(ethylene oxide) “bow-tie” hybrids with tunable molecular weight and architecture. *J Am Chem Soc* **2002**, *124*, 14137-14146. Copyright (2002) American Chemical Society.

In 2011, Weck et al. reported an interesting polyamide-based hyperbranched multifunctional dendrimer platform, which contains nine azide termini, nine amine termini, and fifty-four terminal acid groups.¹⁶ The authors first combined two different dendrons into a “Janus”-type dendrimer, and then reacted with an AB₆C₁ type dendron to construct the hyperbranched multifunctional dendrimer platform (**Figure 3.6**).¹⁶ Further orthogonal functionalization of the multifunctional dendrimer by connecting the nine amine groups with a near-infrared (NIR) cyanine dye gave rise to the final dendrimer conjugate, which shows fluorescence in the NIR region, and no toxicity toward T98G human cells.¹⁶

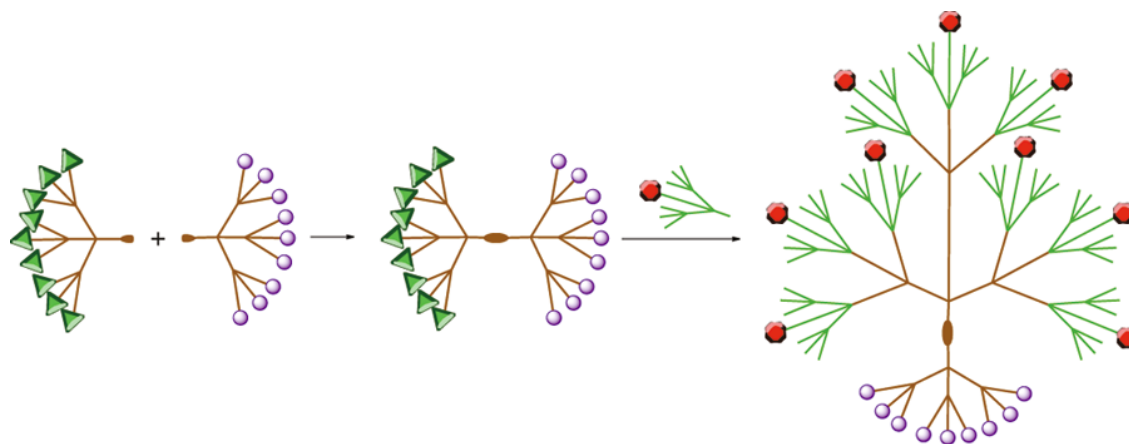


Figure 3.6 Schematic representation of a well-defined polyamide-based hyperbranched multifunctional dendrimer platform. Reprinted with permission from Ornelas, C.; Pennell, R.; Liebes, L. F.; Weck, M. Construction of a Well-Defined Multifunctional Dendrimer for Theranostics. *Org Lett* **2011**, *13*, 976-979. Copyright (2011) American Chemical Society.

In addition, while our research was going on, in 2011, Hartley et al. reported a “diblock” generation 3 (G3) cystamine core PAMAM dendrimer-based scaffold, allowing one half-dendrimer attaching with 16 targeting structures, the other side attaching with 16 peptides or proteins, and a third structure such as fluorochrome could be incorporated into the bifunctional linker (**Figure 3.7**).¹⁷

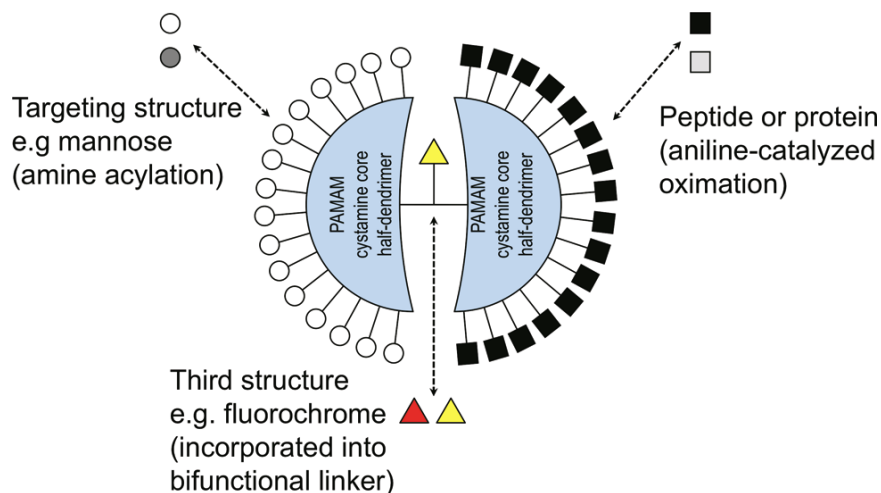


Figure 3.7 Schematic representation of “diblock” PAMAM cystamine core dendrimer-based conjugate for synthesis of bioactive nanoparticles. Reprinted with permission from Gaertner, H. F.; Cerini, F.; Kamath, A.; Rochat, A. F.; Siegrist, C. A.; Menin, L.; Hartley, O. Efficient orthogonal bioconjugation of dendrimers for synthesis of bioactive nanoparticles. *Bioconjugate Chem* **2011**, *22*, 1103-1114. Copyright (2011) American Chemical Society.

§ 3.1.3 Applications of Dendrimer in Anticancer Drug Delivery

Dendrimers have been used for various applications in different fields including biological, chemical, medical, polymer and nanotechnology.¹⁸ In term of anticancer drug delivery, dendrimers are attractive platforms because of their unique properties including: i) Well-defined architectures, molecular weights and functionalities; ii) anticancer drugs could be encapsulated into the interior space of dendrimers to greatly increase the water solubility of the drug; iii) anticancer drugs, targeting moieties and other functionality groups could also be conjugated to the terminal groups on the surface of dendrimers to increase the payload of the drugs, targeting efficacy of the conjugate and other biological and physiological properties; iv) passive targeting of the conjugated could be achieved based on size of the functionalized dendrimers by employing the enhanced permeability and retention (EPR) effect; and v) lack of immunogenicity of certain types of dendrimers make them safer than synthetic peptides or natural proteins.^{19,20}

As illustrated in **Figure 3.8**, dendrimers can be used as anticancer drug delivery vehicles by employing both receptor-mediated active targeting (large amount of small targeting molecules and cytotoxic agents could be conjugated to the surface of a dendrimer or anticancer drugs could be encapsulated inside a dendrimer) and size-mediated passive targeting (by taking advantage of the enhanced permeability and retention (EPR) effect).¹⁹ The multifunctional characteristics of the dendritic constructs make them appealing platforms for anticancer drug delivery.

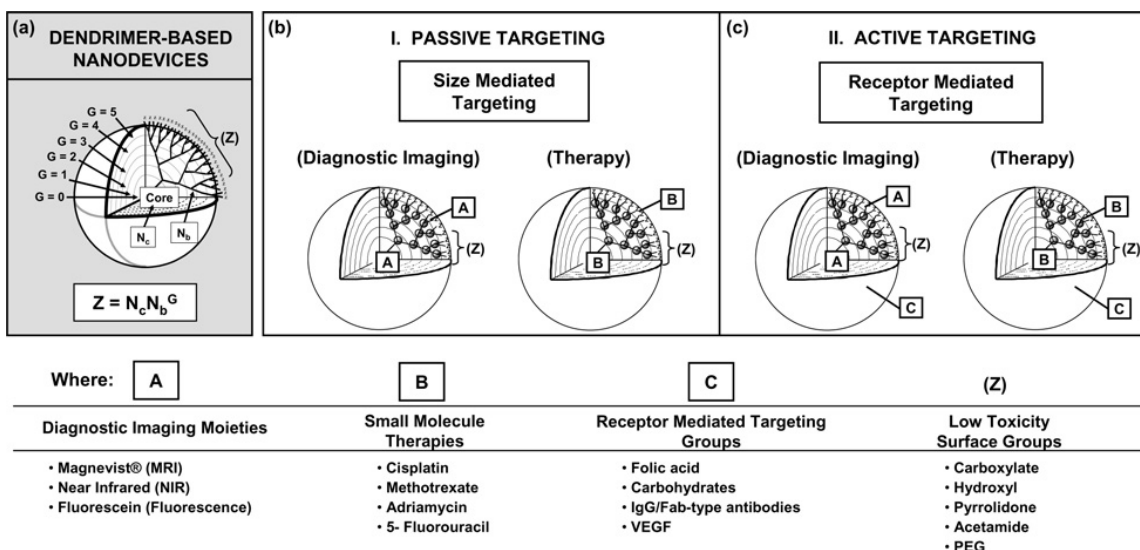


Figure 3.8 Dendrimers as multi-purpose nanodevices for anticancer drug delivery and diagnostic imaging. Reprinted from Tomalia, D. A.; Reyna, L. A.; Svenson, S. Dendrimers as multi-purpose nanodevices for oncology drug delivery and diagnostic imaging. *Biochem Soc Trans* **2007**, *35*, 61-67, with permission from Portland Press.

A proof-of-concept example of using dendrimer as an anticancer drug delivery platform via conjugation with chemotherapeutic drugs, targeting moieties and other functionalities is shown below in **Figure 3.9**. In 2005, Baker and his coworkers reported the synthesis of such conjugate by partial acetylation of the surface amino groups of a generation 5 (G5) PAMAM dendrimer and surface-functionalized with fluorescein isothiocyanate (FITC), folic acid (FA) and methotrexate (MTX) in a multistep sequential manner.^{21,22} This conjugate has shown in vitro and in vivo cellular internalization through the folate receptor and improved efficacy to kill tumor cells.^{23,24} A similar construct using taxol as the warhead instead of methotrexate (MTX) was also reported by the same group in 2006.²⁵

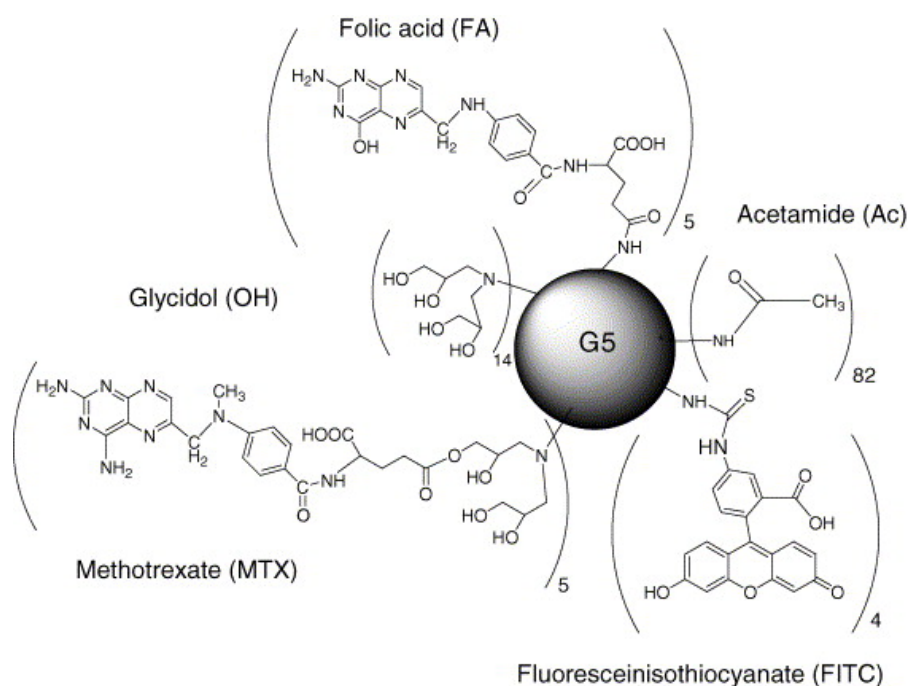


Figure 3.9 Schematic representation of generation 5 (G5) PAMAM dendrimer surface-functionalized with FITC, FA and MTX. Reprinted from *J Chromatogr B Analyt Technol Biomed Life Sci*, 822, Islam, M. T.; Majoros, I. J.; Baker, J. R., Jr. HPLC analysis of PAMAM dendrimer based multifunctional devices, 21-26, Copyright (2005), with permission from Elsevier.

However, recently their studies suggested that possibly less than 5% of the material contain the desired number of 4 folic acids (FA) and 5 methotrexates (MTX) in the multifunctional dendrimer conjugate (**Figure 3.10**).²⁶ When they scaled up the synthesis for clinical trial studies, markedly less cytotoxicity in vitro and insignificant anticancer activity in vivo was found compared to small batches of the material, presumably because of the polydispersity of the synthesized multifunctional dendrimer conjugates.²⁷

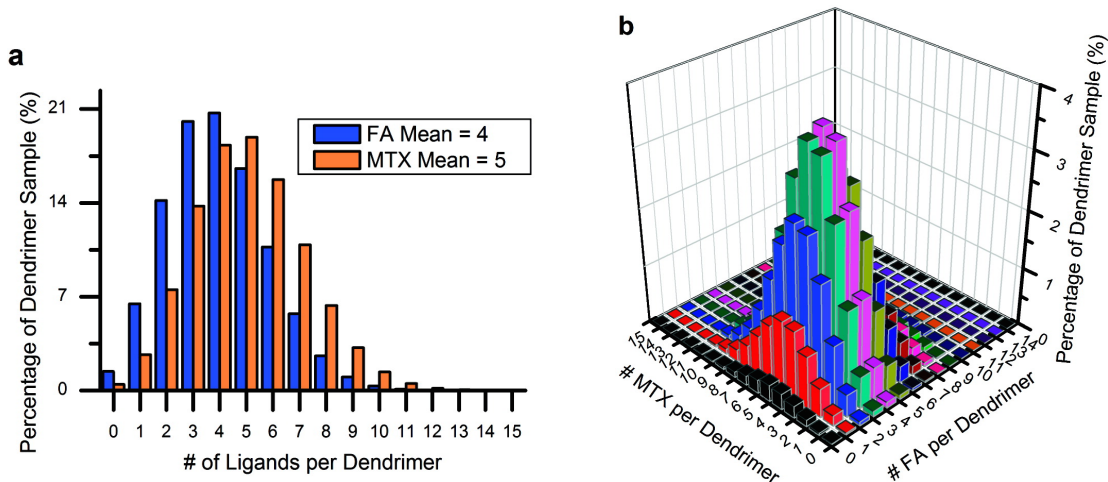


Figure 3.10 A quantitative assessment of ligand distribution of the multifunctional dendrimer conjugate. Reprinted with permission from Mullen, D. G.; Fang, M.; Desai, A.; Baker, J. R.; Orr, B. G.; Holl, M. M. B. A Quantitative Assessment of Nanoparticle-Ligand Distributions: Implications for Targeted Drug and Imaging Delivery in Dendrimer Conjugates. *ACS Nano* **2010**, *4*, 657-670. Copyright (2010) American Chemical Society.

Now they are trying to solve this problem by employing different synthetic strategies, such as define the ratio of FA to MTX via a triazine core scaffold, or conjugate the MTX through a serum-stable amide linker instead of a ester linkage and via copper-free click chemistry (**Figure 3.11**).^{27,28}

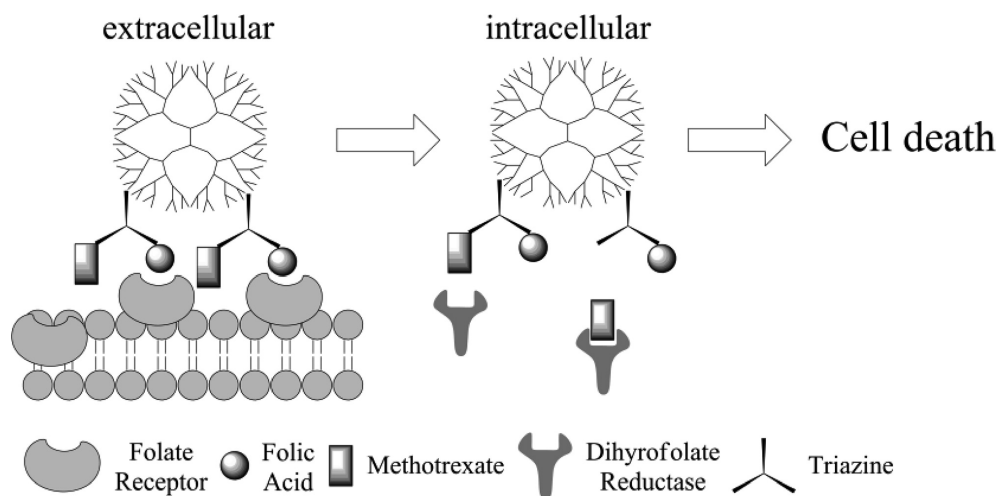


Figure 3.11 Bifunctional dendrimer conjugates of folic acid and methotrexate with defined ratio. Reprinted with permission from Zong, H.; Thomas, T. P.; Lee, K. H.; Desai, A. M.; Li, M. H.; Kotlyar, A.; Zhang, Y.; Leroueil, P. R.; Gam, J. J.; Banaszak Holl, M. M.; Baker, J. R., Jr. Bifunctional PAMAM dendrimer conjugates of folic acid and methotrexate with defined ratio. *Biomacromolecules* **2012**, *13*, 982-991. Copyright (2012) American Chemical Society.

§ 3.1.4 Enhanced Permeability and Retention (EPR) Effect

The concept of the enhanced permeability and retention (EPR) effect was first proposed and described by Maeda and co-workers in 1986.²⁹ Tumor growth is angiogenesis dependent, that is to say, tumor cells are capable of building new blood vessels for obtaining nutrients and oxygen to support their rapid growth.³⁰ These newly developed blood vessels are very different from those in the normal tissue, as they usually have irregular shapes, leakages, and defective architectures.³¹ As shown in **Figure 3.12**, macromolecules or nanoparticles have much greater chance to enter tumor tissue than normal tissue due to such anatomical defectiveness of neovasculature in tumor tissues.³² Moreover, the lymphatic drainage system in tumor tissue is not well developed, resulting poor clearance of the macromolecules or nanoparticles, therefore, such large molecules have longer retention time in the tumor.³² This phenomenon, was termed enhanced permeability and retention (EPR) effect, and is widely used as the theoretical basis for selective targeting tumors by using macromolecules or nanoparticles nowadays. This targeting strategy employing the EPR effect is also commonly classified as passive targeting, while targeting receptors or antigens that overexpressed on tumor cells is named active targeting.

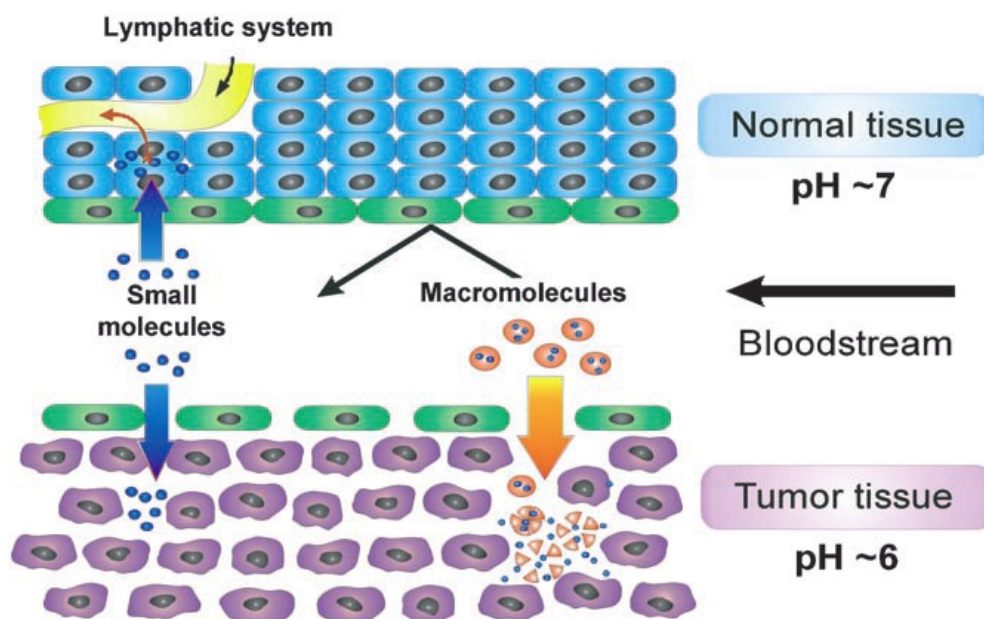


Figure 3.12 Schematic representation of enhanced permeability and retention (EPR) effect. Reprinted from Kratz, F.; Muller, I. A.; Ryppa, C.; Warnecke, A. Prodrug strategies in anticancer chemotherapy. *Chemmedchem* **2008**, *3*, 20-53, with permission from John Wiley & Sons.

§ 3.1.5 Biotin as Tumor-Targeting Module

Vitamins, such as vitamin B₁₂, folic acid, biotin, and riboflavin, are essential nutrients required by living systems.³³ All living cells require such vitamins for survival, however, rapidly dividing cells such as cancer cells require substantially more vitamins than normal cells in order to sustain enhanced proliferation.³³ As a result, the receptors involved in uptake of the vitamins are found to be overexpressed in certain cancer cells, and could be used as therapeutic targets for delivering highly toxic anticancer drugs specifically into these cancer cells.³³ The folate receptor has been extensively studied as a tumor-specific biomarker, and biotin receptor is emerging as a potential target as well.³³⁻³⁶

Biotin (also called vitamin B₇, vitamin H, or coenzyme R), as shown in **Figure 3.13** below, is a water-soluble vitamin and serves a covalently bound coenzyme for five carboxylases including acetyl-CoA carboxylases 1 and 2, pyruvate carboxylase, propionyl-CoA carboxylase, and 3-methylcrotonyl-CoA carboxylase.³⁷ Biotin plays a vital role in epigenetic regulation, fatty acid biosynthesis, energy production, as well as metabolism of fats and amino acids.^{37,38}

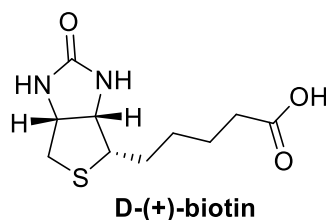


Figure 3.13 Chemical structure of D-(+)-biotin

However, using biotin receptor as a potential tumor-specific target was not well recognized until Russell-Jones and his colleagues reported the high overexpression level of biotin receptors in a wide range of tumor cells in 2004.³³ The authors used Rhodamine-labeled HPMA polymer conjugated with various targeting agents including folic acid, vitamin B₁₂, and biotin, and evaluated the uptake levels of these conjugates.³³ It was found that those cancer cells overexpressing folate or vitamin B₁₂ receptors also overexpress biotin receptors, and moreover, certain types of cancer cells have more overexpression level of biotin receptors than the other two receptors, such as L1210FR, Colo-26, P815, RD995, 4T1, JC, and MMT060562 cell lines.³³ Therefore, biotin receptor became a potential new target for tumor-targeted drug delivery, and was subsequently used in the Ojima laboratory in a number of drug conjugates.³⁹⁻⁴²

Table 3.2 The relative expression levels of vitamin receptors in cancer cells. Reprinted from *J Inorg Biochem*, 98, Russell-Jones, G.; McTavish, K.; McEwan, J.; Rice, J.; Nowotnik, D. Vitamin-mediated targeting as a potential mechanism to increase drug uptake by tumours, 1625-1633, Copyright (2004), with permission from Elsevier.

Tumor	Mouse	Type	Folate	B ₁₂	Biotin
O157	Balb/C	Bcell lymph	+/-	+/-	+/-
BW5147	AKR/J	Lymphoma	+/-	+/-	+/-
B16	C57/Bl	Melanoma	-	-	-
LL-2	C57/Bl	Lung	-	-	-
HCT-116	Balb/C-Nu	Colon	-	-	-
L1210	DBA/2	Leukemia	+/-	+/-	-
L1210FR	DBA/2	Leukemia	++	+	+++
Ov 2008	Balb/C-Nu	Ovarian	+++	-	++
ID8	C57/Bl	Ovarian	+++	-	++
Ovcar-3		Ovarian	+++	-	+++
Colo-26	Balb/C	Colon	+/-	++	+++
P815	DBA/2	Mastocytoma	+/-	++	+++
M109	Balb/C	Lung	+	+++	+++
RENCA	Balb/C	Renal cell	+	+++	+++
RD995	C3H/HeJ	Renal cell	+	++	+++
4T1	Balb/C	Breast	+	++	+++
JC	Balb/C	Breast	+	++	+++
MMT060562	Balb/C	Breast	+	++	+++

§ 3.1.6 Multivalent Binding Effect

Multivalent protein-ligand binding is frequently used by nature to achieve tight binding when univalent binding is weak.⁴³ Various types of multivalent interactions have been extensively studied, such as antibody-antigen interactions,^{44,45} protein-carbohydrate interactions,^{46,47} and folate receptor-folic acid interactions.⁴⁸⁻⁵⁰

In 2007, G5 dendrimer-based nanodevices with different numbers of folic acid targeting moieties attached were used to assess the multivalent interactions between folate receptors (FAR) and folic acid (FA).⁴⁸ Quantitative assessments of the dissociation constants (K_d) between surface-bound folate-binding protein (FBP) and G5 dendrimer-based nanodevices using surface plasmon resonance (SPR) indicates the binding avidity is dramatically increased when increasing the number of folic acid (FA) attached to the nanodevice from 0 to 4.7, however, the binding avidity does not further increase when

more than 4.7 folic acid (FA) are attached, presumably due to saturation of the receptors (**Figure 3.14**).⁴⁸

Nanodevices ^a	Nominal Equiv. #FA Added for FA Conjugation	#FA (GPC) ^b	#FA (UV) ^c	Targeted Nanodevice	Dissociation Constant K_D (M) ^a	Fold Increase over Free FA ^b	Fold Increase over Free FA ^c
G5-Ac-AF488-FA ₀	0	—	—	Free FA	$5 \pm 3 \times 10^{-6}$	—	—
G5-Ac-AF488-FA _{2.6}	3	2.6	1.3 ± 0.3	G5-Ac-AF488-FA _{2.6}	$2 \pm 1 \times 10^{-9}$	2,500	1,000
G5-Ac-AF488-FA _{4.7}	6	4.7	3.0 ± 0.2	G5-Ac-AF488-FA _{4.7}	$7 \pm 6 \times 10^{-11}$	71,400	15,200
G5-Ac-AF488-FA _{7.2}	9	7.2	5.3 ± 0.2	G5-Ac-AF488-FA _{7.2}	$7 \pm 2 \times 10^{-11}$	71,400	9,900
G5-Ac-AF488-FA _{11.5}	12	11.5	8.3 ± 0.9	G5-Ac-AF488-FA _{11.5}	$5 \pm 1 \times 10^{-11}$	100,000	8,700
G5-Ac-AF488-FA _{13.7}	15	13.7	10.6 ± 1.8	G5-Ac-AF488-FA _{13.7}	$3 \pm 2 \times 10^{-11}$	166,700	12,200

Figure 3.14 Quantitative assessments of multivalent interactions between folate-binding protein (FBP) and G5 dendrimer-based nanodevices using surface plasmon resonance (SPR). Reprinted from *Chem Biol*, 14, Hong, S.; Leroueil, P. R.; Majoros, I. J.; Orr, B. G.; Baker, J. R.; Holl, M. M. B. The binding avidity of a nanoparticle-based multivalent targeted drug delivery platform, 107-115, Copyright (2007), with permission from Elsevier.

Qualitative assessments of multivalent interactions between folate receptors (FAR) and G5 dendrimer-based nanodevices with FAR-overexpressed KB cells using flow cytometry gave similar trend after incubation at 37 °C for 1 hour (**Figure 3.15**).⁴⁸ The results indicate a multivalent binding effect for folic-acid-targeted dendritic nanodevice.

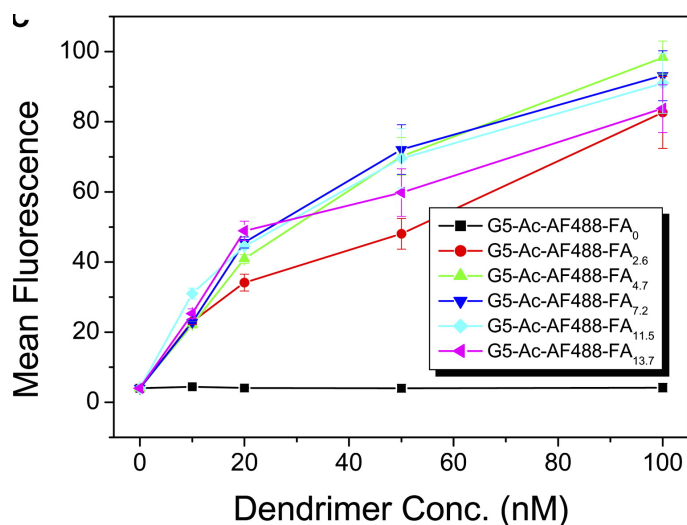


Figure 3.15 Qualitative assessments of multivalent interactions between folate receptors (FAR) and G5 dendrimer-based nanodevices using flow cytometry. Reprinted from *Chem Biol*, 14, Hong, S.; Leroueil, P. R.; Majoros, I. J.; Orr, B. G.; Baker, J. R.; Holl, M. M. B. The binding avidity of a nanoparticle-based multivalent targeted drug delivery platform, 107-115, Copyright (2007), with permission from Elsevier.

However, to date, there are few literature reports about the multivalent binding interactions between biotin receptors (BR) and biotin. In 2009, Palakurthi and his coworkers reported biotinylated PAMAM dendrimers with about 2, 3, 6, and 7 biotin molecules attached to G1, G2, G3, and G4 PAMAM dendrimers respectively, but there was no clear comparison of the cellular uptake between these conjugates.⁵¹

Moreover, the actual impact of different numbers of targeting ligands on the multivalent binding avidity has been difficult to analyze, because the heterogeneous ligand-nanodevice distributions generated by stochastic conjugation chemistries employed in the synthesis.^{16,52} Therefore, there is great need to evaluate the multivalent binding effect using structurally well-defined conjugates with exact numbers of ligands attached.

§ 3.1.7 Theranostics

Theranostics are combination of therapeutic drugs and diagnostic imaging agents, which could be simultaneously delivered with the same dose.⁵³ For example, therapeutics such as chemotherapy, gene therapy, hyperthermia, photodynamic, and radiation therapy could be used to combine with either *in vitro* or *in vivo* imaging functionalities, such as fluorescent probes, magnetic resonance imaging (MRI) contrast agents, and/or positron emission tomography (PET)/single photon emission computed tomography (SPECT) imaging agents (**Figure 3.16**).⁵³

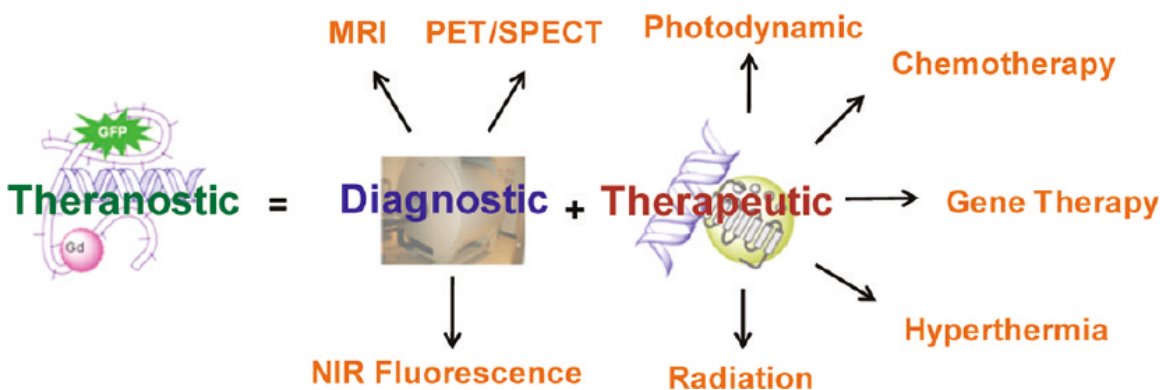


Figure 3.16 Schematic representation of the concept of theranostic. Reprinted with permission from Kelkar, S. S.; Reineke, T. M. Theranostics: Combining Imaging and Therapy. *Bioconjugate Chem* **2011**, *22*, 1879-1903. Copyright (2011) American Chemical Society.

For example, in 2014, Guo and his colleagues reported platinum (II)-gadolinium (III) complexes as potential theranostic agents for cancer treatment (**Figure 3.17**).⁵⁴ These bifunctional Pd-Gd complexes could partially dissociate in cancer cells to release the cytotoxic Pt moieties, and the Gd component and the untouched complex could be used for *in vivo* MRI imaging.⁵⁴ It was found that the proton relaxivity of these

complexes is even higher than commercial MRI contrast agent Gd-DTPA, and showed stronger signal intensity.⁵⁴

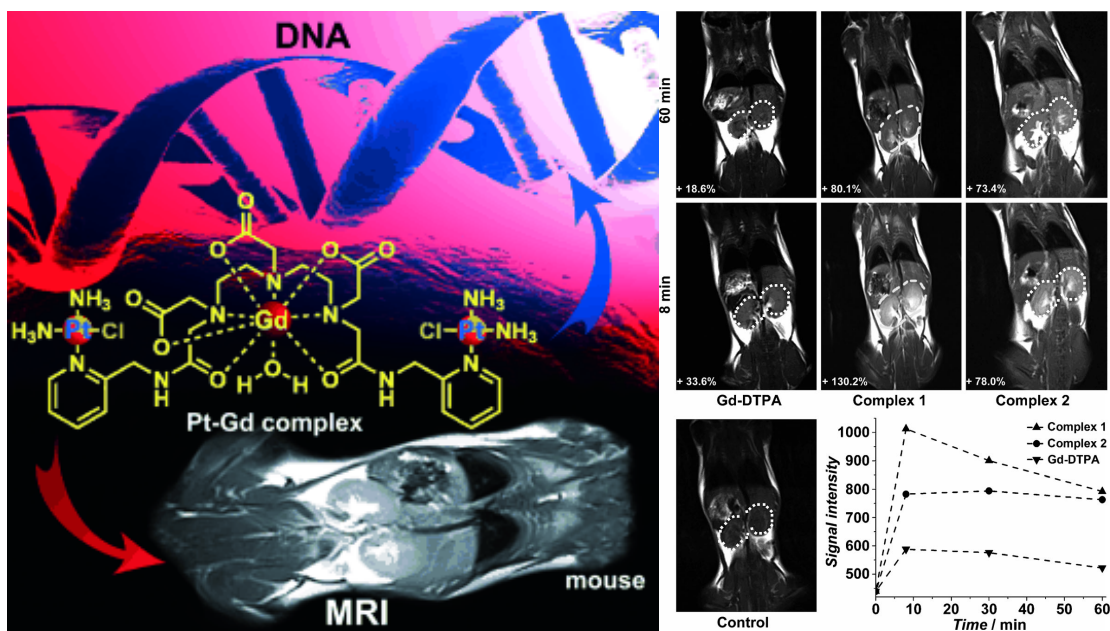


Figure 3.17 Platinum (II)-gadolinium (III) complexes as potential theranostic agents for cancer treatment. Reprinted from Zhu, Z.; Wang, X.; Li, T.; Aime, S.; Sadler, P. J.; Guo, Z. Platinum(II)-Gadolinium(III) Complexes as Potential Single-Molecular Theranostic Agents for Cancer Treatment. *Angew Chem Int Ed* **2014**, *53*, 13225-13228, with permission from John Wiley & Sons.

The Ojima group has been developing trifunctional theranostic agents using triazine splitter, in which tumor-targeting module such as biotin, cytotoxic warhead new-generation taxoid, and an imaging module such as fluorescent probe, MRI contrast agent, or PET/SPECT imaging module could be incorporated into the same conjugate.

Theranostic vitamin-linker-taxoid conjugates bearing FITC for *in vitro* imaging or ¹⁸F for *in vivo* PET imaging have been constructed by Dr. Jacob Vineberg, and published in 2015 (**Figure 3.18**).⁴²

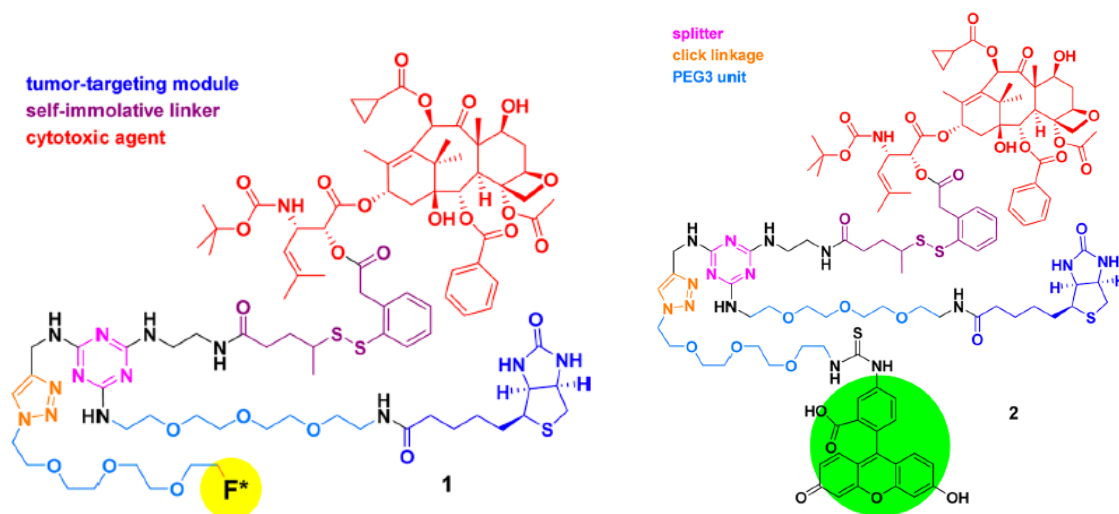


Figure 3.18 Theranostic vitamin-linker-taxoid conjugates bearing FITC for *in vitro* imaging or ^{18}F for *in vivo* imaging. Reprinted with permission from Vineberg, J. G.; Wang, T.; Zuniga, E. S.; Ojima, I. Design, Synthesis, and Biological Evaluation of Theranostic Vitamin-Linker-Taxoid Conjugates. *J Med Chem* **2015**, *58*, 2406-2416. Copyright (2015) American Chemical Society.

Theranostic vitamin-linker-taxoid conjugates bearing chelated radiotracer for potential *in vivo* PET/SPECT/MRI imaging have been constructed by Dr. Tao Wang (Figure 3.19).⁵⁵

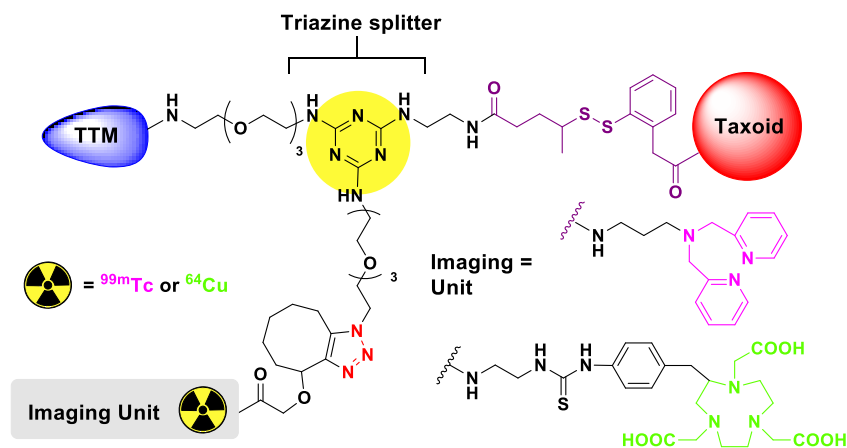


Figure 3.19 Theranostic vitamin-linker-taxoid conjugates bearing chelated radiotracer for potential *in vivo* PET/SPECT/MRI imaging. Adapted with permission from Wang, T.

Design, synthesis, and biological evaluation of novel taxoid-based small-molecule theranostic PET/SPECT imaging agents and nano-scale asymmetric bow-tie dendrimer drug conjugates towards tumor-targeted chemotherapy (Doctoral Dissertation). Stony Brook University, 2015.

§ 3.2 PAMAM Dendrimer-based Tumor-Targeting Taxoid/FITC Conjugates

§ 3.2.1 Rational Design

To avoid the heterogeneous ligand distribution problem found in the traditional dendrimer-based drug delivery, a different strategy was adopted by using PAMAM dendrimer with a cleavable cystamine core and amine surface (**Figure 3.20**).⁵⁵ First, different generations of such PAMAM dendrimer could be surface fully functionalized with one functional group, subsequently cleavage of the disulfide core by reducing agent allows the attachment of other functionalities via a thiol-maleimido type Michael addition though a suitable spacer.

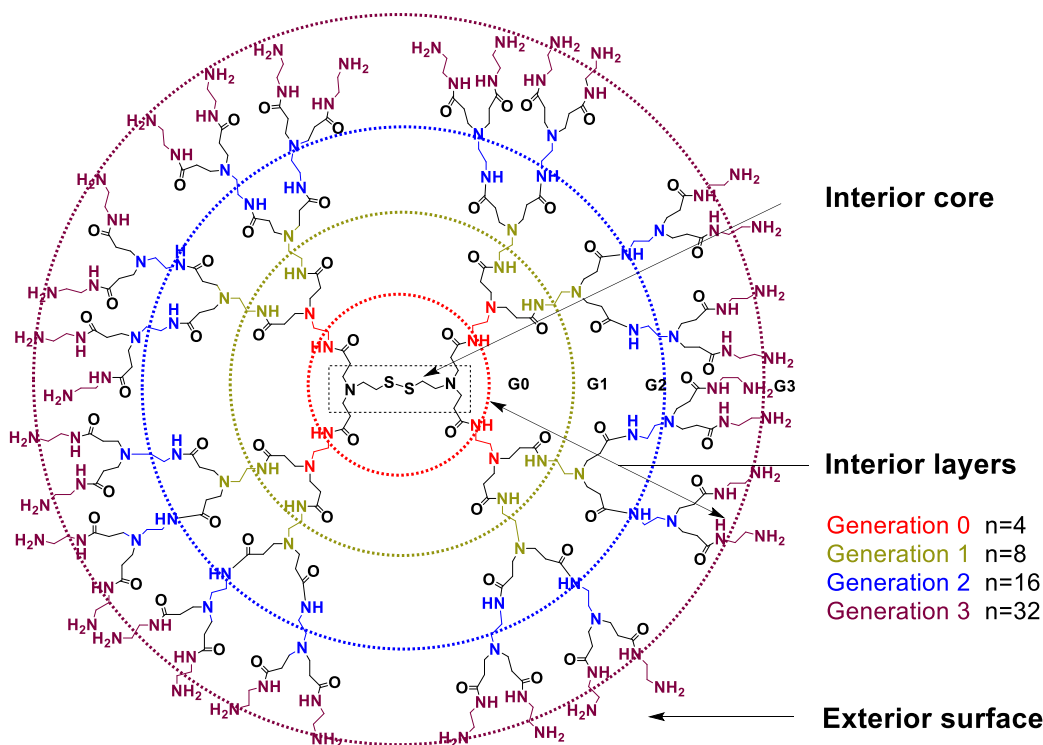


Figure 3.20 Chemical structure of PAMAM dendrimers with a cleavable cystamine core and amine surface. Adapted with permission from Wang, T. Design, synthesis, and biological evaluation of novel taxoid-based small-molecule theranostic PET/SPECT imaging agents and nano-scale asymmetric bow-tie dendrimer drug conjugates towards tumor-targeted chemotherapy (Doctoral Dissertation). Stony Brook University, 2015.

Novel PAMAM dendrimer-based biotin-linker-taxoid (**Figure 3.21**) and biotin-FITC (**Figure 3.22**) conjugates, with 4 or 16 biotins as tumor-targeting modules, were subsequently designed. For synthesizing these conjugates, G1/G3 PAMAM dendrimer with cleavable cystamine core was first fully functionalized with biotins, and then the disulfide bond inside the dendrimer was cleaved and connected to a bifunctional maleimido-alkyne spacer. After that, the functionalized G1/G3 half dendron with biotins

on the surface and alkyne group on the tail was reacted with taxoid-linker-azide and FITC-linker-azide via click chemistry to afford the final conjugates. The synthesized conjugates were evaluated against biotin-receptor overexpressed cancer cell lines to study the multivalent binding effect.

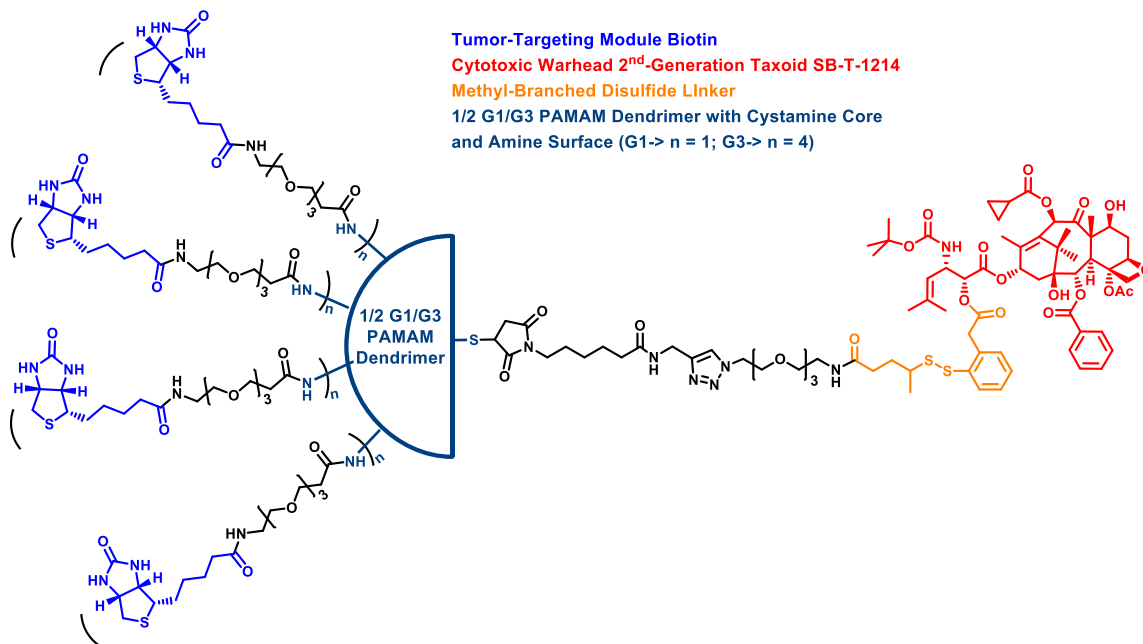


Figure 3.21 Designed PAMAM dendrimer-based biotin-linker-taxoid conjugates

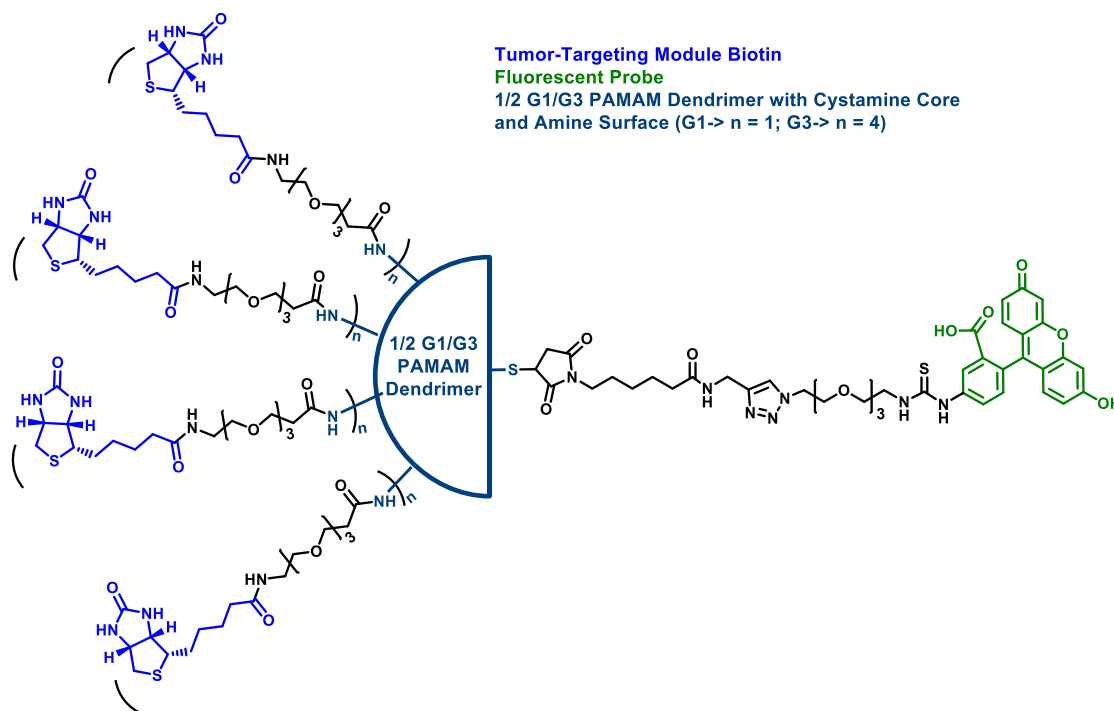
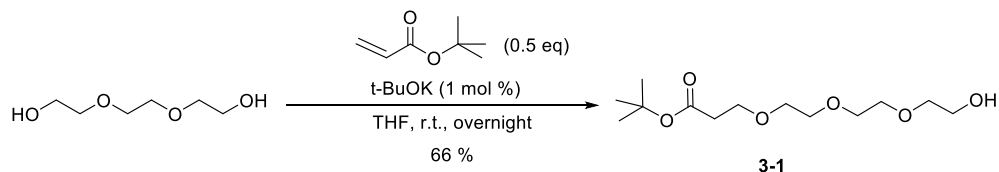


Figure 3.22 Designed PAMAM dendrimer-based biotin-FITC conjugates

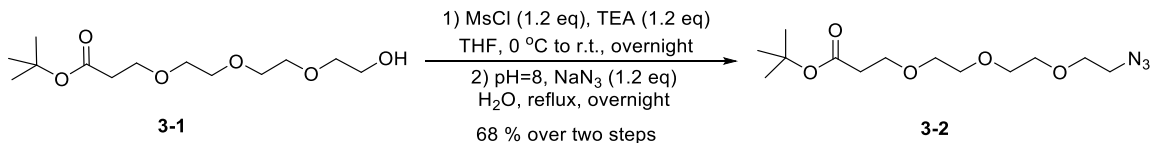
§ 3.2.2 Synthesis of Biotin-PEGylated-G1/G3 PAMAM Dendrimers

The synthesis of biotin-PEGylated-G1/G3 PAMAM dendrimers begins with mono protection of triethylene glycol (**Scheme 3.1**).⁵⁶ This is a Michael addition, and triethylene glycol is used in much excess to ensure mono protection is favored than di-protection. Also, *tert*-butyl acrylate should be added very slowly to favor the mono-protected product. Desired product *tert*-butyl 12-hydroxy-4,7,10-trioxadodecanoate **3-1** was obtained in 66% yield with a small amount of di-protected side product formed.



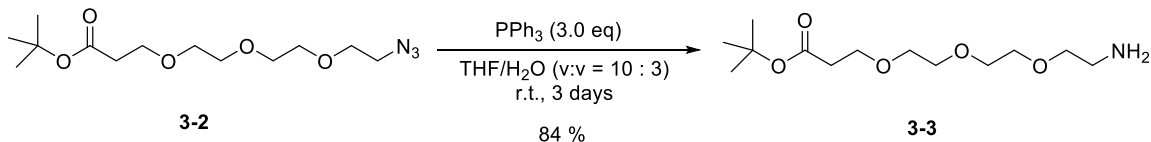
Scheme 3.1 Mono protection of triethylene glycol

Then, the hydroxyl functional group in **3-1** was converted to azide functional group by a two-step sequence to give *tert*-butyl 12-azido-4,7,10-trioxadodecanoate **3-2** in 68% yield (**Scheme 3.2**).^{57,58} The presence of azide functional group in the product was confirmed by IR spectrum. Before treated with sodium azide in the second step, the pH was adjusted to 8~9 to by sodium bicarbonate to ensure hydrazoic acid, an explosive liquid, would not be formed.



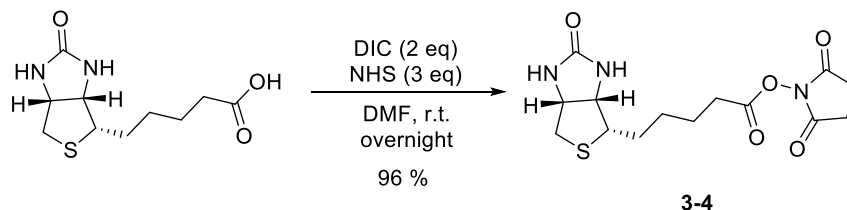
Scheme 3.2 Conversion of hydroxyl group in **3-1** to azide group

Then azide functional group was further converted to amine group by Staudinger reduction (**Scheme 3.3**).⁵⁷ This reaction is a mild method of reducing an azide to an amine. Triphenylphosphine is commonly used as the reducing agent in Staudinger reduction, yielding triphenylphosphine oxide as the side product in addition to the amine. Desired product *tert*-butyl 12-amino-4,7,10-trioxadodecanoate **3-3** was obtained in 84% yield. Side product triphenylphosphine oxide could be removed by extracting with small amount of toluene.



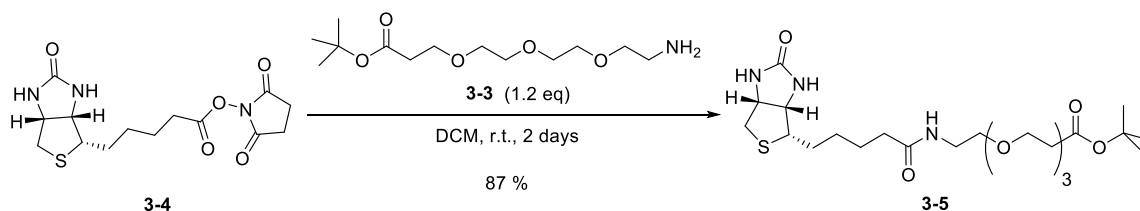
Scheme 3.3 Staudinger reduction of azide to amine

On the other hand, biotin-OSu activated ester **3-4** was obtained in 96% yield by reacting biotin with NHS *via* DIC coupling (**Scheme 3.4**).⁵⁹ First, biotin reacts with the coupling agent DIC to form a highly unstable activated intermediate, and then NHS reacts with the intermediate to form a less labile activated ester **3-4**.



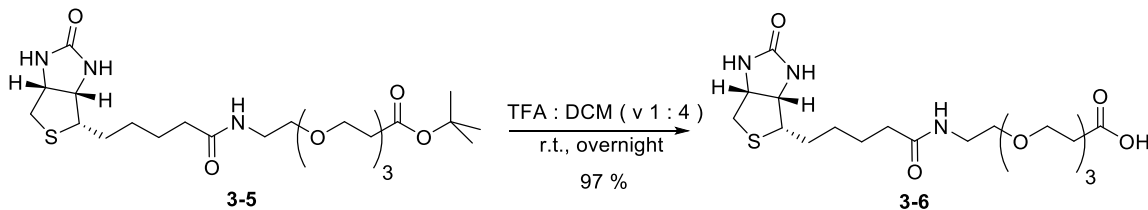
Scheme 3.4 Synthesis of biotin-OSu activated ester **3-4**

Then, the biotin-OSu activated ester **3-4** was used to react with the PEG derivative *tert*-butyl-12-amino-4,7,10-trioxadodecanoate **3-3** to form **3-5** in 87% yield (**Scheme 3.5**).⁵⁷



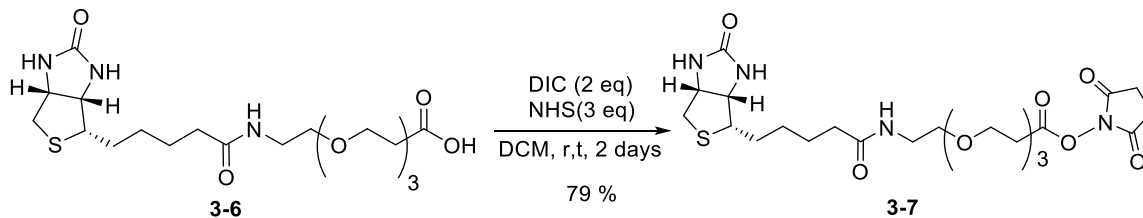
Scheme 3.5 Synthesis of biotin-PEG-*tert*-butyl ester **3-5**

Subsequently, biotin-PEG-*tert*-butyl ester **3-5** was deprotected by trifluoroacetic acid (TFA) in DCM to give biotin-PEG-carboxylic acid **3-6** in 96% to 97% yield (**Scheme 3.6**).⁵⁷



Scheme 3.6 TFA deprotection of biotin-PEG-*tert*-butyl ester **3-5**

In order to react with the surfaces amino groups on the PAMAM dendrimers, the carboxylic acid group in **3-6** was reacted with NHS by DIC coupling to form activated ester **3-7** in 79% isolated yield (**Scheme 3.7**).

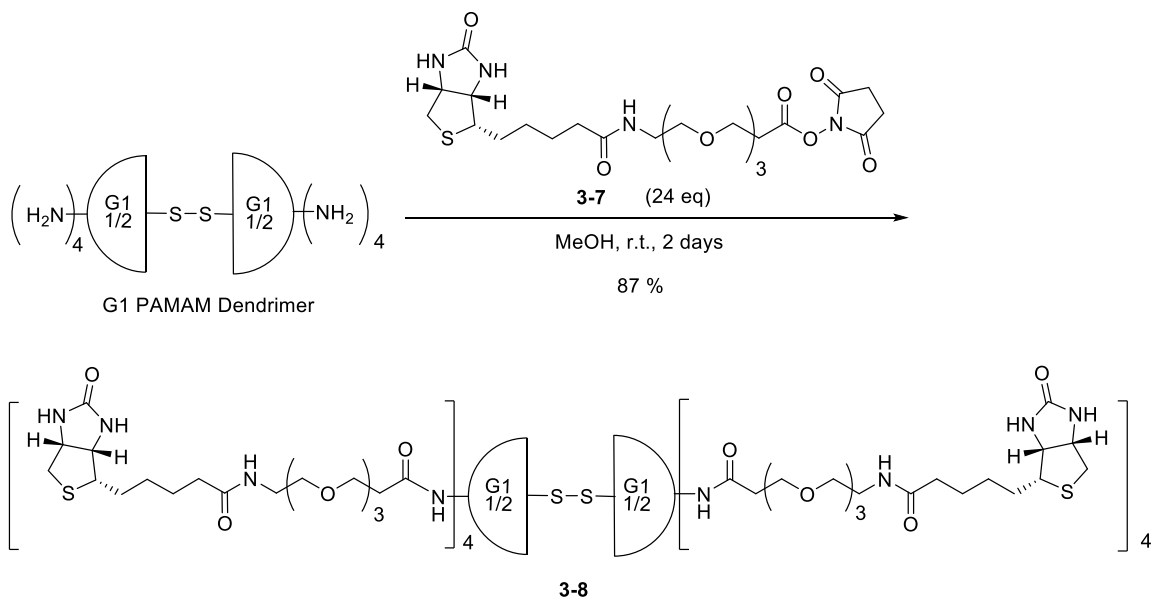


Scheme 3.7 Synthesis of biotin-PEG-Osu activated ester **3-7**

Then, G1 PAMAM dendrimer with cystamine core was reacted with excess activated ester **3-7** to afford biotin PEGylated G1 PAMAM dendrimer **3-8** as a white solid in 87% yield after dialysis against methanol for 3 days (**Scheme 3.8**). The excess activated ester **3-7** also reacted with methanol solution to give biotin-PEG3- methyl ester as a side product. This methyl ester side product obtained from dialysis could be recycled, and undergo hydrolysis to give biotin-PEG-carboxylic acid **3-6** by treating with LiOH.

Biotin PEGylated G1 PAMAM dendrimer **3-8** (chemical formula: $C_{216}H_{380}N_{50}O_{60}S_{10}$) has exact mass 4954.54, molecular weight 4958.31, and m/z 4956.55 (100%) and 4955.55 (86%). In the matrix-assisted laser desorption/ionization-time of flight (MALDI-TOF) analysis using 2,5-dihydroxybenzoic acid (DHB) as the matrix, mass signals of 4958.6 ($[M+H]^+$, calculated 4955.6, $\Delta = 3.0$ Da), 4979.4 ($[M+Na]^+$, calculated 4977.6, $\Delta = 1.8$ Da), 2480.0 ($[M+2H]^{2+}$, calculated 2478.3, $\Delta = 1.7$ Da), and 2502.7 ($[M+2Na]^{2+}$, calculated 2500.3, $\Delta = 2.4$ Da) were observed (**Figure 3.23**). The difference between observed mass and calculated mass is presumably due to two reasons: 1) because of the low resolution of the mass signals in the MALDI-TOF spectrum for measuring dendrimer samples, the processing method used in the experiment is centroid, which measures the “center of mass” instead of isotopic peaks, and as a result, the observed mass is closer to the molecular weight instead of m/z ; 2) the calibration of the method was performed using external peptides standards in a linear protocol, which could not give the best calibration agreement when measuring dendrimer samples.

ESI-MS spectra of biotin PEGylated G1 PAMAM dendrimer **3-8** before purification by dialysis (**Figure 3.24**) and after dialysis (**Figure 3.25**) indicates that dialysis was able to remove most of the small molecule impurities, but could not completely remove the impurities. In the ESI-MS spectra, multiple charge states (+4, +5, and +6) of the product were observed.



Scheme 3.8 Synthesis of biotin PEGylated G1 PAMAM dendrimer **3-8**

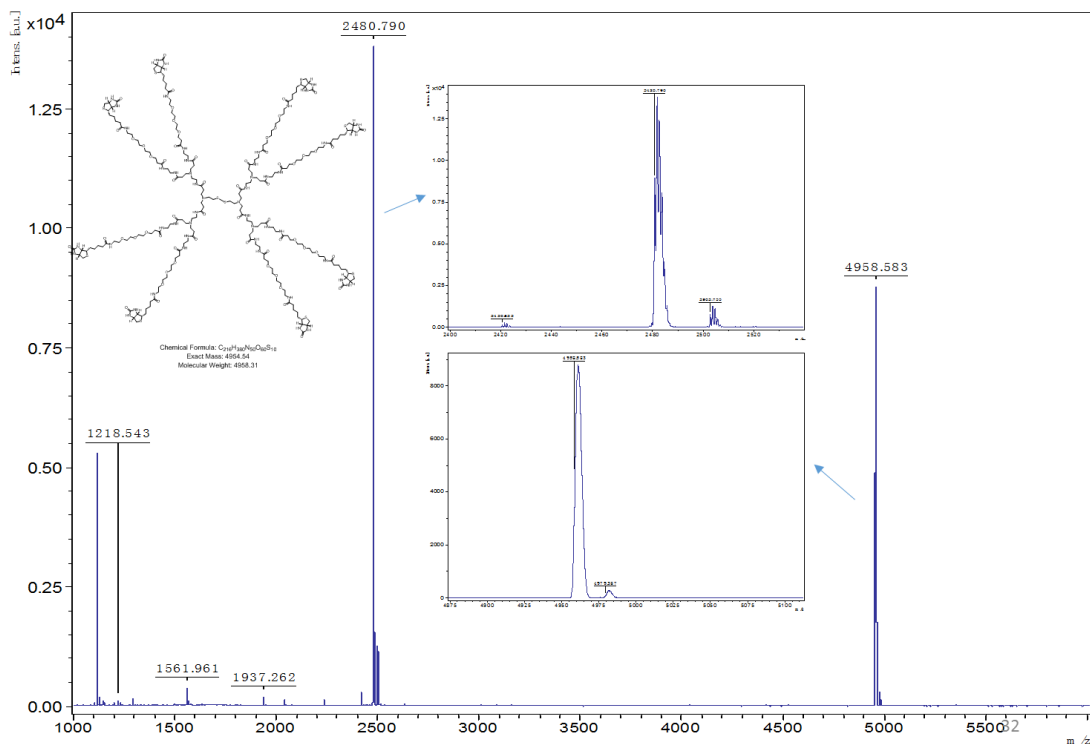


Figure 3.23 MALDI-TOF spectrum of biotin PEGylated G1 PAMAM dendrimer



Figure 3.24 ESI-MS spectrum of biotin PEGylated G1 PAMAM dendrimer before dialysis

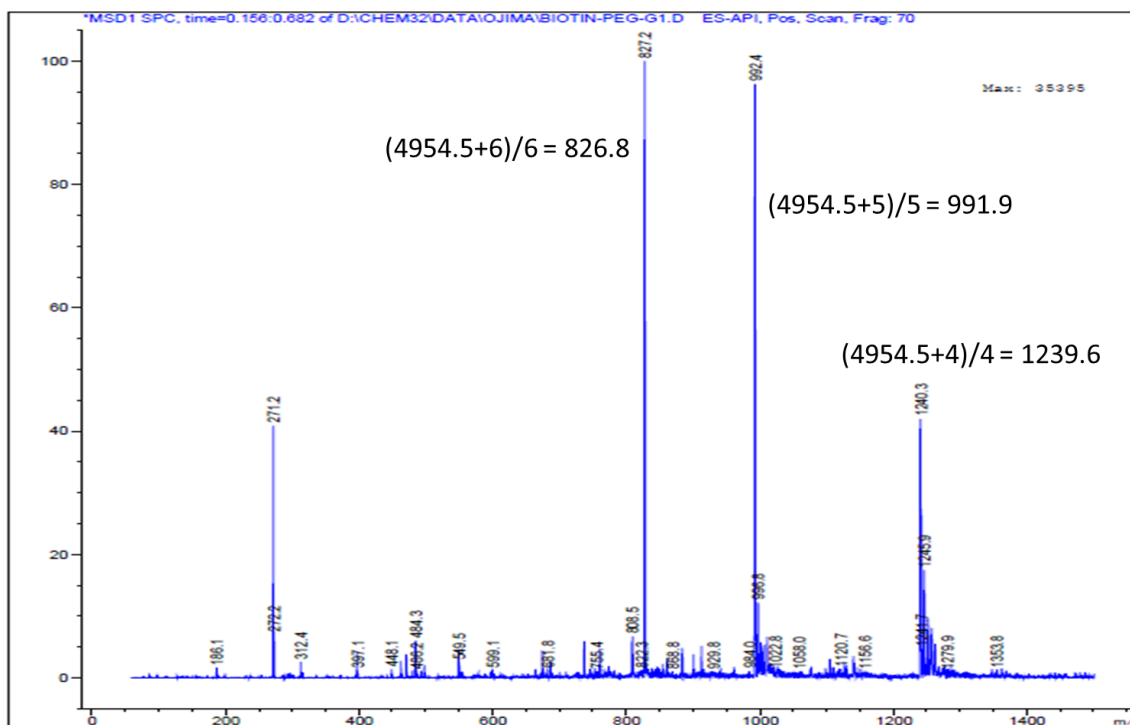
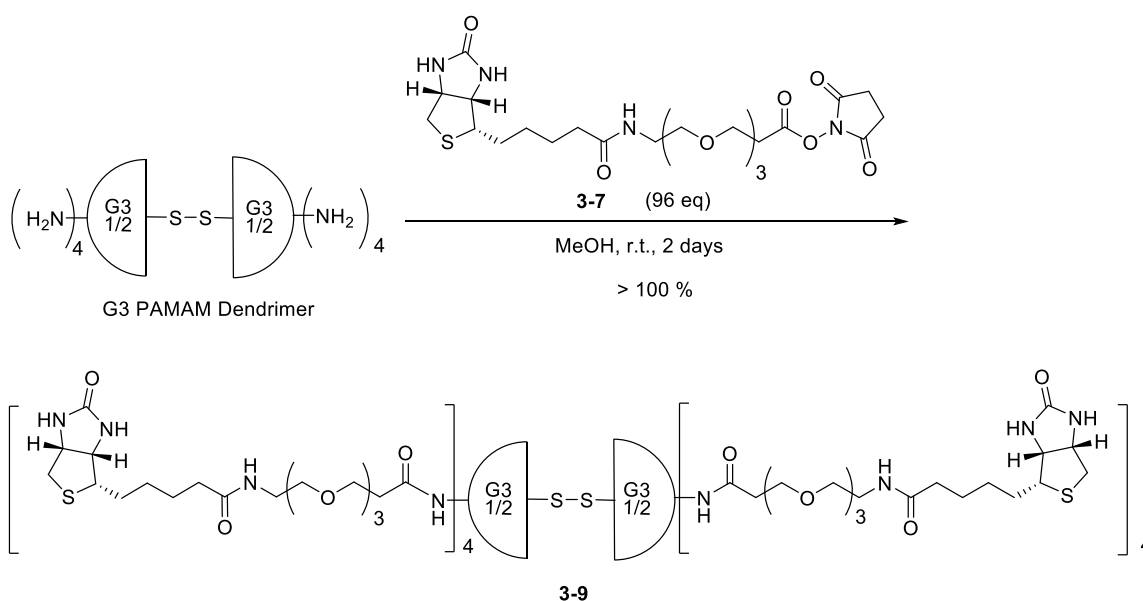


Figure 3.25 ESI-MS spectrum of biotin PEGylated G1 PAMAM dendrimer after dialysis

Similarly, G3 PAMAM dendrimer with cystamine core was reacted with excess activated ester **3-7** to afford biotin PEGylated G3 PAMAM dendrimer **3-9** as a white solid in > 100% yield after dialysis against methanol for 3 days (**Scheme 3.9**). The yield is higher than 100% is because dialysis could not completely remove the impurities. Biotin PEGylated G3 PAMAM dendrimer **3-9** (chemical formula: C₉₁₂H₁₆₀₄N₂₁₈O₂₅₂S₃₄) has exact mass 20730.99, and molecular weight 20746.01. In the MALDI-TOF analysis using DHB as the matrix, mass signals of 20736.0 ([M+H]⁺, calculated 20731.0, Δ = 5.0 Da), and 10370.4 ([M+2H]²⁺, calculated 10366.5, Δ = 3.9 Da) were observed (**Figure 3.26**). Because the molecular weight of desired product is over 20 kDa, ESI-MS could not give any obvious signal of the desired product.



Scheme 3.9 Synthesis of biotin PEGylated G3 PAMAM dendrimer **3-9**

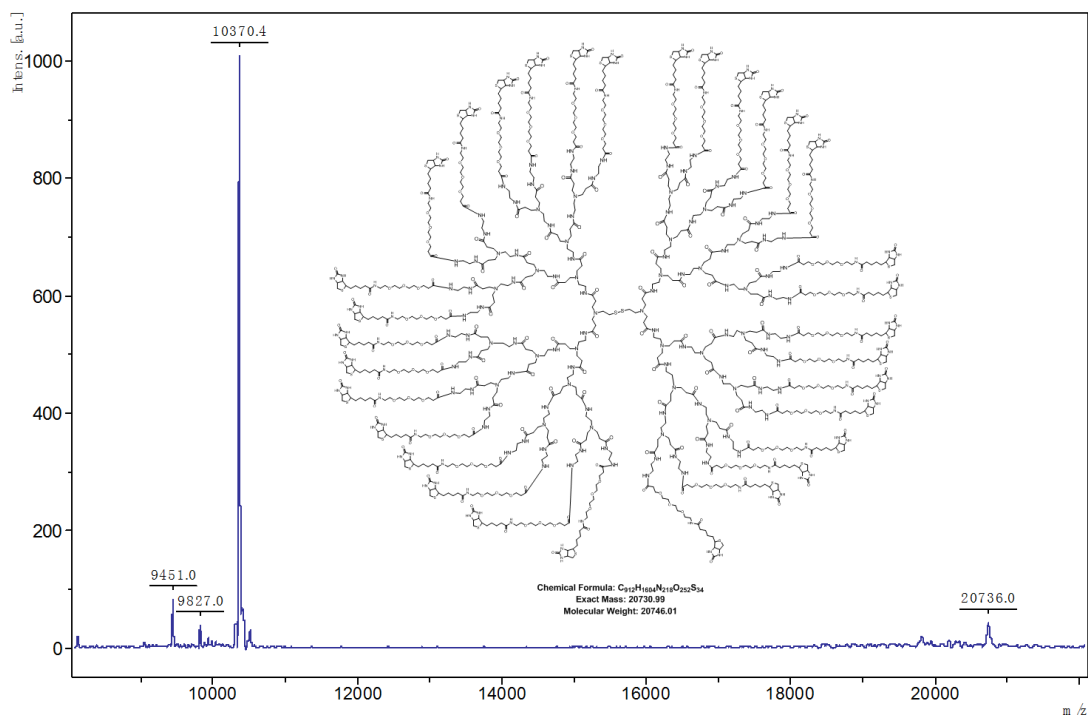
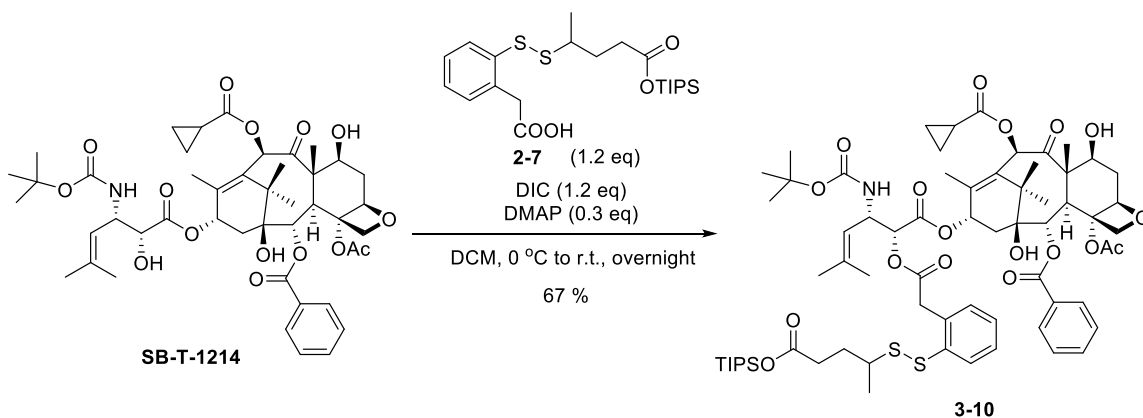


Figure 3.26 MALDI-TOF spectrum of biotin PEGylated G3 PAMAM dendrimer

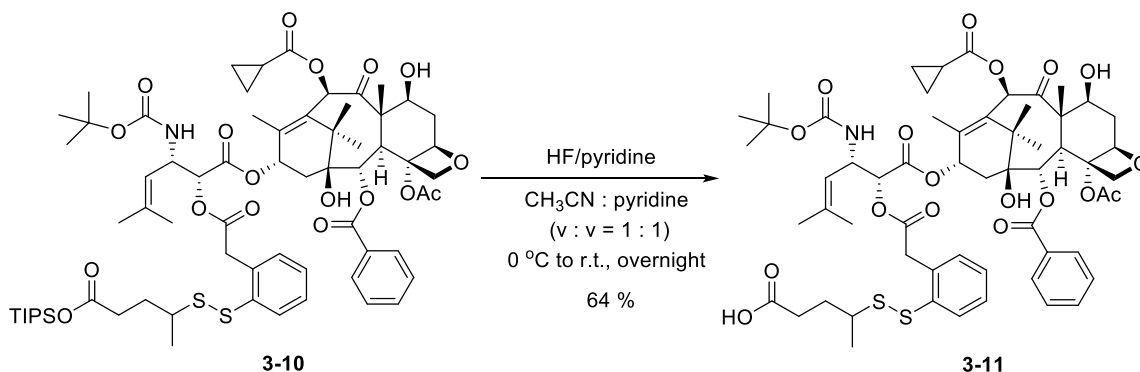
§ 3.2.3 Synthesis of SB-T-1214-Linker-PEG-Azide and FITC-PEG-Azide Click Ready Probes

In order to synthesize SB-T-1214-linker-PEG-azide click ready probe for constructing the PAMAM dendrimer-based biotin-taxoid conjugate, first, SB-T-1214-linker conjugate **3-10** was synthesized by DMAP catalyzed DIC coupling of SB-T-1214 and methyl-branched disulfide linker **2-7** (**Scheme 3.10**). The C-2' hydroxyl is the most reactive site of the taxoid and cold temperature was maintained during the reaction to avoid multiple couplings. Desired conjugate **3-10** was obtained in 67% yield after purification by column chromatography.



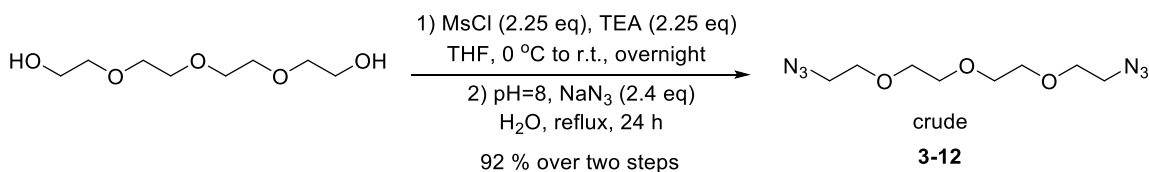
Scheme 3.10 Synthesis of SB-T-1214-linker conjugate **3-10**

Then, TIPS protecting group on the linker moiety was removed by HF/pyridine to give **3-11** in 64% yield (**Scheme 3.11**).



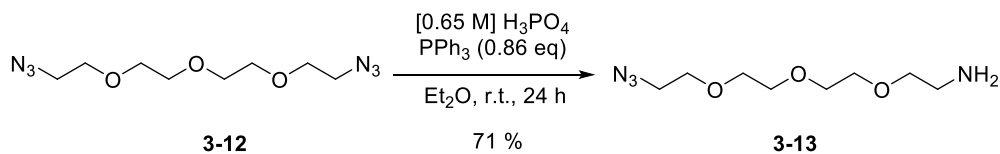
Scheme 3.11 Removal of the TIPS protecting group in **3-10**

In order to prepare the amino-PEG-azide to coupling with the acid group in **3-11**, diazide **3-12** was prepared by reacting tetraethyleneglycol with excess MsCl, followed by reacting with excess sodium azide under basic condition to afford diazide **3-12** in 92% crude yield over two steps (**Scheme 3.12**).



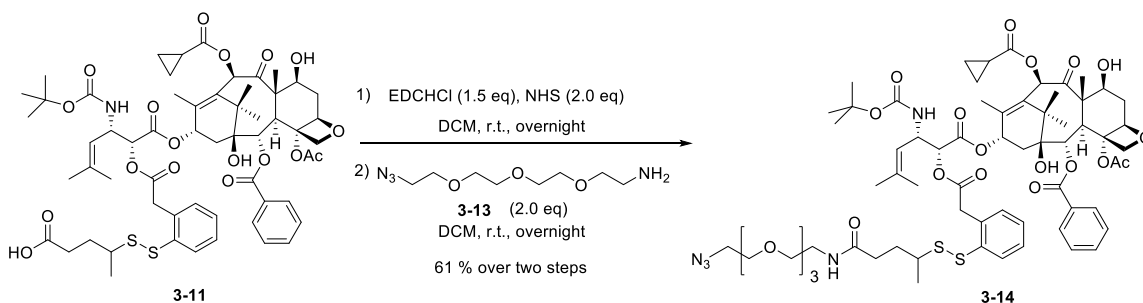
Scheme 3.12 Synthesis of diazide **3-12**

Subsequent selective mono Staudinger reduction of the azide group in **3-12** by triphenylphosphine in the presence of phosphoric acid in a mixture of water/ethyl ether as solvent gave rise to amino-PEG-azide **3-13** in 71% yield (**Scheme 3.13**). The mono reduction was achieved because once product is formed, it goes to water layer in the acid condition to avoid over-reduction of the other azide group. Excess diazide **3-12** could be easily removed by a simple workup.



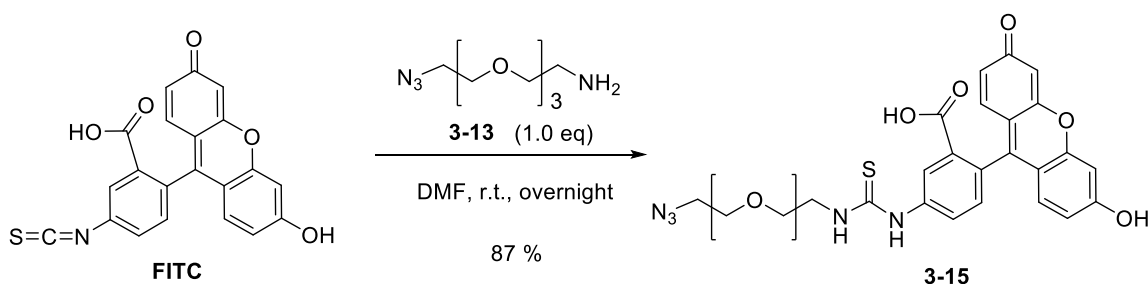
Scheme 3.13 Mono-reduction of diazide **3-12**

Then, the carboxylic acid group in **3-11** was activated with NHS by EDC coupling, followed by reacting with amino-PEG-azide **3-13** to afford SB-T-1214-linker-PEG-azide click ready probe **3-14** in 61% yield over two steps (**Scheme 3.14**).



Scheme 3.14 Synthesis of SB-T-1214-linker-PEG-azide click ready probe **3-14**

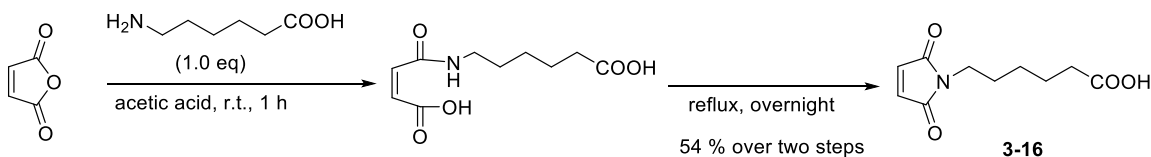
For synthesis of FITC-PEG-azide click ready probe, commercially available FITC was reacted with amino-PEG-azide **3-13** in DMF to give the desire product **3-15** in 87% yield (**Scheme 3.15**). The reaction was done in dark, and the product was kept in freezer to avoid isomerization of the product.



Scheme 3.15 Synthesis of FITC-PEG-azide click ready probe **3-15**

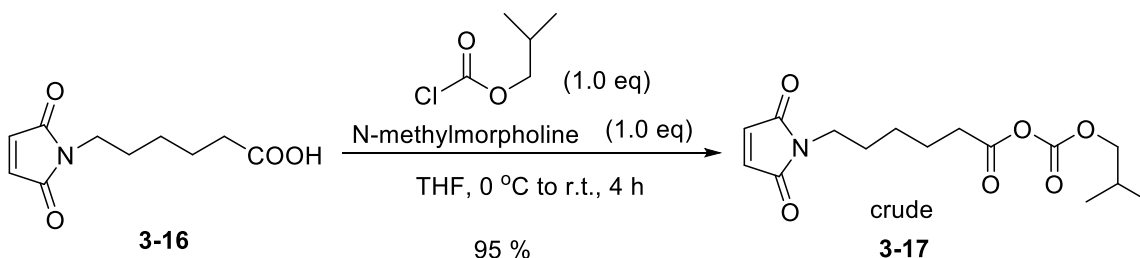
§ 3.2.4 Construct of Final Dendrimer Conjugates

In order to connect the biotin-PEGylated G1/G3 PAMAM dendrimers with click ready SB-T-1214-linker-azide or FITC-PEG-azide probes, a bifunctional maleimido-alkyne spacer was prepared. First, maleic anhydride was reacted with 6-aminocaproic acid in acetic acid under reflux condition to give 6-maleimidocaproic acid **3-16** in 54% yield (**Scheme 3.16**).



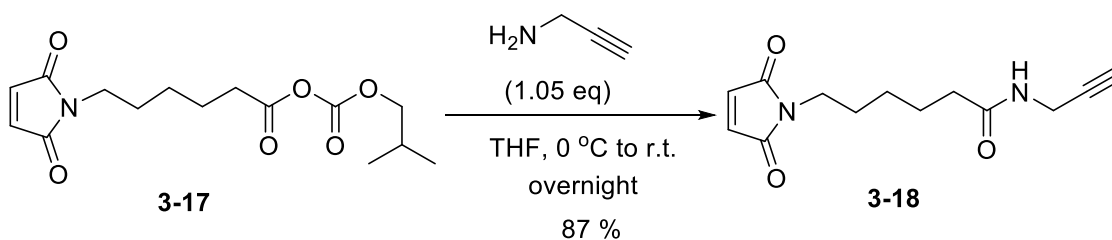
Scheme 3.16 Synthesis of 6-maleimidocaproic acid **3-16**

6-maleimidocaproic acid **3-16** was subsequently activated by isobutyl chloroformate in the presence of N-methylmorpholine to give mixed anhydride **3-17** in 95% crude yield (**Scheme 17**). This product is unstable, and was directly used in the next step after workup without further purification, as column purification would decompose the product back to starting material.



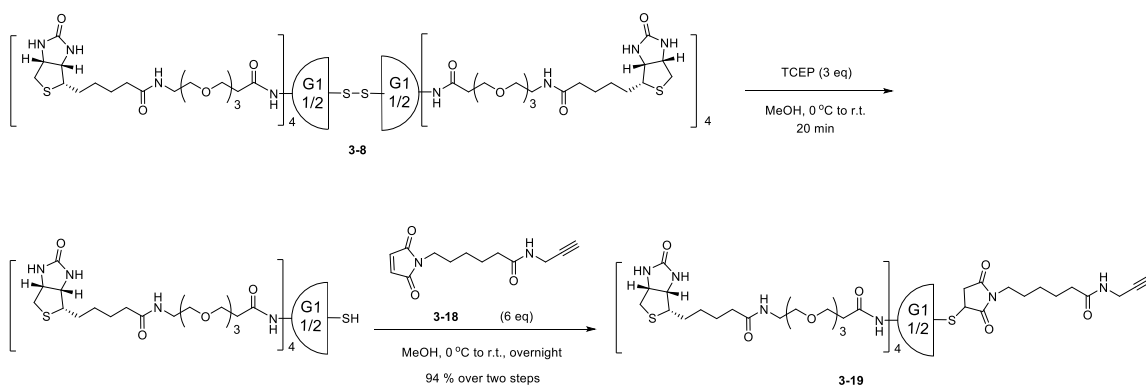
Scheme 3.16 Synthesis of mixed anhydride **3-17**

Mixed anhydride **3-17** was then treated with propargylamine to give desired maleimido-alkyne spacer **3-18** in 87% yield (**Scheme 3.18**).



Scheme 3.18 Synthesis of maleimido-alkyne spacer **3-18**

Then, the disulfide bond inside the biotin PEGylated G1 PAMAM dendrimer was cleaved by reducing agent TCEP, and subsequently connected to a bifunctional maleimido-alkyne spacer to afford biotin PEGylated G1 alkyne conjugate **3-19** in 94% yield after dialysis (**Scheme 3.19**). The product was further purified by prep-HPLC. The purified product was characterized by MALDI-TOF, ESI-MS, LC-MS, and NMR. Biotin PEGylated G1 alkyne conjugate **3-19** (chemical formula: C₁₂₁H₂₀₇N₂₇O₃₃S₅) has exact mass 2726.40, molecular weight 2728.44, and *m/z* 2726.40 (76.4%) and 2727.40 (100%). In the MALDI-TOF analysis using DHB as the matrix, mass signals of 2728.7 ([M+H]⁺, calculated 2727.4, Δ = 1.3 Da), and 2750.7 ([M+Na]⁺, calculated 2749.4, Δ = 1.3 Da) were observed (**Figure 3.27**). In the ESI-MS spectrum (**Figure 3.28**), multiple charge states (+2, +3, and +4) of the product were observed. In the LC-MS analysis (**Figure 3.29** to **Figure 3.33**), it was found that desired mass of product was observed, and the purity of the product was 99%. Interestingly, the 1% impurity has a mass of only 16 unit larger than the desired mass, and presumably this is the product when the sulfonyl group of one biotin was oxidized during the synthesis.



Scheme 3.19 Synthesis of biotin PEGylated G1 alkyne conjugate **3-19**

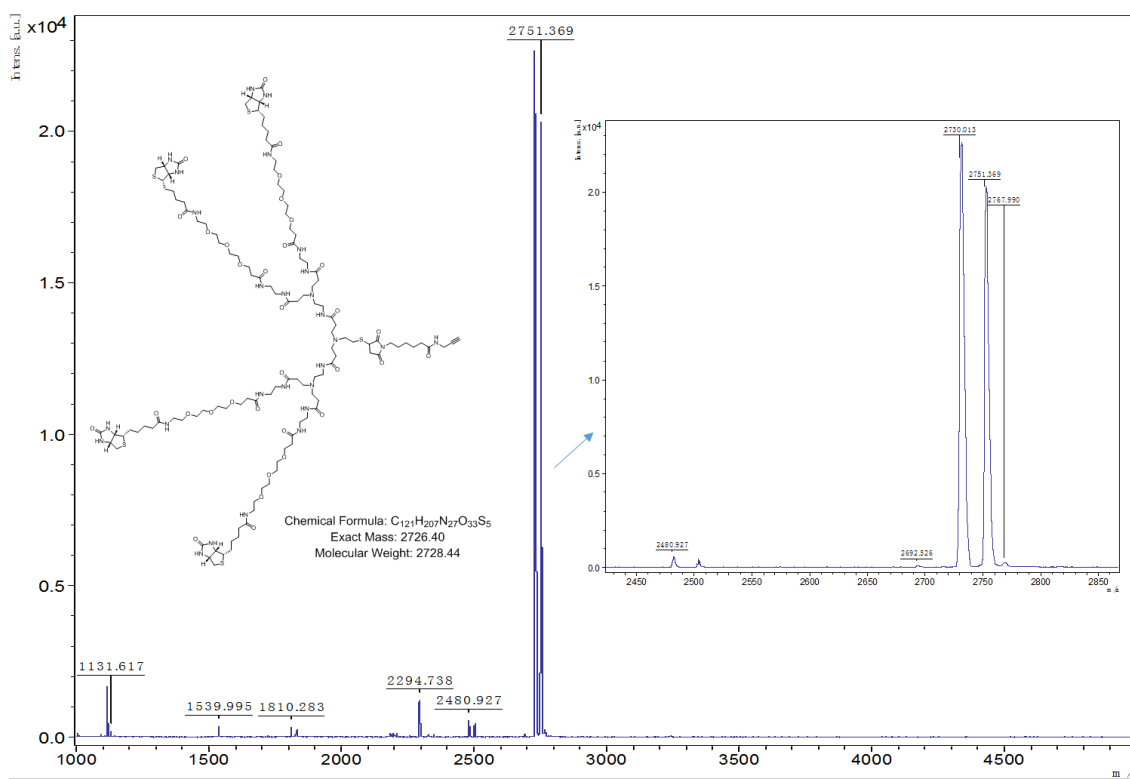


Figure 3.27 MALDI-TOF spectrum of biotin PEGylated G1 alkyne conjugate **3-19**

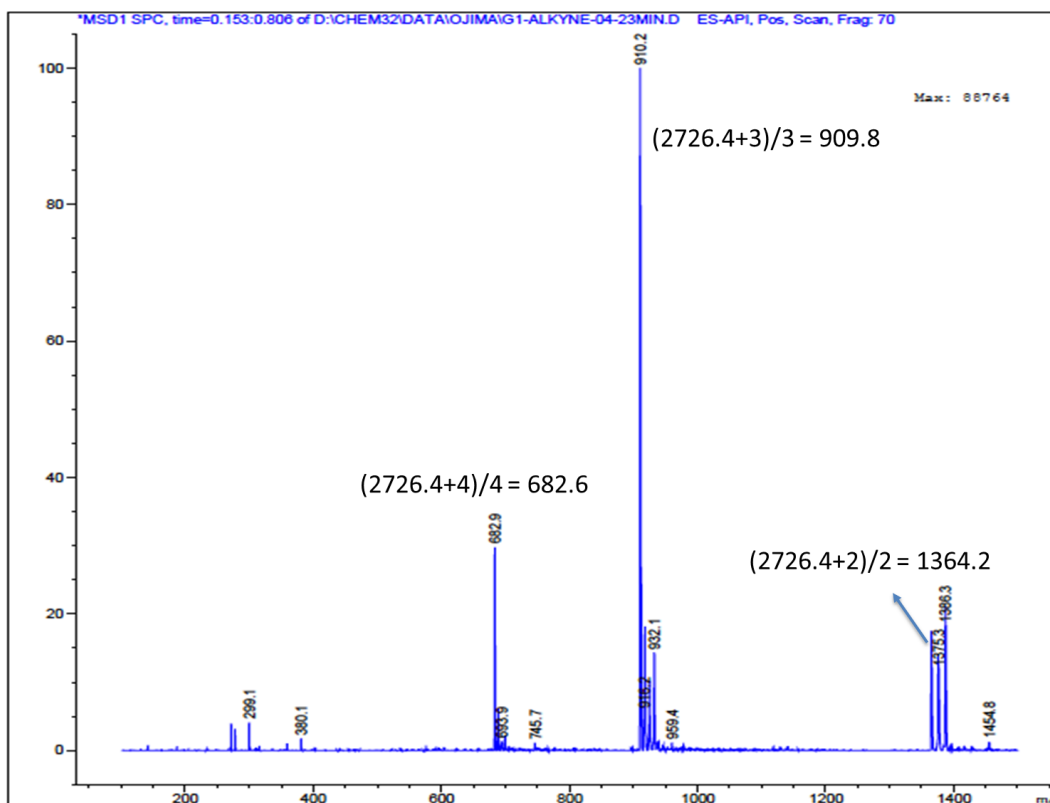
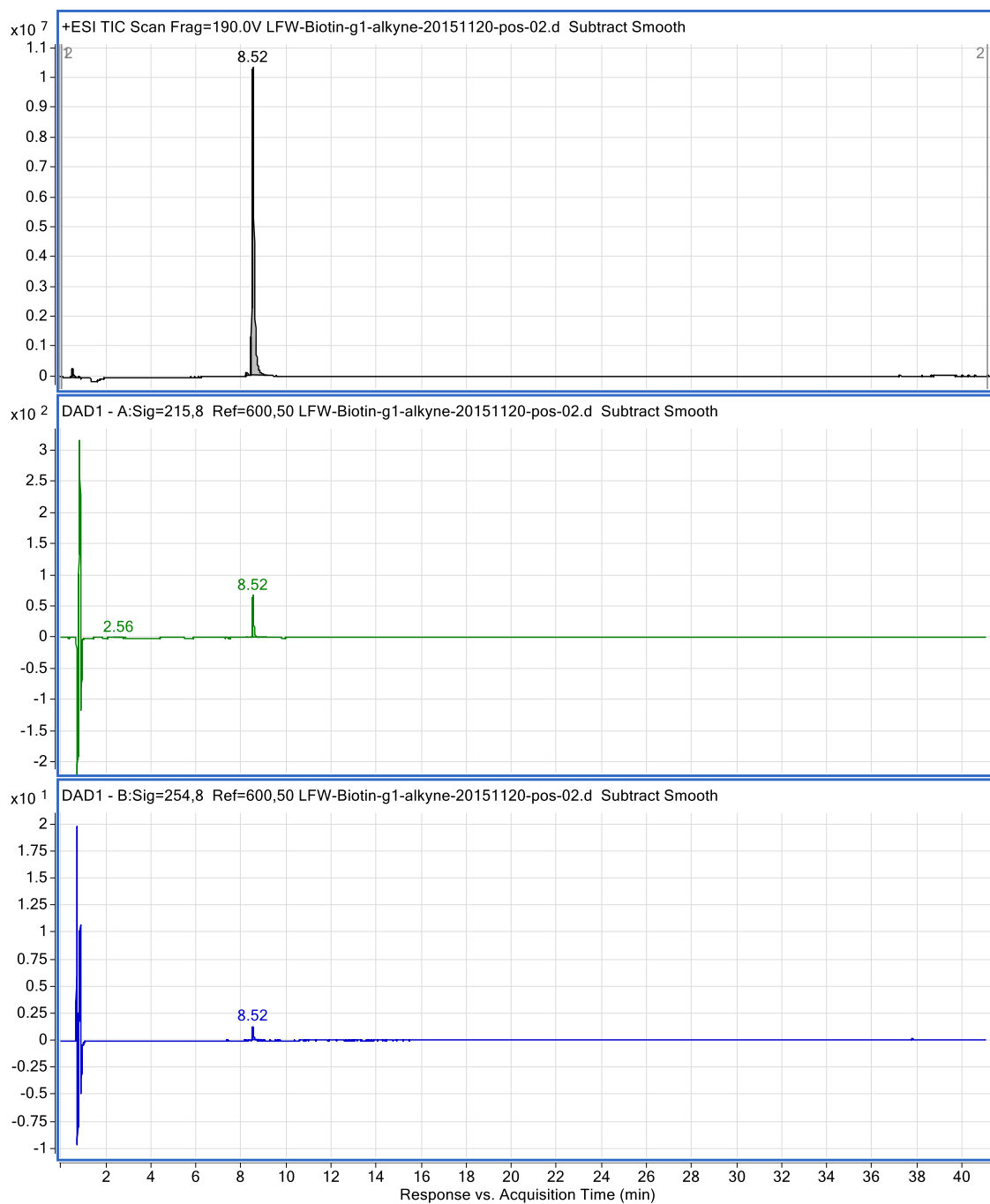
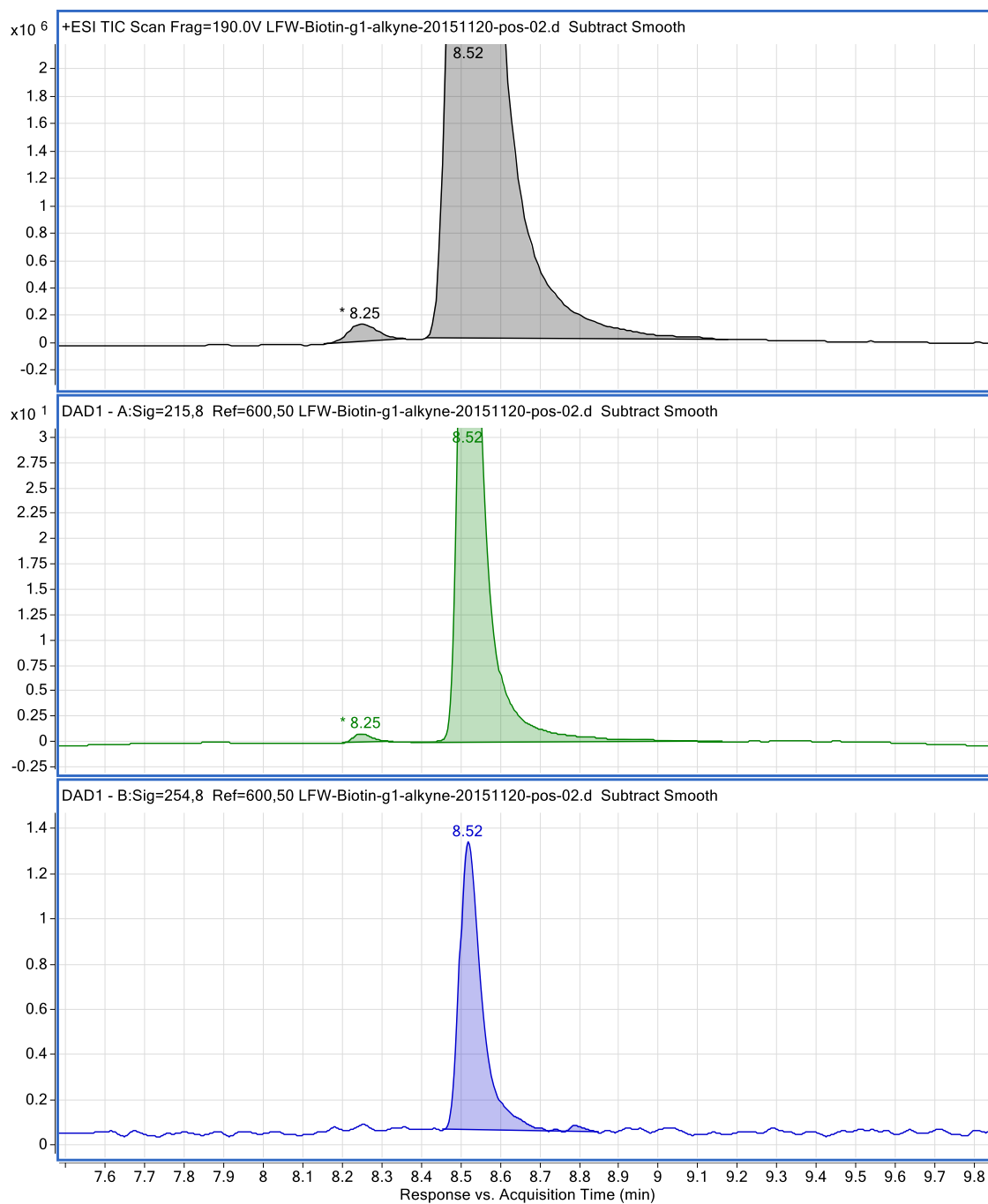


Figure 3.28 ESI-MS spectrum of biotin PEGylated G1 alkyne conjugate **3-19**



ESI⁺, TIC (m/z=100-3200) chromatogram for Biotin-PEG-G1-Alkyne
 DAD1-A, UV=215nm chromatogram for Biotin- PEG-G1-Alkyne
 DAD1-B, UV=254nm chromatogram for Biotin- PEG-G1-Alkyne
Figure 3.29 LC-MS spectrum of biotin PEGylated G1 alkyne conjugate **3-19**

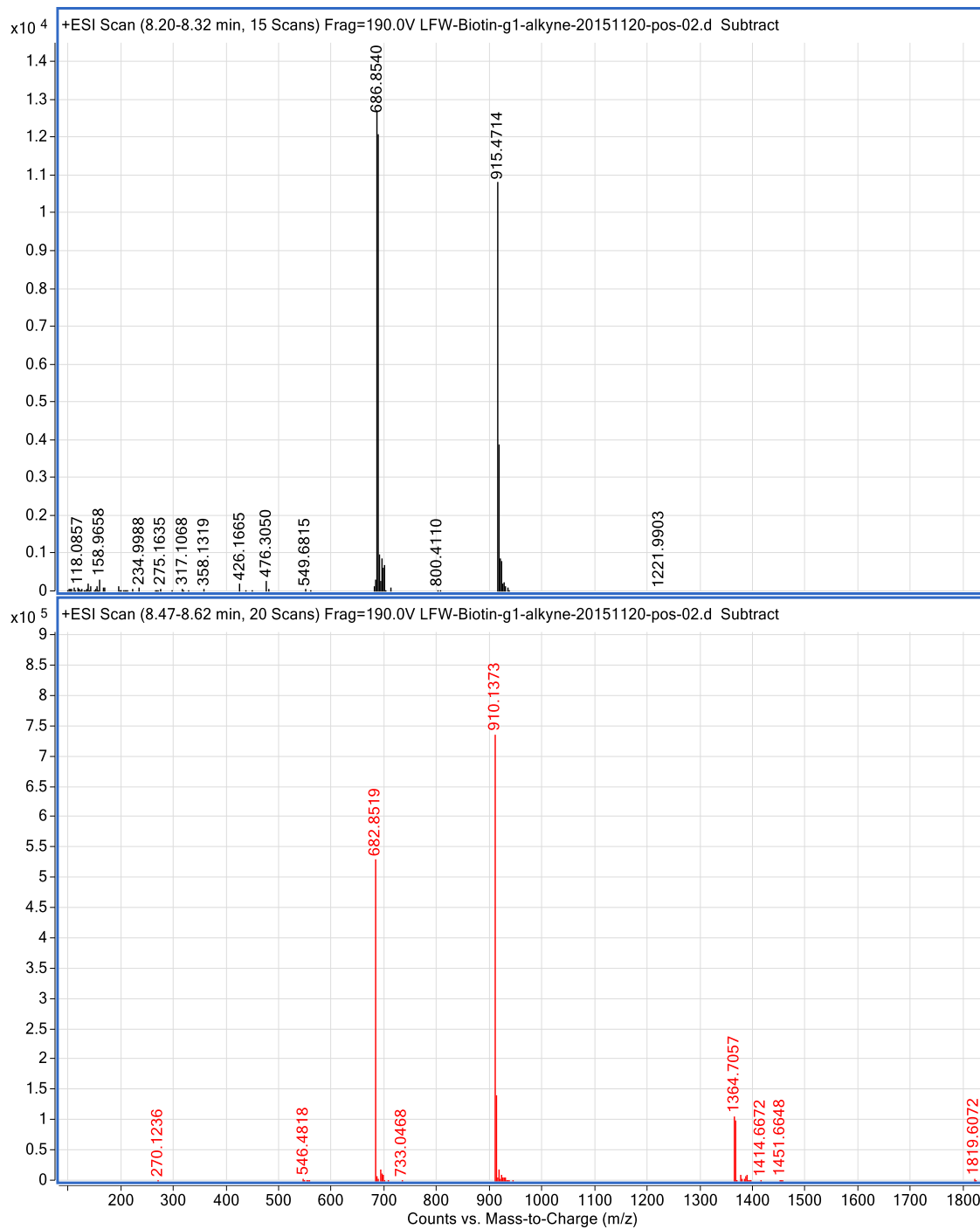


ESI⁺, TIC (m/z=100-3200) chromatogram for Biotin-PEG-G1-Alkyne

DAD1-A, UV=215nm chromatogram for Biotin- PEG-G1-Alkyne

DAD1-B, UV=254nm chromatogram for Biotin- PEG-G1-Alkyne

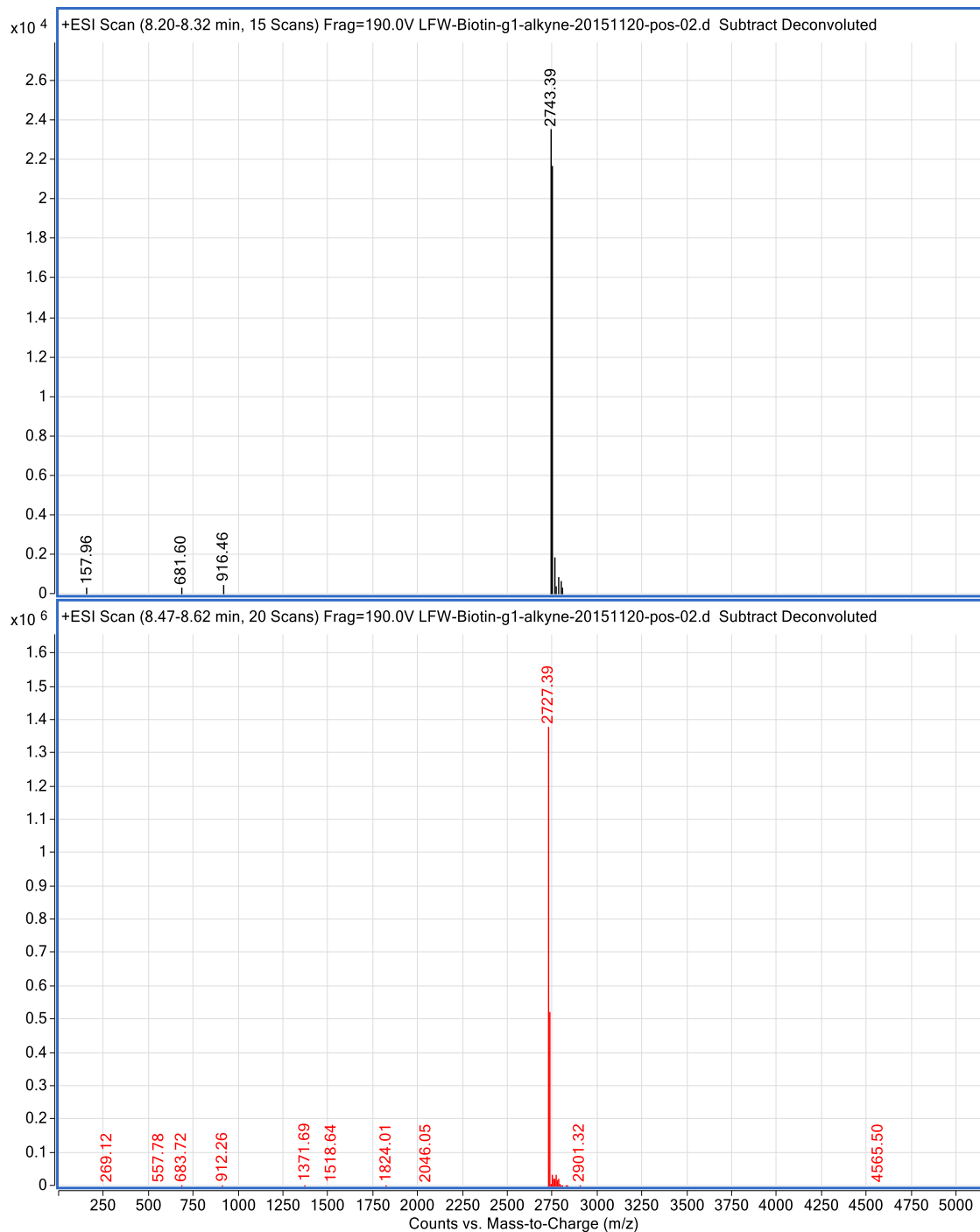
Figure 3.30 Expanded LC-MS spectrum of biotin PEGylated G1 alkyne conjugate **3-19**



Extracted Mass Spectra from TIC, Rt = 8.25'

Extracted Mass Spectra from TIC, Rt = 8.52'

Figure 3.31 Extracted mass spectra from TIC in LC-MS analysis of biotin PEGylated G1 alkyne conjugate **3-19**



Deconvolution of Extracted Mass Spectra from TIC, Rt = 8.25'

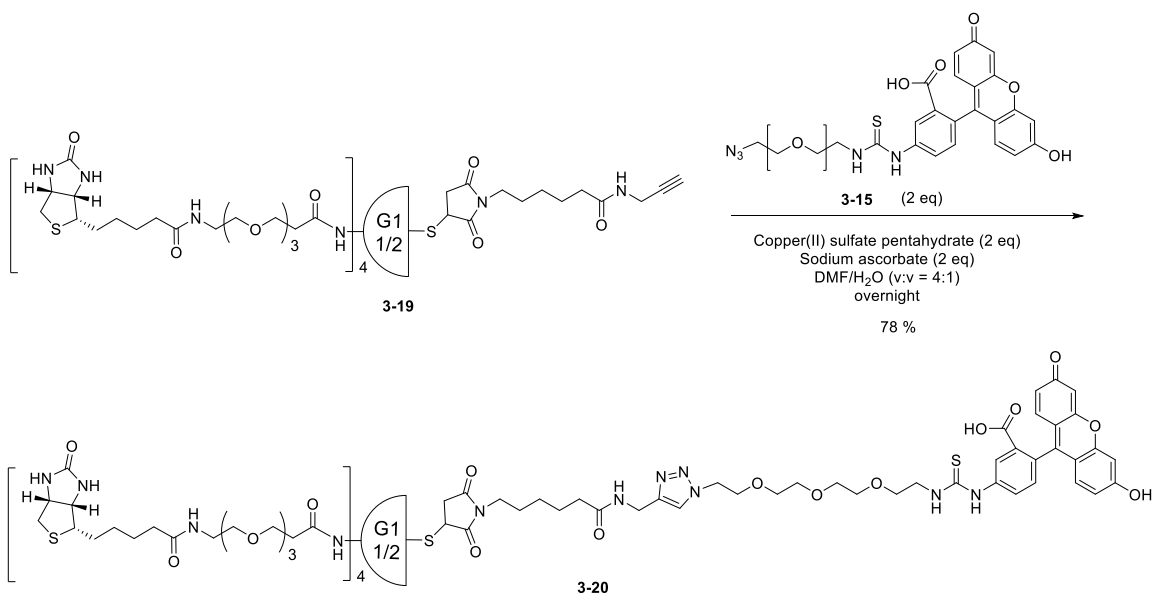
Deconvolution of Extracted Mass Spectra from TIC, Rt = 8.52'

Figure 3.32 Deconvolution of Extracted mass spectra from TIC in LC-MS analysis of biotin PEGylated G1 alkyne conjugate **3-19**

Species				Biotin-PEG-G1-Alkyne			
MW expected	MW observed	Δ mass (ppm)	RT	TIC Area	TIC Area %	UV-215 Area	UV-215 Area %
2742.3902	2742.388	-0.8	8.25	684910	1.0%	3.1	1.1%
2726.3953	2726.385	-3.7	8.52	68790537	99.0%	279.6	98.9%
				69475447		282.7	

Figure 3.33 Integration of peak area from TIC and UV-215 in LC-MS analysis of biotin PEGylated G1 alkyne conjugate **3-19**

Then, biotin PEGylated G1 alkyne **3-19** was reacted with FITC-PEG3-azide **3-15** via copper(I)-catalyzed alkyne-azide cycloaddition (CuAAC) to give biotin-G1-FITC conjugate **3-20** in 78% yield (**Scheme 3.20**). The product was purified by prep-HPLC, and was characterized by MALDI-TOF, ESI-MS, LC-MS, and NMR. Biotin-G1-FITC conjugate **3-20** (chemical formula: C₁₅₀H₂₃₆N₃₂O₄₁S₆) has exact mass 3333.57, molecular weight 3336.08, and *m/z* 3334.57 (100%) and 3335.58 (80.6%). In the MALDI-TOF analysis using DHB as the matrix, mass signals of 3336.0 ([M+H]⁺, calculated 3334.6, Δ = 1.4 Da), 3359.5 ([M+Na]⁺, calculated 3356.6, Δ = 2.9 Da), and 3373.9 ([M+K]⁺, calculated 3372.6, Δ = 1.3 Da) were observed (**Figure 3.34**). Because high laser energy was used in the MALDI-TOF experiment in order to get a decent signal intensity of the product, a number of fragmentation peaks were also observed in the MALDI-TOF spectrum. In the ESI-MS spectrum of the crude product before purification (**Figure 3.35**), multiple charge states (+3, +4, and +5) of the product were observed. In the LC-MS analysis after prep-HPLC purification (**Figure 3.36** to **Figure 3.39**), it was found that desired mass of product was observed, and the product has high purity (retention time 9.77 min) with trace amounts of impurities (retention time 9.55 and 10.46 min).



Scheme 3.20 Synthesis of biotin-G1-FITC conjugate via CuAAC

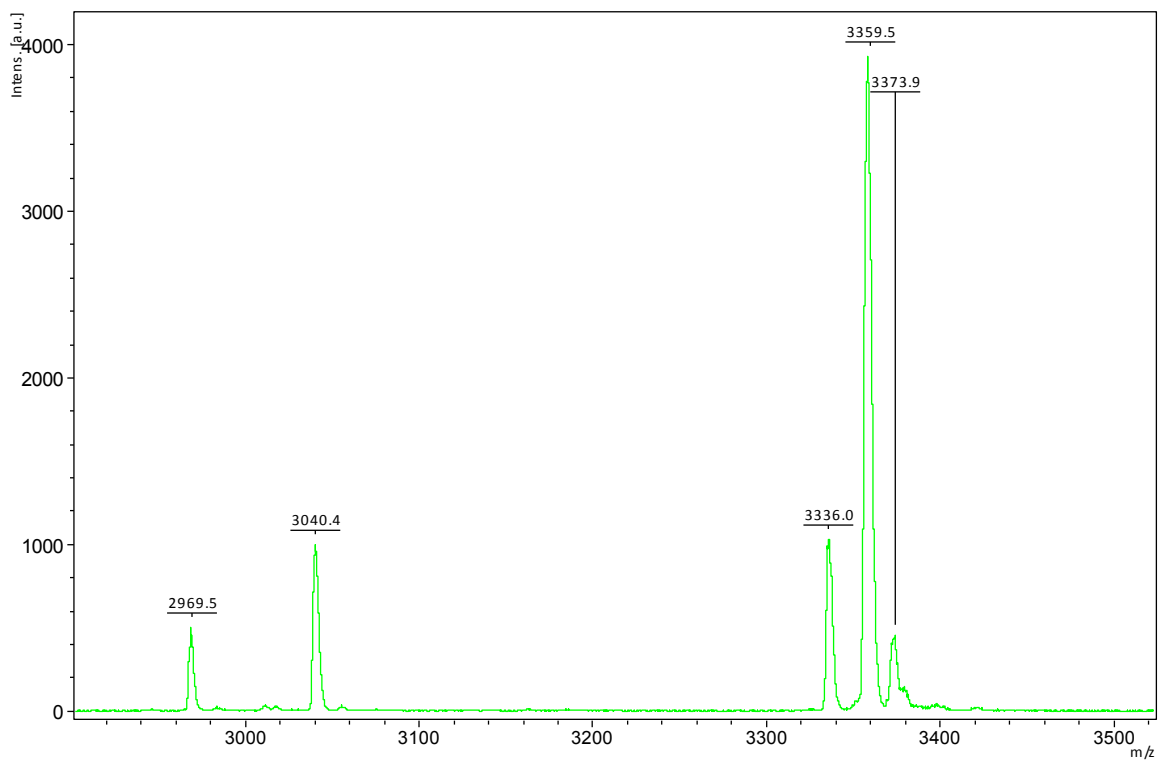


Figure 3.34 MALDI-TOF spectrum of biotin-G1-FITC conjugate **3-20**

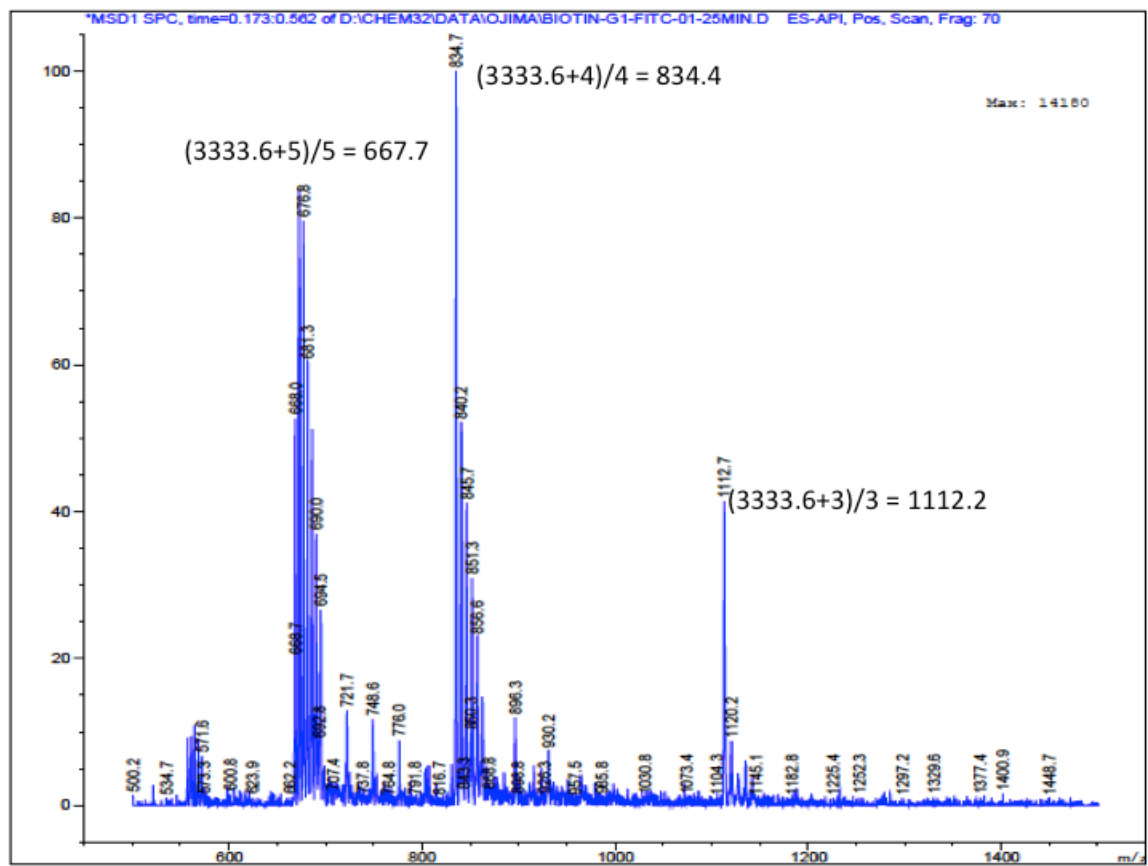
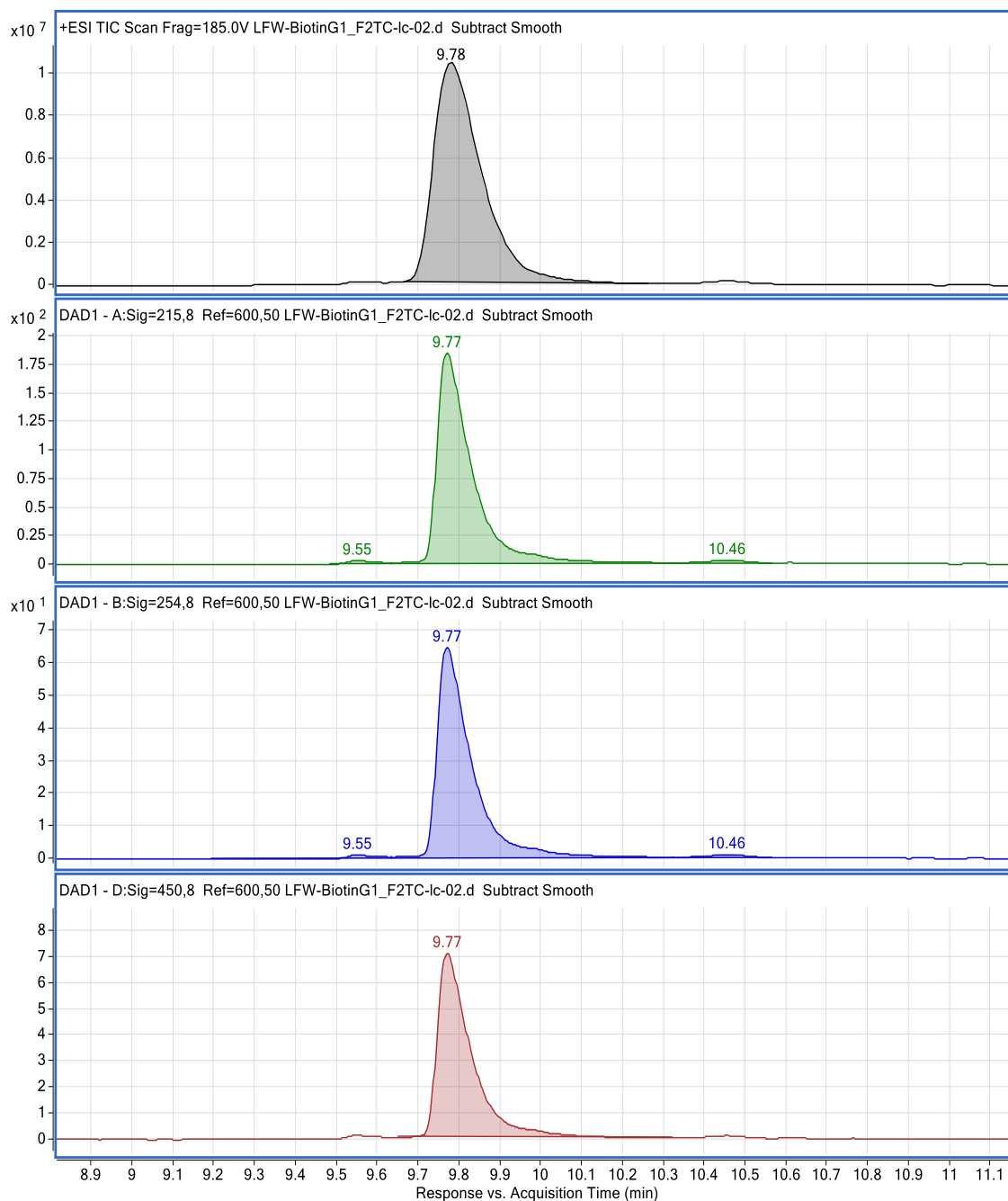


Figure 3.35 ESI-MS spectrum of biotin-G1-FITC conjugate 3-20



ESI⁺, TIC (m/z=100-3200) chromatogram for Biotin-G1-FITC
 DAD1-A, UV=215nm chromatogram for Biotin-G1-FITC
 DAD1-B, UV=254nm chromatogram for Biotin-G1-FITC
 DAD1-D, UV=450nm chromatogram for Biotin-G1-FITC
Figure 3.36 LC-MS spectrum of biotin-G1-FITC conjugate **3-20**



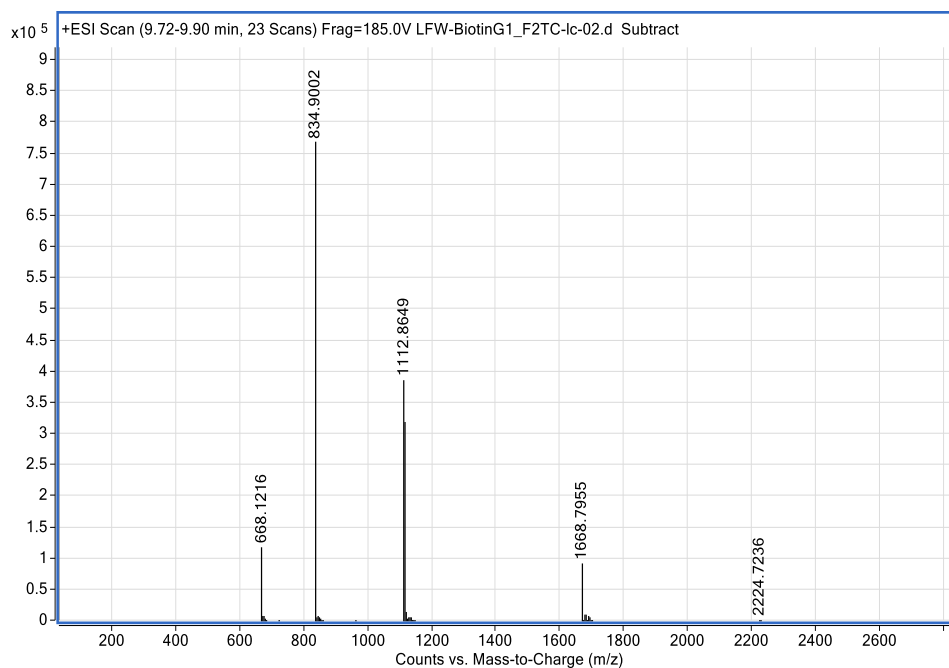
ESI⁺, TIC (m/z=100-3200) chromatogram for Biotin-G1-FITC

DAD1-A, UV=215nm chromatogram for Biotin-G1-FITC

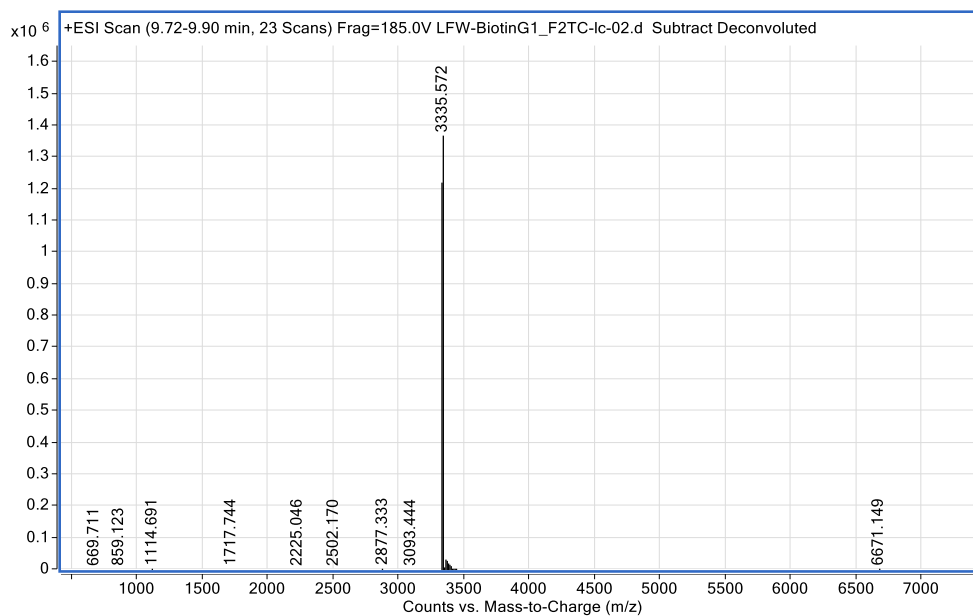
DAD1-B, UV=254nm chromatogram for Biotin-G1-FITC

DAD1-D, UV=450nm chromatogram for Biotin-G1-FITC

Figure 3.37 Expanded LC-MS spectrum of biotin-G1-FITC conjugate **3-20**

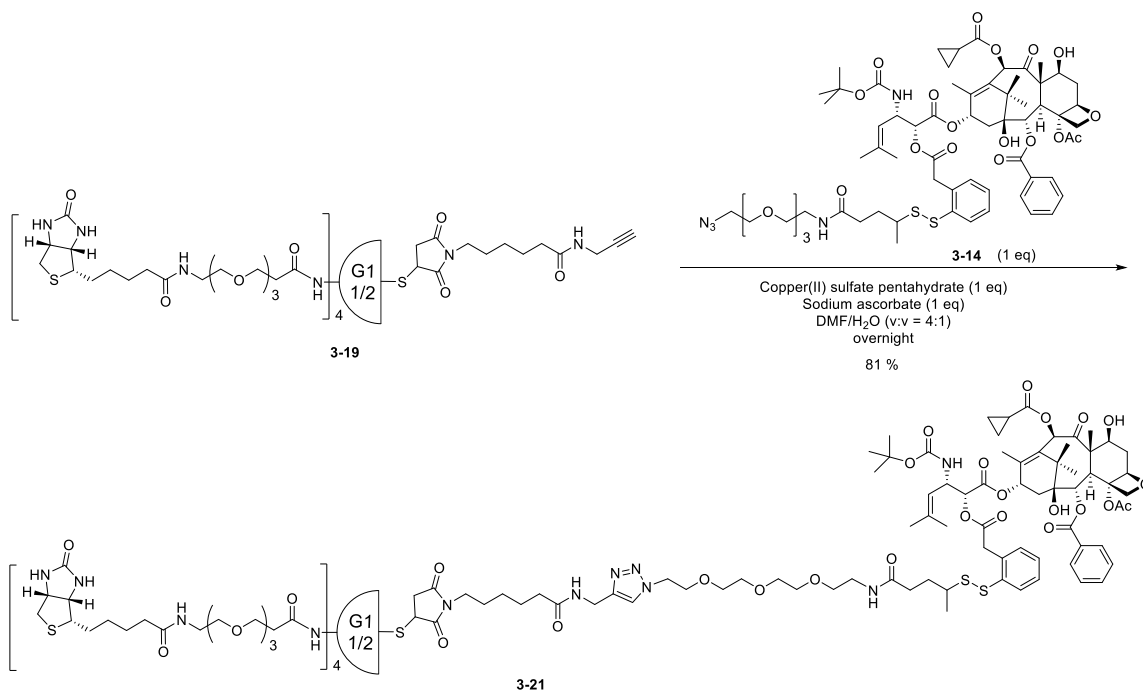


Extracted Mass Spectra from TIC, Rt = 9.78'
Figure 3.38 Extracted mass spectra from TIC in LC-MS analysis of biotin-G1-FITC conjugate **3-20**



Deconvolution of Extracted Mass Spectra from TIC, Rt = 9.78'
Figure 3.39 Deconvolution of extracted mass spectra from TIC in LC-MS analysis of biotin-G1-FITC conjugate **3-20**

Similarly, biotin PEGylated G1 alkyne **3-19** was reacted with SB-T-1214-linker-PEG-azide **3-14** via CuAAC to give biotin-G1-SB-T-1214 conjugate **3-21** in 81% yield (**Scheme 3.21**). The product was purified by prep-HPLC, and was characterized by MALDI-TOF, ESI-MS, LC-MS, and NMR. Biotin-G1-SB-T-1214 conjugate **3-21** (chemical formula: C₁₈₇H₂₉₆N₃₂O₅₃S₇) has exact mass 4061.95, molecular weight 4065.02, and *m/z* 4062.95 (99.4%) and 4063.96 (100%). In the MALDI-TOF analysis using DHB as the matrix, mass signals of 4065.9 ([M+H]⁺, calculated 4063.0, Δ = 2.9 Da), and 4087.8 ([M+Na]⁺, calculated 4085.0, Δ = 2.8 Da) were observed (**Figure 3.40**). Because high laser energy was used in the MALDI-TOF experiment in order to get a decent signal intensity of the product, a number of fragmentation peaks were also observed in the MALDI-TOF spectrum. In the ESI-MS spectrum (**Figure 3.41**), multiple charge states (+3, +4, and +5) of the product were observed. In the LC-MS analysis (**Figure 3.42** to **Figure 3.46**), it was found that desired mass of product was observed, and the purity of the product was around 95%. The 5% impurity again has a mass of only 16 unit larger than the desired mass, and presumably this is the product when the sulfonyl group of one biotin was oxidized during the synthesis.



Scheme 3.21 Synthesis of biotin-G1-SB-T-1214 conjugate **3-21** via CuAAC

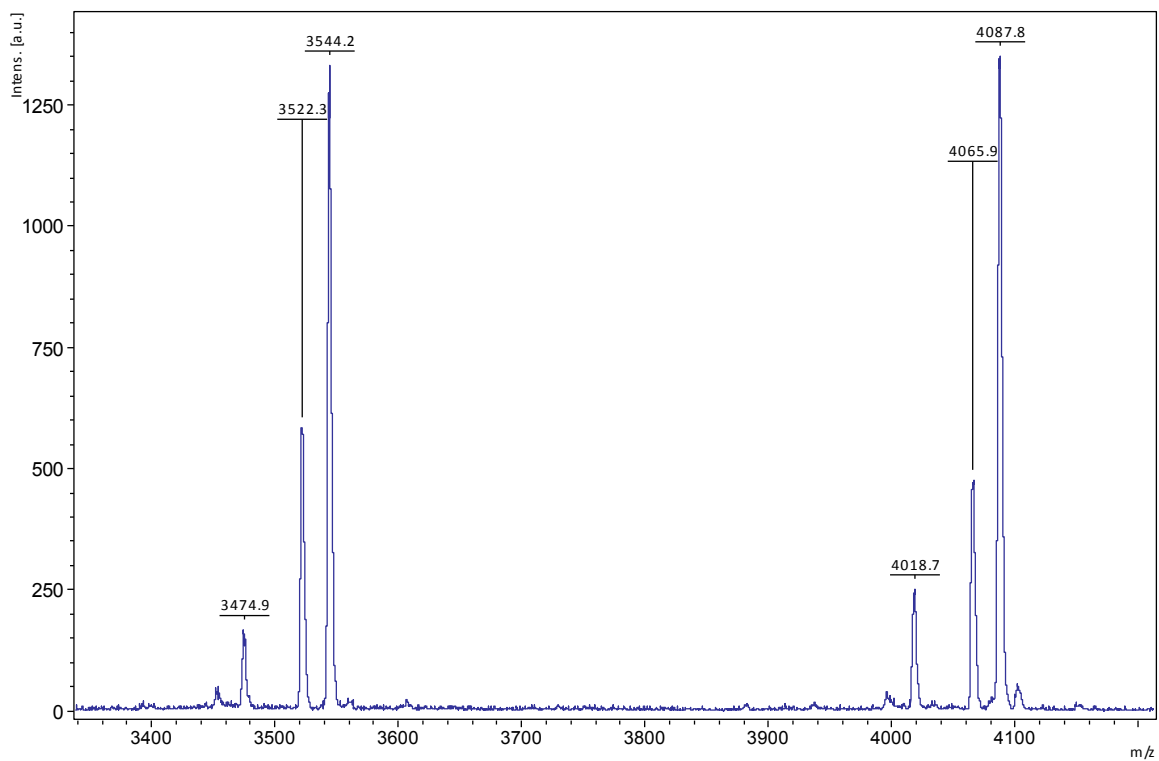


Figure 3.40 MALDI-TOF spectrum of biotin-G1-SB-T-1214 conjugate 3-21

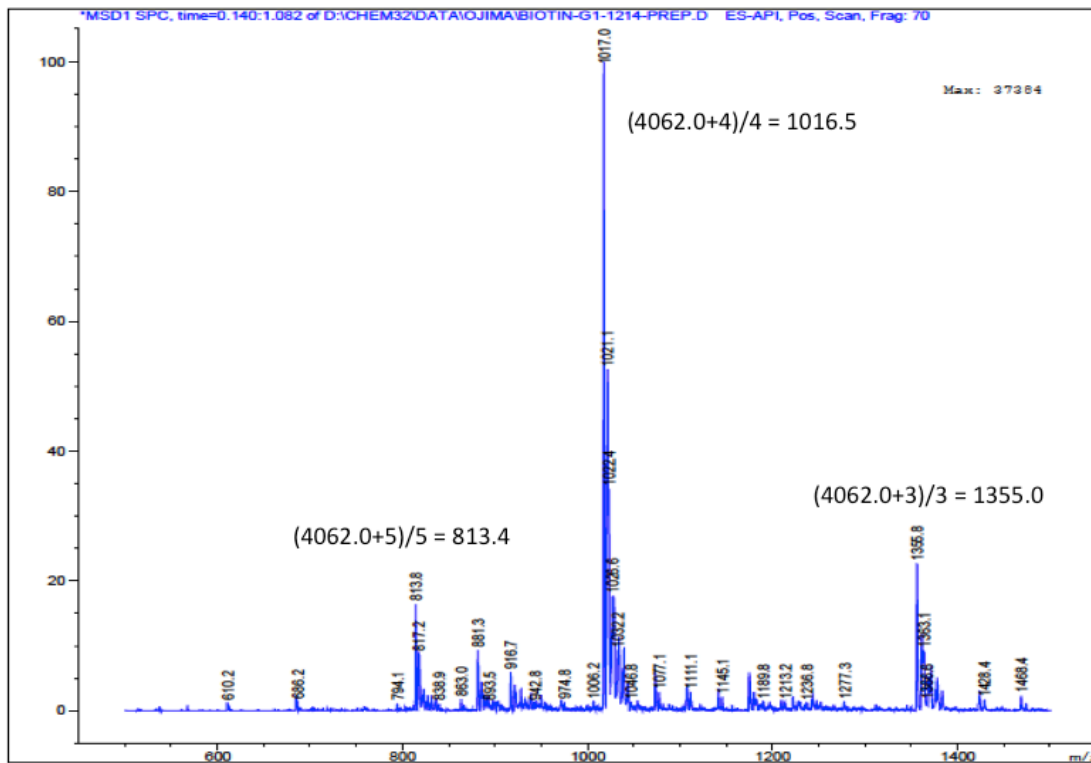
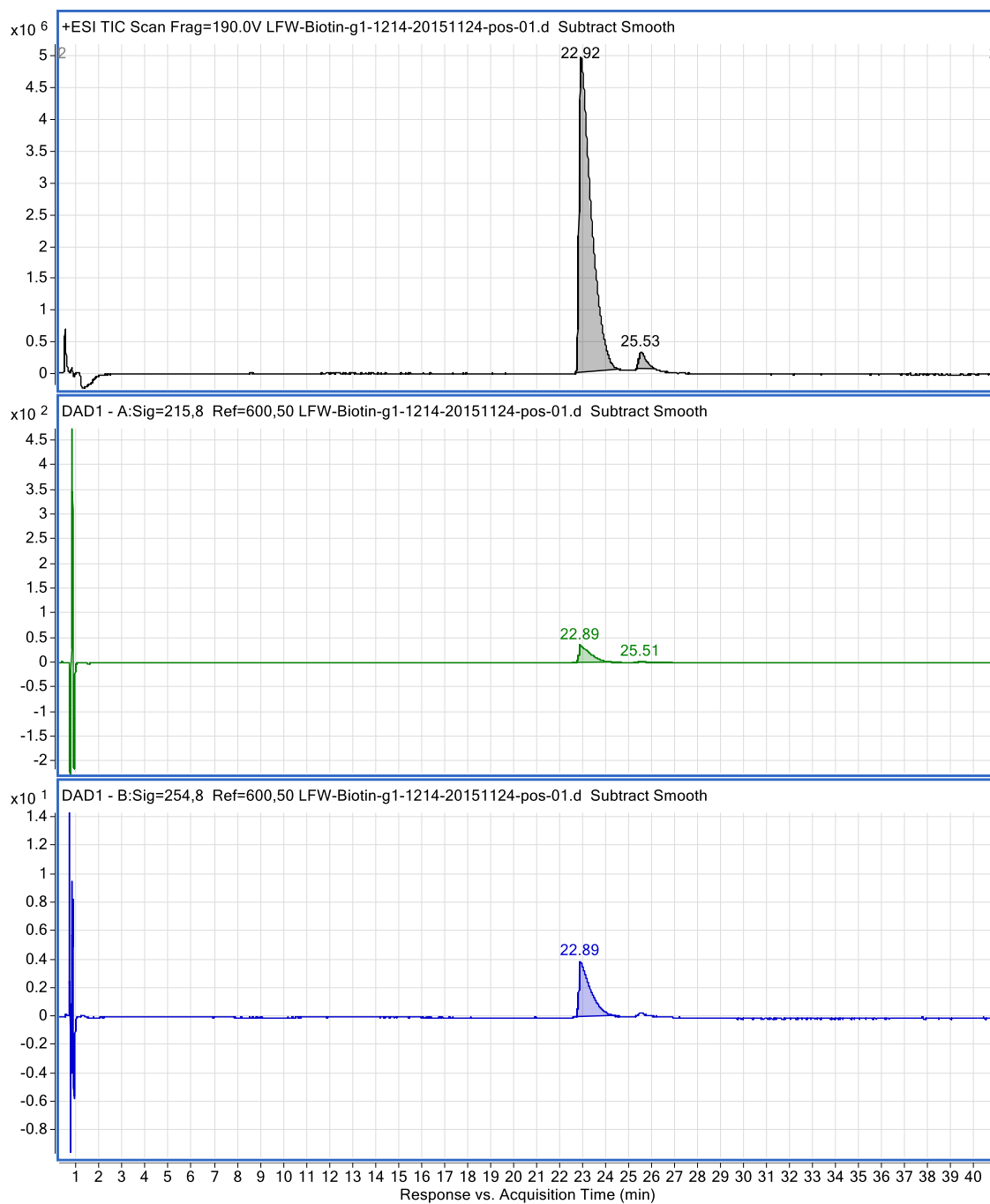
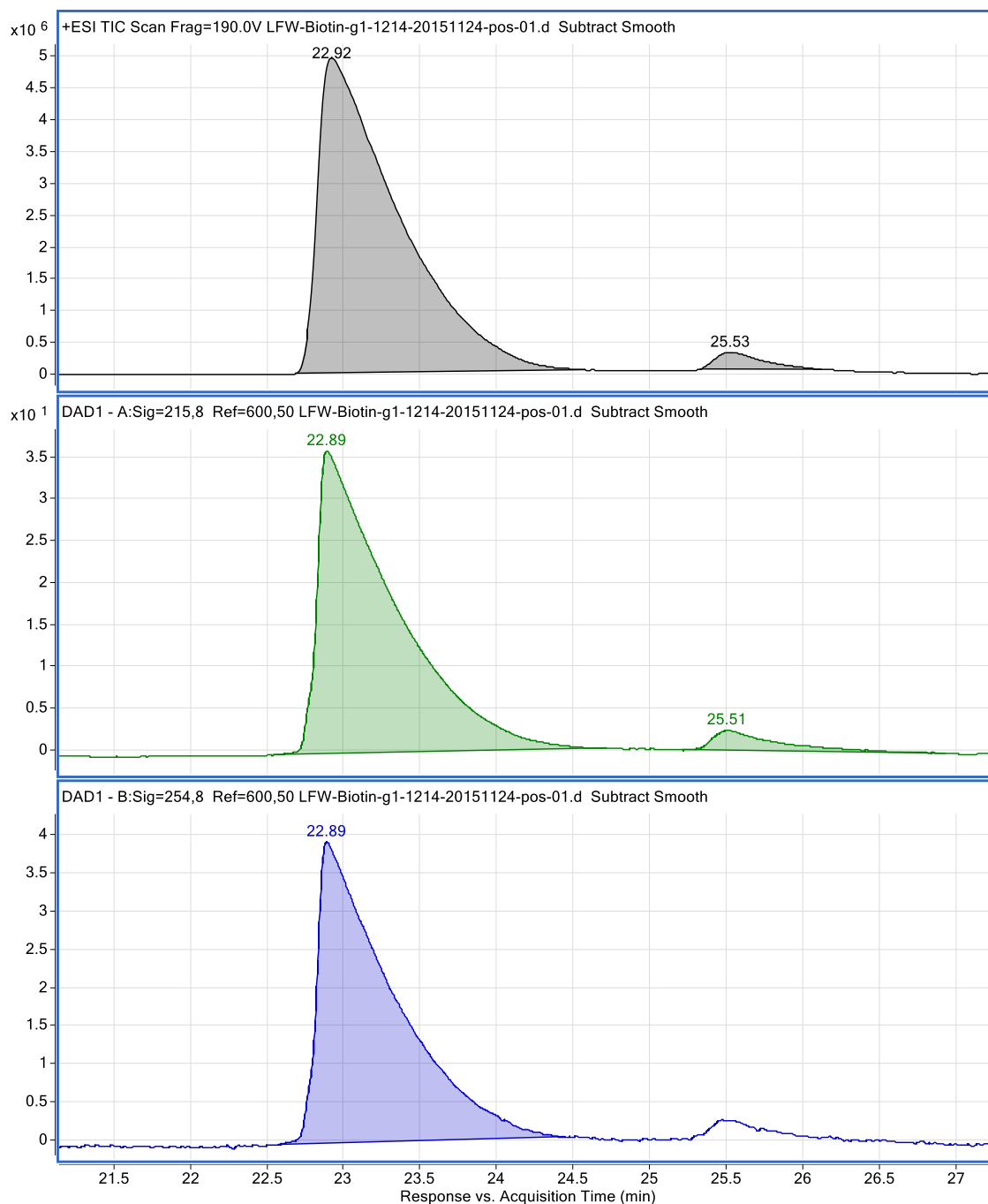


Figure 3.41 ESI-MS spectrum of biotin-G1-SB-T-1214 conjugate 3-21



ESI⁺, TIC (m/z=100-3200) chromatogram for Biotin-G1-SB-T-1214
 DAD1-A, UV=215nm chromatogram for Biotin-PEG-G1-SB-T-1214
 DAD1-B, UV=254nm chromatogram for Biotin-G1-SB-T-1214
Figure 3.42 LC-MS spectrum of biotin-G1-SB-T-1214 conjugate **3-21**

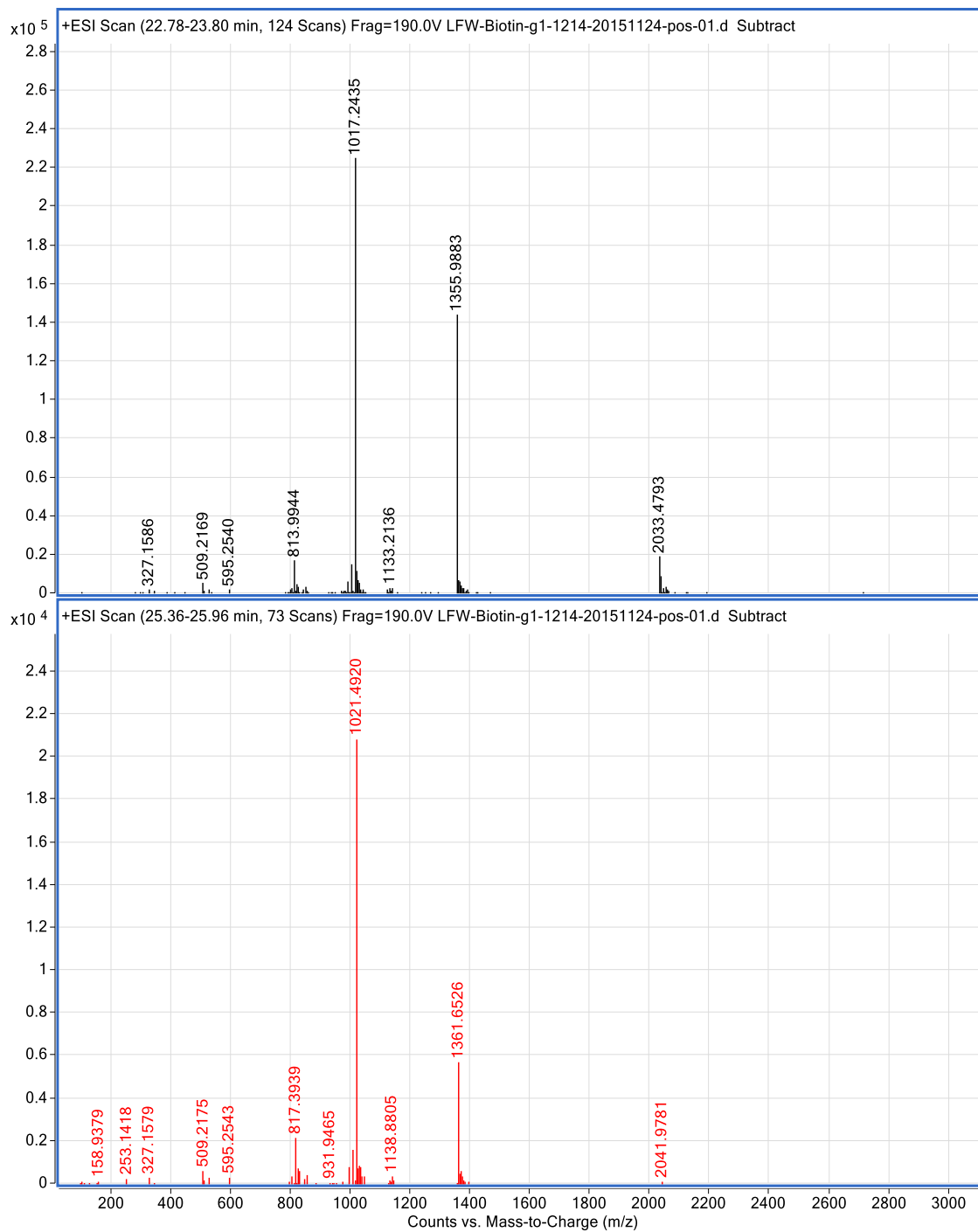


ESI⁺, TIC (m/z=100-3200) chromatogram for Biotin-G1-SB-T-1214

DAD1-A, UV=215nm chromatogram for Biotin- PEG-G1-SB-T-1214

DAD1-B, UV=254nm chromatogram for Biotin-G1-SB-T-1214

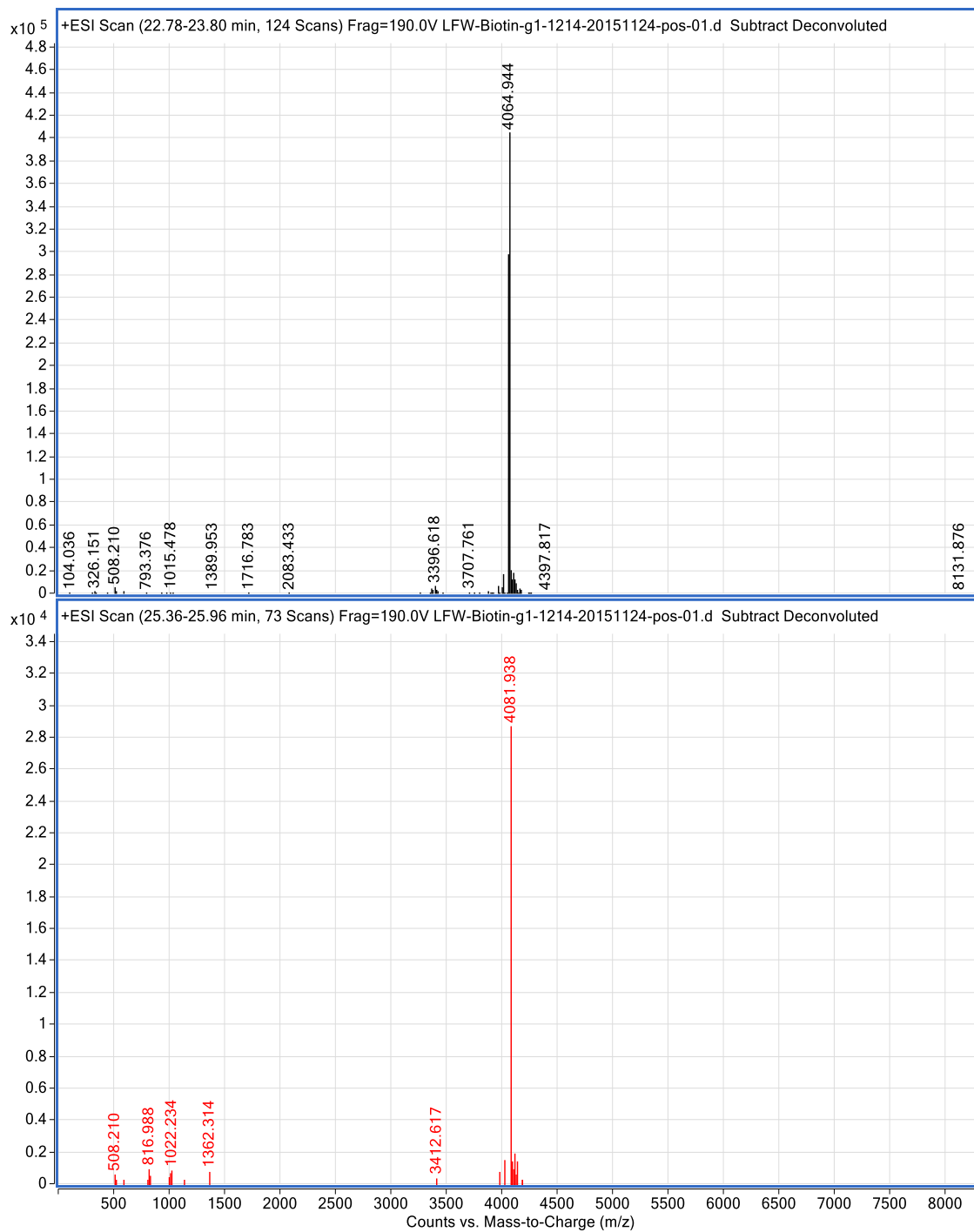
Figure 3.43 Expanded LC-MS spectrum of biotin-G1-SB-T-1214 conjugate **3-21**



Extracted Mass Spectra from TIC, Rt = 22.92'

Extracted Mass Spectra from TIC, Rt = 25.53'

Figure 3.44 Extracted mass spectra from TIC in LC-MS analysis of biotin-G1-SB-T-1214 conjugate **3-21**



Deconvolution of Extracted Mass Spectra from TIC, Rt = 22.92'

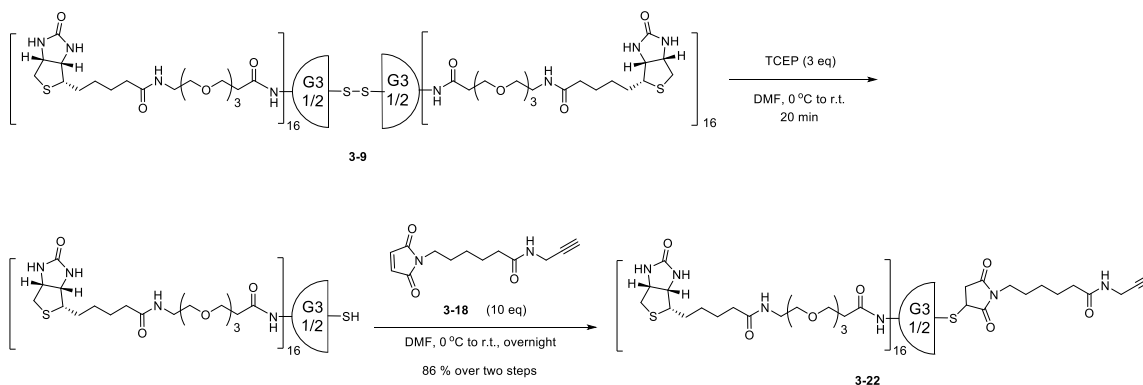
Deconvolution of Extracted Mass Spectra from TIC, Rt = 25.53'

Figure 3.45 Deconvolution of extracted mass spectra from TIC in LC-MS analysis of biotin-G1-SB-T-1214 conjugate **3-21**

Species		Biotin-PEG-G1-SBT-1214					
MW expected	MW observed	Δ mass (ppm)	RT	TIC Area	TIC Area %	UV-215 Area	UV-215 Area %
4061.9495	4062.938	243.4	22.90	180892825	96.9%	1275.8	94.4%
	4078.928		22.52	5794382	3.1%	76.2	5.6%
				186687207		1352.0	

Figure 3.46 Integration of peak area from TIC and UV-215 in LC-MS analysis of biotin-G1-SB-T-1214 conjugate **3-21**

For the synthesis of G3 PAMAM dendrimer conjugates, first, the disulfide bond inside the biotin PEGylated G3 PAMAM dendrimer **3-9** was cleaved by reducing agent TCEP and connected to the bifunctional maleimido-alkyne spacer to afford biotin PEGylated G3 alkyne conjugate **3-22** in 86% yield after dialysis (**Scheme 3.22**). The product was characterized MALDI-TOF and ESI-MS. Biotin PEGylated G3 alkyne conjugate **3-22** (chemical formula: $C_{469}H_{819}N_{111}O_{129}S_{17}$) has exact mass 10614.62, molecular weight 10622.38, and m/z 10619.64 (100%). In the MALDI-TOF analysis using DHB as the matrix, mass signals of 10621.5 ($[M+H]^+$, calculated 10620.6 from most abundant isotope, $\Delta = 0.9$ Da), and 10643.4 ($[M+Na]^+$, calculated 10642.6 from most abundant isotope, $\Delta = 0.8$ Da) were observed (**Figure 3.47**). Because high laser energy was used in the MALDI-TOF experiment in order to get a decent signal intensity of the product, a number of fragmentation peaks were also observed in the MALDI-TOF spectrum. In the ESI-MS spectrum (**Figure 3.48**), multiple charge states (+8, +9, and +10) of the product were observed.



Scheme 3.22 Synthesis of biotin PEGylated G3 alkyne conjugate **3-22**

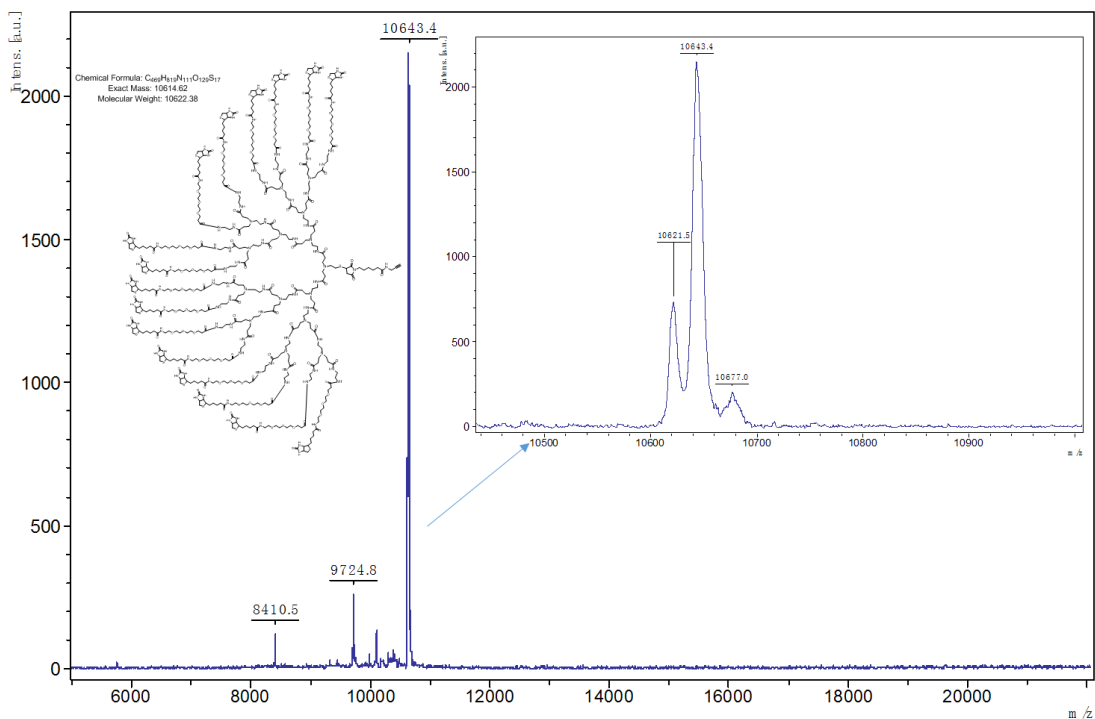


Figure 3.47 MALDI-TOF spectrum of biotin PEGylated G3 alkyne conjugate 3-22

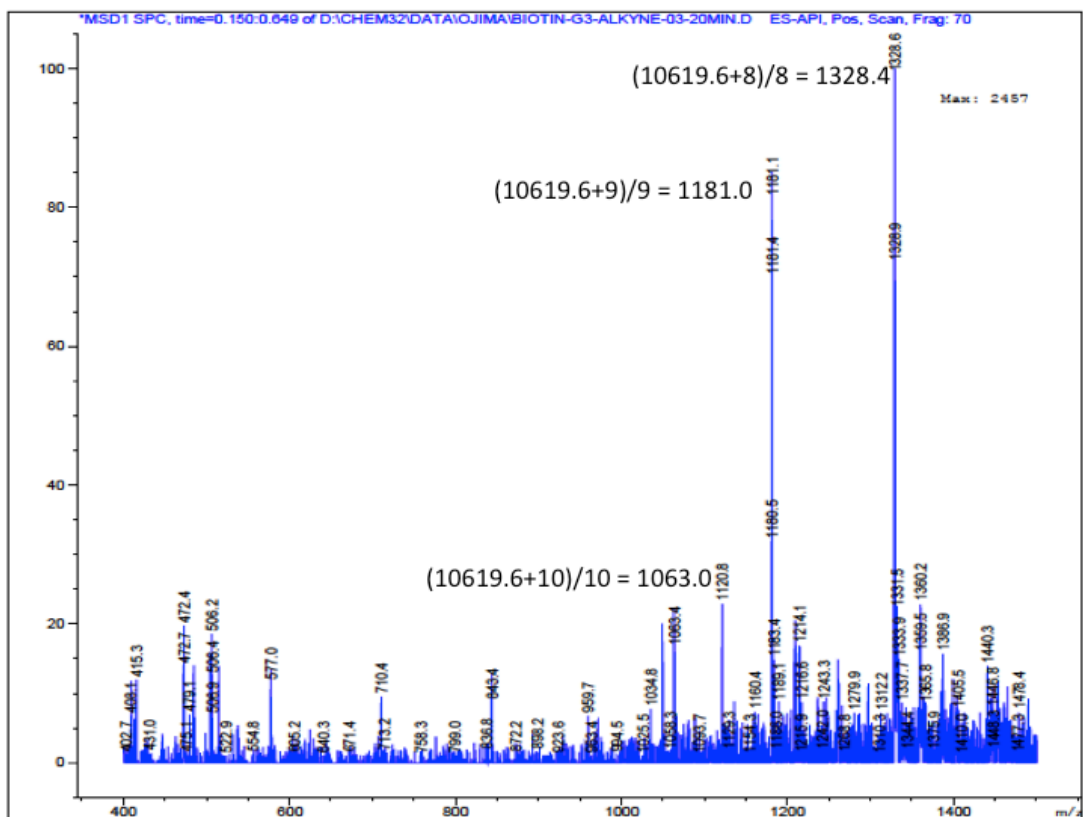
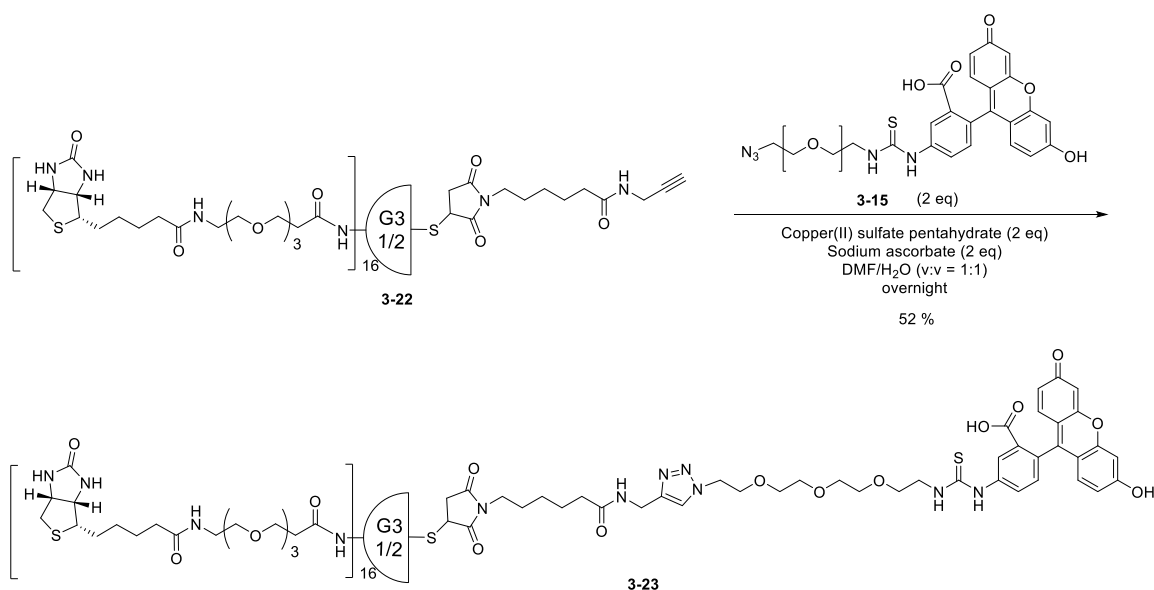


Figure 3.48 ESI-MS spectrum of biotin PEGylated G3 alkyne conjugate 3-22

Then, biotin PEGylated G3 alkyne **3-22** was reacted with FITC-PEG-azide via CuAAC to give biotin-G3-FITC conjugate **3-23** in 52% yield (**Scheme 3.23**). The product was purified by prep-HPLC, and was characterized by MALDI-TOF, ESI-MS, HR-MS, and NMR (**Figure 3.49** to **Figure 3.51**). Biotin-G3-FITC conjugate **3-23** (chemical formula: $C_{498}H_{848}N_{116}O_{137}S_{18}$) has exact mass 11221.79, molecular weight 11230.62, and m/z 11226.81 (100%). In the MALDI-TOF analysis using DHB as the matrix, mass signal of 11242.0 ($[M+Na]^+$, calculated 11244.8, $\Delta = -2.8$ Da) was observed (**Figure 3.49**). Because high laser energy was used in the MALDI-TOF experiment in order to get a decent signal intensity of the product, a number of fragmentation peaks were also observed in the MALDI-TOF spectrum. In the ESI-MS spectrum (**Figure 3.50**), multiple charge states (+8, and +9) of the product were observed.



Scheme 3.23 Synthesis of biotin-G3-FITC conjugate **3-23** via CuAAC

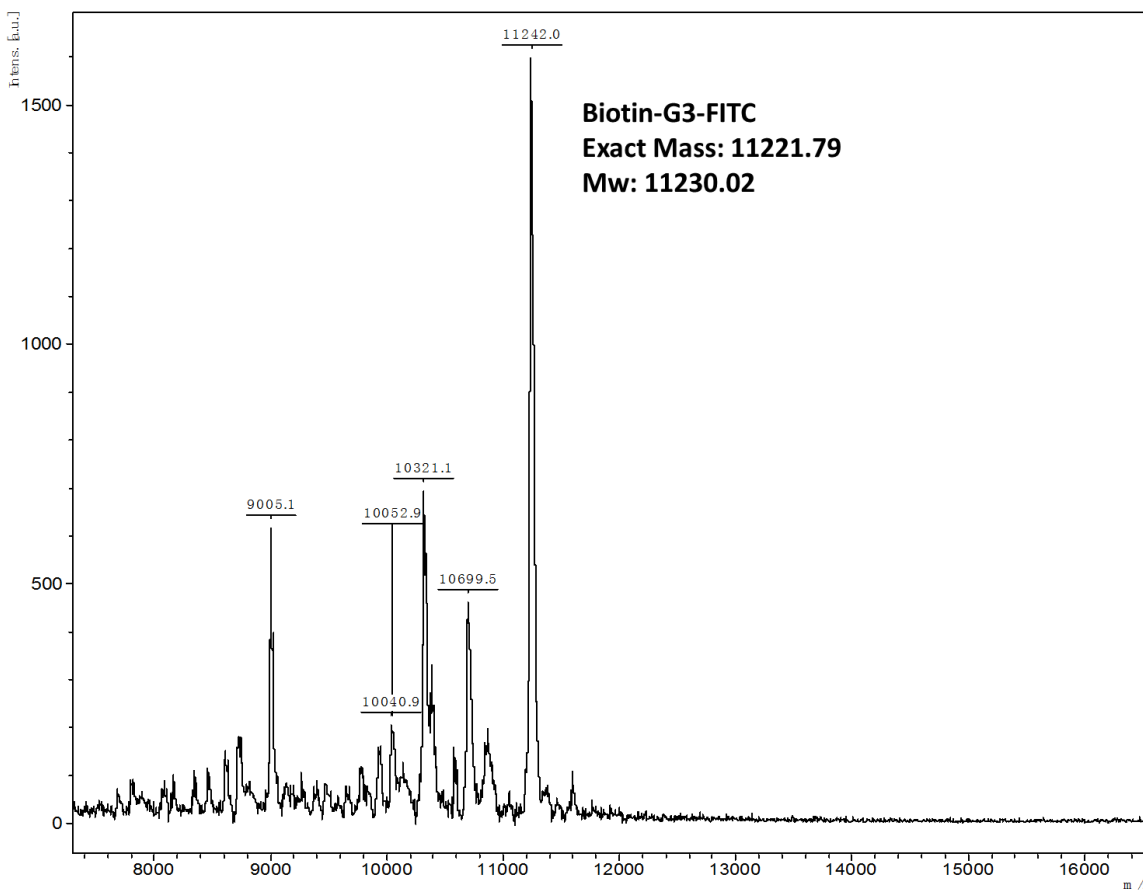


Figure 3.49 MALDI-TOF spectrum of biotin-G3-FITC conjugate **3-23**

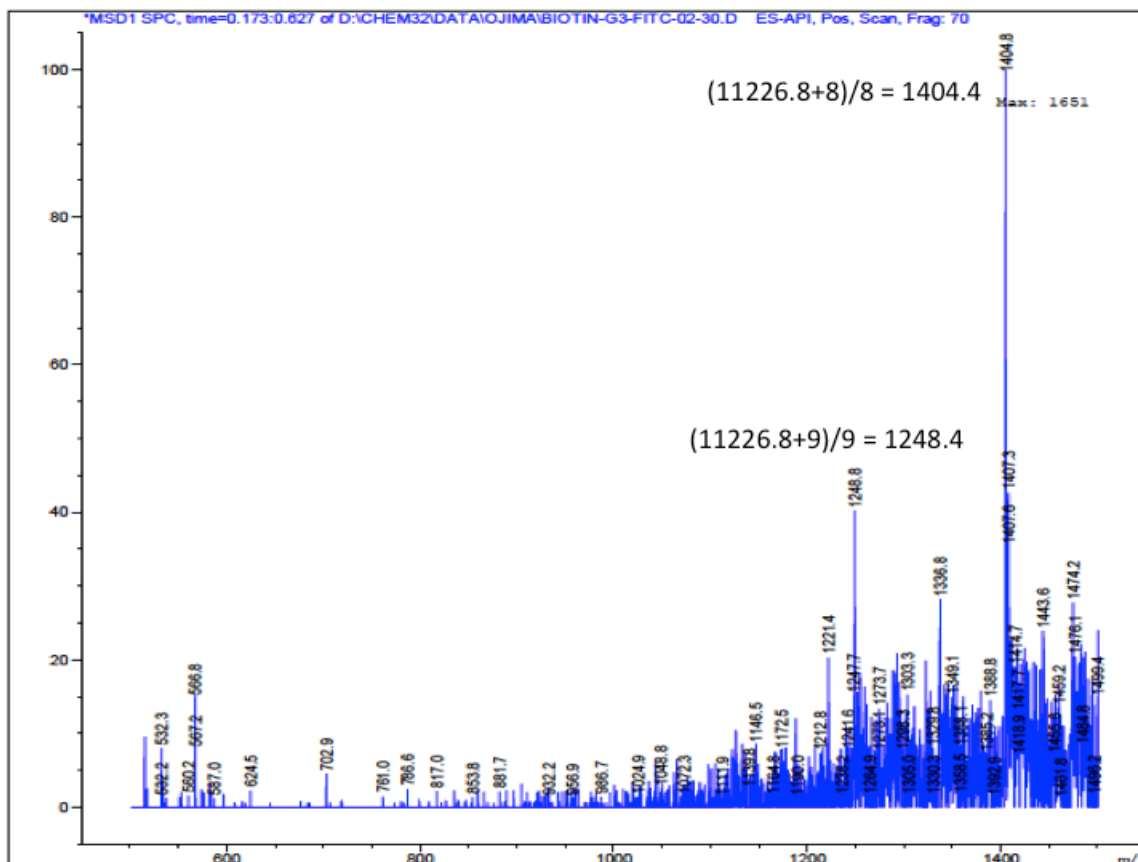


Figure 3.50 ESI-MS spectrum of biotin-G3-FITC conjugate 3-23

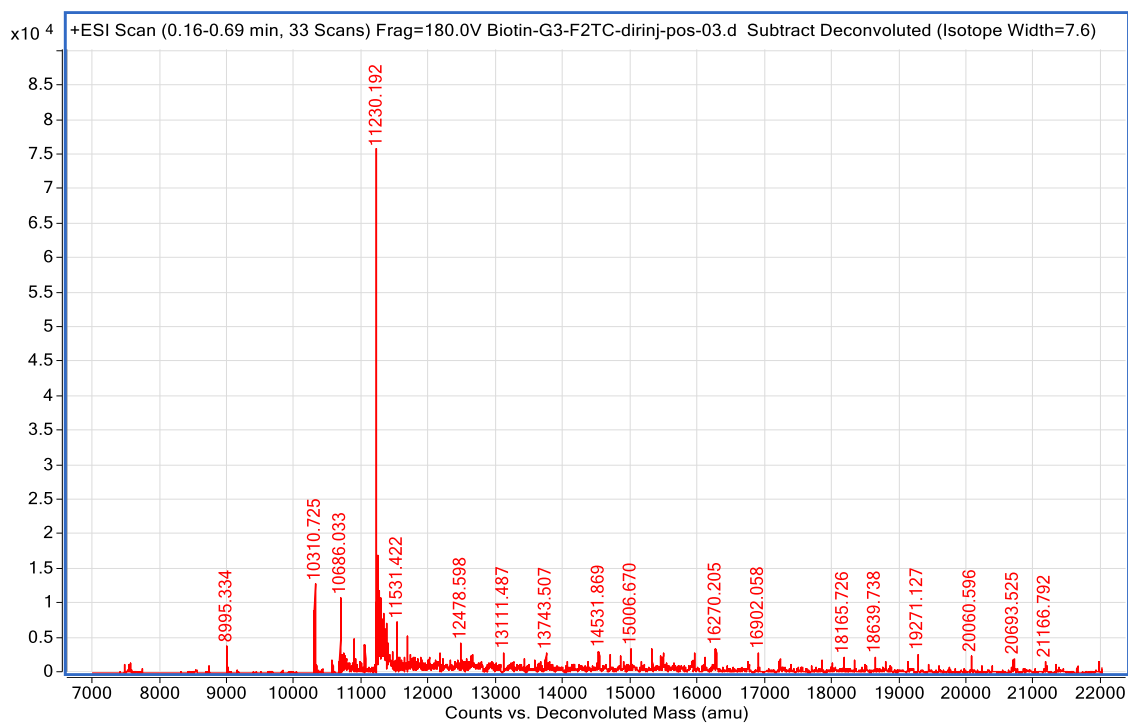
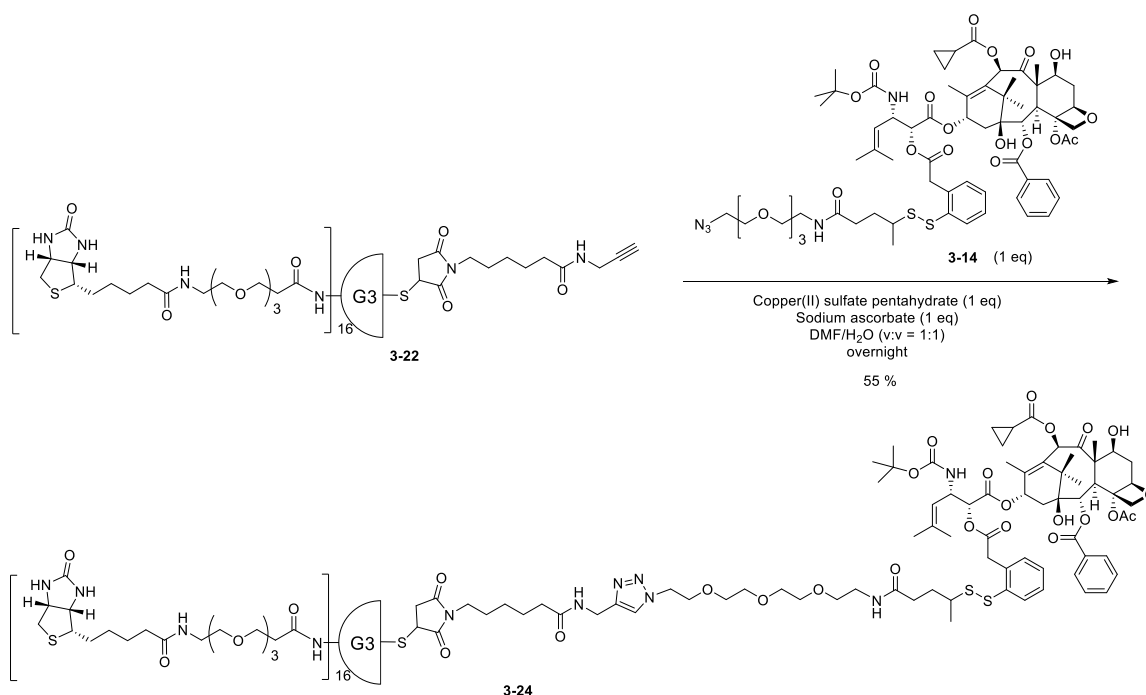


Figure 3.51 HR-MS deconvolution spectrum of biotin-G3-FITC conjugate 3-23

Similarly, biotin PEGylated G3 alkyne **3-22** was reacted with SB-T-1214-linker-PEG-azide via CuAAC to give biotin-G3-SB-T-1214 conjugate **3-24** in 55% yield (**Scheme 3.24**). The product was purified by prep-HPLC, and was characterized by MALDI-TOF and ESI-MS. Biotin-G3-SB-T-1214 conjugate **3-24** (chemical formula: C₅₃₅H₉₀₈N₁₁₆O₁₄₉S₁₉) has exact mass 11950.17, molecular weight 11958.95, and *m/z* 11955.19 (100%). In the MALDI-TOF analysis using DHB as the matrix, mass signal of 11966.6 ([M+Na]⁺, calculated 11972.2, Δ = -5.6 Da) was observed (**Figure 3.52**). Because high laser energy was used in the MALDI-TOF experiment in order to get a decent signal intensity of the product, a number of fragmentation peaks were also observed in the MALDI-TOF spectrum. In the ESI-MS spectrum (**Figure 3.53**), multiple charge states (+8, and +9) of the product were observed.



Scheme 3.24 Synthesis of biotin-G1-SB-T-1214 conjugate **3-24** via CuAAC

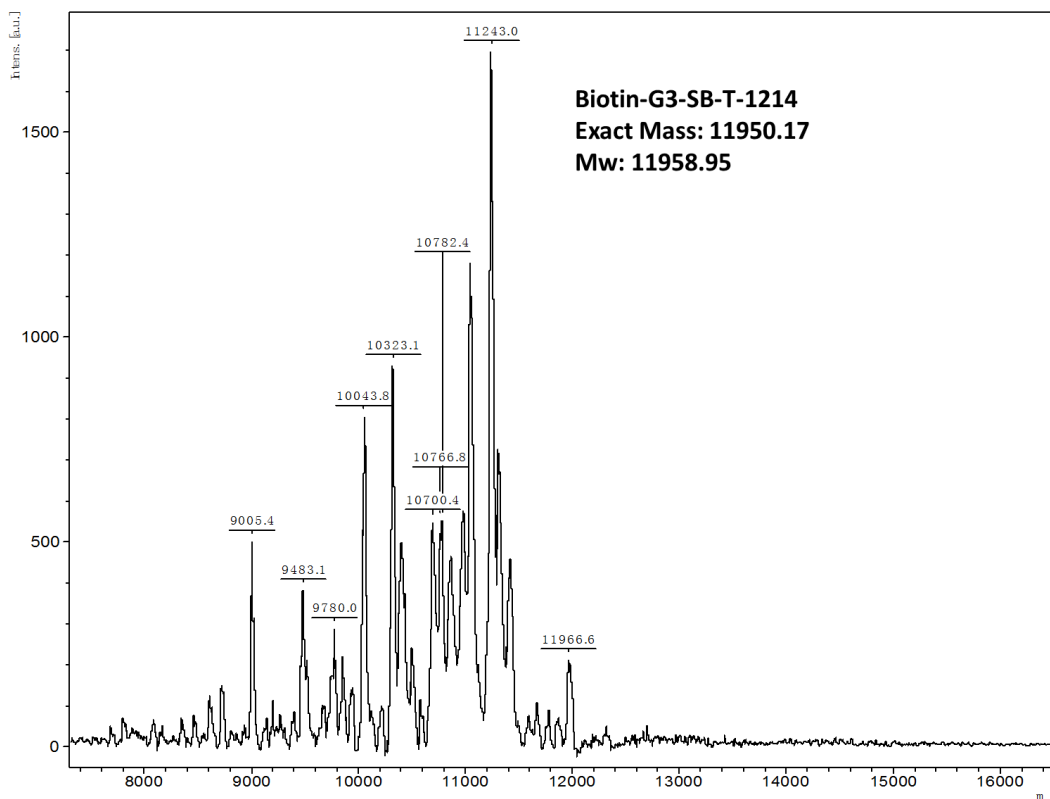


Figure 3.52 MALDI-TOF spectrum of biotin-G3-SB-T-1214 conjugate 3-24

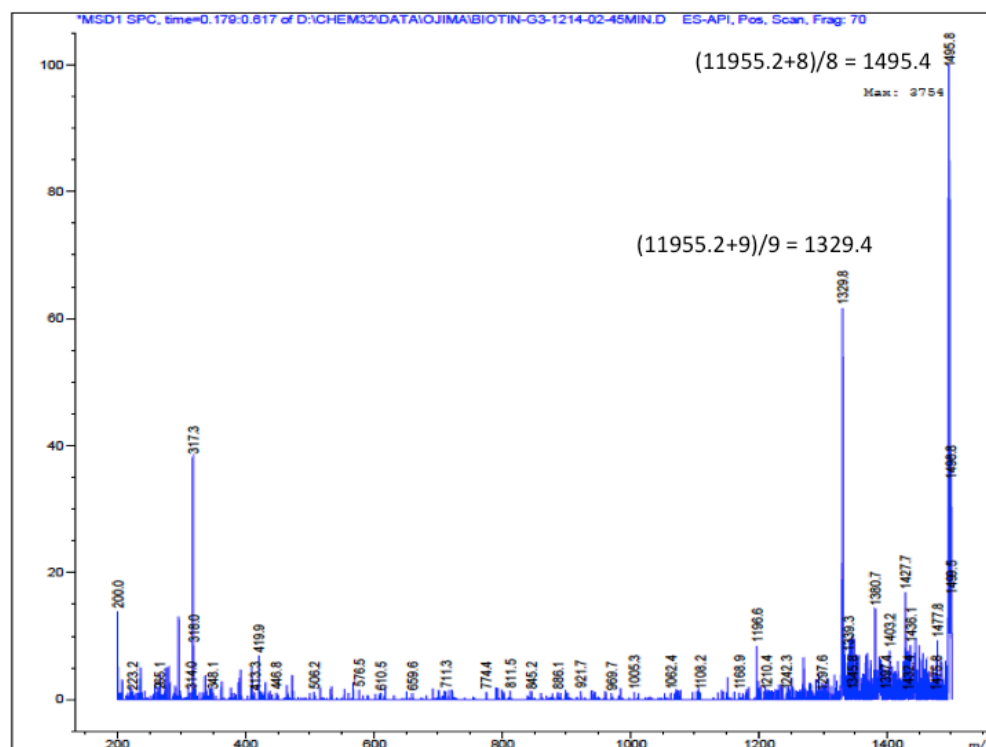
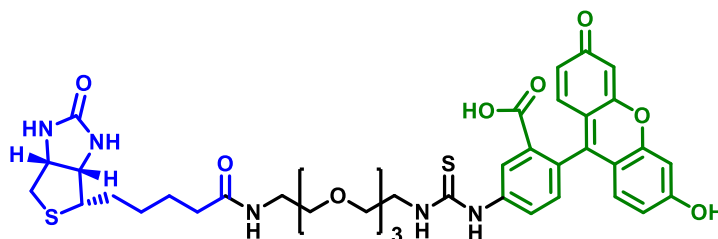


Figure 3.53 ESI-MS spectrum of biotin-G3-SB-T-1214 conjugate 3-24

§ 3.2.5 Biological Evaluation of PAMAM Dendrimer-based Tumor-Targeting Taxoid/FITC Conjugates

Cell internalization of three probes, biotin-PEG-FITC, biotin-G1-FITC conjugate, and biotin-G3-FITC conjugates, were evaluated against three cancer cell lines ID8 (murine ovarian carcinoma cell line), HCT116 (human colon carcinoma cell line), and MCF7 (human breast carcinoma cell line) via confocal fluorescence microscopy (CFM) imaging. In the first set of experiments, 5 μM of each probe was incubated with ID8 and MCF7 cell lines at 37 $^{\circ}\text{C}$ for 1 h. In ID8 cell line, CFM images (**Figure 3.54**, **Figure 3.57**, and **Figure 3.60**) clearly show internalization of three probes, however, the fluorescence signals were not very strong. In MCF7 cell line, barely fluorescence signals were observed. In the second set of experiments, higher concentration of each probe (10 μM) and longer incubation time (24 h) were used with HCT116 and MCF7 cell lines. In HCT116 cell line (**Figure 3.55**, **Figure 3.58**, and **Figure 3.61**), CFM images show strong fluorescence signals for all three probes, and in MCF7 cell line (**Figure 3.56**, **Figure 3.59**, and **Figure 3.62**), weak fluorescence signals were observed. In contrast, the control experiments using these three cancer cell lines without adding any fluorescent probe, or using a normal human fibroblast cell line WI-38 with adding each of the fluorescent probe, showed no fluorescence signals in the CFM imaging. These results clearly indicate ID8, HCT116, and MCF7 all three cancer cell lines have overexpression of biotin-receptors, and the overexpression levels are different (HCT116/ID8 > MCF7).



Biotin-PEG-FITC



Figure 3.54 Confocal fluorescence microscopy (CFM) images of ID8 cell line after incubation with 5 μM Biotin-PEG-FITC at 37 $^{\circ}\text{C}$ for 1 h.

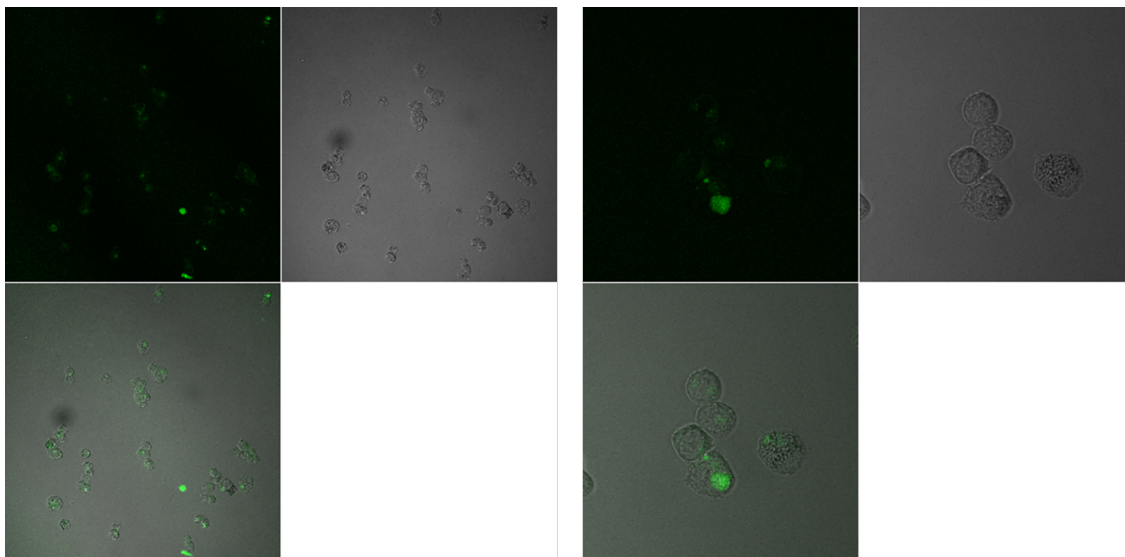


Figure 3.55 Confocal fluorescence microscopy (CFM) images of HCT116 cell line after incubation with 10 μ M Biotin-PEG-FITC at 37 $^{\circ}$ C for 24 h.

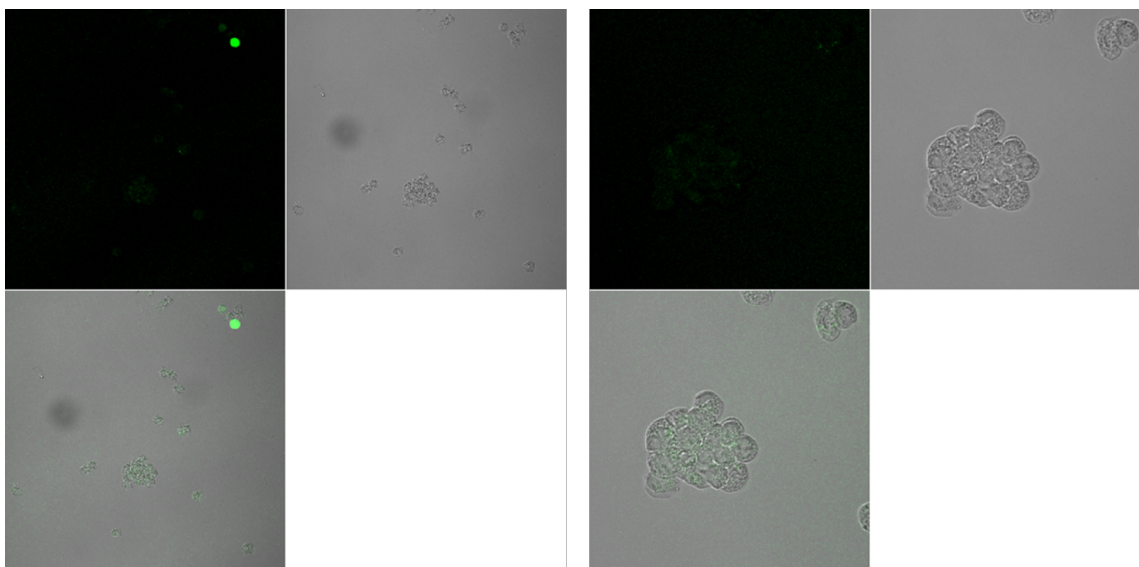
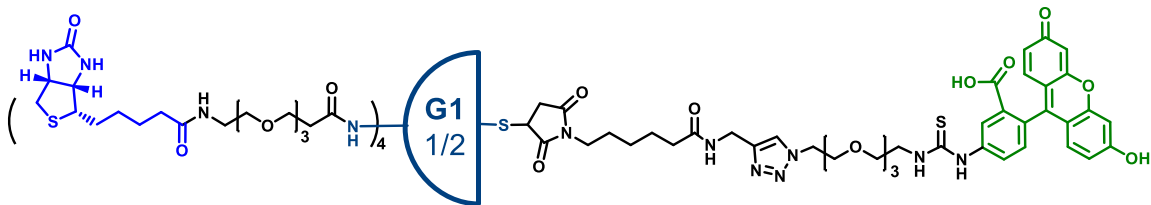


Figure 3.56 Confocal fluorescence microscopy (CFM) images of MCF7 cell line after incubation with 10 μ M Biotin-PEG-FITC at 37 $^{\circ}$ C for 24 h.



Biotin-G1-FITC conjugate

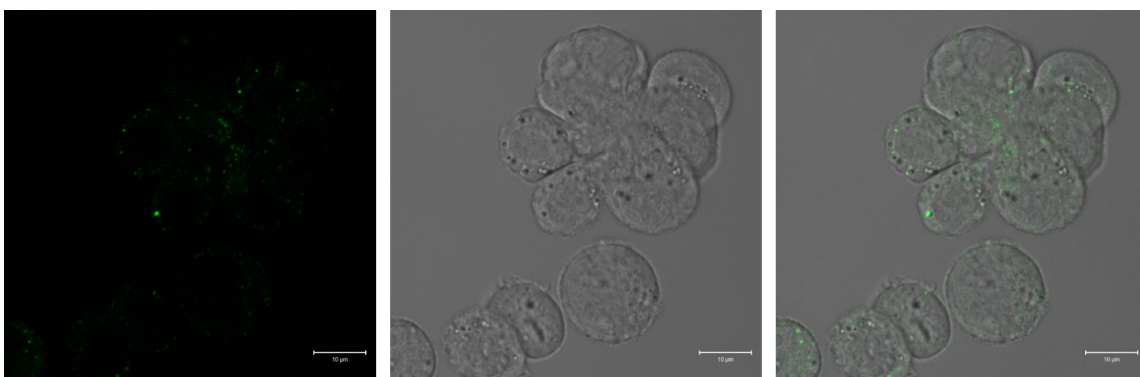


Figure 3.57 Confocal fluorescence microscopy (CFM) images of ID8 cell line after incubation with 5 μM Biotin-G1-FITC conjugate at 37 $^{\circ}\text{C}$ for 1 h.

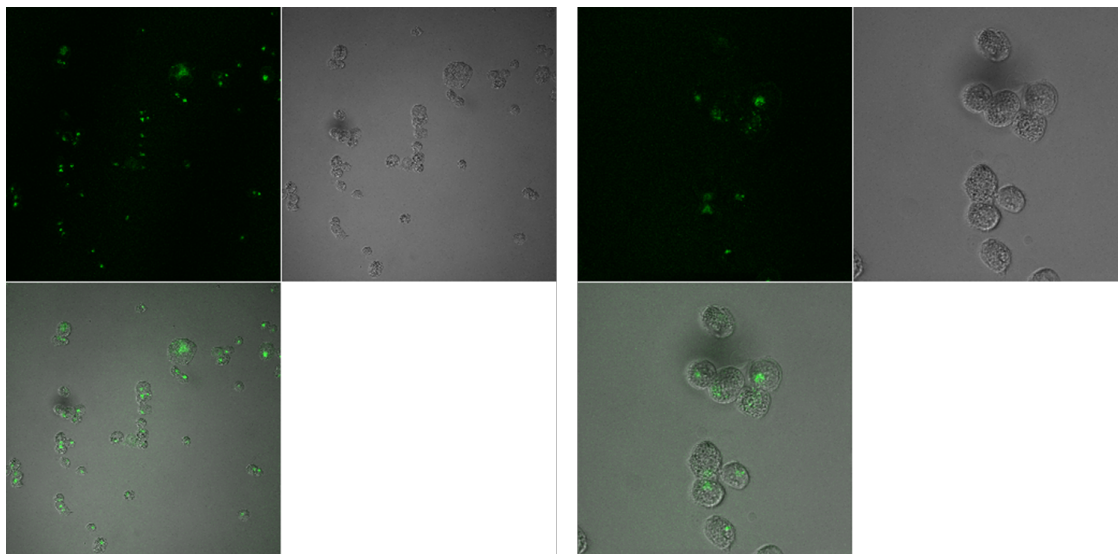


Figure 3.58 Confocal fluorescence microscopy (CFM) images of HCT116 cell line after incubation with 10 μM Biotin-G1-FITC conjugate at 37 $^{\circ}\text{C}$ for 24 h.

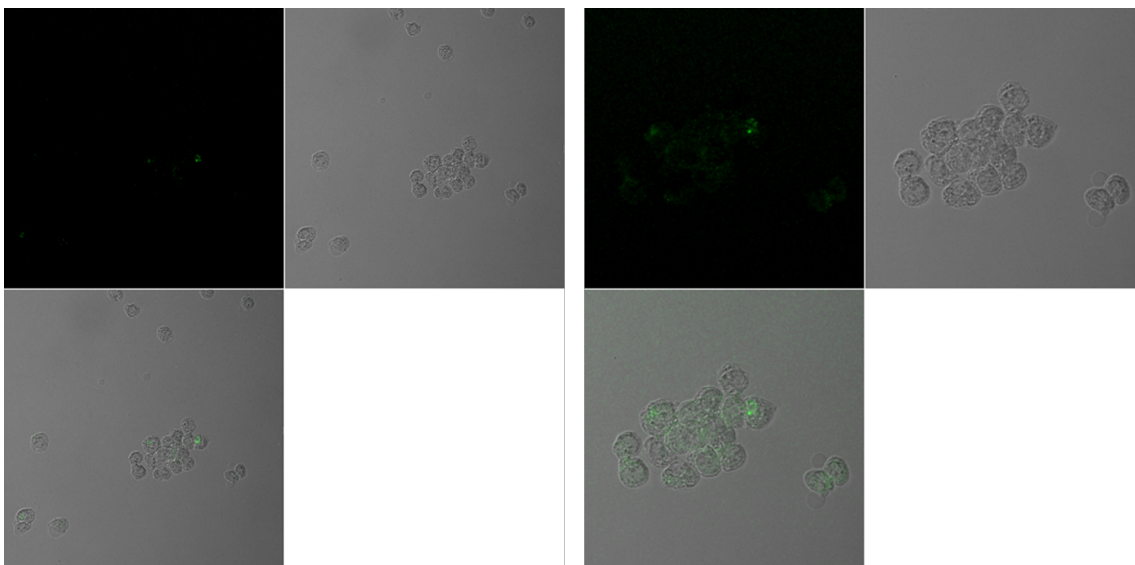
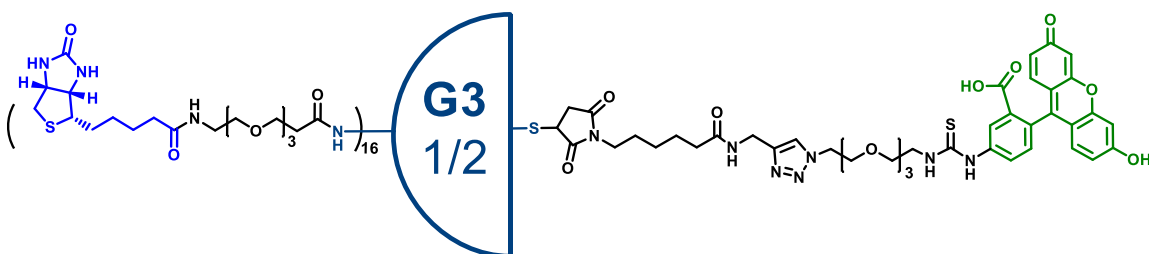


Figure 3.59 Confocal fluorescence microscopy (CFM) images of MCF7 cell line after incubation with 10 μM Biotin-G1-FITC conjugate at 37 $^{\circ}\text{C}$ for 24 h.



Biotin-G3-FITC conjugate

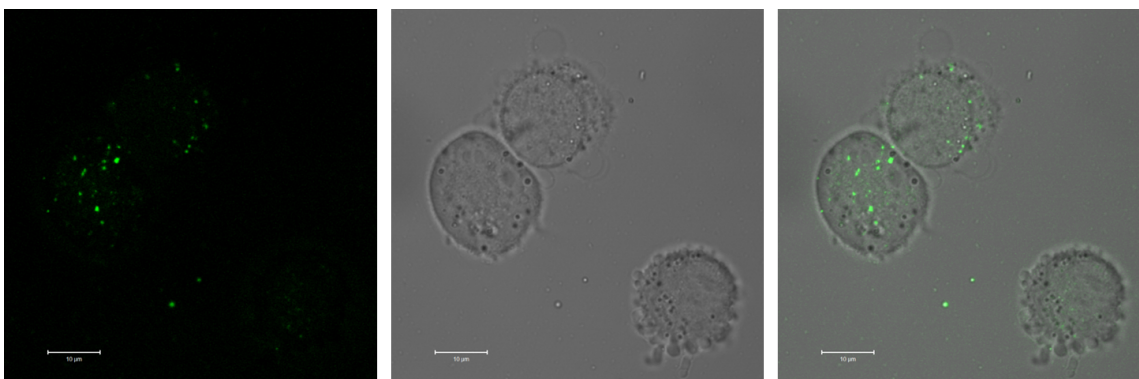


Figure 3.60 Confocal fluorescence microscopy (CFM) images of ID8 cell line after incubation with 5 μM Biotin-G3-FITC conjugate at 37 $^{\circ}\text{C}$ for 1 h.

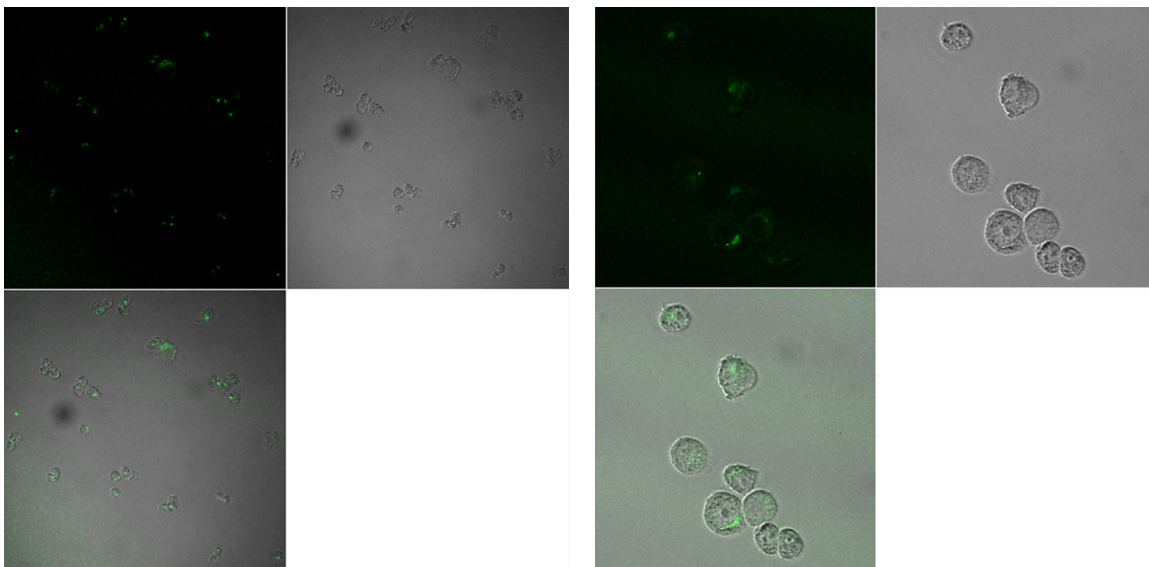


Figure 3.61 Confocal fluorescence microscopy (CFM) images of HCT116 cell line after incubation with 10 μM Biotin-G3-FITC conjugate at 37 $^{\circ}\text{C}$ for 24 h.

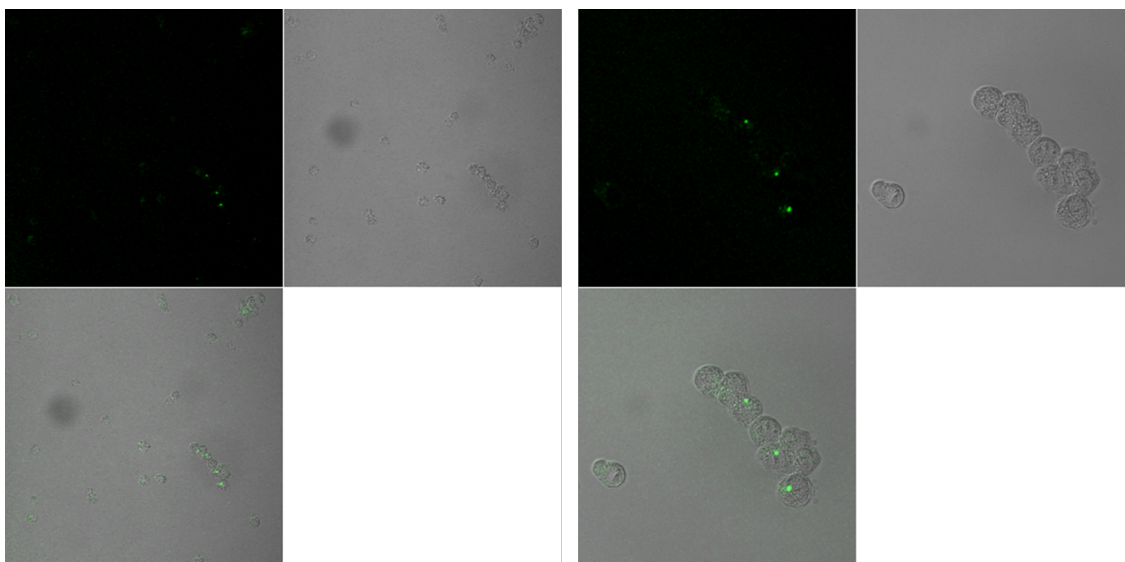


Figure 3.62 Confocal fluorescence microscopy (CFM) images of MCF7 cell line after incubation with 10 μM Biotin-G3-FITC conjugate at 37 $^{\circ}\text{C}$ for 24 h.

To further quantify the fluorescence intensity, flow cytometry experiments were conducted. In the first set of experiments, 5 μM of each probe was incubated with ID8 cell line at 37 $^{\circ}\text{C}$ for 1 h (**Figure 3.63**). Flow cytometry analysis indicates the intensity of fluorescence signal in the order of biotin-G3-FITC > biotin-PEG-FITC ~ biotin-G1-FITC > control. However, due to the low concentration and short incubation time, the fluorescence intensity was not strong enough compared with control.

In the second set of experiments, higher concentration of each probe (10 μM) was used with HCT116 and MCF7 cell lines at different time intervals (4 h, 8 h, 12 h, 24 h). **Figure 3.64**, **Figure 3.65**, and **Figure 3.66** clearly show a time-dependent internalization of each probe. Fast internalization rates were observed from the beginning to 4 h, and the internalization process slowed down and gradually reached saturation at around 12 h, presumably due to saturation of the biotin receptors. Moreover, HCT116 cell line showed slower internalization than MCF7 in the beginning, but stronger fluorescence intensity after 4 h. The fluorescence intensity of HCT116 at 24 h for each probe is around two times of MCF7 cell line, which is consistent with the CFM imaging results.

However, there was no obvious fluorescence intensity difference between the three fluorescent probes at each time interval for both HCT116 and MCF7 cell lines (**Figure 3.67** and **Figure 3.68**), which is unexpected and contradictory to the literature report for the observed multivalent interactions between folate receptors and folic acids in a flow cytometry analysis (**Figure 3.15**). This unexpected results could be because of the difference between biotin receptors and folate receptors. It is also possible that at high concentration (10 μM) and long incubation time (> 4 h), saturation of the biotin receptors was easily achieved by three different probes, and one biotin targeting moiety may be enough at this condition. Indeed, in the case of folate receptors and folic acids shown in **Figure 3.15**, there is a clear difference at the concentration of 50 nM between different number of folic acid targeting moieties, but the difference becomes much smaller and even within errors at the concentration of 100 nM.

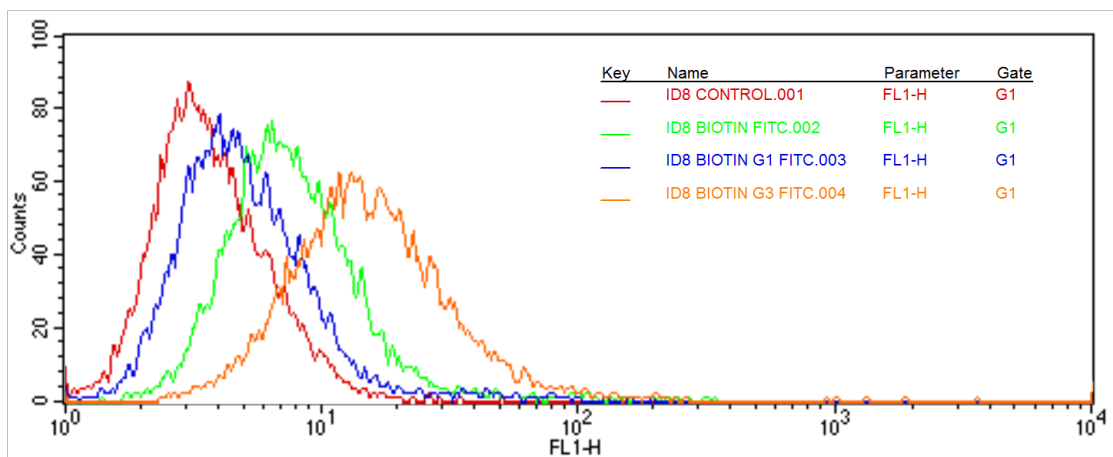


Figure 3.63 Flow cytometry analysis of ID8 cell line after incubation with 5 μM Biotin-PEG-FITC, Biotin-G1-FITC or Biotin-G3-FITC conjugates at 37 $^{\circ}\text{C}$ for 1 h.

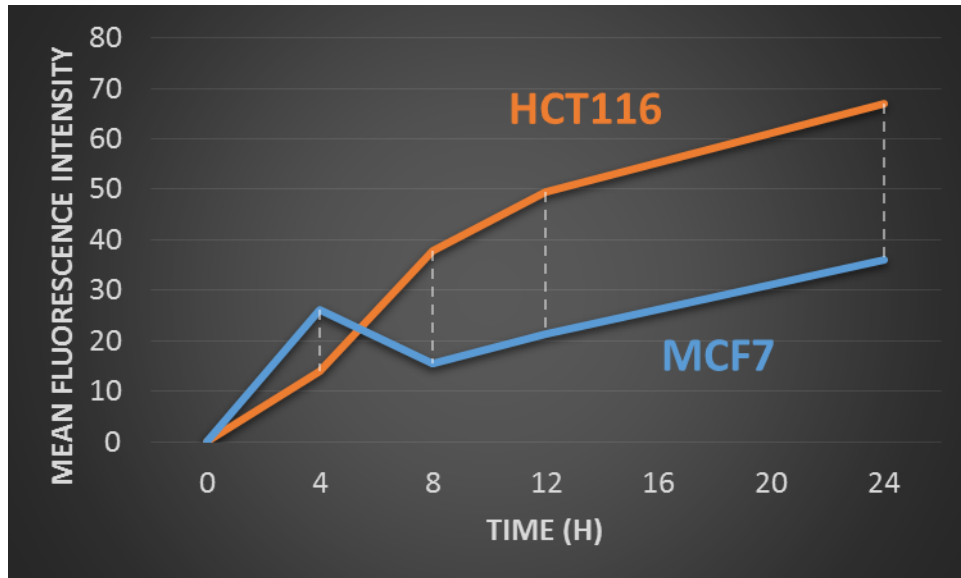


Figure 3.64 Flow cytometry analysis of HCT116 and MCF7 cell lines after incubation with 10 μ M Biotin-PEG-FITC at 37 °C at different time intervals.

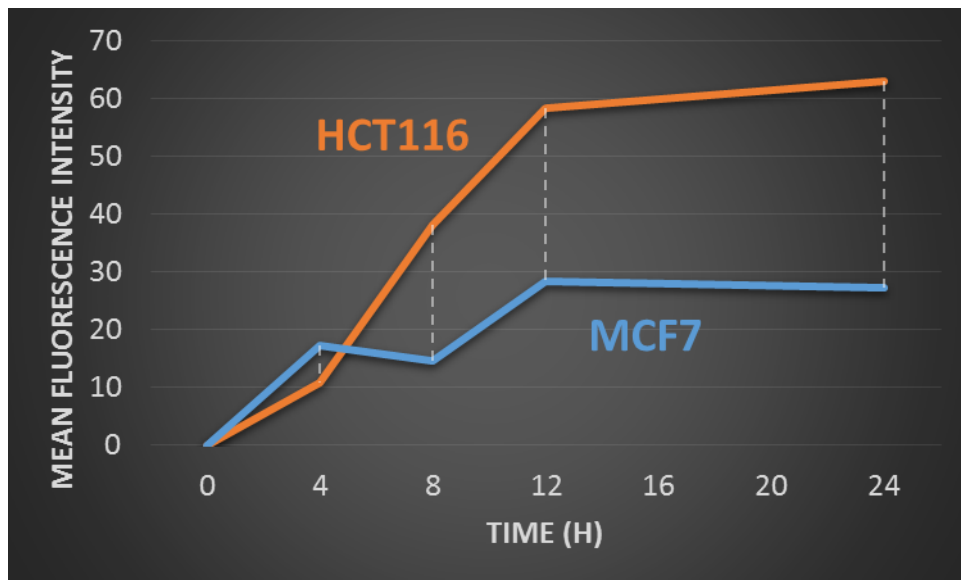


Figure 3.65 Flow cytometry analysis of HCT116 and MCF7 cell lines after incubation with 10 μ M Biotin-G1-FITC conjugate at 37 °C at different time intervals.

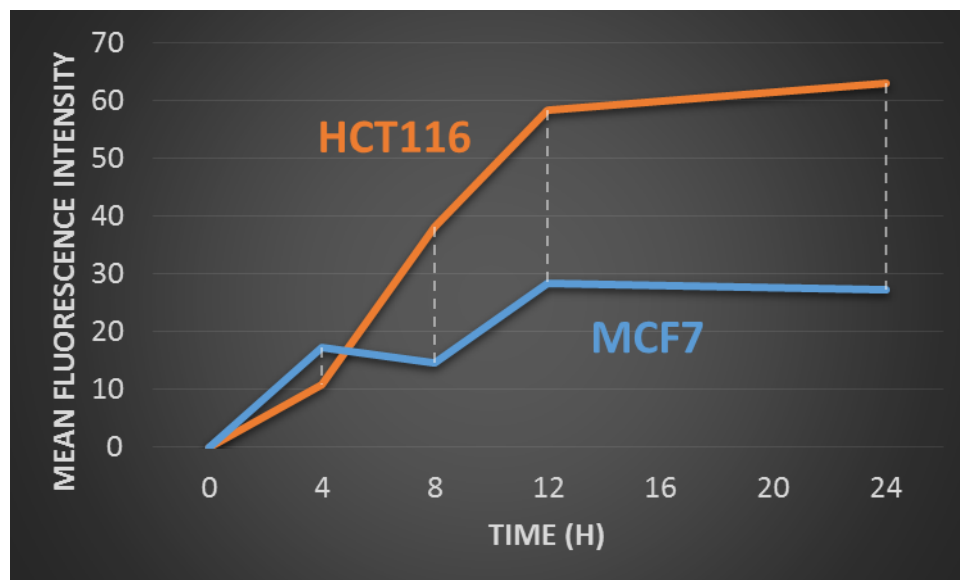


Figure 3.66 Flow cytometry analysis of HCT116 and MCF7 cell lines after incubation with 10 μ M Biotin-G3-FITC conjugate at 37 $^{\circ}$ C at different time intervals.

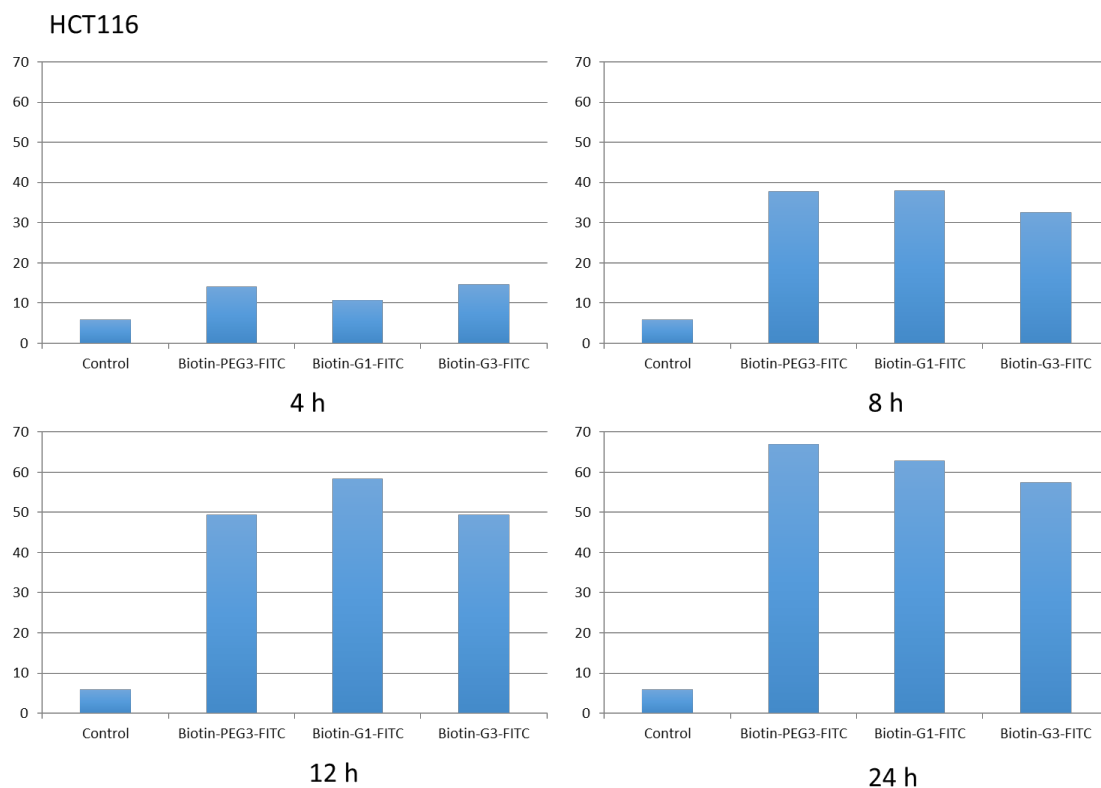


Figure 3.67 Flow cytometry analysis of HCT 116 cell line after incubation with 10 μ M Biotin-PEG-FITC, Biotin-G1-FITC or Biotin-G3-FITC conjugates at 37 $^{\circ}$ C at different time intervals.

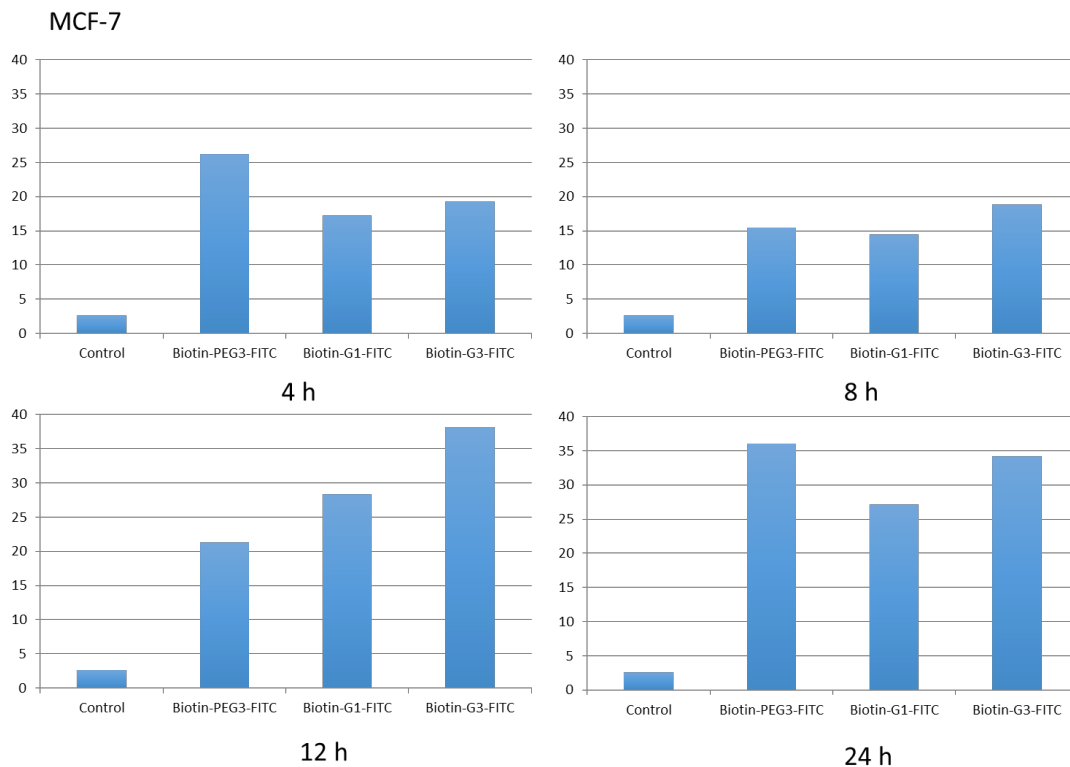
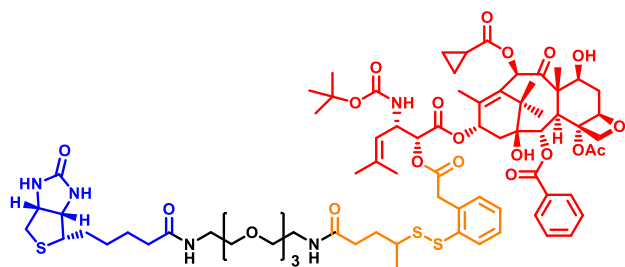
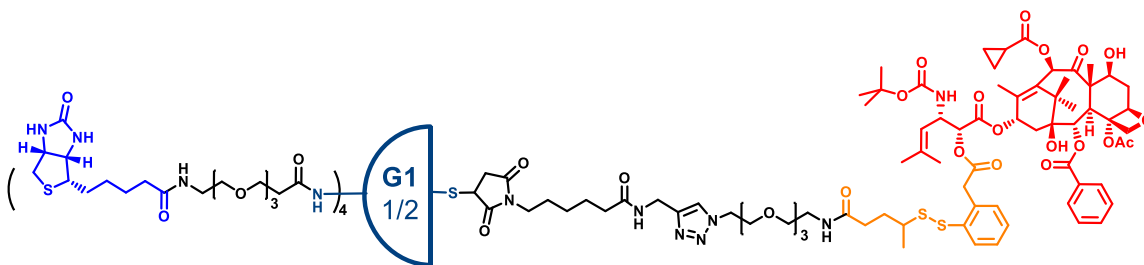


Figure 3.68 Flow cytometry analysis of MCF7 cell line after incubation with 10 μ M Biotin-PEG-FITC, Biotin-G1-FITC or Biotin-G3-FITC conjugates at 37 $^{\circ}$ C at different time intervals.

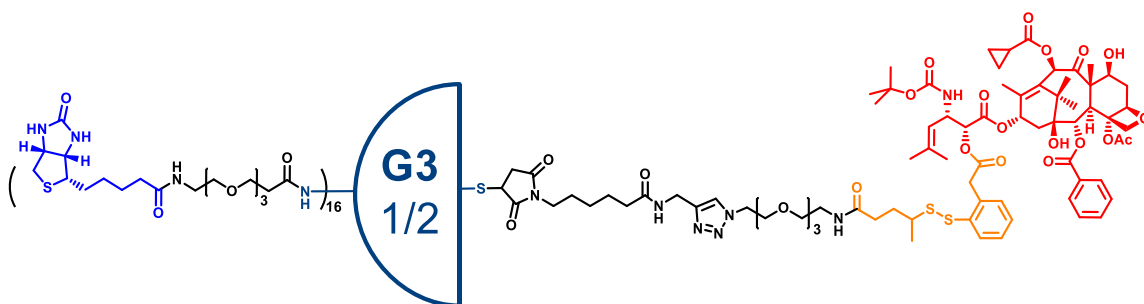
The results of cytotoxicity assays of SB-T-1214, BLT-s, biotin-G1-SB-T-1214, and biotin-G3-SB-T-1214 against MCF7 and ID8 cell lines are shown in **Table 3.3** below. All three drug conjugates were less potent than the parent taxoid SB-T-1214 in both cell lines, which were expected, since release of the drug moiety would highly depend on the amount of endogenous thiols inside the cancer cells. Between the three different drug conjugates, biotin-G1-SB-T-1214 showed similar cytotoxicity as BLT-s, whereas biotin-G3-SB-T-1214 is more potent than the other two drug conjugates, indicating an enhanced cell internalization ability at nM range low concentrations.



BLT-s



Biotin-G1-SB-T-1214



Biotin-G3-SB-T-1214

Table 3.3 Cytotoxicity (IC_{50} , nM) of SB-T-1214, BLT-s, Biotin-G1-SB-T-1214, and Biotin-G3-SB-T-1214 against MCF7 and ID8 cell lines

entry	SB-T-1214	BLT-s	Biotin-G1-SB-T-1214	Biotin-G3-SB-T-1214
MCF-7	1.7 ± 0.3	3.5 ± 0.6	3.1 ± 0.7	2.1 ± 0.5
ID8	5.1 ± 0.9	11.3 ± 1.2	11.9 ± 2.4	7.9 ± 2.2

§ 3.3 Asymmetric Bow-Tie Dendrimer-based (ABTD) Tumor-Targeted Drug Delivery Systems

§ 3.3.1 Rational Design

The original design of asymmetric bow-tie dendrimer-based (ABTD) tumor-targeted drug delivery systems was based on Dr. Yu-Han Gary Teng's PhD research proposal in 2010, and was later extensively developed by Dr. Tao Wang. **Figure 3.69** shows the schematic representation of ABTD tumor-targeted drug delivery systems.

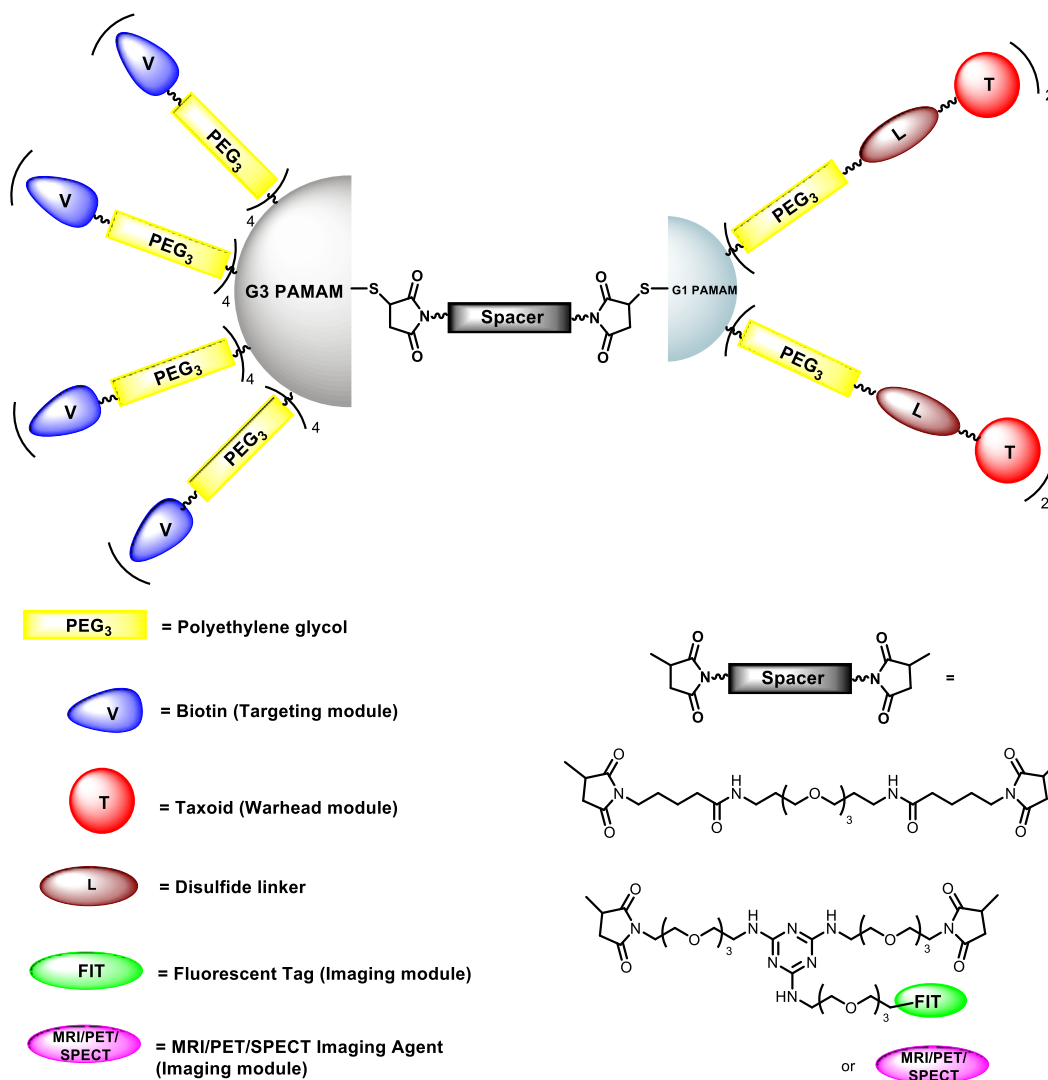


Figure 3.69 Schematic representation of asymmetric bow-tie dendrimer-based (ABTD) tumor-targeted drug delivery systems. Adapted with permission from Wang, T. Design, synthesis, and biological evaluation of novel taxoid-based small-molecule theranostic PET/SPECT imaging agents and nano-scale asymmetric bow-tie dendrimer drug conjugates towards tumor-targeted chemotherapy (Doctoral Dissertation). Stony Brook University, 2015.

In the design ABTD conjugates (**Figure 3.68**), biotin (shown in blue) is used as the tumor targeting molecule, as biotin receptors are found to be overexpressed in certain cancer cell lines. 2nd-generation taxoid SB-T-1214 (shown in red), is used as cytotoxic agent. New generation taxoids have shown excellent cytotoxicity against certain drug-sensitive and drug-resistant cancer cell lines. Fluorescent probe could be used to replace the taxoid warhead to study the internalization and release of the drug conjugate. PEG chains (shown in yellow) are inserted between biotin and G3 PAMAM dendrimer, and also between cytotoxic agent and G1 PAMAM dendrimer, for improving solubility of the conjugate and other pharmaceutical properties. Bismaleimide crosslinkers is used for connecting the G3 PAMAM dendrimer part and G1 PAMAM dendrimer part. The bifunctional bismaleimide crosslinker could be replaced by a trifunctional triazine splitter, in which a fluorescent tag (shown in green) or MRI/PET/SPECT imaging module (shown in magenta) could be attached.

The synthetic strategy for constructing the designed multifunctional ABTD dendrimer conjugate is shown in **Figure 3.70**. The conjugate takes advantage of the primary amino groups on the surface of the dendrimer, which could be fully functionalized by typical coupling conditions. The disulfide in the core could be subsequently cleaved by reducing agent (*tris*(2-carboxyethyl)phosphine (TCEP)). The asymmetric bow-tie scaffold could be built from half G3 PAMAM cystamine core dendrimer surface-functionalized with 16 targeting biotin molecules through PEG chains, and half G1 PAMAM cystamine core dendrimer surface-functionalized with 4 alkyne groups through PEG chains via a suitable bifunctional bismaleimide crosslinker. This asymmetric bow-tie platform could conjugate with the cytotoxic agent SB-T-1214 or fluorescent probe via click chemistry. The chemical structures of designed ABTD conjugates are shown in **Figure 3.71**.

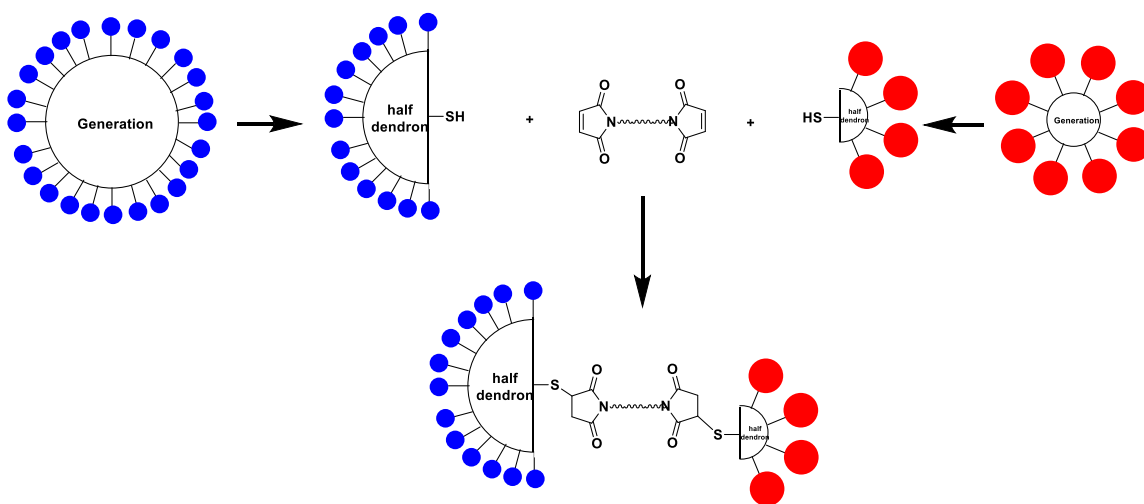


Figure 3.70 Synthetic strategy for constructing asymmetric bow-tie dendrimer-based (ABTD) tumor-targeted drug delivery systems. Adapted with permission from Wang, T.

Design, synthesis, and biological evaluation of novel taxoid-based small-molecule theranostic PET/SPECT imaging agents and nano-scale asymmetric bow-tie dendrimer drug conjugates towards tumor-targeted chemotherapy (Doctoral Dissertation). Stony Brook University, 2015.

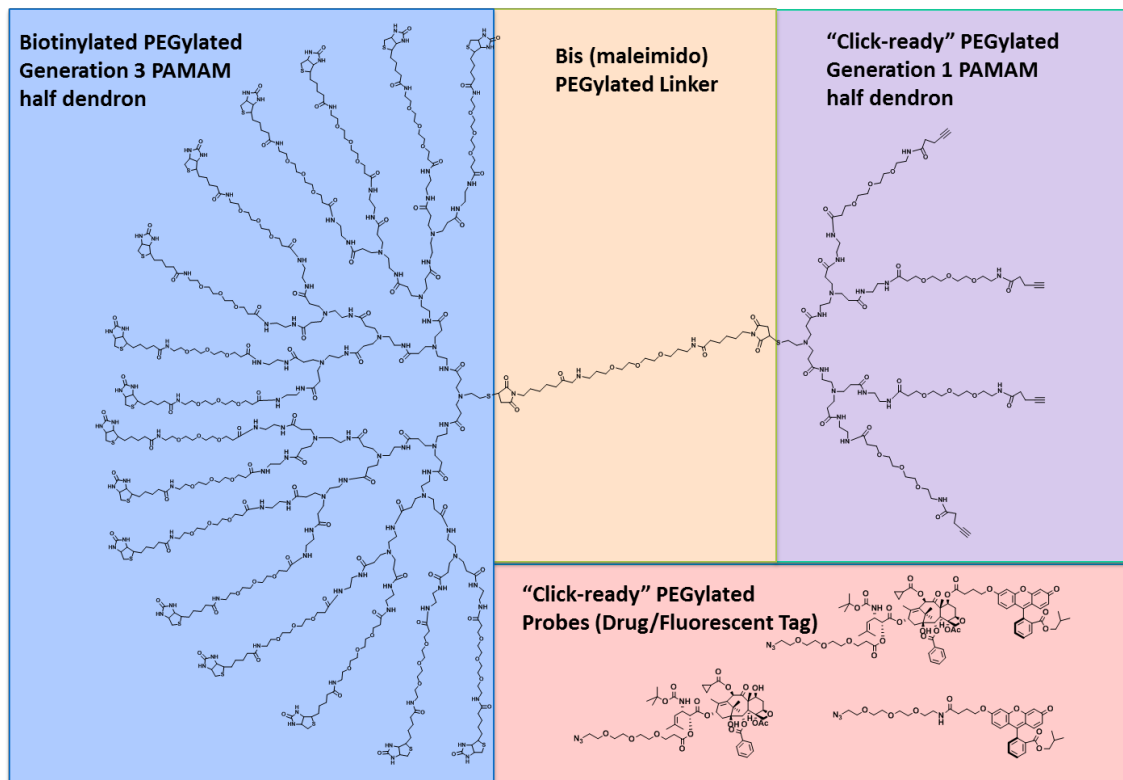


Figure 3.71 Chemical structures of designed asymmetric bow-tie dendrimer-based (ABTD) tumor-targeted drug delivery systems. Adapted with permission from Wang, T.

Design, synthesis, and biological evaluation of novel taxoid-based small-molecule theranostic PET/SPECT imaging agents and nano-scale asymmetric bow-tie dendrimer drug conjugates towards tumor-targeted chemotherapy (Doctoral Dissertation). Stony Brook University, 2015.

The advantages of the designed asymmetric bow-tie PAMAM dendrimer-based multifunctional conjugate include: i) the surface of the asymmetric dendrimer could be coupled with 16 targeting molecules and 4 cytotoxic agents within one conjugate, greatly increasing the payload of drug and its internalization efficiency; ii) the architecture of the conjugate and number of targeting moieties and drugs are well-defined, and ideally this will afford consistent synthetic results and biological evaluation results; iii) accumulation of the conjugate in tumor tissue could be achieved via both passive targeting by employing the enhanced permeability and retention (EPR) effect and receptor-mediated active targeting; iv) solubility of the conjugate could be significantly improved through PEGylation.

§ 3.3.2 Synthesis of ABTD Conjugates

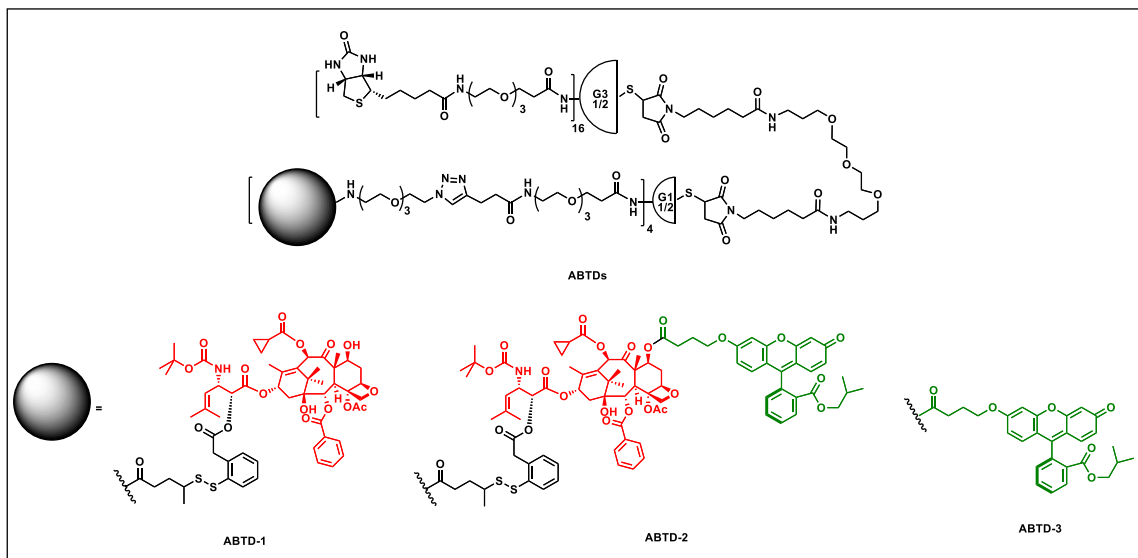
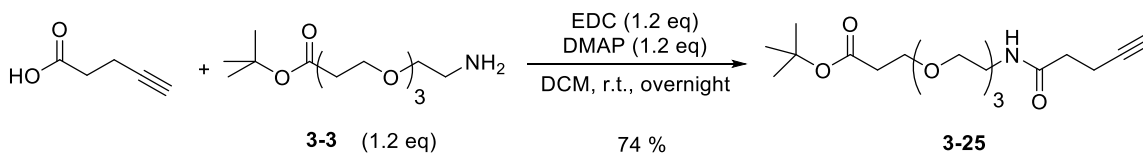


Figure 3.72 Designed ABTD conjugates. Adapted with permission from Wang, T. Design, synthesis, and biological evaluation of novel taxoid-based small-molecule theranostic PET/SPECT imaging agents and nano-scale asymmetric bow-tie dendrimer drug conjugates towards tumor-targeted chemotherapy (Doctoral Dissertation). Stony Brook University, 2015.

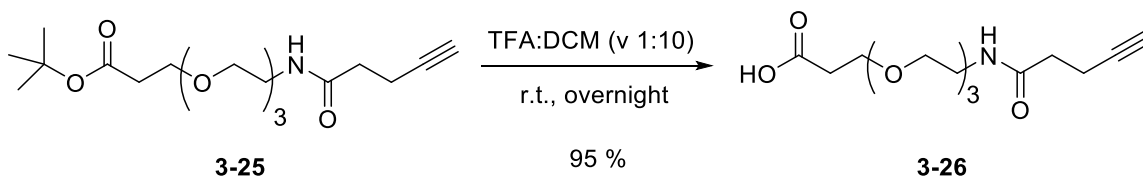
For synthesis of designed ABTD conjugates shown in **Figure 3.72**, first, alkyne PEGylated G1 PAMAM dendrimer was synthesized.

For the synthesis of alkyne PEGylated G1 PAMAM dendrimer, commercially available 4-pentynoic acid was reacted with *tert*-butyl 12-amino-4,7,10-trioxadocecanoate **3-3** via EDC coupling to yield amide **3-25** in 74% yield (**Scheme 3.25**).



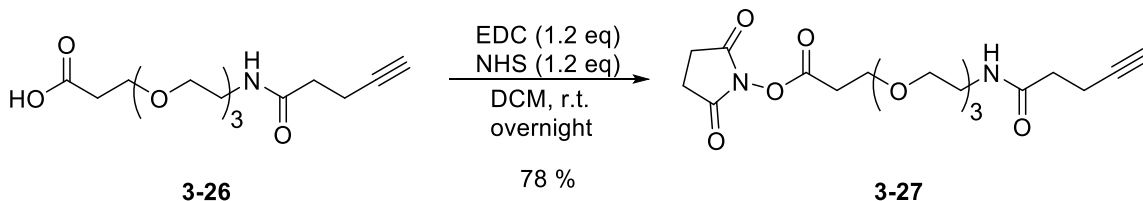
Scheme 3.25 Synthesis of amide **3-25**

Then, TFA deprotection of **3-25** afforded the free carboxylic acid **3-26** in 95% yield (**Scheme 3.26**).



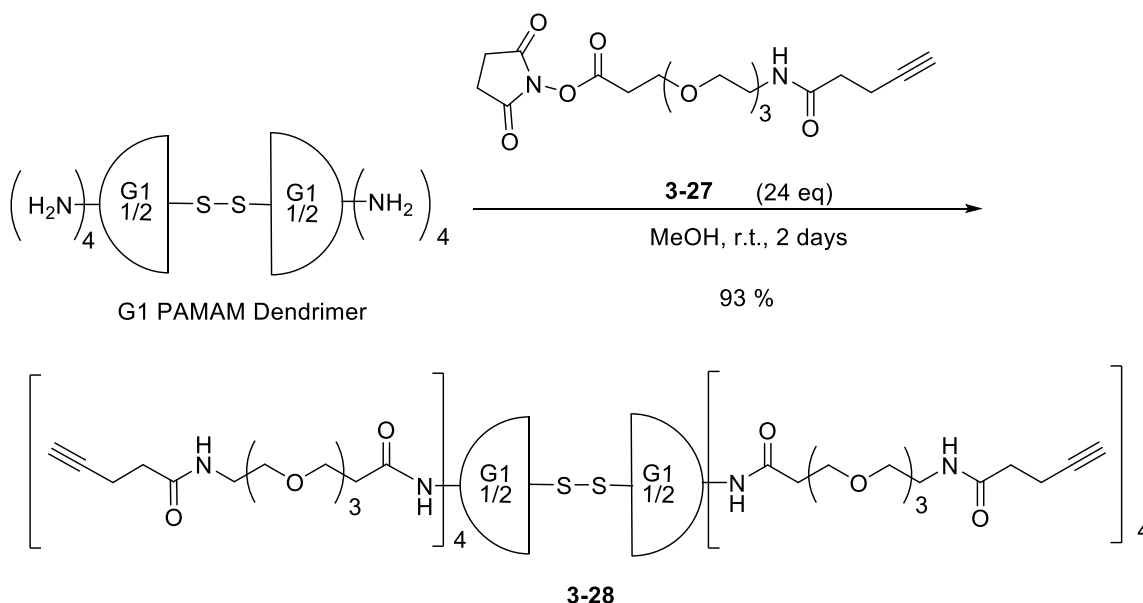
Scheme 3.26 TFA deprotection of **3-25**

Carboxylic acid group of **3-26** was subsequently activated by coupling with NHS via EDC coupling to generate OSu-activated ester **3-27** in 78% yield (**Scheme 3.27**).



Scheme 3.27 Synthesis of activated ester **3-27**

Finally, activated ester **3-27**, connecting PEG chain and alkyne functional group via an amide bond, could be coupled to the surface amine groups of G1 dendrimer, affording alkyne PEGylated G1 PAMAM dendrimer **3-28** in 93% yield (**Scheme 3.28**). Alkyne PEGylated G1 PAMAM dendrimer **3-28** was purified by dialysis against methanol for three days, and characterized by MALDI-TOF and ESI-MS (**Figure 3.73** and **Figure 3.74**).



Scheme 3.28 Synthesis of alkyne PEGylated G1 PAMAM dendrimer **3-28**

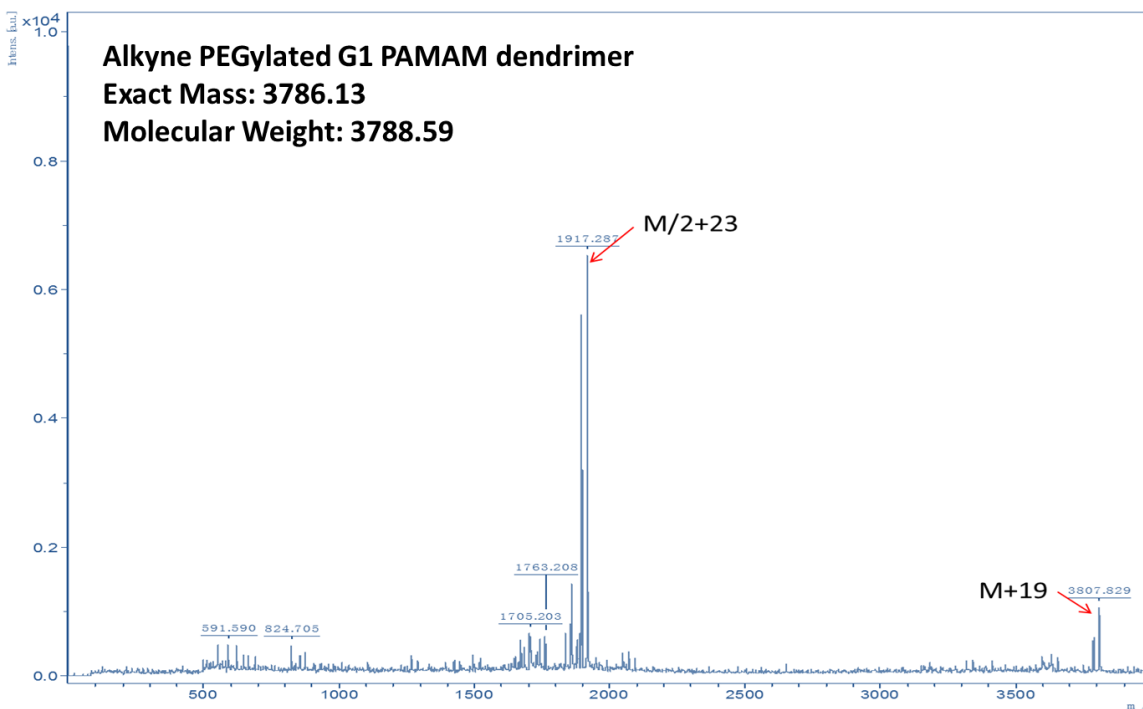


Figure 3.73 MALDI-TOF spectrum of alkyne PEGylated G1 PAMAM dendrimer **3-28**

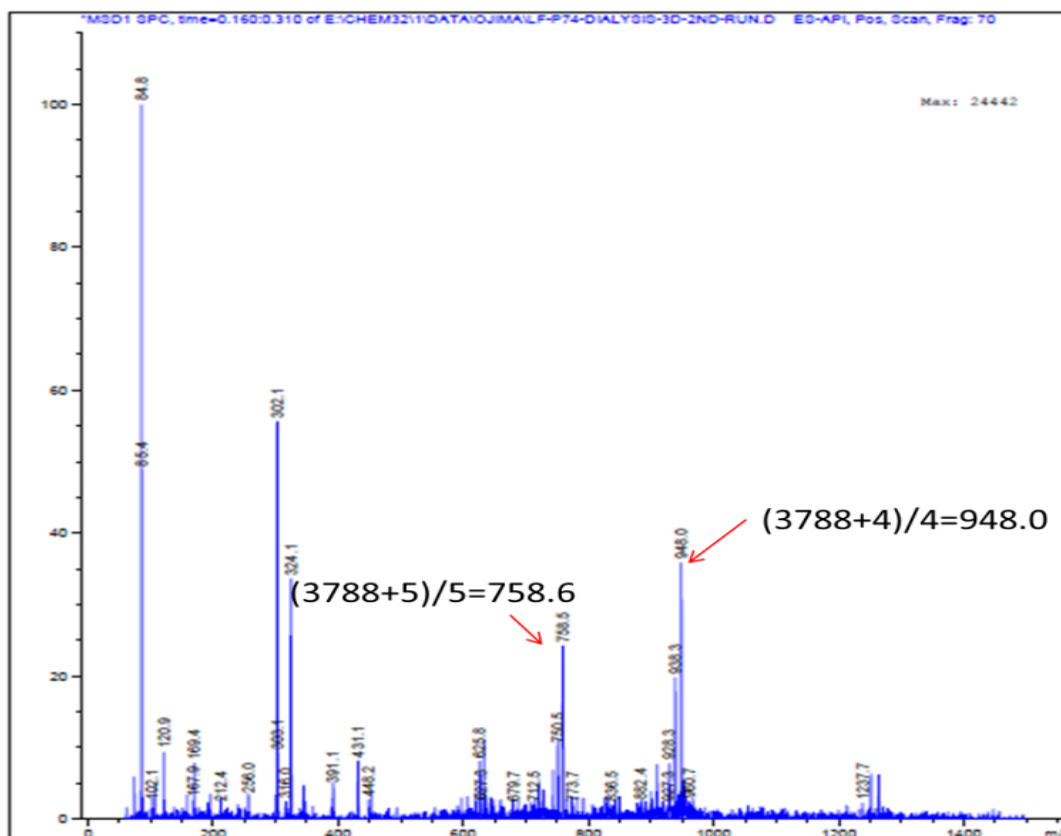
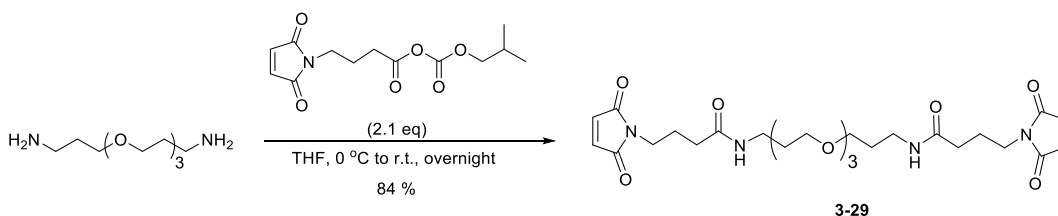


Figure 3.74 ESI-MS spectrum of alkyne PEGylated G1 PAMAM dendrimer **3-28**

Next, bismaleimide crosslinker **3-29** bearing PEG chain for conjugation of alkyne PEGylated G1 PAMAM dendrimer and biotin PEGylated G3 dendrimers was synthesized. Mixed anhydride generated in the same manner as mentioned in previous section was used to couple with commercially available PEG-diamine to afford desired crosslinker **3-29** in 84% yield (**Scheme 3.29**). The diamine was added very slowly to make sure it reacts with excess amount of mixed anhydride during the reaction. The reaction is very effective and most starting materials were converted to product when finishing adding diamine. The reaction was monitored by TLC to make sure the reaction went to completion.



Scheme 3.29 Synthesis of bismaleimide crosslinker **3-29**

ABTD versatile platform biotin-G3-G1-alkyne (**Figure 3.75**) was then prepared by Dr. Tao Wang using the method shown in **Scheme 3.30**. The biotin-G3-G1-alkyne obtained from Dr. Tao Wang was further purified by prep-HPLC, and characterized by ESI-MS before the final click reactions (**Figure 3.76** and **Figure 3.77**). The purity of this material as well as the other starting material SB-T-1214-linker-PEG-azide for the click reaction to construct ABTD1 were both confirmed by HPLC (**Figure 3.78** and **Figure 3.79**).

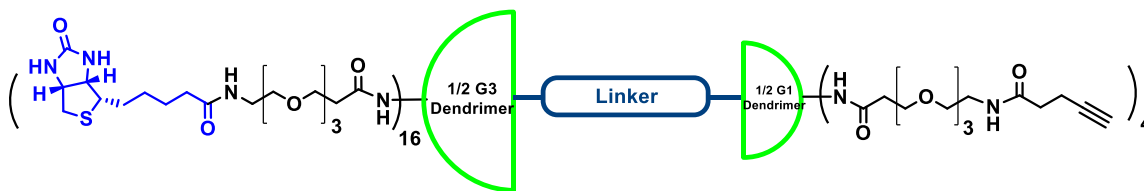
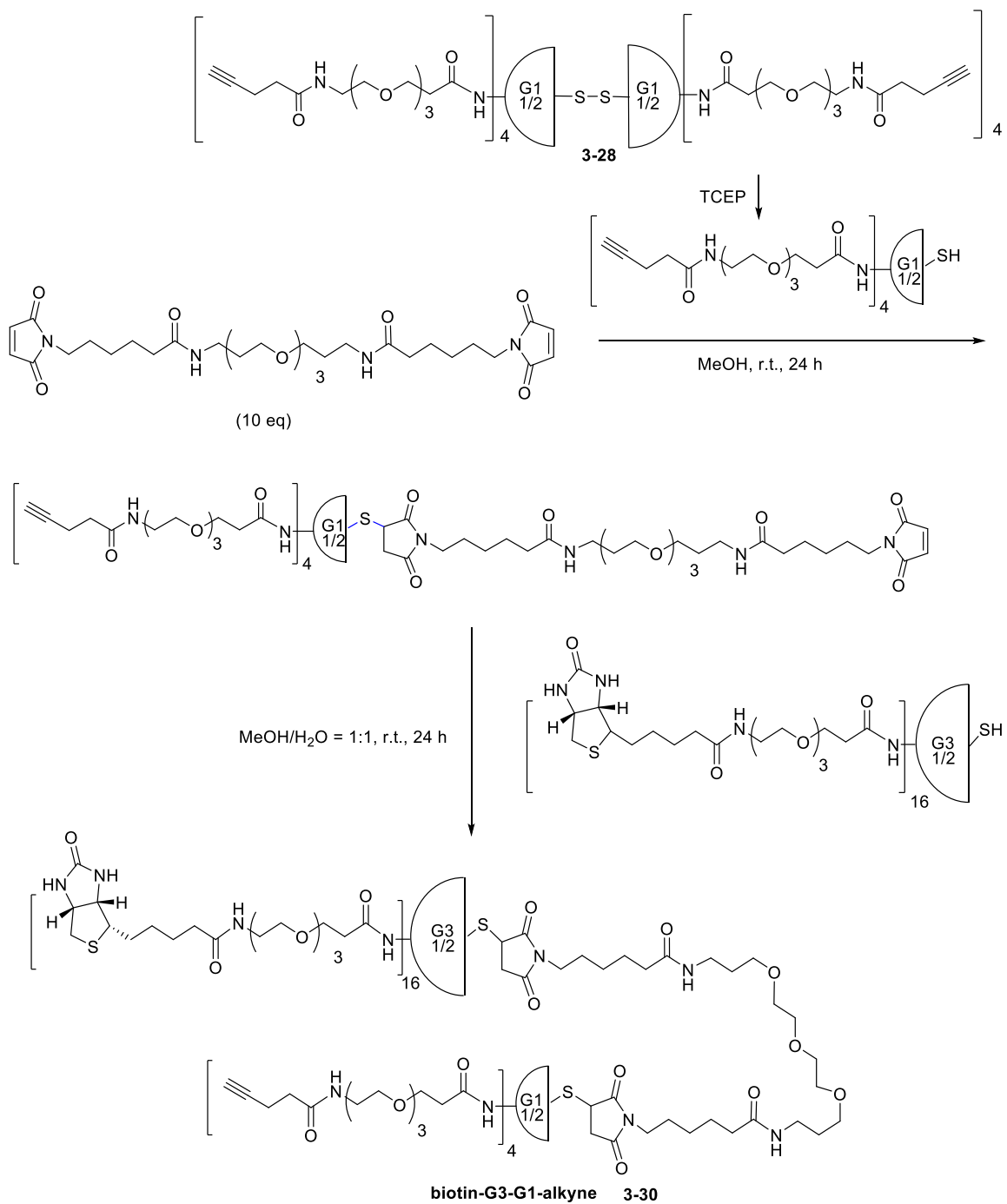


Figure 3.75 Schematic representation of biotin-G3-G1-alkyne



Scheme 3.30 Construct of biotin-G3-G1-alkyne

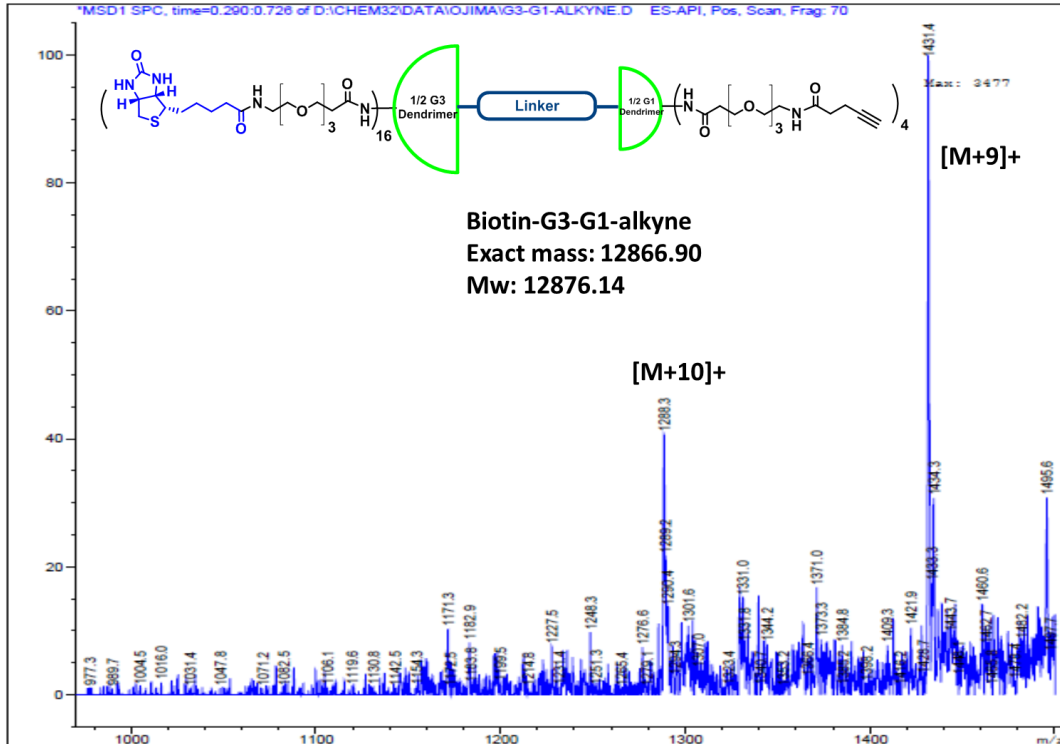


Figure 3.76 ESI-MS MS spectrum of biotin-G3-G1-Alkyne

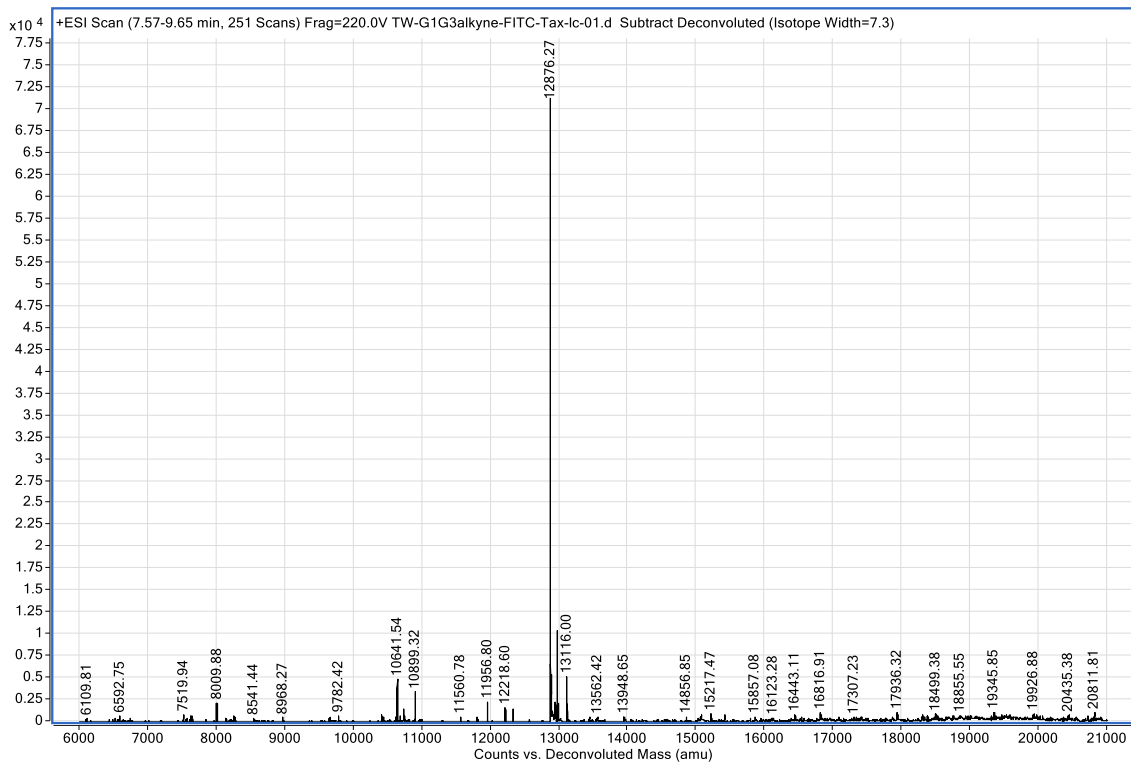


Figure 3.77 Deconvolution MS spectrum of biotin-G3-G1-Alkyne

Biotin-G3-G1-Alkyne-HPLC:

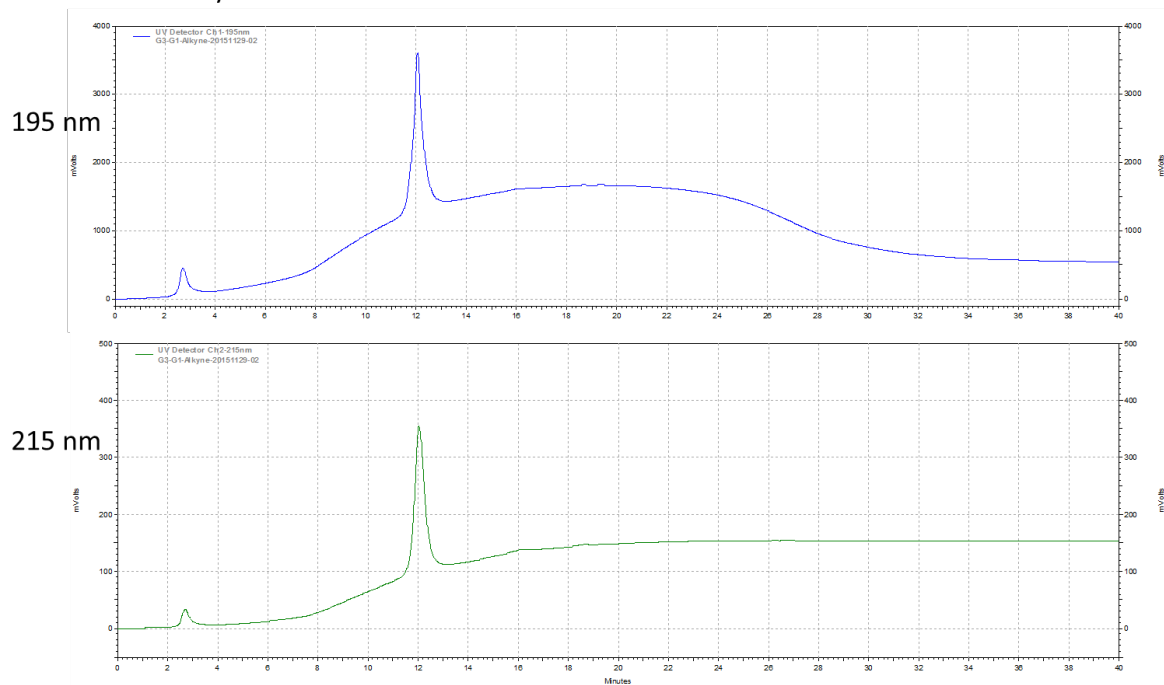


Figure 3.78 HPLC spectra of biotin-G3-G1-Alkyne

SB-T-1214-linker-PEG-azide-HPLC:

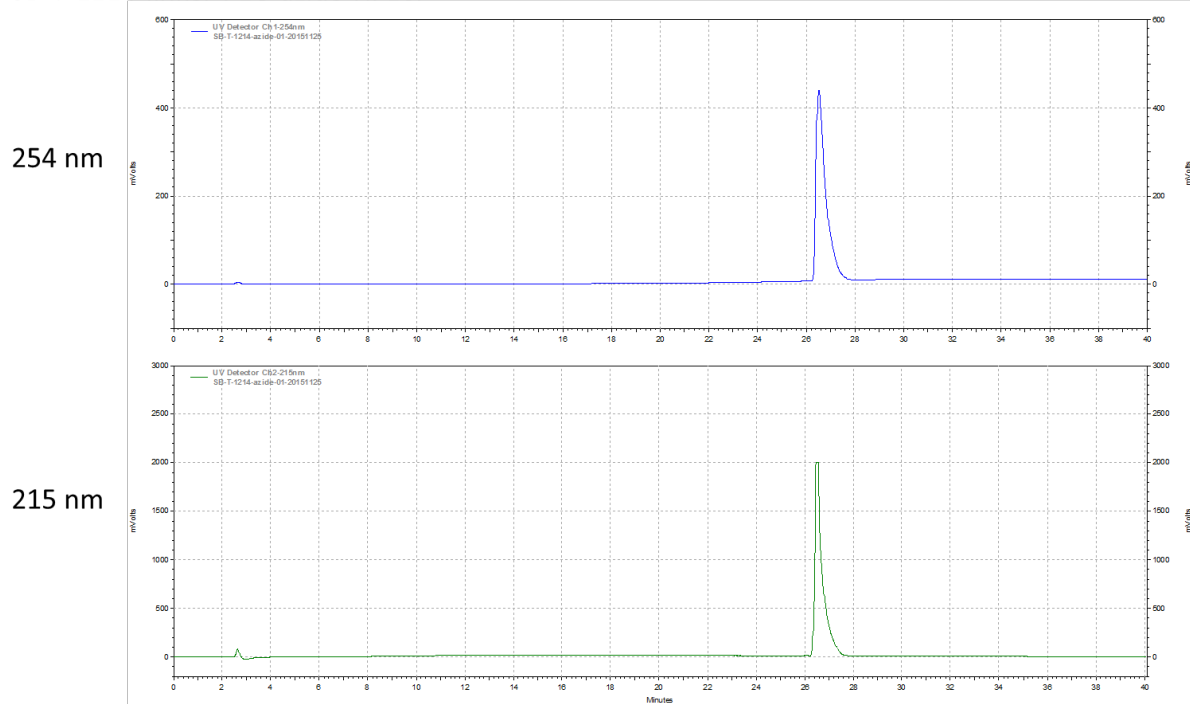
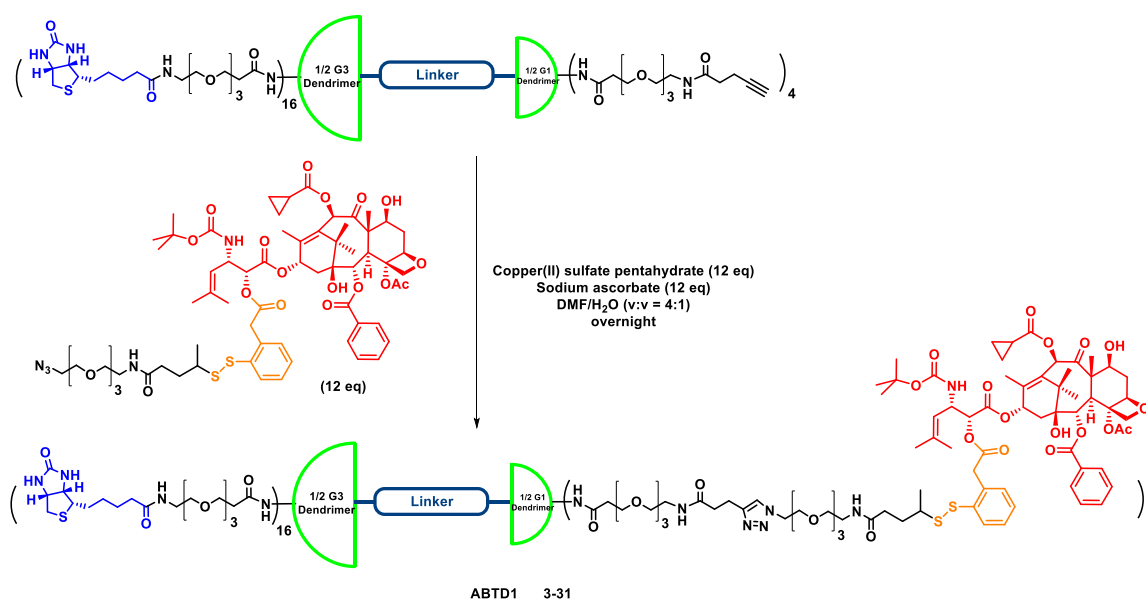


Figure 3.79 HPLC spectra of SB-T-1214-linker-PEG-azide

Then biotin-G3-G1-alkyne was reacted with excess SB-T-1214-linker-PEG-azide via CuAAC to afford ABTD1 (**Scheme 3.31**). Unfortunately, attempts to characterize the product by MALDI-TOF, ESI-MS, LC-MS, and HPLC were not successful. However, GPC analysis of the reaction mixture and starting material clearly indicates the click reaction went completion, since all the biotin-G3-G1-alkyne starting material disappeared, and the expected product, which has a larger molecular weight than the starting material, showed up as a single peak (**Figure 3.80**). GPC analysis was performed with a Shimadzu L-2010A HPLC HT series HPLC assembly, using a Waters Ultrahydrogel 500 GPC column (7.8 mm × 300 mm, 10 μm, 500 Å), using CH₃CN/water as the solvent system with a flow rate of 0.5 mL/min and a UV detector at 215nm.



Scheme 3.31 Synthesis of ABTD1 via CuAAC

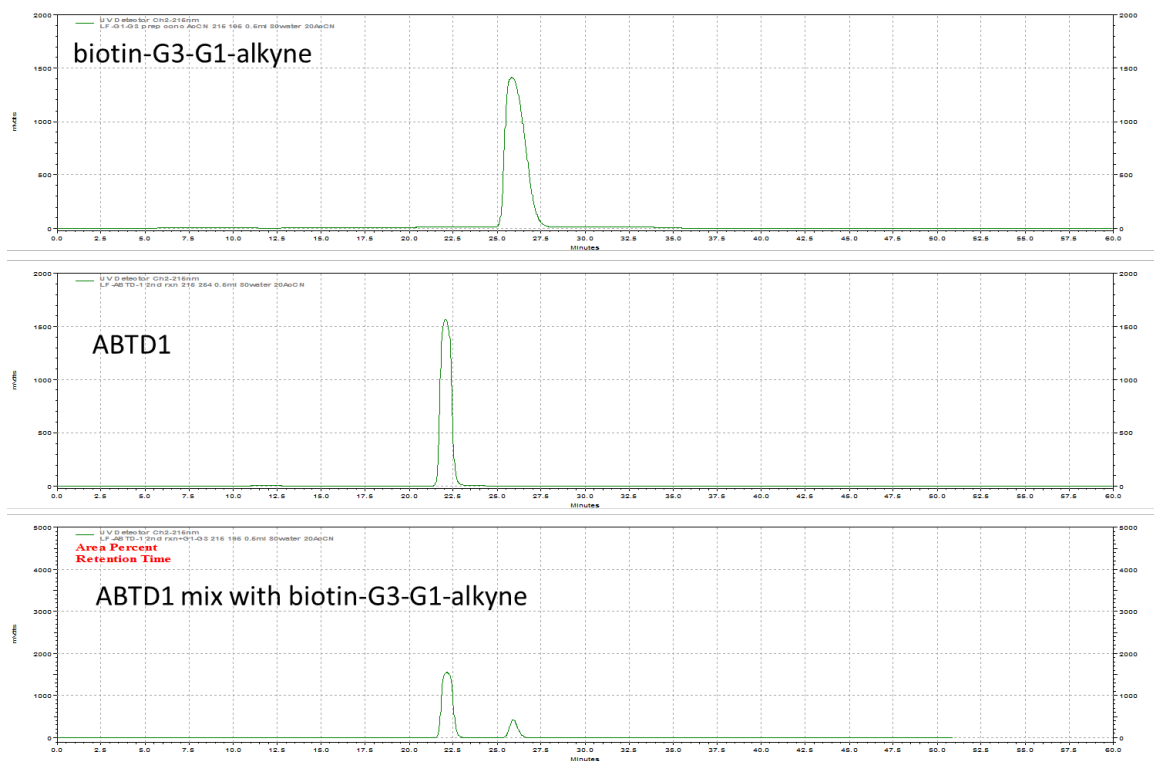
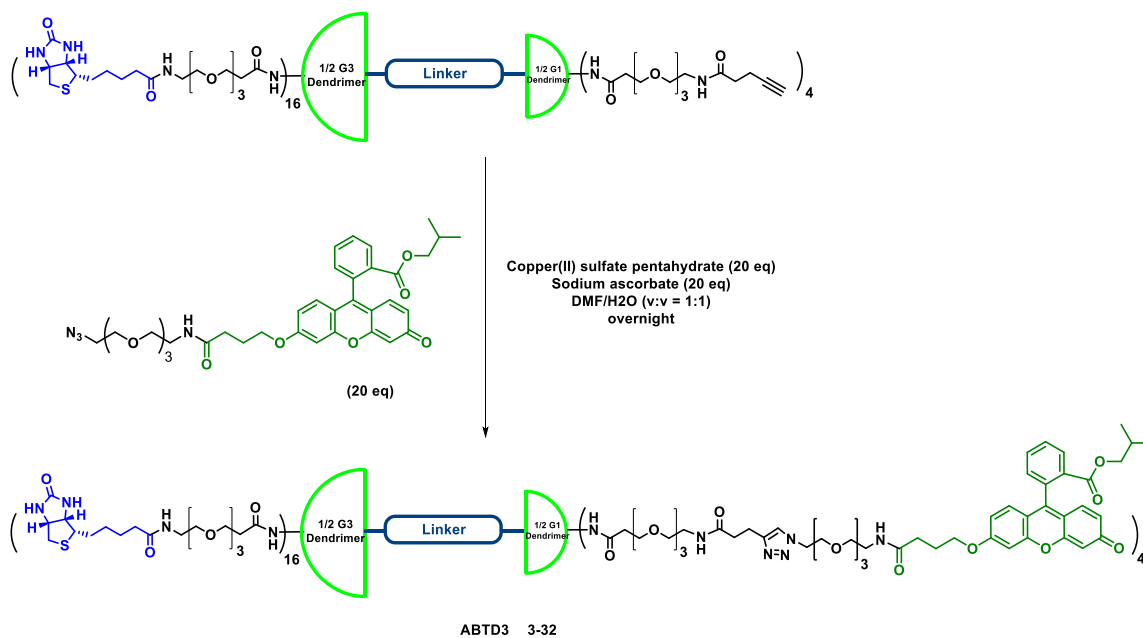


Figure 3.80 GPC analysis of ABTD1 and biotin-G3-G1-alkyne

Then, biotin-G3-G1-alkyne was reacted with excess FITC-PEG-azide via CuAAC to afford ABTD3 (**Scheme 3.32**). GPC analysis of this product again showed complete conversion of the starting material to a larger molecular weight product as a single peak (**Figure 3.81**). GPC analysis was performed with a Shimadzu L-2010A HPLC HT series HPLC assembly, using a Waters Ultrahydrogel 500 GPC column (7.8 mm × 300 mm, 10 μm, 500 Å), using CH₃CN/water as the solvent system with a flow rate of 0.5 mL/min and a UV detector at 215 nm.



Scheme 3.32 Synthesis of ABTD3 via CuAAC

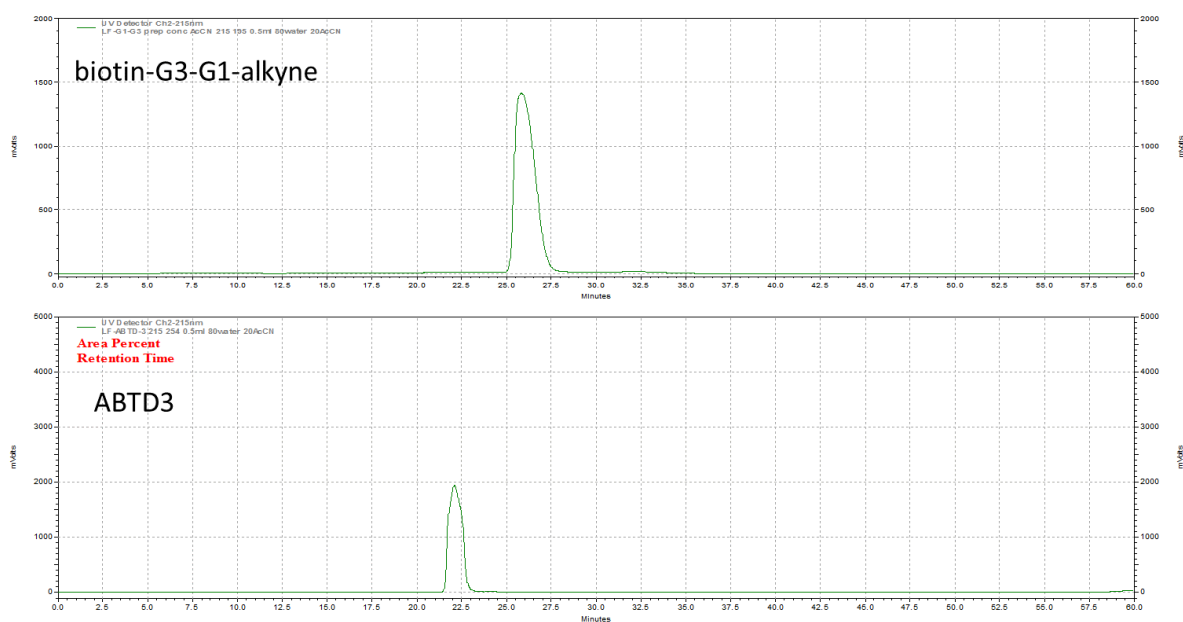


Figure 3.81 GPC analysis of ABTD3 and biotin-G3-G1-alkyne

§ 3.4 Tri-branched PAMAM Dendrimer-based Tumor-Targeting Theranostic Conjugates

§ 3.4.1 Rational Design

The initial design of tri-branched PAMAM dendrimer-based theranostic conjugate bearing tumor-targeting modules, cytotoxic warheads and MRI contrast agent is shown in **Figure 3.82**. The strategy for constructing this conjugate is similar as synthesizing the ABTD conjugates. The difference is using a tri-branched spacer bearing a triazine splitter to incorporate the MRI contrast agent instead of using a bismaleimide spacer. However, the problem found later on during the synthesis of this theranostic conjugate was that large excess of the tri-branched spacer is needed to ensure mono thiol-maleimido type Michael reaction proceeds when connecting the functionalized G1 and G3 dendrimers through the spacer. This was not a big problem when constructing the ABTD conjugates, because the bismaleimide spacer could be easily synthesized in large quantities in short steps, and also removal of the excess spacer used in the reaction by dialysis and prep-HPLC was not so difficult, since the property of the spacer is quite different from the functionalized dendrimers in terms of both molecular weight and polarity. In the synthesis of theranostic conjugate shown in **Figure 3.82**, however, removal the excess tri-branched spacer from reaction mixture was found to be not a trivial task. In addition, the tri-branched spacer is much more difficult to synthesize compared to the bismaleimide spacer, and using excess amount (10 eq) during the reaction made the overall synthesis inefficient.

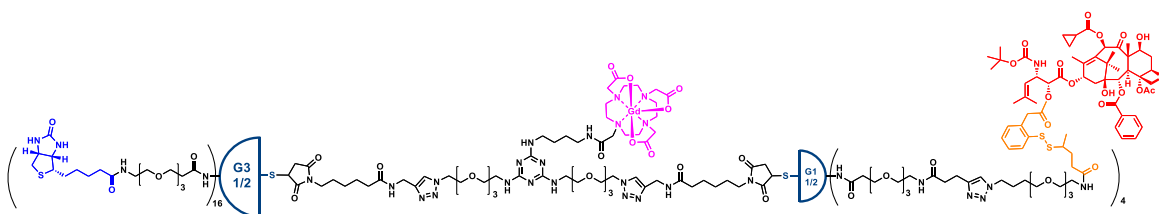


Figure 3.82 Designed tri-branched PAMAM dendrimer-based theranostic conjugate bearing tumor-targeting modules, cytotoxic warheads and MRI contrast agent.

To solve this problem, second-generation theranostic dendrimer conjugates were designed (**Figure 3.83** and **Figure 3.84**). The major difference is that a versatile tri-branched platform bearing taxoid warhead(s), tumor-targeting modules, and a terminal azide group could be constructed first, final attachment of the imaging modules through copper-catalyzed click reaction for attaching a fluorescent probe or copper-free click reaction for attaching a DOTA radionuclide chelator could be achieved in the late stage.

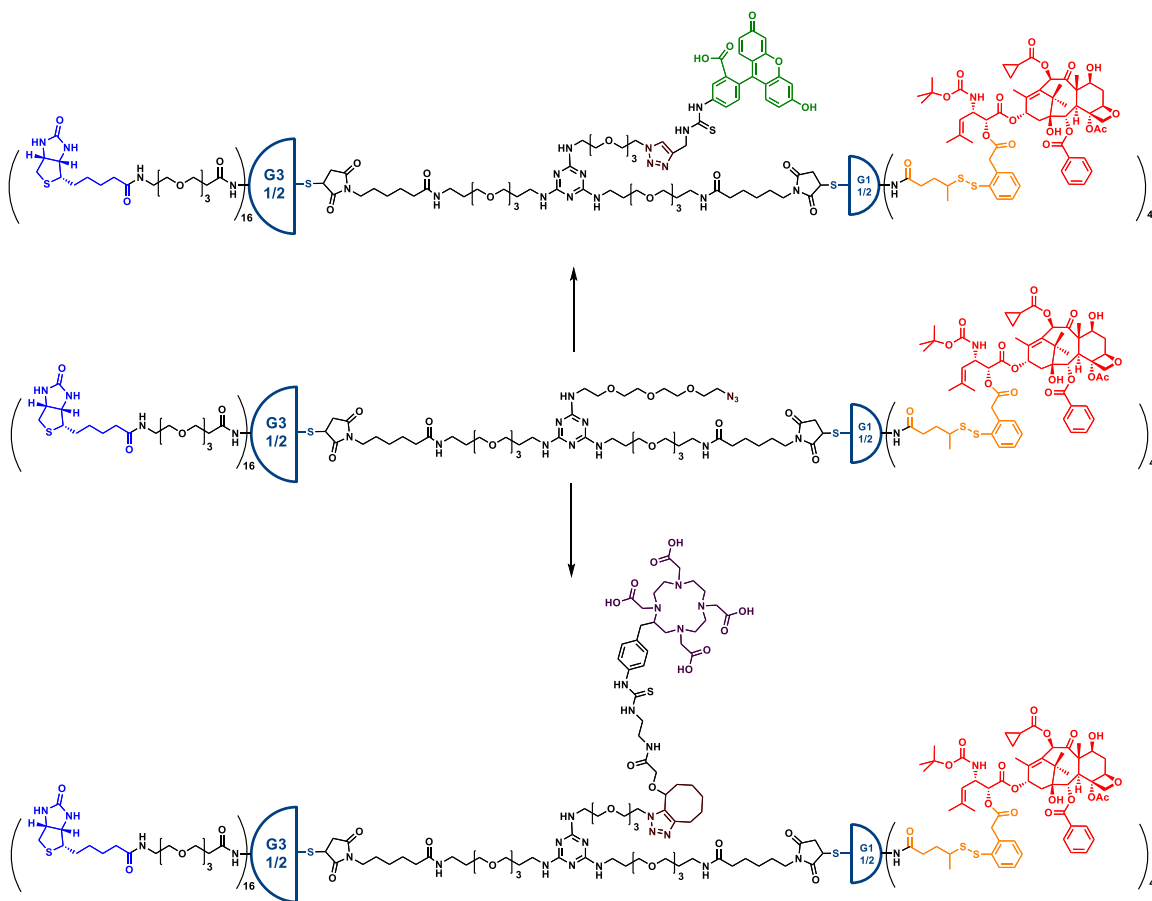


Figure 3.83 Designed tri-branched PAMAM dendrimer-based theranostic conjugates bearing tumor-targeting modules, cytotoxic warheads and fluorescent probe for *in vitro* internalization study, or DOTA radionuclide chelator for *in vivo* PET/SPECT imaging.

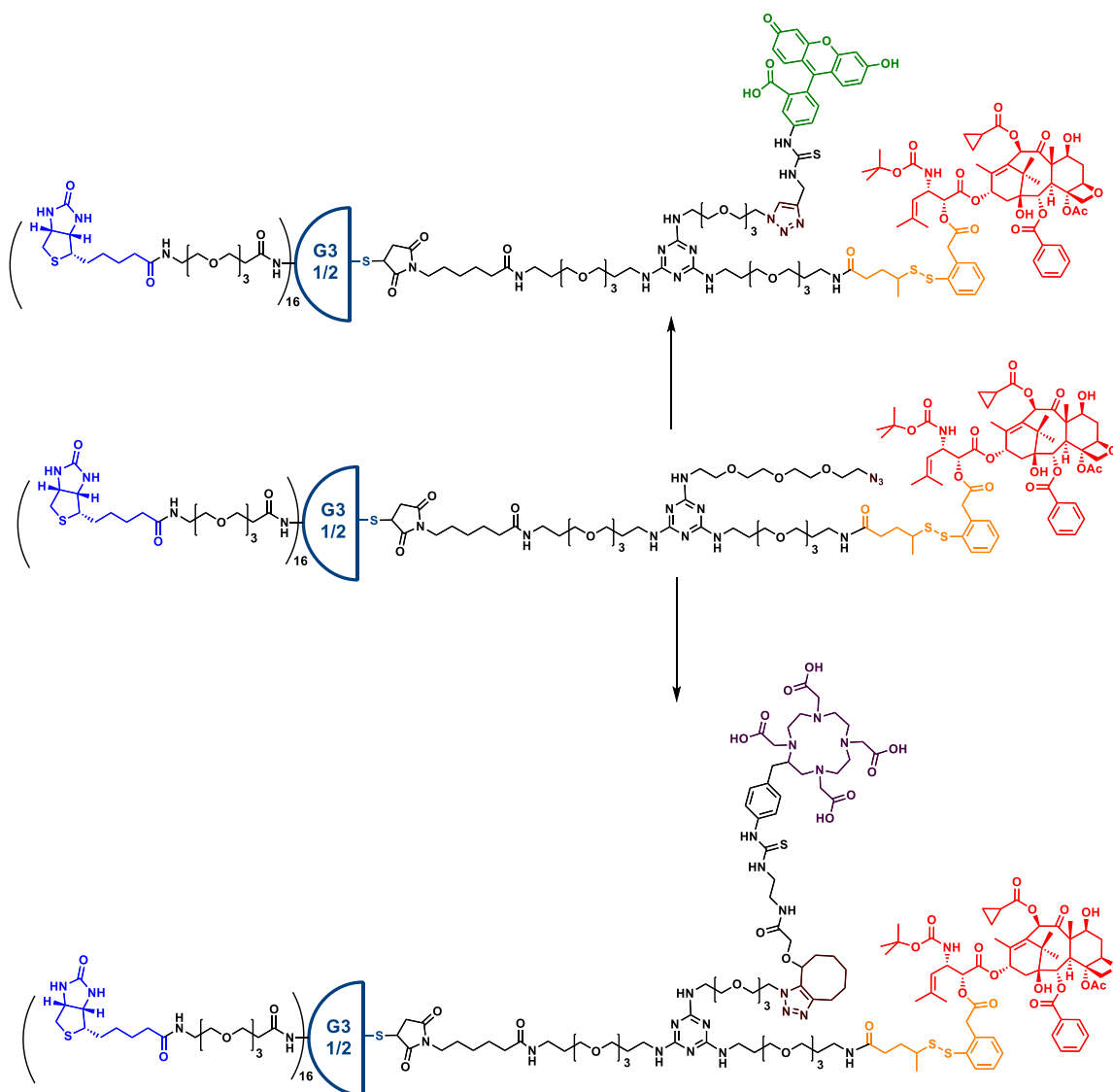
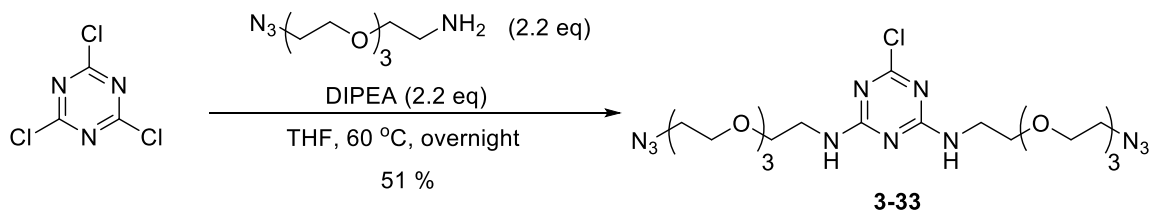


Figure 3.84 Designed tri-branched PAMAM dendrimer-based theranostic conjugates bearing single taxoid warhead.

§ 3.4.2 Towards Synthesis of a Tri-branched PAMAM Dendrimer-based Tumor-Targeting Theranostic Conjugate bearing MRI Contrast Agent

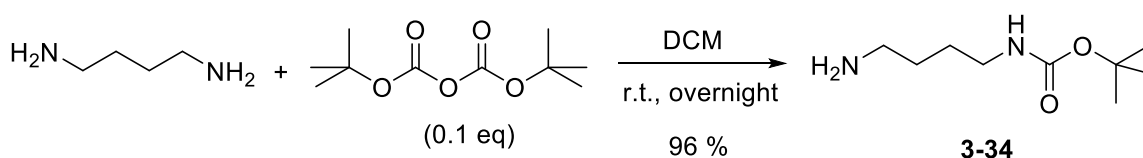
For constructing the PAMAM dendrimer-based theranostic conjugate bearing MRI contrast agent shown in **Figure 3.82**, a tri-branched spacer was synthesized.

First, cyanuric chloride was used to react with 2.2 eq amino-PEG-azide to give desired di-azide **3-33** in 51% yield (**Scheme 3.33**). Mono-azide was also obtained as side product (27%), and could be easily separated by column chromatography.



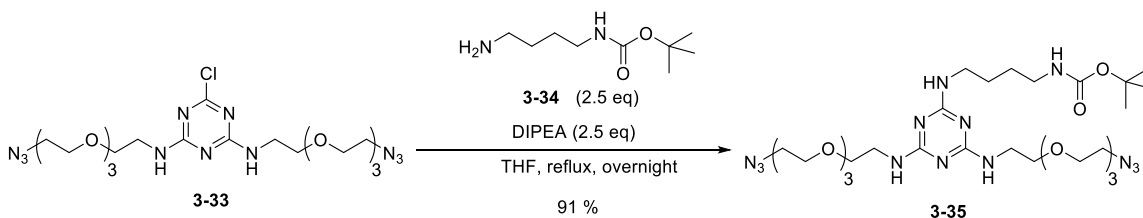
Scheme 3.33 Synthesis of diazide **3-33**

For attaching the third branch, 1,4-diaminobutane was reacted with Boc anhydride to give mono-Boc-1,4-diaminobutane **3-34** in 96% crude yield (**Scheme 3.34**). To ensure minimum formation of di-Boc side product, the reaction was performed in very dilute condition, and Boc anhydride was added very slow.



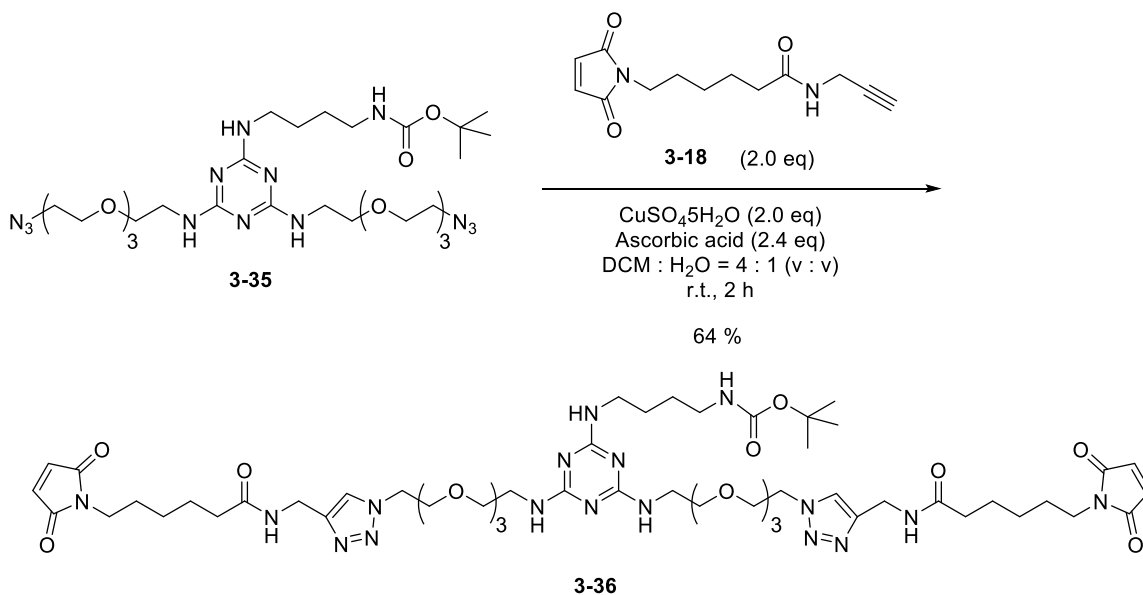
Scheme 3.34 Synthesis of mono-Boc-1,4-diaminobutane **3-34**

Then, diazide **3-33** was reacted with excess mono-Boc-1,4-diaminobutane **3-34** under reflux condition in THF to give tri-branched intermediate **3-35** in 91% yield (**Scheme 3.35**).



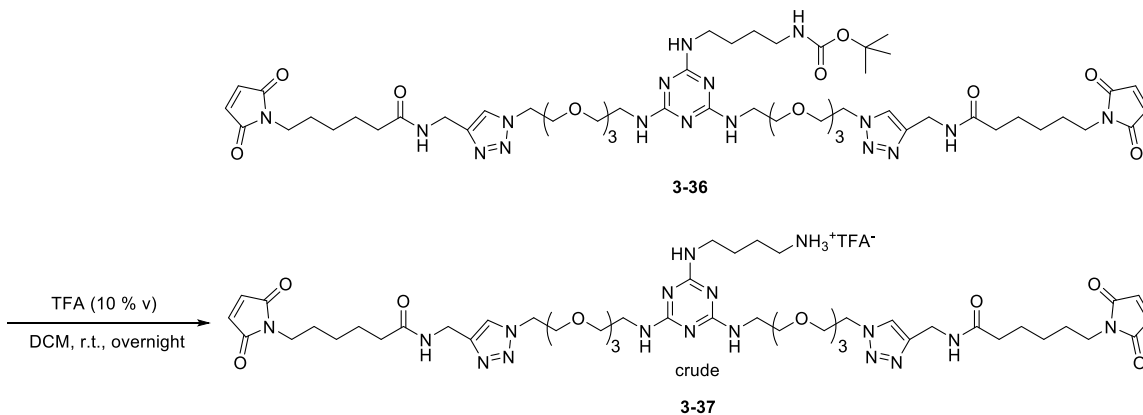
Scheme 3.35 Synthesis of tri-branched intermediate **3-35**

Tri-branched intermediate **3-35** was then reacted with two equivalents of maleimido-alkyne **3-18** *via* copper-catalyzed click chemistry to give tri-branched spacer **3-36** in 64% yield (**Scheme 3.36**).



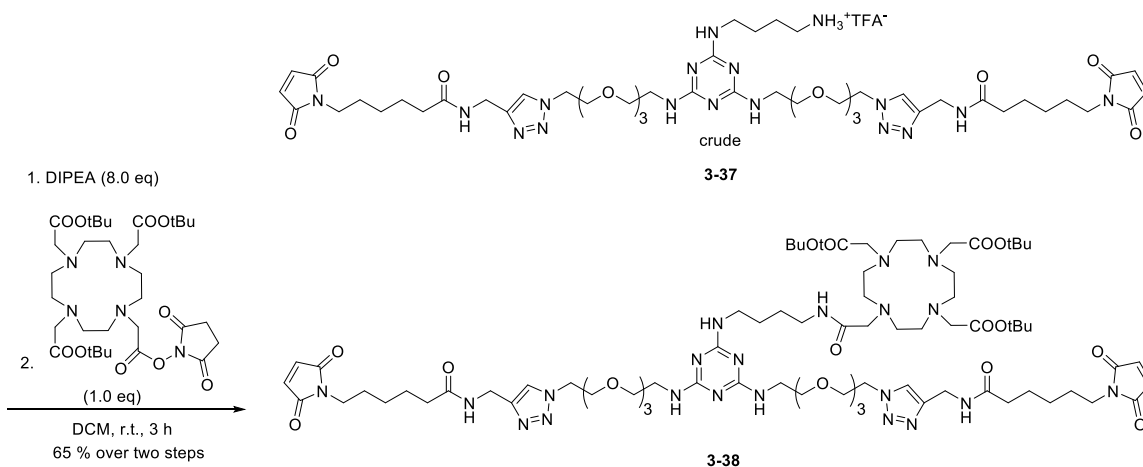
Scheme 3.36 Synthesis of tri-branched spacer **3-36**

Tri-branched spacer **3-36** was subjected to TFA deprotection condition to remove the Boc protecting group, giving crude product **3-37** as a TFA salt (**Scheme 3.37**).



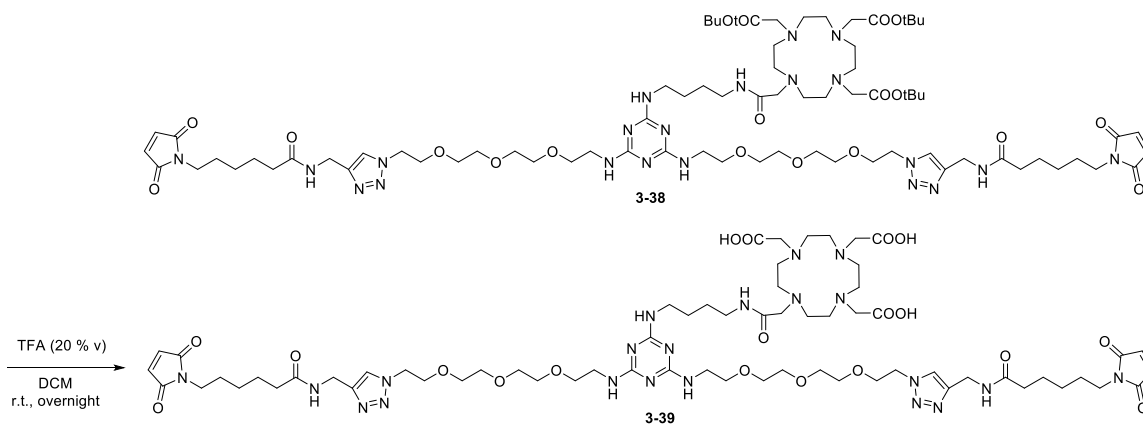
Scheme 3.37 TFA deprotection of **3-36**

Then, intermediate **3-37** was treated with excess base DIPEA to remove TFA, and the free amine could then react with DOTA-tri-*t*Bu-mono-NHS ester to give compound **3-38** in 65% yield over two steps (**Scheme 3.38**).



Scheme 3.38 Attachment of DOTA chelator onto tri-branched spacer **3-37**

Compound **3-38** was then treated with TFA to remove all three t-Bu protecting groups on the DOTA chelating group to give compound **3-39** as a crude product (**Scheme 3.39**). This product was characterized by MALDI-TOF (**Figure 3.85**).



Scheme 3.39 TFA deprotection of **3-38**

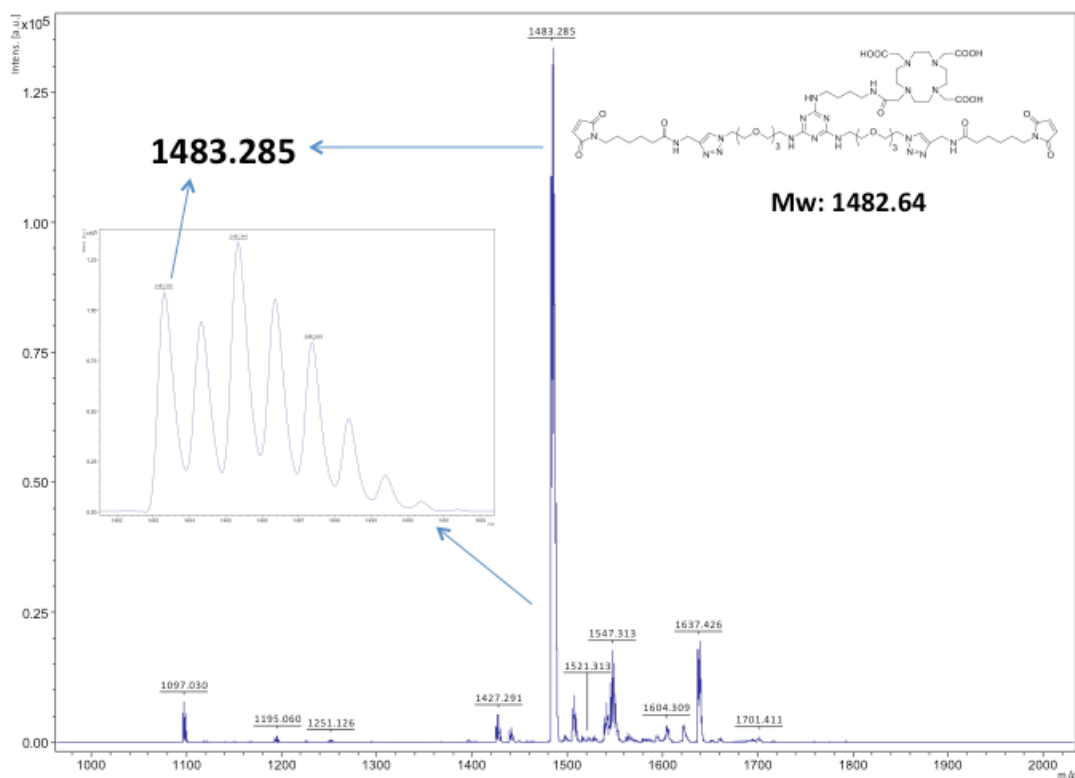
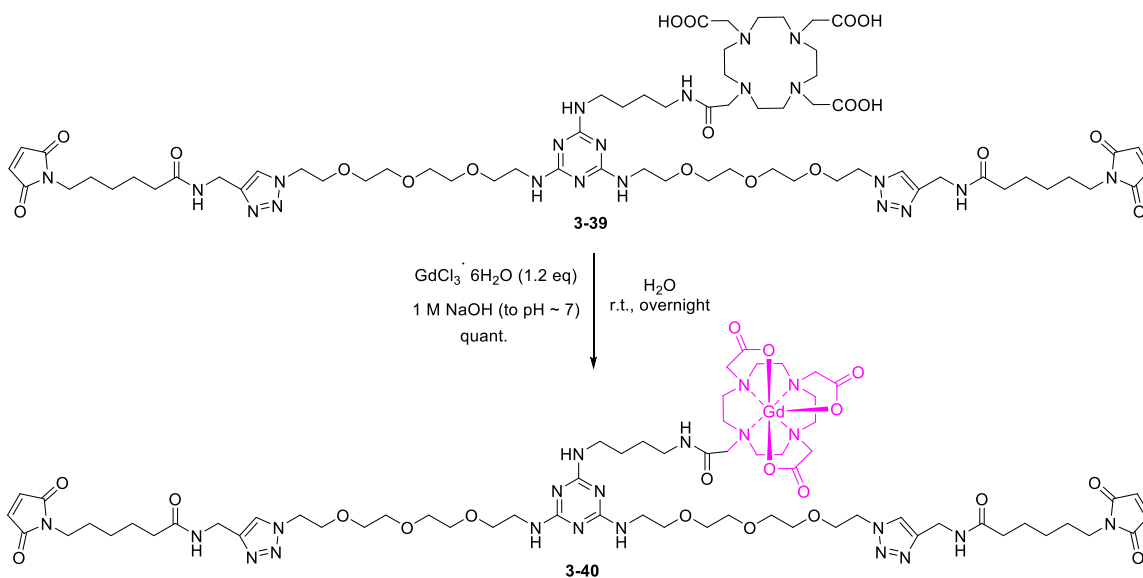


Figure 3.85 MALDI-TOF spectrum of compound **3-39**

With tri-branched spacer bearing DOTA chelating group **3-39** in hand, chelation with gadolinium (III) was attempted. In the first attempt, potassium hydroxide was used as the base to adjust the pH to 14, and water/methanol was used as solvent. It was clearly observed during the experiment that while the chelation was happening when adjusting the pH, the solution turned from white-milky color to pink color. Also, excess gadolinium (III) reacted with potassium hydroxide to afford gadolinium (III) hydroxide, which showed as a white precipitate during the reaction. However, on the MALDI-TOF spectrum, the product showed as a methanol adduct. In the second attempt, sodium hydroxide was used as the base to adjust the pH to 7, and water was used as solvent (**Scheme 3.40**). In this condition, desired product **3-40** was clearly observed on MALDI-TOF spectrum (**Figure 3.86**).



Scheme 3.40 Chelation of tri-branched spacer **3-39** with Gd (III)

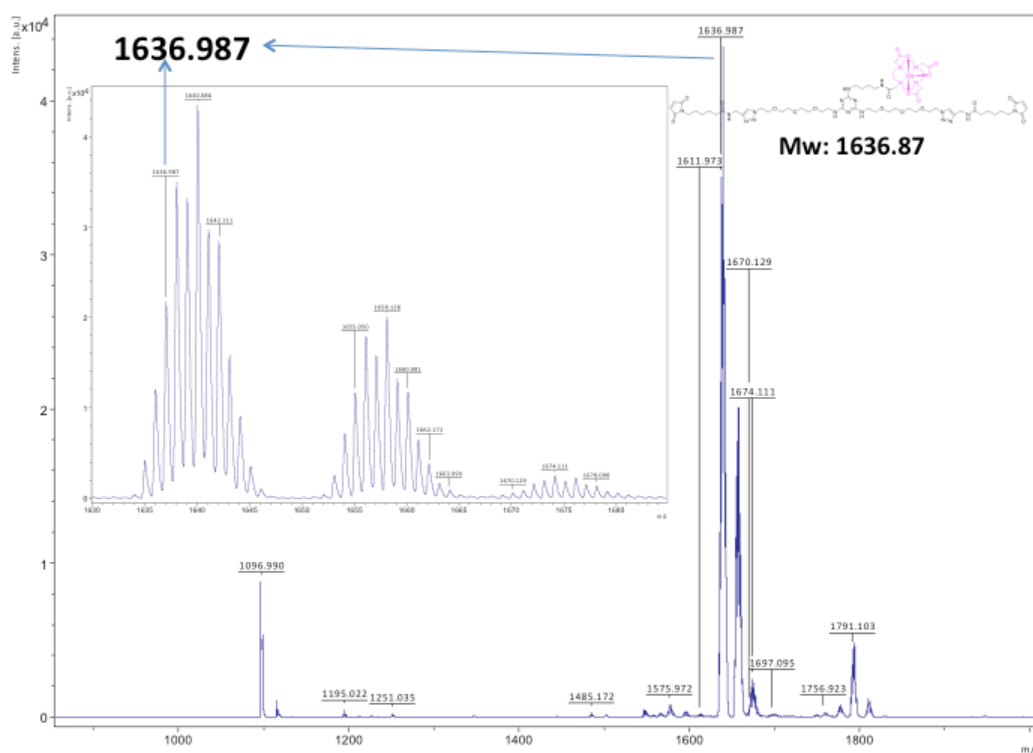
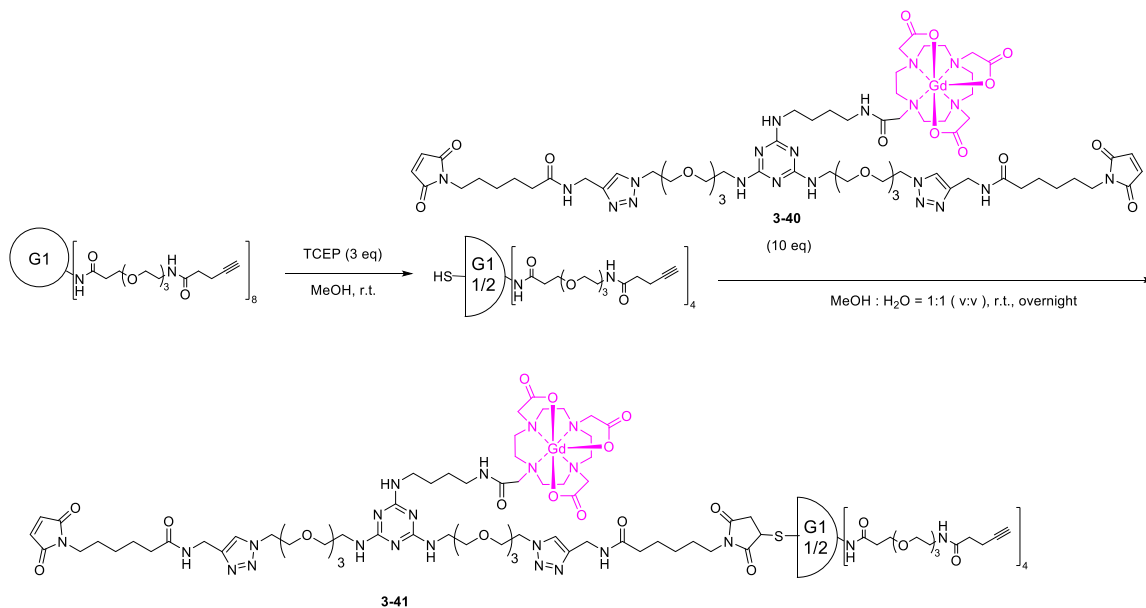


Figure 3.86 MALDI-TOF spectrum of compound **3-40**

After successfully chelating tri-branched spacer with gadolinium (III), conjugation of alkyne-PEGylated-G1 PAMAM half dendron onto this spacer was attempted. Alkyne-PEGylated-G1 PAMAM dendrimer was first treated with excess TCEP to reduce the

disulfide bond in the core to give the half dendron bearing free thiol. Then this thiol intermediate was reacted with excess tri-branched spacer bearing MRI contrast agent **3-40** to give conjugate **3-41** (Scheme 3.41). The product formation was observed on MALDI-TOF spectrum (Figure 3.87). However, purification of the product by dialysis with Mw cut-off 2000 membrane to remove the excess tri-branched spacer bearing MRI contrast agent **3-40** was unsuccessful. Unfortunately, the retention time of the excess tri-branched spacer bearing MRI contrast agent **3-40** is very close to the desired product **3-41**, purification by preparative HPLC is also not practical.



Scheme 3.41 Conjugation of alkyne PEGylated half G1 dendron onto tri-branched spacer

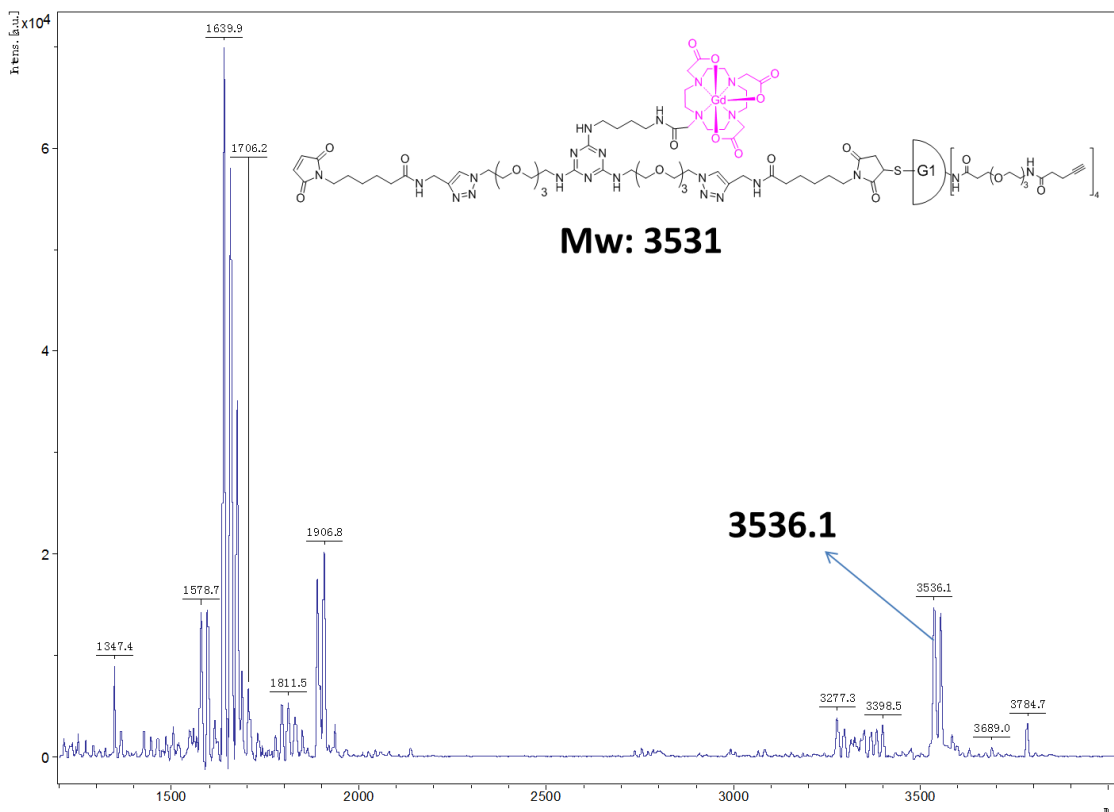


Figure 3.87 MALDI-TOF spectrum of conjugate 3-41

§ 3.4.3 Towards Synthesis of Second-Generation Versatile Tri-branched PAMAM Dendrimer-based Tumor-Targeting Theranostic Conjugates-Route 1

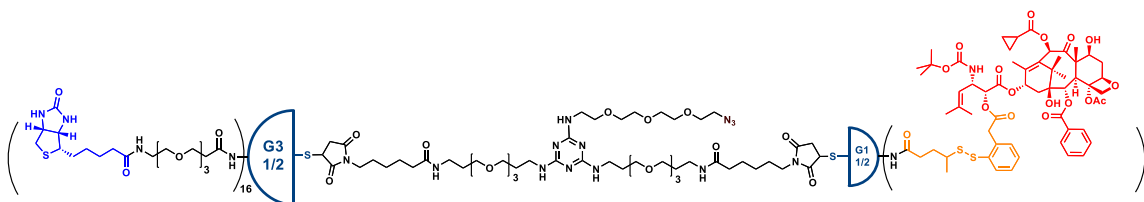


Figure 3.88 Designed tri-branched PAMAM dendrimer platform bearing four taxoids

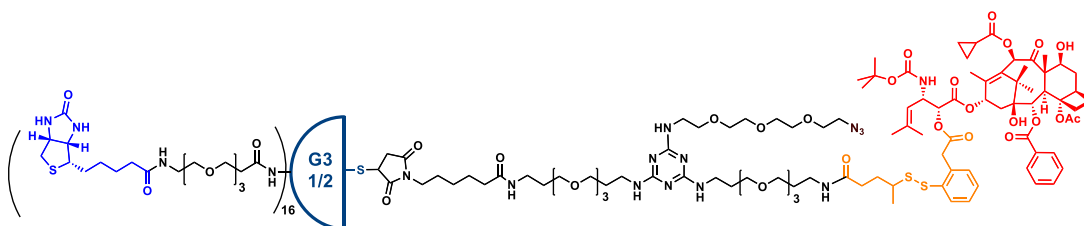


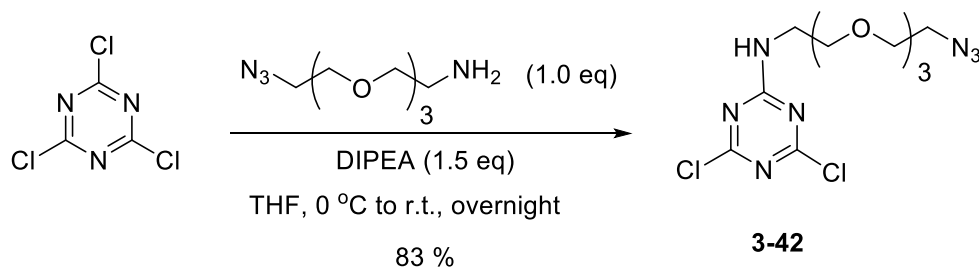
Figure 3.89 Designed tri-branched PAMAM dendrimer platform bearing single taxoid

To solve the problem mentioned above, second-generation versatile tri-branched PAMAM dendrimer platforms bearing either four taxoids on a half G1 dendron (**Figure**

3.88) or just single taxoid warhead (**Figure 3.89**) were designed. A terminal azide on the third branch could be used for final attachment of imaging module.

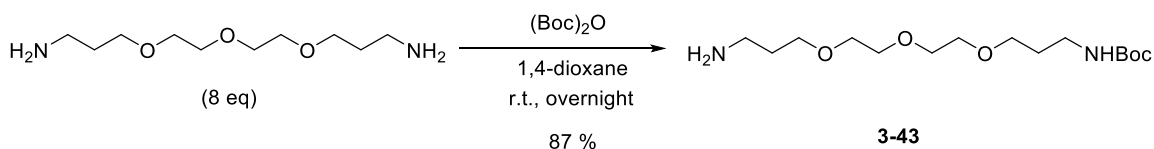
For the synthesis of tri-branched platform shown in **Figure 3.88**, two different synthetic routes were explored.

In the first synthetic route, first, cyanuric chloride was used to react with 1 eq of amino-PEG-azide to give mono reacted product **3-42** 83% yield (**Scheme 3.42**).



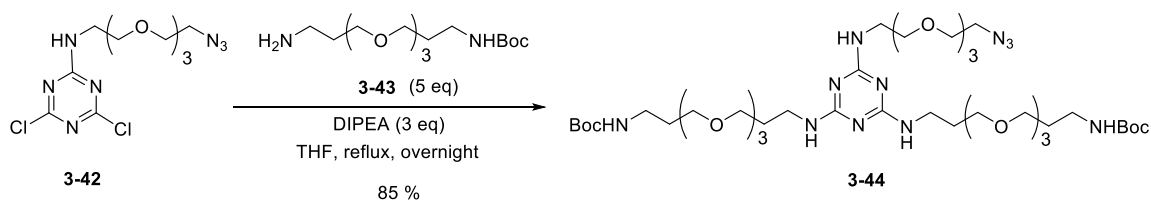
Scheme 3.42 Synthesis of mono-azide **3-42**

Then, commercially available PEG-diamine was treated with Boc anhydride to give mono-Boc-PEG-diamine **3-43** in 87% yield (**Scheme 3.43**). PEG-diamine was used in large excess to avoid di-Boc protected side product. The desired product could be separated from excess PEG-diamine by a simple workup, since the starting material is highly water soluble.



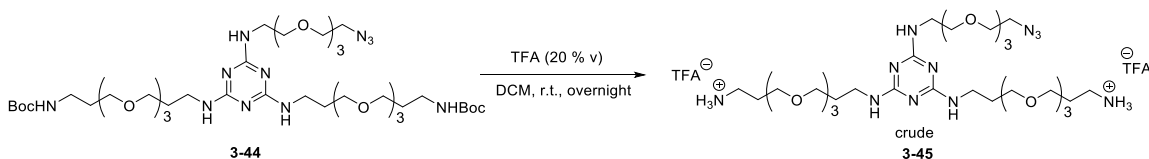
Scheme 3.43 Synthesis of mono-Boc-PEG-diamine **3-43**

Then, compound **3-42** was reacted with excess amount of mono-Boc-PEG-diamine **3-43** to afford triazine intermediate **3-44** in 85% yield under reflux condition in THF (**Scheme 3.44**). Large excess of mono-Boc-PEG-diamine **3-43** (5 eq) was used to push the reaction to go completion. It was found that when only slight excess of mono-Boc-PEG-diamine **3-43** (3 eq) was used under same condition, the conversion of this reaction is very low (~ 50%).



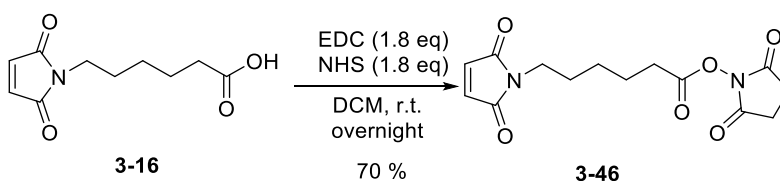
Scheme 3.44 Synthesis of triazine intermediate **3-44**

Subsequent TFA deprotection of both Boc protecting groups in **3-44** gives crude product **3-45** as a TFA salt (**Scheme 3.45**).



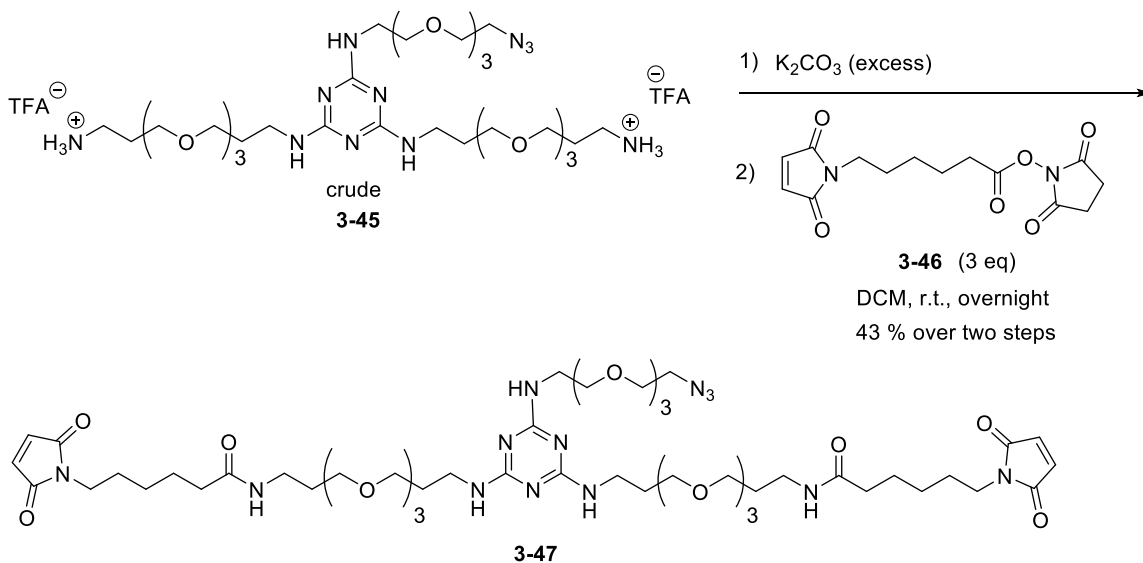
Scheme 3.45 TFA deprotection of **3-44**

On the other hand, 6-maleimidocaproic acid was activated with NHS by EDC coupling to give the activated ester **3-46** in 70% yield (**Scheme 3.46**).



Scheme 3.46 Synthesis of activated ester **3-46**

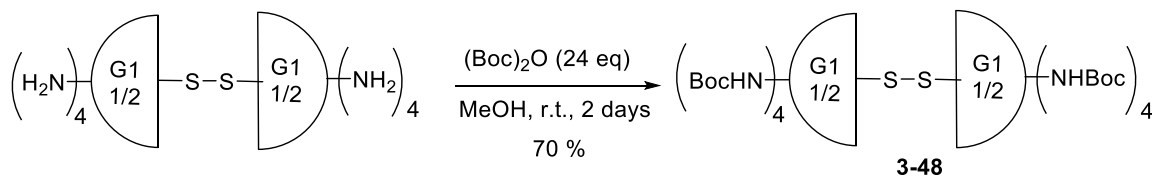
After that, excess potassium carbonate was used to neutralize TFA in the crude product **3-45**, the resulting free diamine product was directly treated with activated ester **3-46** to give tri-branched spacer **3-47** in 43% yield over two steps (**Scheme 3.47**).



Scheme 3.47 Synthesis of tri-branched spacer **3-47**

G1 PAMAM dendrimer was then treated with excess Boc anhydride to give Boc protected G1 PAMAM dendrimer **3-48** in 70% yield after dialysis (**Scheme 3.48**). The

product was characterized by ESI-MS, showing the multiple charge states (+2, +3, +3) of desired mass (**Figure 3.90**).



Scheme 3.48 Synthesis Boc protected G1 PAMAM dendrimer **3-48**

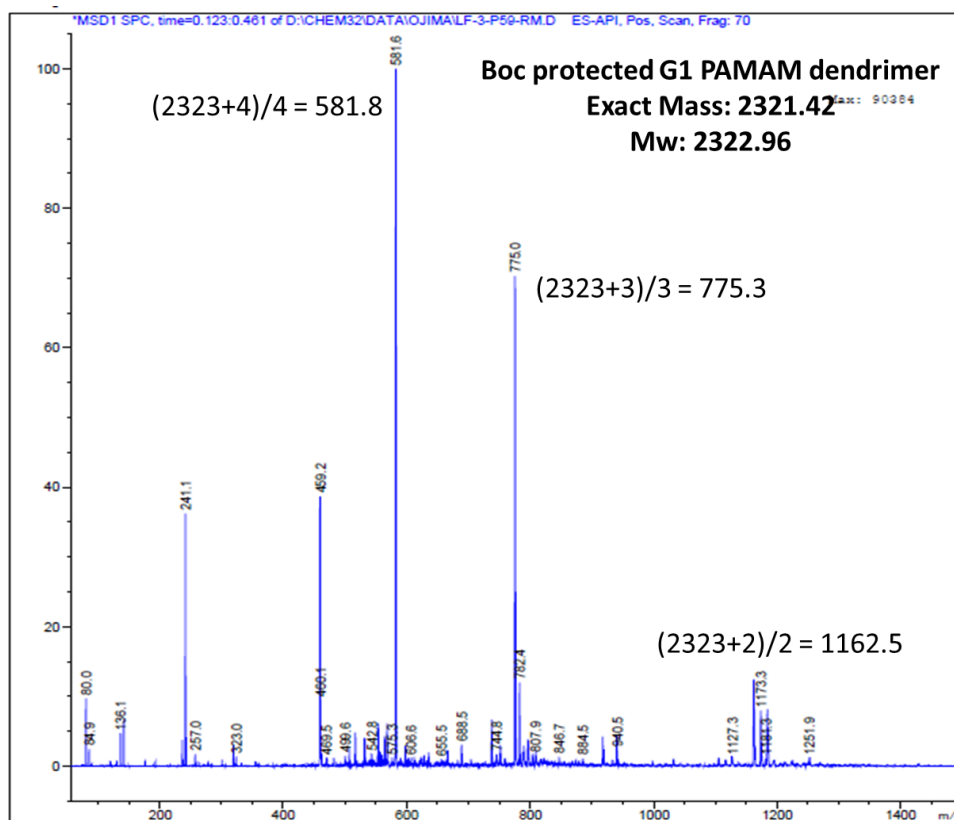
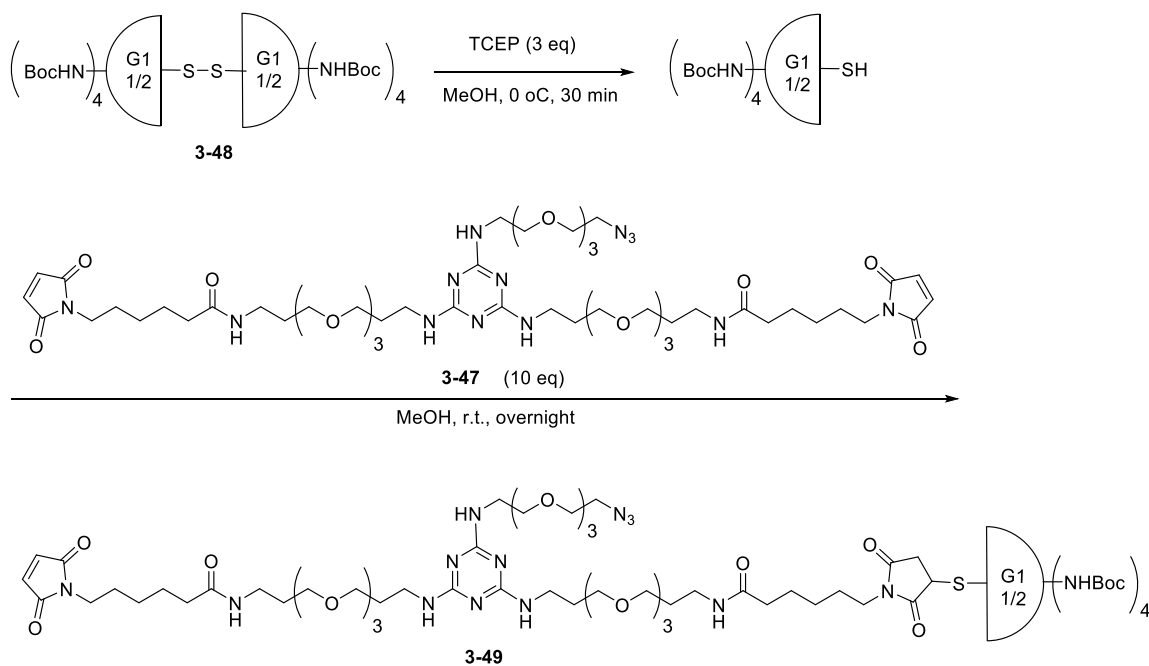


Figure 3.90 ESI-MS spectrum of Boc protected G1 PAMAM dendrimer **3-48**

Subsequently, Boc protected G1 PAMAM dendrimer **3-48** was treated with excess reducing agent TCEP to cleave the disulfide bond in the core, and the half Boc protected G1 dendron was reacted with excess tri-branched spacer **3-47** to give conjugate **3-49** (**Scheme 3.49**). The product was purified by dialysis, and characterized by MALD-TOF and ESI-MS, however, it was found that dialysis could not remove the excess tri-branched spacer **3-47**, and prep-HPLC need to be used to obtain pure product (**Figure 3.91** and **Figure 3.92**).



Scheme 3.49 Synthesis of conjugate **3-49**

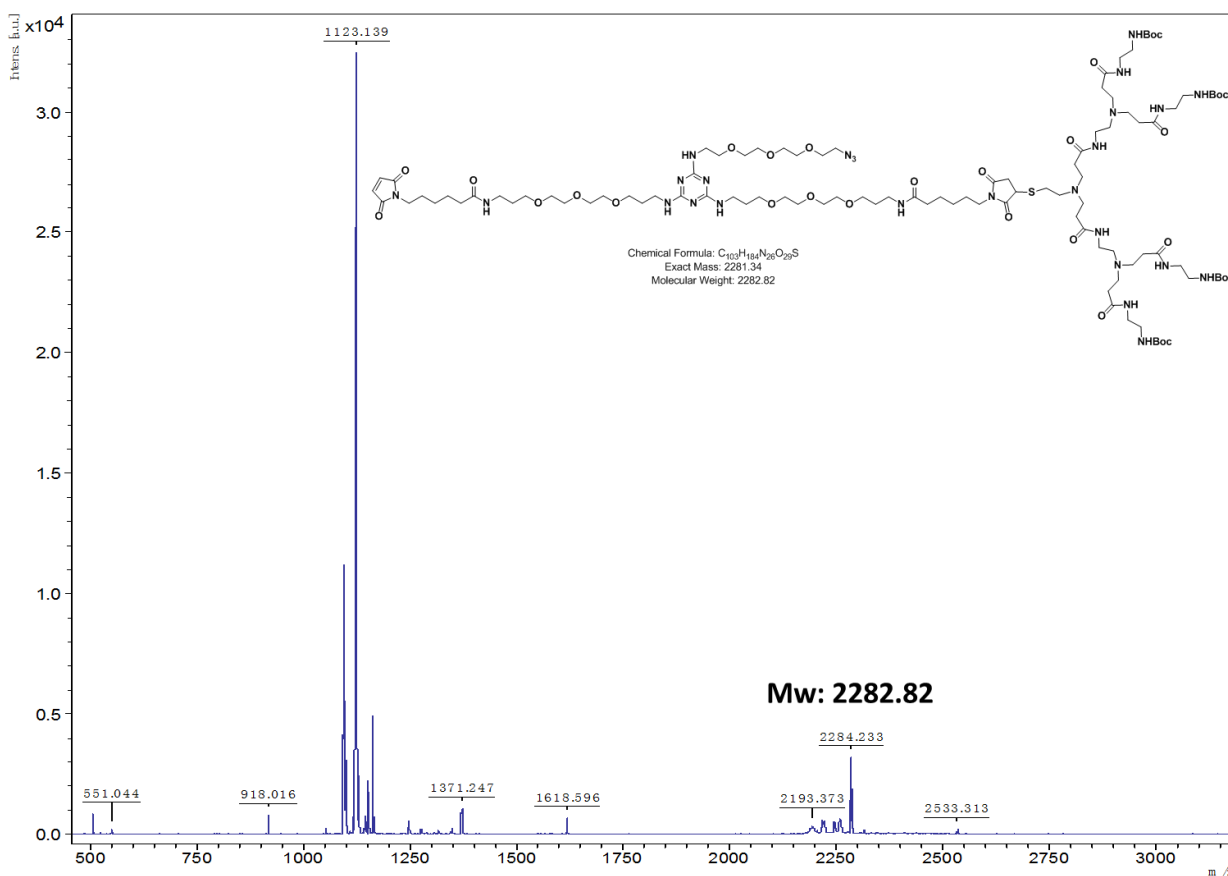


Figure 3.91 MALDI-TOF spectrum of conjugate **3-49**

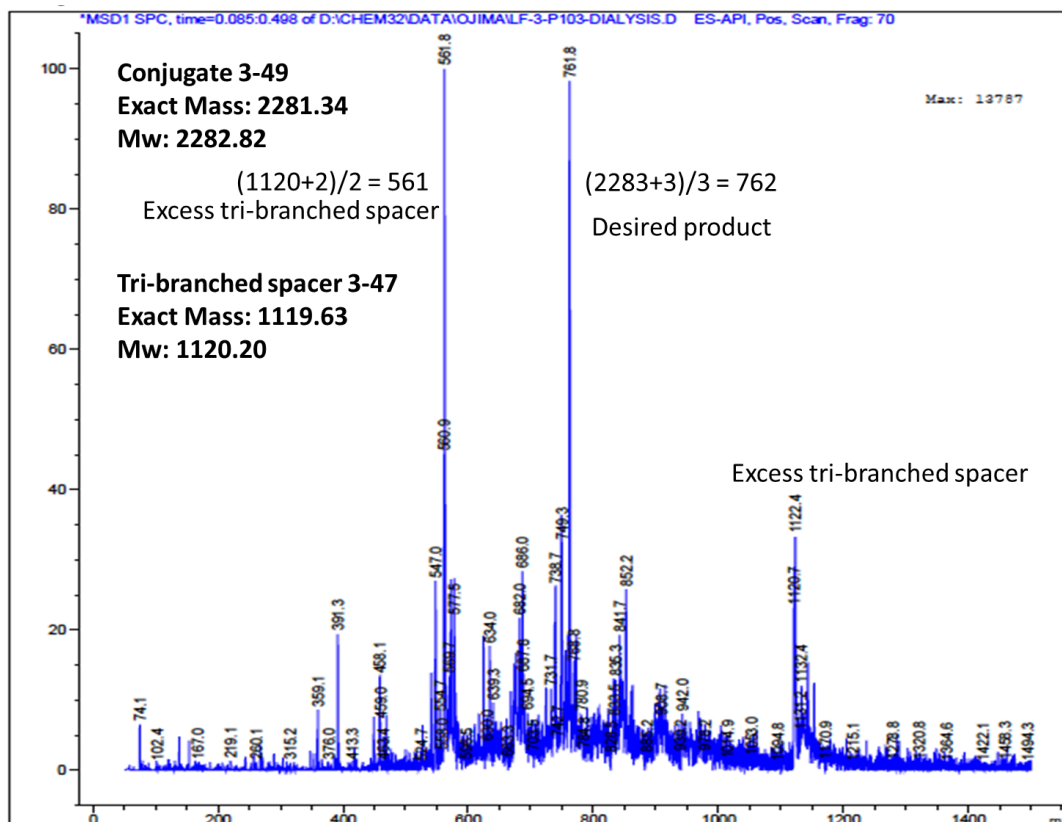
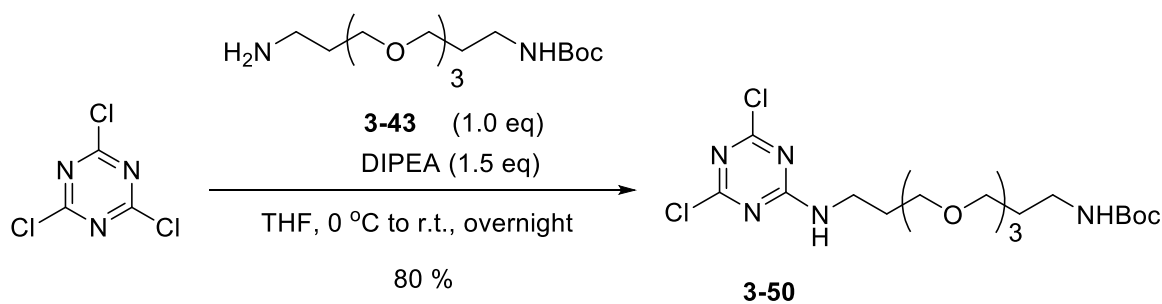


Figure 3.92 ESI-MS spectrum of conjugate 3-49 after dialysis

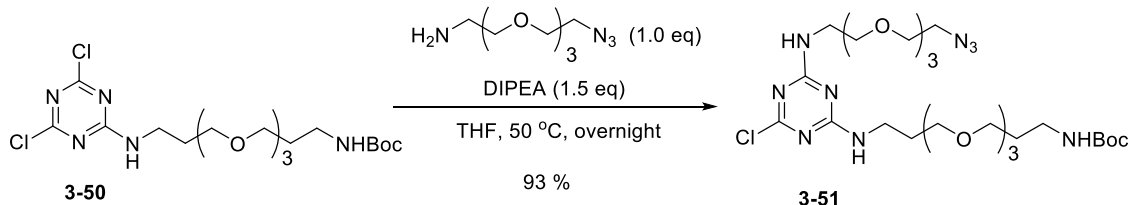
§ 3.4.4 Towards Synthesis of Second-Generation Versatile Tri-branched PAMAM Dendrimer-based Tumor-Targeting Theranostic Conjugates-Route 2

To avoid using large excess of tri-branched spacer, a second synthetic route was investigated. In this route, first, cyanuric acid was reacted with only one equivalent of mono-Boc- PEG-diamine **3-43** in the presence of DIPEA to give **3-50** in 80% yield (Scheme 3.50).



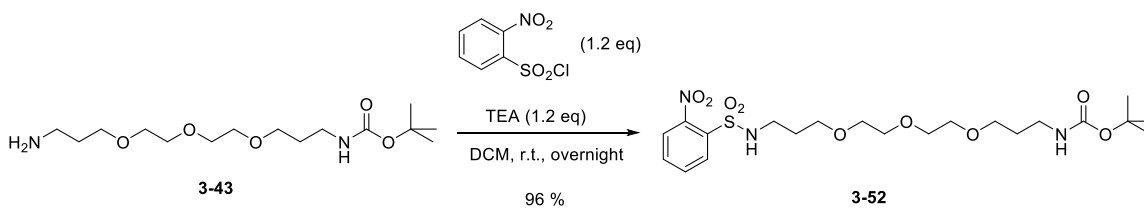
Scheme 3.50 Synthesis of 3-50

Then, **3-50** was reacted with one equivalent of amino-PEG-azide at 50 °C to give intermediate **3-51** in 93% yield (Scheme 3.51).



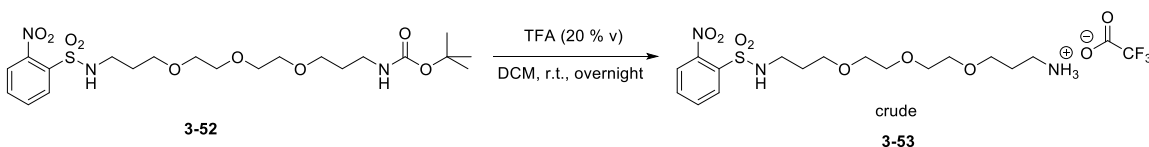
Scheme 3.51 Synthesis of **3-51**

On the other hand, mono-Boc-PEG-diamine **3-43** was treated with NsCl in the presence of TEA to give **3-52** in 96% yield (**Scheme 3.52**).



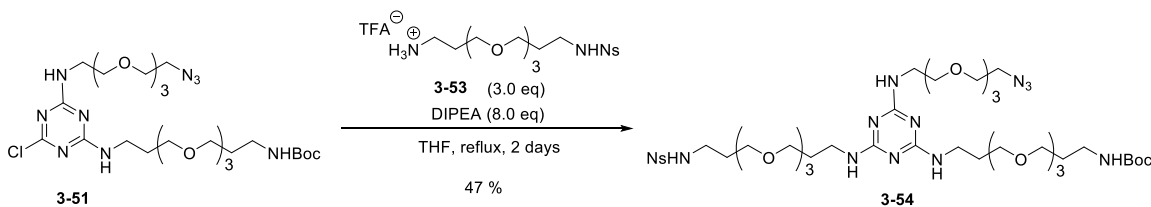
Scheme 3.52 Synthesis of Ns protected Boc-PEG-diamine

Subsequent deprotection of Boc group by TFA gave mono-Ns-PEG-diamine **3-53** as a crude TFA salt (**Scheme 3.53**).



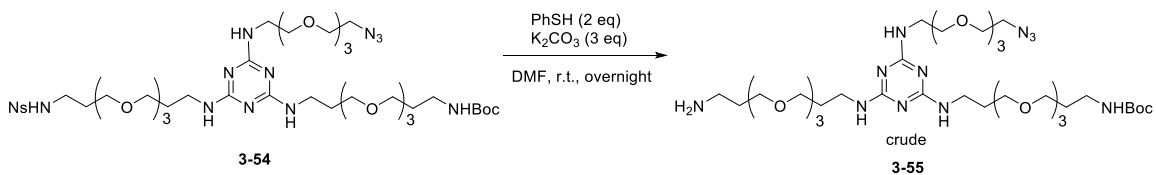
Scheme 3.53 TFA deprotection of **3-52**

Then, intermediate **3-51** was reacted with excess mono-Ns-PEG-diamine **3-53** under reflux condition in THF, desired product **3-54** was formed, and was isolated in 47% yield (**Scheme 3.54**). The yield for this step is low because the reaction could not go to completion even after reflux for two days.



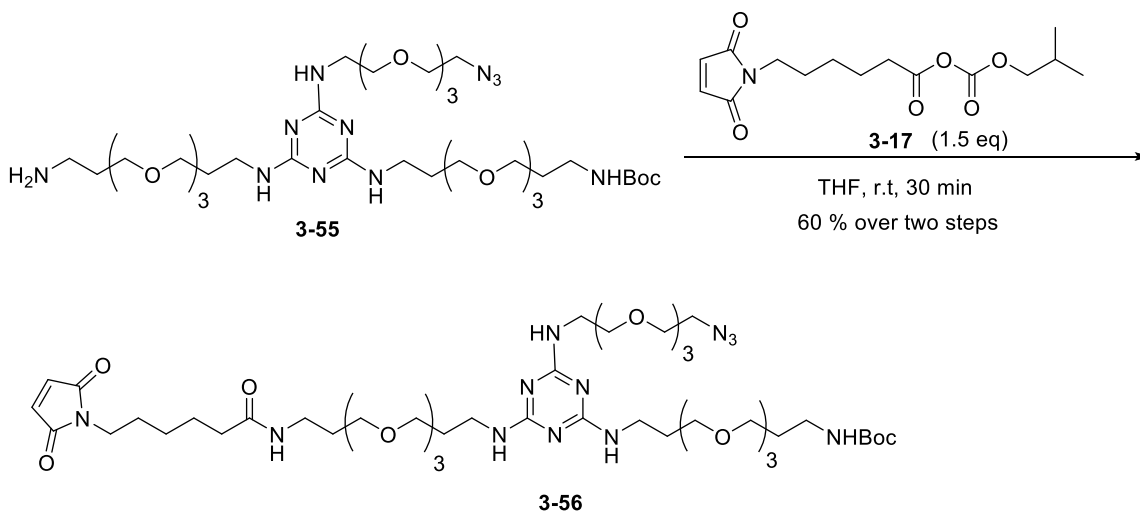
Scheme 3.54 Synthesis of tri-branched intermediate **3-54**

Tri-branched intermediate **3-54** with a terminal azide group, a Boc protected amine group, and an Ns protected amine group was then treated with thiophenol to remove the Ns group to give free amine **3-55** as a crude product (**Scheme 3.55**).



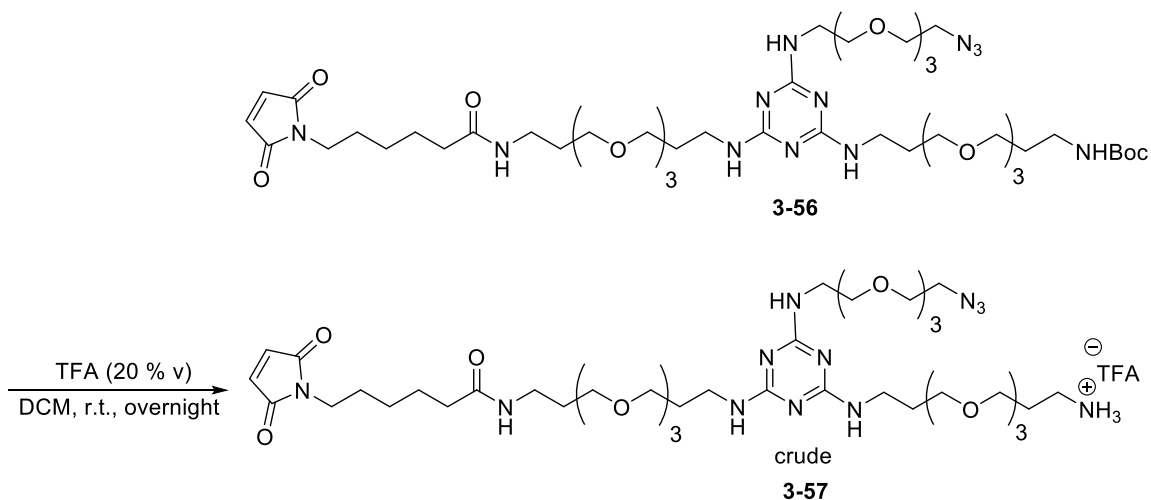
Scheme 3.55 Removal of Ns group by thiophenol

Free amine **3-55** was then treated with mixed anhydride **3-17** to give intermediate **3-56** in 60% yield over two steps (**Scheme 3.56**).



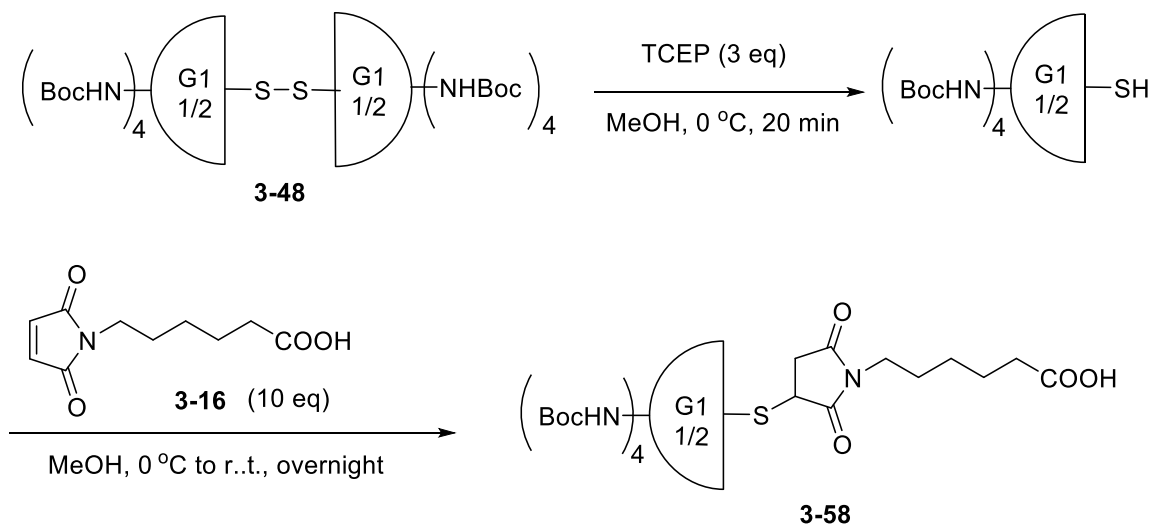
Scheme 3.56 Synthesis of intermediate **3-56**

Subsequent TFA deprotection of the Boc protecting group in **3-56** give amine **3-57** as a crude TFA salt (**Scheme 3.57**).



Scheme 3.57 TFA deprotection of **3-56**

In the meantime, Boc protected G1 PAMAM dendrimer **3-48** was treated with reducing agent TCEP, and the disulfide core was cleaved and subsequently reacted with excess amount of 6-maleimidocaproic acid **3-16** to afford conjugate **3-58** in 88% yield over two steps (**Scheme 3.58**). The product was purified by dialysis, and characterized by ESI-MS (**Figure 3.93**).



Scheme 3.58 Synthesis of conjugate **3-58**

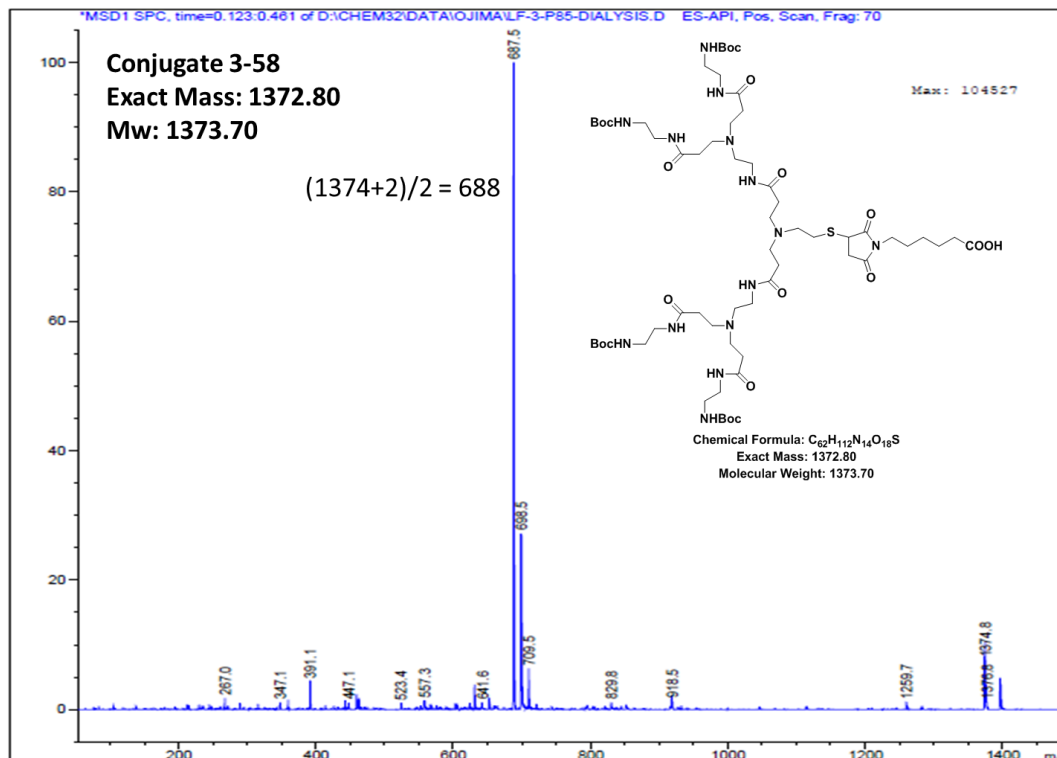
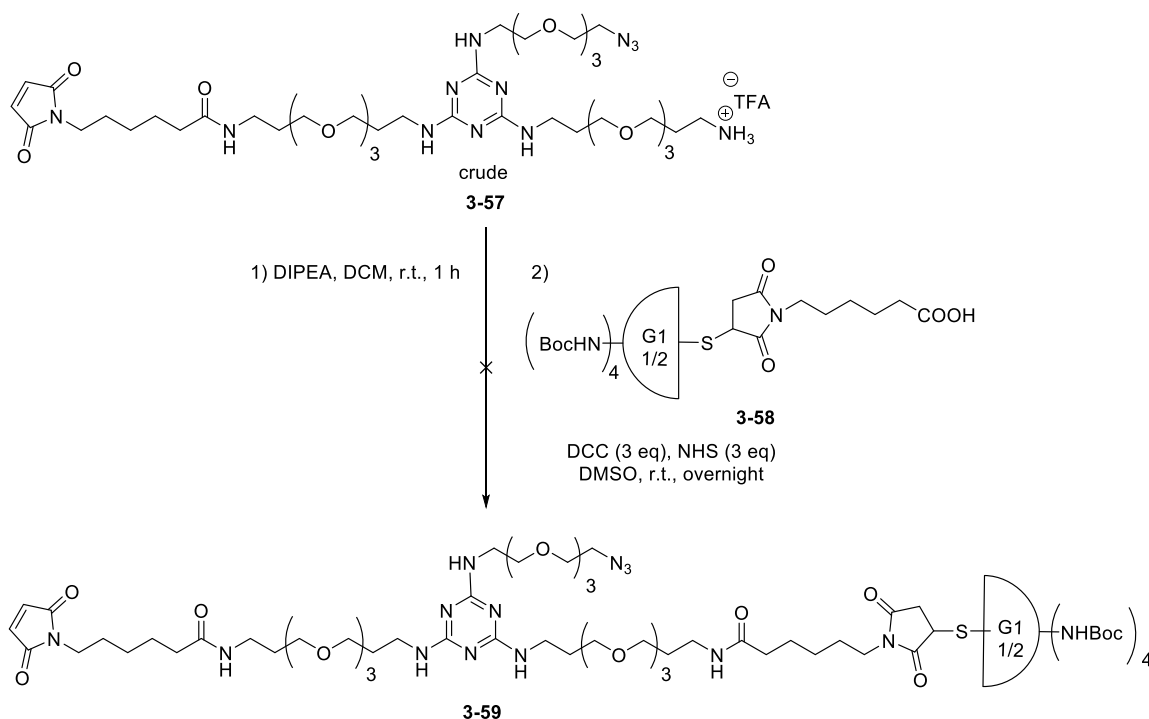


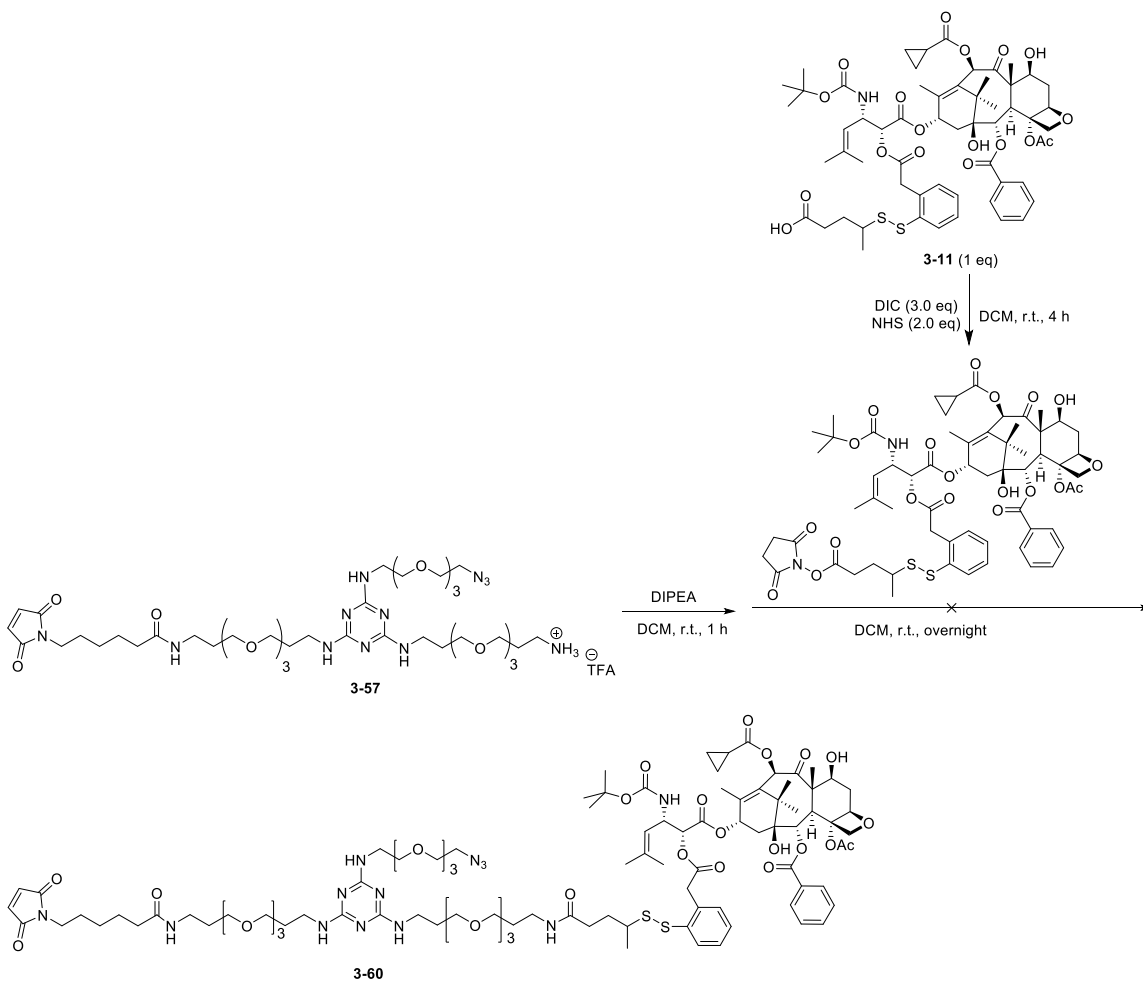
Figure 3.93 ESI-MS spectrum of conjugate **3-58** after dialysis

After that, crude **3-57** was treated with excess amount of DIPEA to remove TFA, and the resulting free amine was reacted with acid **3-58** under DCC coupling condition (**Scheme 3.59**). However, the reaction did not proceed, and no desired product was observed. Attempts to activate the acid **3-58** via mixed anhydride or HBTU were also not successful, presumably because of the extremely low solubility of acid **3-58** in common organic solvents, and DMSO was thus used in the reactions for solubilizing it at dilute conditions.



Scheme 3.59 Attempts towards conjugate **3-59**

Attempts were also made towards conjugate **3-60**, which could be served as a versatile tri-branched platform for constructing PAMAM dendrimer based theranostic agents bearing single taxoid warhead. Crude **3-57** was treated with excess amount of DIPEA to remove TFA, and the resulting free amine was reacted with NHS activated ester of SB-T-1214-linker-COOH in DCM (**Scheme 3.60**). The coupling did proceed smoothly this time as confirmed by MALDI-TOF and ESI-MS (**Figure 3.94** and **Figure 3.95**), however, the product obtained has a molecular mass which is 10 units less than the desired product (observed Mw 2035 instead of desired Mw 2045), presumably due to some side reaction under this condition.



Scheme 3.60 Attempts towards conjugate **3-60**

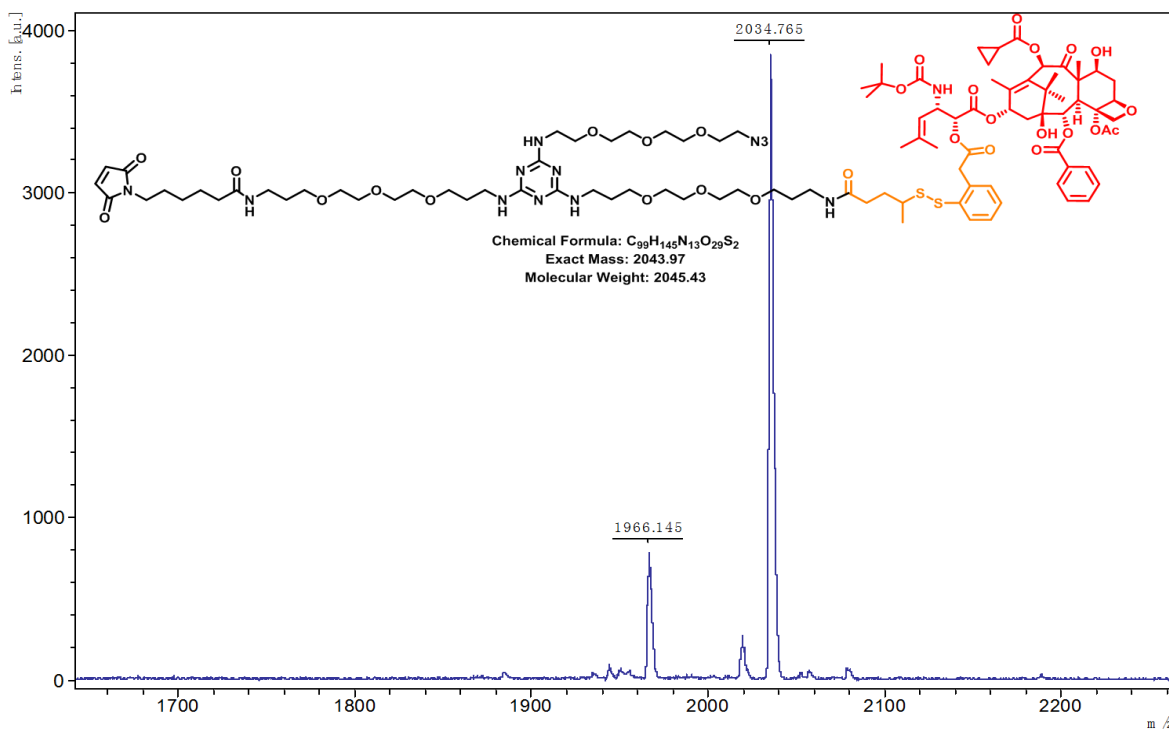


Figure 3.94 MALDI-TOF spectrum of conjugate 3-60

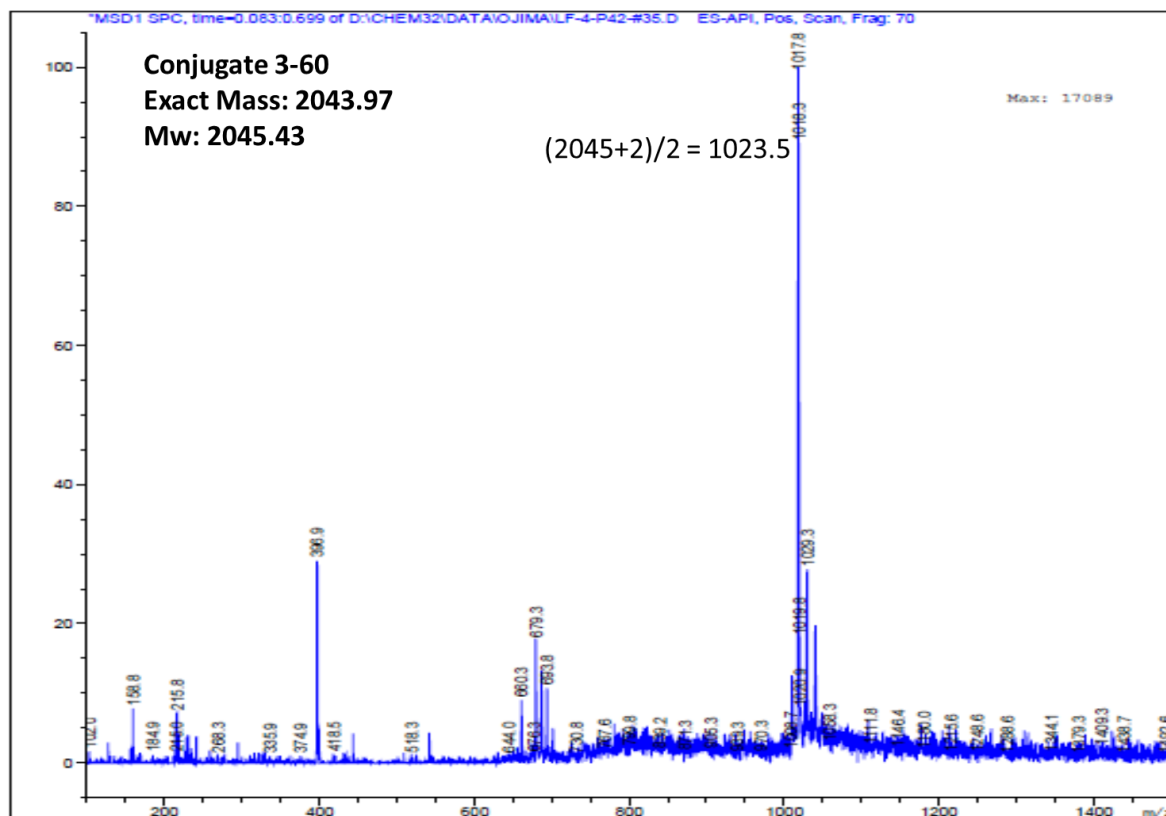


Figure 3.95 ESI-MS spectrum of conjugate 3-60

§ 3.5 Summary

PAMAM dendrimer-based biotin-taxoid/FITC tumor-targeting conjugates have been designed, synthesized, and evaluated *via* MTT cytotoxicity assays, confocal fluorescence microscopy (CFM) imaging, and flow cytometry analysis. Biological evaluations of the dendrimer-based conjugates show excellent cell internalization *via* RME and high drug delivery efficiency. No obvious multivalent binding effect was observed presumably because of saturation of the biotin receptors at high concentration and long incubation time.

A versatile asymmetric bow-tie PAMAM dendrimer-based (ABTD) platform has been developed. Purification and analysis methods have been developed for dendrimer intermediates and final conjugates.

Tri-branched theranostic dendrimer-based conjugates have been designed, and different synthetic routes have been investigated.

§ 3.6 Experimental

Caution

Taxoids have been classified as highly potent cytotoxic agents. Thus, all taxoids and structurally related compounds and derivatives must be considered as mutagens and potential reproductive hazards for both males and females. Appropriate precautions (i.e. use of gloves, goggles, lab coat and fume hood) must be taken while handling these compounds.

General Methods

¹H NMR and ¹³C NMR spectra were measured on a Varian 300 spectrometer or a Bruker 400 MHz, 500 MHz, or 700 MHz NMR spectrometer. Melting points were measured on a Thomas-Hoover capillary melting point apparatus and are uncorrected. Optical rotations were measured on Perkin-Elmer Model 241 polarimeter. TLC analyses were performed on Sorbent Technologies aluminum-backed Silica G TLC plates (Sorbent Technologies, 200 μm, 20 cm × 20 cm), and were visualized with UV light and stained with sulfuric acid-EtOH, 10% phosphomolybdic acid (PMA)-EtOH, 10% vanillin-EtOH with 1% sulfuric acid, ninhydrin-butanol with 10% AcOH, or DACA stain. Column chromatography was carried out on silica gel 60 (Merck; 230-400 mesh ASTM). Chemical purity was determined with a Shimadzu L-2010A HPLC HT series HPLC assembly, using a Kinetex PFP column (4.6 mm × 100 mm, 2.6 μm, 100 Å), using CH₃CN/water as the solvent system with a flow rate of 1 mL/min, or a Jupiter C18 column (2.0 mm × 150 mm, 3 μm, 300 Å), using CH₃CN/water as the solvent system

with a flow rate of 0.3 mL/min. GPC analysis was performed with a Shimadzu L-2010A HPLC HT series HPLC assembly, using a Waters Ultrahydrogel 500 GPC column (7.8 mm × 300 mm, 10 μm, 500 Å), using CH₃CN/water as the solvent system with a flow rate of 0.5 mL/min. LC-MS or HR-MS analysis was carried out on an Agilent LC-UV-TOF mass spectrometer, using Jupiter C18 analytical column (2.1 × 100 mm, 2.6 μm, 100 Å), with 0.1% TFA in water (optima grade) as solvent A and 0.1% TFA in CH₃CN (optima grade) as solvent B, at the Institute of Chemical Biology and Drug Discovery (ICB&DD), Stony Brook, NY. Preparative HPLC purification was performed using Jupiter C18 semi-preparative HPLC column (10 x 250 mm, 5 μm, 300 Å) or Jupiter C18 preparative HPLC column (21.2 x 250, 5 μm, 300 Å) on a Shimadzu CBM-10AW VP communications bus module, Shimadzu SPD-10A VP UV-Vis detector, and Shimadzu LC-6AD liquid chromatography assembly. Matrix-assisted laser desorption/ionization (MALDI)-TOF analysis for determination of molecular weight was carried out using 2, 5-dihydroxybenzoic acid (DHB) as matrix at the Institute of Chemical Biology and Drug Discovery (ICB&DD), Stony Brook, NY. DHB matrix was prepared by dissolving 10 mg ultrapure DHB in a mixture of 500 μL CH₃CN (contain 0.1% TFA) and 500 μL proteomics grade water (contain 0.1% TFA), and vortex vigorously. For preparing MALDI samples, 1 μL of the sample dissolved in methanol was mixed with 10 μL of the DHB matrix solution, and 1 μL of the mixed solution was applied onto the MALDI sample plate, and was allowed to co-crystallize through evaporation at room temperature.

Materials

All chemicals were purchased from Sigma Aldrich, Fisher Scientific or VWR International and used as received or purified before use by standard methods. Dichloromethane and methanol were dried before use by distillation over calcium hydride under nitrogen. Ether and tetrahydrofuran were dried before use by distillation over sodium-benzophenone kept under nitrogen. 10-Deacetylbaccatin III was obtained from Indena, S.p.A, Italy. Reaction flasks were dried in a 100 °C oven and allowed to cool to room temperature in a desiccator over calcium sulfate and assembled under an inert nitrogen gas atmosphere. The PAMAM dendrimers bearing cystamine cores were purchased as methanol solution from Dendritic Nanotechnologies, Inc®. G3 cystamine-PAPAM dendrimer, DNT-296 (MW: 7,001 g/mol) (10.1% in methanol) and G1 cystamine-PAPAM dendrimer, DNT-294 (MW: 1,522 g/mol) (20.1% in methanol), were used as received. Biological materials including RPMI-1640 cell culture media, DPBS buffer, fetal bovine serum, PenStrep, and TrypLE were obtained from Gibco and VWR International, and used as received for cell-based assays.

Experimental Procedures

Chemical Synthesis

***tert*-Butyl 12-hydroxy-4,7,10-trioxadodecanoate (3-1)⁵⁶**

To a 250-mL round-bottom flask were added dry THF (50 mL), triethylene glycol (15.0 g, 100 mmol), and potassium *tert*-butoxide (115 mg, 1.0 mmol). The mixture was allowed to stir at room temperature under inert condition. A solution of *tert*-butyl acrylate (6.18 g, 48 mmol) in 50 mL dry THF was then slowly added to the mixture via an additional funnel within 2.5 h. The reaction mixture was allowed to stir overnight, and was monitored by TLC (stained with vanillin). Upon completion, the solvent was evacuated, and the crude mixture was purified by column chromatography on silica gel (gradient eluent: hexanes/ethyl acetate from 10/1 to 1/4) to give *tert*-butyl 12-hydroxy-4,7,10-trioxadodecanoate **3-1** (8.81g, 31.7 mmol) as colorless oil in 66% yield. Side product di-*tert*-butyl 4,7,10,13-tetraoxahexadecane-1,16-dioate (595 mg) was also obtained as colorless oil. Product *tert*-butyl 12-hydroxy-4,7,10-trioxadodecanoate **3-1**: ¹H NMR (500 MHz, CDCl₃): δ 1.44 (s, 9H), 2.44 (t, J = 6.0 Hz, 1H), 2.51 (t, J = 6.6 Hz, 2H), 3.61 (m, 4H), 3.67 (m, 6H), 3.71 (t, J = 6.6 Hz, 2H), 3.72 (m, 2H). ¹³C NMR (125 MHz, CDCl₃): δ 28.1, 36.2, 61.8, 66.9, 70.4, 70.4, 70.5, 70.7, 72.5, 80.6, 170.9. ESI-MS *m/z* : 301.1 [M+Na]⁺. Side product di-*tert*-butyl 4,7,10,13-tetraoxahexadecane-1,16-dioate: ¹H NMR (300 MHz, CDCl₃): δ 1.44 (s, 18H), 2.50 (t, J = 6.6 Hz, 4H), 3.62 (m, 12H), 3.70 (t, J = 6.6 Hz, 4H). All data are in agreement with literature values.⁵⁶

***tert*-Butyl 12-azido-4,7,10-trioxadocecanoate (3-2)^{57,58}**

To a 50-mL round-bottom flask were added *tert*-butyl 12-hydroxy-4,7,10-trioxadocecanoate **3-1** (5.45 g, 29.6 mmol), methanesulfonyl chloride (2.69 g, 23.5 mmol) and THF (20 mL). The mixture was allowed to stir at 0 °C in an ice bath. Then triethylamine (2.38 g, 23.5 mmol) was added dropwise. White precipitate came out immediately. The reaction mixture was allowed to slowly warm to room temperature and stir at room temperature for 2 hours. The reaction was monitored by TLC (stained with vanillin). Upon completion, the white precipitate was removed by vacuum filtration and washed with ether. The filtrate was concentrated to remove solvent to afford pale yellow oil. The resulting oil was diluted with 15 mL distilled water and cooled to 0 °C. Sodium bicarbonate was added to adjust the pH of the mixture to 8-9. Then sodium azide (1.53 g, 23.5 mmol) was added and the resulting solution was heated up to reflux at 100 °C overnight. The reaction was monitored by TLC (stained with vanillin). Upon completion, the reaction mixture was extract with ethyl acetate (3 x 50 mL). The organic layer was collected, washed with brine (3 x 30 mL), and dried over anhydrous magnesium sulfate. The magnesium sulfate was subsequently removed by vacuum filtration, and the filtrate was concentrated to afford crude product as pale yellow oil. Purification was down by column chromatography on silica gel (gradient eluent: hexanes/ethyl acetate from 8/1 to 2/1) to give *tert*-butyl 12-azido-4,7,10-trioxadocecanoate **3-2** (4.06 g, 13.4 mmol) as colorless oil in 68% yield. ¹H NMR (500 MHz, CDCl₃): δ 1.45 (s, 9H), 2.50 (t, J = 6.6 Hz, 2H), 3.39 (t, J = 5.1 Hz, 2H), 3.63 (m, 10H), 3.71 (t, J = 6.6 Hz, 2H). ¹³C NMR (125

MHz, CDCl₃): δ 28.1, 36.3, 50.7, 66.9, 70.1, 70.4, 70.6, 70.7, 70.7, 80.5, 170.9. IR: 2871 cm⁻¹ (alkyl), 2105 cm⁻¹ (N₃), 1732 cm⁻¹ (COOR). All data are in agreement with literature values.^{57,58}

***tert*-Butyl 12-amino-4,7,10-trioxadocecanoate (3-3)⁵⁷**

To a 100-mL round-bottom flask were added *tert*-butyl 12-azido-4,7,10-trioxadocecanoate **3-2** (1.00 g, 3.30 mmol) in THF (30 mL) and triphenylphosphine (1.73 g, 6.60 mmol). The mixture was allowed to stir at room temperature for 30 min. Then distilled water (10 mL) was added. The resulting solution was allowed to stir at room temperature for overnight. The reaction was monitored by TLC (stained with ninhydrin). Upon completion, the resulting solution was concentrated in vacuo to remove THF. After THF was removed, white precipitate (mixture of triphenylphosphine and triphenylphosphine oxide) slowly came out and was removed by vacuum filtration and washed with water. The filtrate was diluted with water (~300 mL), and washed with toluene 3 x 20 mL to remove triphenylphosphine oxide. The water layer was concentrated by rotavapor and water was further removed by freezer drier overnight to give *tert*-butyl 12-amino-4,7,10-trioxadocecanoate **3-3** (770 mg, 2.77 mmol) as pale yellow oil in 84% yield. ¹H NMR (500 MHz, CDCl₃): δ 1.38 (s, 2H), 1.45 (s, 9H), 2.50 (t, J = 6.6 Hz, 2H), 2.86 (t, J = 5.3 Hz), 3.50 (t, J = 5.3 Hz), 3.62 (m, 8H), 3.65 (t, J = 6.6 Hz, 2H). ¹³C NMR (125 MHz, CDCl₃): δ 28.1, 36.3, 41.9, 66.9, 70.3, 70.4, 70.5, 70.6, 73.6, 80.5, 170.9. ESI-MS *m/z* : 278.1 [M+H]⁺. All data are consisted with literature values.⁵⁷

***D*-(+)-Biotin-OSu (3-4)⁵⁹**

To a 50-mL round-bottom flask were added *D*-(+)-biotin (1.00 g, 4.09 mmol) and anhydrous DMF (20 mL). The mixture was slowly heated up to 70 °C to afford a clear solution. The mixture was then cooled down to room temperature. *N*-hydroxysuccinimide (NHS) (1.41 g, 12.3 mmol) was added to the mixture and after that *N,N*-diisopropylcarbodiimide (DIC) (1.03 g, 8.18 mmol) was slowly added dropwise. The reaction mixture was allowed to stir at room temperature overnight. The reaction was monitored by TLC (stained with DACA). Upon completion, DMF was removed by freezer drier overnight to give crude product as a white solid. The crude product was further purified by column chromatography on silica gel (gradient eluent: DCM/methanol from 50/1 to 10/1) to give *D*-(+)-biotin-OSu **3-4** (1.35 g, 3.95 mmol) as white solid in 96% yield. ¹H NMR (500 MHz, DMSO-*d*₆): δ 1.43 (m, 2H), 1.50 (m, 1H), 1.63 (m, 3H), 2.570 (d, J = 12.5 Hz, 1H), 2.67 (t, J = 7.4 Hz, 2H), 2.81 (br. s, 4H), 2.84 (dd, J = 12.5 Hz, J = 5.2 Hz, 1H), 3.11 (m, 1H), 4.13 (m, 1H), 4.30 (dd, J = 7.6 Hz, J = 5.2 Hz, 1H), 6.36 (s, 1H), 6.42 (s, 1H). All data are in agreement with literature values.⁵⁹

***D*-(+)-Biotin-*tert*-butyl 12-amino-4,7,10-trioxadocecanoate (3-5)⁵⁷**

To a solution of *tert*-butyl 12-amino-4,7,10-trioxadocecanoate **3-3** (770 mg, 2.77 mmol) in DCM (24 mL), was added D -(+)-biotin-OSu **3-4** (998 mg, 2.92 mmol). D -(+)-biotin-OSu **3-4** could not be completely dissolved in the beginning, but slowly fully dissolved as the reaction goes. The reaction mixture was allowed to stir at room temperature under inert condition for 2 days. The reaction was monitored by TLC (stained with DACA). Upon the reaction was completed, the solvent was evacuated and the crude was purified by column chromatography on silica gel (gradient eluent: DCM/methanol from 50/1 to 10/1) to give D -(+)-biotin-*tert*-butyl 12-amino-4,7,10-trioxadocecanoate **3-5** (1.21 g, 2.41 mmol) as pale yellow solid in 87% yield. ^1H NMR (500 MHz, CDCl_3): δ 1.44 (m, 11H), 1.69 (m, 4H), 2.22 (m, 2H), 2.50 (t, $J = 6.6$ Hz, 2H), 2.74 (d, $J = 12.8$ Hz, 1H), 2.91 (dd, $J = 12.8$ Hz, $J = 5.0$ Hz, 1H), 3.14 (m, 1H), 3.42 (m, 2H), 3.56 (t, $J = 5.0$ Hz, 2H), 3.62 (m, 8H), 3.71 (t, $J = 6.6$ Hz, 2H), 4.32 (dd, $J = 7.2$ Hz, $J = 5.0$ Hz, 1H), 4.50 (dd, $J = 7.6$ Hz, 5.0 Hz, 1H), 5.44 (s, 1H), 6.41 (s, 1H), 6.66 (t, $J = 5.3$ Hz, 1H). All data are consisted with literature values.⁵⁷

D -(+)-Biotin-*tert*-butyl 12-amino-4,7,10-trioxadocecanoic acid (3-6**)⁵⁷**

To a solution of D -(+)-biotin-*tert*-butyl 12-amino-4,7,10-trioxadocecanoate **3-5** (1.20 g, 2.39 mmol) in DCM (40 mL), was added TFA (10 mL) dropwise. The reaction mixture was allowed to stir at room temperature overnight. Upon the reaction was completed, the solvent was evacuated and the crude was purified by column chromatography on silica gel (gradient eluent: DCM/methanol from 50/1 to 6/1) to give D -(+)-biotin-*tert*-butyl 12-amino-4,7,10-trioxadocecanoic acid **3-6** as pale yellow solid (1.03 g, 2.30 mmol) in 97% yield. ^1H NMR (500 MHz, DMSO-d_6): δ 1.30 (m, 2H), 1.46 (m, 3H), 1.60 (m, 1H), 2.06 (t, $J = 7.4$ Hz, 2H), 2.44 (t, $J = 6.3$ Hz, 2H), 2.57 (d, $J = 12.4$ Hz, 1H), 2.82 (dd, $J = 12.4$ Hz, $J = 5.1$ Hz, 1H), 3.09 (m, 1H), 3.38 (t, $J = 6.0$ Hz, 2H), 3.49 (m, 8H), 3.59 (t, $J = 6.3$ Hz, 2H), 4.13 (m, 1H), 4.30 (dd, $J = 7.5$ Hz, 5.2 Hz, 1H), 6.35 (s, 1H), 6.41 (s, 1H), 7.82 (t, $J = 5.5$ Hz, 1H). ^{13}C NMR (125 MHz, DMSO-d_6): δ 25.7, 28.5, 28.7, 35.2, 35.6, 38.9, 55.9, 59.7, 61.5, 66.7, 69.6, 70.0, 70.1, 70.2, 70.3, 163.2, 172.6, 173.1. All data are consisted with literature values.⁵⁷

D -(+)-Biotin-12-amino-4,7,10-trioxadocecanoic acid *N*-hydroxysuccinimidyl ester (3-7**)**

To a solution of D -(+)-biotin-*tert*-butyl 12-amino-4,7,10-trioxadocecanoic acid **3-6** (566 mg, 1.27 mmol) in DCM (30 mL) (starting material could not fully dissolved), was added DIC (2 eq) and NHS (3 eq). The reaction mixture was allowed to stir at room temperature overnight. Starting material slowly dissolved as the reactions goes, and white precipitate slowly came out (DIU). Upon the reaction was completed, the solvent was evacuated, and the crude was purified by column chromatography on silica gel (gradient eluent: DCM/methanol from 50/1 to 10/1) to give D -(+)-biotin-12-amino-4,7,10-trioxadocecanoic acid *N*-hydroxysuccinimidyl ester **3-7** as white solid (547 mg, 1.00

mmol) in 79% isolated yield. ^1H NMR (500 MHz, CDCl_3): δ 1.44 (m, 2H), 1.68 (m, 4H), 2.23 (m, 2H), 2.74 (d, $J = 12.8$ Hz, 1H), 2.85 (br.s, 4H), 2.91 (m, 1H), 3.16 (m, 1H), 3.43 (m, 2H), 3.56 (t, $J = 5.1$ Hz, 2H), 3.63 (m, 6H), 3.65 (s, 1H), 3.69 (s, 1H), 3.76 (t, $J = 6.4$ Hz, 1H), 3.85 (t, $J = 6.4$ Hz, 1H), 4.34 (t, $J = 6.0$ Hz, 1H), 4.51 (t, $J = 6.0$ Hz, 1H), 5.38 (s, 1H), 6.11 (s, 1H), 6.51 (d, $J = 5.7$ Hz).

Biotin PEGylated G1 PAMAM Dendrimer (3-8)

To a solution of G1 dendrimer (DNT-294, 20 w% in methanol) (40 mg, 0.026 mmol) in methanol (1 mL) was added $\text{D-}(+)\text{-biotin-12-amino-4,7,10-trioxadocecanoic acid } N\text{-hydroxysuccinimidyl ester } \mathbf{3-7}$ (344 mg, 0.632 mmol). The reaction mixture was allowed to stir at room temperature for two days. Upon the reaction was completed, the reaction mixture was directly purified by dialysis against methanol (3 x 1000 mL) for three days. Then the solvent was removed by evaporation to give biotin PEGylated G1 PAMAM dendrimer **3-8** as a white solid (112 mg, 0.023 mmol) in 87% yield. ^1H NMR (700 MHz, MeOH-d_4): δ 1.42 (m, 16H), 1.61 (m, 8H), 1.65 (m, 16H), 1.74 (m, 8H), 2.21 (t, $J = 7.4$ Hz, 16H), 2.45 (t, $J = 6.3$ Hz, 16H), 2.70 (d, $J = 12.6$ Hz, 8H), 2.74 (m, 16H), 2.91 (m, 12H), 3.21 (m, 8H), 3.34 (m, 16H), 3.41 (m, 32H), 3.53 (m, 32H), 3.61 (m, 64H), 3.72 (t, $J = 6.3$ Hz, 16H), 4.30 (m, 8H), 4.49 (m, 8H). MALTI-TOF-MS: 4958.6 ($[\text{M}+\text{H}]^+$, calculated 4955.6, $\Delta = 3.0$ Da), 4979.4 ($[\text{M}+\text{Na}]^+$, calculated 4977.6, $\Delta = 1.8$ Da), 2480.0 ($[\text{M}+2\text{H}]^{2+}$, calculated 2478.3, $\Delta = 1.7$ Da), and 2502.7 ($[\text{M}+2\text{Na}]^{2+}$, calculated 2500.3, $\Delta = 2.4$ Da). ESI-MS: 1240.3 $[\text{M}+4\text{H}]^{4+}$, 992.4 $[\text{M}+5\text{H}]^{5+}$, 827.2 $[\text{M}+6\text{H}]^{6+}$.

Biotin PEGylated G3 PAMAM Dendrimer (3-9)

To a solution of G3 dendrimer (DNT-296, 20 w% in methanol) (27 mg, 0.0038 mmol) in methanol (1 mL) was added $\text{D-}(+)\text{-biotin-12-amino-4,7,10-trioxadocecanoic acid } N\text{-hydroxysuccinimidyl ester } \mathbf{3-7}$ (196 mg, 0.360 mmol). The reaction mixture was allowed to stir at room temperature for two days. Upon the reaction was completed, the reaction mixture was directly purified by dialysis against methanol (3 x 1000 mL) for three days. Then the solvent was removed by evaporation to give biotin PEGylated G3 PAMAM dendrimer **3-9** as a white solid (99 mg, 0.0048 mmol) in > 100% yield. ^1H NMR (700 MHz, MeOH-d_4): δ 1.42 (m, 64H), 1.61 (m, 32H), 1.65 (m, 64H), 1.74 (m, 32H), 2.21 (t, $J = 7.4$ Hz, 64H), 2.45 (t, $J = 6.3$ Hz, 64H), 2.70 (d, $J = 12.6$ Hz, 32H), 2.74 (m, 64H), 2.87 (br.s 64H), 2.91 (m, 32H), 3.21 (m, 32H), 3.34 (m, 64H), 3.41 (m, 128H), 3.53 (m, 128H), 3.61 (m, 256H), 3.72 (m, 64H), 4.33 (m, 32H), 4.50 (m, 32H). MALTI-TOF-MS: 20736.0 ($[\text{M}+\text{H}]^+$, calculated 20731.0, $\Delta = 5.0$ Da), and 10370.4 ($[\text{M}+2\text{H}]^{2+}$, calculated 10366.5, $\Delta = 3.9$ Da).

SB-T-1214-linker-TIPS ester conjugate (3-10)⁴¹

To a mixture of SB-T-1214 (180 mg, 0.211 mmol), methyl-branched disulfide linker **2-7** (120 mg, 0.263 mmol) and DMAP (9.6 mg, 0.079 mmol) dissolved in DCM (5 mL) and

cooled to 0 °C in an ice bath was added DIC (33 mg, 0.026 mmol) dropwise. The mixture was allowed to stir at 0 °C and the reaction was monitored via TLC. Upon reaction completion after overnight, the reaction mixture was purified immediately by column chromatography on silica gel (gradient eluent: hexanes/ethyl acetate from 10/1 to 1/1) to give SB-T-1214-linker-TIPS ester conjugate **3-10** (183 mg, 0.142 mmol) as white solid in 67% yield. ¹H NMR (400 MHz, CDCl₃): δ 1.00 (m, 2H), 1.05 (m, 21H), 1.13 (m, 6H), 1.26 (m, 12H), 1.34 (s, 6H), 1.67 (s, 3H), 1.72 (s, 3H), 1.74 (s, 3H), 1.77 (m, 2H), 1.86 (m, 1H), 1.90 (s, 3H), 2.37 (s, 3H), 2.40 (m, 2H), 2.55 (m, 1H), 2.58 (d, J = 3.7 Hz, 1H), 3.80 (d, J = 6.9 Hz, 1H), 4.18 (d, J = 8.4 Hz, 1H), 4.31 (d, J = 8.4 Hz, 1H), 4.44 (m, 1H), 4.79 (m, 1H), 4.94 (m, 2H), 5.07 (d, J = 8.8 Hz), 5.67 (d, J = 6.9 Hz, 1H), 6.19 (t, J = 8.2 Hz, 1H), 6.28 (s, 1H), 7.30 (m, 3H), 7.47 (t, J = 7.3 Hz, 2H), 7.60 (t, J = 7.6 Hz, 1H), 7.80 (d, J = 7.7 Hz, 1H), 8.11 (d, J = 7.4 Hz, 2H). All data are consisted with literature values.⁴¹

SB-T-1214-linker-carboxylic acid conjugate (3-11)⁴¹

To SB-T-1214-linker-TIPS ester conjugate **3-10** (182 mg, 0.141 mmol) dissolved in a 1/1 mixture of CH₃CN/pyridine [0.01 M] cooled to 0 °C was added HF/pyridine (1 mL) dropwise. The mixture was stirred at room temperature and the reaction was monitored via TLC. After 16 hours, the reaction was quenched with 10% citric acid (10 mL) and extracted with ethyl acetate (3 x 15 mL). The organic layer was extracted and washed with aqueous CuSO₄ (3 x 30 mL), then washed with brine (3 x 30 mL), and dried over MgSO₄. The MgSO₄ was subsequently removed by vacuum filtration and the filtrate was concentrated in vacuo. The resulting crude was purified via flash column chromatography on silica gel (gradient eluent: hexanes/ethyl acetate from 10/1 to 1/4) to yield SB-T-1214-linker-carboxylic acid conjugate **3-11** as a white solid (102 mg, 0.0899 mmol) in 64% yield. ¹H NMR (500 MHz, CDCl₃): δ 1.00 (m, 2H), 1.13 (m, 6H), 1.26 (m, 12H), 1.34 (s, 6H), 1.67 (s, 3H), 1.72 (s, 3H), 1.74 (s, 3H), 1.77 (m, 2H), 1.86 (m, 1H), 1.90 (s, 3H), 2.37 (s, 3H), 2.40 (m, 2H), 2.55 (m, 1H), 2.58 (d, J = 3.7 Hz, 1H), 3.80 (d, J = 6.9 Hz, 1H), 4.18 (d, J = 8.4 Hz, 1H), 4.31 (d, J = 8.4 Hz, 1H), 4.44 (m, 1H), 4.79 (m, 1H), 4.94 (m, 2H), 5.07 (d, J = 8.8 Hz), 5.67 (d, J = 6.9 Hz, 1H), 6.19 (t, J = 8.2 Hz, 1H), 6.28 (d, J = 4.8 Hz, 1H), 7.22 (m, 2H), 7.30 (m, 1H), 7.47 (t, J = 7.8 Hz, 2H), 7.60 (t, J = 7.4 Hz, 1H), 7.80 (t, J = 9.5 Hz, 1H), 8.10 (d, J = 7.5 Hz, 2H). All data are consisted with literature values.⁴¹

PEG-diazide (3-12)⁶⁰

To a 250-mL round-bottom flask was added tetraethyleneglycol (20.0 g, 103 mmol), methanesulfonyl chloride (2.25 eq) and THF (100 mL). The mixture was allowed to stir at 0 °C in an ice bath. Then triethylamine (2.25 eq) was added dropwise. White precipitate came out immediately. The reaction mixture was allowed to slowly warm to room temperature. The reaction was monitored by TLC (stained with vanillin). Upon

completion after 5 hour, the white precipitate was removed by vacuum filtration and washed with ether. The filtrate was concentrated to remove solvent to afford pale yellow oil. The resulting oil was diluted with 50 mL distilled water and cooled to 0 °C. Sodium bicarbonate was added to adjust the pH of the mixture to 8. Then sodium azide (2.4 eq) was added and the resulting solution was heated up to reflux at 100 °C overnight. The reaction was monitored by TLC and stained with vanillin. Upon completion, the reaction mixture was cooled to room temperature and was extracted with ether (3 x 50 mL). The organic layer was collected, washed with brine (3 x 50 mL), and dried over anhydrous magnesium sulfate. The magnesium sulfate was subsequently removed by vacuum filtration and the filtrate was concentrated in vacuo to afford crude product **3-12** as pale yellow oil (23.1 g, 95 mmol) in 92% yield. ¹H NMR (400 MHz, CDCl₃): δ 3.38 (t, J = 5.2 Hz, 4H), 3.67 (m, 12H). All data are in agreement with literature values.⁶⁰

Amino-PEG-azide (3-13)⁶⁰

To a 250-mL round-bottom flask was added PEG diazide **3-12** (8.54 g, 35.0 mmol) in 60 mL ether and triphenylphosphine (8.00 g, 30.5 mmol). Then phosphoric acid [0.65 M] in 80 mL water was added. The mixture was allowed to stir at room temperature for 24 h. The reaction was monitored by TLC (stained with vanillin). Upon completion, the water layer was separated from organic layer, treated with potassium carbonate, and extracted with DCM (10 x 100 mL). The magnesium sulfate was subsequently removed by vacuum filtration and the filtrate was concentrated in vacuo to afford crude product **3-13** as pale yellow oil (5.40 g, 24.8 mmol) in 71% yield. ¹H NMR (400 MHz, CDCl₃): δ 2.98 (t, J = 5.3 Hz, 2H), 3.38 (m, 2H), 3.62 (m, 12H), 4.04 (br s, 2H). All data are in agreement with literature values.⁶⁰

SB-T-1214-linker-PEG3-azide (3-14)

To a mixture of SB-T-1214-linker-carboxylic acid conjugate **3-11** (96 mg, 0.085 mmol) and NHS (20 mg, 0.17 mmol) dissolved in DCM (5 mL) was added EDCHCl (24 mg, 0.13 mmol). The reaction was stirred at room temperature and monitored via TLC and ESI-MS. After overnight, the reaction was quenched with saturated NH₄Cl (10 mL). The residue was extracted with ethyl acetate (4 x 30 mL). The organic layer was washed with brine (2 x 30 mL), collected, and dried over MgSO₄. and concentrated *in vacuo*. The resulting crude was characterized by ESI-MS *m/z* : 1250.5 [M+H]⁺. To this crude SB-T-1214-linker-OSu conjugate dissolved in DCM (1 mL) was added amino-PEG3-azide **3-13** (36 mg, 0.169 mmol). The reaction was stirred at room temperature and monitored via TLC and ESI-MS. After overnight, the reaction was quenched with saturated NH₄Cl (10 mL). The residue was extracted with ethyl acetate (4 x 30 mL). The organic layer was washed with brine (2 x 30 mL), collected, and dried over MgSO₄. The MgSO₄ was subsequently removed by vacuum filtration and the filtrate was concentrated in vacuo. The resulting crude was purified via flash column chromatography on silica gel (gradient

eluent: hexanes/ethyl acetate from 10/1 to 1/2) to yield SB-T-1214-linker-PEG3-azide **3-14** as a white solid (70 mg, 0.052 mmol) in 61% yield over two steps. ¹H NMR (500 MHz, CDCl₃): δ 0.96 (m, 3H), 1.12 (m, 2H), 1.14 (s, 3H), 1.25 (s, 3H), 1.28 (d, J = 6.8 Hz, 3H), 1.34 (s, 9H), 1.60 (br. s 9H), 1.66 (s, 3H), 1.70 (s, 2H), 1.72 (s, 2H), 1.75 (m, 2H), 1.85 (m, 2H), 1.90 (s, 3H), 2.20 (m, 2H), 2.31 (m, 1H), 2.35 (s, 3H), 2.52 (m, 1H), 2.65 (d, J = 3.9 Hz, 1H), 2.91 (m, 1H), 3.38 (m, 3H), 3.48 (d, J = 5.0 Hz, 4H), 3.51 (m, 2H), 3.62 (m, 2H), 3.67 (m, 6H), 3.80 (d, J = 7.0 Hz, 1H), 3.96 (dd, J = 13.7 Hz, J = 2.6 Hz, 1H), 4.10 (d, J = 16.4 Hz, 1H), 4.18 (d, J = 8.4 Hz, 1H), 4.30 (d, J = 8.4 Hz, 1H), 4.42 (m, 1H), 4.95 (m, 3H), 5.11 (br. s, 1H), 5.67 (d, J = 7.0 Hz, 1H), 6.02 (br. s, 1H), 6.18 (t, J = 8.8 Hz, 1H), 6.29 (s, 1H), 7.24 (m, 1H), 7.28 (m, 1H), 7.32 (m, 1H), 7.47 (t, J = 7.8 Hz, 2H), 7.60 (t, J = 7.4 Hz, 1H), 7.79 (d, J = 7.6 Hz, 1H), 8.11 (d, J = 7.4 Hz, 2H). ESI-MS *m/z* : 1355.9 [M+H]⁺.

FITC-PEG3-azide (3-15)

To FITC (100 mg, 0.26 mmol) dissolved in DMF (5 mL) was added amino-PEG3-azide **3-13** (64 mg, 0.30 mmol). The reaction was stirred at room temperature and monitored via TLC and ESI-MS. After overnight, DMF was removed by freezer-drier. The resulting crude was purified via flash column chromatography on silica gel (gradient eluent: DCM/methanol from 50/1 to 10/1) to yield FITC-PEG3-azide **3-15** as an orange solid (135 mg, 0.22 mmol) in 87% yield. ¹H NMR (500 MHz, DMSO-d₆): δ 3.31 (m, 16 H), 3.55 (s, 1H), 3.59 (s, 1H), 6.54 (d, J = 8.8 Hz, 1H), 6.60 (d, J = 8.7 Hz, 1H), 6.66 (s, 1H), 7.16 (d, J = 8.2 Hz, 1H), 7.73 (d, J = 7.9 Hz, 1H), 8.08 (s, 1H), 8.25 (s, 1H), 10.25 (s, 1H), 10.12 (s, 1H). ESI-MS *m/z* : 608.2 [M+H]⁺.

6-Maleimidocaproic acid (3-16)⁶¹

To a solution of maleic anhydride (5.00 g, 51.0 mmol) dissolved in acetic acid (30 mL), was added 6-aminocaproic acid (6.69 g, 51.0 mmol). White precipitate came out slowly. The reaction mixture was heated up to reflux for 3 h. White precipitate slowly dissolved during the heating process. Then the reaction mixture was concentrated and dried by freeze drier to afford crude product as yellow solid. The crude was purified by column chromatography on silica gel (gradient eluent: DCM/methanol from 50/1 to 10/1) to give 6-maleimidocaproic acid **2-5** (5.77 g, 27.3 mmol) as white solid in 54% yield. ¹H NMR (400 MHz, CDCl₃): δ 1.32 (m, 2H), 1.64 (m, 4H), 2.34 (t, J = 7.4 Hz, 2H), 3.52 (t, J = 7.2 Hz, 2H), 6.69 (s, 2H), 11.33 (br.s, 1H). ¹³C NMR (100 MHz, CDCl₃): δ 24.1, 26.1, 28.2, 33.7, 37.6, 134.1, 170.9, 179.4. All data are in agreement with literature values.⁶¹

6-Maleimidocaproic acid anhydride with 2-methylpropyl carbonate (mixed anhydride, 3-17)

To a solution of 6-maleimidocaproic acid **3-16** (2.11 g, 10.0 mmol) dissolved in 40 mL THF, was added *N*-methylmorpholine (1.02 g, 10.0 mmol), followed by adding isobutyl

chloroformate (1.37 g, 10.0 mmol) dropwise. White precipitate came out immediately. The reaction mixture was allowed to stir at room temperature under nitrogen for 4 h. Then the white precipitate was removed by vacuum filtration. Water was added to the filtrate and the mixture was extracted with ethyl acetate (3 x 100 mL). The organic layer was combined, and dried over anhydrous MgSO₄. The MgSO₄ was subsequently removed by vacuum filtration and the filtrate was concentrated in vacuo to give crude product mixed anhydride **3-17** (2.96 g, 9.52 mmol) as pale yellow viscous oil in 95% yield. The crude product was directly used in the next step without further purification, because the product is very unstable and purification by column chromatography may decompose the product. ¹H NMR (400 MHz, CDCl₃): δ 0.96 (d, J = 6.7 Hz, 6H), 1.35 (m, 2H), 1.60 (m, 2H), 1.68 (m, 2H), 2.02 (m, 1H), 2.46 (t, J = 7.4 Hz, 2H), 3.52 (t, J = 7.2 Hz, 2H), 4.03 (d, J = 6.7 Hz, 2H), 6.68 (s, 2H).

Maleimido alkyne spacer (3-18)

To a solution of mixed anhydride **3-17** (2.96 g, 9.52 mmol) in 25 mL THF, was added propargylamine (550 mg, 10.0 mmol) diluted with 5 mL THF dropwise at 0 °C. The reaction mixture was allowed to warm to room temperature and stir under nitrogen overnight. Upon completion, the reaction mixture was extracted with DCM (3 x 100 mL). The organic layer was combined, and dried over anhydrous MgSO₄. The MgSO₄ was subsequently removed by vacuum filtration and the filtrate was concentrated in vacuo to give crude product as brown oil. The crude product was purified by column chromatography on silica gel (gradient eluent: DCM/methanol from 50/1 to 20/1) to give maleimido alkyne spacer **3-18** (2.05 g, 8.26 mmol) as white solid in 87% yield. ¹H NMR (400 MHz, CDCl₃): δ 1.32 (m, 2H), 1.60 (m, 2H), 1.68 (m, 2H), 2.18 (t, J = 7.4 Hz, 2H), 2.23 (t, J = 2.6 Hz, 1H), 3.52 (t, J = 7.2 Hz, 2H), 4.04 (dd, J = 5.2 Hz, J = 2.6 Hz, 2H), 6.68 (s, 2H).

Biotin PEGylated G1 alkyne conjugate (3-19)

To a solution of biotin PEGylated G1 PAMAM dendrimer **3-8** (65 mg, 0.013 mmol) in methanol (1 mL) was added TCEP (0.5 M) (80 μL, 0.040 mmol) dropwise. The reaction mixture was allowed to stir at 0 °C for 20 min. Maleimido alkyne spacer **3-18** (20 mg, 0.081 mmol) was then added. The reaction mixture was allowed to stir at room temperature for 2 days. Upon the reaction was completed, the reaction mixture was directly purified by dialysis against methanol (3 x 1000 mL) for three days. Then the solvent was removed by evaporation to give biotin PEGylated G1 alkyne conjugate **3-19** as white solid (67 mg, 0.025 mmol) in 94% yield. The product was further purified by preparative HPLC before use in the next step. ¹H NMR (700 MHz, DMSO-d₆): δ 1.20 (m, 2H), 1.27 (m, 8H), 1.46 (m, 16H), 1.60 (m, 4H), 2.06 (t, J = 7.4 Hz, 10H), 2.31 (t, J = 6.4 Hz, 8H), 2.40 (s, 1H), 2.58 (m, 8H), 2.82 (dd, J = 12.4 Hz, 5.1 Hz, 4H), 3.08 (m, 24H), 3.18 (m, 12H), 3.36 (m, 24H), 3.49 (m, 32H), 3.58 (t, J = 6.5 Hz, 8H), 3.82 (dd, J =

5.4 Hz, 2.5 Hz, 2H), 4.12 (m, 4H), 4.30 (m, 4H), 6.37 (s, 4H), 6.42 (s, 4H), 6.55 (br. s, 2H), 7.84 (t, J = 5.6 Hz, 4H), 8.23 (s, 4H), 8.43 (br. s, 2H), 9.43 (s, 2H), 9.58 (s, 1H). MALTI-TOF-MS: observed Mw 2730.0 (calculated exact mass 2726.40; calculated Mw 2728.44). ESI-MS: 1364.8 [M+2H]²⁺, 910.2 [M+3H]³⁺, 682.9 [M+4H]⁴⁺.

Biotin PEGylated G1 FITC conjugate (3-20)

To a 5 mL vial biotin PEGylated G1 alkyne conjugate **3-19** (9.0 mg, 0.0033 mmol) and FITC-PEG₃-azide **3-15** (4.0 mg, 0.0066 mmol) were dissolved in DMF (0.8 mL). The vial was purged with nitrogen for three times. After that, copper sulfate pentahydrate (1.7 mg, 0.0066 mmol) dissolved in water (0.1 mL) was added into the mixture under nitrogen. Sodium ascorbate (1.4 mg, 0.0066 mmol) dissolved in water (0.1 mL) was then added into the reaction mixture under nitrogen to afford an orange solution. The reaction was monitored by ESI-MS. Upon the reaction was completed, the reaction mixture was directly purified by preparative HPLC, and the solvent was removed by freezer-drier to give biotin PEGylated G1 FITC conjugate **3-20** as an orange solid (8.6 mg, 0.0026 mmol) in 78% yield. ¹H NMR (700 MHz, DMSO-d₆): δ 1.20 (m, 2H), 1.27 (m, 8H), 1.46 (m, 16H), 1.60 (m, 4H), 2.06 (t, J = 7.4 Hz, 10H), 2.31 (t, J = 6.4 Hz, 8H), 2.58 (m, 8H), 2.82 (dd, J = 12.4 Hz, 5.1 Hz, 4H), 3.08 (m, 24H), 3.18 (m, 12H), 3.31 (m, 16 H), 3.36 (m, 24H), 3.49 (m, 32H), 3.58 (t, J = 6.5 Hz, 8H), 3.82 (dd, J = 5.4 Hz, 2.5 Hz, 2H), 4.12 (m, 4H), 4.30 (m, 4H), 6.37 (s, 4H), 6.42 (s, 4H), 6.55 (br. s, 3H), 6.60 (d, J = 8.7 Hz, 1H), 6.66 (s, 1H), 7.84 (t, J = 5.6 Hz, 4H), 8.23 (s, 4H), 8.43 (br. s, 2H), 9.43 (s, 2H), 9.58 (s, 1H), 7.16 (d, J = 8.2 Hz, 1H), 7.73 (d, J = 7.9 Hz, 1H), 8.08 (s, 1H), 8.25 (s, 1H), 9.63 (s, 2H), 9.77 (s, 1H), 10.12 (m, 3H). MALTI-TOF-MS: observed Mw 3336.0 (calculated exact mass 3333.57; calculated Mw 3336.08). ESI-MS: 1112.7 [M+3H]³⁺, 834.7 [M+4H]⁴⁺, 668.0 [M+5H]⁵⁺.

Biotin PEGylated G1 linker SB-T-1214 conjugate (3-21)

To a 5 mL vial biotin PEGylated G1 alkyne conjugate **3-19** (9.7 mg, 0.0036 mmol) and SB-T-1214-linker-PEG₃-azide **3-14** (4.8 mg, 0.0036 mmol) were dissolved in DMF (0.8 mL). The vial was purged with nitrogen for three times. After that, copper sulfate pentahydrate (0.9 mg, 0.0036 mmol) dissolved in water (0.1 mL) was added into the mixture under nitrogen. Sodium ascorbate (0.7 mg, 0.0036 mmol) dissolved in water (0.1 mL) was then added into the reaction mixture under nitrogen to afford a colorless solution. The reaction was monitored by ESI-MS. Upon the reaction was completed, the reaction mixture was directly purified by preparative HPLC, and the solvent was removed by freezer-drier to give biotin PEGylated G1 linker SB-T-1214 conjugate **3-21** as a white solid (11.8 mg, 0.0029 mmol) in 81% yield. ¹H NMR (700 MHz, DMSO-d₆): δ 0.88 (m, 1H), 0.96 (m, 2H), 1.03 (m, 4H), 1.18 (m, 4H), 1.29 (m, 8H), 1.39 (s, 9H), 1.45 (m, 16H), 1.60 (m, 6H), 1.72 (m, 3H), 1.82 (s, 3H), 2.06 (m, 9H), 2.30 (m, 9H), 2.58 (m, 10H), 2.65 (br. s, 3H), 2.80 (dd, J = 12.4 Hz, J = 5.1 Hz, 4H), 2.96 (m, 1H), 3.08 (m,

16H), 3.18 (m, 12H), 3.38 (m, 20H), 3.49 (m, 36H), 3.55 (m, 2H), 3.58 (t, J = 6.5 Hz, 8H), 3.65 (d, J = 7.1 Hz), 3.78 (t, J = 5.3 Hz, 2H), 3.97 (m, 2H), 4.03 (m, 2H), 4.08 (m, 2H), 4.13 (m, 4H), 4.26 (m, 2H), 4.31 (m, 4H), 4.48 (t, J = 5.2 Hz, 2H), 4.70 (m, 1H), 4.80 (d, J = 7.8 Hz, 1H), 4.93 (m, 2H), 5.14 (m, 1H), 5.46 (d, J = 7.1 Hz, 1H), 5.98 (s, 1H), 6.31 (s, 1H), 6.37 (m, 3H), 6.42 (m, 4H), 7.23 (m, 1H), 7.26 (m, 1H), 7.31 (m, 1H), 7.37 (m, 1H), 7.53 (t, J = 7.9 Hz, 2H), 7.66 (t, J = 7.4 Hz, 1H), 7.74 (d, J = 7.8 Hz, 1H), 7.84 (m, 4H), 7.94 (m, 3H), 8.00 (d, J = 7.6 Hz, 2H), 8.26 (m, 4H), 8.44 (s, 2H), 9.43 (s, 2H), 9.59 (s, 1H). MALTI-TOF-MS: observed Mw 4065.9 (calculated exact mass 4061.95; calculated Mw 4065.02). ESI-MS: 1356.8 [M+3H]³⁺, 1017.0 [M+4H]⁴⁺, 813.8 [M+5H]⁵⁺.

Biotin PEGylated G3 alkyne conjugate (3-22)

To a solution of biotin PEGylated G3 PAMAM dendrimer **3-9** (87 mg, 0.0042 mmol) in DMF (1 mL) was added TCEP (0.5 M) (26 μ L, 0.013 mmol) dropwise. The reaction mixture was allowed to stir at 0 °C for 20 min. Maleimido alkyne spacer **3-18** (10 mg, 0.040 mmol) was then added. The reaction mixture was allowed to stir at room temperature for 2 days. Upon the reaction was completed, the reaction mixture was directly purified by dialysis against methanol (3 x 1000 mL) for three days. Then the solvent was removed by evaporation to give biotin PEGylated G3 alkyne conjugate **3-22** as white solid (77 mg, 0.0072 mmol) in 86% yield. The product was further purified by preparative HPLC before use in the next step. MALTI-TOF-MS: observed Mw 10621.5 (calculated exact mass 10614.62; calculated Mw 10622.38). ESI-MS: 1328.6 [M+8H]⁸⁺, 1181.1 [M+9H]⁹⁺, 1063.4 [M+10H]¹⁰⁺.

Biotin PEGylated G3 FITC conjugate (3-23)

To a 5 mL vial biotin PEGylated G3 alkyne conjugate **3-22** (24.5 mg, 0.0023 mmol) and FITC-PEG₃-azide **3-15** (2.8 mg, 0.0046 mmol) were dissolved in DMF (0.8 mL). The vial was purged with nitrogen for three times. After that, copper sulfate pentahydrate (1.2 mg, 0.0046 mmol) dissolved in water (0.1 mL) was added into the mixture under nitrogen. Sodium ascorbate (0.9 mg, 0.0046 mmol) dissolved in water (0.1 mL) was then added into the reaction mixture under nitrogen to afford an orange solution. The reaction was monitored by ESI-MS. Upon the reaction was completed, the reaction mixture was directly purified by preparative HPLC, and the solvent was removed by freezer-drier to give biotin PEGylated G3 FITC conjugate **3-23** as an orange solid (13.4 mg, 0.0012 mmol) in 52% yield. MALTI-TOF-MS: observed Mw 11242.0 (calculated exact mass 11221.79; calculated Mw 11230.02). ESI-MS: 1404.8 [M+8H]⁸⁺, 1247.7 [M+9H]⁹⁺.

Biotin PEGylated G3 linker SB-T-1214 conjugate (3-24)

To a 5 mL vial biotin PEGylated G3 alkyne conjugate **3-22** (30.3 mg, 0.0029 mmol) and SB-T-1214-linker-PEG₃-azide **3-14** (3.8 mg, 0.0029 mmol) were dissolved in DMF (0.8

mL). The vial was purged with nitrogen for three times. After that, copper sulfate pentahydrate (0.7 mg, 0.0029 mmol) dissolved in water (0.1 mL) was added into the mixture under nitrogen. Sodium ascorbate (0.6 mg, 0.0029 mmol) dissolved in water (0.1 mL) was then added into the reaction mixture under nitrogen to afford a colorless solution. The reaction was monitored by ESI-MS. Upon the reaction was completed, the reaction mixture was directly purified by preparative HPLC, and the solvent was removed by freezer-drier to give biotin PEGylated G3 linker SB-T-1214 conjugate **3-24** as a white solid (18.8 mg, 0.0016 mmol) in 55% yield. MALTI-TOF-MS: observed Mw 11966.6 (calculated exact mass 11950.17; calculated Mw 11958.95). ESI-MS: 1495.8 [M+8H]⁸⁺, 1329.8 [M+9H]⁹⁺.

***tert*-Butyl 14-oxo-4,7,10-trioxa-13-azaoctadec-17-yn-1-oate (3-25)**

To a solution of 4-pentynoic acid (800 mg, 8.15 mmol), DIPEA (1.55 g, 12.0 mmol), EDCHCl (2.30 g, 12.0 mmol) and DMAP (1.47 g, 12.0 mmol) dissolved in DCM (40 mL), was added a solution of *tert*-butyl 12-amino-4,7,10-trioxadecanoate **3-3** (2.78 g, 10.0 mmol) in DCM (20 mL) dropwise. The reaction mixture was allowed to stir at room temperature overnight. Upon the reaction was completed, the solvent was evacuated and the crude was purified by column chromatography on silica gel (gradient eluent: DCM/methanol from 50/1 to 20/1) to give *tert*-butyl 14-oxo-4,7,10-trioxa-13-azaoctadec-17-yn-1-oate **3-25** as pale yellow oil (2.16 g, 6.05 mmol) in 74% yield. ¹H NMR (400 MHz, CDCl₃): δ 1.44 (s, 9H), 2.01 (t, J = 2.6 Hz, 1H), 2.41 (t, J = 6.8 Hz, 2H), 2.2.51 (m, 4H), 3.46 (m, 2H), 3.56 (t, J = 4.8 Hz, 2H), 3.64 (m, 8H), 3.72 (t, J = 2.6 Hz, 2H), 6.26 (s, 1H). ESI-MS *m/z* : 358.2 [M+H]⁺.

14-Oxo-4,7,10-trioxa-13-azaoctadec-17-yn-1-oic acid (3-26)

To a solution of *tert*-butyl 14-oxo-4,7,10-trioxa-13-azaoctadec-17-yn-1-oate **3-25** (2.16 g, 6.05 mmol) in DCM (20 mL), was added TFA (5 mL) dropwise. The reaction mixture was allowed to stir at room temperature overnight. Upon the reaction was completed, the solvent was evacuated and the crude was purified by column chromatography on silica gel (gradient eluent: DCM/methanol from 50/1 to 10/1) to give 14-oxo-4,7,10-trioxa-13-azaoctadec-17-yn-1-oic acid **3-26** as pale yellow oil (1.73 g, 5.76 mmol) in 95% yield. ¹H NMR (400 MHz, CDCl₃): δ 2.01 (t, J = 2.6 Hz, 1H), 2.45 (t, J = 6.4 Hz, 2H), 2.53 (m, 2H), 2.63 (t, J = 6.0 Hz, 2H), 3.49 (m, 2H), 3.59 (t, J = 5.0 Hz, 2H), 3.64 (m, 8H), 3.79 (t, J = 5.9 Hz, 2H), 6.58 (br s, 1H).

2,5-Dioxopyrrolidin-1-yl 14-oxo-4,7,10-trioxa-13-azaoctadec-17-yn-1-oate (3-27)

To a solution of 14-oxo-4,7,10-trioxa-13-azaoctadec-17-yn-1-oic acid **3-26** (1.73 g, 5.76 mmol) in DCM (40 mL) was added EDCHCl (1.33 g, 6.91 mmol) and NHS (785 mg, 6.91 mmol). The reaction mixture was allowed to stir at room temperature overnight. Upon the reaction was completed, the solvent was evacuated and the crude was purified

by column chromatography on silica gel (gradient eluent: DCM/methanol from 50/1 to 10/1) to give 2,5-dioxopyrrolidin-1-yl 14-oxo-4,7,10-trioxa-13-azaoctadec-17-yn-1-oate **3-27** as pale yellow oil (1.78 g, 4.47 mmol) in 78% yield. ¹H NMR (400 MHz, CDCl₃): δ 2.02 (m, 1H), 2.43 (m, 2H), 2.52(m, 2H), 2.62 (m, 1H), 2.75 (s, 4H), 2.84 (m, 3H), 2.94 (m, 2H), 3.46 (m, 2H), 3.59 (m, 10H), 3.78 (m, 1H), 3.84 (m, 1H), 5.30 (s, 1H). ESI-MS *m/z* : 399.1 [M+H]⁺.

Alkyne PEGylated G1 PAMAM dendrimer (3-28)

To a solution of G1 PAMAM dendrimer (DNT-294, 20 w% in methanol) (80 mg, 0.0525 mmol) in methanol (2 mL) was added a solution of 2,5-dioxopyrrolidin-1-yl 14-oxo-4,7,10-trioxa-13-azaoctadec-17-yn-1-oate **3-27** (500 mg, 1.26 mmol) in methanol (4 mL). The reaction mixture was allowed to stir at room temperature for three days. Upon the reaction was completed, the reaction mixture was directly purified by dialysis against methanol (3 x 1000 mL) for three days. Then the solvent was removed by evaporation to give alkyne PEGylated G1 PAMAM dendrimer **3-28** as pale yellow solid (186 mg, 0.0491 mmol) in 93% yield. MALTI-TOF-MS: observed Mw 3807.8 (calculated exact mass 3786.13; calculated Mw 3788.59). ESI-MS: 948.0 [M+4H]⁴⁺, 758.6 [M+5H]⁵⁺.

Bismaleimido linker (3-29)

To a solution of mixed anhydride (1.12 g, 3.96 mmol) in 20 mL THF, was added PEG-diamine (418 mg, 1.90 mmol) diluted with 5 mL THF dropwise at 0 °C. The reaction mixture was allowed to warm to room temperature and stir under nitrogen for overnight. The reaction mixture was then concentrated to remove solvent and purified by column chromatography on silica gel (gradient eluent: DCM/methanol from 50/1 to 10/1) to give bismaleimide crosslinker *N,N'*-(((oxybis(ethane-2,1-diyl))bis(oxy))bis(propane-3,1-diyl))bis(4-(2,5-dioxo-2,5-dihydro-1H-pyrrol-1-yl)butanamide) **3-29** (873 mg, 1.59 mmol) as white solid in 84% yield. ¹H NMR (400 MHz, CDCl₃): δ 1.78 (m, 4H), 1.93 (m, 4H), 2.15 (t, J = 7.2 Hz, 4H), 3.34 (dd, J = 6.6 Hz, J = 12.6 Hz, 4H), 3.60 (m, 16H), 6.35 (br. s, 2H), 6.70 (s, 4H).

ABTD1 (3-31)

To a 2 mL vial biotin-G3-G1-alkyne conjugate **3-30** (5.5 mg, 0.00043 mmol) and SB-T-1214-linker-PEG₃-azide **3-14** (12 eq) were dissolved in DMF (0.4 mL). The vial was purged with nitrogen for three times. After that, copper sulfate pentahydrate (12 eq) dissolved in water (0.05 mL) was added into the mixture under nitrogen. Sodium ascorbate (12 eq) dissolved in water (0.05 mL) was then added into the reaction mixture under nitrogen to afford a colorless solution. After overnight reaction, 200 μL of the reaction mixture was taken out, diluted with CH₃CN/H₂O (4/1) and directly characterized by GPC.

ABTD3 (3-32)

To a 2 mL vial biotin-G3-G1-alkyne conjugate **3-30** (3.0 mg, 0.00023 mmol) and FITC-PEG3-azide (20 eq) were dissolved in DMF (0.4 mL). The vial was purged with nitrogen for three times. After that, copper sulfate pentahydrate (20 eq) dissolved in water (0.05 mL) was added into the mixture under nitrogen. Sodium ascorbate (20 eq) dissolved in water (0.05 mL) was then added into the reaction mixture under nitrogen to afford a yellow solution. After overnight reaction, 200 μ L of the reaction mixture was taken out, diluted with CH₃CN/H₂O (4/1) and directly characterized by GPC.

*N*²,*N*⁴-Bis-(2-(2-(2-(2-azidoethoxy)ethoxy)ethoxy)ethyl)-6-chloro-1,3,5-triazin-2,4-diamine (3-33)

To cyanuric chloride (500 mg, 2.71 mmol) dissolved in freshly distilled anhydrous THF (15 mL) in a 50 mL round bottomed flask, was added amino-PEG₃-azide **3-13** (1.30 g, 5.96 mmol) in freshly distilled anhydrous THF (10 mL) dropwise. DIPEA (700 mg, 5.42 mmol) was then slowly added dropwise. The reaction mixture was allowed to slowly warm up to 60 °C in an oil bath and stirred overnight. Upon the reaction was completed, the solvent was evacuated and the crude was purified by column chromatography on silica gel (gradient eluent: DCM/methanol from 50/1 to 10/1) to give product *N*²,*N*⁴-Bis-(2-(2-(2-(2-azidoethoxy)ethoxy)ethoxy)ethyl)-6-chloro-1,3,5-triazin-2,4-diamine **3-33** as white solid (838 mg, 1.53 mmol) in 57% yield and side product *N*-(2-(2-(2-(2-azidoethoxy)ethoxy)ethoxy)ethyl)-4,6-dichloro-1,3,5-triazin-2-amine **3-42** as colorless oil (275 mg, 0.751 mmol) in 28% yield. Product: ¹H NMR (400 MHz, CDCl₃): δ 3.40 (t, *J* = 4.9 Hz, 4H), 3.64 (m, 28 H), 5.75 (br. s, 1H), 5.87 (br. s, 1H). ¹³C NMR (100 MHz, CDCl₃): δ 40.6, 40.7, 50.7, 69.4, 69.7, 70.1, 70.3, 70.5, 70.6, 70.7, 70.8. ESI-MS *m/z* : 548.3 [M+H]⁺. Side product: ¹H NMR (400 MHz, CDCl₃): δ 3.40 (t, *J* = 4.9 Hz, 4H), 3.70 (m, 14 H), 6.65 (br. s, 1H). ¹³C NMR (100 MHz, CDCl₃): δ 41.3, 50.7, 68.9, 70.1, 70.5, 70.6, 70.7, 70.8. ESI-MS *m/z* : 366.0 [M+H]⁺.

Mono-Boc-1,4-diaminobutane (3-34)

To 1,4-diaminobutane (4.41 g, 50.0 mmol) dissolved in DCM (1.25 L), was added di-*tert*-butyl dicarbonate (1.09 g, 5.00 mmol) in DCM (100 mL) dropwise within 4 hours *via* an additional funnel. The reaction mixture turned milky and was allowed to stir overnight at room temperature. Upon completion, the reaction mixture was concentrated and water was added to dissolve the white precipitate. Then the mixture was extracted with DCM (3 x 80 mL). The organic layer was collected, washed with brine (3 x 30 mL), and dried over anhydrous magnesium sulfate. The magnesium sulfate was subsequently removed by vacuum filtration and the filtrate was concentrated in vacuo to afford product mono-Boc-1,4-diaminobutane **3-34** as pale yellow oil (902 mg, 4.77 mmol) in 95% yield. ¹H

NMR (400 MHz, CDCl₃): δ 1.42 (s, 9H), 1.48 (m, 4H), 2.70 (t, J = 6.4 Hz, 2H), 3.11 (m, 2H), 4.69 (br. s, 1H). ESI-MS m/z : 189.1 [M+H]⁺.

***tert*-Butyl (4-((4,6-bis((2-(2-(2-(2-azidoethoxy)ethoxy)ethoxy)ethyl)amino)-1,3,5-triazin-2-yl)amino)butyl)carbamate (3-35)**

To *N*²,*N*⁴-bis-(2-(2-(2-(2-azidoethoxy)ethoxy)ethoxy)ethyl)-6-chloro-1,3,5-triazin-2,4-diamine **3-33** (480 mg, 0.878 mmol) dissolved in freshly distilled anhydrous THF (16 mL) in a 50-mL round-bottom flask, was added mono-Boc-1,4-diaminobutane **3-34** (412 mg, 2.19 mmol). DIPEA (283 mg, 2.19 mmol) was then slowly added dropwise. The reaction mixture was allowed to slowly heat up to reflux in an oil bath and stirred overnight. Upon the reaction was completed, the solvent was removed in vacuo and the crude was purified by column chromatography on silica gel (gradient eluent: DCM/methanol from 100/1 to 100/3) to give product *tert*-butyl (4-((4,6-bis((2-(2-(2-(2-azidoethoxy)ethoxy)ethoxy)ethyl)amino)-1,3,5-triazin-2-yl)amino)butyl)carbamate **3-35** as pale yellow sticky oil (558 mg, 0.797 mmol) in 91% yield. ¹H NMR (400 MHz, CDCl₃): δ 1.44 (s, 9H), 1.54 (m, 4H), 3.14 (m, 2H), 3.35 (m, 2H), 3.38 (t, J = 5.1 Hz, 4H), 3.64 (m, 28H), 4.83 (br. s, 1H), 5.25 (br. s, 1H). ESI-MS m/z : 700.4 [M+H]⁺.

Tri-branched spacer (3-36)

To a solution of *tert*-butyl (4-((4,6-bis((2-(2-(2-(2-azidoethoxy)ethoxy)ethoxy)ethyl)amino)-1,3,5-triazin-2-yl)amino)butyl)carbamate **3-35** (100 mg, 0.143 mmol) in THF/H₂O (1 mL/1 mL) in a 10 mL round-bottomed flask, was added maleimido alkyne spacer **3-18** (71 mg, 0.29 mmol), copper sulfate pentahydrate (71 mg, 0.29 mmol) and ascorbic acid (60 mg, 0.34 mmol). The reaction mixture was allowed to stir at room temperature under inert condition and solution shows yellow color. The reaction was monitored by TLC and was completed after 2 h. The mixture was dried in vacuo to remove THF, and aqueous layer was extracted with DCM (~ 5 x 30 mL). The organic layer was combined and dried in vacuo. The crude was further purified by column chromatography on neutral alumina gel (gradient eluent: DCM/methanol from 50/1 to 20/1) to give tri-branched spacer **3-36** as pale yellow sticky oil (117 mg, 0.0978 mmol) in 68% yield. ¹H NMR (400 MHz, CDCl₃): δ 1.26 (m, 4H), 1.41 (s, 9H), 1.60 (m, 12H), 2.15 (t, J = 7.5 Hz, 4H), 3.11 (dd, J = 12 Hz, J = 5.8 Hz, 2H), 3.33 (m, 2H), 3.46 (t, J = 7.2 Hz, 4H), 3.57 (m, 24H), 3.85 (t, J = 4.4 Hz, 4H), 4.47 (m, 8H), 6.66 (s, 4H), 7.70 (s, 2H). ¹³C NMR (100 MHz, CDCl₃): δ 25.0, 26.4, 27.2, 28.3, 28.4, 34.9, 36.1, 37.6, 40.5, 50.3, 53.4, 69.4, 69.8, 70.3, 70.5, 79.1, 123.3, 134.1, 144.5, 156.1, 170.8, 172.8. ESI-MS m/z : 1196.6 [M+H]⁺.

Compound 3-37

To a solution of tri-branched spacer **3-36** (117 mg, 0.0978 mmol) in DCM (5 mL) was added TFA (0.5 mL) dropwise. The reaction mixture was stirred at room temperature

overnight. Upon the reaction was completed, the reaction mixture was concentrated in vacuo to give crude product **3-37** as pale yellow sticky oil (183 mg, contain some TFA). ESI-MS m/z : 548.8 $[M+2H]^{2+}$.

Compound 3-38

To a solution of compound **3-37** (0.0978 mmol, theoretical) in DCM (5 mL), was added DIPEA (103 mg, 0.80 mmol) dropwise. DOTA-tris-*t*Bu-mono-NHS ester (67 mg, 0.10 mmol) was then added to the reaction mixture. The reaction mixture was stirred at room temperature for 3 h. Upon the reaction was completed, the solvent was evacuated and the crude was purified by column chromatography on neutral alumina gel (gradient eluent: DCM/methanol from 50/1 to 20/1) to give product **3-38** as white sticky solid (104 mg, 0.0630 mmol) in 65% yield. ^1H NMR (400 MHz, CDCl_3): δ 1.26 (m, 4H), 1.43 (m, 27H), 1.60 (m, 12H), 2.20 (t, $J = 7.5$ Hz, 4H), 2.34 (br. m, 24 H), 3.19 (m, 2H), 3.33 (m, 2H), 3.46 (m, 6H), 3.45 (m, 8H), 3.57 (m, 24H), 3.85 (t, $J = 5.1$ Hz, 4H), 4.47 (m, 8H), 5.05 (br. s, 1H), 5.27 (br. s, 2H), 6.65 (s, 4H), 7.10 (br. s, 2H), 7.76 (s, 2H), 8.84 (br. s, 1H). ^{13}C NMR (100 MHz, CDCl_3): δ 25.1, 26.4, 27.3, 28.0, 28.3, 35.0, 36.1, 37.7, 38.9, 40.3, 50.2, 53.4, 55.8, 56.1, 69.5, 70.1, 70.2, 70.5, 81.8, 81.9, 123.3, 134.1, 144.8, 170.8, 171.5, 172.3, 173.0. ESI-MS m/z : 826.5 $[M+2H]^{2+}$, 551.1 $[M+3H]^{3+}$.

Compound 3-39

To a solution of compound **3-38** (104 mg, 0.0630 mmol) in DCM (5 mL) was added TFA (1.5 mL) dropwise. The reaction mixture was stirred at room temperature overnight. Upon the reaction was completed, the reaction mixture was concentrated in vacuo to give crude product **3-39** as pale yellow sticky solid (120 mg, TFA salt). MALTI-TOF-MS: observed Mw 1483.3 (calculated exact mass 1481.77, calculated Mw 1482.67). ESI-MS m/z : 798.5 $[M+2H]^{2+}$, 532.4 $[M+3H]^{3+}$.

Compound 3-40

To crude **3-39** (60 mg, 0.0315 mmol theoretically) in 4 mL water (milky solution) was added gadolinium (III) chloride hexahydrate (14.2 mg, 0.0382 mmol). 1 M NaOH solution was slowly added via a syringe. The solution slowly turned into light pink color after 0.20 mL 1 M NaOH solution was added ($\text{pH} = 7$ at this point) while some white precipitate slowly came out (gadolinium (III) hydroxide). The mixture was allowed to stir at room temperature overnight and the reaction was monitored by MALDI-TOF-MS. Upon the reaction was completed, the white precipitate was filtered off, and the filtrate was concentrated in vacuo to afford product **3-40** as a light pink solid (66 mg) in quantitative yield. MALTI-TOF-MS: observed Mw 1636.9 (calculated exact mass 1636.67, calculated Mw 1636.89).

Conjugate 3-41

To alkyne PEGylated G1 PAMAM dendrimer **3-28** (12 mg, 0.0032 mmol) dissolved in MeOH (1.2 mL) was added TCEPHCl (0.5 M solution in water, 20 μ L, 0.010 mmol) dropwise. The reaction mixture was allowed to stir at room temperature for 20 min. Then compound **3-40** in water (1.2 mL) was added dropwise. The reaction mixture was allowed to stir at room temperature overnight. Upon the reaction was completed, the solvent was removed by freezer-drier to give crude product **3-41** as pink solid (90 mg). MALTI-TOF-MS: observed Mw 3536.1 (calculated Mw 3532.16).

***N*-(2-(2-(2-(2-azidoethoxy)ethoxy)ethoxy)ethyl)-4,6-dichloro-1,3,5-triazin-2-amine (3-42)**

To cyanuric chloride (366 mg, 1.99 mmol) dissolved in THF (16 mL) and cooled to 0 °C was added DIPEA dropwise. Amino-PEG₃-azide **3-13** (433 mg, 1.99 mmol) in THF (8 mL) was then added dropwise. White precipitate came out. The reaction mixture was allowed to stir at room temperature overnight. Upon the reaction was completed, water was added, and the mixture was extracted with ethyl acetate (3 x 50 mL). The organic layer was collected, washed with brine (3 x 30 mL), and dried over anhydrous magnesium sulfate. The magnesium sulfate was subsequently removed by vacuum filtration and the filtrate was concentrated in vacuo. The resulting crude was further purified by flash column chromatography on silica gel (gradient eluent: DCM/methanol from 100/1 to 50/1) to afford *N*-(2-(2-(2-(2-azidoethoxy)ethoxy)ethoxy)ethyl)-4,6-dichloro-1,3,5-triazin-2-amine **3-42** as pale yellow oil (601 mg, 1.64 mmol) in 83% yield. ¹H NMR (400 MHz, CDCl₃): δ 3.40 (t, J = 4.9 Hz, 2H), 3.70 (m, 14 H), 6.65 (br. s, 1H). ¹³C NMR (100 MHz, CDCl₃): δ 41.3, 50.7, 68.9, 70.1, 70.5, 70.6, 70.7, 165.8, 169.9, 170.8. ESI-MS m/z : 366.0 [M+H]⁺.

Mono-Boc-PEG₃-diamine (3-43)

To a solution of PEG₃-diamine (1 eq) in 1,4-dioxane [0.60 M] was added a solution of Boc anhydride (8 eq) in 1,4-dioxane [0.15 M] dropwise via an additional funnel. The reaction mixture was allowed to stir at room temperature overnight. Upon the reaction was completed, solvent 1,4-dioxane was removed by freezer-drier. Then water was added, and the mixture was extracted with ethyl acetate (4 x 100 mL). The organic layer was collected, washed with brine (3 x 30 mL), and dried over anhydrous magnesium sulfate. The magnesium sulfate was subsequently removed by vacuum filtration and the filtrate was concentrated in vacuo to afford product mono-Boc-PEG₃-diamine **3-43** as pale yellow oil in 87% yield. ¹H NMR (400 MHz, CDCl₃): δ 1.43 (br. s, 11H), 1.74 (m, 4H), 2.80 (m, 2H), 3.22 (m, 2H), 3.53 (m, 4H), 3.58 (m, 4H), 3.62 (m, 4H), 5.09 (s, 1H). ¹³C NMR (100 MHz, CDCl₃): δ 28.5, 29.6, 33.3, 38.5, 39.7, 69.5, 69.6, 70.2, 70.3, 70.6, 70.7, 78.9, 156.1. ESI-MS m/z : 321.2 [M+H]⁺.

Compound 3-44

To *N*-(2-(2-(2-(2-azidoethoxy)ethoxy)ethoxy)ethyl)-4,6-dichloro-1,3,5-triazin-2-amine **3-42** (1 eq) dissolved in THF [0.20 M] was added DIPEA (3 eq) and mono-Boc-PEG₃-diamine **3-43** (5 eq). The reaction mixture was allowed to heat up to reflux and stir at reflux overnight. Upon the reaction was completed, water was added, and the mixture was extracted with DCM (3 x 50 mL). The organic layer was collected, washed with brine (3 x 30 mL), and dried over anhydrous magnesium sulfate. The magnesium sulfate was subsequently removed by vacuum filtration and the filtrate was concentrated in vacuo. The resulting crude was further purified by flash column chromatography on silica gel (gradient eluent: DCM/methanol from 50/1 to 10/1) to afford compound **3-44** as pale yellow oil in 85% yield. ¹H NMR (400 MHz, CDCl₃): δ 1.43 (br. s, 18H), 1.76 (m, 8H), 3.21 (m, 4H), 3.38 (m, 4H), 3.60 (m, 40 H), 5.04 (br. s, 2H). ¹³C NMR (100 MHz, CDCl₃): δ 28.5, 29.6, 38.3, 50.7, 69.3, 69.6, 70.0, 70.1, 70.2, 70.3, 70.4, 70.5, 70.6, 70.7, 156.1. ESI-MS *m/z* : 934.5 [M+H]⁺.

Compound 3-45

To compound **3-44** (200 mg, 0.214 mmol) dissolved in DCM (1.6 mL) was added TFA (0.4 mL). The reaction mixture was allowed to stir at room temperature overnight. The reaction was monitored by ESI-MS. Upon the reaction was completed, solvent and TFA was evaporated in vacuo to give compound **3-45** as a yellow oil (crude TFA salt). The crude was directly used in the next step without further purification. ESI-MS *m/z* : 734.5 [M+H]⁺.

6-Maleimidocaproic acid OSu ester (3-46)

To 6-maleimidocaproic acid **3-16** (211 mg, 1.00 mmol) dissolved in DCM (10 mL) was added EDCHCl (345 mg, 1.80 mmol) and NHS (207 mg, 1.80 mmol). The reaction mixture was allowed to stir at room temperature for overnight. Upon the reaction was completed, water was added, and the mixture was extracted with DCM (3 x 30 mL). The organic layer was collected, washed with brine (3 x 30 mL), and dried over anhydrous magnesium sulfate. The magnesium sulfate was subsequently removed by vacuum filtration and the filtrate was concentrated in vacuo. The resulting crude was further purified by flash column chromatography on silica gel (gradient eluent: DCM/methanol from 50/1 to 20/1) to afford 6-maleimidocaproic acid OSu ester **3-46** as a colorless oil (217 mg, 0.704 mmol) in 70% yield. ¹H NMR (400 MHz, CDCl₃): δ 1.40 (m, 2H), 1.63 (m, 2H), 1.77 (m, 2H), 2.60 (t, J = 7.4 Hz, 2H), 2.83 (br. s, 4H), 3.53 (t, J = 7.2 Hz, 2H), 6.68 (s, 2H).

Tri-branched spacer (3-47)

To tri-branched intermediate crude **3-45** in DCM (1 mL) was added excess potassium carbonate (200 mg, 1.45 mmol) was added to neutralize TFA. 6-Maleimidocaproic acid OSu ester **3-46** (198 mg, 0.642 mmol) was then added to the mixture. The reaction

mixture was allowed to stir at room temperature for overnight. Upon the reaction was completed, water was added, and the mixture was extracted with DCM (3 x 30 mL). The organic layer was collected, washed with brine (3 x 30 mL), and dried over anhydrous magnesium sulfate. The magnesium sulfate was subsequently removed by vacuum filtration and the filtrate was concentrated in vacuo. The resulting crude was further purified by flash column chromatography on silica gel (gradient eluent: DCM/methanol from 50/1 to 10/1) to afford compound **3-47** as pale yellow oil (102 mg, 0.0912 mmol) in 43% yield. ¹H NMR (400 MHz, CDCl₃): δ 1.29 (m, 6H), 1.62 (m, 8H), 1.75 (m, 4H), 1.82 (m, 4H), 2.12 (t, J = 7.4 Hz, 4H), 3.34 (m, 4H), 3.39 (t, J = 5.2 Hz, 2H), 3.43 (m, 4H), 3.50 (m, 4H), 3.54 (m, 8H), 3.60 (m, 12H), 3.67 (m, 16H), 6.20 (br. s, 3H), 6.68 (s, 4H).

Boc protected G1 PAMAM dendrimer (3-48)

To G1 PAMAM dendrimer (DNT-294) (100 mg, 0.0657 mmol) in methanol (3 mL) was added Boc anhydride (344 mg, 1.58 mmol). The reaction mixture was allowed to stir at room temperature for two days. Upon the reaction was completed, the reaction mixture was directly purified by dialysis against methanol (3 x 1000 mL) for three days. Then the solvent was removed by evaporation to give Boc protected G1 PAMAM dendrimer **3-48** as a white solid (107 mg, 0.0461 mmol) in 70% yield. ESI-MS *m/z* : 775.0 [M+3H]³⁺, 581.6 [M+4H]⁴⁺.

Conjugate 3-49

To a solution of Boc protected G1 PAMAM dendrimer **3-48** (18 mg, 0.0078 mmol) in methanol (1 mL) was added a solution TCEPHCl (0.5 M solution in water, 47 μL, 0.024 mmol) dropwise. Tri-branched spacer **3-47** (90 mg, 0.080 mmol) was then added to the mixture. The reaction mixture was allowed to stir at room temperature for 2 days. Upon the reaction was completed, the reaction mixture was directly purified by dialysis against methanol (3 x 1000 mL) for three days. Then the solvent was removed by evaporation to give conjugate **3-49** as pale yellow solid. MALDI-TOF-MS: observed Mw 2284.2 (calculated exact mass 2281.34; calculated Mw 2282.82). ESI-MS: 761.8 [M+3H]³⁺.

Compound 3-50

To cyanuric chloride (309 mg, 1.68 mmol) dissolved in THF (15 mL) and cooled to 0 °C was added DIPEA dropwise. Mono-Boc-PEG₃-diamine **3-43** (537 mg, 1.68 mmol) in THF (5 mL) was then added dropwise. White precipitate came out. The reaction mixture was allowed to stir at room temperature overnight. Upon the reaction was completed, water was added, and the mixture was extracted with ethyl acetate (3 x 50 mL). The organic layer was collected, washed with brine (3 x 30 mL), dried over anhydrous magnesium sulfate, and concentrated in vacuo. The resulting crude was further purified by flash column chromatography with increasing amount of (hexanes : ethyl acetate) to

afford compound **3-50** as pale yellow oil (628 mg, 1.34 mmol) in 80% yield. ^1H NMR (300 MHz, CDCl_3): δ 1.43 (s, 9H), 1.77 (m, 2H), 1.87 (m, 2H), 3.22 (m, 2H), 3.56 (t, $J = 6.0$ Hz, 2H), 3.64 (m, 12H), 4.93 (br. s, 1H), 7.01 (br. s, 1H).

Compound 3-51

To compound **3-50** (614 mg, 1.32 mmol) in THF (8 mL) was added DIPEA (255 mg, 1.97 mmol) dropwise. Amino-PEG₃-azide **3-13** (287 mg, 1.32 mmol) in THF (2 mL) was then added dropwise. The reaction mixture was allowed to heat up to 50 °C and stir overnight. Upon the reaction was completed, water was added, and the mixture was extracted with DCM (3 x 50 mL). The organic layer was collected, washed with brine (3 x 30 mL), and dried over anhydrous magnesium sulfate. The magnesium sulfate was subsequently removed by vacuum filtration and the filtrate was concentrated in vacuo. The resulting crude was further purified by flash column chromatography on silica gel (gradient eluent: DCM/methanol from 50/1 to 10/1) to afford compound **3-51** as pale yellow oil (789 mg, 1.22 mmol) in 93% yield. ^1H NMR (400 MHz, CDCl_3): δ 1.43 (s, 9H), 1.75 (m, 2H), 1.84 (m, 2H), 3.22 (m, 2H), 3.40 (m, 2H), 3.62 (m, 24H), 4.99 (br. s, 1H), 5.81 (m, 2H). ^{13}C NMR (100 MHz, CDCl_3): δ 28.5, 28.8, 29.6, 40.7, 50.7, 69.5, 70.1, 70.3, 70.5, 70.6, 70.7, 156.1, 165.8, 168.6.

Compound 3-52

To mono-Boc-PEG₃-diamine **3-43** (842 mg, 2.63 mmol) in DCM (12 mL) was added NsCl (700 mg, 3.16 mmol). TEA (320 mg, 3.16 mmol) was then added dropwise. White precipitate slowly came out. The reaction mixture was allowed to stir at room temperature overnight. Upon the reaction was completed, water was added, and the mixture was extracted with DCM (3 x 50 mL). The organic layer was collected, washed with brine (3 x 30 mL), and dried over anhydrous magnesium sulfate. The magnesium sulfate was subsequently removed by vacuum filtration and the filtrate was concentrated in vacuo. The resulting crude was further purified by flash column chromatography on silica gel (gradient eluent: hexanes/ethyl acetate from 3/1 to 1/4) to afford compound **3-52** as pale yellow oil (1.28 g, 2.53 mmol) in 96% yield. ^1H NMR (400 MHz, CDCl_3): δ 1.41 (s, 9H), 1.74 (m, 4H), 3.22 (m, 4H), 3.57 (m, 8H), 3.64 (m, 2H), 4.98 (br. s, 1H), 6.02 (m, 1H), 7.71 (m, 2H), 7.81 (m, 1H), 8.10 (m, 1H). ^{13}C NMR (100 MHz, CDCl_3): δ 28.4, 28.9, 29.0, 29.6, 38.6, 42.5, 42.6, 69.6, 69.7, 69.8, 70.2, 70.3, 70.4, 70.5, 70.6, 78.8, 125.2, 131.0, 132.6, 132.6, 133.4, 133.8, 133.9, 148.1, 156.0. ESI-MS m/z : 506.3 $[\text{M}+\text{H}]^+$.

Compound 3-53

To compound **3-52** (628 mg, 1.24 mmol) in DCM (2 mL) was added TFA (0.5 mL). The reaction mixture was allowed to stir at room temperature overnight. The reaction was monitored by ESI-MS. Upon the reaction was completed, solvent and TFA was

evaporated in vacuo to give compound **3-53** as a yellow oil. The crude was directly used in the next step without further purification. ESI-MS m/z : 406.3 $[M+H]^+$.

Compound 3-54

To compound **3-53** (1.24 mmol) in THF (5 mL) was added DIPEA (491 mg, 3.80 mmol) to remove TFA. Compound **3-51** (260 mg, 0.400 mmol) was then added. The reaction mixture was allowed to heat up to reflux and stir at reflux overnight. Upon the reaction was completed, water was added, and the mixture was extracted with DCM (3 x 50 mL). The organic layer was collected, washed with brine (3 x 30 mL), and dried over anhydrous magnesium sulfate. The magnesium sulfate was subsequently removed by vacuum filtration and the filtrate was concentrated in vacuo. The resulting crude was further purified by flash column chromatography on silica gel (gradient eluent: DCM/methanol from 50/1 to 20/1) to afford compound **3-54** as pale yellow oil (191 mg, 0.188 mmol) in 47% yield. ^1H NMR (400 MHz, CDCl_3): δ 1.42 (s, 9H), 1.77 (m, 8H), 3.21 (m, 4H), 3.40 (m, 6H), 3.55 (m, 20H), 3.66 (m, 18H), 5.04 (br. s, 1H), 5.39 (br. s, 2H), 6.01 (br. s, 1H), 7.70 (m, 2H), 7.82 (m, 1H), 8.11 (m, 1H). ESI-MS m/z : 1019.5 $[M+H]^+$.

Compound 3-55

To compound **3-54** (182 mg, 0.179 mmol) in DMF (2 mL) was added potassium carbonate (74 mg, 0.537 mmol) and thiophenol (39 mg, 0.358 mmol). The reaction mixture was allowed to stir at room temperature for overnight. Upon the reaction was completed, DMF was removed by freezer drier. The resulting crude was further purified by flash column chromatography on neutral alumina gel (gradient eluent: DCM/methanol from 50/1 to 6/1) to afford compound **3-55** as pale yellow oil (106 mg, 0.127 mmol) in 71% yield. ESI-MS m/z : 833.8 $[M+H]^+$.

Compound 3-56

To compound **3-55** (106 mg, 0.127 mmol) in THF (2 mL) and cooled to 0 °C was added mixed anhydride **3-17** (44 mg, 0.140 mmol). The reaction mixture was allowed to stir at room temperature for overnight. Upon the reaction was completed, water was added, and the mixture was extracted with DCM (3 x 30 mL). The organic layer was collected, washed with brine (3 x 30 mL), and dried over anhydrous magnesium sulfate. The magnesium sulfate was subsequently removed by vacuum filtration and the filtrate was concentrated in vacuo. The resulting crude was further purified by flash column chromatography on silica gel (gradient eluent: DCM/methanol from 50/1 to 10/1) to afford compound **3-56** as pale yellow oil (74 mg, 0.072 mmol) in 57% yield. ^1H NMR (400 MHz, CDCl_3): δ 1.23 (m, 4H), 1.40 (s, 9H), 1.55 (m, 4H), 1.71 (m, 4H), 1.79 (m, 4H), 2.07 (t, J = 7.5 Hz, 2H), 3.18 (m, 2H), 3.30 (m, 2H), 3.42 (m, 6H), 3.56 (m, 36H), 3.73 (m, 1H), 3.84 (m, 1H), 3.96 (m, 1H), 4.11 (m, 1H), 4.57 (d, J = 11.0 Hz, 1H), 5.08

(br. s, 1H), 4.29 (br. s, 2H), 4.49 (d, J = 11.0 Hz, 1H), 6.29 (br. s, 1H). ESI-MS m/z : 1026.7 $[M+H]^+$.

Compound 3-57

To compound **3-56** dissolved in DCM [0.1 M] was added TFA (20% v). The reaction mixture was allowed to stir at room temperature overnight. The reaction was monitored by ESI-MS. Upon the reaction was completed, solvent and TFA was evaporated in vacuo to give compound **3-57** as a yellow oil. The crude was directly used in the next step without further purification.

Compound 3-58

To a solution of Boc protected G1 PAMAM dendrimer **3-48** (50 mg, 0.022 mmol) in methanol (1 mL) was added a solution TCEPHCl (0.5 M solution in water, 130 μ L, 0.065 mmol) dropwise. 6-Maleimidocaproic acid **3-16** (9.0 mg, 0.043 mmol) was then added to the mixture. The reaction mixture was allowed to stir at room temperature for 2 days. Upon the reaction was completed, the reaction mixture was directly purified by dialysis against methanol (3 x 1000 mL) for three days. Then the solvent was removed by evaporation to give compound **3-58** as a white solid. ESI-MS m/z : 1374.8 $[M+H]^+$, 687.5 $[M+2H]^{2+}$.

Cell Culture

ID8 (ovary), MCF7 (breast) and HCT116 (colon) cell lines were cultured as monolayers on 100 mm tissue culture dishes in the RPMI-1640 cell culture medium (Gibco) supplemented with 10% (v/v) heat-inactivated fetal bovine serum (FBS) as well as 1% (v/v) penicillin and streptomycin (P/S) at 37 °C in a humidified atmosphere with 5% CO₂. The cells were harvested and collected by centrifugation at 950 rpm for 5 min, and finally suspended in fresh cell culture medium containing different cell densities for subsequent biological experiments and analysis.

Incubation of Cells with the fluorescent probes

The cell suspension at 5×10^5 cells/well was split into each well of a 6-well plate with 3 mL RPMI-1640 cell culture medium and allowed to grow for 24 h. The fluorescent probe in DMSO was diluted in RPMI-1640 cell culture medium (3 mL) at final concentration of 10 μ M for multi-binding effect study and internalization through receptor-mediated endocytosis (RME) study, respectively, and was used to replace the medium in each well followed by incubated at 37 °C for different periods. One well with cells was incubated without any fluorescent probes as control for different periods. After incubation, the medium was aspirated and the cells were washed twice with PBS, collected by

centrifugation, and resuspended in 300 μ L PBS for flow cytometry fluorescein measurement and confocal microscopy imaging.

Flow Cytometry Fluorescent Measurements of the Cells

Flow cytometry analysis of the treated cells was performed with a flow cytometer, FACSCalibur, operating at a 488 nm excitation wavelength and detecting emission wavelengths with a 530/30 nm bandpass filter. At least 10,000 cells were counted for each experiment using CellQuest 3.3 software (Becton Dickinson) and the distribution of FITC fluorescence was analyzed using WinMDI 2.8 freeware (Joseph Trotter, Scripps Research Institute). Propidium iodide staining was used in all experiments to rule out dead cell count in the analysis.

Confocal Microscopy Imaging of the Treated Cells

Cells treated as described above were dropped onto an uncoated glass dish (MatTek Corp.). Confocal fluorescence microscopy (CFM) experiments were performed using a Zeiss LSM 510 META NLO two-photon laser scanning confocal microscope system, operating at a 488 nm excitation wavelength and at 527 (23 nm detecting emission wavelength using a 505-550 nm bandpass filter. Images were captured using a C-Apochromat 63 \times /1.2 water (corr.) objective or a Plan-Apochromat 100 \times /1.45 oil objective. Acquired data were analyzed using LSM 510 META software.

***In Vitro* Cytotoxicity Assay**

The cytotoxicity of taxoids and conjugates were evaluated by means of a quantitative colorimetric assay using a tetrazolium salt-based analysis (“MTT assay”; MTT = 3-(4,5-dimethylthiazol-2-yl)-2,5-diphenyltetrazolium bromide; Sigma Chemical Co.). The inhibitory activity of each compound is represented by the IC₅₀ value, which is defined as the concentration required for inhibiting 50% of the cell growth. Cells were harvested, collected, and resuspended in 200 μ L medium at a concentration of $\sim 0.5 \times 10^6$ cells per well over a 96-well plate. Cells were allowed to descend to the bottom of the plates overnight and fresh medium was added to each well upon removal of the old medium. A drug or drug conjugate in DMSO stock solution was diluted to a series of concentrations in the cell culture medium to prepare test solutions. These test solutions at different concentrations ranging from 500 pM to 5 μ M (100 μ L each) were added to the wells in the 96-well plate and cells were subsequently cultured for 72 h. After removing the old medium by aspiration, 50 μ L DPBS buffer containing MTT (0.5 mg/mL) was added to each well and incubated at 37 $^{\circ}$ C for 3 h. The resulting DPBS buffer was then removed and as-produced insoluble violet formazan crystals were dissolved into 50 μ L 0.1 N HCl in isopropanol to give a violet solution. The plate was allowed to shake for 8 minutes to fully dissolve the violet formazan crystal, then the spectrophotometric absorbance measurement of each well in the 96-well plate was run at 568 nm. The IC₅₀ values and

their standard errors were calculated from the viability-concentration curve using the Four Parameter Logistic Model of Sigmaplot. The concentration of DMSO per well was $\leq 1\%$ in all cases.

§ 3.7 References

- (1) Peer, D.; Karp, J. M.; Hong, S.; Farokhzad, O. C.; Margalit, R.; Langer, R. Nanocarriers as an emerging platform for cancer therapy. *Nat Nanotechnol* **2007**, *2*, 751-760.
- (2) Duncan, R. Polymer conjugates as anticancer nanomedicines. *Nat Rev Cancer* **2006**, *6*, 688-701.
- (3) Maeda, H. SMANCS and polymer-conjugated macromolecular drugs: advantages in cancer chemotherapy. *Adv Drug Deliver Rev* **2001**, *46*, 169-185.
- (4) Duncan, R.; Seymour, L. W.; Ohare, K. B.; Flanagan, P. A.; Wedge, S.; Hume, I. C.; Ulbrich, K.; Strohalm, J.; Subr, V.; Spreafico, F.; Grandi, M.; Ripamonti, M.; Farao, M.; Suarato, A. Preclinical Evaluation of Polymer-Bound Doxorubicin. *J Control Release* **1992**, *19*, 331-346.
- (5) Thomson, A. H.; Vasey, P. A.; Murray, L. S.; Cassidy, J.; Fraier, D.; Frigerio, E.; Twelves, C. Population pharmacokinetics in phase I drug development: a phase I study of PK1 in patients with solid tumours. *Brit J Cancer* **1999**, *81*, 99-107.
- (6) Vasey, P. A.; Kaye, S. B.; Morrison, R.; Twelves, C.; Wilson, P.; Duncan, R.; Thomson, A. H.; Murray, L. S.; Hilditch, T. E.; Murray, T.; Burtles, S.; Fraier, D.; Frigerio, E.; Cassidy, J.; Comm, C. R. C. P. I. I. Phase I clinical and pharmacokinetic study of PK1 [N-(2-hydroxypropyl)methacrylamide copolymer doxorubicin]: First member of a new class of chemotherapeutic agents - Drug-polymer conjugates. *Clin Cancer Res* **1999**, *5*, 83-94.
- (7) Duncan, R.; Kopecek, J.; Rejmanova, P.; Lloyd, J. B. Targeting of N-(2-Hydroxypropyl)Methacrylamide Co-Polymers to Liver by Incorporation of Galactose Residues. *Biochim Biophys Acta* **1983**, *755*, 518-521.
- (8) Julyan, P. J.; Seymour, L. W.; Ferry, D. R.; Daryani, S.; Boivin, C. M.; Doran, J.; David, M.; Anderson, D.; Christodoulou, C.; Young, A. M.; Hesselwood, S.; Kerr, D. J. Preliminary clinical study of the distribution of HPMA copolymers bearing doxorubicin and galactosamine. *J Control Release* **1999**, *57*, 281-290.
- (9) Li, C.; Yu, D. F.; Newman, R. A.; Cabral, F.; Stephens, L. C.; Hunter, N.; Milas, L.; Wallace, S. Complete regression of well-established tumors using a novel

water-soluble poly(L-glutamic acid) paclitaxel conjugate. *Cancer Res* **1998**, *58*, 2404-2409.

(10) Shaffer, S. A.; Baker Lee, C.; Kumar, A.; Singer, J. W. Proteolysis of xyotax by lysosomal cathepsin B; metabolic profiling in tumor cells using LC-MS. *Eur J Cancer* **2002**, *38*, S129-S129.

(11) Mintzer, M. A.; Grinstaff, M. W. Biomedical applications of dendrimers: a tutorial. *Chem Soc Rev* **2011**, *40*, 173-190.

(12) Bharali, D. J.; Khalil, M.; Gurbuz, M.; Simone, T. M.; Mousa, S. A. Nanoparticles and cancer therapy: A concise review with emphasis on dendrimers. *Int J Nanomed* **2009**, *4*, 1-7.

(13) Tomalia, D. A.; Baker, H.; Dewald, J.; Hall, M.; Kallos, G.; Martin, S.; Roeck, J.; Ryder, J.; Smith, P. A New Class of Polymers - Starburst-Dendritic Macromolecules. *Polym J* **1985**, *17*, 117-132.

(14) Hawker, C. J.; Frechet, J. M. J. Preparation of Polymers with Controlled Molecular Architecture - a New Convergent Approach to Dendritic Macromolecules. *J Am Chem Soc* **1990**, *112*, 7638-7647.

(15) Gillies, E. R.; Frechet, J. M. J. Designing macromolecules for therapeutic applications: Polyester dendrimer-poly(ethylene oxide) "bow-tie" hybrids with tunable molecular weight and architecture. *J Am Chem Soc* **2002**, *124*, 14137-14146.

(16) Ornelas, C.; Pennell, R.; Liebes, L. F.; Weck, M. Construction of a Well-Defined Multifunctional Dendrimer for Theranostics. *Org Lett* **2011**, *13*, 976-979.

(17) Gaertner, H. F.; Cerini, F.; Kamath, A.; Rochat, A. F.; Siegrist, C. A.; Menin, L.; Hartley, O. Efficient orthogonal bioconjugation of dendrimers for synthesis of bioactive nanoparticles. *Bioconjugate Chem* **2011**, *22*, 1103-1114.

(18) Bosman, A. W.; Janssen, H. M.; Meijer, E. W. About Dendrimers: Structure, Physical Properties, and Applications. *Chem Rev* **1999**, *99*, 1665-1688.

(19) Tomalia, D. A.; Reyna, L. A.; Svenson, S. Dendrimers as multi-purpose nanodevices for oncology drug delivery and diagnostic imaging. *Biochem Soc Trans* **2007**, *35*, 61-67.

(20) Astruc, D.; Boisselier, E.; Ornelas, C. Dendrimers Designed for Functions: From Physical, Photophysical, and Supramolecular Properties to Applications in Sensing, Catalysis, Molecular Electronics, Photonics, and Nanomedicine. *Chem Rev* **2010**, *110*, 1857-1959.

- (21) Majoros, I. J.; Thomas, T. P.; Mehta, C. B.; Baker, J. R., Jr. Poly(amidoamine) dendrimer-based multifunctional engineered nanodevice for cancer therapy. *J Med Chem* **2005**, *48*, 5892-5899.
- (22) Islam, M. T.; Majoros, I. J.; Baker, J. R., Jr. HPLC analysis of PAMAM dendrimer based multifunctional devices. *J Chromatogr B Analyt Technol Biomed Life Sci* **2005**, *822*, 21-26.
- (23) Thomas, T. P.; Majoros, I. J.; Kotlyar, A.; Kukowska-Latallo, J. F.; Bielinska, A.; Myc, A.; Baker, J. R., Jr. Targeting and inhibition of cell growth by an engineered dendritic nanodevice. *J Med Chem* **2005**, *48*, 3729-3735.
- (24) Kukowska-Latallo, J. F.; Candido, K. A.; Cao, Z.; Nigavekar, S. S.; Majoros, I. J.; Thomas, T. P.; Balogh, L. P.; Khan, M. K.; Baker, J. R., Jr. Nanoparticle targeting of anticancer drug improves therapeutic response in animal model of human epithelial cancer. *Cancer Res* **2005**, *65*, 5317-5324.
- (25) Majoros, I. J.; Myc, A.; Thomas, T.; Mehta, C. B.; Baker, J. R., Jr. PAMAM dendrimer-based multifunctional conjugate for cancer therapy: synthesis, characterization, and functionality. *Biomacromolecules* **2006**, *7*, 572-579.
- (26) Mullen, D. G.; Fang, M.; Desai, A.; Baker, J. R.; Orr, B. G.; Holl, M. M. B. A Quantitative Assessment of Nanoparticle-Ligand Distributions: Implications for Targeted Drug and Imaging Delivery in Dendrimer Conjugates. *ACS Nano* **2010**, *4*, 657-670.
- (27) Zong, H.; Thomas, T. P.; Lee, K. H.; Desai, A. M.; Li, M. H.; Kotlyar, A.; Zhang, Y.; Leroueil, P. R.; Gam, J. J.; Banaszak Holl, M. M.; Baker, J. R., Jr. Bifunctional PAMAM dendrimer conjugates of folic acid and methotrexate with defined ratio. *Biomacromolecules* **2012**, *13*, 982-991.
- (28) Thomas, T. P.; Huang, B. H.; Choi, S. K.; Silpe, J. E.; Kotlyar, A.; Desai, A. M.; Zong, H.; Gam, J.; Joice, M.; Baker, J. R. Polyvalent Dendrimer-Methotrexate as a Folate Receptor-Targeted Cancer Therapeutic. *Mol Pharm* **2012**, *9*, 2669-2676.
- (29) Matsumura, Y.; Maeda, H. A New Concept for Macromolecular Therapeutics in Cancer-Chemotherapy - Mechanism of Tumor-tropic Accumulation of Proteins and the Antitumor Agent Smancs. *Cancer Res* **1986**, *46*, 6387-6392.
- (30) Folkman, J. What Is the Evidence That Tumors Are Angiogenesis Dependent. *J Natl Cancer I* **1990**, *82*, 4-6.
- (31) Skinner, S. A.; Tutton, P. J.; O'Brien, P. E. Microvascular architecture of experimental colon tumors in the rat. *Cancer Res* **1990**, *50*, 2411-2417.

- (32) Kratz, F.; Muller, I. A.; Ryppa, C.; Warnecke, A. Prodrug strategies in anticancer chemotherapy. *Chemmedchem* **2008**, *3*, 20-53.
- (33) Russell-Jones, G.; McTavish, K.; McEwan, J.; Rice, J.; Nowotnik, D. Vitamin-mediated targeting as a potential mechanism to increase drug uptake by tumours. *J Inorg Biochem* **2004**, *98*, 1625-1633.
- (34) Lu, Y. J.; Low, P. S. Folate-mediated delivery of macromolecular anticancer therapeutic agents. *Adv Drug Deliver Rev* **2002**, *54*, 675-693.
- (35) Leamon, C. P. Folate-targeted drug strategies for the treatment of cancer. *Curr Opin Invest Drugs* **2008**, *9*, 1277-1286.
- (36) Leamon, C. P.; Reddy, J. A.; Vetzal, M.; Dorton, R.; Westrick, E.; Parker, N.; Wang, Y.; Vlahov, I. Folate Targeting Enables Durable and Specific Antitumor Responses from a Therapeutically Null Tubulysin B Analogue. *Cancer Res* **2008**, *68*, 9839-9844.
- (37) Zempleni, J.; Wijeratne, S. S. K.; Hassan, Y. I. Biotin. *Biofactors* **2009**, *35*, 36-46.
- (38) Zempleni, J. Uptake, localization, and noncarboxylase roles of biotin. *Annu Rev Nutr* **2005**, *25*, 175-196.
- (39) Chen, J. Y.; Chen, S. Y.; Zhao, X. R.; Kuznetsova, L. V.; Wong, S. S.; Ojima, I. Functionalized Single-Walled Carbon Nanotubes as Rationally Designed Vehicles for Tumor-Targeted Drug Delivery. *J Am Chem Soc* **2008**, *130*, 16778-16785.
- (40) Chen, S. Y.; Zhao, X. R.; Chen, J. Y.; Chen, J.; Kuznetsova, L.; Wong, S. S.; Ojima, I. Mechanism-Based Tumor-Targeting Drug Delivery System. Validation of Efficient Vitamin Receptor-Mediated Endocytosis and Drug Release. *Bioconjugate Chem* **2010**, *21*, 979-987.
- (41) Vineberg, J. G.; Zuniga, E. S.; Kamath, A.; Chen, Y. J.; Seitz, J. D.; Ojima, I. Design, Synthesis, and Biological Evaluations of Tumor-Targeting Dual-Warhead Conjugates for a Taxoid-Camptothecin Combination Chemotherapy. *J Med Chem* **2014**, *57*, 5777-5791.
- (42) Vineberg, J. G.; Wang, T.; Zuniga, E. S.; Ojima, I. Design, Synthesis, and Biological Evaluation of Theranostic Vitamin-Linker-Taxoid Conjugates. *J Med Chem* **2015**, *58*, 2406-2416.
- (43) Kitov, P. I.; Bundle, D. R. On the nature of the multivalency effect: A thermodynamic model. *J Am Chem Soc* **2003**, *125*, 16271-16284.

- (44) Rudnick, S. I.; Adams, G. P. Affinity and Avidity in Antibody-Based Tumor Targeting. *Cancer Biother Radio* **2009**, *24*, 155-161.
- (45) Vorup-Jensen, T. On the roles of polyvalent binding in immune recognition: Perspectives in the nanoscience of immunology and the immune response to nanomedicines. *Adv Drug Deliver Rev* **2012**, *64*, 1759-1781.
- (46) Kiessling, L. L.; Gestwicki, J. E.; Strong, L. E. Synthetic multivalent ligands in the exploration of cell-surface interactions. *Curr Opin Chem Biol* **2000**, *4*, 696-703.
- (47) Kiessling, L. L.; Strong, L. E.; Gestwicki, J. E. Principles for multivalent ligand design. *Annu Rep Med Chem* **2000**, *35*, 321-330.
- (48) Hong, S.; Leroueil, P. R.; Majoros, I. J.; Orr, B. G.; Baker, J. R.; Holl, M. M. B. The binding avidity of a nanoparticle-based multivalent targeted drug delivery platform. *Chem Biol* **2007**, *14*, 107-115.
- (49) Silpe, J. E.; Sumit, M.; Thomas, T. P.; Huang, B. H.; Kotlyar, A.; van Dongen, M. A.; Holl, M. M. B.; Orr, B. G.; Choi, S. K. Avidity Modulation of Folate-Targeted Multivalent Dendrimers for Evaluating Biophysical Models of Cancer Targeting Nanoparticles. *ACS Chem Biol* **2013**, *8*, 2063-2071.
- (50) van Dongen, M. A.; Silpe, J. E.; Dougherty, C. A.; Kanduluru, A. K.; Choi, S. K.; Orr, B. G.; Low, P. S.; Holl, M. M. B. Avidity Mechanism of Dendrimer-Folic Acid Conjugates. *Mol Pharm* **2014**, *11*, 1696-1706.
- (51) Yellepeddi, V. K.; Kumar, A.; Palakurthi, S. Biotinylated poly(amido)amine (PAMAM) dendrimers as carriers for drug delivery to ovarian cancer cells in vitro. *Anticancer Res* **2009**, *29*, 2933-2943.
- (52) Mullen, D. G.; Holl, M. M. B. Heterogeneous Ligand-Nanoparticle Distributions: A Major Obstacle to Scientific Understanding and Commercial Translation. *Acc Chem Res* **2011**, *44*, 1135-1145.
- (53) Kelkar, S. S.; Reineke, T. M. Theranostics: Combining Imaging and Therapy. *Bioconjugate Chem* **2011**, *22*, 1879-1903.
- (54) Zhu, Z.; Wang, X.; Li, T.; Aime, S.; Sadler, P. J.; Guo, Z. Platinum(II)-Gadolinium(III) Complexes as Potential Single-Molecular Theranostic Agents for Cancer Treatment. *Angew Chem Int Ed* **2014**, *53*, 13225-13228.
- (55) Wang, T.: Design, synthesis, and biological evaluation of novel taxoid-based small-molecule theranostic PET/SPECT imaging agents and nano-scale asymmetric

bow-tie dendrimer drug conjugates towards tumor-targeted chemotherapy (Doctoral Dissertation). Stony Brook University. 2015.

(56) Seitz, O.; Kunz, H. HYCRON, an Allylic Anchor for High-Efficiency Solid Phase Synthesis of Protected Peptides and Glycopeptides. *J Org Chem* **1997**, *62*, 813-826.

(57) McReynolds, K. D.; Hadd, M. J.; Gervay-Hague, J. Synthesis of Biotinylated Glycoconjugates and Their Use in a Novel ELISA for Direct Comparison of HIV-1 Gp120 Recognition of GalCer and Related Carbohydrate Analogues. *Bioconjugate Chem* **1999**, *10*, 1021-1031.

(58) Wong, L. S.; Janusz, S. J.; Sun, S.; Leggett, G. J.; Micklefield, J. Nanoscale Biomolecular Structures on Self-Assembled Monolayers Generated from Modular Pegylated Disulfides. *Chem Eur J* **2010**, *16*, 12234-12243.

(59) Chan, E. W. S.; Chattopadhyaya, S.; Panicker, R. C.; Huang, X.; Yao, S. Q. Developing Photoactive Affinity Probes for Proteomic Profiling: Hydroxamate-based Probes for Metalloproteases. *J Am Chem Soc* **2004**, *126*, 14435-14446.

(60) Schwabacher, A. W.; Lane, J. W.; Schiesher, M. W.; Leigh, K. M.; Johnson, C. W. Desymmetrization Reactions: Efficient Preparation of Unsymmetrically Substituted Linker Molecules. *J Org Chem* **1998**, *63*, 1727-1729.

(61) Han, J.; Sun, L.; Chu, Y.; Li, Z.; Huang, D.; Zhu, X.; Qian, H.; Huang, W. Design, Synthesis, and Biological Activity of Novel Dicoumarol Glucagon-like Peptide 1 Conjugates. *J Med Chem* **2013**, *56*, 9955-9968.

Chapter 4

Identification of Potential Binding Sites of Novel Benzimidazole Inhibitors with FtsZ Proteins via Molecular Modeling for Antitubercular Drug Discovery

Chapter Contents

§ 4.1 Introduction.....	237
§ 4.1.1 FtsZ as the Target for Antitubercular Drug Discovery	237
§ 4.1.2 Crystal Structures of FtsZ Proteins	238
§ 4.1.3 Novel Benzimidazole Inhibitors Targeting FtsZ Proteins.....	241
§ 4.2 Identification of Potential Binding Sites of Novel Benzimidazole Inhibitors with FtsZ Proteins via Molecular Modeling.....	243
§ 4.2.1 Docking Study of Benzimidazole Inhibitors into <i>Mtb</i> FtsZ Head-to-Head Lateral Dimer Crystal Structures.....	243
§ 4.2.2 Docking Study of Benzimidazole Inhibitors into <i>Mj</i> FtsZ Head-to-Tail Longitudinal Dimer Crystal Structure.....	245
§ 4.2.3 Construction of <i>Mtb</i> FtsZ Head-to-Tail Longitudinal Dimer Models via Homology Modeling/Protein Alignment	246
§ 4.2.4 Docking Study of Benzimidazole Inhibitors into <i>Mtb</i> FtsZ Head-to-Tail Longitudinal Dimer Models	249
§ 4.2.5 Docking Study of Benzimidazole Inhibitors into <i>Mtb</i> FtsZ Head-to-Tail Curved Longitudinal Trimer Crystal Structure.....	257
§ 4.2.6 Proposed Mechanism of Action	261
§ 4.3 Summary	262
§ 4.4 References.....	262

§ 4.1 Introduction

§ 4.1.1 FtsZ as the Target for Antitubercular Drug Discovery

Tuberculosis (TB), an infectious disease caused by *Mycobacterium tuberculosis* (*Mtb*), is a global threat especially because of the emerging multidrug-resistant TB (MDR-TB) and extensively drug-resistant-TB (XDR-TB).¹ It was reported by the World Health Organization (WHO) that 9.6 million new cases and 1.5 million deaths of TB occurred worldwide in 2014.¹

Filamentous temperature-sensitive protein Z (FtsZ), an essential bacterial cell-division protein and tubulin homolog, is a promising target for the development of new antitubercular agents.^{2,3} As shown in **Figure 4.1**, FtsZ polymerizes into head-to-tail longitudinal filaments in the presence GTP *in vivo*.³ These filaments self-assembles into a ring structure at the septum of the cell, which is termed “Z-ring”.³ During cell division, FtsZ recruits other cell division proteins to undergo Z-ring contraction by using the energy produced by the hydrolysis of GTP into GDP.^{3,4} Therefore, inhibition of FtsZ assembly would block cell division, and lead to bacterial death, which makes FtsZ a highly promising therapeutic target for antitubercular drug discovery.

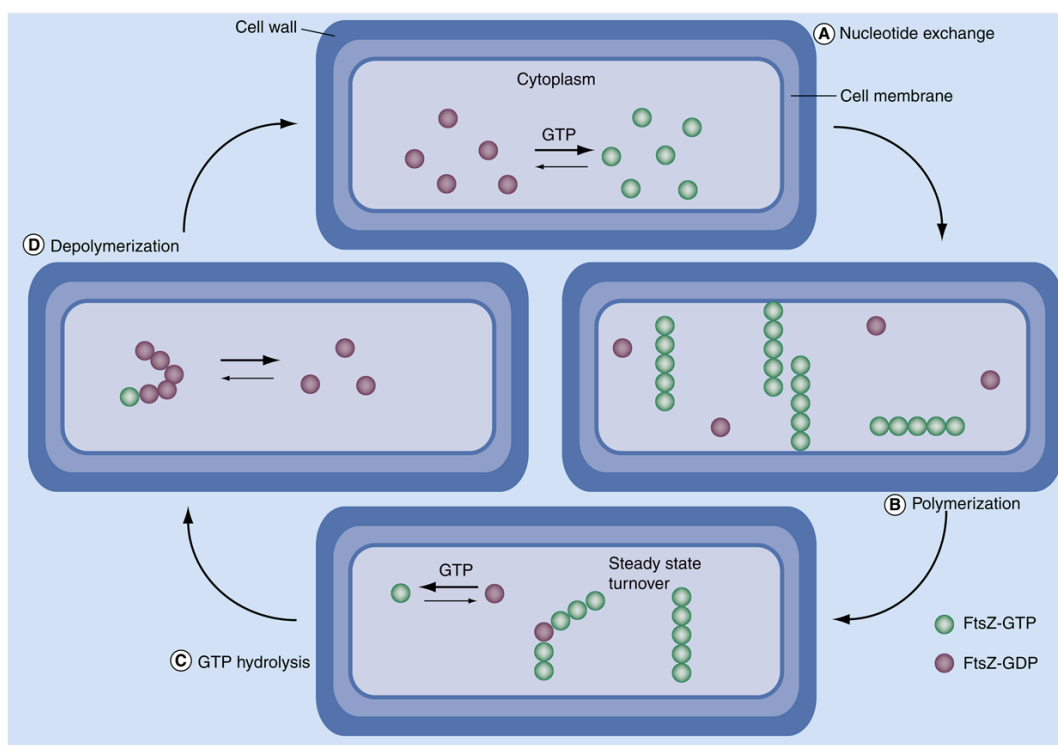


Figure 4.1 Mechanism of FtsZ inhibition. Reprinted from Kumar, K.; Awasthi, D.; Berger, W. T.; Tonge, P. J.; Slayden, R. A.; Ojima, I. Discovery of anti-TB agents that target the cell-division protein FtsZ. *Future Med Chem* **2010**, 2, 1305-1323, with permission from Future Science Ltd.

§ 4.1.2 Crystal Structures of FtsZ Proteins

Crystal structures of FtsZ proteins have been reported since the pioneer work reported by Jan Lowe's group at MRC Laboratory of Molecular Biology in 1998.⁵ A crystal structure of FtsZ protein from *M. jannaschii* at 2.8 Å resolution was determined, which has a similar three-dimensional structure as α - and β - tubulin (**Figure 4.2**).⁵ The crystal structure shows FtsZ contains two domains, a GTPase domain and a carboxy-terminal domain, which arranged around a central helix.⁵ Since then, a number of FtsZ protein crystal structures from different bacterial species have been reported.⁶⁻⁸ A search of RCSB Protein Data Bank (PDB) reveals that 82 crystal structures of FtsZ proteins have been released to date.

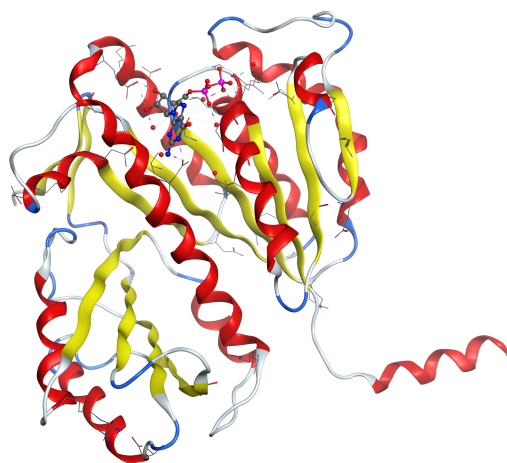


Figure 4.2 First reported crystal structure of FtsZ protein from *M. jannaschii*. (Generated based on PDB code 1FSZ)

However, there are only a few reports of crystal structures of FtsZ protein from the source of *Mycobacterium tuberculosis* (*Mtb*). In 2004, Leung et al. reported the first set of FtsZ crystal structures from *Mtb*, which includes *Mtb*FtsZ in complex with GTP-gamma-S (PDB code 1RLU), GDP (PDB code 1RQ7), and citrate (PDB code 1RQ2) respectively (**Figure 4.3**).⁹ In all three crystal structures, FtsZ protein crystallized as a tight, laterally oriented dimer, which is different from the longitudinal polymer of $\alpha\beta$ tubulin, suggesting FtsZ not only polymerize in a head-to-tail manner to form protofilaments, but also could assembly in the lateral direction.⁹ In addition to these three crystal structures, similar *Mtb*FtsZ structures in complex with citrate (PDB code 2Q1X) or GTP-gamma-S (PDB code 2Q1Y) were released in PDB in 2008, however, no literature has been published for these two new crystal structures yet.

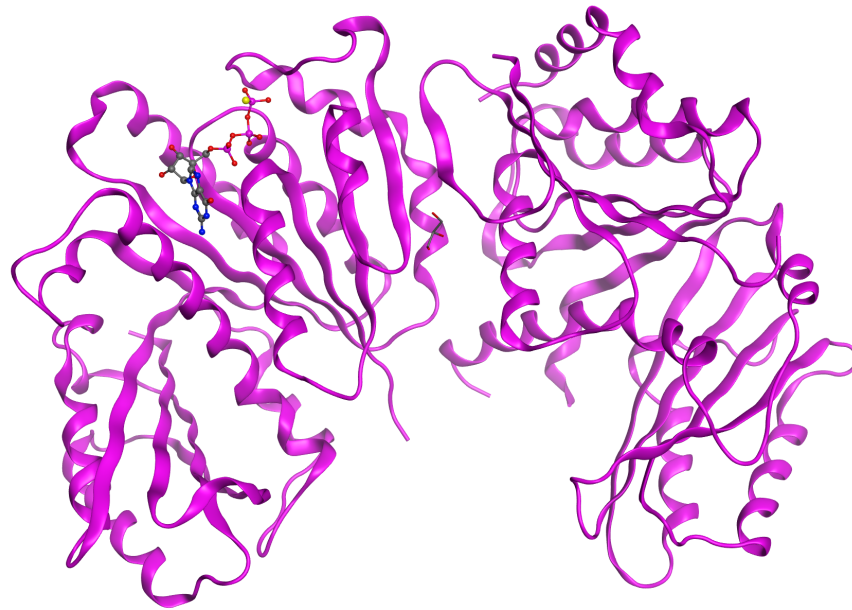


Figure 4.3 *MtbFtsZ* lateral dimer crystal structure in complex with GTP-gamma-S.
(Generated based on PDB code 1RLU)

Recently in 2013, Li et al. reported an interesting new curved trimer *MtbFtsZ* crystal structure in complex with GDP in head-to-tail longitudinal arrangement (**Figure 4.4**).⁴ This crystal structure shows T3 loop adopts a relaxed conformation (R state), and far away from T7 loop in the top subunit. In contrast, in the *MtbFtsZ* straight head-to-tail model, T3 loop adopts a tension conformation (T state), and interacts with T7 loop in the top subunit extensively.⁴ The authors proposed a hinge-opening mechanism for the straight-to-curved conformational change at the longitudinal interface induced by GTP hydrolysis (**Figure 4.5**).⁴ This hydrolysis-dependent conformational switch between straight and curved structures may generate the constrictive force to drive cytokinesis (**Figure 4.6**).^{4,10,11}

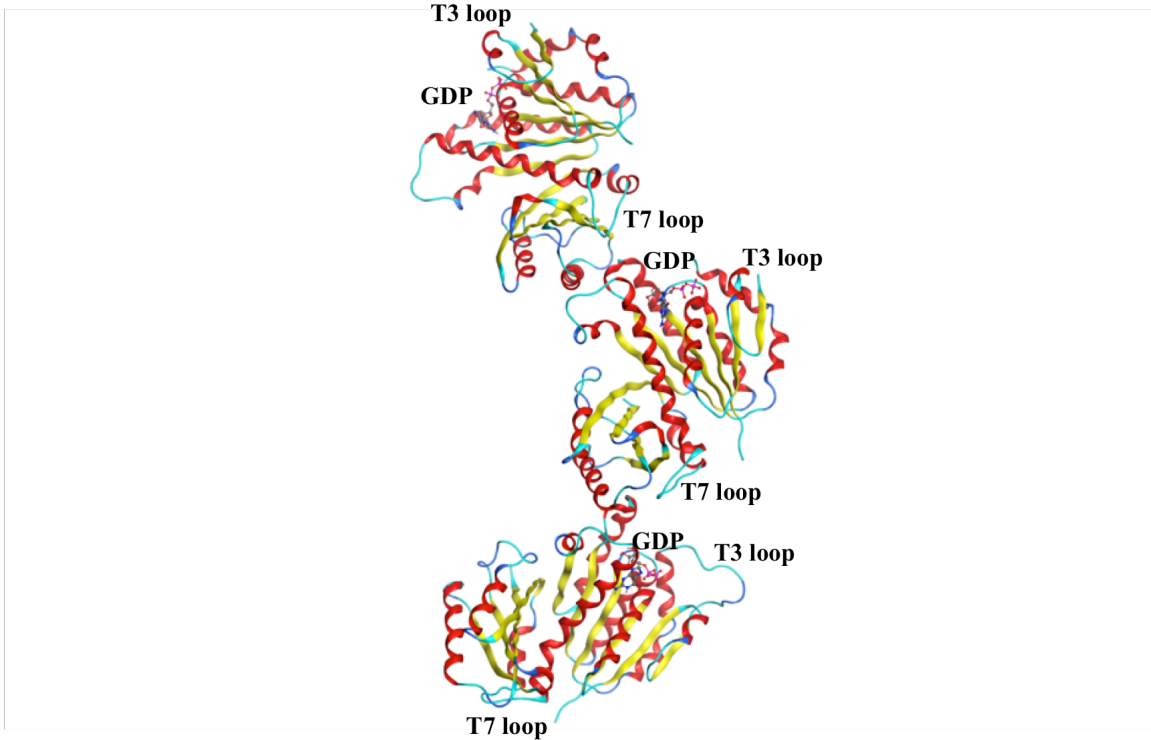


Figure 4.4 *MtbFtsZ* curved trimer head-to-tail crystal structure in complex with GDP. (Generated based on PDB code 4KWE)

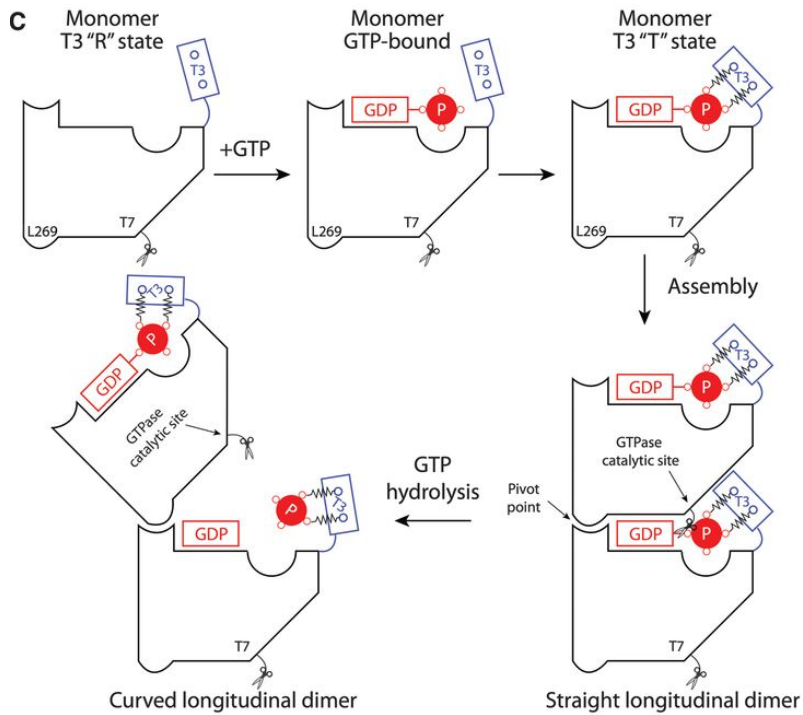


Figure 4.5 Hinge-opening mechanism for the straight-to-curved conformational change at the longitudinal interface induced by GTP hydrolysis. Reprinted from Li, Y.; Hsin, J.;

Zhao, L. Y.; Cheng, Y. W.; Shang, W. N.; Huang, K. C.; Wang, H. W.; Ye, S. FtsZ Protofilaments Use a Hinge-Opening Mechanism for Constrictive Force Generation. *Science* **2013**, *341*, 392-395, with permission from AAAS.

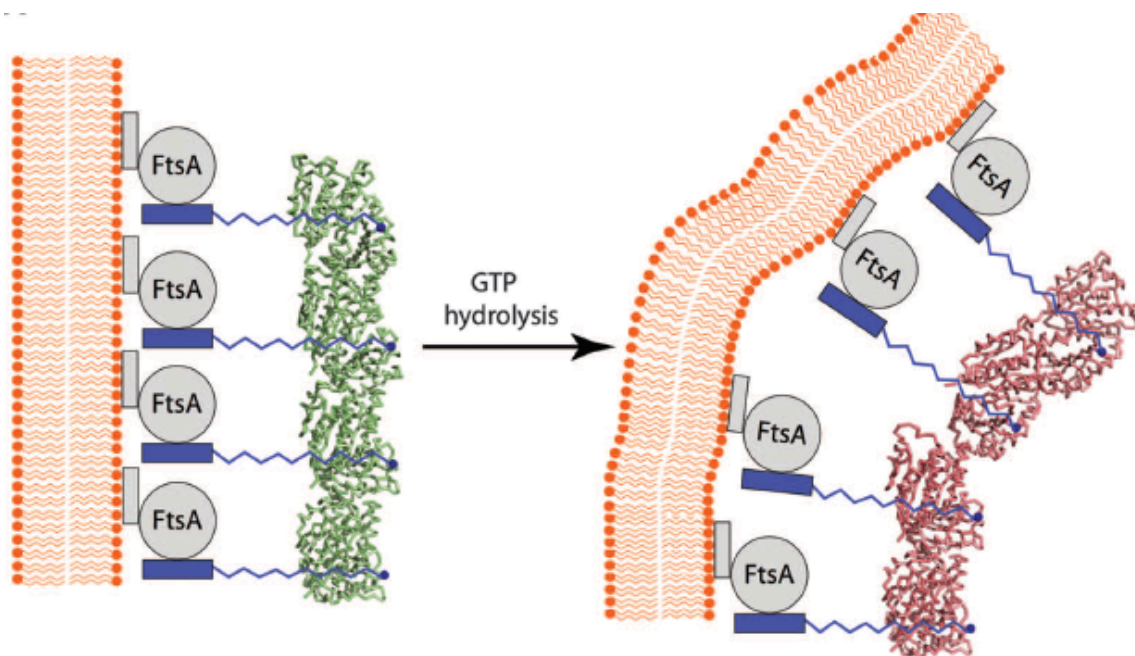


Figure 4.6 Schematic representation of membrane deformation due to the force produced by hydrolysis-induced FtsZ bending. Reprinted from Li, Y.; Hsin, J.; Zhao, L. Y.; Cheng, Y. W.; Shang, W. N.; Huang, K. C.; Wang, H. W.; Ye, S. FtsZ Protofilaments Use a Hinge-Opening Mechanism for Constrictive Force Generation. *Science* **2013**, *341*, 392-395, with permission from AAAS.

Although there is no straight *MtbFtsZ* head-to-tail form crystal structure available to represent the longitude interface of *MtbFtsZ* protofilament, there is *MjFtsZ* head-to-tail longitude dimer crystal structure with GTP and Mg^{2+} soaked reported by Lowe et al. in 2004 (PDB code: 1W5A).⁸ The authors used refolded *MjFtsZ* to crystallize a tubulin-like protofilament, in which N- and C-terminal domains in two consecutive subunits in the filament forms the GTPase catalytic site.⁸ This provides a structural basis for building straight *MtbFtsZ* head-to-tail model.

§ 4.1.3 Novel Benzimidazole Inhibitors Targeting FtsZ Proteins

Series of novel trisubstituted benzimidazoles targeting FtsZ have been designed, synthesized and evaluated in the Ojima laboratory.^{3,12-15} Many of these novel FtsZ inhibitors exhibit excellent activities against drug-sensitive and drug-resistant tuberculosis strains.^{3,12-15}

As shown in **Figure 4.7**, early screening of libraries of 2,5,6- and 2,5,7-trisubstituted benzimidazoles against *Mtb* H37Rv strain at 5 $\mu\text{g/ml}$ gave rise to a good number of hit compounds.^{12,13} Selected lead compounds showed excellent MIC values in the range of 0.39-6.1 $\mu\text{g/ml}$.^{12,13} After extensive optimization, more potent compounds were obtained. For example, one of the lead compounds SB-P17G-C2 has a MIC value 0.06 $\mu\text{g/ml}$, and the dose-dependent inhibition of FtsZ polymerization by this compound is shown in **Figure 4.8**.¹⁴

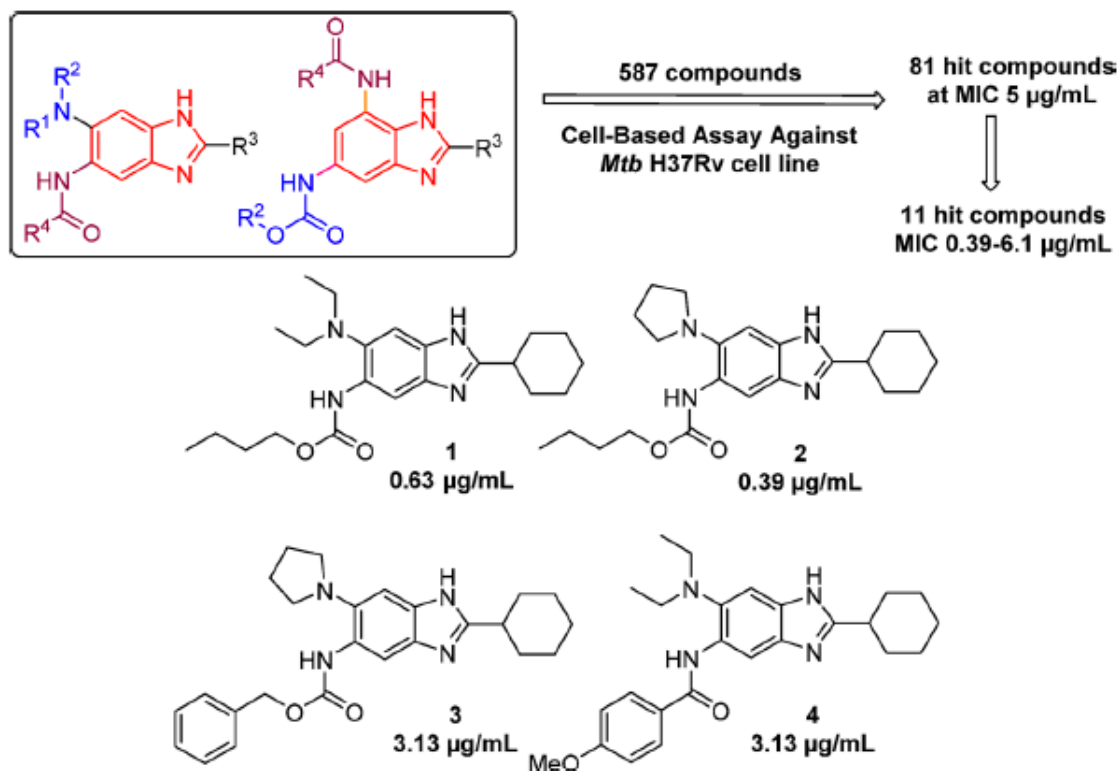


Figure 4.7 Early lead compounds from optimization of hit benzimidazoles. Reprinted with permission from Kumar, K.; Awasthi, D.; Lee, S. Y.; Zanardi, I.; Ruzsicska, B.; Knudson, S.; Tonge, P. J.; Slayden, R. A.; Ojima, I. Novel Trisubstituted Benzimidazoles, Targeting *Mtb* FtsZ, as a New Class of Antitubercular Agents. *J Med Chem* **2011**, *54*, 374-381. Copyright(2011) American Chemical Society.

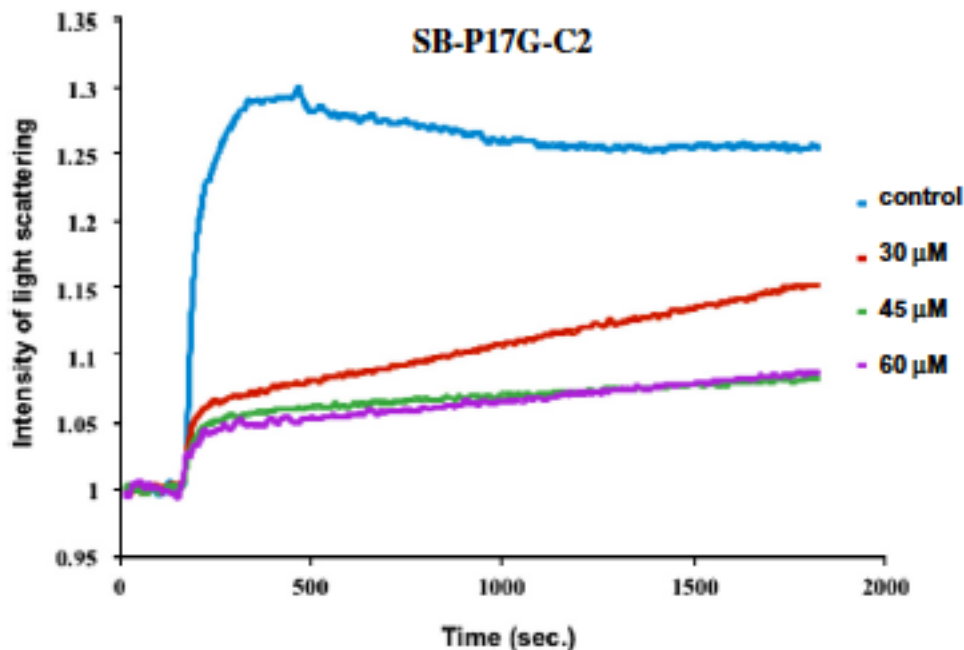


Figure 4.8 Dose-dependent inhibition of FtsZ polymerization by SB-P17G-C2. Reproduced with permission from Awasthi, D.; Kumar, K.; Knudson, S. E.; Slayden, R. A.; Ojima, I. SAR Studies on Trisubstituted Benzimidazoles as Inhibitors of Mtb FtsZ for the Development of Novel Antitubercular Agents. *J Med Chem* **2013**, *56*, 9756-9770. Copyright (2013) American Chemical Society.

It was found that these highly potent lead compounds inhibit FtsZ polymerization through accelerating GTPase activity.^{3,12} However, currently the binding site(s) of FtsZ with these highly potent antitubercular agents is still unclear. Attempts to co-crystallize the lead compounds with *Mtb*FtsZ protein were also not successful. Thus, computational approaches have been employed to investigate the binding sites of these novel benzimidazole inhibitors with *Mtb*FtsZ for antitubercular drug discovery and possible binding sites have been identified.

§ 4.2 Identification of Potential Binding Sites of Novel Benzimidazole Inhibitors with FtsZ Proteins via Molecular Modeling

§ 4.2.1 Docking Study of Benzimidazole Inhibitors into *Mtb*FtsZ Head-to-Head Lateral Dimer Crystal Structures

Initially, AutoDock 4.2¹⁶ is used to docking selected novel trisubstituted benzimidazoles (**Figure 4.9**) into *Mtb*FtsZ head-to-head dimer crystal structure in complex with GTP-gamma-S (PDB code 1RLU).⁹

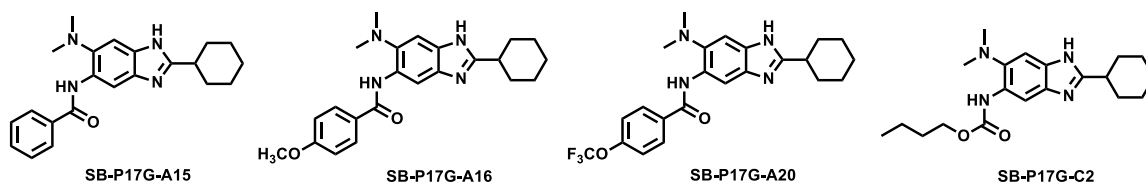


Figure 4.9 Chemical structures of selected benzimidazole inhibitors used in the initial docking study

It was anticipated that the binding site might be close to the GTPase catalytic site, since benzimidazole inhibitors function as accelerators of GTPase activity. However, in a global docking search of the entire space of the protein, interestingly, the two potential binding sites identified by AutoDock are close to the T7 loop and far away from GTP-gamma-S. When the inhibitors were forced to dock into the space close to GTP-gamma-S, less favored energy scores were obtained. These results are surprising in the beginning, but after carefully examine the positions of these two potential binding sites, it was found that these binding sites might be close to the another GTP site of the FtsZ subunit adjacent to this FtsZ subunit in the head-to-tail longitudinal FtsZ protofilament. Indeed, T7 loop has been known to be critical for GTPase activity of FtsZ by extensively interacting with the T3 loop next the GTP site. These results provided a hypothesis that benzimidazole inhibitors might bind the interface of two FtsZ subunits in the head-to-tail FtsZ protofilament.

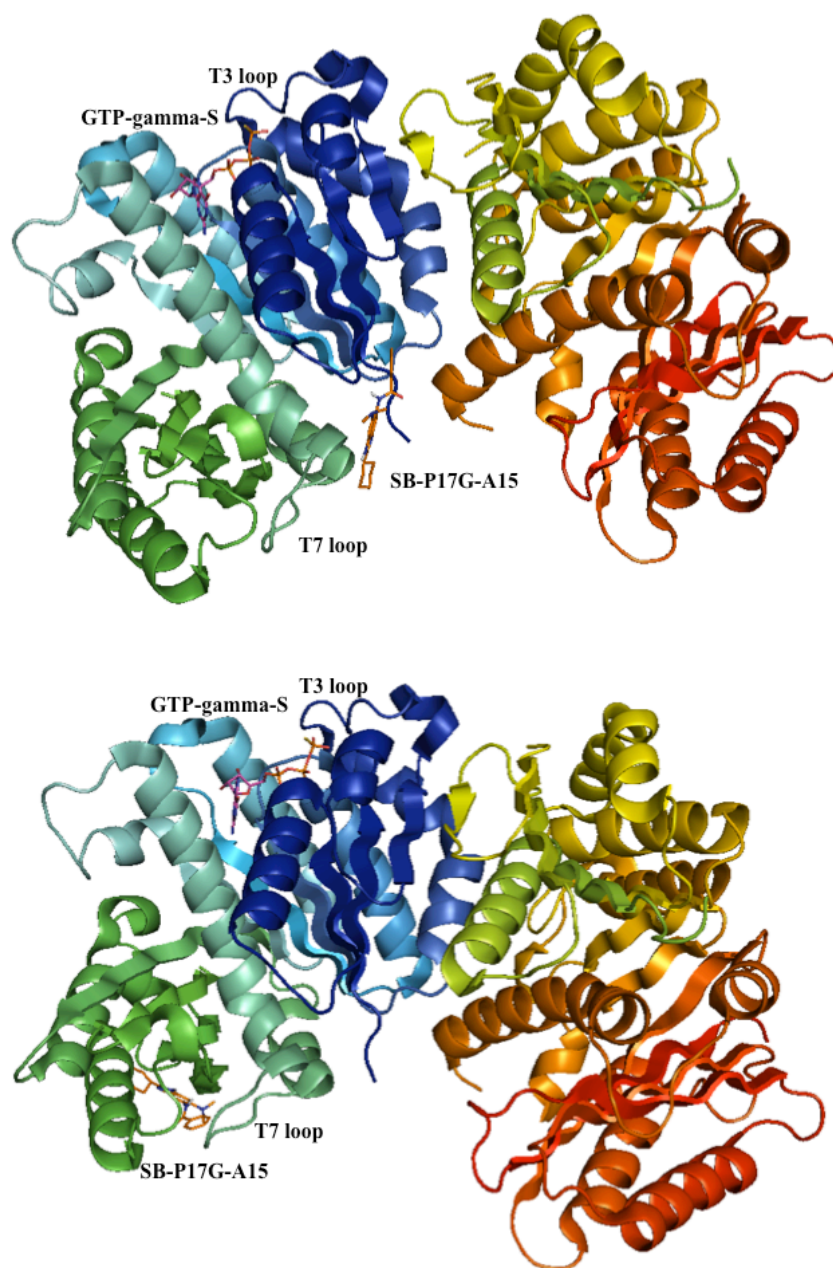


Figure 4.10 Potential binding sites of selected benzimidazole inhibitors in the initial docking study against 1RLU by AutoDock

§ 4.2.2 Docking Study of Benzimidazole Inhibitors into *MjFtsZ* Head-to-Tail Longitudinal Dimer Crystal Structure

Because FtsZ forms protofilaments *in vivo* by repeating its subunits in a head-to-tail manner, it is important to study potential binding site(s) of novel benzimidazole

inhibitors with *MtbFtsZ* based on a head-to-tail crystal structure. *M. jannaschii* FtsZ head-to-tail dimer crystal structure with GTP bound (PDB code 1W5A) was then selected for computational docking study, as no *MtbFtsZ* straight head-to-tail crystal structure was available. The potential binding site by AutoDock 4.2 was found to be in the middle interface of the two subunits, close to T7 loop and GTP (Figure 4.11).

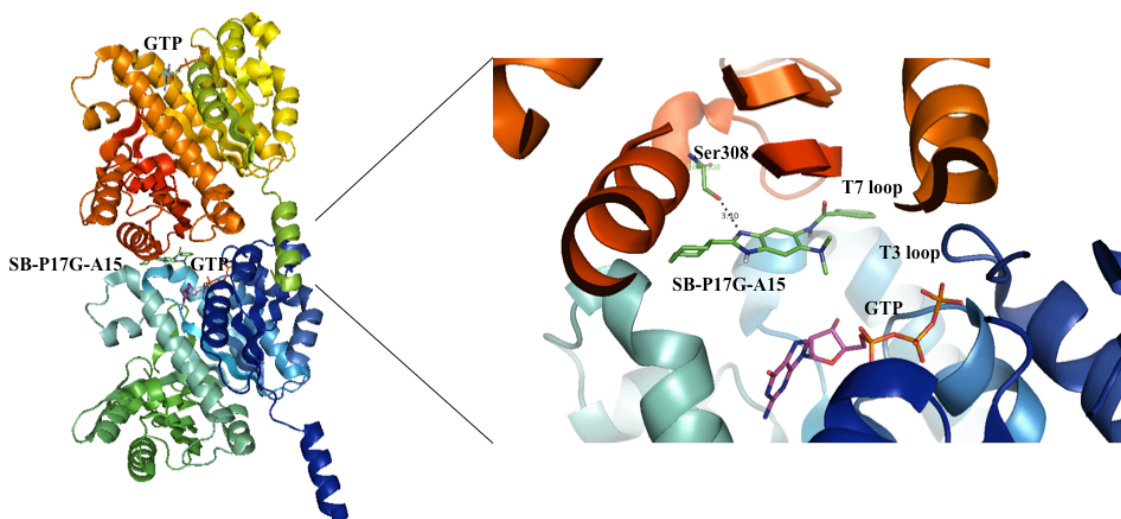


Figure 4.11 Potential binding sites of selected benzimidazole inhibitors in the initial docking study against 1W5A by AutoDock

§ 4.2.3 Construction of *MtbFtsZ* Head-to-Tail Longitudinal Dimer Models via Homology Modeling/Protein Alignment

Based on *M. jannaschii* FtsZ head-to-tail dimer GTP bound crystal structure (PDB code 1W5A) and protein sequence of *Mtb-FtsZ*, a homology model (Figure 4.12) was generated using Modeller v9.11¹⁷, which is a program for comparative protein structure modeling by satisfaction of spatial restraints developed in the Andrej Sali Lab. This homology model of head-to-tail *MtbFtsZ* dimer (purple) showed overall good overlay with the template *MjFtsZ* structure 1W5A (cyan), however, the problem is the position of GTP is difficult to model in this case, as the sequence of *MtbFtsZ* only contains the protein residues without GTP. Attempts to re-dock GTP into this homology model give a pose quite different from the expected position, presumably due to the flexibility of the GTP ligand compared to the large space in the interface to accommodate this nucleotide. As a result, the expected contacts of GTP with the protein residues were not observed.



Figure 4.12 Homology model of head-to-tail *MtbFtsZ* dimer (purple) based on template *MjFtsZ* structure 1W5A (cyan).

To solve this problem, protein alignment was employed using MOE (version 2015.10)¹⁸. α -Subunit of *MtbFtsZ* lateral dimer crystal structures with GTP γ S, GDP or citrate bound (PDB codes 1RLU, 1RQ7, and 1RQ2) were aligned based on *MjFtsZ* head-to-tail dimer crystal structure, respectively. **Figure 4.13** and **Figure 4.14** show the protein alignment of *MtbFtsZ* with GTP γ S bound (1RLU, purple) and *MjFtsZ* with GTP and Mg²⁺ soaked (1W5A, blue), which gives a rmsd of ~ 1.4 Å in the alignment. Zoom-in GTPase site shows good overlay of the nucleotides. Similarly, head-to-tail *MtbFtsZ* dimer models with GDP bound or citrate bound were also generated in the same manner for docking study.

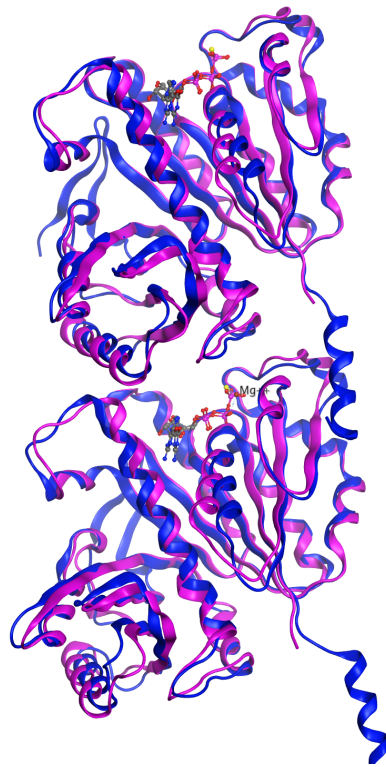


Figure 4.13 Protein alignment of *MtbFtsZ* and *MjFtsZ*

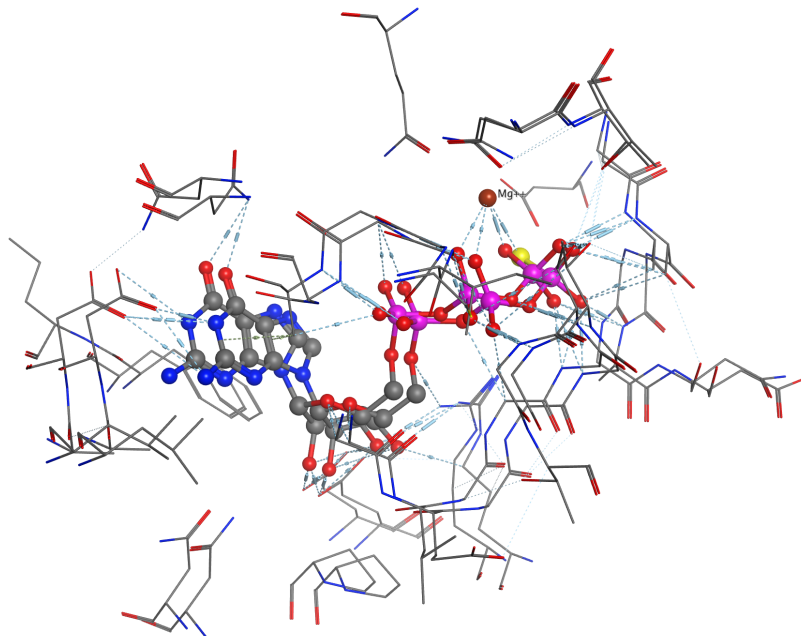


Figure 4.14 Zoom-in GTPase site of aligned *MtbFtsZ* and *MjFtsZ* structures

§ 4.2.4 Docking Study of Benzimidazole Inhibitors into *MtbFtsZ* Head-to-Tail Longitudinal Dimer Models

MtbFtsZ head-to-tail dimer model in complex with GTP γ S generated by protein alignment is shown in **Figure 4.15**. The head-to-tail dimer model could better represent the longitudinal interface in *MtbFtsZ* protofilament, and was used for recent docking study.



Figure 4.15 *MtbFtsZ* head-to-tail dimer model in complex with GTP γ S generated by protein alignment

After *MtbFtsZ* head-to-tail dimer models were generated, SB-P17G-A38 (SBZ013251) and SB-P17G-A42 (SBZ013221) (**Figure 4.16**) were docked into them using MOE (version 2015.10).

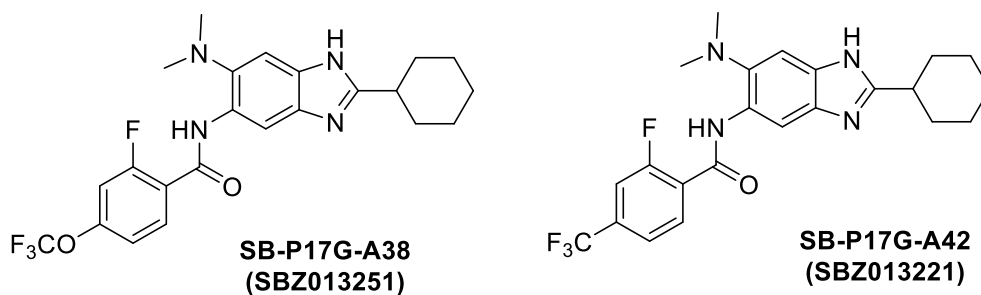


Figure 4.16 Chemical structures of SB-P17G-A38 (SBZ013251) and SB-P17G-A42 (SBZ013221)

Figure 4.17 shows the docked pose of SB-P17G-A38 with *MtbFtsZ* head-to-tail dimer model with GTP γ S bound (energy score -8.4897 kcal/mol). SB-P17G-A38 was found to bind to the hydrophobic interface of two subunits, adjacent to the T7 loop in the top subunit, and close to the GTP γ S in the bottom subunit (~ 4.27 Å). As mentioned previously, T7 loop was found to be critical in FtsZ and tubulin polymerization and GTPase activities. **Figure 4.18** shows the 2D interaction diagram of SB-P17G-A38 with *MtbFtsZ* head-to-tail dimer model with GTP γ S bound, indicating Van der Waals interactions between the inhibitor with two FtsZ subunits, and no specific hydrogen bonding was observed.

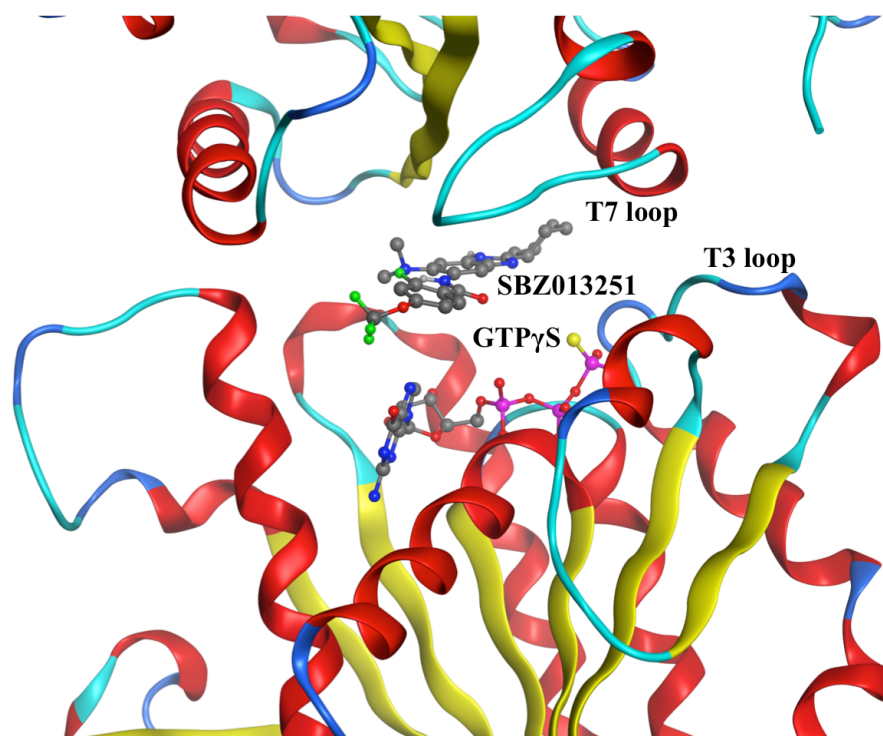


Figure 4.17 Docked pose of SB-P17G-A38 (SBZ013251) with *MtbFtsZ* head-to-tail dimer model with GTP γ S bound

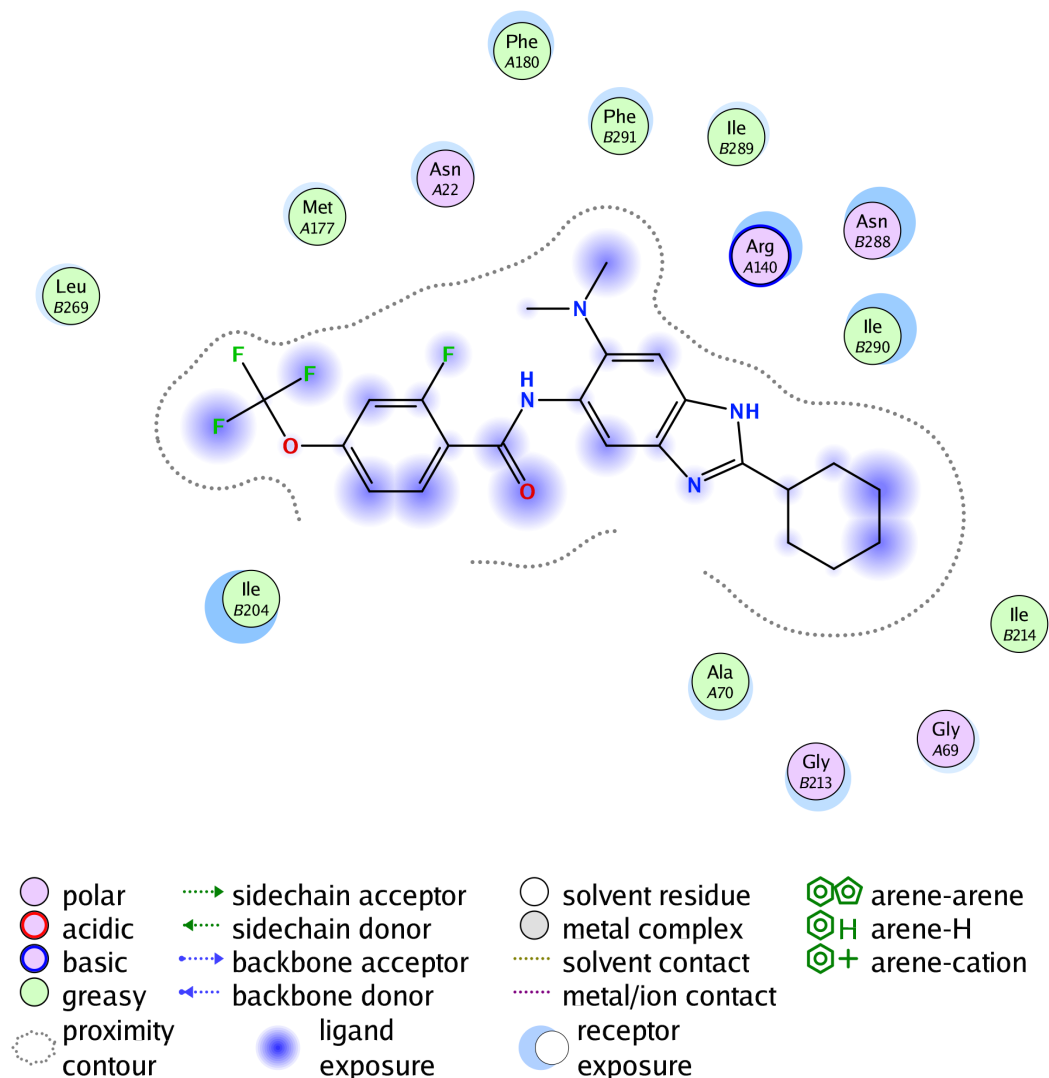


Figure 4.18 2D interaction diagram of SB-P17G-A38 (SBZ013251) with *MtbFtsZ* head-to-tail dimer model with GTP γ S bound

Similarly, SB-P17G-A42 was docked into the same *MtbFtsZ* head-to-tail dimer model with GTP γ S bound. **Figure 4.19** shows the docked pose of SB-P17G-A42 (energy score -8.7284 kcal/mol). SB-P17G-A42 adopted essentially the same pose as SB-P17G-A38. **Figure 4.20** shows the 2D interaction diagram of SB-P17G-A42 with *MtbFtsZ* head-to-tail dimer model with GTP γ S bound, indicating Van der Waals interactions between the inhibitor with two FtsZ subunits, and no specific hydrogen bonding was observed similar as the results for SB-P17G-A38.

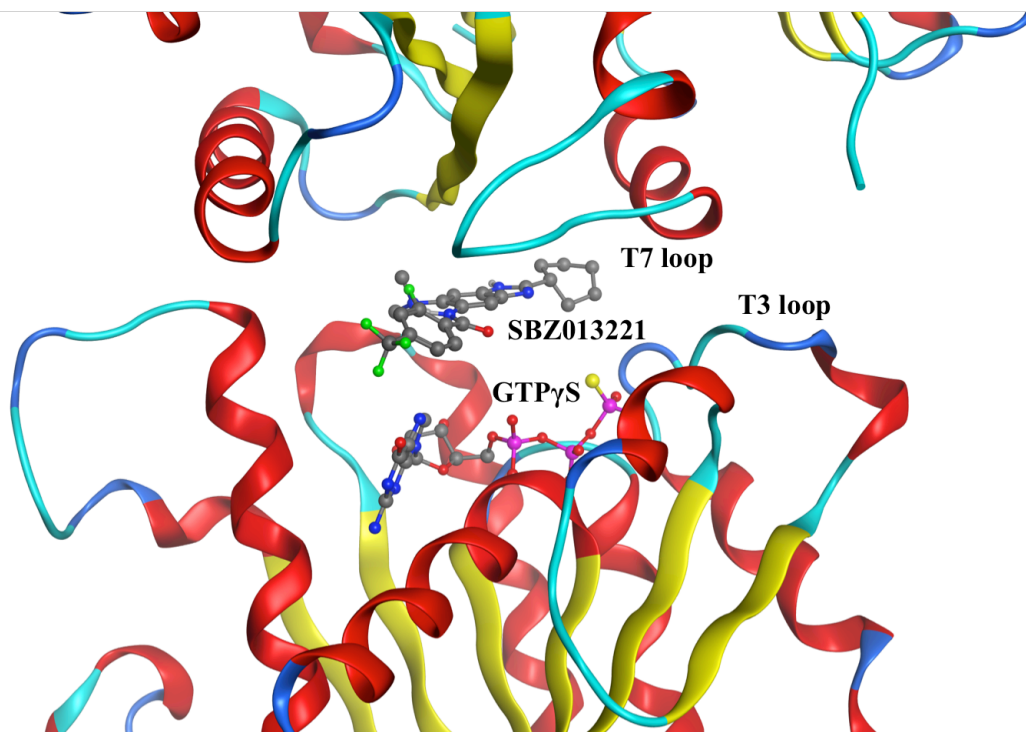


Figure 4.19 Docked pose of SB-P17G-A42 (SBZ013221) with *Mtb*FtsZ head-to-tail dimer model with GTP γ S bound

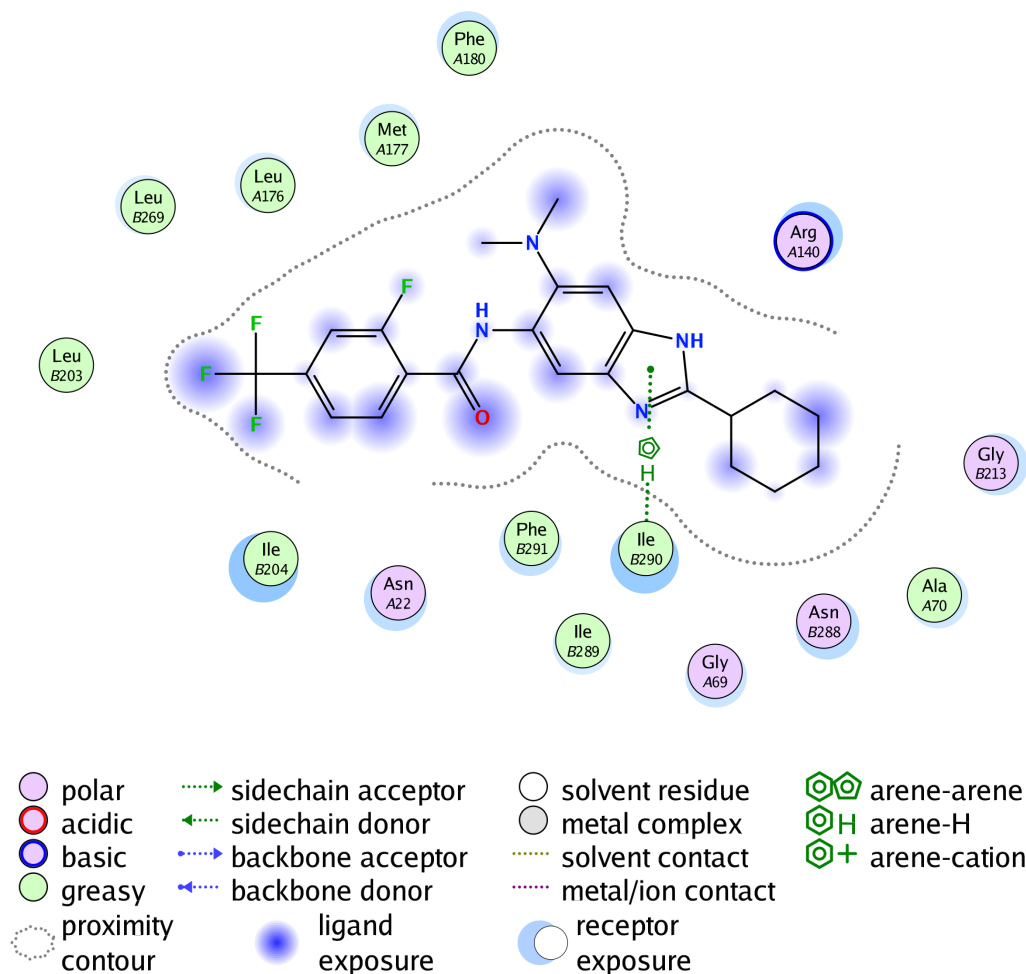


Figure 4.20 2D interaction diagram of SB-P17G-A42 (SBZ013221) with *MtbFtsZ* head-to-tail dimer model with GTP γ S bound

Subsequently, SB-P17G-A38 was docked into *MtbFtsZ* head-to-tail dimer model with GDP bound. **Figure 4.21** shows the docked pose of SB-P17G-A38 (energy score - 8.8896 kcal/mol). Interestingly, SB-P17G-A38 was found to bind to the same pocket, but adopted an opposite pose as compared with the previous GTP γ S model. **Figure 4.22** shows the 2D interaction diagram of SB-P17G-A38 with *MtbFtsZ* head-to-tail dimer model with GDP bound through Van der Waals interactions between the inhibitor with two FtsZ subunits.

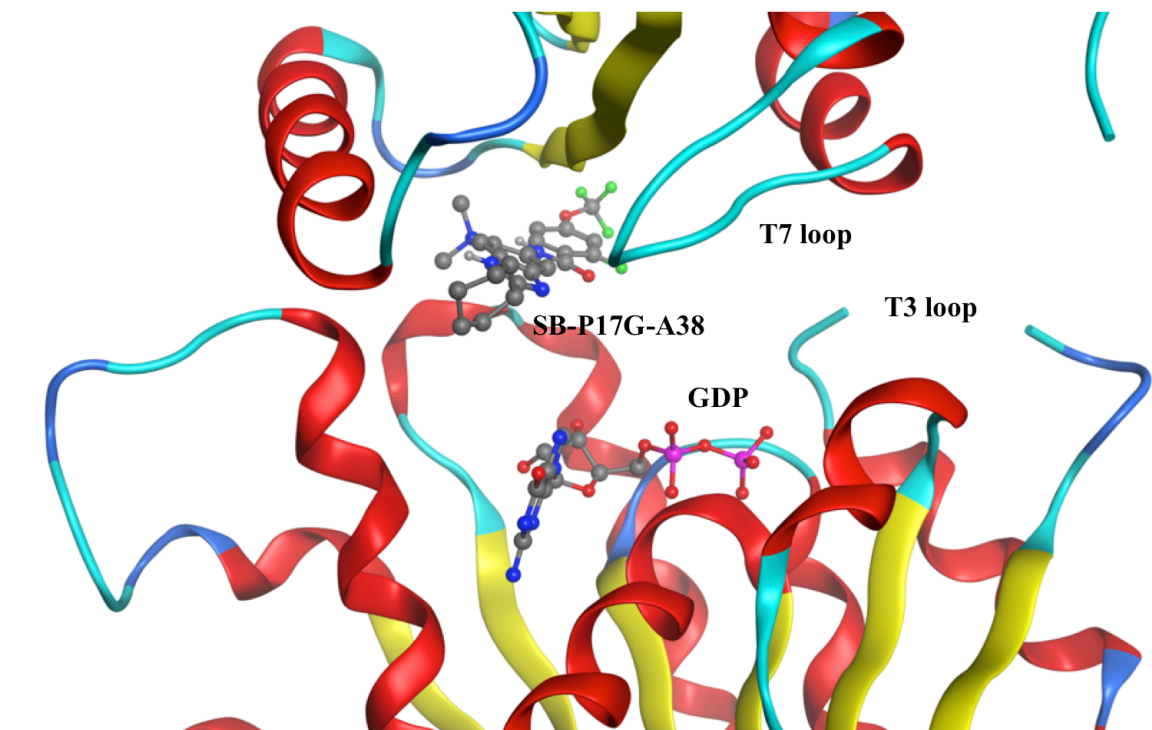


Figure 4.21 Docked pose of SB-P17G-A38 (SBZ013251) with *MtbFtsZ* head-to-tail dimer model with GDP bound

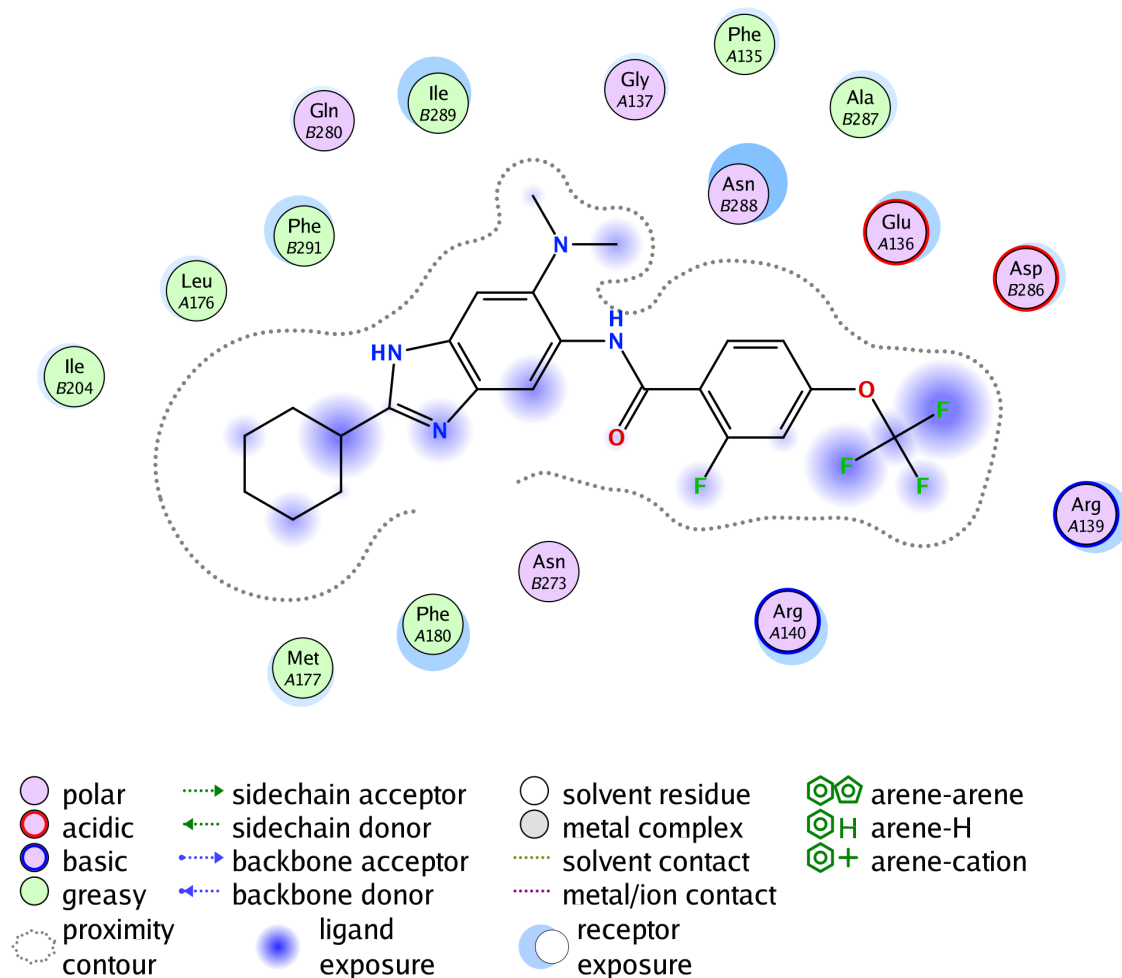


Figure 4.22 2D interaction diagram of SB-P17G-A38 (SBZ013251) with *MtbFtsZ* head-to-tail dimer model with GDP bound

After that, SB-P17G-A38 was docked into *MtbFtsZ* head-to-tail dimer model with citrate bound. **Figure 4.23** shows the docked pose of SB-P17G-A38 (energy score - 7.5046 kcal/mol). In the absence of nucleotide, SB-P17G-A38 was found to move closer into the nucleotide-binding site, with a less favored binding energy score. **Figure 4.24** shows the 2D interaction diagram of SB-P17G-A38 with *MtbFtsZ* head-to-tail dimer model with citrate bound. In this case, the carbonyl group forms hydrogen bond with the backbone of Met177.

These docking results suggested that in the straight head-to-tail longitudinal *MtbFtsZ* dimer models, benzimidazole inhibitors prefer to bind to the interface of two FtsZ subunits close the T7 loop in the presence of nucleotide rather than nucleotide-free conformation. The pose difference between GTP γ S model and GDP model indicates the benzimidazole inhibitors may bind differently *in vivo* in FtsZ protofilament when GTP hydrolyzed into GDP.

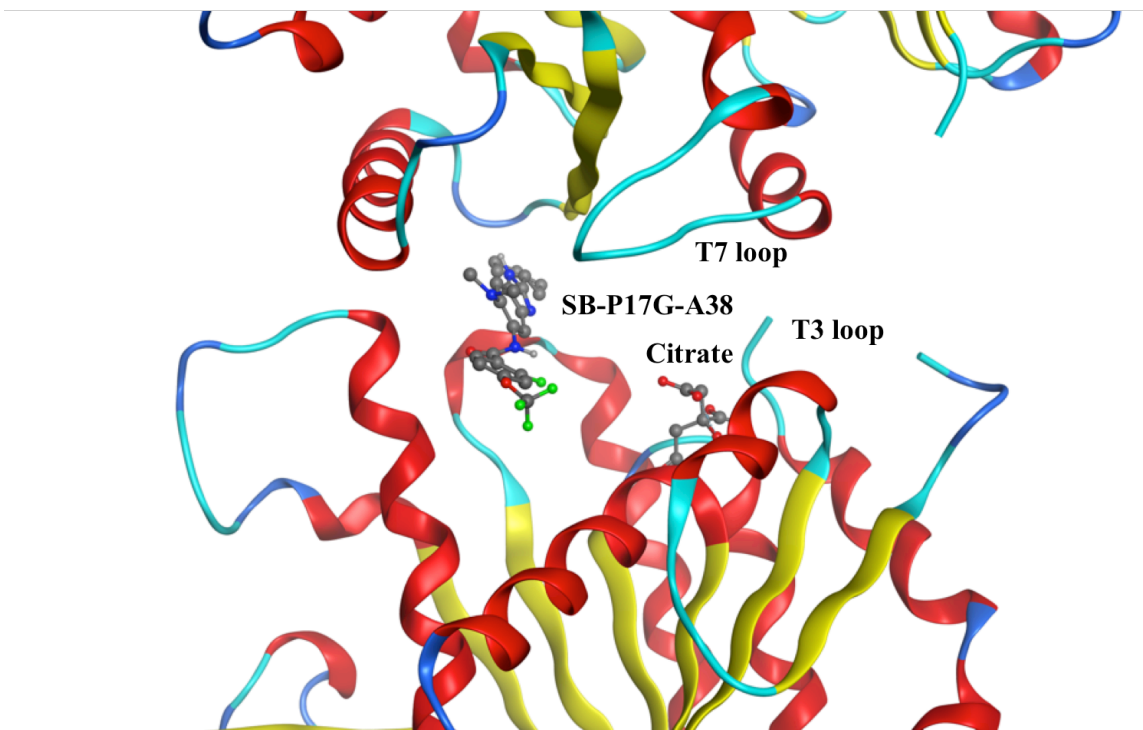


Figure 4.23 Docked pose of SB-P17G-A38 (SBZ013251) with *MtbFtsZ* head-to-tail dimer model with citrate bound

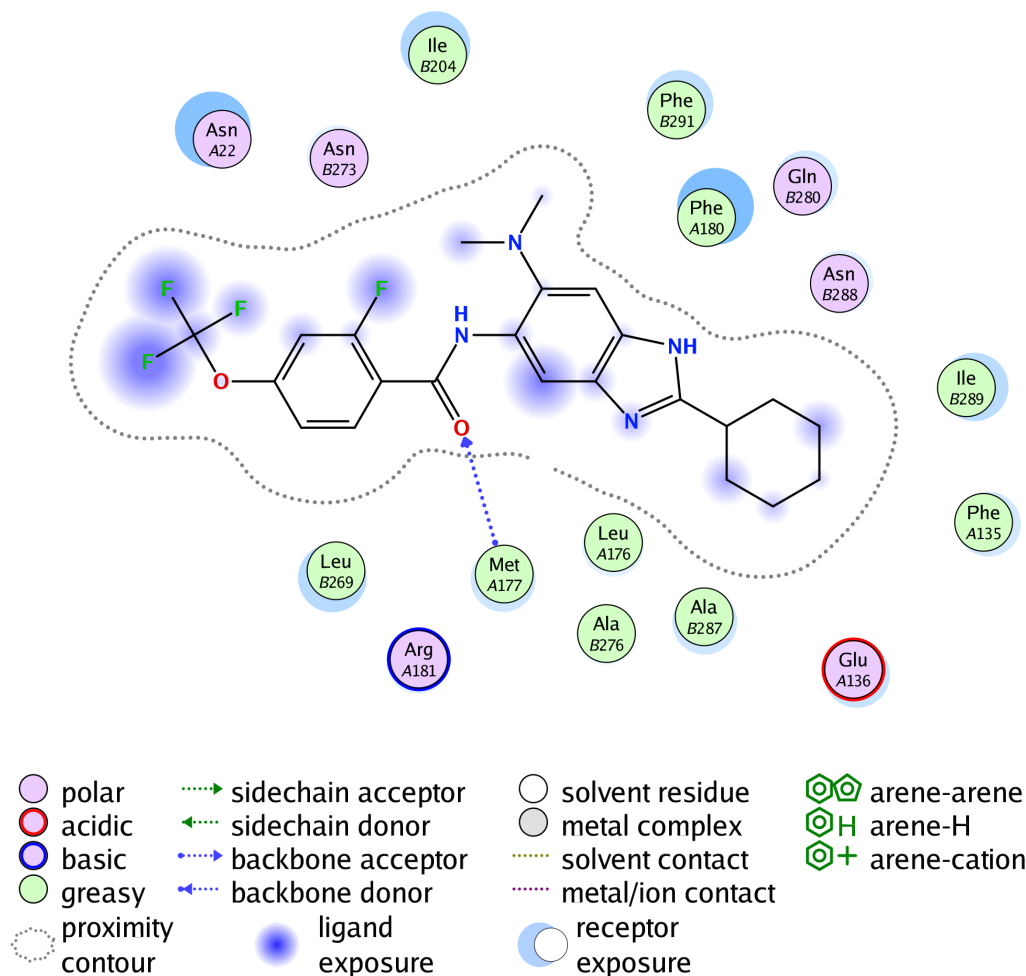


Figure 4.24 2D interaction diagram of SB-P17G-A38 (SBZ013251) with *MtbFtsZ* head-to-tail dimer model with citrate bound

§ 4.2.5 Docking Study of Benzimidazole Inhibitors into *MtbFtsZ* Head-to-Tail Curved Longitudinal Trimer Crystal Structure

In 2013, an interesting new *MtbFtsZ* curved head-to-tail crystal structure with GDP bound was reported (PDB code 4KWE). The authors proposed a hinge-opening mechanism for the straight-to-curved conformational change at the longitudinal interface induced by GTP hydrolysis (**Figure 4.5**).⁴ It is hypothesized that benzimidazole inhibitors may prefer to bind to the straight *MtbFtsZ* protofilament longitudinal interface with GTP bound, catalyzing the hydrolysis of GTP to GDP, and might be kicked out while *MtbFtsZ* protofilament adopts a straight-to-curved conformation change. To test this hypothesis computationally, SB-P17G-A38 was docked to the GDP site and T7 loop of *MtbFtsZ* curved head-to-tail crystal structure respectively. Neither of these two binding sites gave as good binding energy scores as in the straight head-to-tail models. In the GDP site docked pose (**Figure 4.25**), SB-P17G-A38 is very close to GDP, the

carbonyl group forms hydrogen bond with Arg140 (**Figure 4.26**), and the energy score is -7.1755 kcal/mol. In the T7 loop docked pose (**Figure 4.27**), the carbonyl group of SB-P17G-A38 forms hydrogen bond with backbone of Arg139 (**Figure 4.28**), and the energy score is -7.0868 kcal/mol. These results indicate that indeed, benzimidazole inhibitors prefer to bind to the straight *MtbFtsZ* protofilament longitudinal interface rather than the curved FtsZ structure.

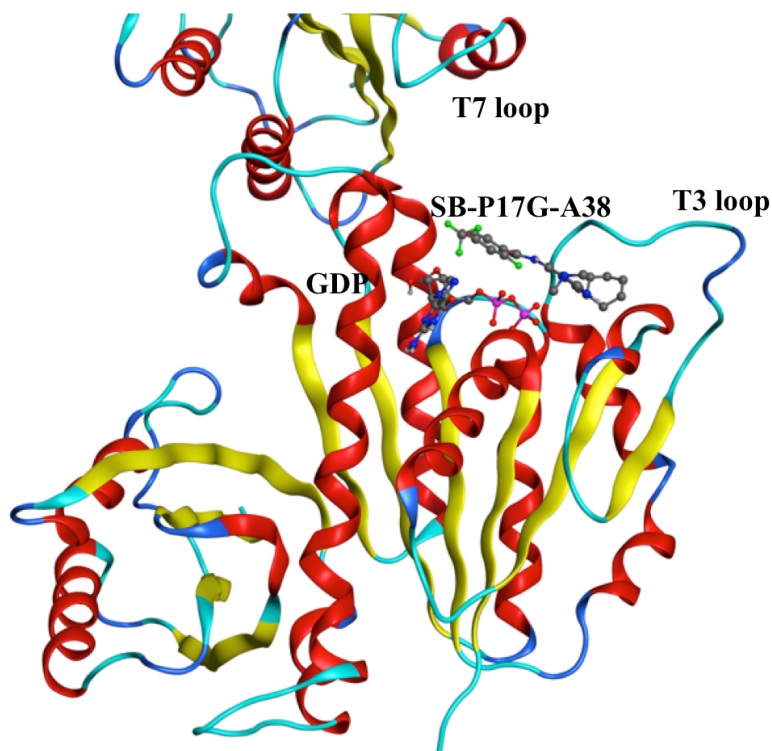


Figure 4.25 Docked pose of SB-P17G-A38 with *MtbFtsZ* curved head-to-tail crystal structure with GDP bound (GDP site)

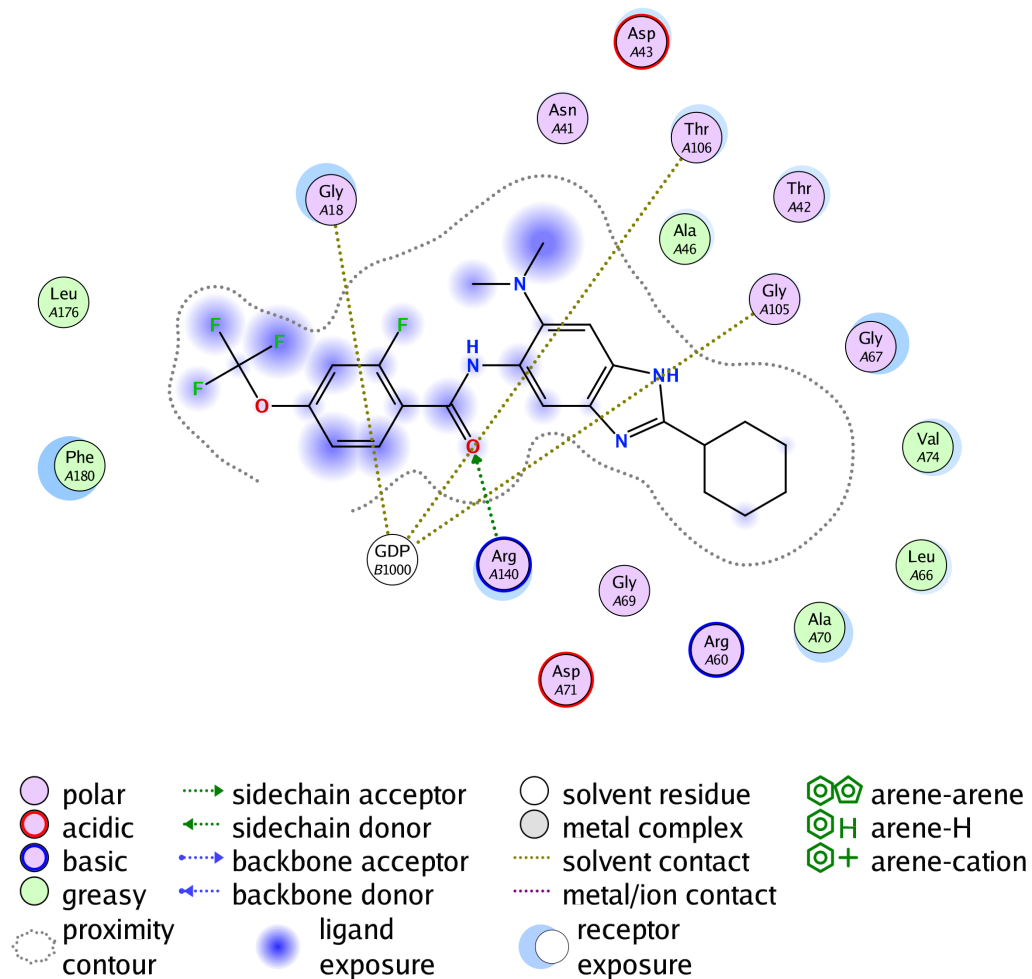


Figure 4.26 2D interaction diagram of SB-P17G-A38 with *MtbFtsZ* curved head-to-tail crystal structure with GDP bound (GDP site)

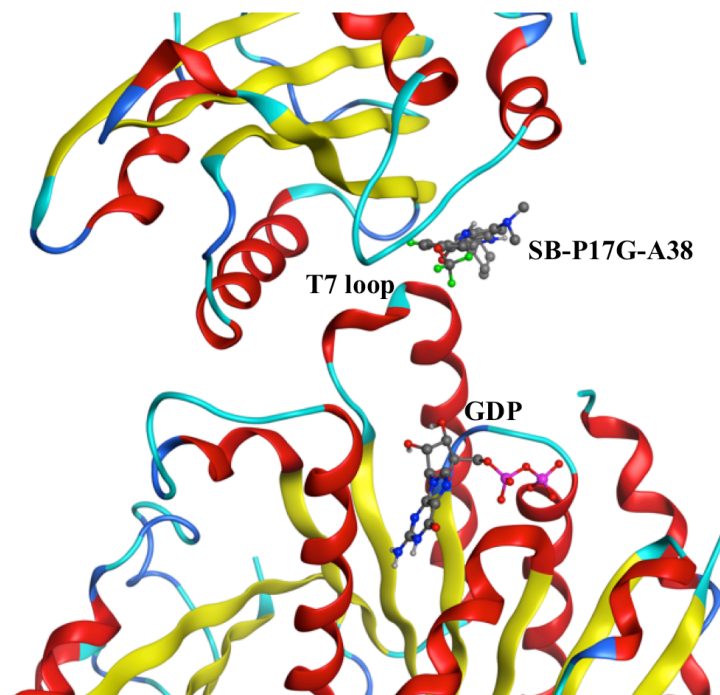


Figure 4.27 Docked pose of SB-P17G-A38 with *MtbFtsZ* curved head-to-tail crystal structure with GDP bound (T7 loop site)

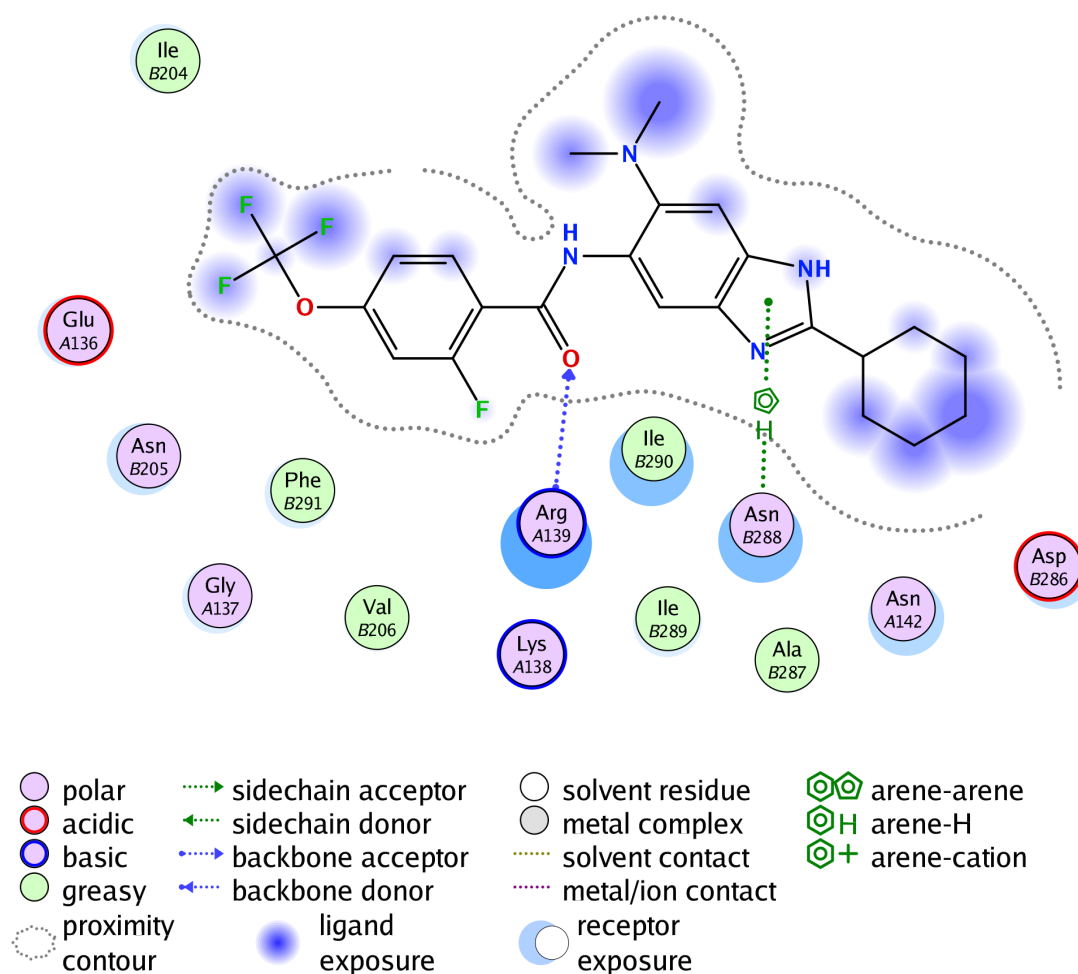


Figure 4.28 2D interaction diagram of SB-P17G-A38 with *MtbFtsZ* curved head-to-tail crystal structure with GDP bound (T7 loop site)

§ 4.2.6 Proposed Mechanism of Action

Based on the docking results and the hinge-opening mechanism for FtsZ protofilaments reported by Li et al.⁴, a plausible mechanism of action (MOA) of the benzimidazole inhibitors is proposed. As shown in **Figure 4.29**, during bacterial cell division, GTP binds to FtsZ monomers to promote the formation of FtsZ straight protofilaments. However, in the presence of the benzimidazole inhibitors, which bind to FtsZ close to T7 loop and GTP binding site and accelerate the GTP hydrolysis, FtsZ monomers cannot form normal long straight FtsZ protofilaments. After that, GTP is hydrolyzed to GDP, and induces a straight-to-curve FtsZ conformation change. In the meantime, benzimidazole inhibitors have finished their job, and get kicked out from the binding site at FtsZ subunits interface.

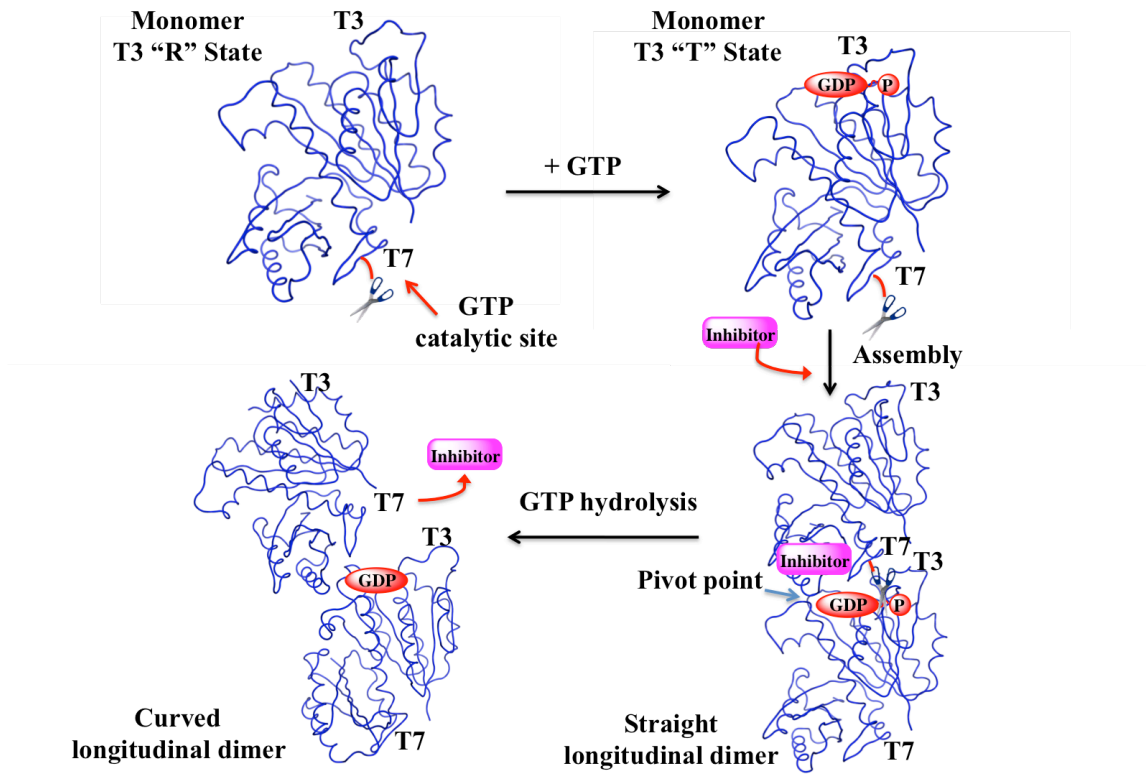


Figure 4.29 Proposed mechanism of action for benzimidazole inhibitors

§ 4.3 Summary

Potential binding site of tri-substituted benzimidazole FtsZ inhibitors has been identified through molecular docking, homology modeling, and protein alignment for antitubercular drug discovery. The identified potential binding site is located at the interface of longitudinal *Mtb* FtsZ dimer, close to GTP and T7 loop, suggesting a novel mechanism of action (MOA) to accelerate GTP hydrolysis and inhibit FtsZ polymerization.

§ 4.4 References

- (1) World Health Organization: Tuberculosis Fact sheets. <http://www.who.int/mediacentre/factsheets/fs104/en/>. 2016.
- (2) Huang, Q.; Tonge, P. J.; Slayden, R. A.; Kirikae, J.; Ojima, I. FtsZ: A novel target for tuberculosis drug discovery. *Curr Top Med Chem* **2007**, *7*, 527-543.

- (3) Kumar, K.; Awasthi, D.; Berger, W. T.; Tonge, P. J.; Slayden, R. A.; Ojima, I. Discovery of anti-TB agents that target the cell-division protein FtsZ. *Future Med Chem* **2010**, *2*, 1305-1323.
- (4) Li, Y.; Hsin, J.; Zhao, L. Y.; Cheng, Y. W.; Shang, W. N.; Huang, K. C.; Wang, H. W.; Ye, S. FtsZ Protofilaments Use a Hinge-Opening Mechanism for Constrictive Force Generation. *Science* **2013**, *341*, 392-395.
- (5) Lowe, J.; Amos, L. A. Crystal structure of the bacterial cell-division protein FtsZ. *Nature* **1998**, *391*, 203-206.
- (6) Tan, C. M.; Therien, A. G.; Lu, J.; Lee, S. H.; Caron, A.; Gill, C. J.; Lebeau-Jacob, C.; Benton-Perdomo, L.; Monteiro, J. M.; Pereira, P. M.; Elsen, N. L.; Wu, J.; Deschamps, K.; Petcu, M.; Wong, S.; Daigneault, E.; Kramer, S.; Liang, L.; Maxwell, E.; Claveau, D.; Vaillancourt, J.; Skorey, K.; Tam, J.; Wang, H.; Meredith, T. C.; Sillaots, S.; Wang-Jarantow, L.; Ramtohul, Y.; Langlois, E.; Landry, F.; Reid, J. C.; Parthasarathy, G.; Sharma, S.; Baryshnikova, A.; Lumb, K. J.; Pinho, M. G.; Soisson, S. M.; Roemer, T. Restoring methicillin-resistant *Staphylococcus aureus* susceptibility to beta-lactam antibiotics. *Sci Transl Med* **2012**, *4*, 126-135.
- (7) Oliva, M. A.; Trambaiolo, D.; Lowe, J. Structural insights into the conformational variability of FtsZ. *J Mol Biol* **2007**, *373*, 1229-1242.
- (8) Oliva, M. A.; Cordell, S. C.; Lowe, J. Structural insights into FtsZ protofilament formation. *Nat Struct Mol Biol* **2004**, *11*, 1243-1250.
- (9) Leung, A. K. W.; White, E. L.; Ross, L. J.; Reynolds, R. C.; DeVito, J. A.; Borhani, D. W. Structure of *Mycobacterium tuberculosis* FtsZ reveals unexpected, G protein-like conformational switches. *J Mol Biol* **2004**, *342*, 953-970.
- (10) Lu, C. L.; Reedy, M.; Erickson, H. P. Straight and curved conformations of FtsZ are regulated by GTP hydrolysis. *J Bacteriol* **2000**, *182*, 164-170.
- (11) Hsin, J.; Gopinathan, A.; Huang, K. C. Nucleotide-dependent conformations of FtsZ dimers and force generation observed through molecular dynamics simulations. *P Natl Acad Sci USA* **2012**, *109*, 9432-9437.
- (12) Kumar, K.; Awasthi, D.; Lee, S. Y.; Zanardi, I.; Ruzsicska, B.; Knudson, S.; Tonge, P. J.; Slayden, R. A.; Ojima, I. Novel Trisubstituted Benzimidazoles, Targeting *Mtb* FtsZ, as a New Class of Antitubercular Agents. *J Med Chem* **2011**, *54*, 374-381.

- (13) Awasthi, D.; Kumar, K.; Knudson, S. E.; Slayden, R. A.; Ojima, I. SAR Studies on Trisubstituted Benzimidazoles as Inhibitors of Mtb FtsZ for the Development of Novel Antitubercular Agents. *J Med Chem* **2013**, *56*, 9756-9770.
- (14) Ojima, I.; Kumar, K.; Awasthi, D.; Vineberg, J. G. Drug discovery targeting cell division proteins, microtubules and FtsZ. *Bioorg Med Chem* **2014**, *22*, 5060-5077.
- (15) Park, B.; Awasthi, D.; Chowdhury, S. R.; Melief, E. H.; Kumar, K.; Knudson, S. E.; Slayden, R. A.; Ojima, I. Design, synthesis and evaluation of novel 2,5,6-trisubstituted benzimidazoles targeting FtsZ as antitubercular agents. *Bioorg Med Chem* **2014**, *22*, 2602-2612.
- (16) Morris, G. M.; Huey, R.; Lindstrom, W.; Sanner, M. F.; Belew, R. K.; Goodsell, D. S.; Olson, A. J. AutoDock4 and AutoDockTools4: Automated docking with selective receptor flexibility. *J Comput Chem* **2009**, *30*, 2785-2791.
- (17) Sali, A.; Blundell, T. L. Comparative protein modelling by satisfaction of spatial restraints. *J Mol Biol* **1993**, *234*, 779-815.
- (18) Chemical Computing Group Inc.: Molecular Operating Environment (MOE). Version 2015.10. 2015.

Chapter 5

Design of Novel Fatty Acid Binding Protein (FABP) Inhibitors via Molecular Modeling for Anti-nociceptive and Anti-inflammatory Drug Discovery

Chapter Contents

§ 5.1 Introduction.....	266
§ 5.1.1 Fatty acid-binding proteins (FABPs)	266
§ 5.1.2 Known FABP Inhibitors	268
§ 5.1.3 Discovery and Development of SB-FI-26 as Lead FABP Inhibitor	270
§ 5.1.4 Co-crystal Structure of FABP5 with SB-FI-26.....	272
§ 5.2 Design of Novel SB-FI-26 Analogs as Potential FABP Inhibitors.....	274
§ 5.2.1 Validation of a Pharmacophore-guided Docking Strategy	274
§ 5.2.2 Computational Structural-based Design of New SB-FI-26 Analogs	278
§ 5.3 Summary	281
§ 5.4 References.....	281

§ 5.1 Introduction

§ 5.1.1 Fatty acid-binding proteins (FABPs)

Fatty acid-binding proteins (FABPs), which belong to a superfamily of lipid-binding proteins, are 14-15 kDa proteins that reversibly bind hydrophobic ligands, such as saturated and unsaturated long-chain fatty acids, with high affinity.^{1,2} The primary role of all FABPs is regulation of fatty acid uptake and intracellular transport.³ Since the initial discovery of FABPs in 1972⁴, at least nine members have been identified in human genome (FABP1-9, or liver- (L-FABP), intestine- (I-FABP), heart- (H-FABP), adipocyte- (A-FABP), epidermal- (E-FABP), ileal- (Il-FABP), brain- (B-FABP), myelin- (M-FABP) and testis- (T-FABP)) (Table 5.1).⁵ These different isoforms were named after the organ in which they were first discovered or mostly predominate, however, this classification is somewhat misleading, as no FABP is exclusively specific for a given tissue or cell type.^{1,2} For example, B-FABP (FABP7) is not only expressed in brain, but also in central nervous system (CNS), glial cell, retina and mammary gland.⁵

Table 5.1 Family members of fatty acid-binding proteins (FABPs). Reproduced from Smathers, R. L.; Petersen, D. R. The human fatty acid-binding protein family: evolutionary divergences and functions. *Human genomics* **2011**, 5, 170-191, with permission from BioMed Central.

Gene	Common Name	Alternative Names	Expression	# of Amino Acids
FABP1	Liver FABP	L-FABP, hepatic FABP, Z protein, heme-binding Protein	Liver, intestine, pancreas, kidney, lung, stomach	127
FABP2	Intestinal FABP	I-FABP, gut FABP (gFABP)	Intestine, liver	132
FABP3	Heart FABP	H-FABP, O-FABP, mammary-derived growth inhibitor (MDGI)	Cardiac and skeletal muscle, brain, kidney, lung, stomach, testis, adrenal gland, mammary gland, placenta, ovary, brown adipose tissue	133
FABP4	Adipocyte FABP	A-FABP, aP2	Adipocytes, macrophages, dendritic cells, skeletal muscle fibres	132
FABP5	Epidermal FABP	E-FABP, keratinocyte-type FABP (KFABP),	Skin, tongue, adipocyte, macrophage, dendritic cells,	135

		psoriasis-associated-FABP (PA-FABP)	mammary gland, brain, stomach, intestine, kidney, liver, lung, heart, skeletal muscle, testis, retina, lens, spleen, placenta	
FABP6	Ileal FABP	Il-FABP, Ileal lipid-binding protein (ILLBP), intestinal bile acid-binding protein (I-BABP), gastraphin	Ileum, ovary, adrenal gland, stomach	128
FABP7	Brain FABP	B-FABP, brain lipid-binding protein (BLBP), MRG	Brain, central nervous system (CNS), glial cell, retina, mammary gland	132
FABP8	Myelin FABP	M-FABP, peripheral myelin protein 2 (PMP2)	Peripheral nervous system, Schwann cell	132
FABP9	Testis FABP	T-FABP, testis lipid-binding protein (TLBP), PERF, PERF 15	Testis, salivary gland, mammary gland	132

Interestingly, although FABPs show only moderate amino acids sequence homology, ranging from 20% to 70%, they share almost identical tertiary structures.⁶ All FABPs are composed of ten antiparallel β strands that form a β barrel, and the bound ligand is located within the β barrel in a central internal water-filled cavity.¹ The ten antiparallel β strands are organized into two five-stranded β sheets that orient nearly orthogonally, and on one end of the barrel is capped by a small helix-loop-helix motif.³ The interior of the cavity is determined by the side chains of both hydrophobic and polar amino acid residues, which probably determines the volume of the cavity and the binding specificity. Internal water molecules within the cavity are assumed to contribute to the protein stability.¹

An example for demonstrating the structure of FABP in complex with long chain fatty acid is shown below (**Figure 5.1**). Like the conformations of other FABPs in complex with fatty acids, human brain fatty acid-binding protein (B-FABP or FABP7) binds oleic acid in a U-shaped way.² One oxygen of the carboxylate group of oleic acid (OLA) hydrogen bonds to the hydroxyl group of Tyr128 (2.8 Å) and to an ordered water molecule (3.0 Å), which in turn hydrogen bonds to the side chain oxygen of Thr53 and the guanidinium group of Arg106 (3.2 and 3.3 Å, respectively). The other oxygen is within direct hydrogen bonding distance to the guanidinium group of Arg126 (2.9 Å).

Carbon atoms of the fatty acids' aliphatic chain form van der Waals interactions with several residues of the protein and ordered water molecules.⁷

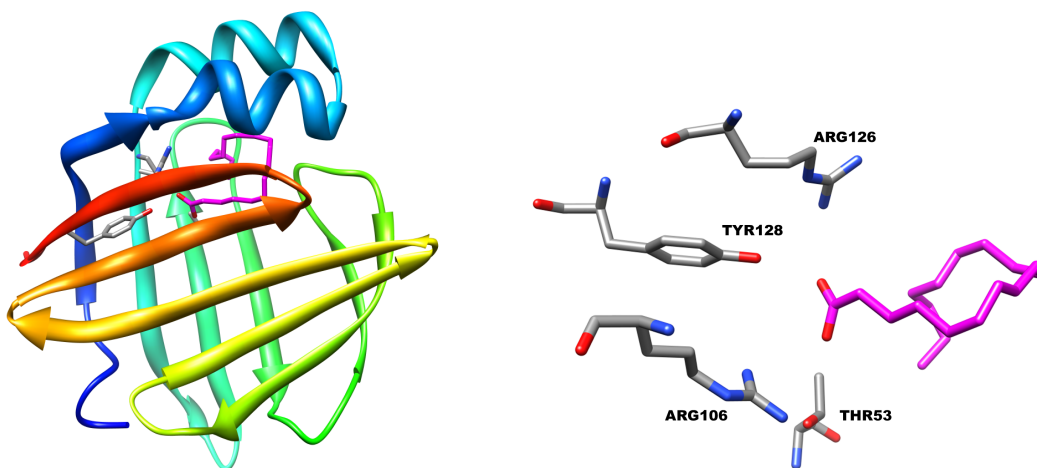


Figure 5.1 Crystal structure of oleic acid (OLA) bound to human B-FABP. Generated based on PDB code 1FE3 with UCSF Chimera.⁸

§ 5.1.2 Known FABP Inhibitors

Because adipocyte/macrophage FABPs, A-FABP (FABP4) and E-FABP (FABP5), have a central role in many aspects of metabolic diseases such as obesity, diabetes and atherosclerosis, a series of FABPs inhibitors have been identified recently against them (**Figure 5.2** and **Table 5.2**), among which orally active small molecule BMS309403 (**1c**), discovered by Sulsky *et al.* from Bristol Myer-Squibb (BMS) Pharmaceutical Research Institute in 2007, has the most promising biology activity profile.^{2,9-15} This promising hit compound has a K_i value of less than 2 nM, and remarkably selectivity over muscle fatty acid-binding protein (M-FABP) and epidermal fatty acid-binding protein (E-FABP).¹²

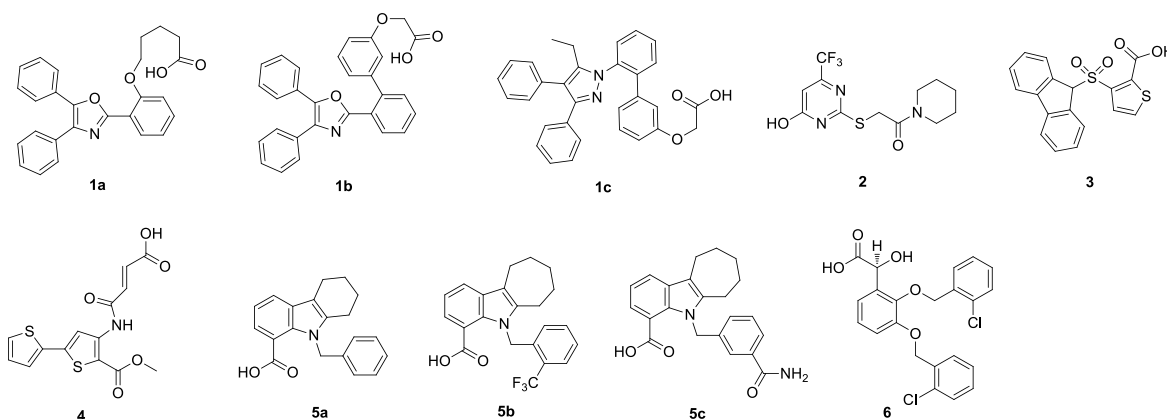


Figure 5.2 Representative chemical structures of known inhibitors of FABPs in development

Table 5.2 Binding affinities for known inhibitors of FABPs in development

Compound Name	IC ₅₀ (μM) or Ki* (μM)					PDB code	Refs
	A-FABP	E-FABP	M-FABP	H-FABP	I-FABP		
1a	0.058*	>2*	>1*				12
1b	0.006*	>2*	>1*				12
1c	<0.002*	0.350*	0.250*			2NNQ	12
2	1					1TOU	9
3	0.57	6.7		<0.6	>100	1TOW	10
4	0.67*	3.40*		9.07*	6.57*	3HK1	13
5a	0.59			3.88		3FR2	14
5b	0.65			<0.4		3FR4	14
5c	0.45			>10		3FR5	14
6	<0.002*	<0.002*					11

X-ray crystallography studies¹² suggested that BMS309403 interact with key amino acid residues such as Ser53, Arg106, Arg126 and Thr128, within the fatty acid binding pocket of A-FABP, accounting for its high binding affinity *in vitro* and selectivity for A-FABP over other FABPs (**Figure 5.3**).

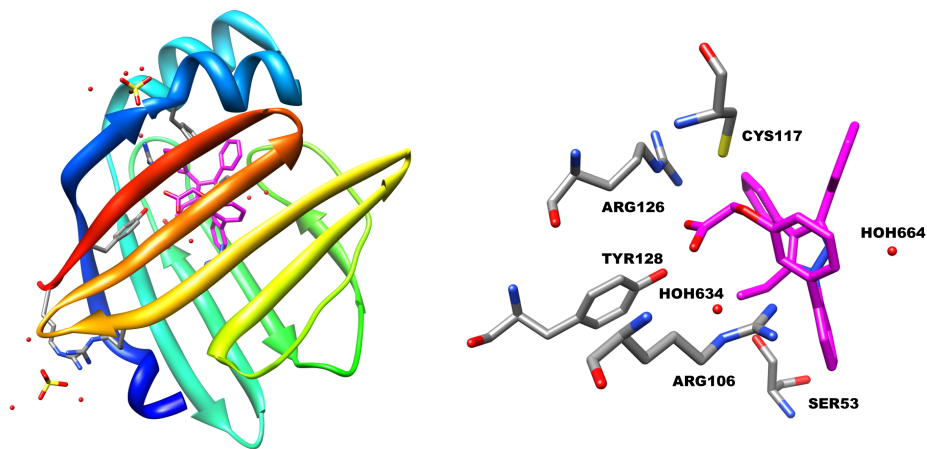


Figure 5.3 Crystal structure of BMS309403 bound to human A-FABP¹². Generated based on PDB code 2NNQ with UCSF Chimera.⁸

§ 5.1.3 Discovery and Development of SB-FI-26 as Lead FABP Inhibitor

Despite the fact that a number of inhibitors targeting FABPs have been reported recently, almost all of these inhibitors were developed for targeting A-FABP (FABP4). Our collaborator Professor Dale Deutsch and his colleagues have recently discovered that FABPs are intracellular carriers for transporting endocannabinoid anandamide (AEA) from outside of the cell to its breakdown enzyme fatty acid amide hydrolase (FAAH).¹⁶ Because arachidonoyl ethanolamide (anandamide, AEA) is a naturally occurring brain component that binds to a specific brain cannabinoid receptor (CBR1), three FABPs which are known to be expressed in brain were examined as possible AEA carriers.^{16,17} Their experimental results suggest that uptake and subsequent hydrolysis of AEA are enhanced by E-FABP (FABP5) and B-FABP (FABP7), and reduced by inhibition of FABPs.¹⁶ Therefore, inhibitors of these FABPs will inactivate endocannabinoid AEA, which may lead to new treatment of a variety of disorders, including addiction, pain, inflammation, and appetite regulation.^{18,19}

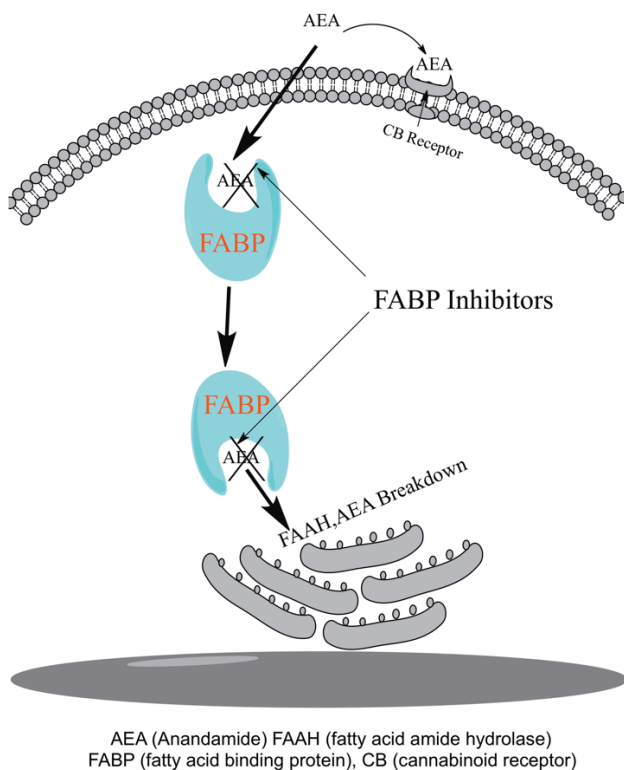


Figure 5.4 Schematic representation of anandamide inactivation FABP drug target. Reprinted with permission from Berger, W. T.; Ralph, B. P.; Kaczocha, M.; Sun, J.; Balias, T. E.; Rizzo, R. C.; Haj-Dahmane, S.; Ojima, I.; Deutsch, D. G. Targeting Fatty Acid Binding Protein (FABP) Anandamide Transporters - A Novel Strategy for Development of Anti-Inflammatory and Anti-Nociceptive Drugs. *Plos One* **2012**, *7*, e50968.

Previous Ojima laboratory group member Dr. William Berger performed a large scale virtual screening with the program DOCK²⁰ of over one million compounds against FABP7, and employed molecular footprint similarity (FPS) scoring²¹, a rescoring method developed in Professor Robert Rizzo's laboratory by Dr. Trent Balias, using oleic acid as the reference molecule (**Figure 5.5**). Forty-eight top scoring compounds were purchased and four of them were found to have greater than 50 % inhibition in a fluorescence displacement assay (**Figure 5.6**).

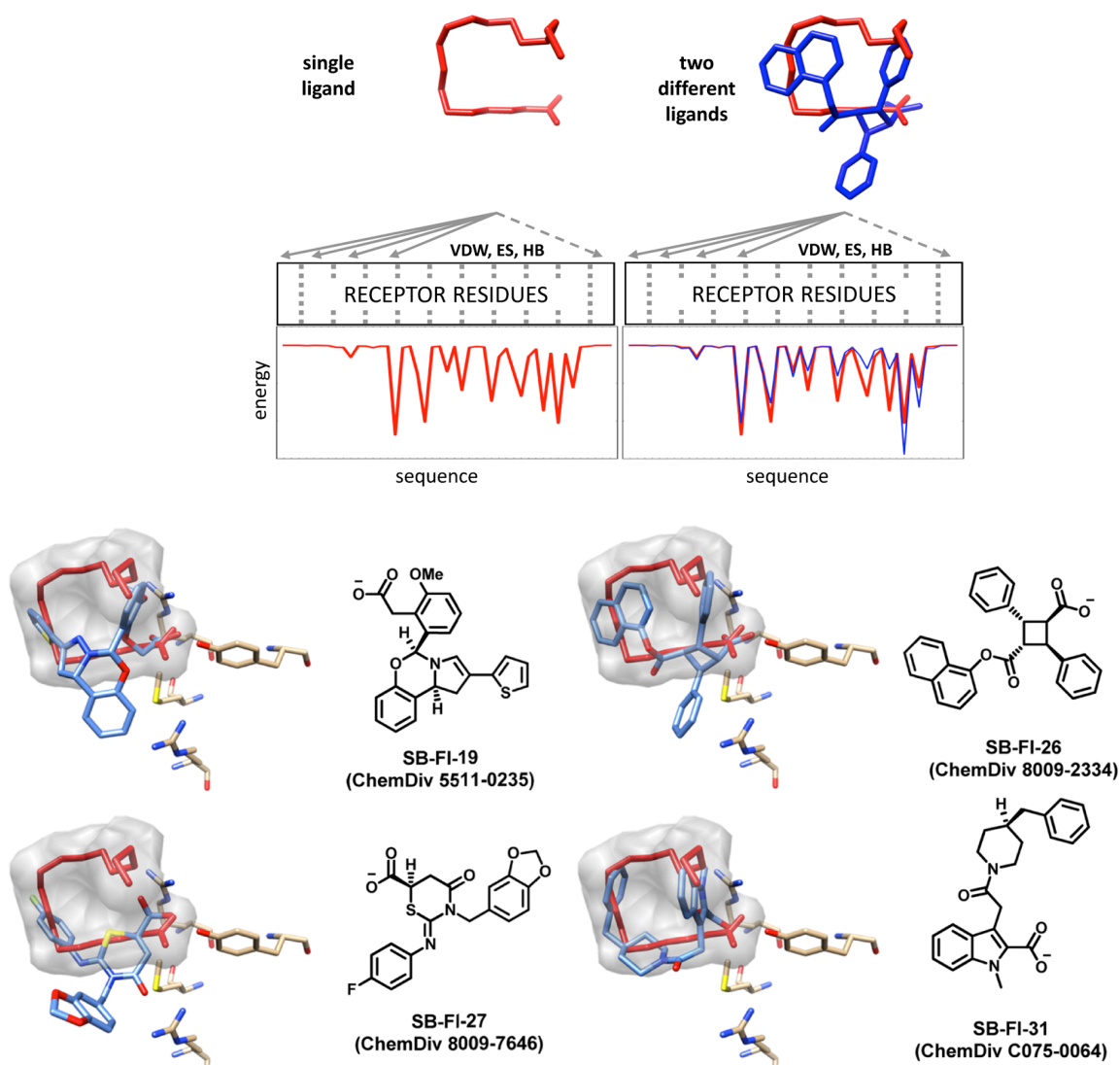


Figure 5.5 Initial hit compounds from virtual screening using footprint similarity method. Reprinted with permission from Berger, W. T.; Ralph, B. P.; Kaczocha, M.; Sun, J.; Balias, T. E.; Rizzo, R. C.; Haj-Dahmane, S.; Ojima, I.; Deutsch, D. G. Targeting Fatty Acid Binding Protein (FABP) Anandamide Transporters - A Novel Strategy for Development of Anti-Inflammatory and Anti-Nociceptive Drugs. *Plos One* **2012**, *7*, e50968.

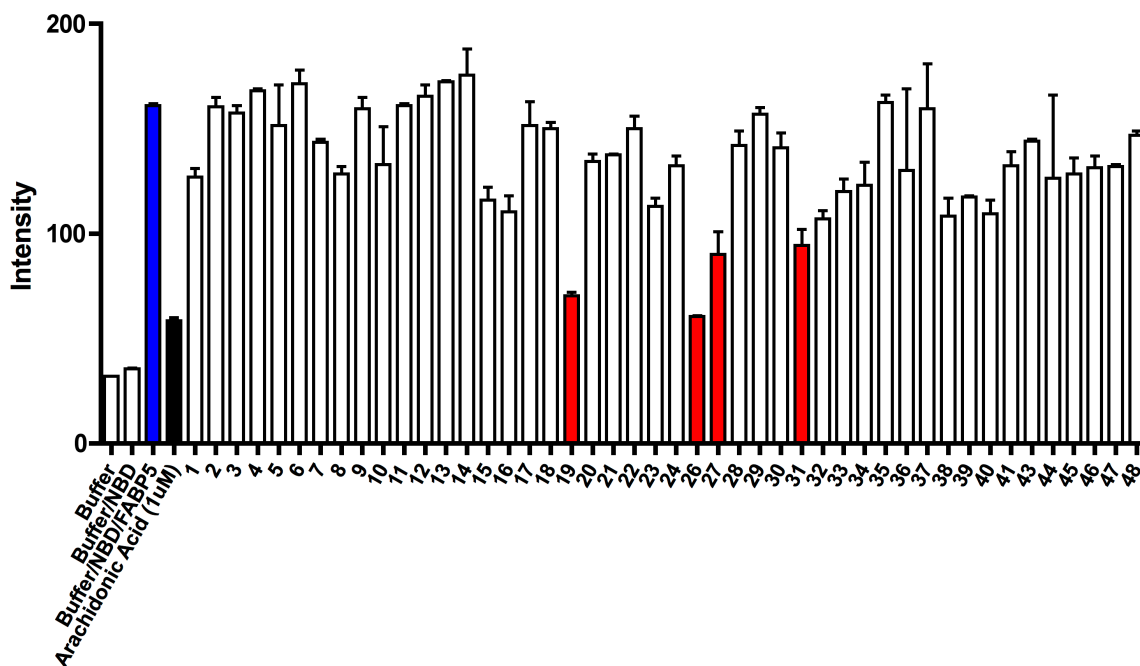


Figure 5.6 Fluorescence displacement assay for purchased 48 top scoring compounds. Reprinted with permission from Berger, W. T.; Ralph, B. P.; Kaczocha, M.; Sun, J.; Balias, T. E.; Rizzo, R. C.; Haj-Dahmane, S.; Ojima, I.; Deutsch, D. G. Targeting Fatty Acid Binding Protein (FABP) Anandamide Transporters - A Novel Strategy for Development of Anti-Inflammatory and Anti-Nociceptive Drugs. *Plos One* **2012**, *7*, e50968.

Biological evaluation of hit compounds were performed in our collaborator Professor Dale Deutsch's laboratory. One of the initial hit compounds purchased from ChemDiv was found out to be γ -truxillic acid 1-naphthyl mono-ester (SB-FI-49) instead of the α - isoform (SB-FI-26), and has a K_i value of $0.747 \pm 0.07 \mu\text{M}$ against FABP5.¹⁹ α -Truxillic acid 1-naphthyl mono-ester (SB-FI-26) was subsequently synthesized, and the K_i value was determined as $0.927 \pm 0.08 \mu\text{M}$ against FABP5.¹⁹ Although SB-FI-26 was slightly less potent than the γ - isoform in the initial binding assays, the solubility is much better and was chosen as the lead compound for further evaluation. SB-FI-26 was later found to be a potent anti-nociceptive agent with mild anti-inflammatory activity in mice models.^{19,22}

§ 5.1.4 Co-crystal Structure of FABP5 with SB-FI-26

Co-crystal structures of FABP5 in complex with endocannabinoids AEA, 2-AG, BMS-309403,²³ as well as lead compound SB-FI-26 were subsequently determined at our collaborator Professor Huilin Li's laboratory. The X-ray crystal structure of FABP5 in complex with SB-FI-26 reveals that the carboxylate group of SB-FI-26 forms two key hydrogen bonds with the side chains of Arg129 and Tyr131 (**Figure 5.7** and **Figure 5.8**).

This provided a structural basis for computationally designing new SB-FI-26 analogs with improved potency.

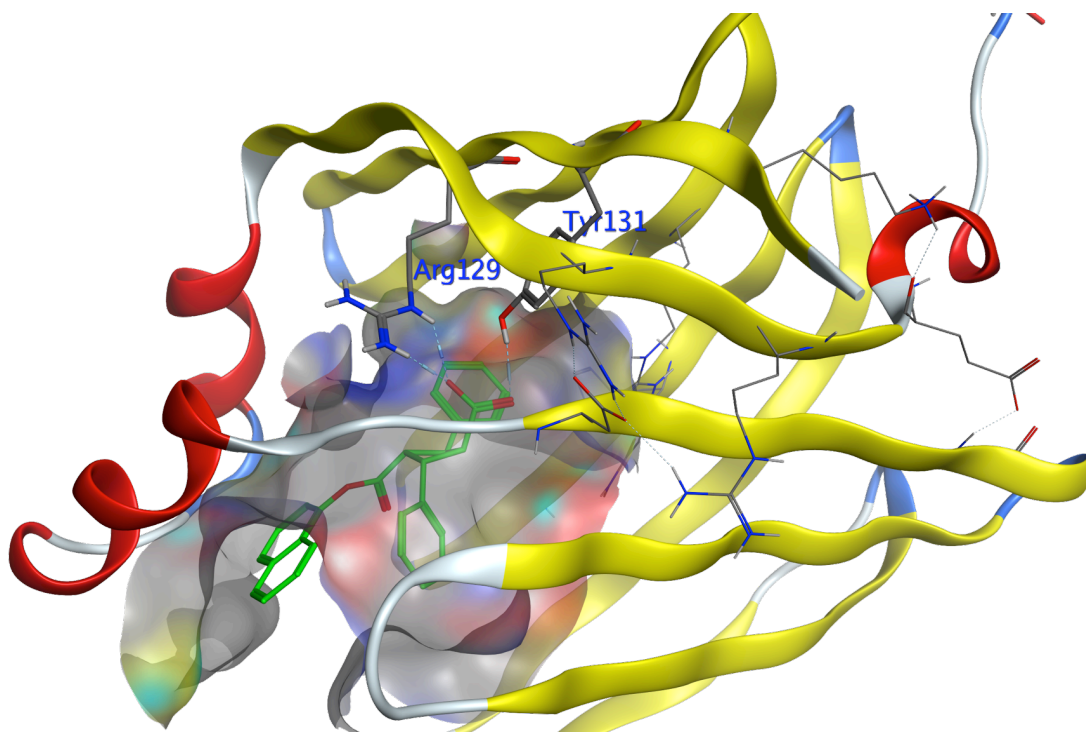


Figure 5.7 Crystal structure of FABP5 in complex with SB-FI-26.

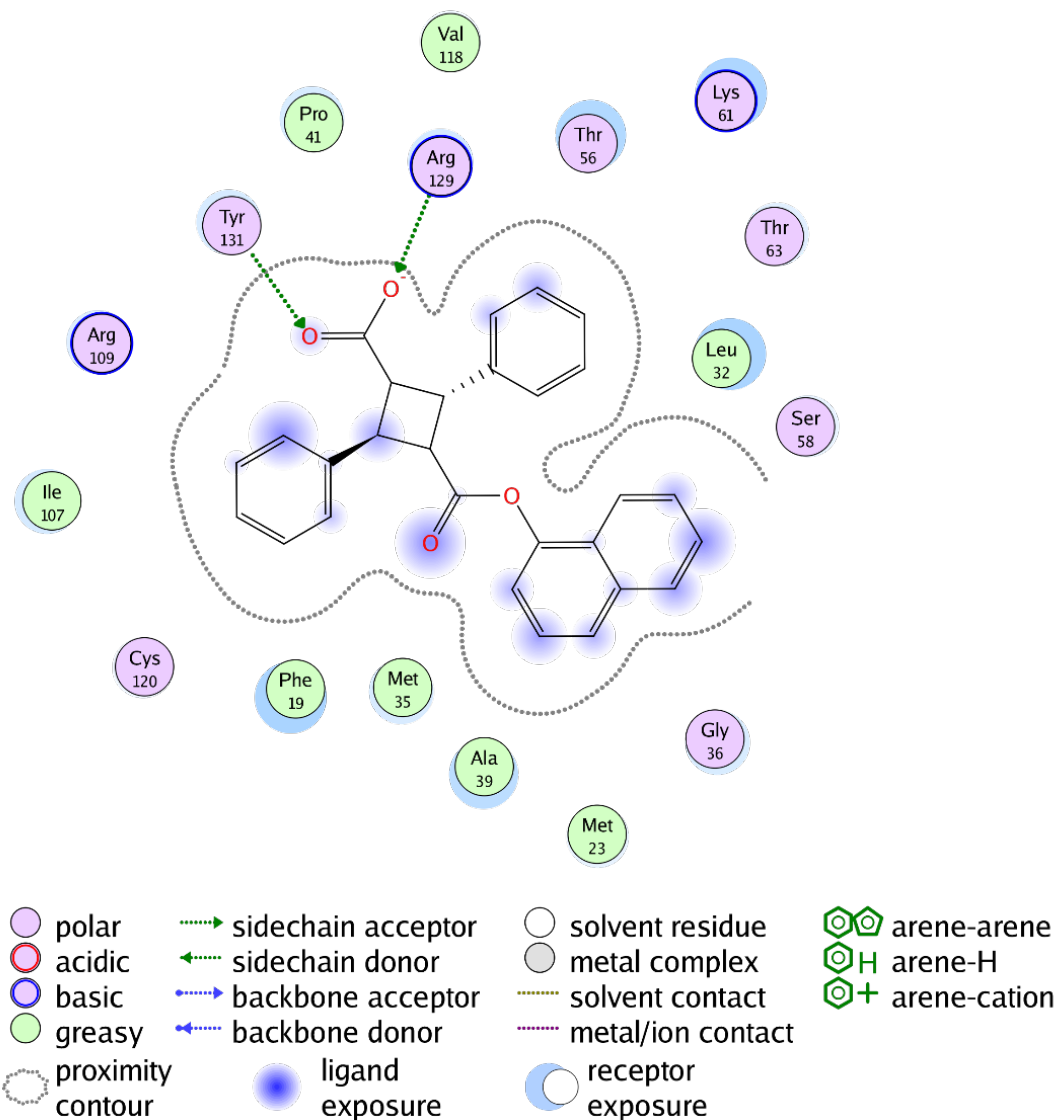


Figure 5.8 2D Interaction diagram of SB-FI-26 with FABP5.

§ 5.2 Design of Novel SB-FI-26 Analogs as Potential FABP Inhibitors

§ 5.2.1 Validation of a Pharmacophore-guided Docking Strategy

Because the X-ray co-crystal structure shows that the carboxylate group of SB-FI-26 forms two key hydrogen bonds with the side chains of Arg129 and Tyr131, combined with fact that the di-ester or di-amide analogs of SB-FI-26 synthesized later in the Ojima laboratory are inactive, as well as the presence of similar hydrogen bonds in the natural occurring fatty acid ligands, strongly suggests these two hydrogen bonds are important for the activity of FABP inhibitors. Thus, these two hydrogen bond interactions were

maintained as pharmacophores during the computational analysis of new SB-FI-26 analogs with the program MOE (**Figure 5.9**).²⁴

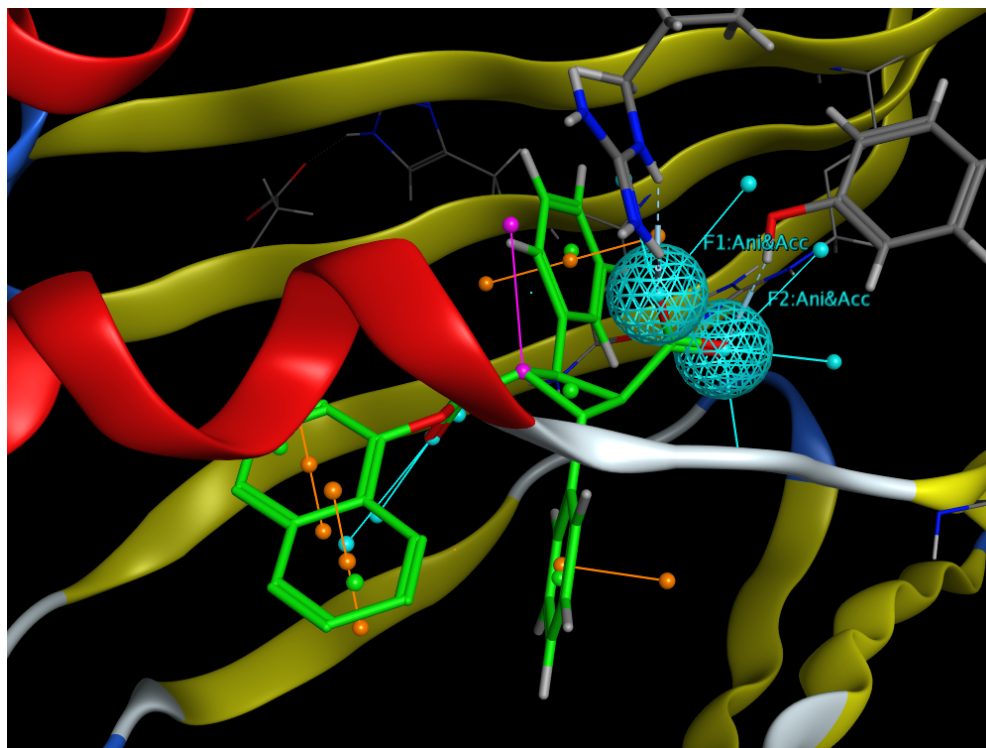


Figure 5.9 Two hydrogen bonds acceptor pharmacophores are used as a filter in the MOE docking protocol.

To validate this docking strategy, first, SB-FI-26 was docked back into FABP5 to compare with the original X-ray crystal structure using this protocol by both rigid-receptor and induced-fit methods (**Figure 5.10** and **Figure 5.11**). The rigid-receptor method shows excellent overlap of the docked pose (magenta) with co-crystal structure ligand (green) with an rmsd of 0.7266 Å. The induced-fit method gave an rmsd of 1.1140 Å, which is also quite reasonable because of the flexibility of the protein receptor in this case.

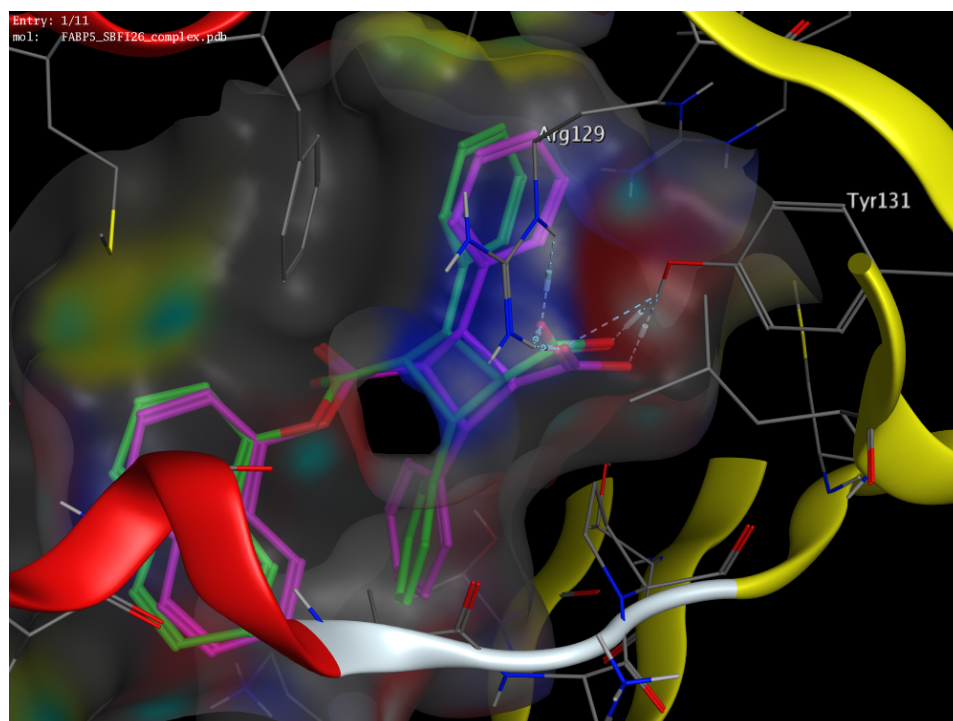


Figure 5.10 Docked poses of SB-FI-26 (magenta) compared with co-crystal structure (green) using rigid-receptor method. Rmsd: 0.7266 Å.

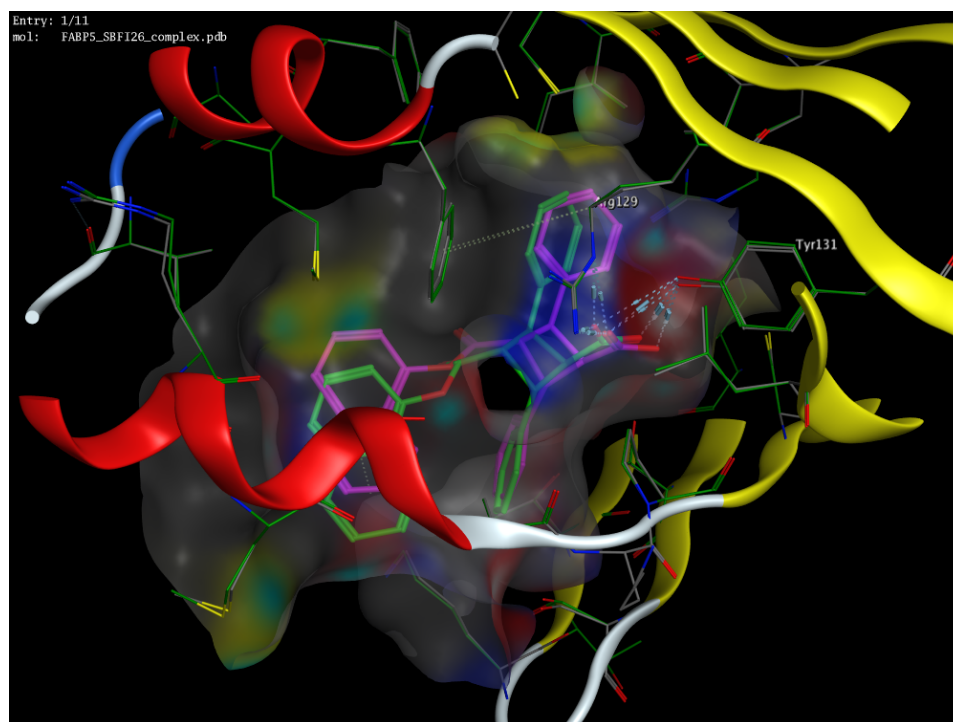
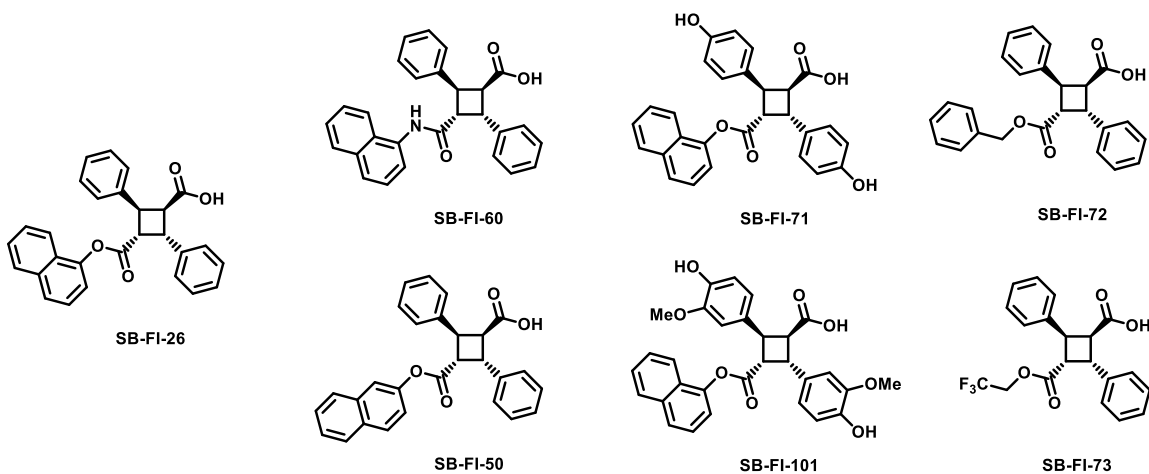


Figure 5.11 Docked poses of SB-FI-26 (magenta) compared with co-crystal structure (green) using induced-fit method. Rmsd: 1.1140 Å.

To further test this docking strategy, docking energy scores with experimental K_i values of a few synthesized SB-FI-26 analogs were compared, and they can correlate very well (**Table 5.3**).

Table 5.3 Comparison of pharmacophore-based docking energy scores by MOE with experimental K_i values.

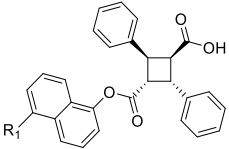
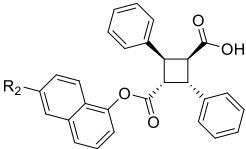


Compound	Rigid Receptor Energy Score (Kcal/mol)	Induced-fit Energy Score (Kcal/mol)	Experimental K_i (μM)
SB-FI-26	-9.0043	-9.1031	0.93 ± 0.05
SB-FI-60	-8.6507	-8.8315	1.55 ± 0.03
SB-FI-50	-8.0667	-8.3427	1.34 ± 0.20
SB-FI-71	-8.0846	-9.1076	>10
SB-FI-101	-8.6793	-9.1948	>10
SB-FI-72	-8.2994	-8.6119	4.11 ± 0.57
SB-FI-73	-7.0679	-7.1707	>10

§ 5.2.2 Computational Structural-based Design of New SB-FI-26 Analogs

Further structure analysis revealed that 5 and 6 positions of the 1-naphthyl group in SB-FI-26 are quite exposed. Based on this, a series of new SB-FI-26 analogs with various substitutions at the 5 or 6 position of the 1-naphthyl group have been designed, and evaluated using a pharmacophore-guided docking strategy (Table 5.4).

Table 5.4 Docking results of new SB-FI-26 analogs

					
Substitution (R ₁ or R ₂)	#	Energy Score-Rigid Receptor (Kcal/mol)	#	Energy Score-Rigid Receptor (Kcal/mol)	
SB-FI-26 (R ₁ = R ₂ = H)		-9.0043			
-CH ₃	1	-8.8692	23	-8.9297	
-CH ₂ CH ₃	2	-8.0851	24	-8.3457	
-CH ₂ CH ₂ CH ₃	3	-8.9415	25	-9.6197	
-CH(CH ₃) ₂	4	-8.6468	26	-8.3183	
-CF ₃	5	-7.7566	27	-8.5033	
-F	6	-8.8467	28	-8.7680	
-Cl	7	-8.8142	29	-8.4908	
-Br	8	-7.9937	30	-8.0883	
-OH	9	-8.9019	31	-8.4021	
-OCH ₃	10	-9.0933	32	-9.1320	
-OCH ₂ CH ₃	11	-8.7818	33	-9.2709	
-OCF ₃	12	-9.3313	34	-8.5033	
-CH ₂ OH	13	-9.0269	35	-8.1564	
-CH ₂ OCH ₃	14	-9.1707	36	-9.4956	
-CH ₂ OCH ₂ CH ₃	15	-8.2089	37	-9.9314	

<chem>-CH2OCF3</chem>	16	-9.4002	38	-8.9880
<chem>-NHCOCH3</chem>	17	-9.2489	39	-9.4251
<chem>-NHCOCH2CH3</chem>	18	-9.0212	40	-9.4553
<chem>-NHCOCH2CH2CH3</chem>	19	-9.1407	41	-10.3273
<chem>CCOCCOCCOCCOCCOCCOCCO</chem>	20	-10.2759	42	-10.0460
<chem>CC(=O)NCCOCCOCCOCCOCCOCCOCCO</chem>	21	-8.1526	43	-10.4708
<chem>CC1=CN(C)N=C1CCOCCOCCOCCOCCOCCO</chem>	22	-10.3944	44	-10.6337

Note: Compounds with better energy scores than parent lead compound SB-FI-26 are shown in red.

As expected, a number of these newly designed analogs showed much better binding than SB-FI-26, while overlapping very well with the binding pose of SB-FI-26 in the X-ray crystallography. Moreover, new analogs with a short PEG chain exhibited much better binding energy scores than SB-FI-26, and would increase the aqueous solubility of the inhibitors (**Figure 5.12** and **Figure 5.13**).

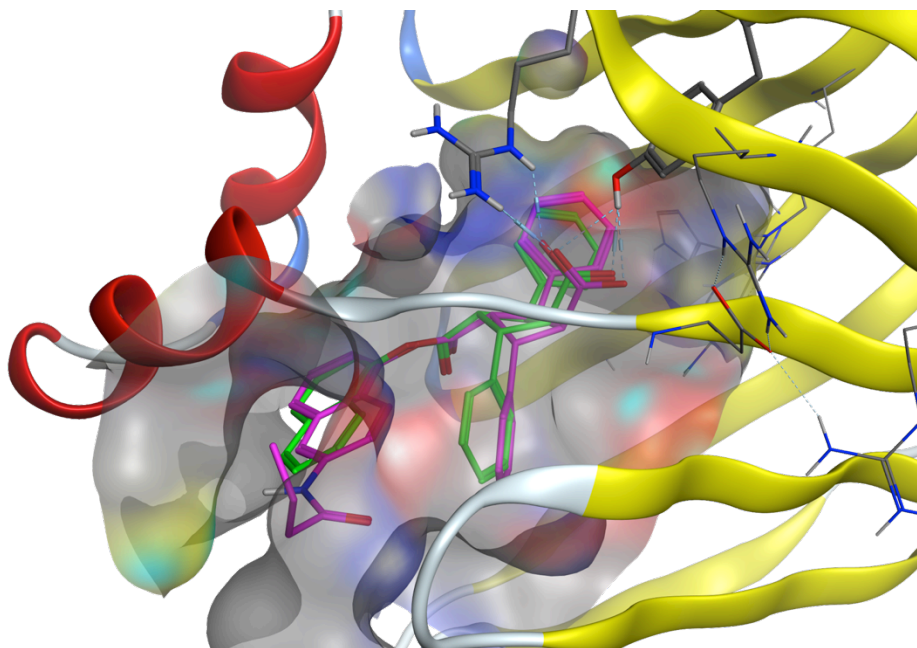


Figure 5.12 Overlay of designed analog (magenta, compound 41) with SB-FI-26 (green)

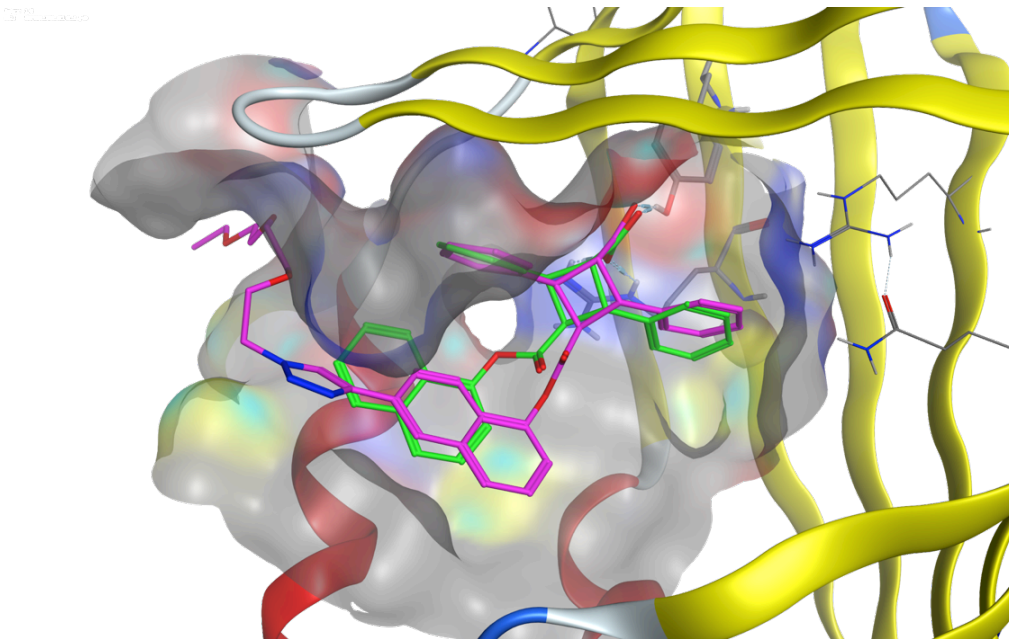


Figure 5.13 Overlay of designed analog (magenta, compound 44) with SB-FI-26 (green)

In addition, a new analog by replacing the 1-naphthyl group with an *m*-triazole-substituted phenyl group was designed, which gave similar better binding energy scores as SB-FI-26. Modifications on this *m*-triazole-substituted phenyl group lead to new analog with much better binding energy score (**Figure 5.14** and **Figure 5.15**). Moreover, these analogs show lower cLogP values than the parent compound SB-FI-26 (cLogP 5.79), which could potentially lead to new candidates with less hydrophobicity for anti-nociceptive and anti-inflammatory drug discovery.

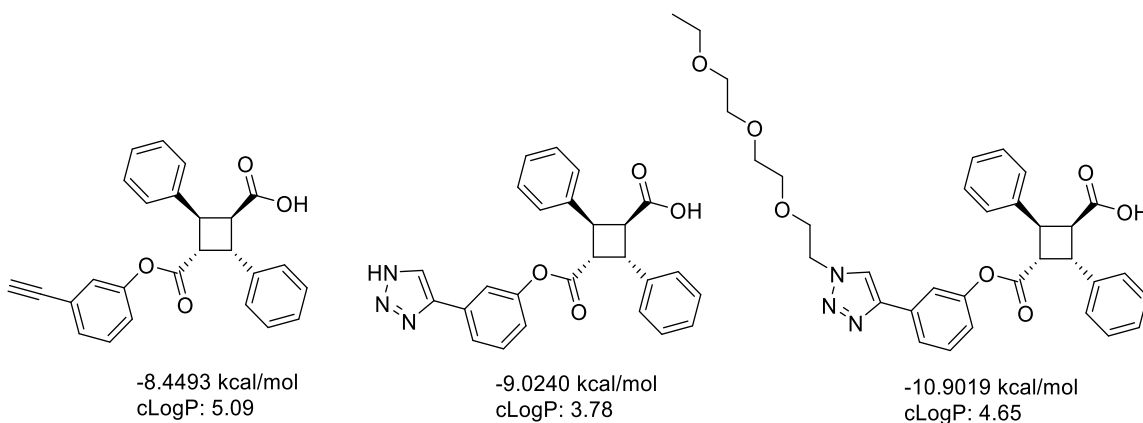


Figure 5.14 Chemical structures, binding energies, and calculated cLogP values for new analogs of SB-FI-26.

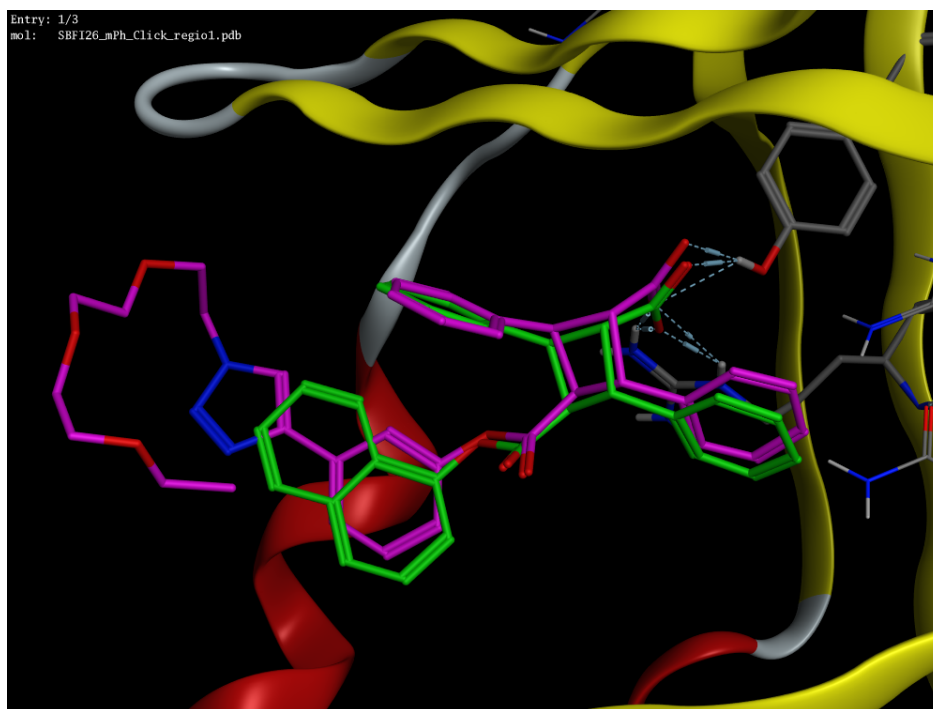


Figure 5.15 Overlay of designed analog (magenta) with SB-FI-26 (green)

§ 5.3 Summary

A pharmacophore-guided docking strategy has been developed for designing FABP inhibitors as anti-nociceptive agents. Docking energy scores have shown good correlation with experimental K_i values. New SB-FI-26 analogs have been designed using the pharmacophore-guided docking strategy, and a number of designed new analogs showed lower binding energy scores as well as smaller cLogP values.

§ 5.4 References

- (1) Zimmerman, A. W.; Veerkamp, J. H. New insights into the structure and function of fatty acid-binding proteins. *Cell Mol Life Sci* **2002**, *59*, 1096-1116.
- (2) Furuhashi, M.; Hotamisligil, G. S. Fatty acid-binding proteins: role in metabolic diseases and potential as drug targets. *Nat Rev Drug Discov* **2008**, *7*, 489-503.
- (3) Chmurzynska, A. The multigene family of fatty acid-binding proteins (FABPs): Function, structure and polymorphism. *J Appl Genetics* **2006**, *47*, 39-48.

- (4) Ockner, R. K.; Ho, W. K. L.; Poppenha.Rb; Manning, J. A. Binding Protein for Fatty-Acids in Cytosol of Intestinal-Mucosa, Liver, Myocardium, and Other Tissues. *Science* **1972**, *177*, 56-58.
- (5) Smathers, R. L.; Petersen, D. R. The human fatty acid-binding protein family: evolutionary divergences and functions. *Human genomics* **2011**, *5*, 170-191.
- (6) Storch, J.; Thumser, A. E. Tissue-specific Functions in the Fatty Acid-binding Protein Family. *J Biol Chem.* **2010**, *285*, 32679-32683.
- (7) Balendiran, G. K.; Schnutgen, F.; Scapin, G.; Borchers, T.; Xhong, N.; Lim, K.; Godbout, R.; Spener, F.; Sacchettini, J. C. Crystal structure and thermodynamic analysis of human brain fatty acid-binding protein. *J Biol Chem* **2000**, *275*, 27045-27054.
- (8) Pettersen, E. F.; Goddard, T. D.; Huang, C. C.; Couch, G. S.; Greenblatt, D. M.; Meng, E. C.; Ferrin, T. E. UCSF chimera - A visualization system for exploratory research and analysis. *J Comput Chem* **2004**, *25*, 1605-1612.
- (9) Lehmann, F.; Haile, S.; Axen, E.; Medina, C.; Uppenberg, J.; Svensson, S.; Lundback, T.; Rondahl, L.; Barf, T. Discovery of inhibitors of human adipocyte fatty acid-binding protein, a potential type 2 diabetes target. *Bioorg Med Chem Lett* **2004**, *14*, 4445-4448.
- (10) Ringom, R.; Axen, E.; Uppenberg, J.; Lundback, T.; Rondahl, L.; Barf, T. Substituted benzylamino-6-(trifluoromethyl)pyrimidin-4(1H)-ones: a novel class of selective human A-FABP inhibitors. *Bioorg Med Chem Lett* **2004**, *14*, 4449-4452.
- (11) McDonnell, P. A.; Constantine, K. L.; Goldfarb, V.; Johnson, S. R.; Sulsky, R.; Magnin, D. R.; Robl, J. A.; Caulfield, T. J.; Parker, R. A.; Taylor, D. S.; Adam, L. P.; Metzler, W. J.; Mueller, L.; Farmer, B. T. NMR structure of a potent small molecule inhibitor bound to human keratinocyte fatty acid-binding protein. *J Med Chem* **2006**, *49*, 5013-5017.
- (12) Sulsky, R.; Magnin, D. R.; Huang, Y.; Simpkins, L.; Taunk, P.; Patel, M.; Zhu, Y.; Stouch, T. R.; Bassolino-Klimas, D.; Parker, R.; Harrity, T.; Stoffel, R.; Taylor, D. S.; Lavoie, T. B.; Kish, K.; Jacobson, B. L.; Sheriff, S.; Adam, L. P.; Ewing, W. R.; Robl, J. A. Potent and selective biphenyl azole inhibitors of adipocyte fatty acid binding pirotein (aFABP). *Bioorg Med Chem Lett* **2007**, *17*, 3511-3515.
- (13) Barf, T.; Lehmann, F.; Hammer, K.; Haile, S.; Axen, E.; Medina, C.; Uppenberg, J.; Svensson, S.; Rondahl, L.; Lundback, T. N-Benzyl-indolo carboxylic acids: Design and synthesis of potent and selective adipocyte fatty-acid binding protein (A-FABP) inhibitors. *Bioorg Med Chem Lett* **2009**, *19*, 1745-1748.

- (14) Hertzelt, A. V.; Hellberg, K.; Reynolds, J. M.; Kruse, A. C.; Juhlmann, B. E.; Smith, A. J.; Sanders, M. A.; Ohlendorf, D. H.; Suttles, J.; Bernlohr, D. A. Identification and Characterization of a Small Molecule Inhibitor of Fatty Acid Binding Proteins. *J Med Chem* **2009**, *52*, 6024-6031.
- (15) Cai, H. Y.; Yan, G. R.; Zhang, X. D.; Gorbenko, O.; Wang, H. Y.; Zhu, W. L. Discovery of highly selective inhibitors of human fatty acid binding protein 4 (FABP4) by virtual screening. *Bioorg Med Chem Lett* **2010**, *20*, 3675-3679.
- (16) Kaczocha, M.; Glaser, S. T.; Deutsch, D. G. Identification of intracellular carriers for the endocannabinoid anandamide. *Proc Natl Acad Sci USA* **2009**, *106*, 6375-6380.
- (17) Koutek, B.; Prestwich, G. D.; Howlett, A. C.; Chin, S. A.; Salehani, D.; Akhavan, N.; Deutsch, D. G. Inhibitors of arachidonoyl ethanolamide hydrolysis. *The J Biol Chem* **1994**, *269*, 22937-22940.
- (18) Di Marzo, V. Targeting the endocannabinoid system: to enhance or reduce? *Nat Rev Drug Discov* **2008**, *7*, 438-455.
- (19) Berger, W. T.; Ralph, B. P.; Kaczocha, M.; Sun, J.; Balius, T. E.; Rizzo, R. C.; Haj-Dahmane, S.; Ojima, I.; Deutsch, D. G. Targeting Fatty Acid Binding Protein (FABP) Anandamide Transporters - A Novel Strategy for Development of Anti-Inflammatory and Anti-Nociceptive Drugs. *Plos One* **2012**, *7*, e50968.
- (20) DOCK6.5 San Francisco, CA: University of California at San Francisco., 2011.
- (21) Balius, T. E.; Mukherjee, S.; Rizzo, R. C. Implementation and evaluation of a docking-rescoring method using molecular footprint comparisons. *J Comput Chem* **2011**, *32*, 2273-2289.
- (22) Kaczocha, M.; Rebecchi, M. J.; Ralph, B. P.; Teng, Y. H. G.; Berger, W. T.; Galbavy, W.; Elmes, M. W.; Glaser, S. T.; Wang, L. Q.; Rizzo, R. C.; Deutsch, D. G.; Ojima, I. Inhibition of Fatty Acid Binding Proteins Elevates Brain Anandamide Levels and Produces Analgesia. *Plos One* **2014**, *9*.
- (23) Sanson, B.; Wang, T.; Sun, J.; Wang, L. Q.; Kaczocha, M.; Ojima, I.; Deutsch, D.; Li, H. L. Crystallographic study of FABP5 as an intracellular endocannabinoid transporter. *Acta Crystallogr D* **2014**, *70*, 290-298.
- (24) Chemical Computing Group Inc.: Molecular Operating Environment (MOE). Version 2015.10. 2015.

References

References for Chapter 1:

- (1) Hanahan, D.; Weinberg, R. A. Hallmarks of Cancer: The Next Generation. *Cell* **2011**, *144*, 646-674.
- (2) Siegel, R. L.; Miller, K. D.; Jemal, A. Cancer Statistics, 2016. *Ca-Cancer J Clin* **2016**, *66*, 7-30.
- (3) American Cancer Society. Cancer Facts & Figures 2016. 2016.
- (4) Ferlay, J.; Soerjomataram, I.; Dikshit, R.; Eser, S.; Mathers, C.; Rebelo, M.; Parkin, D. M.; Forman, D.; Bray, F. Cancer incidence and mortality worldwide: Sources, methods and major patterns in GLOBOCAN 2012. *Int J Cancer* **2015**, *136*, E359-E386.
- (5) Espinosa, E.; Zamora, P.; Feliu, J.; Baron, M. G. Classification of anticancer drugs - a new system based on therapeutic targets. *Cancer Treat Rev* **2003**, *29*, 515-523.
- (6) Wall, M. E.; Wani, M. C. Camptothecin and Taxol - Discovery to Clinic - 13th Bruce-F-Cain-Memorial-Award-Lecture. *Cancer Res* **1995**, *55*, 753-760.
- (7) Wani, M. C.; Taylor, H. L.; Wall, M. E.; Coggon, P.; Mcphail, A. T. Plant Antitumor Agents .6. Isolation and Structure of Taxol, a Novel Antileukemic and Antitumor Agent from *Taxus-Brevifolia*. *J Am Chem Soc* **1971**, *93*, 2325-2327.
- (8) Rowinsky, E. K.; Donehower, R. C. Paclitaxel (Taxol) *New Engl J Med* **1995**, *332*, 1004-1014.
- (9) Schiff, P. B.; Fant, J.; Horwitz, S. B. Promotion of Microtubule Assembly In vitro by Taxol. *Nature* **1979**, *277*, 665-667.
- (10) Schiff, P. B.; Horwitz, S. B. Taxol Stabilizes Microtubules in Mouse Fibroblast Cells. *P Natl Acad Sci-Biol* **1980**, *77*, 1561-1565.
- (11) Jordan, M. A.; Wilson, L. Microtubules as a target for anticancer drugs. *Nat Rev Cancer* **2004**, *4*, 253-265.
- (12) Kingston, D. G. I. Taxol, a molecule for all seasons. *Chem Commun* **2001**, *10*, 867-880.
- (13) National Cancer Institute. FDA approval for docetaxel. <http://www.cancer.gov/about-cancer/treatment/drugs/fda-docetaxel - Anchor-Hea-39459>.

(14) Galsky, M. D.; Dritselis, A.; Kirkpatrick, P.; Oh, W. K. Cabazitaxel. *Nat Rev Drug Discov* **2010**, *9*, 677-678.

(15) Cragg, G. M.; Schepartz, S. A.; Suffness, M.; Grever, M. R. The Taxol Supply Crisis - New Nci Policies for Handling the Large-Scale Production of Novel Natural Product Anticancer and Anti-Hiv Agents. *J Nat Prod* **1993**, *56*, 1657-1668.

(16) Holton, R. A.; Somoza, C.; Kim, H. B.; Liang, F.; Biediger, R. J.; Boatman, P. D.; Shindo, M.; Smith, C. C.; Kim, S. C.; Nadizadeh, H.; Suzuki, Y.; Tao, C. L.; Vu, P.; Tang, S. H.; Zhang, P. S.; Murthi, K. K.; Gentile, L. N.; Liu, J. H. First Total Synthesis of Taxol .1. Functionalization of the B-Ring. *J Am Chem Soc* **1994**, *116*, 1597-1598.

(17) Holton, R. A.; Kim, H. B.; Somoza, C.; Liang, F.; Biediger, R. J.; Boatman, P. D.; Shindo, M.; Smith, C. C.; Kim, S. C.; Nadizadeh, H.; Suzuki, Y.; Tao, C. L.; Vu, P.; Tang, S. H.; Zhang, P. S.; Murthi, K. K.; Gentile, L. N.; Liu, J. H. First Total Synthesis of Taxol .2. Completion of the C-Ring and D-Ring. *J Am Chem Soc* **1994**, *116*, 1599-1600.

(18) Nicolaou, K. C.; Yang, Z.; Liu, J. J.; Ueno, H.; Nantermet, P. G.; Guy, R. K.; Claiborne, C. F.; Renaud, J.; Couladouros, E. A.; Paulvannan, K.; Sorensen, E. J. Total Synthesis of Taxol. *Nature* **1994**, *367*, 630-634.

(19) Nicolaou, K. C.; Nantermet, P. G.; Ueno, H.; Guy, R. K.; Couladouros, E. A.; Sorensen, E. J. Total Synthesis of Taxol .1. Retrosynthesis, Degradation, and Reconstitution. *J Am Chem Soc* **1995**, *117*, 624-633.

(20) Nicolaou, K. C.; Liu, J. J.; Yang, Z.; Ueno, H.; Sorensen, E. J.; Claiborne, C. F.; Guy, R. K.; Hwang, C. K.; Nakada, M.; Nantermet, P. G. Total Synthesis of Taxol .2. Construction of a-Ring and C-Ring Intermediates and Initial Attempts to Construct the Abc Ring-System. *J Am Chem Soc* **1995**, *117*, 634-644.

(21) Nicolaou, K. C.; Yang, Z.; Liu, J. J.; Nantermet, P. G.; Claiborne, C. F.; Renaud, J.; Guy, R. K.; Shibayama, K. Total Synthesis of Taxol .3. Formation of Taxols Abc Ring Skeleton. *J Am Chem Soc* **1995**, *117*, 645-652.

(22) Nicolaou, K. C.; Ueno, H.; Liu, J. J.; Nantermet, P. G.; Yang, Z.; Renaud, J.; Paulvannan, K.; Chadha, R. Total Synthesis of Taxol .4. The Final Stages and Completion of the Synthesis. *J Am Chem Soc* **1995**, *117*, 653-659.

(23) Danishefsky, S. J.; Masters, J. J.; Young, W. B.; Link, J. T.; Snyder, L. B.; Magee, T. V.; Jung, D. K.; Isaacs, R. C. A.; Bornmann, W. G.; Alaimo, C. A.; Coburn, C. A.; DiGrandi, M. J. Total synthesis of baccatin III and taxol. *J Am Chem Soc* **1996**, *118*, 2843-2859.

(24) Wender, P. A.; Badham, N. F.; Conway, S. P.; Floreancig, P. E.; Glass, T. E.; Granicher, C.; Houze, J. B.; Janichen, J.; Lee, D. S.; Marquess, D. G.; McGrane, P. L.; Meng, W.; Mucciario, T. P.; Muhlebach, M.; Natchus, M. G.; Paulsen, H.; Rawlins, D. B.; Satkofsky, J.; Shuker, A. J.; Sutton, J. C.; Taylor, R. E.; Tomooka, K. The pinene path to taxanes .5. Stereocontrolled synthesis of a versatile taxane precursor. *J Am Chem Soc* **1997**, *119*, 2755-2756.

(25) Wender, P. A.; Badham, N. F.; Conway, S. P.; Floreancig, P. E.; Glass, T. E.; Houze, J. B.; Krauss, N. E.; Lee, D. S.; Marquess, D. G.; McGrane, P. L.; Meng, W.; Natchus, M. G.; Shuker, A. J.; Sutton, J. C.; Taylor, R. E. The pinene path to taxanes .6. A concise stereocontrolled synthesis of taxol. *J Am Chem Soc* **1997**, *119*, 2757-2758.

(26) Morihira, K.; Hara, R.; Kawahara, S.; Nishimori, T.; Nakamura, N.; Kusama, H.; Kuwajima, I. Enantioselective total synthesis of taxol. *J Am Chem Soc* **1998**, *120*, 12980-12981.

(27) Mukaiyama, T.; Shiina, I.; Iwadare, H.; Saitoh, M.; Nishimura, T.; Ohkawa, N.; Sakoh, H.; Nishimura, K.; Tani, Y.; Hasegawa, M.; Yamada, K.; Saitoh, K. Asymmetric total synthesis of Taxol (R). *Chem-Eur J* **1999**, *5*, 121-161.

(28) Doi, T.; Fuse, S.; Miyamoto, S.; Nakai, K.; Sasuga, D.; Takahashi, T. A formal total synthesis of taxol aided by an automated synthesizer. *Chem-Asian J* **2006**, *1*, 370-383.

(29) Fukaya, K.; Tanaka, Y.; Sato, A. C.; Kodama, K.; Yamazaki, H.; Ishimoto, T.; Nozaki, Y.; Iwaki, Y. M.; Yuki, Y.; Umei, K.; Sugai, T.; Yamaguchi, Y.; Watanabe, A.; Oishi, T.; Sato, T.; Chida, N. Synthesis of Paclitaxel. 1. Synthesis of the ABC Ring of Paclitaxel by SmI₂-Mediated Cyclization. *Org Lett* **2015**, *17*, 2570-2573.

(30) Fukaya, K.; Kodama, K.; Tanaka, Y.; Yamazaki, H.; Sugai, T.; Yamaguchi, Y.; Watanabe, A.; Oishi, T.; Sato, T.; Chida, N. Synthesis of Paclitaxel. 2. Construction of the ABCD Ring and Formal Synthesis. *Org Lett* **2015**, *17*, 2574-2577.

(31) Hirai, S.; Utsugi, M.; Iwamoto, M.; Nakada, M. Formal Total Synthesis of (-)-Taxol through Pd-Catalyzed Eight-Membered Carbocyclic Ring Formation. *Chem-Eur J* **2015**, *21*, 355-359.

(32) Ojima, I.; Habus, I.; Zhao, M.; Zucco, M.; Park, Y. H.; Sun, C. M.; Brigaud, T. New and Efficient Approaches to the Semisynthesis of Taxol and Its C-13 Side-Chain Analogs by Means of Beta-Lactam Synthons Method. *Tetrahedron* **1992**, *48*, 6985-7012.

(33) Holton, R. A. Method for preparation of taxol. Eur. Pat. Appl. EP 400971, May 30, 1990.

- (34) Chauviere, G.; Guenard, D.; Picot, F.; Senilh, V.; Potier, P. Structural-Analysis and Biochemical-Study of Isolated Products of the Yew - *Taxus-Baccata* L (Taxaceae). *Cr Acad Sci Li* **1981**, *293*, 501-503.
- (35) Denis, J. N.; Greene, A. E.; Guenard, D.; Guerittevoegelein, F.; Mangatal, L.; Potier, P. A Highly Efficient, Practical Approach to Natural Taxol. *J Am Chem Soc* **1988**, *110*, 5917-5919.
- (36) Ojima, I., Kuduk, S. D., Chakravarty, S. Recent advances in the medicinal chemistry of taxoids anticancer agents. *Adv Med Chem* **1999**, *4*, 69-124.
- (37) Ojima, I.; Habus, I. Asymmetric-Synthesis of Beta-Lactams by Chiral Ester Enolate - Imine Condensation. *Tetrahedron Lett* **1990**, *31*, 4289-4292.
- (38) Ojima, I.; Habus, I.; Zhao, M. Z.; Georg, G. I.; Jayasinghe, L. R. Efficient and Practical Asymmetric-Synthesis of the Taxol C-13 Side-Chain, N-Benzoyl-(2r,3s)-3-Phenylisoserine, and Its Analogs Via Chiral 3-Hydroxy-4-Aryl-Beta-Lactams through Chiral Ester Enolate-Imine Cyclocondensation. *J Org Chem* **1991**, *56*, 1681-1683.
- (39) Ojima, I.; Sun, C. M.; Zucco, M.; Park, Y. H.; Duclos, O.; Kuduk, S. A Highly Efficient Route to Taxotere by the Beta-Lactam Synthon Method. *Tetrahedron Lett* **1993**, *34*, 4149-4152.
- (40) Ojima, I.; Zucco, M.; Duclos, O.; Kuduk, S. D.; Sun, C. M.; Park, Y. H. N-Acyl-3-Hydroxy-Beta-Lactams as Key Intermediates for Taxotere and Its Analogs. *Bioorg Med Chem Lett* **1993**, *3*, 2479-2482.
- (41) Staudinger, H. Announcements from the chemical instiute at Strasbourg University in Alsace, France - Ketene. *Liebigs Ann Chem* **1907**, *356*, 51-123.
- (42) Tidwell, T. T. Hugo (ugo) Schiff, Schiff bases, and a century of beta-lactam synthesis. *Angew Chem Int Edit* **2008**, *47*, 1016-1020.
- (43) Sheehan, J. C.: The enchanted ring: the untold story of penicillin. The MIT Press., 1984.
- (44) Ojima, I. Recent Advances in the Beta-Lactam Synthon Method. *Acc Chem Res* **1995**, *28*, 383-389.
- (45) Jiao, L.; Liang, Y.; Xu, J. X. Origin of the relative stereoselectivity of the beta-lactam formation in the Staudinger reaction. *J Am Chem Soc* **2006**, *128*, 6060-6069.
- (46) Cossio, F. P.; Arrieta, A.; Sierra, M. A. The mechanism of the ketene-imine (Staudinger) reaction in its centennial: Still an unsolved problem? *Acc Chem Res* **2008**, *41*, 925-936.

- (47) Brieva, R.; Crich, J. Z.; Sih, C. J. Chemoenzymatic Synthesis of the C-13 Side-Chain of Taxol - Optically-Active 3-Hydroxy-4-Phenyl Beta-Lactam Derivatives. *J Org Chem* **1993**, *58*, 1068-1075.
- (48) Kingston, D. G. I.; Samaranayake, G.; Ivey, C. A. The Chemistry of Taxol, a Clinically Useful Anticancer Agent. *J Nat Prod* **1990**, *53*, 1-12.
- (49) Guenard, D.; Guerittevoegelein, F.; Potier, P. Taxol and Taxotere - Discovery, Chemistry, and Structure-Activity-Relationships. *Acc Chem Res* **1993**, *26*, 160-167.
- (50) Ojima, I.; Slater, J. C.; Michaud, E.; Kuduk, S. D.; Bounaud, P. Y.; Vrignaud, P.; Bissery, M. C.; Veith, J. M.; Pera, P.; Bernacki, R. J. Syntheses and structure-activity relationships of the second-generation antitumor taxoids: Exceptional activity against drug-resistant cancer cells. *J Med Chem* **1996**, *39*, 3889-3896.
- (51) Chen, S. H.; Wei, J. M.; Farina, V. Taxol Structure-Activity-Relationships - Synthesis and Biological Evaluation of 2-Deoxytaxol. *Tetrahedron Lett* **1993**, *34*, 3205-3206.
- (52) Chaudhary, A. G.; Gharpure, M. M.; Rimoldi, J. M.; Chordia, M. D.; Gunatilaka, A. A. L.; Kingston, D. G. I.; Grover, S.; Lin, C. M.; Hamel, E. Unexpectedly Facile Hydrolysis of the 2-Benzoate Group of Taxol and Syntheses of Analogs with Increased Activities. *J Am Chem Soc* **1994**, *116*, 4097-4098.
- (53) Kingston, D. G. I.; Chaudhary, A. G.; Chordia, M. D.; Gharpure, M.; Gunatilaka, A. A. L.; Higgs, P. I.; Rimoldi, J. M.; Samala, L.; Jagtap, P. G.; Giannakakou, P.; Jiang, Y. Q.; Lin, C. M.; Hamel, E.; Long, B. H.; Fairchild, C. R.; Johnston, K. A. Synthesis and biological evaluation of 2-acyl analogues of paclitaxel (Taxol). *J Med Chem* **1998**, *41*, 3715-3726.
- (54) Ojima, I.; Wang, T.; Miller, M. L.; Lin, S. N.; Borella, C. P.; Geng, X. D.; Pera, P.; Bernacki, R. J. Synthesis and structure-activity relationships of new second-generation taxoids. *Bioorg Med Chem Lett* **1999**, *9*, 3423-3428.
- (55) Chordia, M. D.; Chaudhary, A. G.; Kingston, D. G. I.; Jiang, Y. Q.; Hamel, E. Synthesis and Biological Evaluation of 4-Deacetytaxol. *Tetrahedron Lett* **1994**, *35*, 6843-6846.
- (56) Neidigh, K. A.; Gharpure, M. M.; Rimoldi, J. M.; Kingston, D. G. I.; Jiang, Y. Q.; Hamel, E. Synthesis and Biological Evaluation of 4-Deacetylpaclitaxel. *Tetrahedron Lett* **1994**, *35*, 6839-6842.

- (57) Chen, S. H.; Wei, J. M.; Long, B. H.; Fairchild, C. A.; Carboni, J.; Mamber, S. W.; Rose, W. C.; Johnston, K.; Casazza, A. M.; Kadow, J. F.; Farina, V.; Vyas, D. M.; Doyle, T. W. Novel C-4 Paclitaxel (Taxol(R)) Analogs - Potent Antitumor Agents. *Bioorg Med Chem Lett* **1995**, *5*, 2741-2746.
- (58) Samaranayake, G.; Magri, N. F.; Jitrangsri, C.; Kingston, D. G. I. Modified Taxols .5. Reaction of Taxol with Electrophilic Reagents and Preparation of a Rearranged Taxol Derivative with Tubulin Assembly Activity. *J Org Chem* **1991**, *56*, 5114-5119.
- (59) Gunatilaka, A. A. L.; Ramdayal, F. D.; Sarragiotto, M. H.; Kingston, D. G. I.; Sackett, D. L.; Hamel, E. Synthesis and biological evaluation of novel paclitaxel (Taxol) D-ring modified analogues. *J Org Chem* **1999**, *64*, 2694-2703.
- (60) Dubois, J.; Thoret, S.; Gueritte, F.; Guenard, D. Synthesis of 5(20)deoxydocetaxel, a new active docetaxel analogue. *Tetrahedron Lett* **2000**, *41*, 3331-3334.
- (61) Chaudhary, A. G.; Rimoldi, J. M.; Kingston, D. G. I. Modified Taxols .10. Preparation of 7-Deoxytaxol, a Highly Bioactive Taxol Derivative, and Interconversion of Taxol and 7-Epi-Taxol. *J Org Chem* **1993**, *58*, 3798-3799.
- (62) Chen, S. H.; Huang, S.; Kant, J.; Fairchild, C.; Wei, J. M.; Farina, V. Synthesis of 7-Deoxytaxol and 7,10-Dideoxytaxol Via Radical Intermediates. *J Org Chem* **1993**, *58*, 5028-5029.
- (63) Chaudhary, A. G.; Kingston, D. G. I. Synthesis of 10-Deacetoxytaxol and 10-Deoxytaxotere. *Tetrahedron Lett* **1993**, *34*, 4921-4924.
- (64) Samaranayake, G.; Neidigh, K. A.; Kingston, D. G. I. Modified Taxols .8. Deacylation and Reacylation of Baccatin-Iii. *J Nat Prod* **1993**, *56*, 884-898.
- (65) Uoto, K.; Mitsui, I.; Terasawa, H.; Soga, T. First synthesis and cytotoxic activity of novel docetaxel analogs modified at the C18-position. *Bioorg Med Chem Lett* **1997**, *7*, 2991-2996.
- (66) Ojima, I.; Park, Y. H.; Sun, C. M.; Fenoglio, I.; Appendino, G.; Pera, P.; Bernacki, R. J. Structure-Activity-Relationships of New Taxoids Derived from 14-Beta-Hydroxy-10-Deacetylbaaccatin-Iii. *J Med Chem* **1994**, *37*, 1408-1410.
- (67) Ojima, I.; Slater, J. C.; Kuduk, S. D.; Takeuchi, C. S.; Gimi, R. H.; Sun, C. M.; Park, Y. H.; Pera, P.; Veith, J. M.; Bernacki, R. J. Syntheses and structure-activity relationships of taxoids derived from 14 beta-hydroxy-10-deacetylbaaccatin III. *J Med Chem* **1997**, *40*, 267-278.

- (68) Nicoletti, M. I.; Colombo, T.; Rossi, C.; Monardo, C.; Stura, S.; Zucchetti, M.; Riva, A.; Morazzoni, P.; Donati, M. B.; Bombardelli, E.; D'Incalci, M.; Giavazzi, R. IDN5109, a taxane with oral bioavailability and potent antitumor activity. *Cancer Res* **2000**, *60*, 842-846.
- (69) Sharom, F. J. ABC multidrug transporters: structure, function and role in chemoresistance. *Pharmacogenomics* **2008**, *9*, 105-127.
- (70) Szakacs, G.; Paterson, J. K.; Ludwig, J. A.; Booth-Genthe, C.; Gottesman, M. M. Targeting multidrug resistance in cancer. *Nat Rev Drug Discov* **2006**, *5*, 219-234.
- (71) Aller, S. G.; Yu, J.; Ward, A.; Weng, Y.; Chittaboina, S.; Zhuo, R. P.; Harrell, P. M.; Trinh, Y. T.; Zhang, Q. H.; Urbatsch, I. L.; Chang, G. Structure of P-Glycoprotein Reveals a Molecular Basis for Poly-Specific Drug Binding. *Science* **2009**, *323*, 1718-1722.
- (72) Ojima, I.; Zuniga, E. S.; Berger, W. T.; Seitz, J. D. Tumor-targeting drug delivery of new-generation taxoids. *Future Med Chem* **2012**, *4*, 33-50.
- (73) Gueritte-Voegelein, F.; Senilh, V.; David, B.; Guenard, D.; Potier, P. Chemical studies of 10-deacetyl baccatin III. Hemisynthesis of taxol derivatives. *Tetrahedron* **1986**, *42*, 4451-4460.
- (74) Ehrlichova, M.; Vaclavikova, R.; Ojima, I.; Pepe, A.; Kuznetsova, L. V.; Chen, J.; Truksa, J.; Kovar, J.; Gut, I. Transport and cytotoxicity of paclitaxel, docetaxel, and novel taxanes in human breast cancer cells. *Naunyn Schmiedebergs Arch Pharmacol* **2005**, *372*, 95-105.
- (75) Macrae, M. X.; Blake, S.; Mayer, M.; Yang, J. Nanoscale Ionic Diodes with Tunable and Switchable Rectifying Behavior. *J Am Chem Soc* **2010**, *132*, 1766-+.
- (76) Yu, H. W.; Ballard, C. E.; Boyle, P. D.; Wang, B. H. An inexpensive carbohydrate derivative used as a chiral auxiliary in the synthesis of alpha-hydroxy carboxylic acids. *Tetrahedron* **2002**, *58*, 7663-7679.
- (77) Gonzalez, J.; Aurigemma, C.; Truesdale, L. Synthesis of (+)-(1S,2R)- and (-)-(1R,2S)-trans-2-phenylcyclohexanol via Sharpless asymmetric dihydroxylation (AD). *Org Synth* **2003**, *79*, 93-102.
- (78) Kuznetsova, L. V.; Pepe, A.; Ungureanu, I. M.; Pera, P.; Bernacki, R. J.; Ojima, I. Syntheses and structure-activity relationships of novel 3'-difluoromethyl and 3'-trifluoromethyl-taxoids. *J Fluorine Chem* **2008**, *129*, 817-828.
- (79) Kuznetsova, L.; Ungureanu, I. M.; Pepe, A.; Zanardi, I.; Wu, X.; Ojima, I. Trifluoromethyl- and difluoromethyl- β -lactams as useful building blocks for the synthesis

of fluorinated amino acids, dipeptides, and fluoro-taxoids. *J Fluorine Chem* **2004**, *125*, 487-500.

(80) Ojima, I.; Fumero-Oderda, C. L.; Kuduk, S. D.; Ma, Z.; Kirikae, F.; Kirikae, T. Structure-activity relationship study of taxoids for their ability to activate murine macrophages as well as inhibit the growth of macrophage-like cells. *Bioorg Med Chem* **2003**, *11*, 2867-2888.

References for Chapter 2:

(1) Strebhardt, K.; Ullrich, A. Paul Ehrlich's magic bullet concept: 100 years of progress. *Nat Rev Cancer* **2008**, *8*, 473-480.

(2) DeVita, V. T., Jr.; Chu, E. A history of cancer chemotherapy. *Cancer Res* **2008**, *68*, 8643-8653.

(3) National Cancer Institute. <http://www.cancer.gov/about-cancer/treatment/types/targeted-therapies/targeted-therapies-fact-sheet>.

(4) Druker, B. J.; Tamura, S.; Buchdunger, E.; Ohno, S.; Segal, G. M.; Fanning, S.; Zimmermann, J.; Lydon, N. B. Effects of a selective inhibitor of the Abl tyrosine kinase on the growth of Bcr-Abl positive cells. *Nat Med* **1996**, *2*, 561-566.

(5) Presta, L. G.; Chen, H.; O'Connor, S. J.; Chisholm, V.; Meng, Y. G.; Krummen, L.; Winkler, M.; Ferrara, N. Humanization of an anti-vascular endothelial growth factor monoclonal antibody for the therapy of solid tumors and other disorders. *Cancer Res* **1997**, *57*, 4593-4599.

(6) Ferrara, N.; Hillan, K. J.; Gerber, H. P.; Novotny, W. Discovery and development of bevacizumab, an anti-VEGF antibody for treating cancer. *Nat Rev Drug Discov* **2004**, *3*, 391-400.

(7) Jaracz, S.; Chen, J.; Kuznetsova, L. V.; Ojima, L. Recent advances in tumor-targeting anticancer drug conjugates. *Bioorg Med Chem* **2005**, *13*, 5043-5054.

(8) Ojima, I. Guided molecular missiles for tumor-targeting chemotherapy-case studies using the second-generation taxoids as warheads. *Acc Chem Res* **2008**, *41*, 108-119.

(9) Ojima, I. Tumor-targeting drug delivery of chemotherapeutic agents. *Pure Appl Chem* **2011**, *83*, 1685-1698.

- (10) Ojima, I.; Zuniga, E. S.; Berger, W. T.; Seitz, J. D. Tumor-targeting drug delivery of new-generation taxoids. *Future Med Chem* **2012**, *4*, 33-50.
- (11) Ojima, I.; Geng, X. D.; Wu, X. Y.; Qu, C. X.; Borella, C. P.; Xie, H. S.; Wilhelm, S. D.; Leece, B. A.; Bartle, L. M.; Goldmacher, V. S.; Chari, R. V. J. Tumor-specific novel taxoid-monoclonal antibody conjugates. *J Med Chem* **2002**, *45*, 5620-5623.
- (12) Wu, X.; Ojima, I. Tumor specific novel taxoid-monoclonal antibody conjugates. *Curr Med Chem* **2004**, *11*, 429-438.
- (13) Kuznetsova, L.; Chen, J.; Sun, L.; Wu, X. Y.; Pepe, A.; Veith, J. A.; Pera, P.; Bernacki, R. J.; Ojima, I. Syntheses and evaluation of novel fatty acid-second-generation taxoid conjugates as promising anticancer agents. *Bioorg Med Chem Lett* **2006**, *16*, 974-977.
- (14) Seitz, J. D.; Vineberg, J. G.; Herlihy, E.; Park, B.; Melief, E.; Ojima, I. Design, synthesis and biological evaluation of a highly-potent and cancer cell selective folate-taxoid conjugate. *Bioorg Med Chem* **2015**, *23*, 2187-2194.
- (15) Chen, J. Y.; Chen, S. Y.; Zhao, X. R.; Kuznetsova, L. V.; Wong, S. S.; Ojima, I. Functionalized Single-Walled Carbon Nanotubes as Rationally Designed Vehicles for Tumor-Targeted Drug Delivery. *J Am Chem Soc* **2008**, *130*, 16778-16785.
- (16) Chen, S. Y.; Zhao, X. R.; Chen, J. Y.; Chen, J.; Kuznetsova, L.; Wong, S. S.; Ojima, I. Mechanism-Based Tumor-Targeting Drug Delivery System. Validation of Efficient Vitamin Receptor-Mediated Endocytosis and Drug Release. *Bioconjugate Chem* **2010**, *21*, 979-987.
- (17) Vineberg, J. G.; Zuniga, E. S.; Kamath, A.; Chen, Y. J.; Seitz, J. D.; Ojima, I. Design, Synthesis, and Biological Evaluations of Tumor-Targeting Dual-Warhead Conjugates for a Taxoid-Camptothecin Combination Chemotherapy. *J Med Chem* **2014**, *57*, 5777-5791.
- (18) Vineberg, J. G.; Wang, T.; Zuniga, E. S.; Ojima, I. Design, Synthesis, and Biological Evaluation of Theranostic Vitamin-Linker-Taxoid Conjugates. *J Med Chem* **2015**, *58*, 2406-2416.
- (19) Chen, J.; Jaracz, S.; Zhao, X.; Chen, S.; Ojima, I. Antibody-cytotoxic agent conjugates for cancer therapy. *Expert Opin Drug Deliv* **2005**, *2*, 873-890.
- (20) Zheng, Z. B.; Zhu, G.; Tak, H.; Joseph, E.; Eiseman, J. L.; Creighton, D. J. N-(2-hydroxypropyl)methacrylamide copolymers of a glutathione (GSH)-activated

glyoxalase i inhibitor and DNA alkylating agent: synthesis, reaction kinetics with GSH, and in vitro antitumor activities. *Bioconjugate Chem* **2005**, *16*, 598-607.

(21) Wolf, W.; Albright, M. J.; Silver, M. S.; Weber, H.; Reichardt, U.; Sauer, R. Fluorine-19 NMR spectroscopic studies of the metabolism of 5-fluorouracil in the liver of patients undergoing chemotherapy. *Magn Reson Imaging* **1987**, *5*, 165-169.

(22) Ojima, I. Use of fluorine in the medicinal chemistry and chemical biology of bioactive compounds - A case study on fluorinated taxane anticancer agents. *Chembiochem* **2004**, *5*, 628-635.

(23) Seitz, J. D.; Vineberg, J. G.; Wei, L. F.; Khan, J. F.; Lichtenthal, B.; Lin, C. F.; Ojima, I. Design, synthesis and application of fluorine-labeled taxoids as F-19 NMR probes for the metabolic stability assessment of tumor-targeted drug delivery systems. *J Fluorine Chem* **2015**, *171*, 148-161.

(24) Shaabani, A.; Tavasoli-Rad, F.; Lee, D. G. Potassium permanganate oxidation of organic compounds. *Synth Commun* **2005**, *35*, 571-580.

(25) Widdison, W. C.; Wilhelm, S. D.; Cavanagh, E. E.; Whiteman, K. R.; Leece, B. A.; Kovtun, Y.; Goldmacher, V. S.; Xie, H.; Steeves, R. M.; Lutz, R. J.; Zhao, R.; Wang, L.; Blaettler, W. A.; Chari, R. V. J. Semisynthetic Maytansine Analogs for the Targeted Treatment of Cancer. *J Med Chem* **2006**, *49*, 4392-4408.

(26) Banerjee, P. S.; Zuniga, E. S.; Ojima, I.; Carrico, I. S. Targeted and armed oncolytic adenovirus via chemoselective modification. *Bioorg Med Chem Lett* **2011**, *21*, 4985-4988.

(27) Bordwell, F. G.; Fried, H. E. Heterocyclic aromatic anions with $4n + 2 \pi$ electrons. *J Org Chem* **1991**, *56*, 4218-4223.

References for Chapter 3:

(1) Peer, D.; Karp, J. M.; Hong, S.; FaroKHZad, O. C.; Margalit, R.; Langer, R. Nanocarriers as an emerging platform for cancer therapy. *Nat Nanotechnol* **2007**, *2*, 751-760.

(2) Duncan, R. Polymer conjugates as anticancer nanomedicines. *Nat Rev Cancer* **2006**, *6*, 688-701.

(3) Maeda, H. SMANCS and polymer-conjugated macromolecular drugs: advantages in cancer chemotherapy. *Adv Drug Deliver Rev* **2001**, *46*, 169-185.

- (4) Duncan, R.; Seymour, L. W.; Ohare, K. B.; Flanagan, P. A.; Wedge, S.; Hume, I. C.; Ulbrich, K.; Strohalm, J.; Subr, V.; Spreafico, F.; Grandi, M.; Ripamonti, M.; Farao, M.; Suarato, A. Preclinical Evaluation of Polymer-Bound Doxorubicin. *J Control Release* **1992**, *19*, 331-346.
- (5) Thomson, A. H.; Vasey, P. A.; Murray, L. S.; Cassidy, J.; Fraier, D.; Frigerio, E.; Twelves, C. Population pharmacokinetics in phase I drug development: a phase I study of PK1 in patients with solid tumours. *Brit J Cancer* **1999**, *81*, 99-107.
- (6) Vasey, P. A.; Kaye, S. B.; Morrison, R.; Twelves, C.; Wilson, P.; Duncan, R.; Thomson, A. H.; Murray, L. S.; Hilditch, T. E.; Murray, T.; Burtles, S.; Fraier, D.; Frigerio, E.; Cassidy, J.; Comm, C. R. C. P. I. I. Phase I clinical and pharmacokinetic study of PK1 [N-(2-hydroxypropyl)methacrylamide copolymer doxorubicin]: First member of a new class of chemotherapeutic agents - Drug-polymer conjugates. *Clin Cancer Res* **1999**, *5*, 83-94.
- (7) Duncan, R.; Kopecek, J.; Rejmanova, P.; Lloyd, J. B. Targeting of N-(2-Hydroxypropyl)Methacrylamide Co-Polymers to Liver by Incorporation of Galactose Residues. *Biochim Biophys Acta* **1983**, *755*, 518-521.
- (8) Julyan, P. J.; Seymour, L. W.; Ferry, D. R.; Daryani, S.; Boivin, C. M.; Doran, J.; David, M.; Anderson, D.; Christodoulou, C.; Young, A. M.; Hesselwood, S.; Kerr, D. J. Preliminary clinical study of the distribution of HPMA copolymers bearing doxorubicin and galactosamine. *J Control Release* **1999**, *57*, 281-290.
- (9) Li, C.; Yu, D. F.; Newman, R. A.; Cabral, F.; Stephens, L. C.; Hunter, N.; Milas, L.; Wallace, S. Complete regression of well-established tumors using a novel water-soluble poly(L-glutamic acid) paclitaxel conjugate. *Cancer Res* **1998**, *58*, 2404-2409.
- (10) Shaffer, S. A.; Baker Lee, C.; Kumar, A.; Singer, J. W. Proteolysis of xyotax by lysosomal cathepsin B; metabolic profiling in tumor cells using LC-MS. *Eur J Cancer* **2002**, *38*, S129-S129.
- (11) Mintzer, M. A.; Grinstaff, M. W. Biomedical applications of dendrimers: a tutorial. *Chem Soc Rev* **2011**, *40*, 173-190.
- (12) Bharali, D. J.; Khalil, M.; Gurbuz, M.; Simone, T. M.; Mousa, S. A. Nanoparticles and cancer therapy: A concise review with emphasis on dendrimers. *Int J Nanomed* **2009**, *4*, 1-7.
- (13) Tomalia, D. A.; Baker, H.; Dewald, J.; Hall, M.; Kallos, G.; Martin, S.; Roeck, J.; Ryder, J.; Smith, P. A New Class of Polymers - Starburst-Dendritic Macromolecules. *Polym J* **1985**, *17*, 117-132.

- (14) Hawker, C. J.; Frechet, J. M. J. Preparation of Polymers with Controlled Molecular Architecture - a New Convergent Approach to Dendritic Macromolecules. *J Am Chem Soc* **1990**, *112*, 7638-7647.
- (15) Gillies, E. R.; Frechet, J. M. J. Designing macromolecules for therapeutic applications: Polyester dendrimer-poly(ethylene oxide) "bow-tie" hybrids with tunable molecular weight and architecture. *J Am Chem Soc* **2002**, *124*, 14137-14146.
- (16) Ornelas, C.; Pennell, R.; Liebes, L. F.; Weck, M. Construction of a Well-Defined Multifunctional Dendrimer for Theranostics. *Org Lett* **2011**, *13*, 976-979.
- (17) Gaertner, H. F.; Cerini, F.; Kamath, A.; Rochat, A. F.; Siegrist, C. A.; Menin, L.; Hartley, O. Efficient orthogonal bioconjugation of dendrimers for synthesis of bioactive nanoparticles. *Bioconjugate Chem* **2011**, *22*, 1103-1114.
- (18) Bosman, A. W.; Janssen, H. M.; Meijer, E. W. About Dendrimers: Structure, Physical Properties, and Applications. *Chem Rev* **1999**, *99*, 1665-1688.
- (19) Tomalia, D. A.; Reyna, L. A.; Svenson, S. Dendrimers as multi-purpose nanodevices for oncology drug delivery and diagnostic imaging. *Biochem Soc Trans* **2007**, *35*, 61-67.
- (20) Astruc, D.; Boisselier, E.; Ornelas, C. Dendrimers Designed for Functions: From Physical, Photophysical, and Supramolecular Properties to Applications in Sensing, Catalysis, Molecular Electronics, Photonics, and Nanomedicine. *Chem Rev* **2010**, *110*, 1857-1959.
- (21) Majoros, I. J.; Thomas, T. P.; Mehta, C. B.; Baker, J. R., Jr. Poly(amidoamine) dendrimer-based multifunctional engineered nanodevice for cancer therapy. *J Med Chem* **2005**, *48*, 5892-5899.
- (22) Islam, M. T.; Majoros, I. J.; Baker, J. R., Jr. HPLC analysis of PAMAM dendrimer based multifunctional devices. *J Chromatogr B Analyt Technol Biomed Life Sci* **2005**, *822*, 21-26.
- (23) Thomas, T. P.; Majoros, I. J.; Kotlyar, A.; Kukowska-Latallo, J. F.; Bielinska, A.; Myc, A.; Baker, J. R., Jr. Targeting and inhibition of cell growth by an engineered dendritic nanodevice. *J Med Chem* **2005**, *48*, 3729-3735.
- (24) Kukowska-Latallo, J. F.; Candido, K. A.; Cao, Z.; Nigavekar, S. S.; Majoros, I. J.; Thomas, T. P.; Balogh, L. P.; Khan, M. K.; Baker, J. R., Jr. Nanoparticle targeting of anticancer drug improves therapeutic response in animal model of human epithelial cancer. *Cancer Res* **2005**, *65*, 5317-5324.

- (25) Majoros, I. J.; Myc, A.; Thomas, T.; Mehta, C. B.; Baker, J. R., Jr. PAMAM dendrimer-based multifunctional conjugate for cancer therapy: synthesis, characterization, and functionality. *Biomacromolecules* **2006**, *7*, 572-579.
- (26) Mullen, D. G.; Fang, M.; Desai, A.; Baker, J. R.; Orr, B. G.; Holl, M. M. B. A Quantitative Assessment of Nanoparticle-Ligand Distributions: Implications for Targeted Drug and Imaging Delivery in Dendrimer Conjugates. *ACS Nano* **2010**, *4*, 657-670.
- (27) Zong, H.; Thomas, T. P.; Lee, K. H.; Desai, A. M.; Li, M. H.; Kotlyar, A.; Zhang, Y.; Leroueil, P. R.; Gam, J. J.; Banaszak Holl, M. M.; Baker, J. R., Jr. Bifunctional PAMAM dendrimer conjugates of folic acid and methotrexate with defined ratio. *Biomacromolecules* **2012**, *13*, 982-991.
- (28) Thomas, T. P.; Huang, B. H.; Choi, S. K.; Silpe, J. E.; Kotlyar, A.; Desai, A. M.; Zong, H.; Gam, J.; Joice, M.; Baker, J. R. Polyvalent Dendrimer-Methotrexate as a Folate Receptor-Targeted Cancer Therapeutic. *Mol Pharm* **2012**, *9*, 2669-2676.
- (29) Matsumura, Y.; Maeda, H. A New Concept for Macromolecular Therapeutics in Cancer-Chemotherapy - Mechanism of Tumorotropic Accumulation of Proteins and the Antitumor Agent Smancs. *Cancer Res* **1986**, *46*, 6387-6392.
- (30) Folkman, J. What Is the Evidence That Tumors Are Angiogenesis Dependent. *J Natl Cancer I* **1990**, *82*, 4-6.
- (31) Skinner, S. A.; Tutton, P. J.; O'Brien, P. E. Microvascular architecture of experimental colon tumors in the rat. *Cancer Res* **1990**, *50*, 2411-2417.
- (32) Kratz, F.; Muller, I. A.; Ryppa, C.; Warnecke, A. Prodrug strategies in anticancer chemotherapy. *Chemmedchem* **2008**, *3*, 20-53.
- (33) Russell-Jones, G.; McTavish, K.; McEwan, J.; Rice, J.; Nowotnik, D. Vitamin-mediated targeting as a potential mechanism to increase drug uptake by tumours. *J Inorg Biochem* **2004**, *98*, 1625-1633.
- (34) Lu, Y. J.; Low, P. S. Folate-mediated delivery of macromolecular anticancer therapeutic agents. *Adv Drug Deliver Rev* **2002**, *54*, 675-693.
- (35) Leamon, C. P. Folate-targeted drug strategies for the treatment of cancer. *Curr Opin Invest Drugs* **2008**, *9*, 1277-1286.
- (36) Leamon, C. P.; Reddy, J. A.; Vetzal, M.; Dorton, R.; Westrick, E.; Parker, N.; Wang, Y.; Vlahov, I. Folate Targeting Enables Durable and Specific Antitumor Responses from a Therapeutically Null Tubulysin B Analogue. *Cancer Res* **2008**, *68*, 9839-9844.

- (37) Zempleni, J.; Wijeratne, S. S. K.; Hassan, Y. I. Biotin. *Biofactors* **2009**, *35*, 36-46.
- (38) Zempleni, J. Uptake, localization, and noncarboxylase roles of biotin. *Annu Rev Nutr* **2005**, *25*, 175-196.
- (39) Chen, J. Y.; Chen, S. Y.; Zhao, X. R.; Kuznetsova, L. V.; Wong, S. S.; Ojima, I. Functionalized Single-Walled Carbon Nanotubes as Rationally Designed Vehicles for Tumor-Targeted Drug Delivery. *J Am Chem Soc* **2008**, *130*, 16778-16785.
- (40) Chen, S. Y.; Zhao, X. R.; Chen, J. Y.; Chen, J.; Kuznetsova, L.; Wong, S. S.; Ojima, I. Mechanism-Based Tumor-Targeting Drug Delivery System. Validation of Efficient Vitamin Receptor-Mediated Endocytosis and Drug Release. *Bioconjugate Chem* **2010**, *21*, 979-987.
- (41) Vineberg, J. G.; Zuniga, E. S.; Kamath, A.; Chen, Y. J.; Seitz, J. D.; Ojima, I. Design, Synthesis, and Biological Evaluations of Tumor-Targeting Dual-Warhead Conjugates for a Taxoid-Camptothecin Combination Chemotherapy. *J Med Chem* **2014**, *57*, 5777-5791.
- (42) Vineberg, J. G.; Wang, T.; Zuniga, E. S.; Ojima, I. Design, Synthesis, and Biological Evaluation of Theranostic Vitamin-Linker-Taxoid Conjugates. *J Med Chem* **2015**, *58*, 2406-2416.
- (43) Kitov, P. I.; Bundle, D. R. On the nature of the multivalency effect: A thermodynamic model. *J Am Chem Soc* **2003**, *125*, 16271-16284.
- (44) Rudnick, S. I.; Adams, G. P. Affinity and Avidity in Antibody-Based Tumor Targeting. *Cancer Biother Radio* **2009**, *24*, 155-161.
- (45) Vorup-Jensen, T. On the roles of polyvalent binding in immune recognition: Perspectives in the nanoscience of immunology and the immune response to nanomedicines. *Adv Drug Deliver Rev* **2012**, *64*, 1759-1781.
- (46) Kiessling, L. L.; Gestwicki, J. E.; Strong, L. E. Synthetic multivalent ligands in the exploration of cell-surface interactions. *Curr Opin Chem Biol* **2000**, *4*, 696-703.
- (47) Kiessling, L. L.; Strong, L. E.; Gestwicki, J. E. Principles for multivalent ligand design. *Annu Rep Med Chem* **2000**, *35*, 321-330.
- (48) Hong, S.; Leroueil, P. R.; Majoros, I. J.; Orr, B. G.; Baker, J. R.; Holl, M. M. B. The binding avidity of a nanoparticle-based multivalent targeted drug delivery platform. *Chem Biol* **2007**, *14*, 107-115.

- (49) Silpe, J. E.; Sumit, M.; Thomas, T. P.; Huang, B. H.; Kotlyar, A.; van Dongen, M. A.; Holl, M. M. B.; Orr, B. G.; Choi, S. K. Avidity Modulation of Folate-Targeted Multivalent Dendrimers for Evaluating Biophysical Models of Cancer Targeting Nanoparticles. *ACS Chem Biol* **2013**, *8*, 2063-2071.
- (50) van Dongen, M. A.; Silpe, J. E.; Dougherty, C. A.; Kanduluru, A. K.; Choi, S. K.; Orr, B. G.; Low, P. S.; Holl, M. M. B. Avidity Mechanism of Dendrimer-Folic Acid Conjugates. *Mol Pharm* **2014**, *11*, 1696-1706.
- (51) Yellepeddi, V. K.; Kumar, A.; Palakurthi, S. Biotinylated poly(amido)amine (PAMAM) dendrimers as carriers for drug delivery to ovarian cancer cells in vitro. *Anticancer Res* **2009**, *29*, 2933-2943.
- (52) Mullen, D. G.; Holl, M. M. B. Heterogeneous Ligand-Nanoparticle Distributions: A Major Obstacle to Scientific Understanding and Commercial Translation. *Acc Chem Res* **2011**, *44*, 1135-1145.
- (53) Kelkar, S. S.; Reineke, T. M. Theranostics: Combining Imaging and Therapy. *Bioconjugate Chem* **2011**, *22*, 1879-1903.
- (54) Zhu, Z.; Wang, X.; Li, T.; Aime, S.; Sadler, P. J.; Guo, Z. Platinum(II)-Gadolinium(III) Complexes as Potential Single-Molecular Theranostic Agents for Cancer Treatment. *Angew Chem Int Ed.* **2014**, *53*, 13225-13228.
- (55) Wang, T.: Design, synthesis, and biological evaluation of novel taxoid-based small-molecule theranostic PET/SPECT imaging agents and nano-scale asymmetric bow-tie dendrimer drug conjugates towards tumor-targeted chemotherapy (Doctoral Dissertation). Stony Brook University. 2015.
- (56) Seitz, O.; Kunz, H. HYCRON, an Allylic Anchor for High-Efficiency Solid Phase Synthesis of Protected Peptides and Glycopeptides. *J Org Chem* **1997**, *62*, 813-826.
- (57) McReynolds, K. D.; Hadd, M. J.; Gervay-Hague, J. Synthesis of Biotinylated Glycoconjugates and Their Use in a Novel ELISA for Direct Comparison of HIV-1 Gp120 Recognition of GalCer and Related Carbohydrate Analogues. *Bioconjugate Chem* **1999**, *10*, 1021-1031.
- (58) Wong, L. S.; Janusz, S. J.; Sun, S.; Leggett, G. J.; Micklefield, J. Nanoscale Biomolecular Structures on Self-Assembled Monolayers Generated from Modular Pegylated Disulfides. *Chem Eur J* **2010**, *16*, 12234-12243.

(59) Chan, E. W. S.; Chattopadhyaya, S.; Panicker, R. C.; Huang, X.; Yao, S. Q. Developing Photoactive Affinity Probes for Proteomic Profiling: Hydroxamate-based Probes for Metalloproteases. *J Am Chem Soc* **2004**, *126*, 14435-14446.

(60) Schwabacher, A. W.; Lane, J. W.; Schiesher, M. W.; Leigh, K. M.; Johnson, C. W. Desymmetrization Reactions: Efficient Preparation of Unsymmetrically Substituted Linker Molecules. *J Org Chem* **1998**, *63*, 1727-1729.

(61) Han, J.; Sun, L.; Chu, Y.; Li, Z.; Huang, D.; Zhu, X.; Qian, H.; Huang, W. Design, Synthesis, and Biological Activity of Novel Dicoumarol Glucagon-like Peptide 1 Conjugates. *J Med Chem* **2013**, *56*, 9955-9968.

References for Chapter 4:

(1) World Health Organization: Tuberculosis Fact sheets. <http://www.who.int/mediacentre/factsheets/fs104/en/>. 2016.

(2) Huang, Q.; Tonge, P. J.; Slayden, R. A.; Kirikae, J.; Ojima, I. FtsZ: A novel target for tuberculosis drug discovery. *Curr Top Med Chem* **2007**, *7*, 527-543.

(3) Kumar, K.; Awasthi, D.; Berger, W. T.; Tonge, P. J.; Slayden, R. A.; Ojima, I. Discovery of anti-TB agents that target the cell-division protein FtsZ. *Future Med Chem* **2010**, *2*, 1305-1323.

(4) Li, Y.; Hsin, J.; Zhao, L. Y.; Cheng, Y. W.; Shang, W. N.; Huang, K. C.; Wang, H. W.; Ye, S. FtsZ Protofilaments Use a Hinge-Opening Mechanism for Constrictive Force Generation. *Science* **2013**, *341*, 392-395.

(5) Lowe, J.; Amos, L. A. Crystal structure of the bacterial cell-division protein FtsZ. *Nature* **1998**, *391*, 203-206.

(6) Tan, C. M.; Therien, A. G.; Lu, J.; Lee, S. H.; Caron, A.; Gill, C. J.; Lebeau-Jacob, C.; Benton-Perdomo, L.; Monteiro, J. M.; Pereira, P. M.; Elsen, N. L.; Wu, J.; Deschamps, K.; Petcu, M.; Wong, S.; Daigneault, E.; Kramer, S.; Liang, L.; Maxwell, E.; Claveau, D.; Vaillancourt, J.; Skorey, K.; Tam, J.; Wang, H.; Meredith, T. C.; Sillaots, S.; Wang-Jarantow, L.; Ramtohul, Y.; Langlois, E.; Landry, F.; Reid, J. C.; Parthasarathy, G.; Sharma, S.; Baryshnikova, A.; Lumb, K. J.; Pinho, M. G.; Soisson, S. M.; Roemer, T. Restoring methicillin-resistant *Staphylococcus aureus* susceptibility to beta-lactam antibiotics. *Sci Transl Med* **2012**, *4*, 126-135.

(7) Oliva, M. A.; Trambaiolo, D.; Lowe, J. Structural insights into the conformational variability of FtsZ. *J Mol Biol* **2007**, *373*, 1229-1242.

- (8) Oliva, M. A.; Cordell, S. C.; Lowe, J. Structural insights into FtsZ protofilament formation. *Nat Struct Mol Biol* **2004**, *11*, 1243-1250.
- (9) Leung, A. K. W.; White, E. L.; Ross, L. J.; Reynolds, R. C.; DeVito, J. A.; Borhani, D. W. Structure of Mycobacterium tuberculosis FtsZ reveals unexpected, G protein-like conformational switches. *J Mol Biol* **2004**, *342*, 953-970.
- (10) Lu, C. L.; Reedy, M.; Erickson, H. P. Straight and curved conformations of FtsZ are regulated by GTP hydrolysis. *J Bacteriol* **2000**, *182*, 164-170.
- (11) Hsin, J.; Gopinathan, A.; Huang, K. C. Nucleotide-dependent conformations of FtsZ dimers and force generation observed through molecular dynamics simulations. *P Natl Acad Sci USA* **2012**, *109*, 9432-9437.
- (12) Kumar, K.; Awasthi, D.; Lee, S. Y.; Zanardi, I.; Ruzsicska, B.; Knudson, S.; Tonge, P. J.; Slayden, R. A.; Ojima, I. Novel Trisubstituted Benzimidazoles, Targeting Mtb FtsZ, as a New Class of Antitubercular Agents. *J Med Chem* **2011**, *54*, 374-381.
- (13) Awasthi, D.; Kumar, K.; Knudson, S. E.; Slayden, R. A.; Ojima, I. SAR Studies on Trisubstituted Benzimidazoles as Inhibitors of Mtb FtsZ for the Development of Novel Antitubercular Agents. *J Med Chem* **2013**, *56*, 9756-9770.
- (14) Ojima, I.; Kumar, K.; Awasthi, D.; Vineberg, J. G. Drug discovery targeting cell division proteins, microtubules and FtsZ. *Bioorg Med Chem* **2014**, *22*, 5060-5077.
- (15) Park, B.; Awasthi, D.; Chowdhury, S. R.; Melief, E. H.; Kumar, K.; Knudson, S. E.; Slayden, R. A.; Ojima, I. Design, synthesis and evaluation of novel 2,5,6-trisubstituted benzimidazoles targeting FtsZ as antitubercular agents. *Bioorg Med Chem* **2014**, *22*, 2602-2612.
- (16) Morris, G. M.; Huey, R.; Lindstrom, W.; Sanner, M. F.; Belew, R. K.; Goodsell, D. S.; Olson, A. J. AutoDock4 and AutoDockTools4: Automated docking with selective receptor flexibility. *J Comput Chem* **2009**, *30*, 2785-2791.
- (17) Sali, A.; Blundell, T. L. Comparative protein modelling by satisfaction of spatial restraints. *J Mol Biol* **1993**, *234*, 779-815.
- (18) Chemical Computing Group Inc.: Molecular Operating Environment (MOE). Version 2015.10. 2015.

References for Chapter 5:

- (1) Zimmerman, A. W.; Veerkamp, J. H. New insights into the structure and function of fatty acid-binding proteins. *Cell Mol Life Sci* **2002**, *59*, 1096-1116.
- (2) Furuhashi, M.; Hotamisligil, G. S. Fatty acid-binding proteins: role in metabolic diseases and potential as drug targets. *Nat Rev Drug Discov* **2008**, *7*, 489-503.
- (3) Chmurzynska, A. The multigene family of fatty acid-binding proteins (FABPs): Function, structure and polymorphism. *J Appl Genetics* **2006**, *47*, 39-48.
- (4) Ockner, R. K.; Ho, W. K. L.; Poppenha.Rb; Manning, J. A. Binding Protein for Fatty-Acids in Cytosol of Intestinal-Mucosa, Liver, Myocardium, and Other Tissues. *Science* **1972**, *177*, 56-58.
- (5) Smathers, R. L.; Petersen, D. R. The human fatty acid-binding protein family: evolutionary divergences and functions. *Human genomics* **2011**, *5*, 170-191.
- (6) Storch, J.; Thumser, A. E. Tissue-specific Functions in the Fatty Acid-binding Protein Family. *J Biol Chem.* **2010**, *285*, 32679-32683.
- (7) Balendiran, G. K.; Schnutgen, F.; Scapin, G.; Borchers, T.; Xhong, N.; Lim, K.; Godbout, R.; Spener, F.; Sacchettini, J. C. Crystal structure and thermodynamic analysis of human brain fatty acid-binding protein. *J Biol Chem* **2000**, *275*, 27045-27054.
- (8) Pettersen, E. F.; Goddard, T. D.; Huang, C. C.; Couch, G. S.; Greenblatt, D. M.; Meng, E. C.; Ferrin, T. E. UCSF chimera - A visualization system for exploratory research and analysis. *J Comput Chem* **2004**, *25*, 1605-1612.
- (9) Lehmann, F.; Haile, S.; Axen, E.; Medina, C.; Uppenberg, J.; Svensson, S.; Lundback, T.; Rondahl, L.; Barf, T. Discovery of inhibitors of human adipocyte fatty acid-binding protein, a potential type 2 diabetes target. *Bioorg Med Chem Lett* **2004**, *14*, 4445-4448.
- (10) Ringom, R.; Axen, E.; Uppenberg, J.; Lundback, T.; Rondahl, L.; Barf, T. Substituted benzylamino-6-(trifluoromethyl)pyrimidin-4(1H)-ones: a novel class of selective human A-FABP inhibitors. *Bioorg Med Chem Lett* **2004**, *14*, 4449-4452.
- (11) McDonnell, P. A.; Constantine, K. L.; Goldfarb, V.; Johnson, S. R.; Sulsky, R.; Magnin, D. R.; Robl, J. A.; Caulfield, T. J.; Parker, R. A.; Taylor, D. S.; Adam, L. P.; Metzler, W. J.; Mueller, L.; Farmer, B. T. NMR structure of a potent small molecule inhibitor bound to human keratinocyte fatty acid-binding protein. *J Med Chem* **2006**, *49*, 5013-5017.
- (12) Sulsky, R.; Magnin, D. R.; Huanga, Y.; Simpkins, L.; Taunk, P.; Patel, M.; Zhu, Y.; Stouch, T. R.; Bassolino-Klimas, D.; Parker, R.; Harrity, T.; Stoffel, R.; Taylor, D. S.; Lavoie, T. B.; Kish, K.; Jacobson, B. L.; Sheriff, S.; Adam, L. P.; Ewing,

W. R.; Robl, J. A. Potent and selective biphenyl azole inhibitors of adipocyte fatty acid binding pirotein (aFABP). *Bioorg Med Chem Lett* **2007**, *17*, 3511-3515.

(13) Barf, T.; Lehmann, F.; Hammer, K.; Haile, S.; Axen, E.; Medina, C.; Uppenberg, J.; Svensson, S.; Rondahl, L.; Lundback, T. N-Benzyl-indolo carboxylic acids: Design and synthesis of potent and selective adipocyte fatty-acid binding protein (A-FABP) inhibitors. *Bioorg Med Chem Lett* **2009**, *19*, 1745-1748.

(14) Hertzfel, A. V.; Hellberg, K.; Reynolds, J. M.; Kruse, A. C.; Juhlmann, B. E.; Smith, A. J.; Sanders, M. A.; Ohlendorf, D. H.; Suttles, J.; Bernlohr, D. A. Identification and Characterization of a Small Molecule Inhibitor of Fatty Acid Binding Proteins. *J Med Chem* **2009**, *52*, 6024-6031.

(15) Cai, H. Y.; Yan, G. R.; Zhang, X. D.; Gorbenko, O.; Wang, H. Y.; Zhu, W. L. Discovery of highly selective inhibitors of human fatty acid binding protein 4 (FABP4) by virtual screening. *Bioorg Med Chem Lett* **2010**, *20*, 3675-3679.

(16) Kaczocha, M.; Glaser, S. T.; Deutsch, D. G. Identification of intracellular carriers for the endocannabinoid anandamide. *Proc Natl Acad Sci USA* **2009**, *106*, 6375-6380.

(17) Koutek, B.; Prestwich, G. D.; Howlett, A. C.; Chin, S. A.; Salehani, D.; Akhavan, N.; Deutsch, D. G. Inhibitors of arachidonoyl ethanolamide hydrolysis. *The J Biol Chem* **1994**, *269*, 22937-22940.

(18) Di Marzo, V. Targeting the endocannabinoid system: to enhance or reduce? *Nat Rev Drug Discov* **2008**, *7*, 438-455.

(19) Berger, W. T.; Ralph, B. P.; Kaczocha, M.; Sun, J.; Balius, T. E.; Rizzo, R. C.; Haj-Dahmane, S.; Ojima, I.; Deutsch, D. G. Targeting Fatty Acid Binding Protein (FABP) Anandamide Transporters - A Novel Strategy for Development of Anti-Inflammatory and Anti-Nociceptive Drugs. *Plos One* **2012**, *7*, e50968.

(20) DOCK6.5 San Francisco, CA: University of California at San Francisco., 2011.

(21) Balius, T. E.; Mukherjee, S.; Rizzo, R. C. Implementation and evaluation of a docking-rescoring method using molecular footprint comparisons. *J Comput Chem* **2011**, *32*, 2273-2289.

(22) Kaczocha, M.; Rebecchi, M. J.; Ralph, B. P.; Teng, Y. H. G.; Berger, W. T.; Galbavy, W.; Elmes, M. W.; Glaser, S. T.; Wang, L. Q.; Rizzo, R. C.; Deutsch, D. G.; Ojima, I. Inhibition of Fatty Acid Binding Proteins Elevates Brain Anandamide Levels and Produces Analgesia. *Plos One* **2014**, *9*.

(23) Sanson, B.; Wang, T.; Sun, J.; Wang, L. Q.; Kaczocha, M.; Ojima, I.; Deutsch, D.; Li, H. L. Crystallographic study of FABP5 as an intracellular endocannabinoid transporter. *Acta Crystallogr D* **2014**, *70*, 290-298.

(24) Chemical Computing Group Inc.: Molecular Operating Environment (MOE). Version 2015.10. 2015.

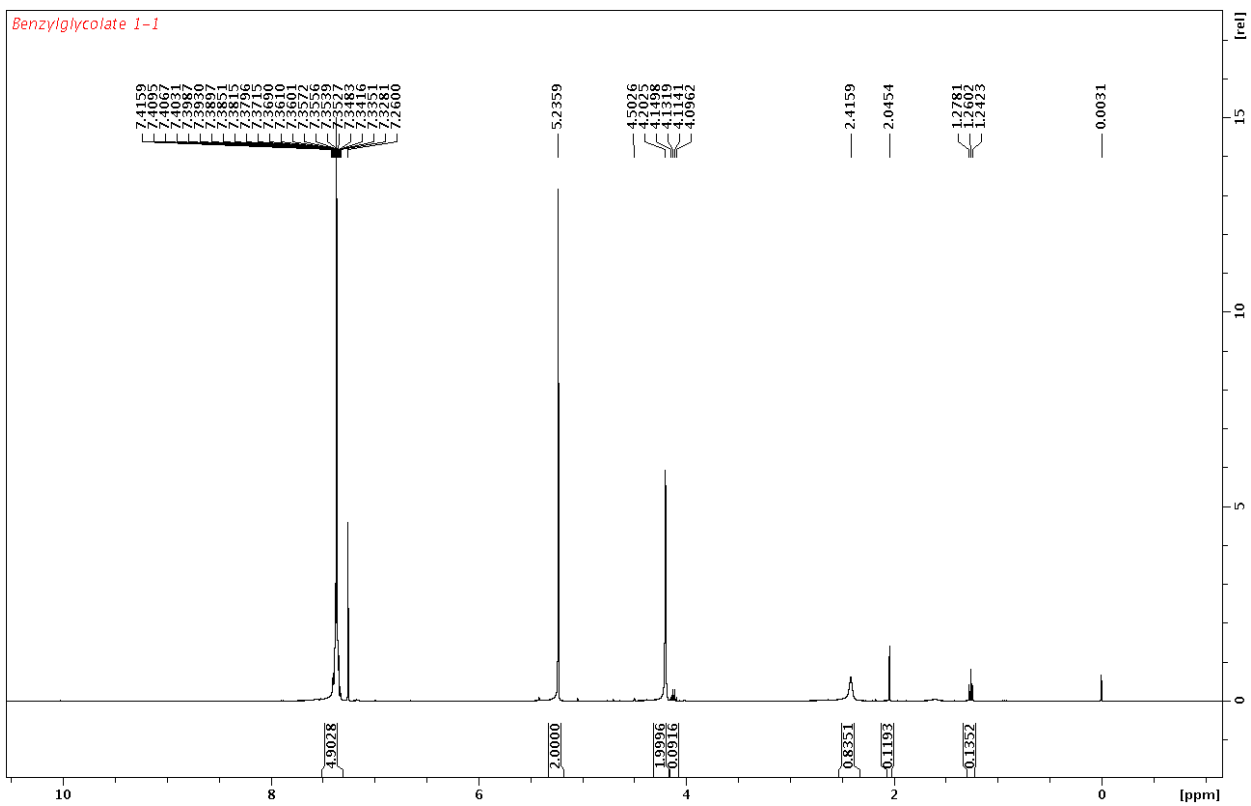
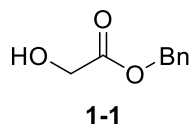
Appendix

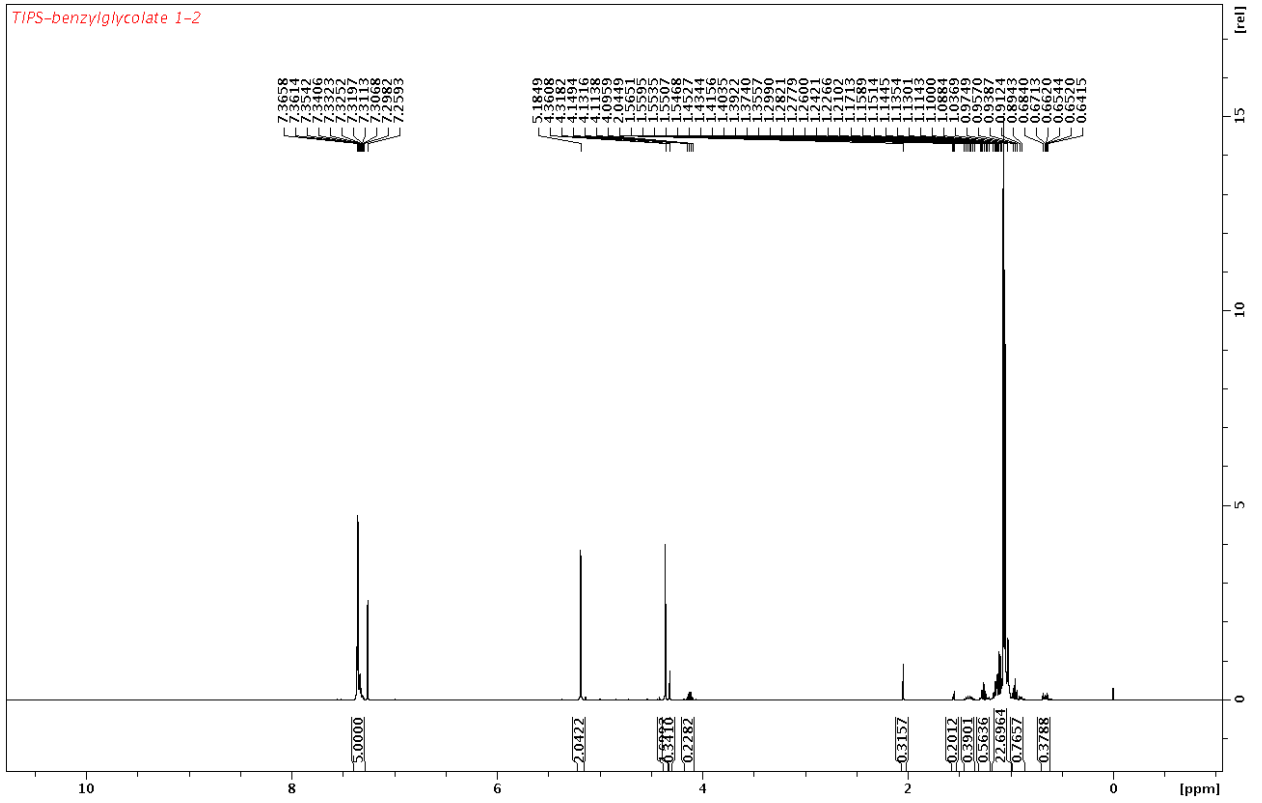
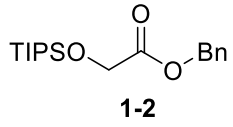
Appendix Chapter 1 NMR Spectra.....A305-A349

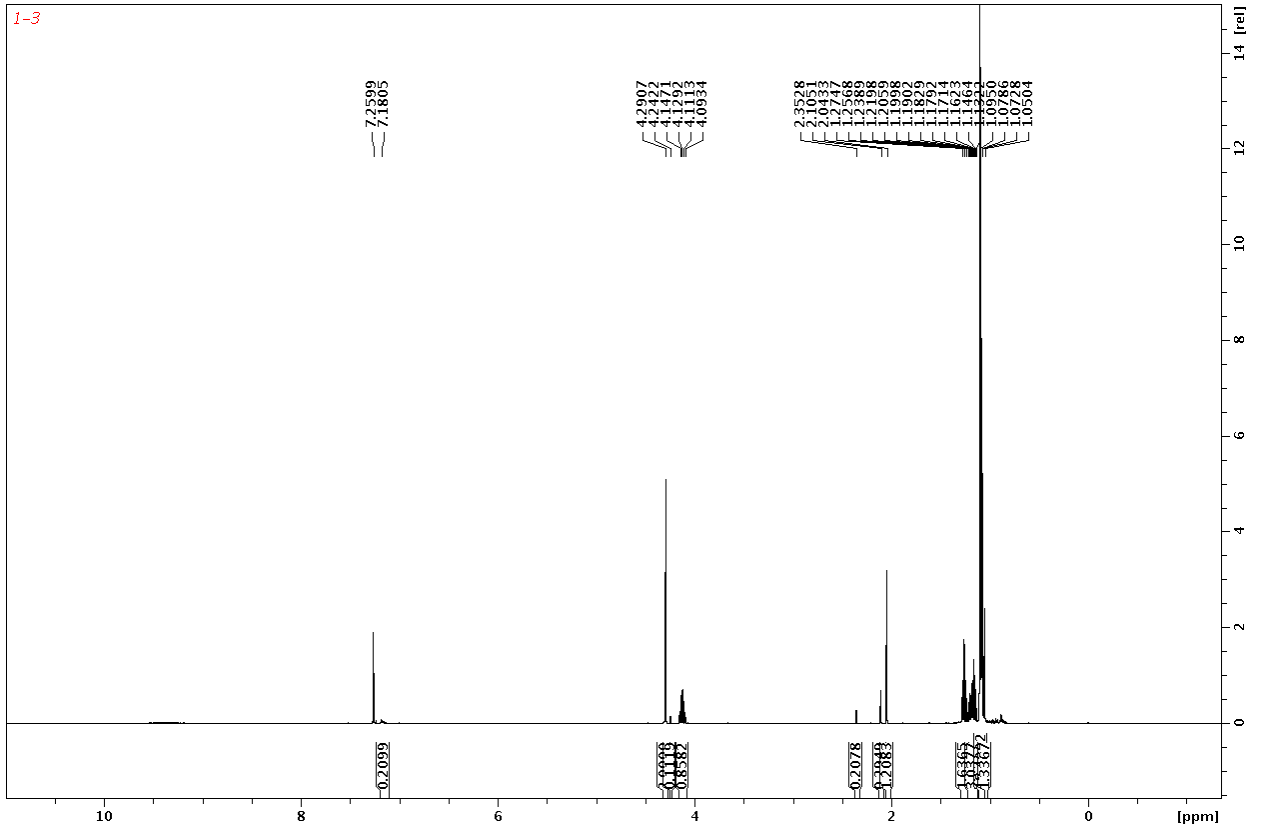
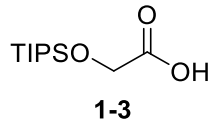
Appendix Chapter 2 NMR Spectra.....A350-A356

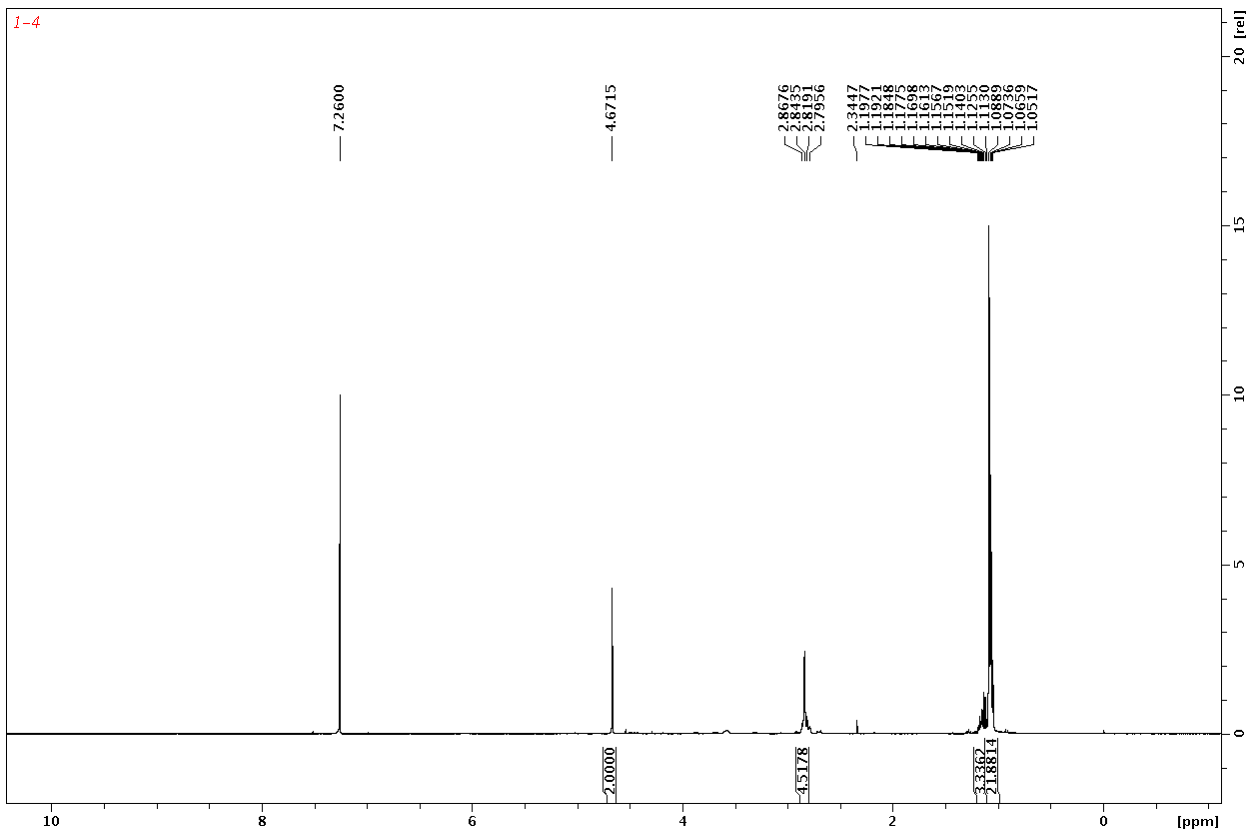
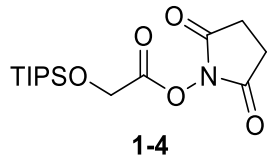
Appendix Chapter 3 NMR Spectra.....A357-A413

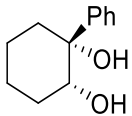
Appendix Chapter 1 NMR Spectra:



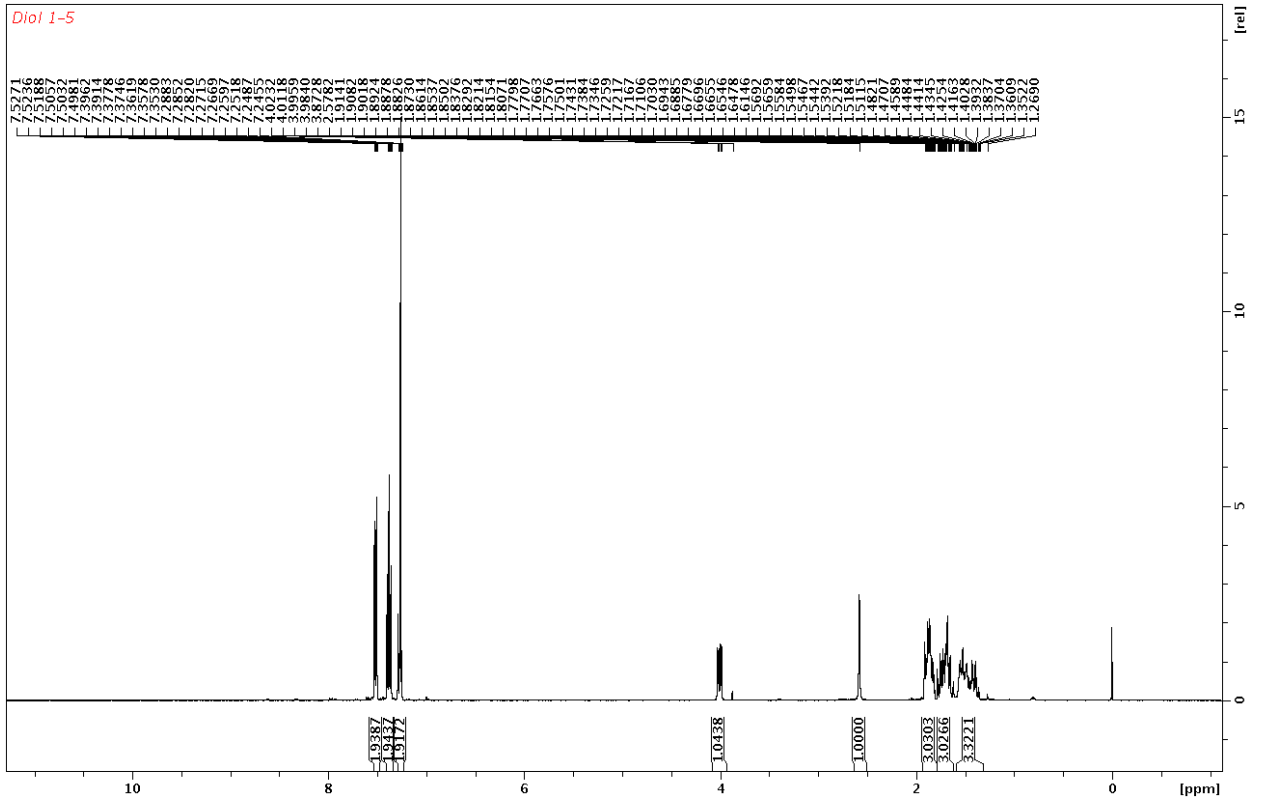


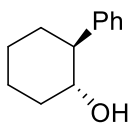




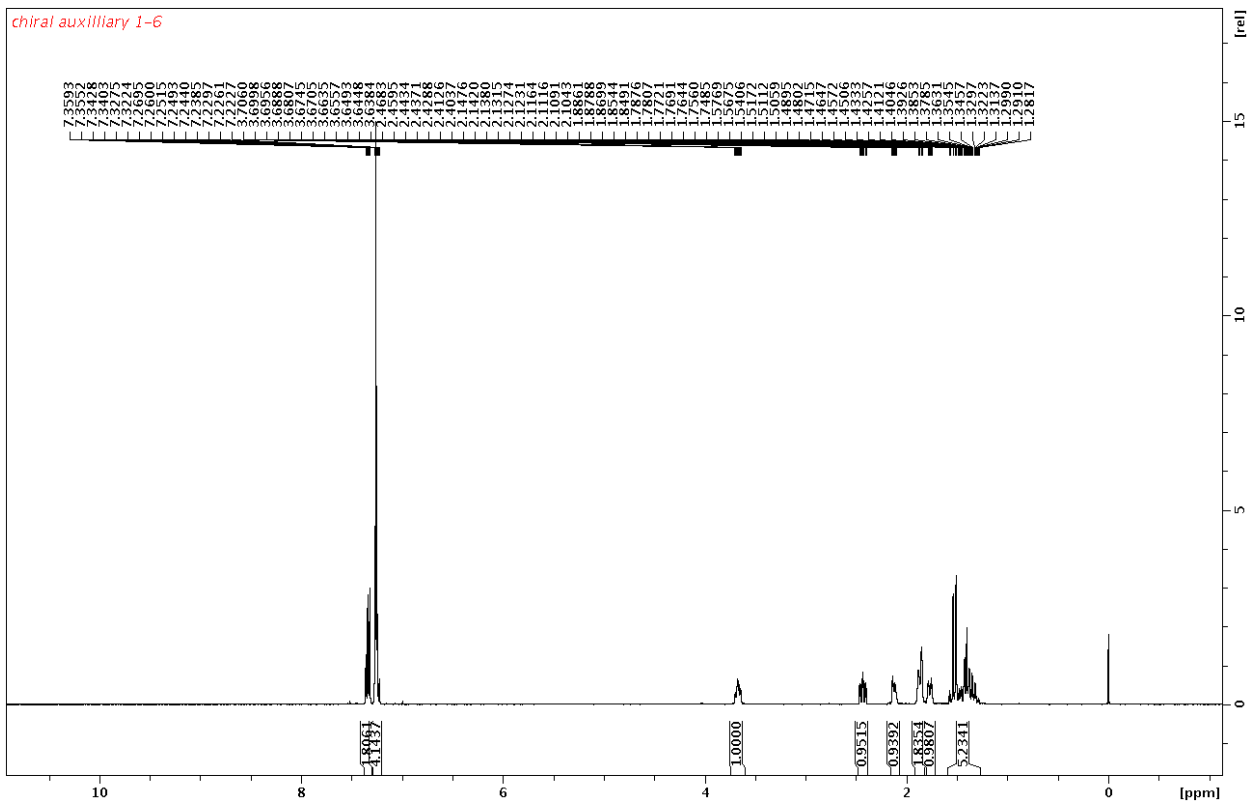


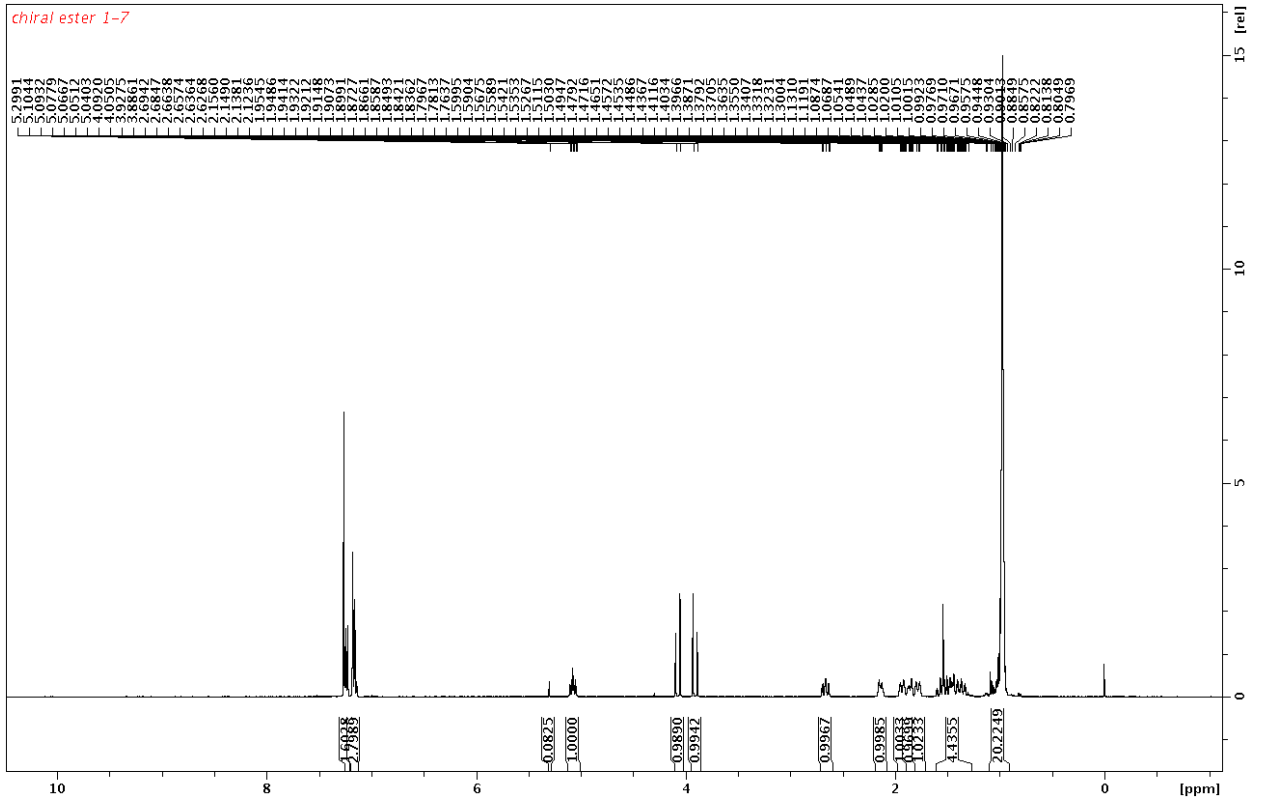
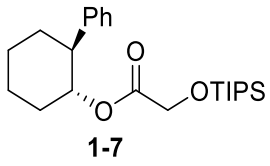
1-5

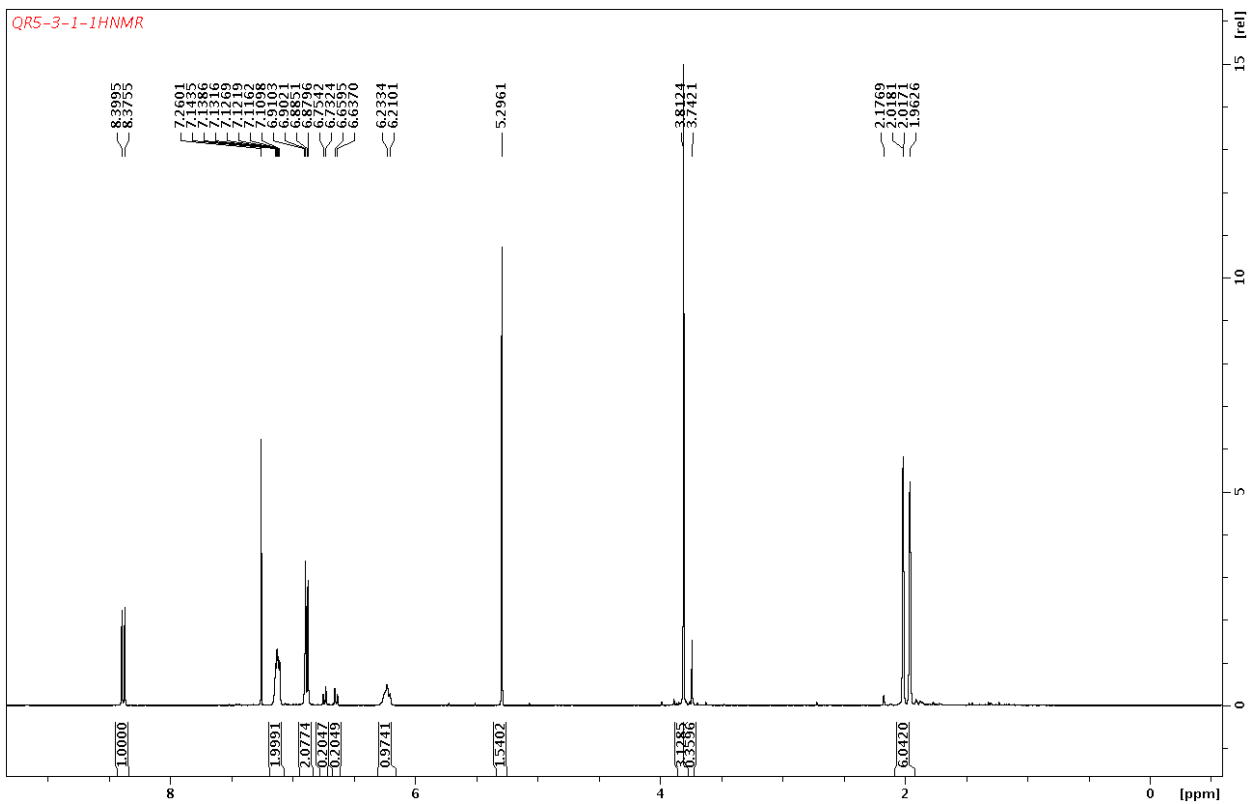
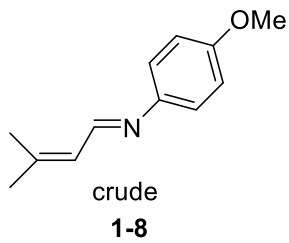


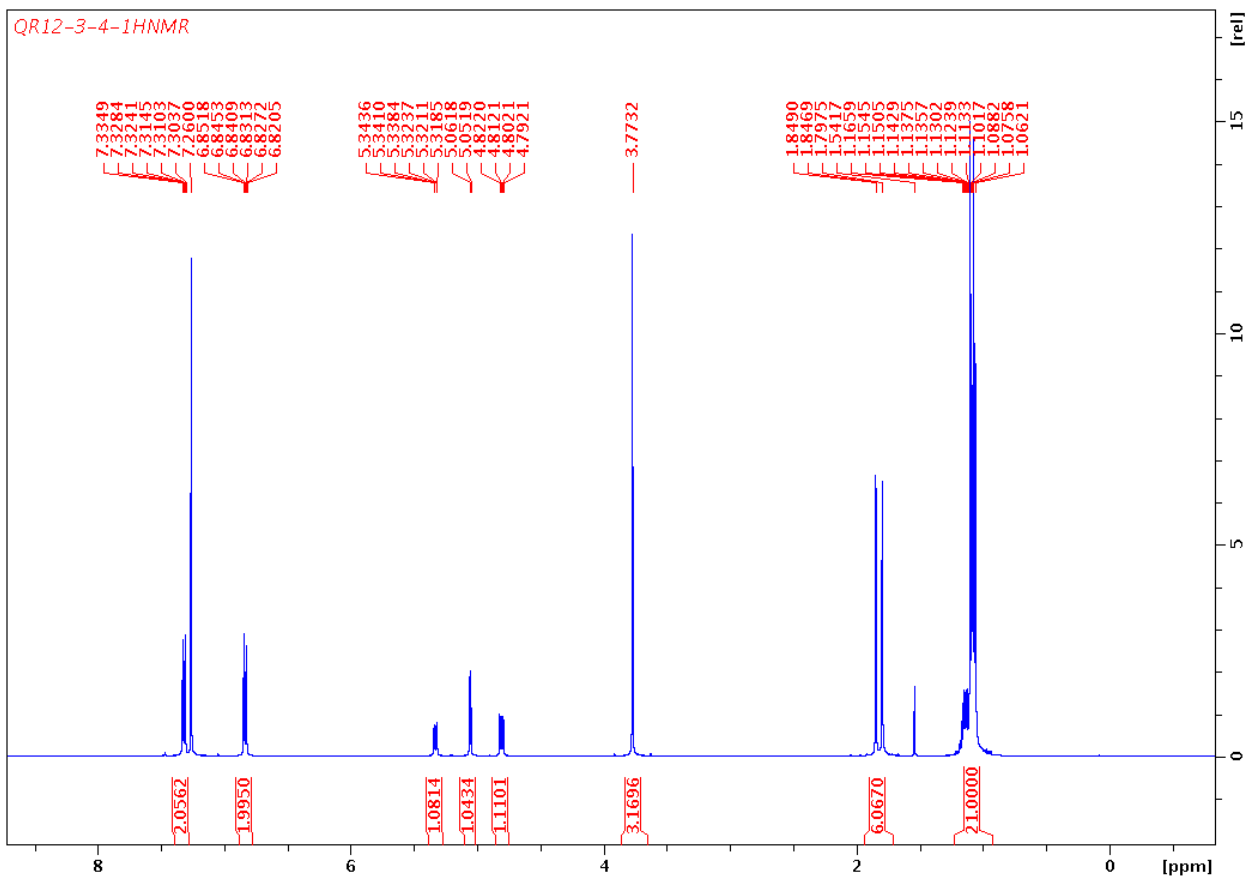
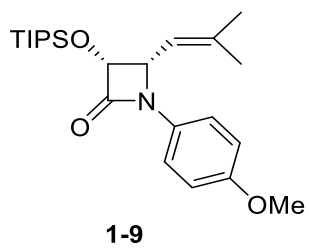


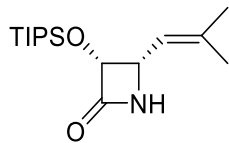
1-6



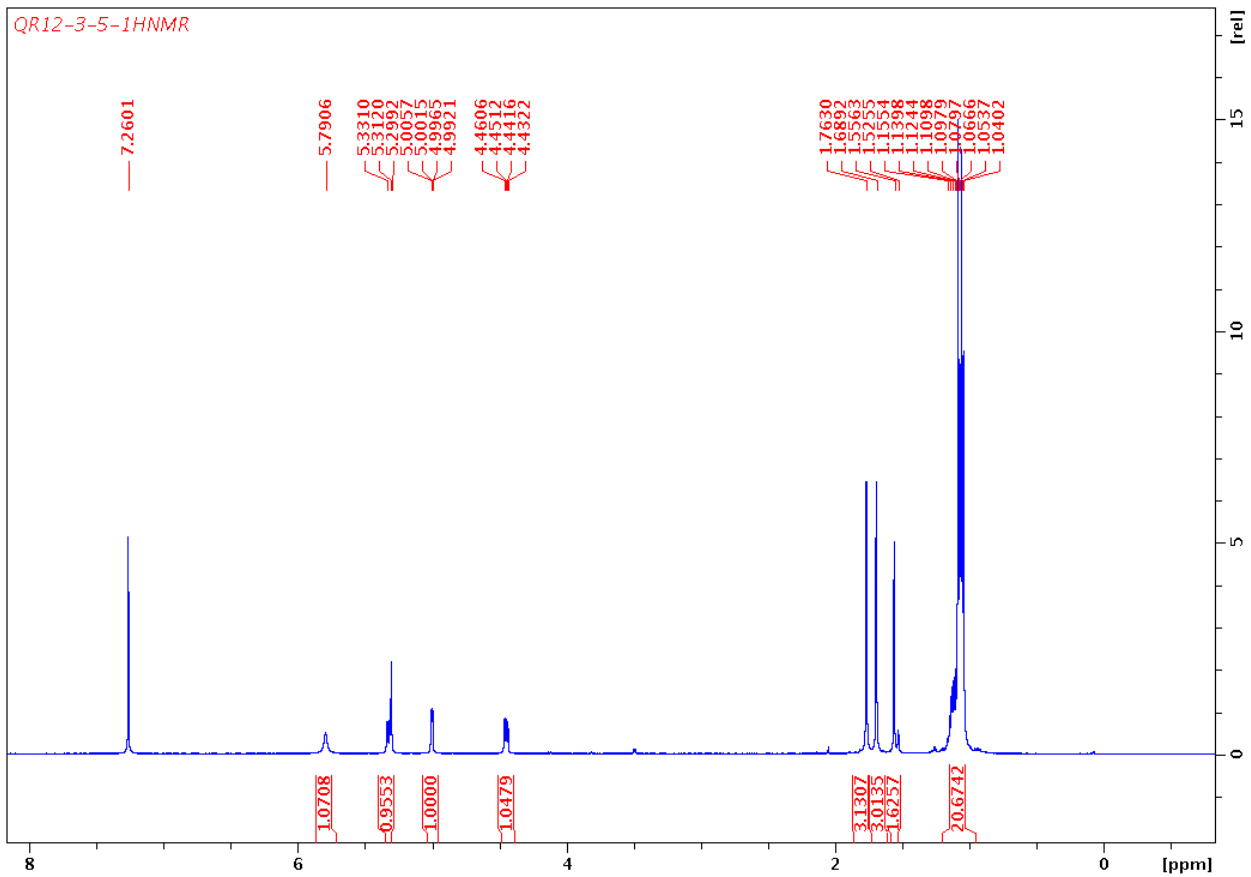


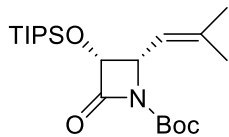




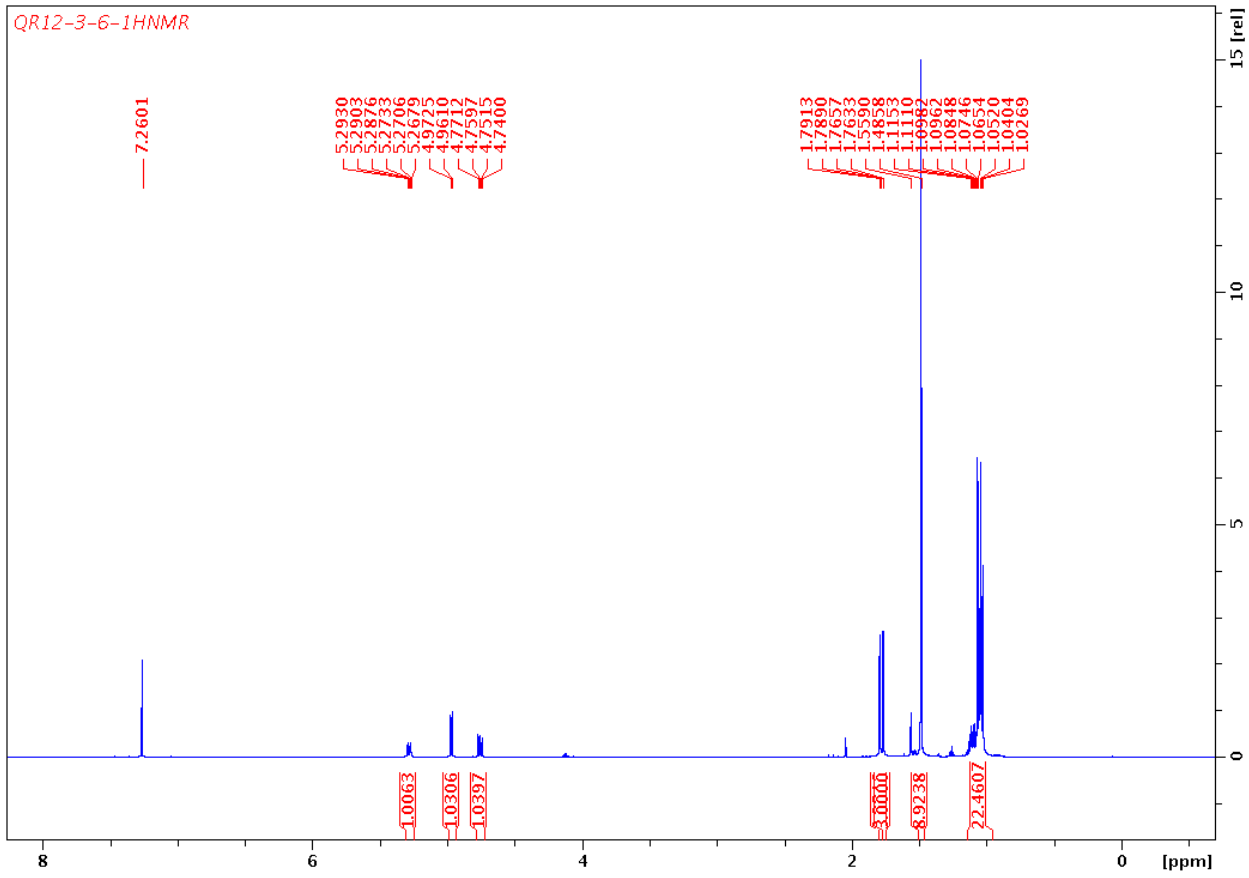


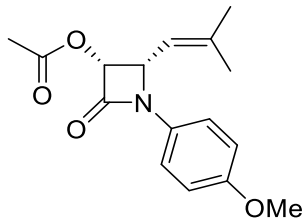
1-10



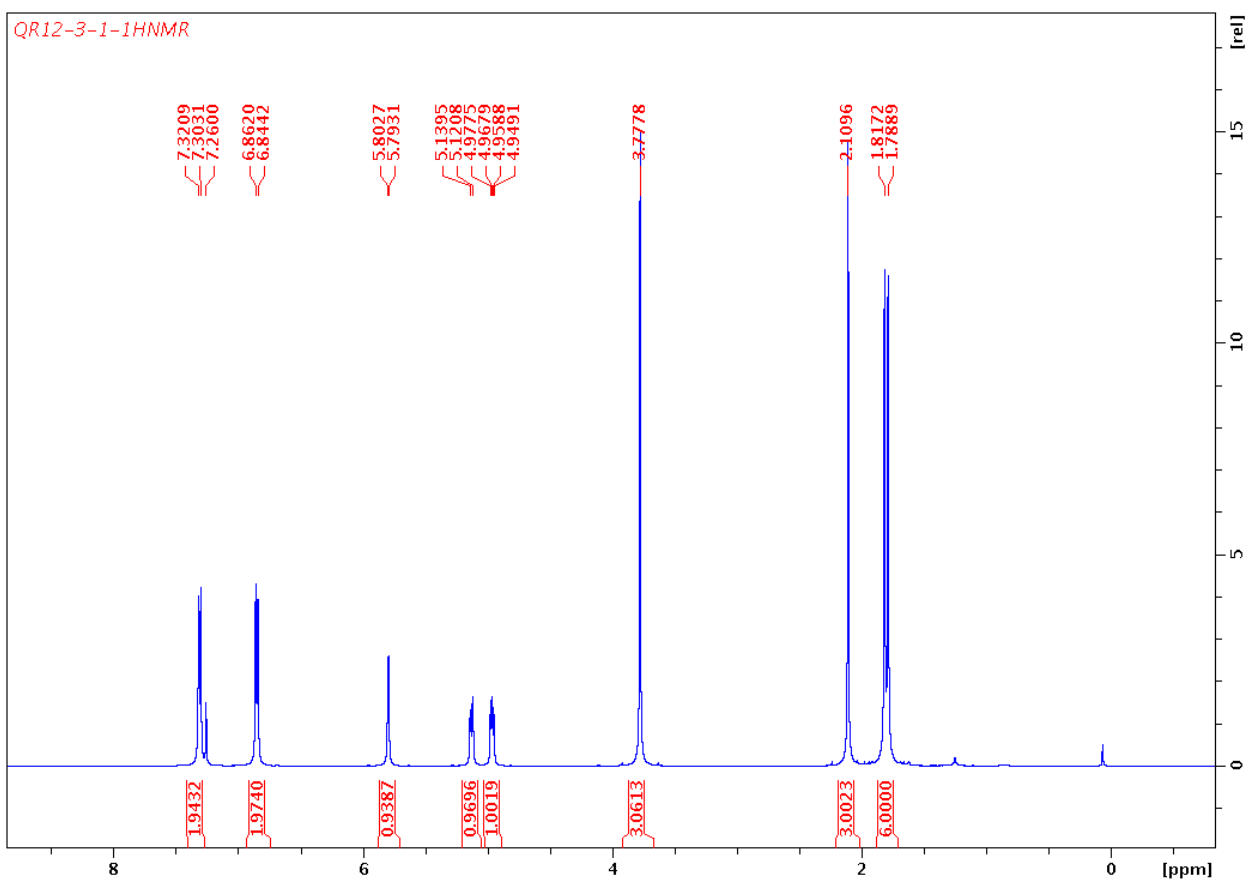


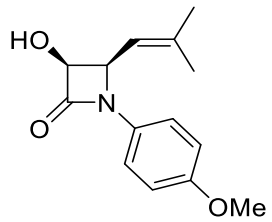
1-11



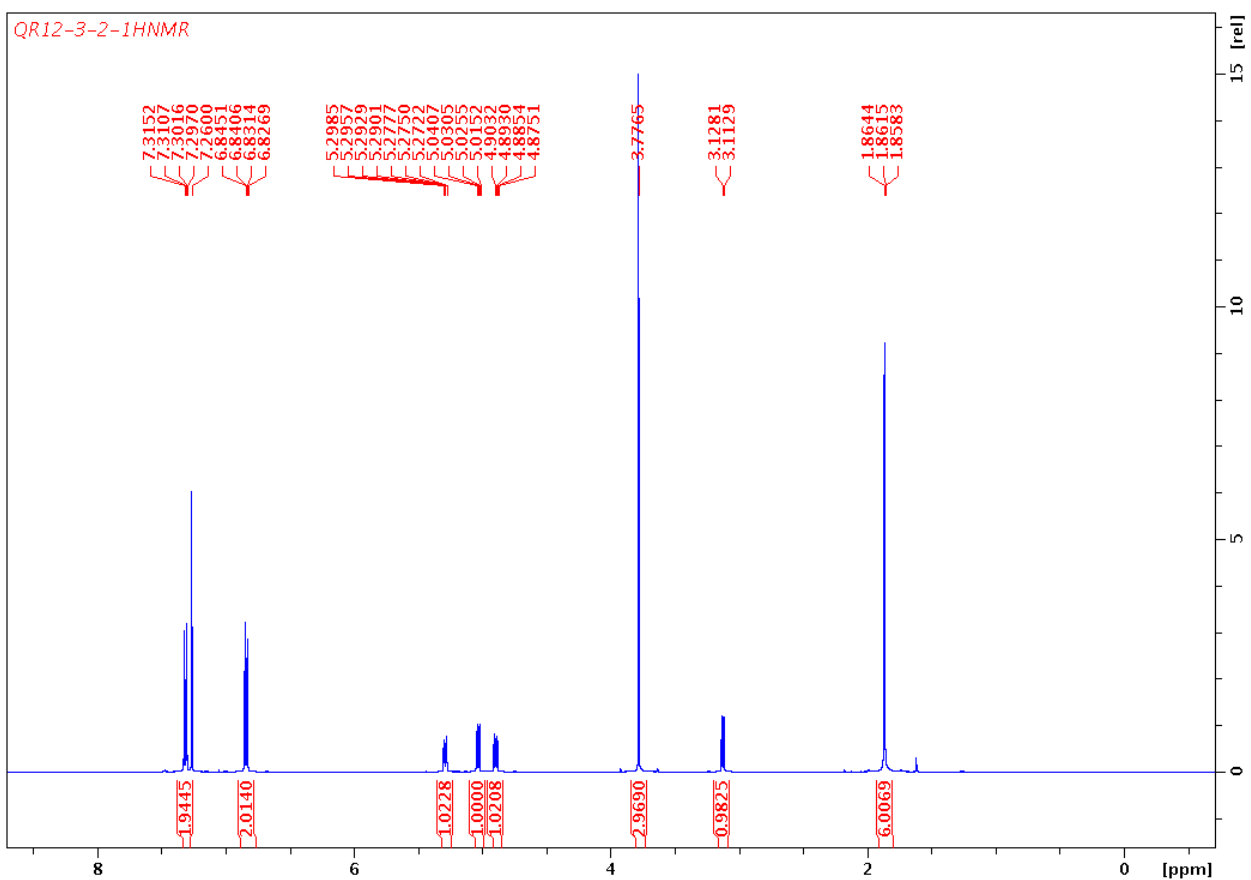


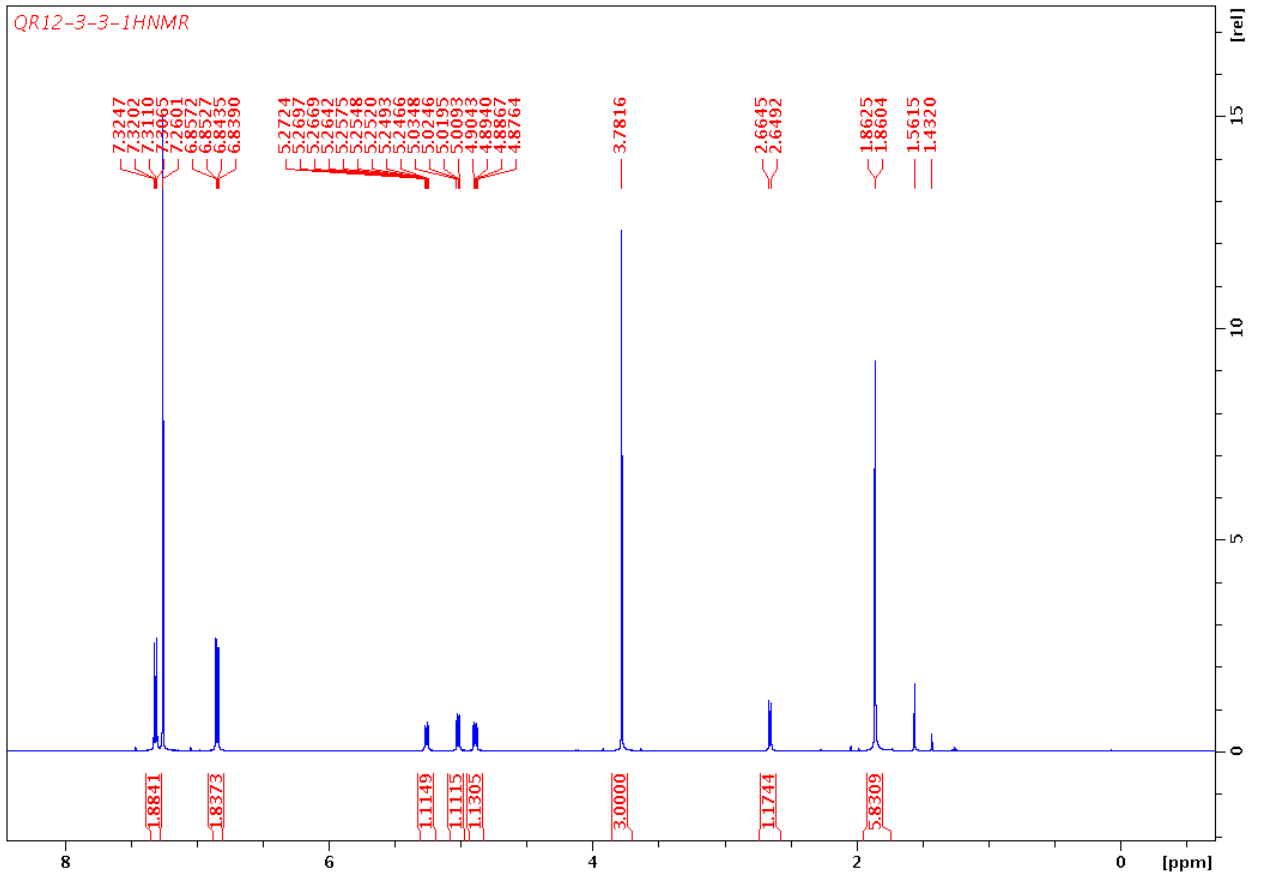
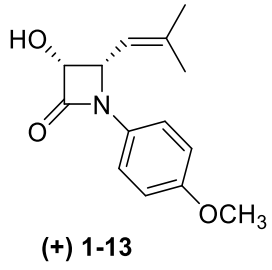
(+) 1-12

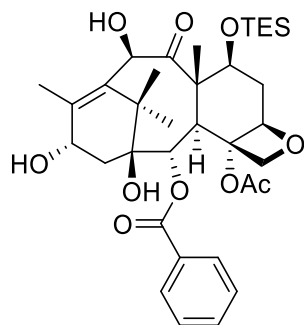




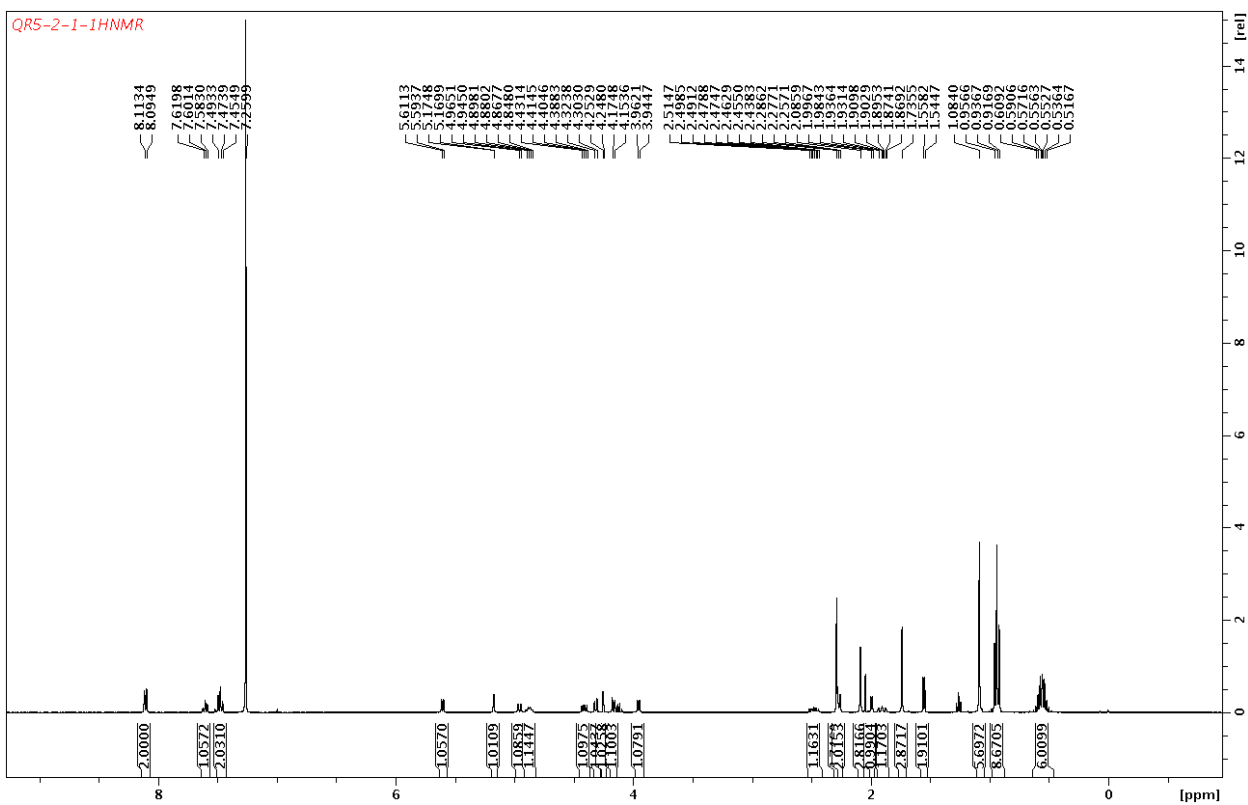
(-)- 1-13

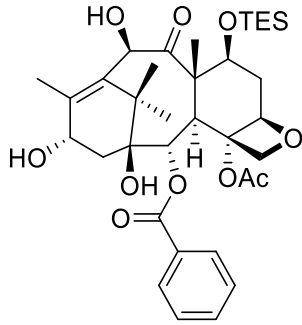




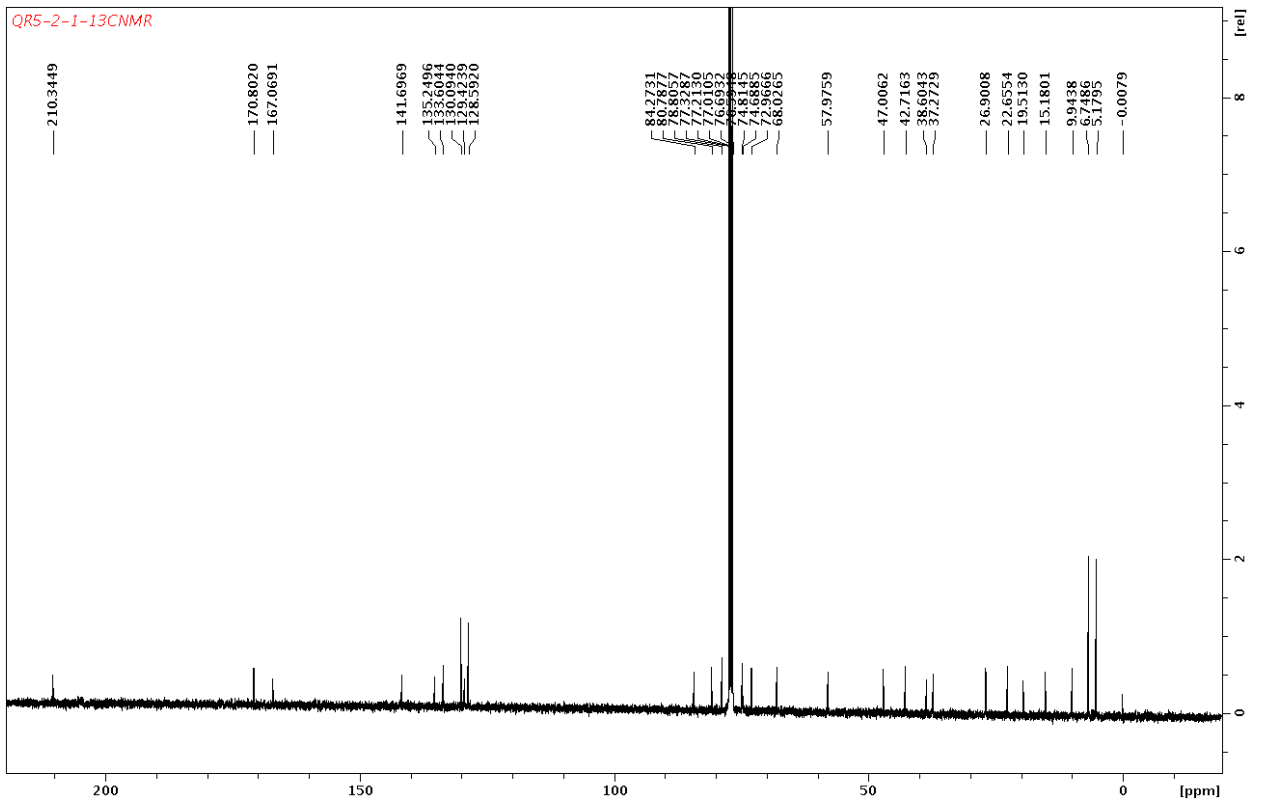


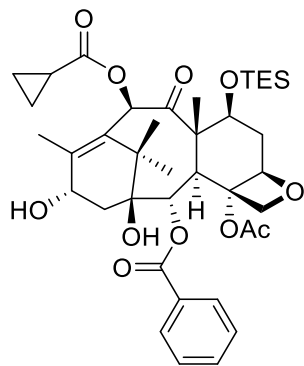
1-14



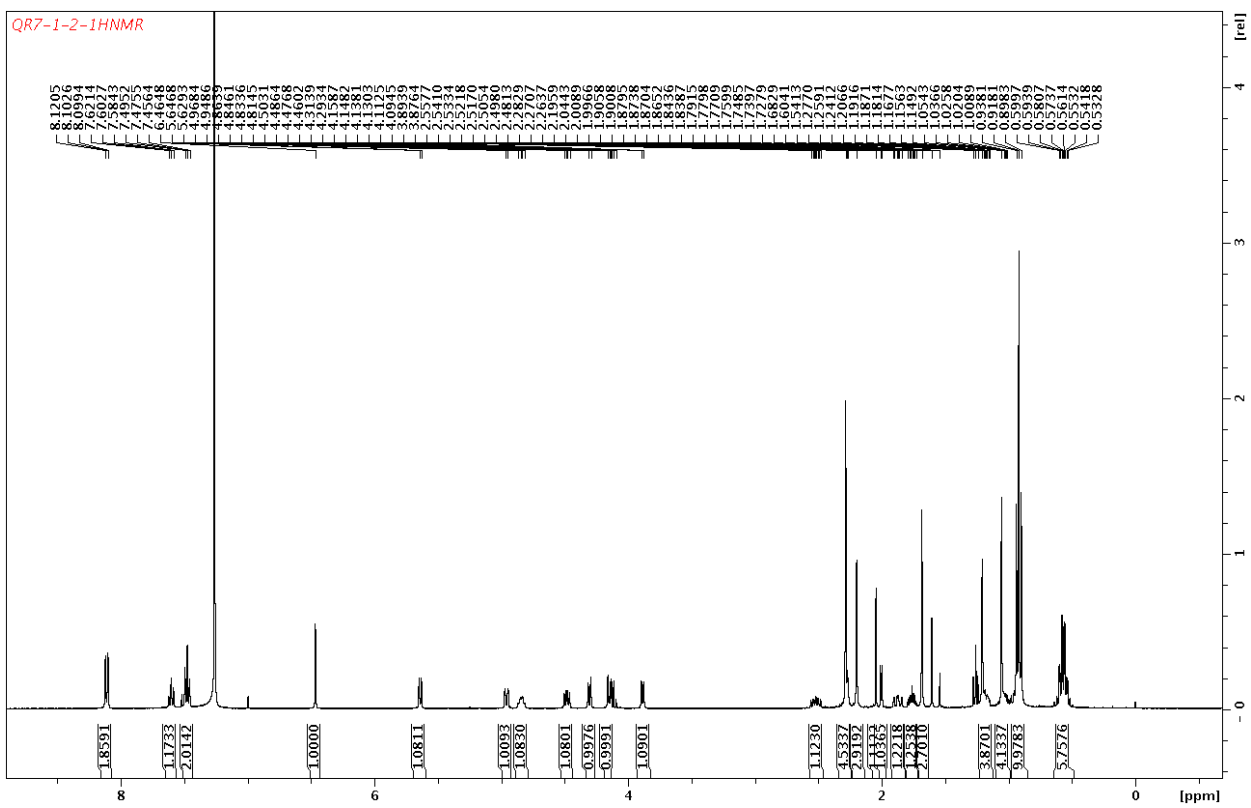


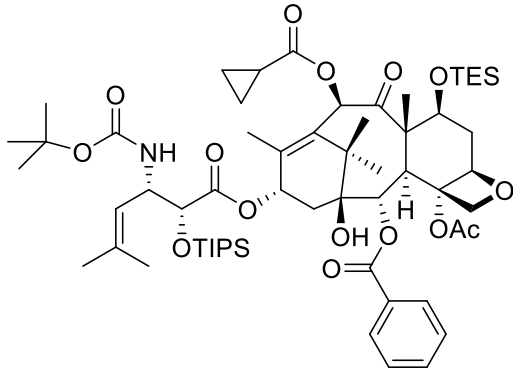
1-14



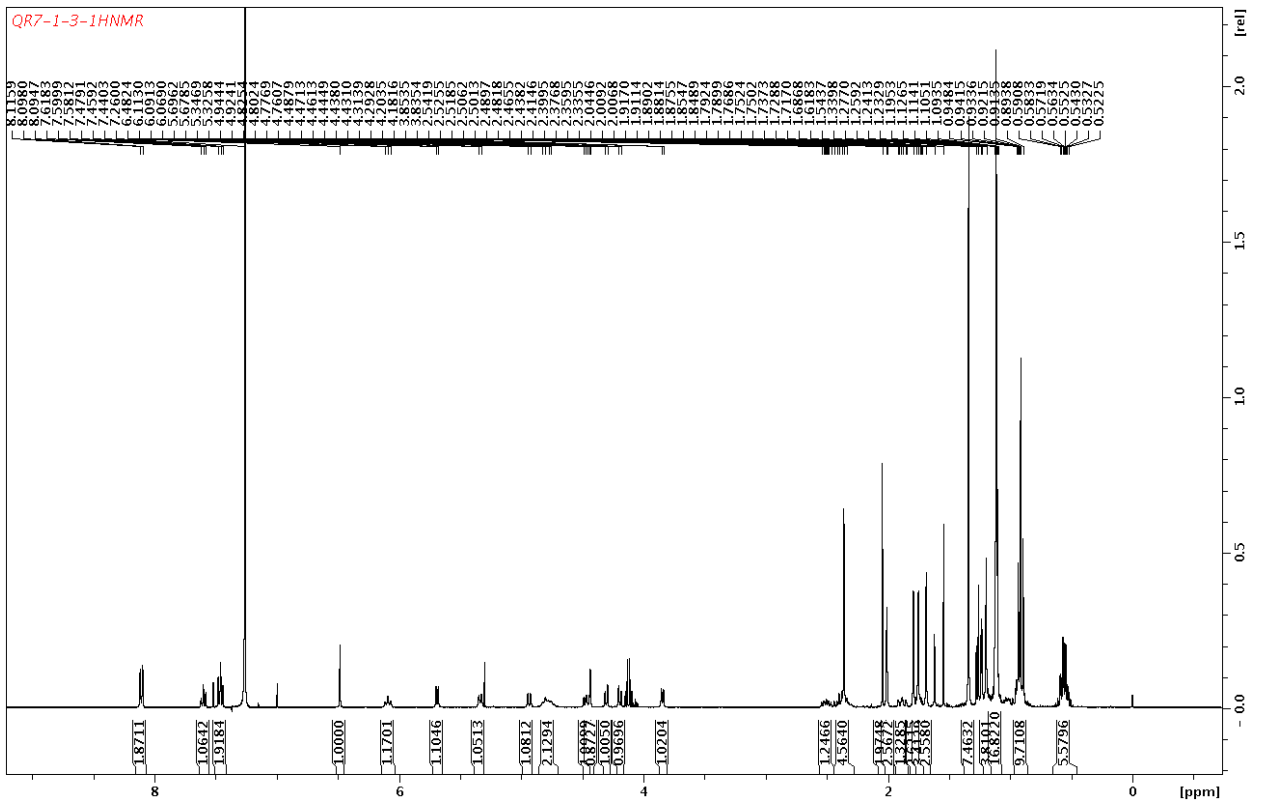


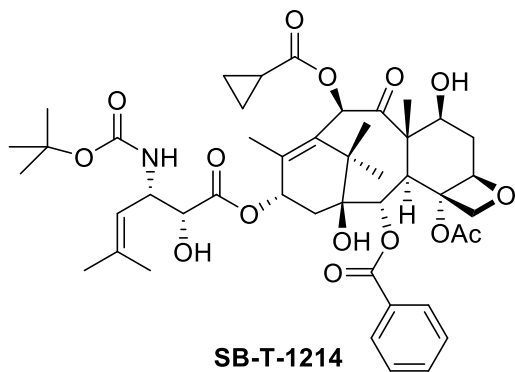
1-15



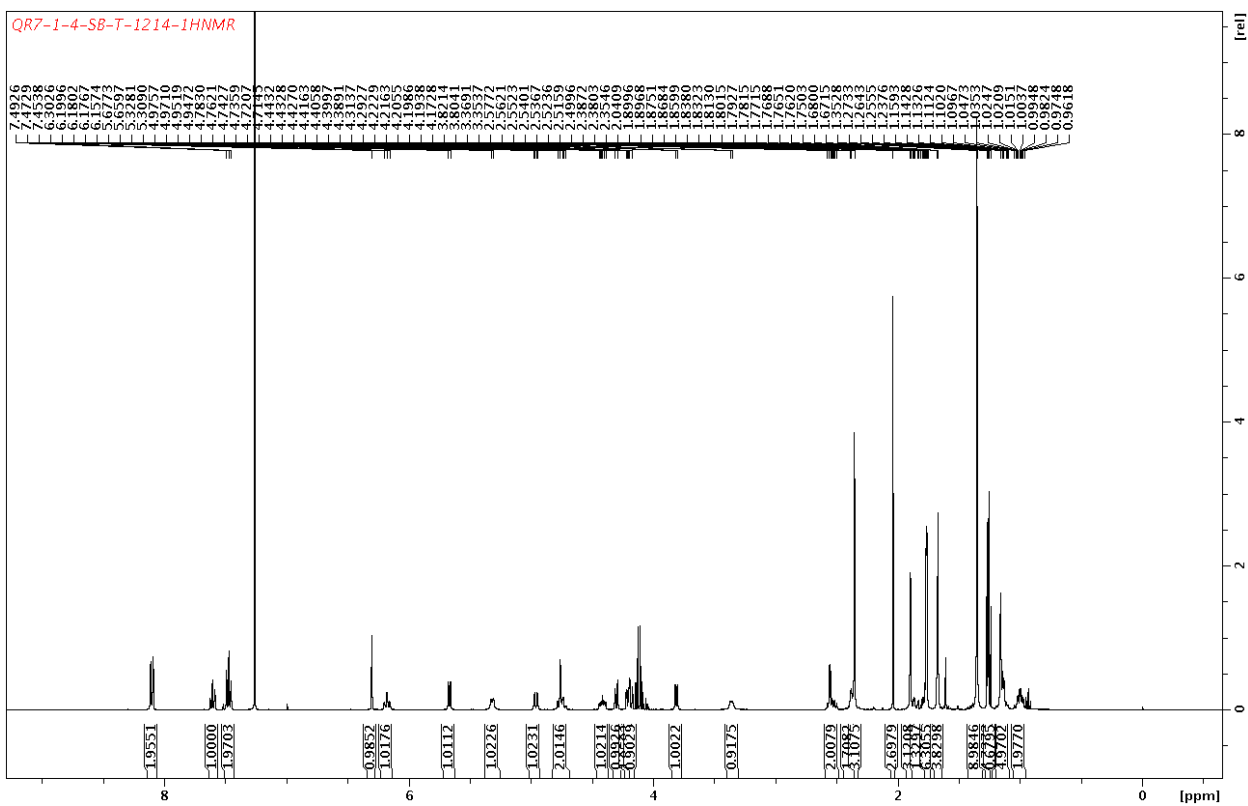


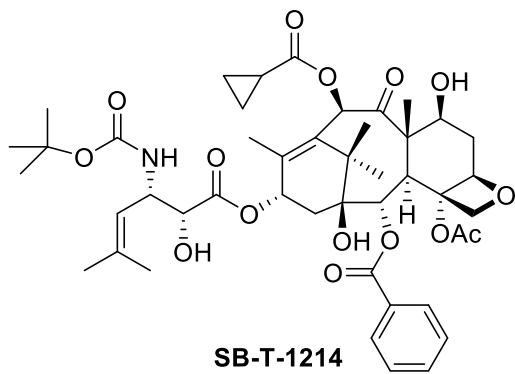
1-16



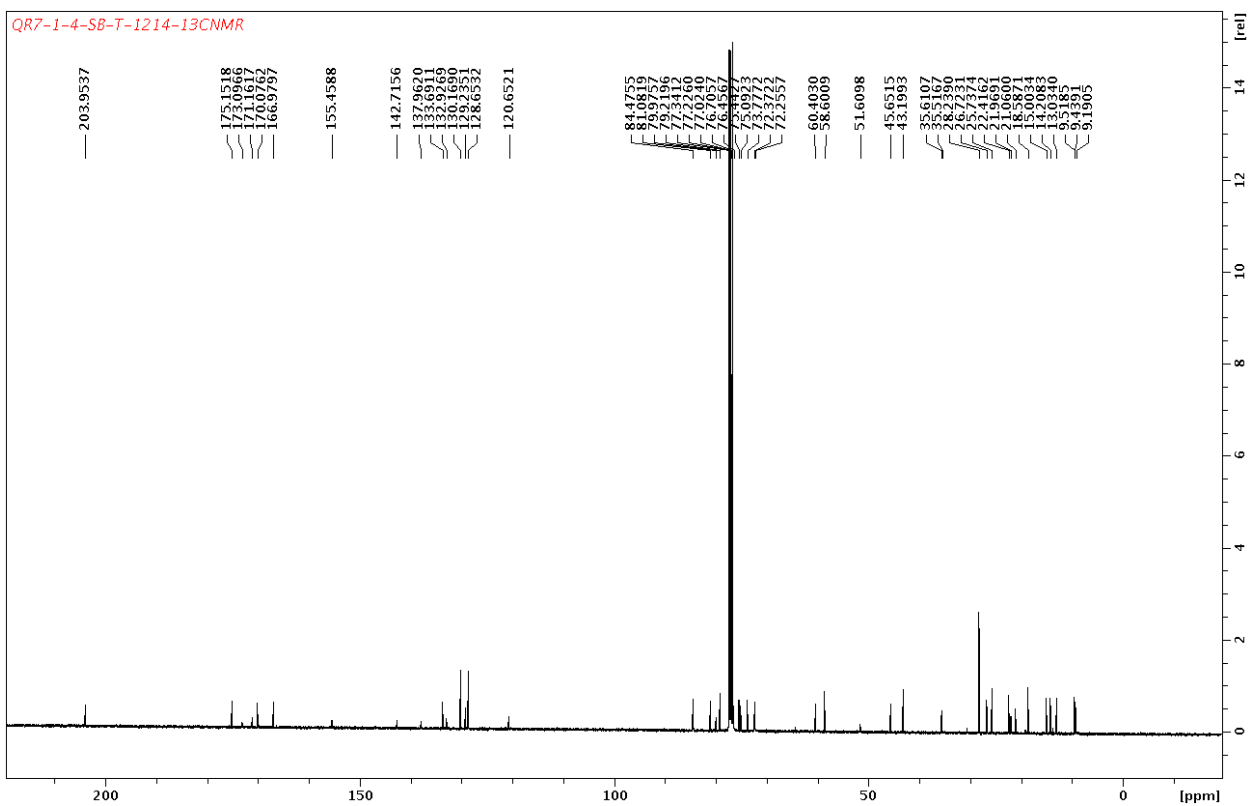


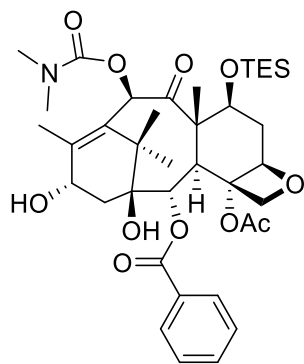
1-17



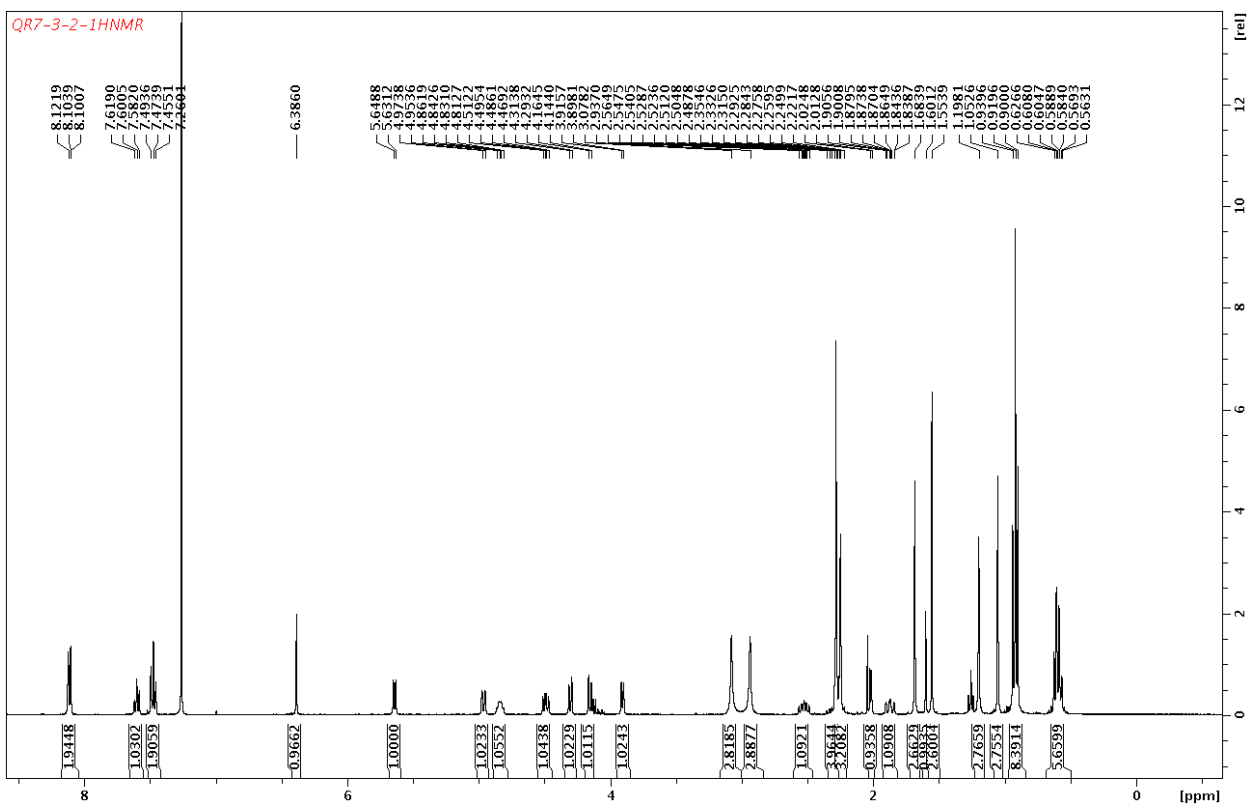


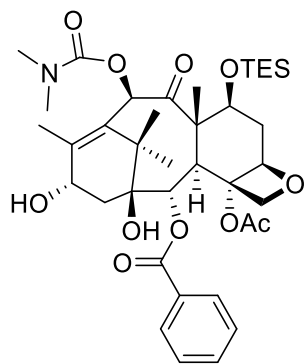
1-17



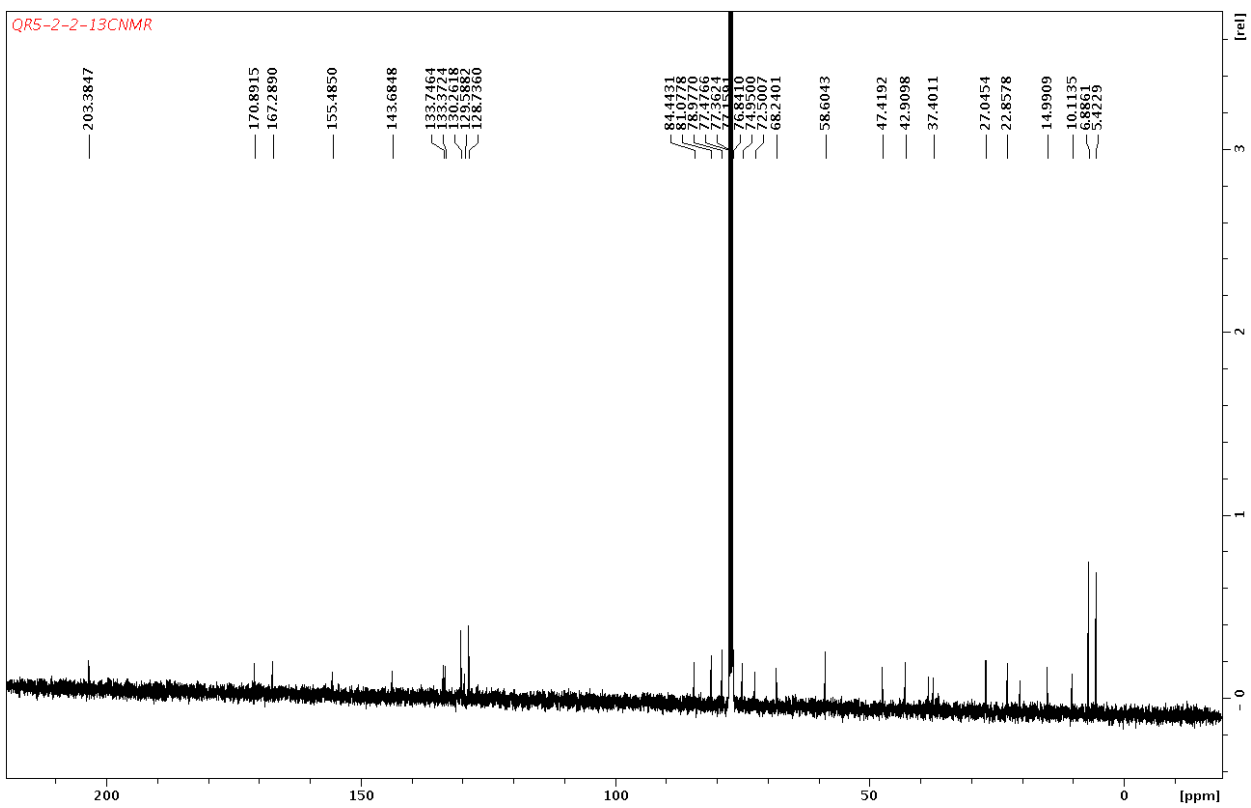


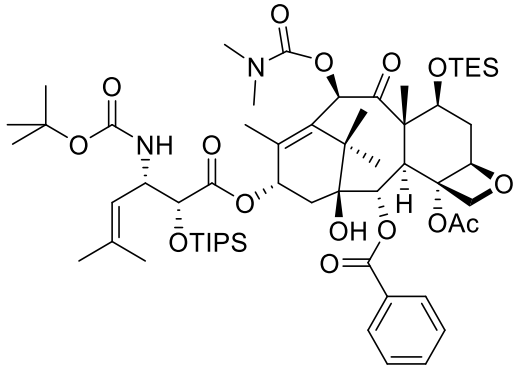
1-18



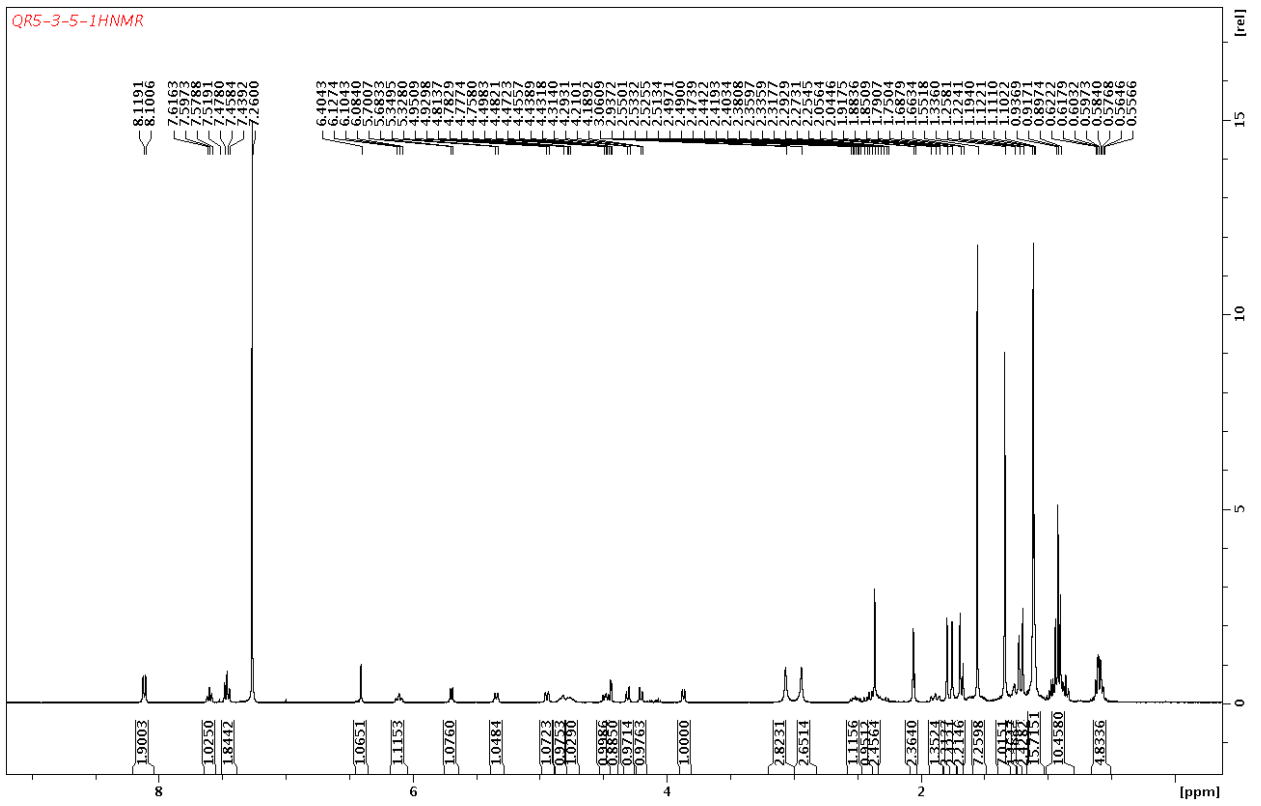


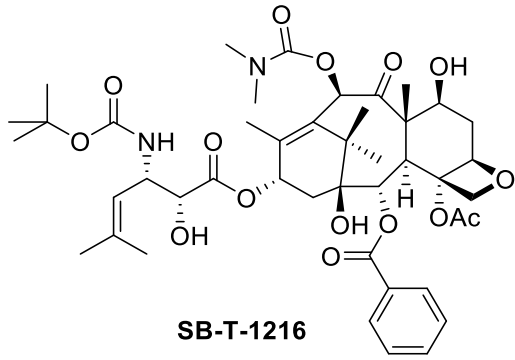
1-18



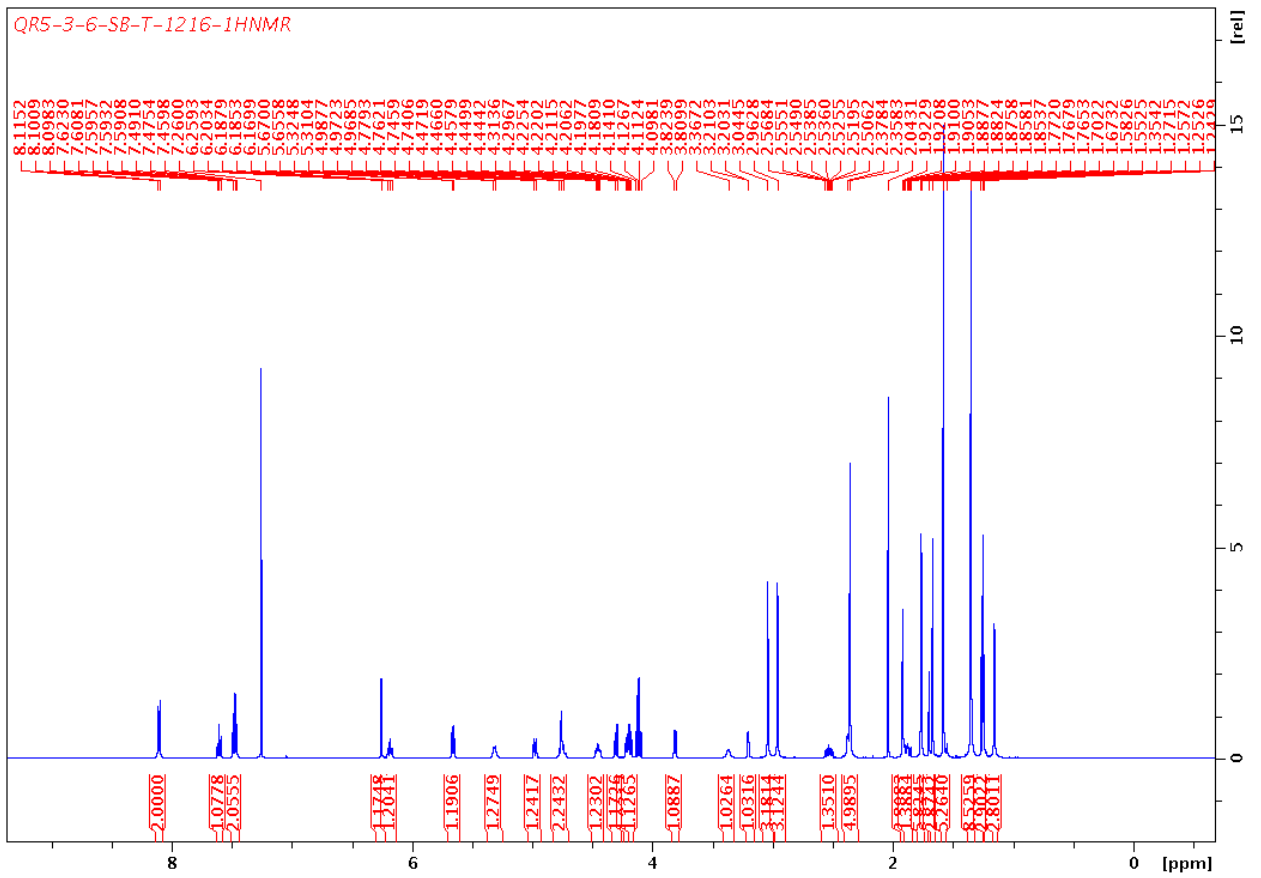


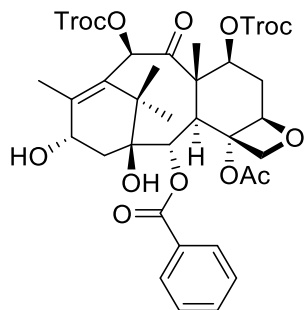
1-19



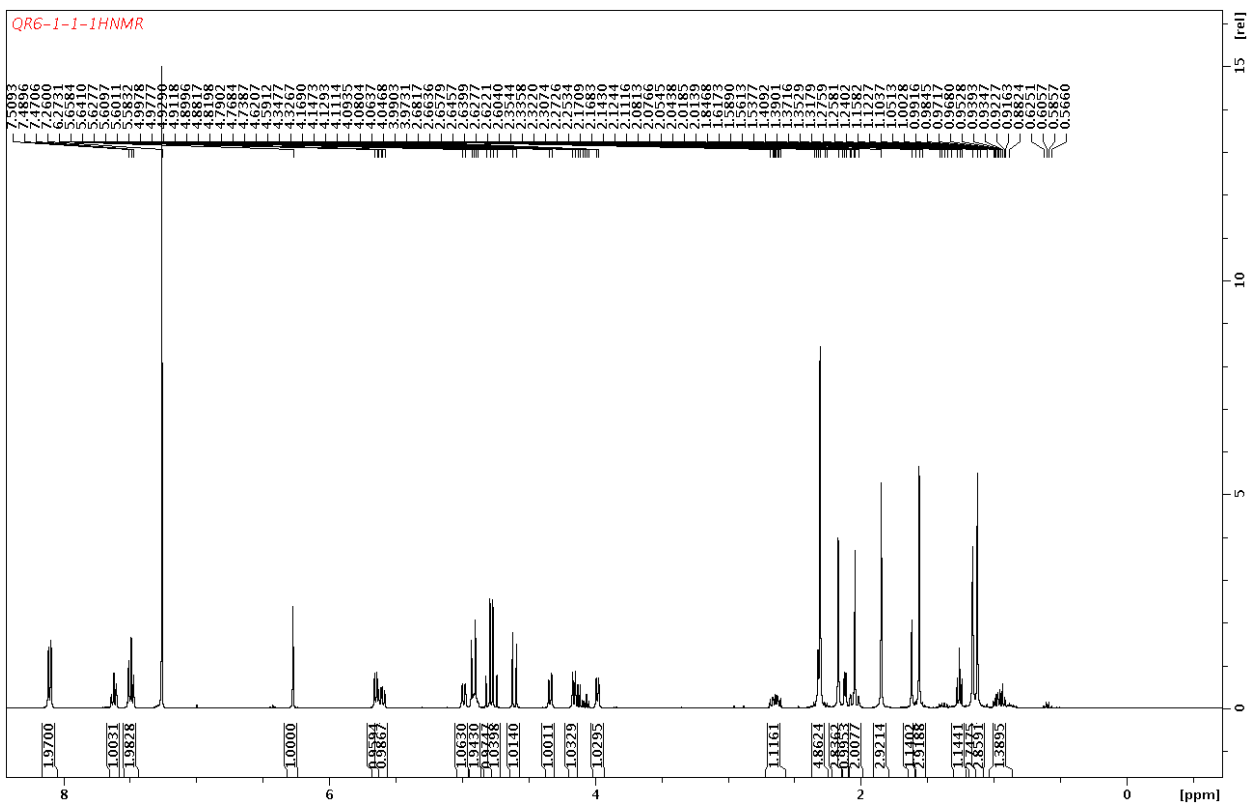


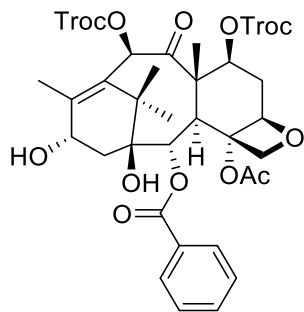
1-20



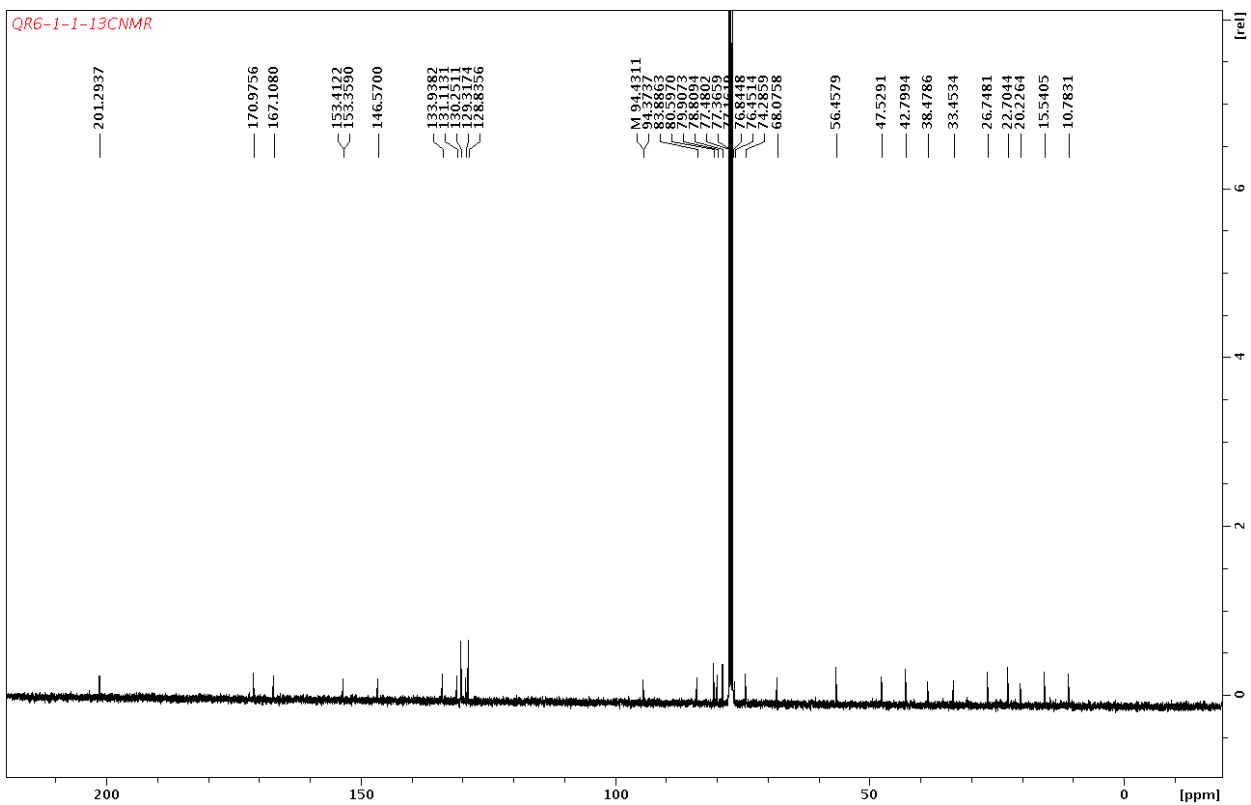


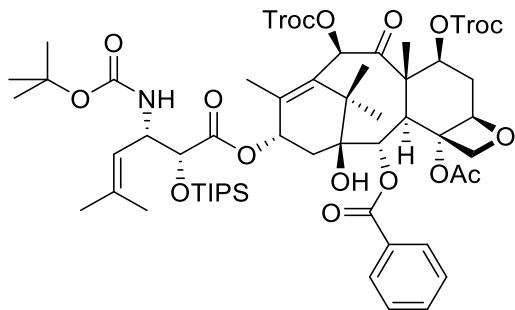
1-21



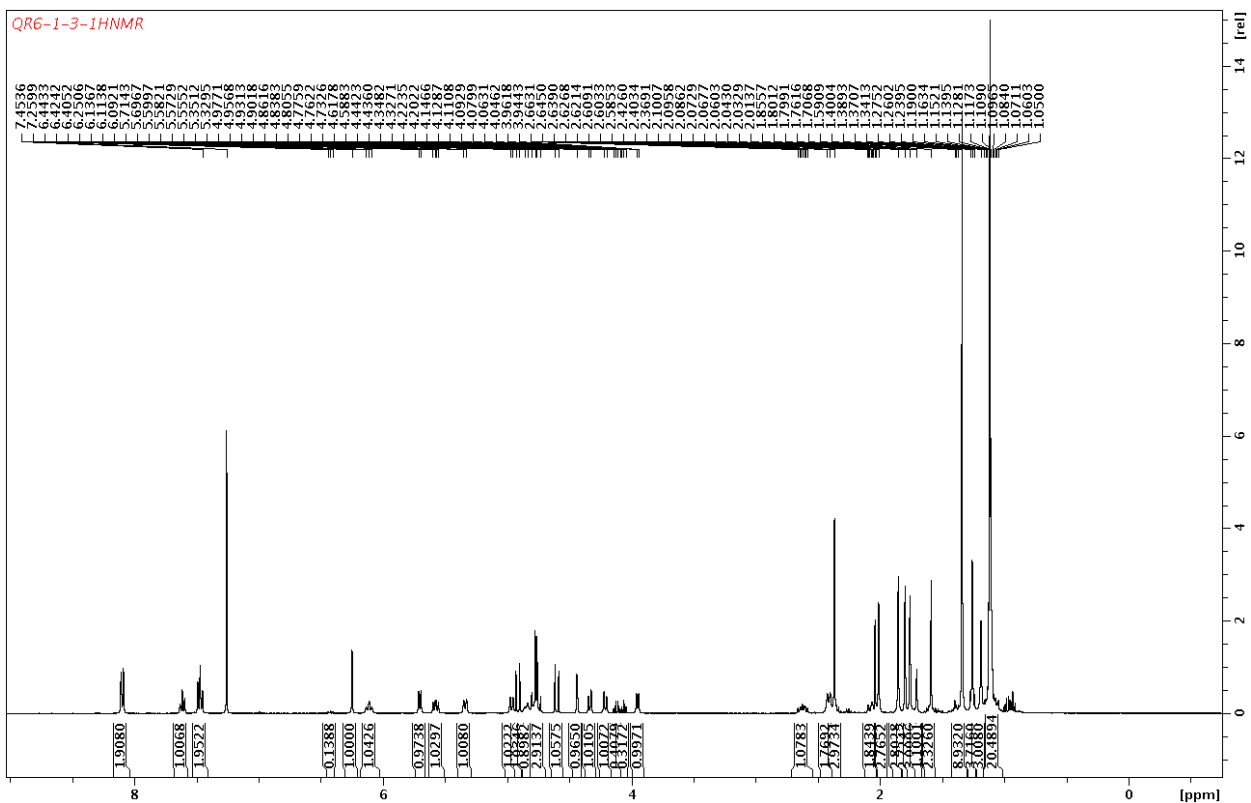


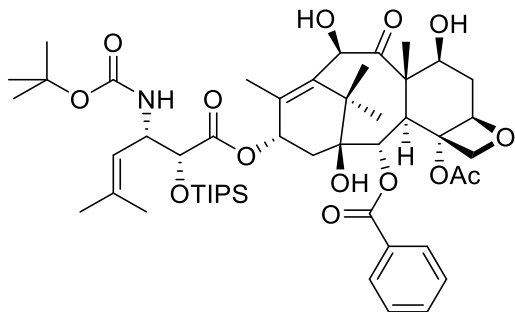
1-21



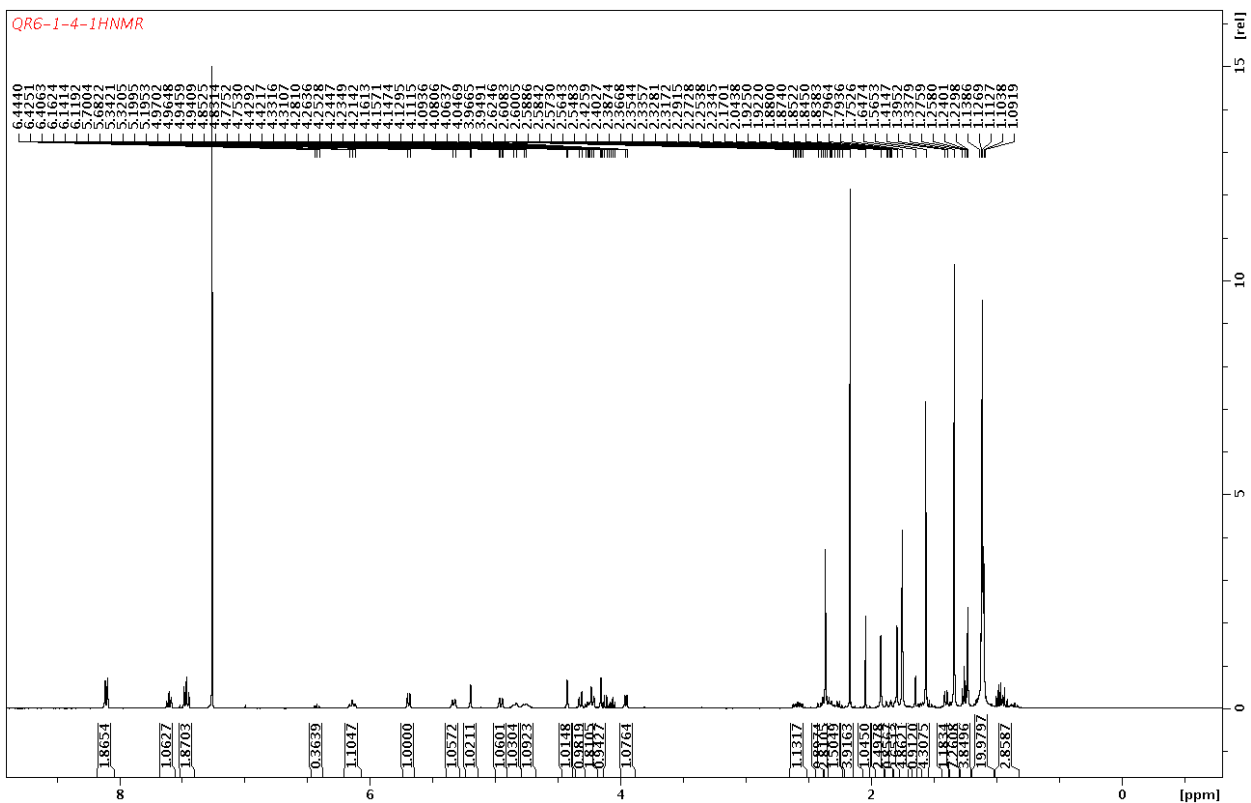


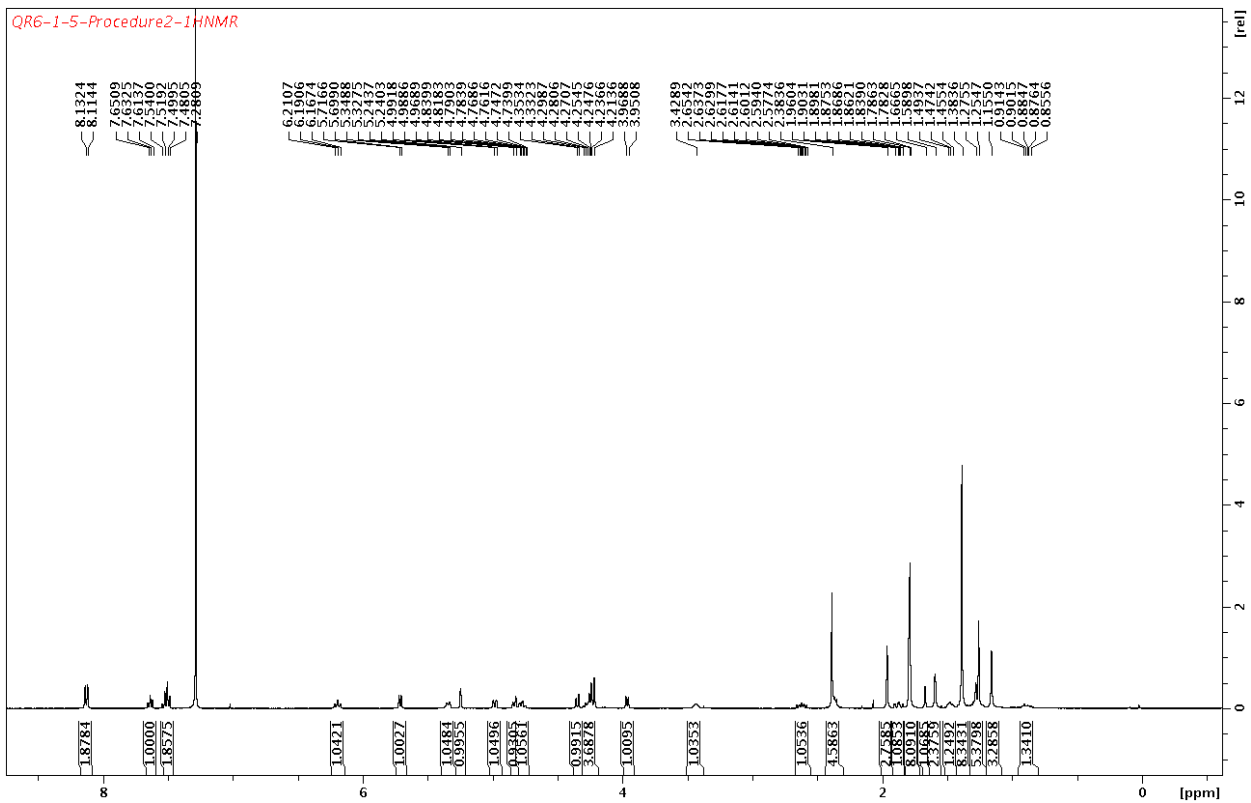
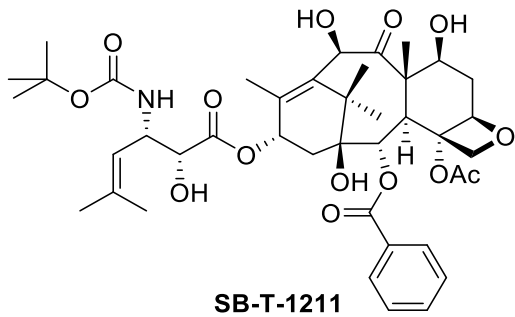
1-22

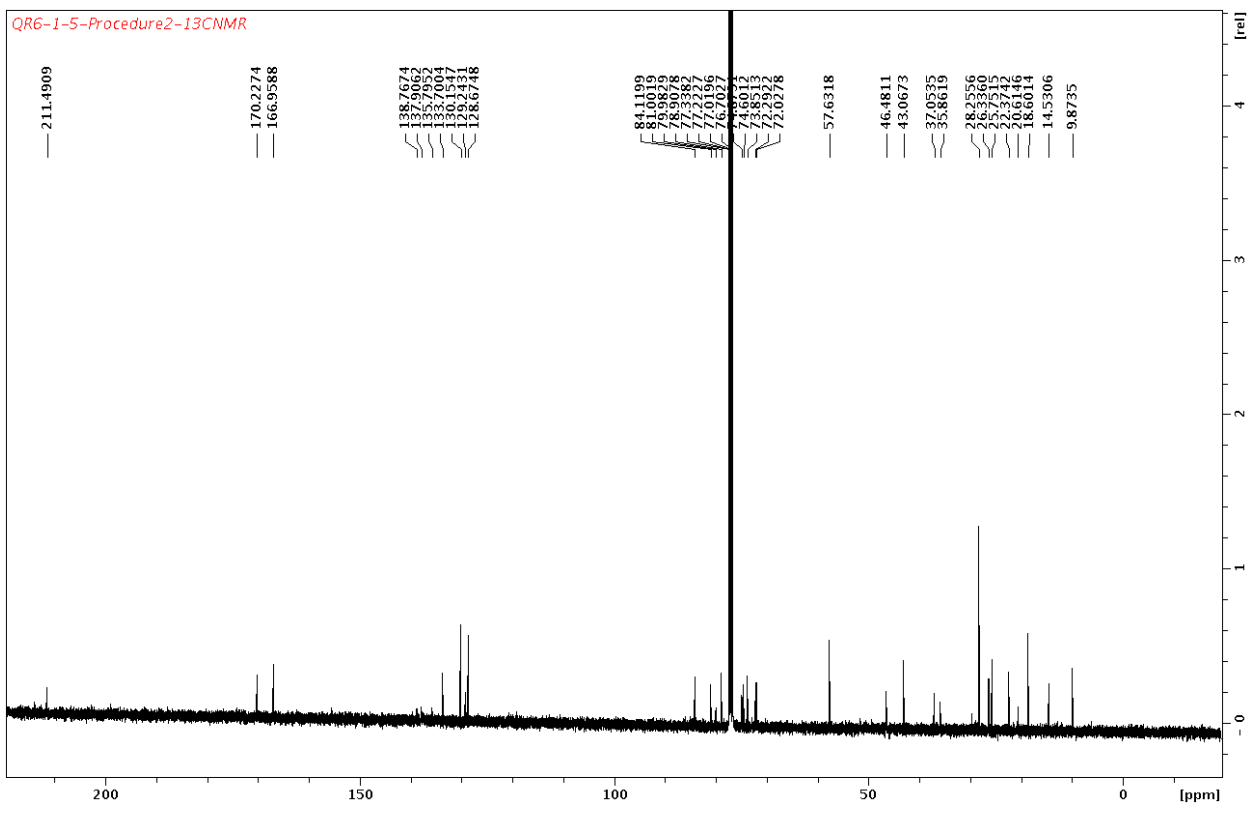
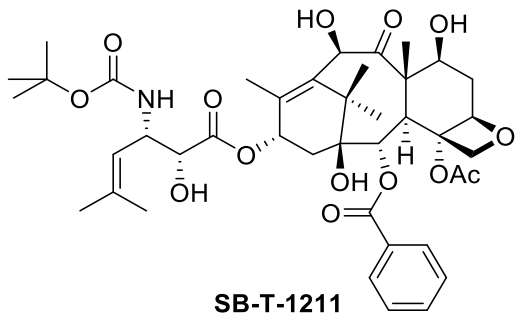


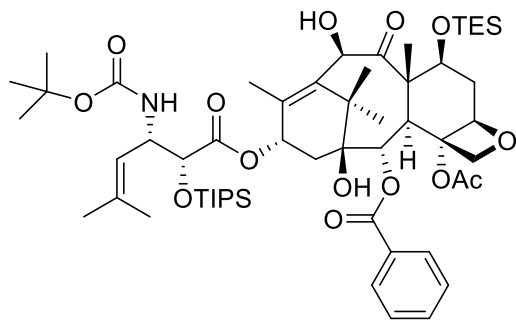


1-23

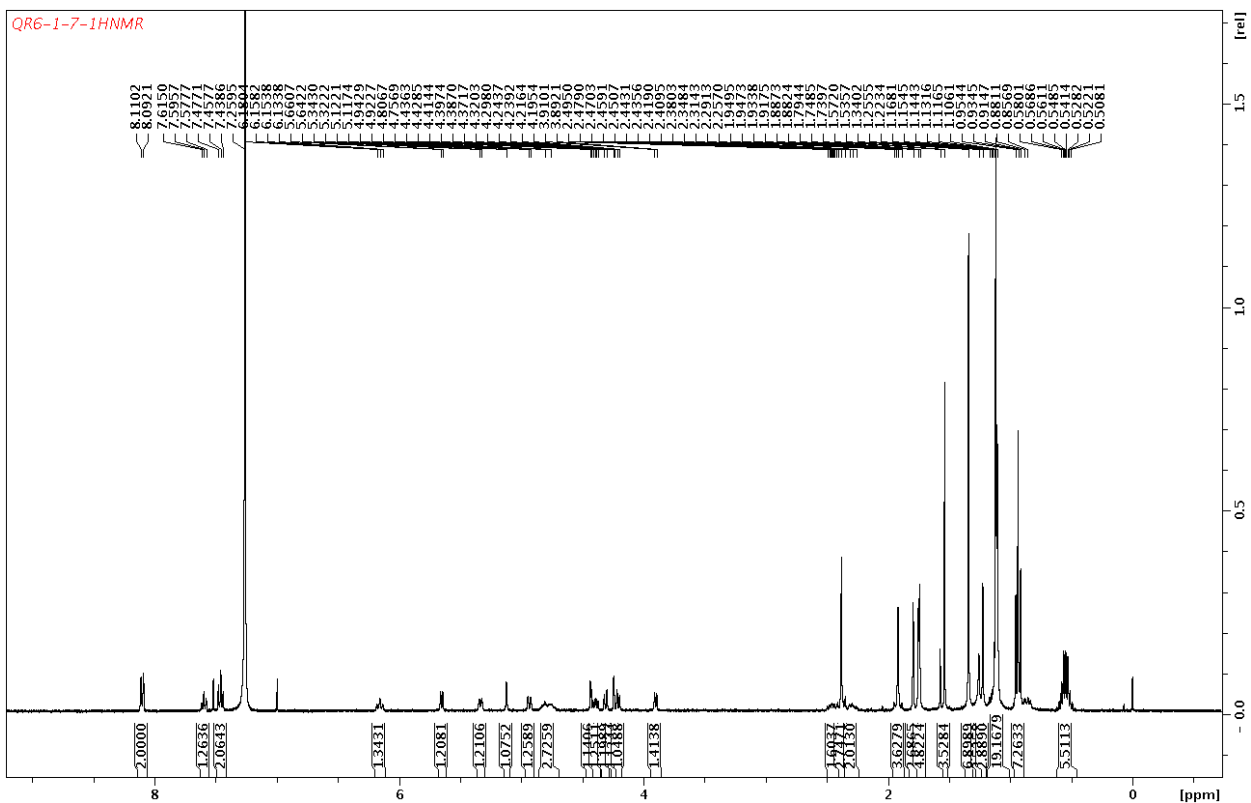


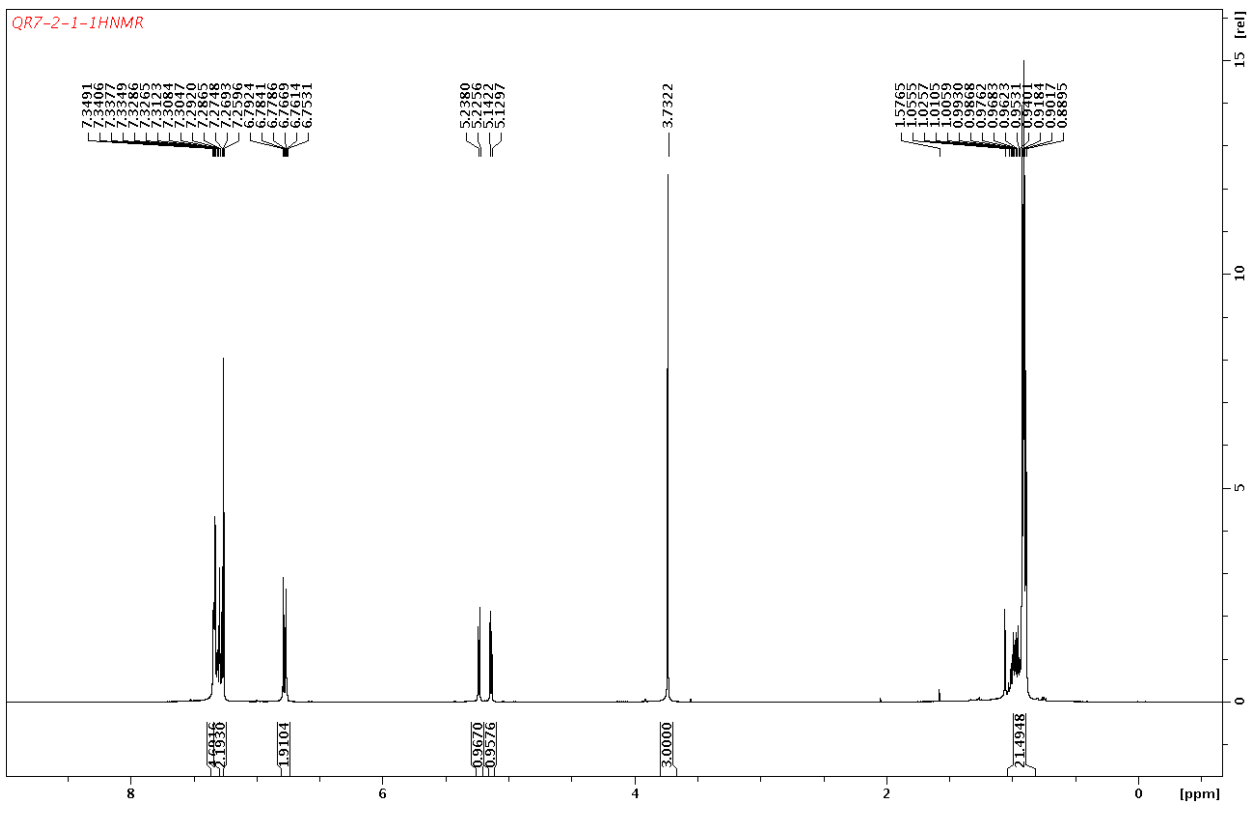
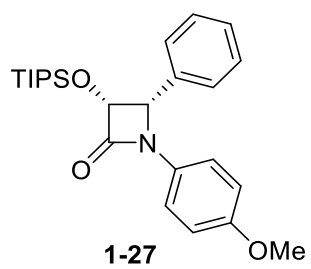


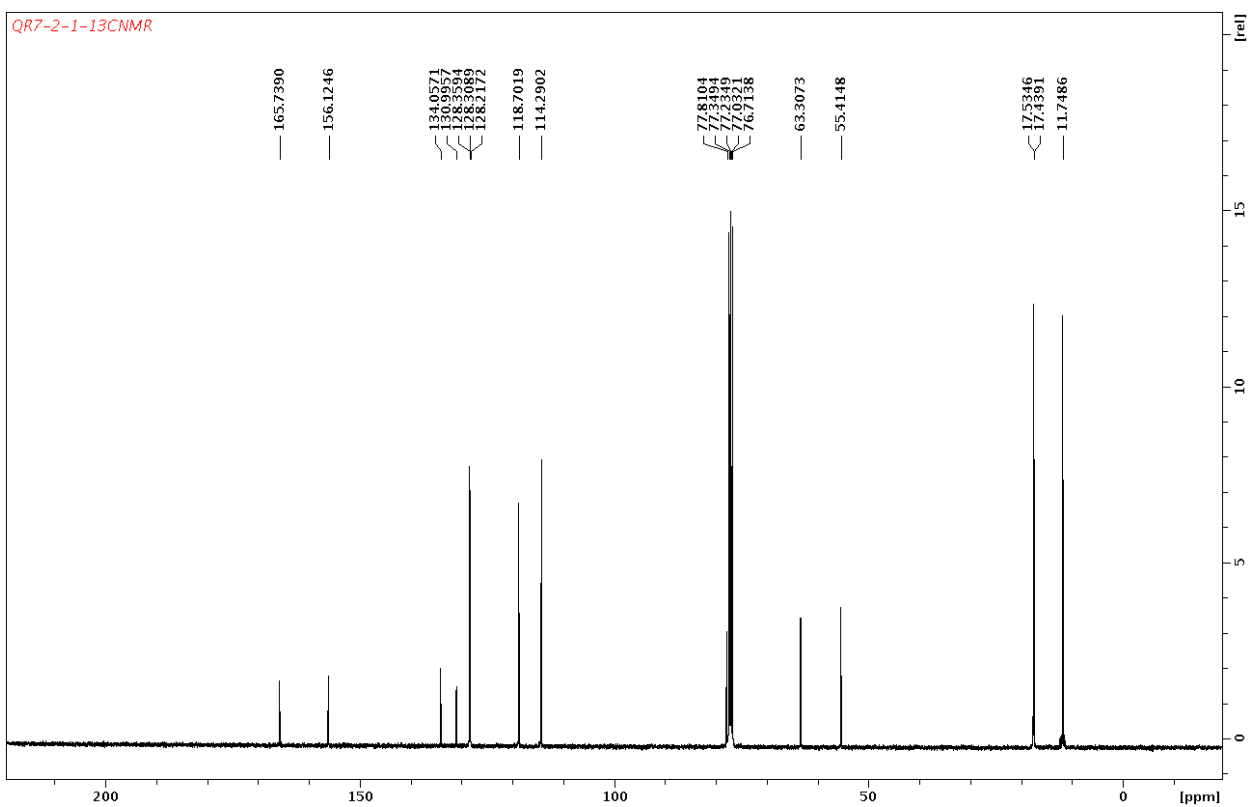
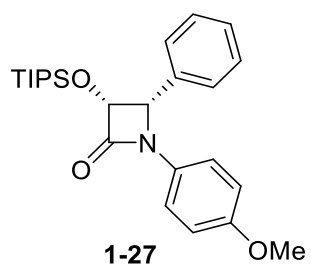


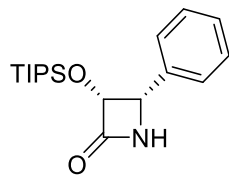


1-26

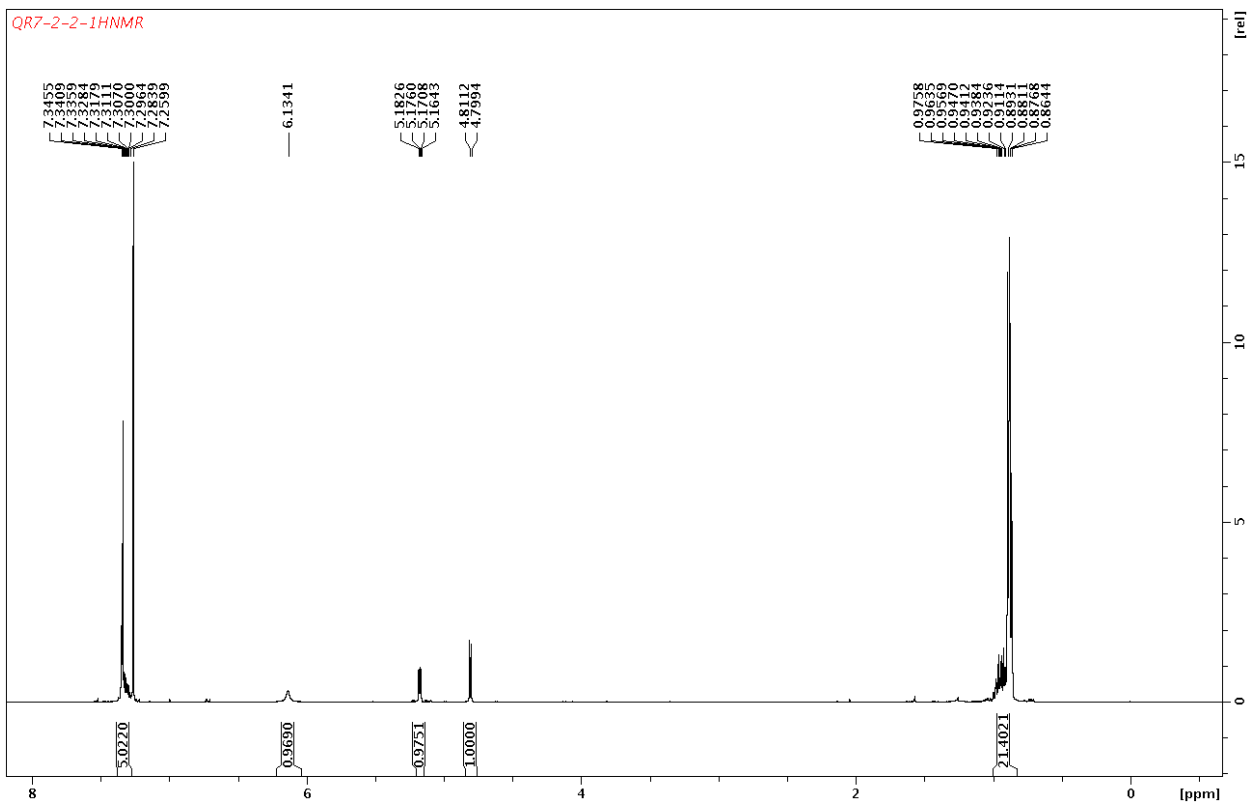


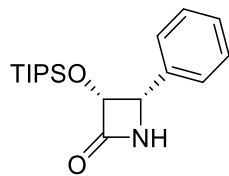




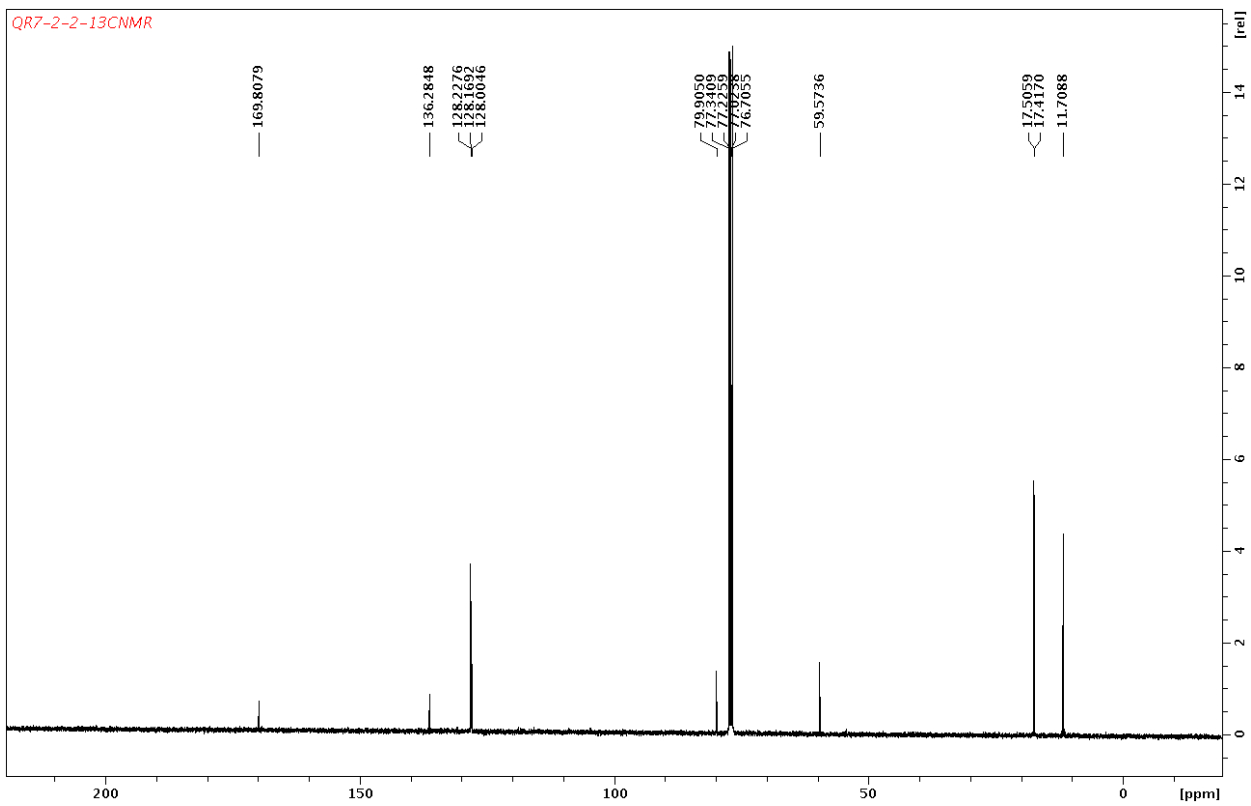


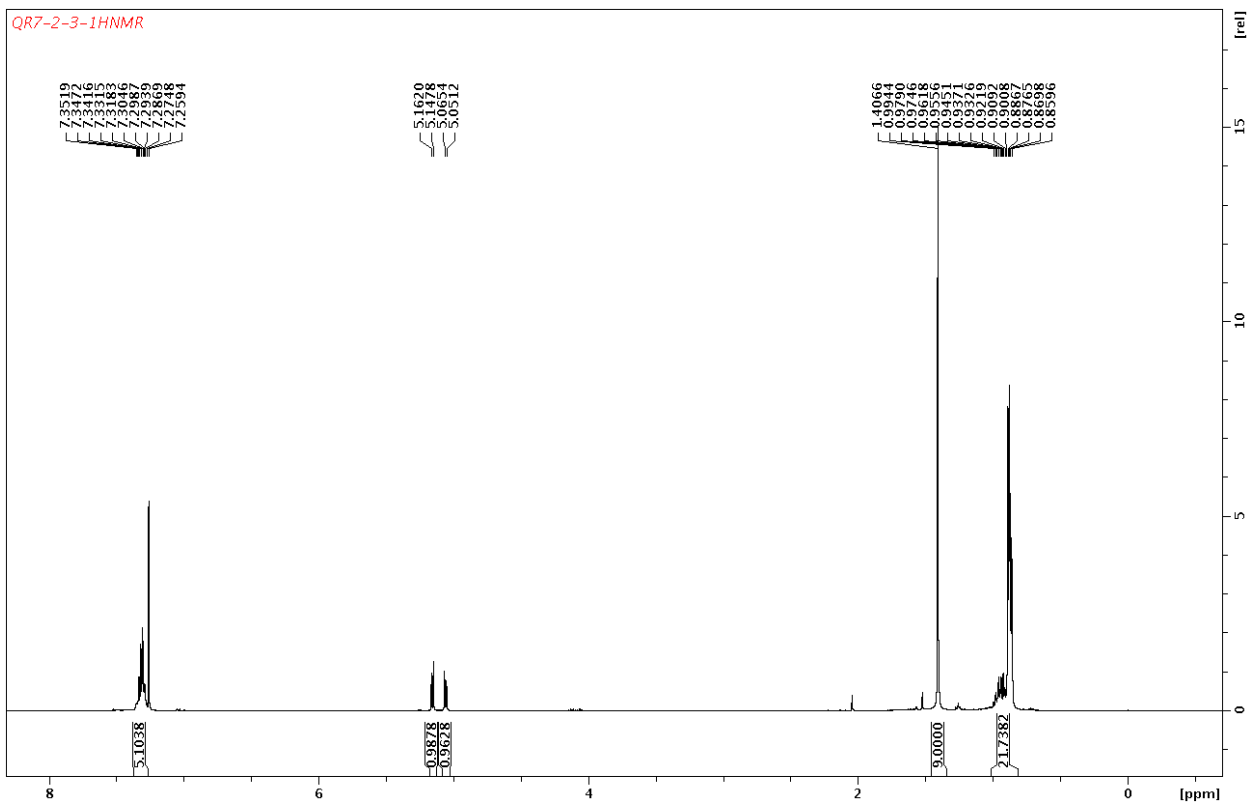
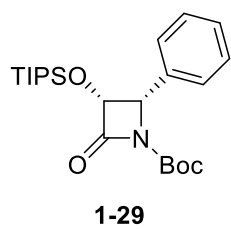
1-28

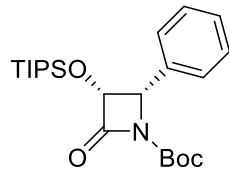




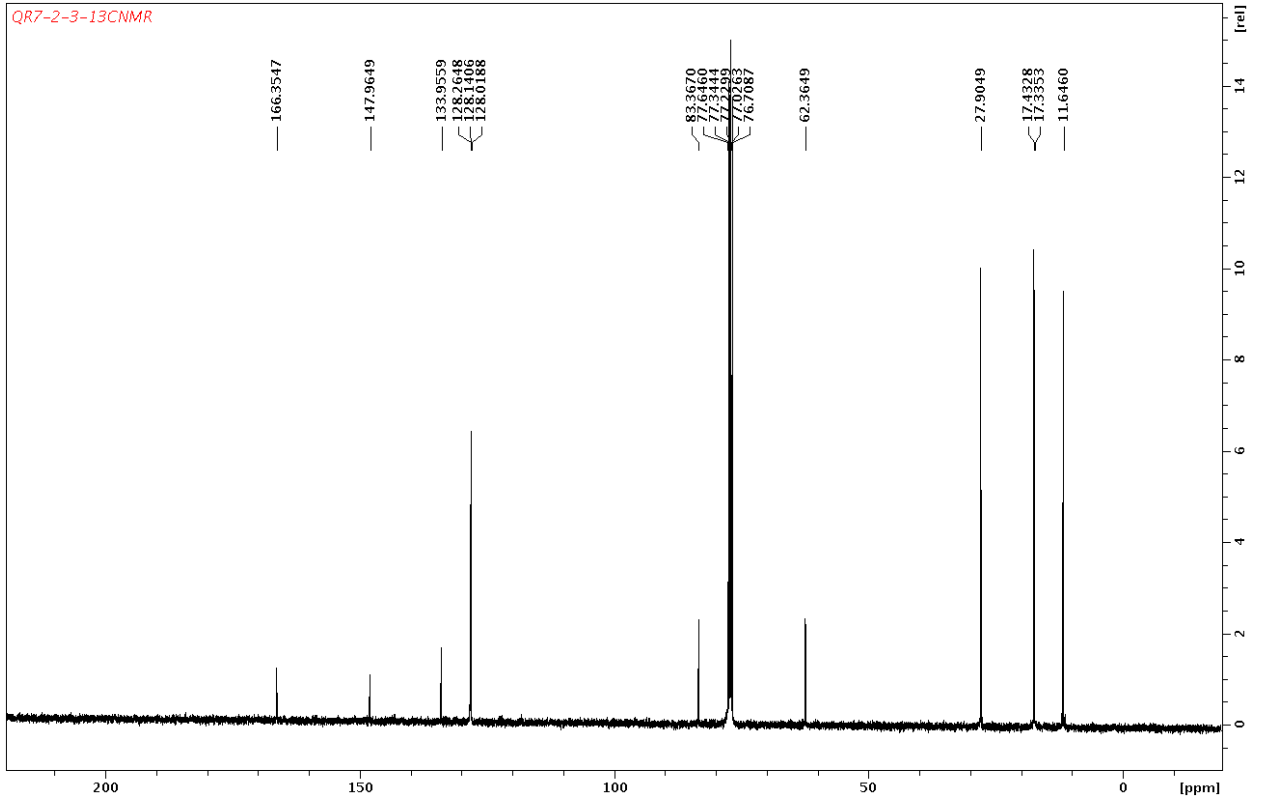
1-28

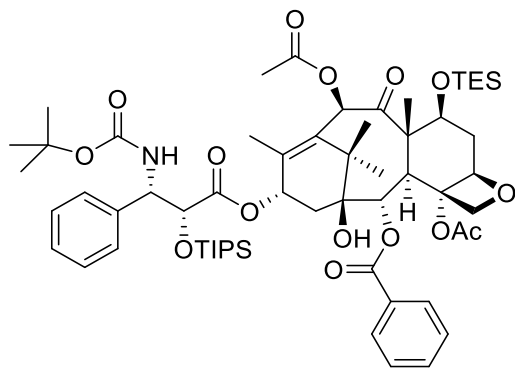




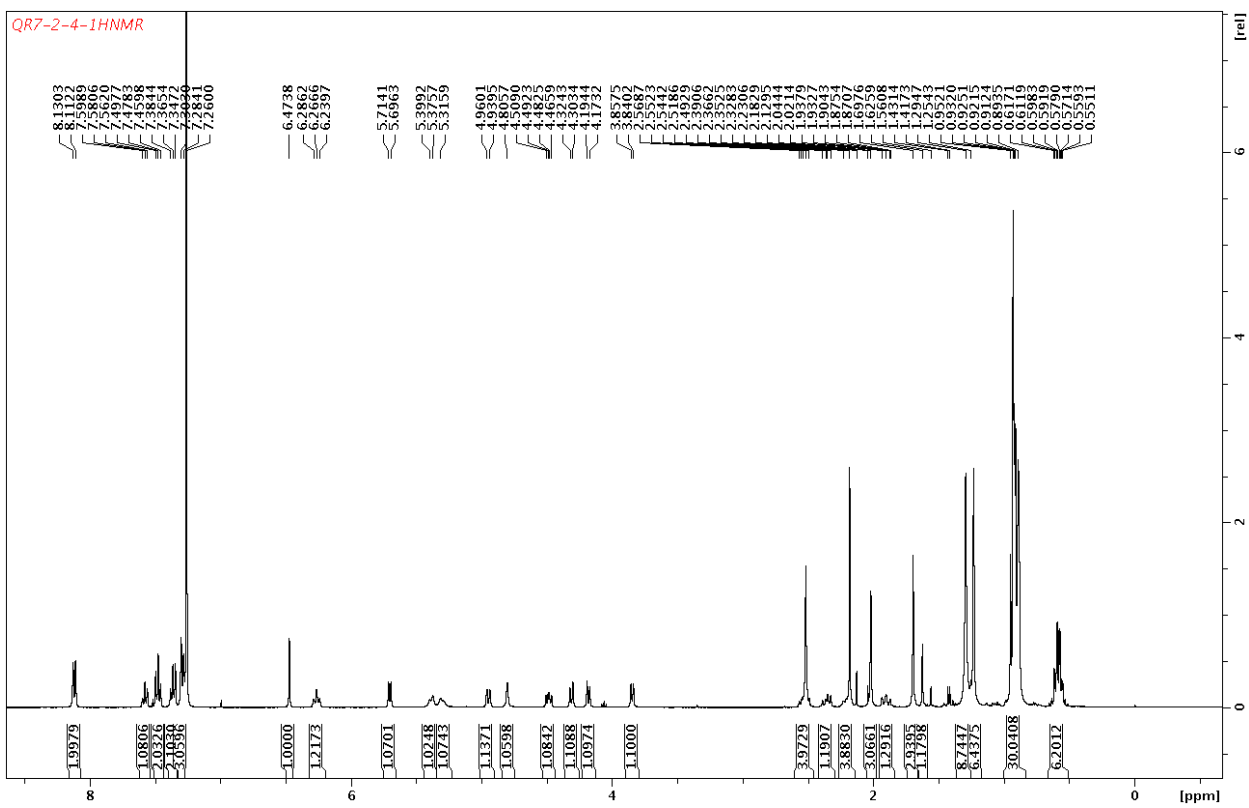


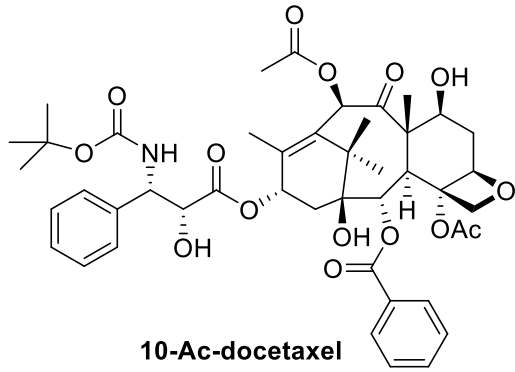
1-29



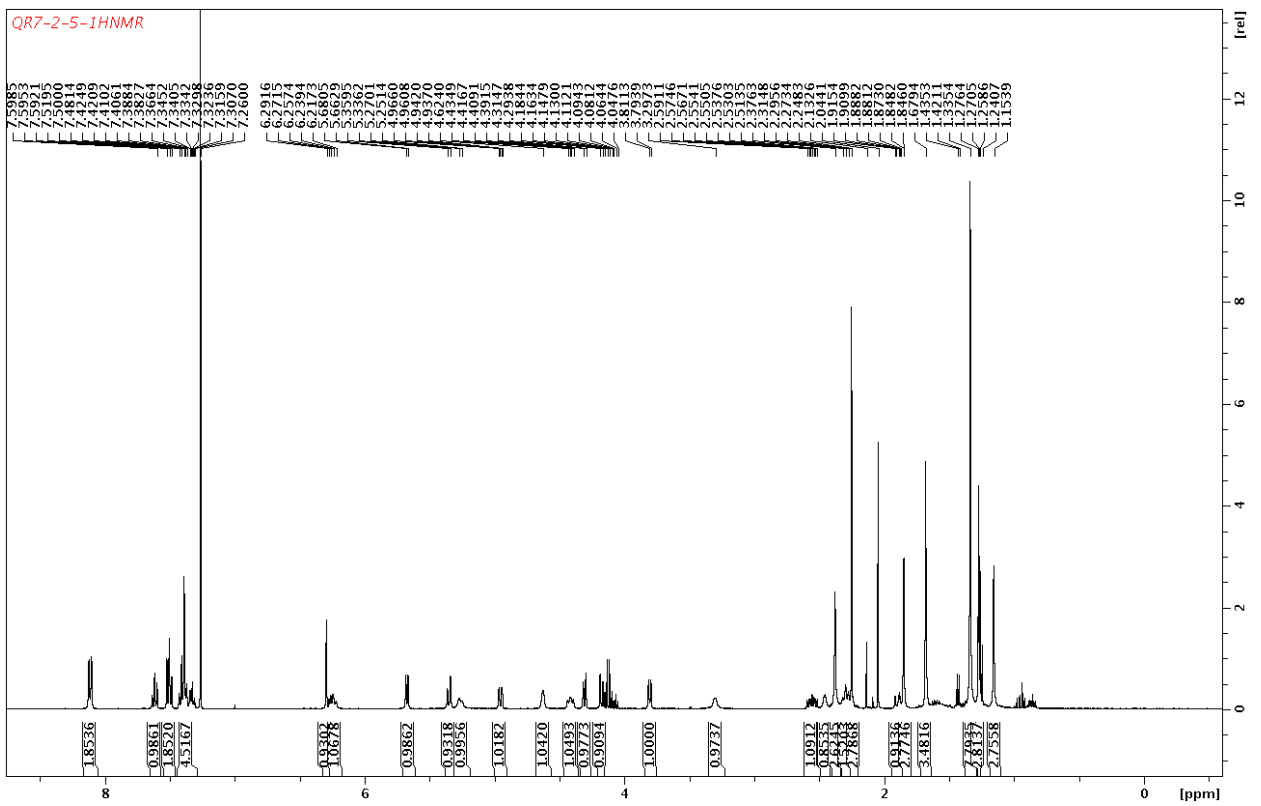


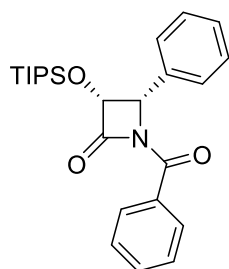
1-30



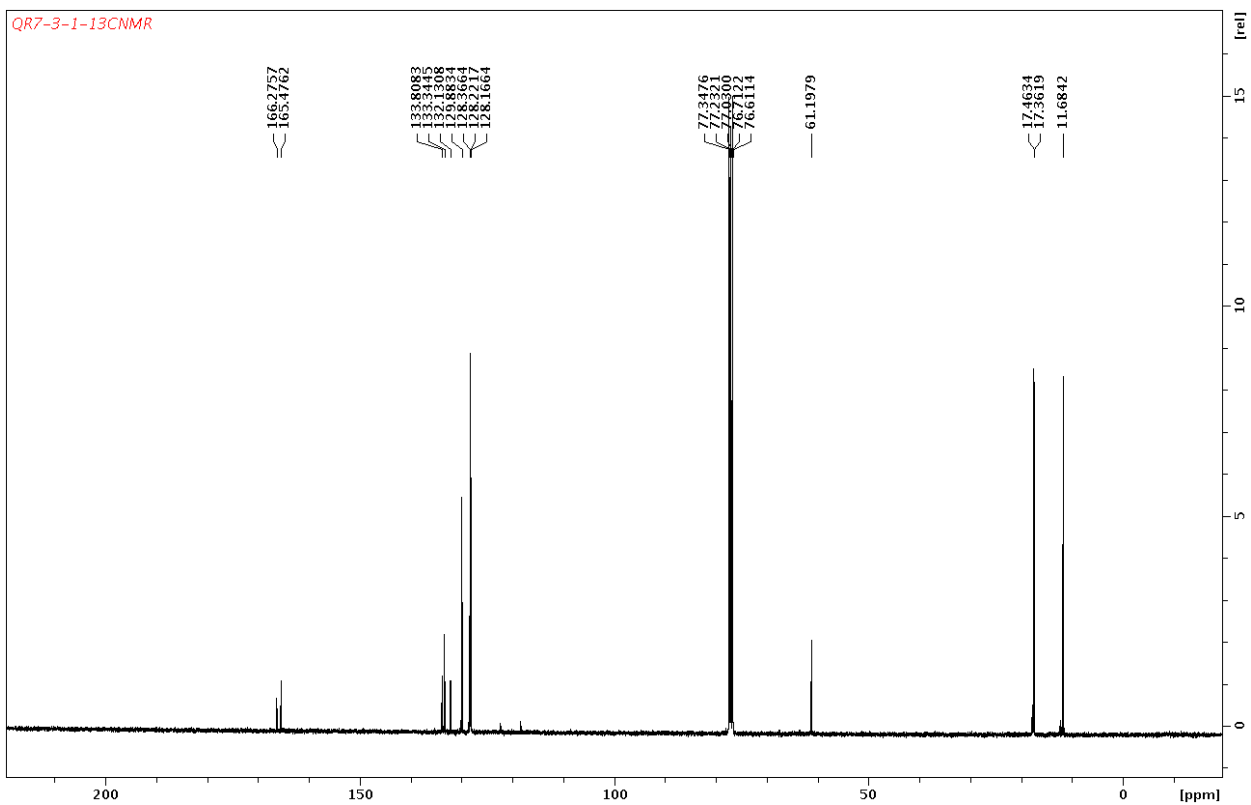


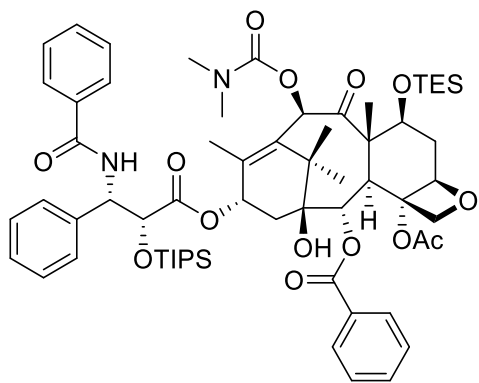
1-31



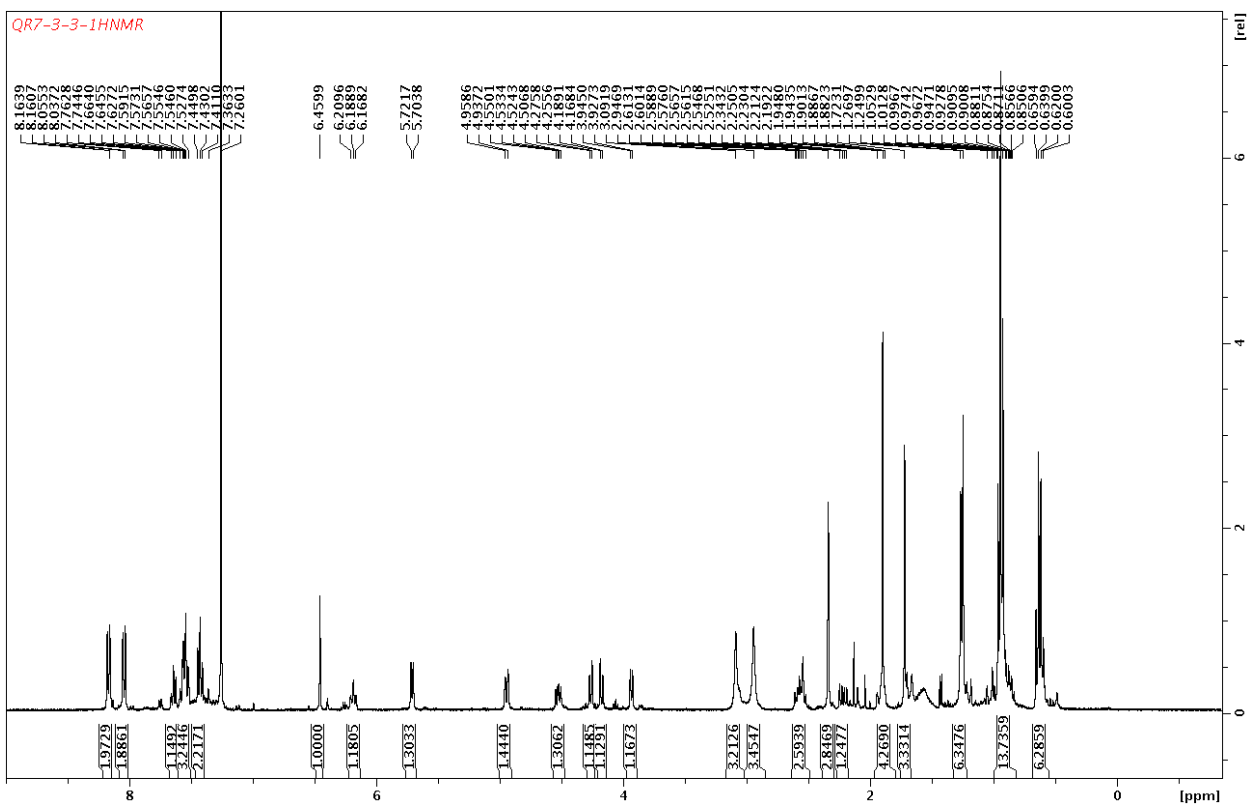


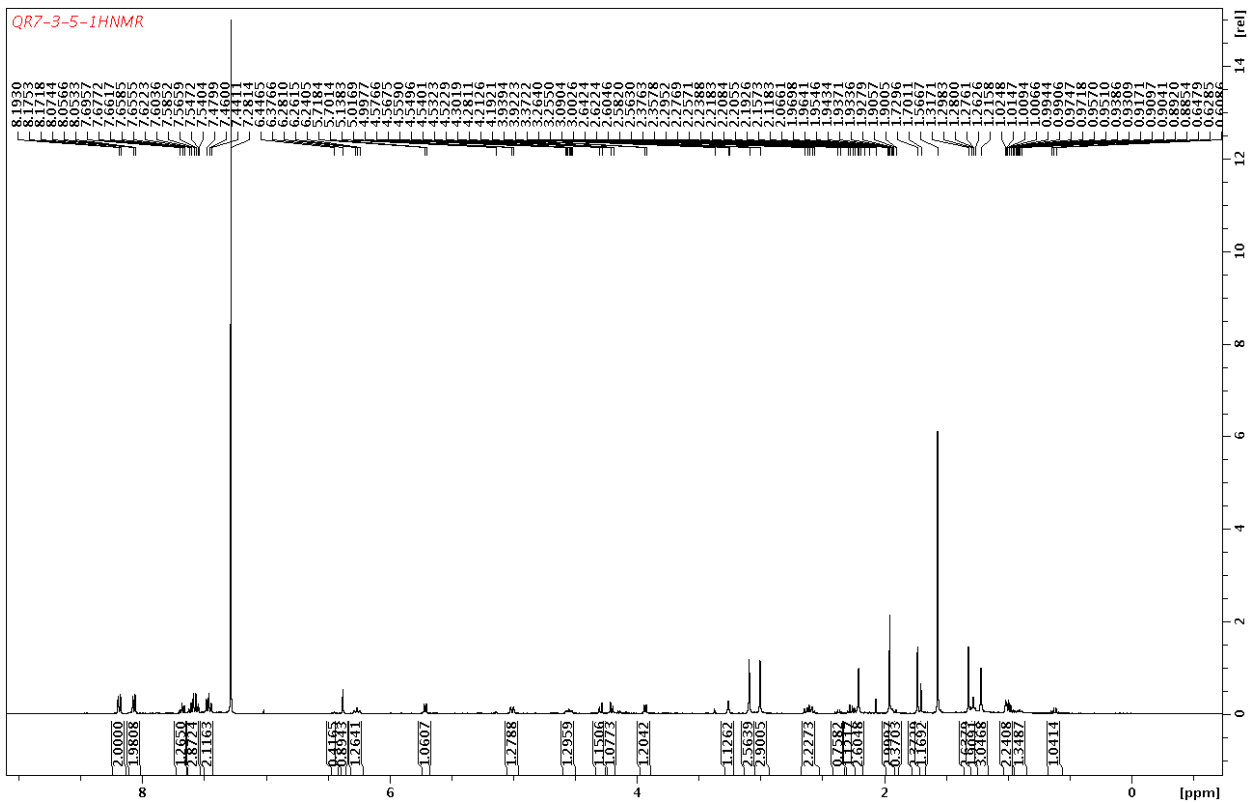
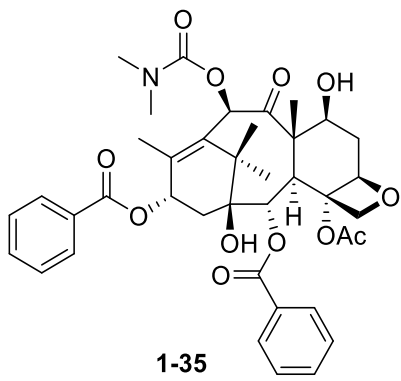
1-32



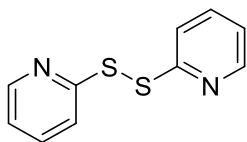


1-33

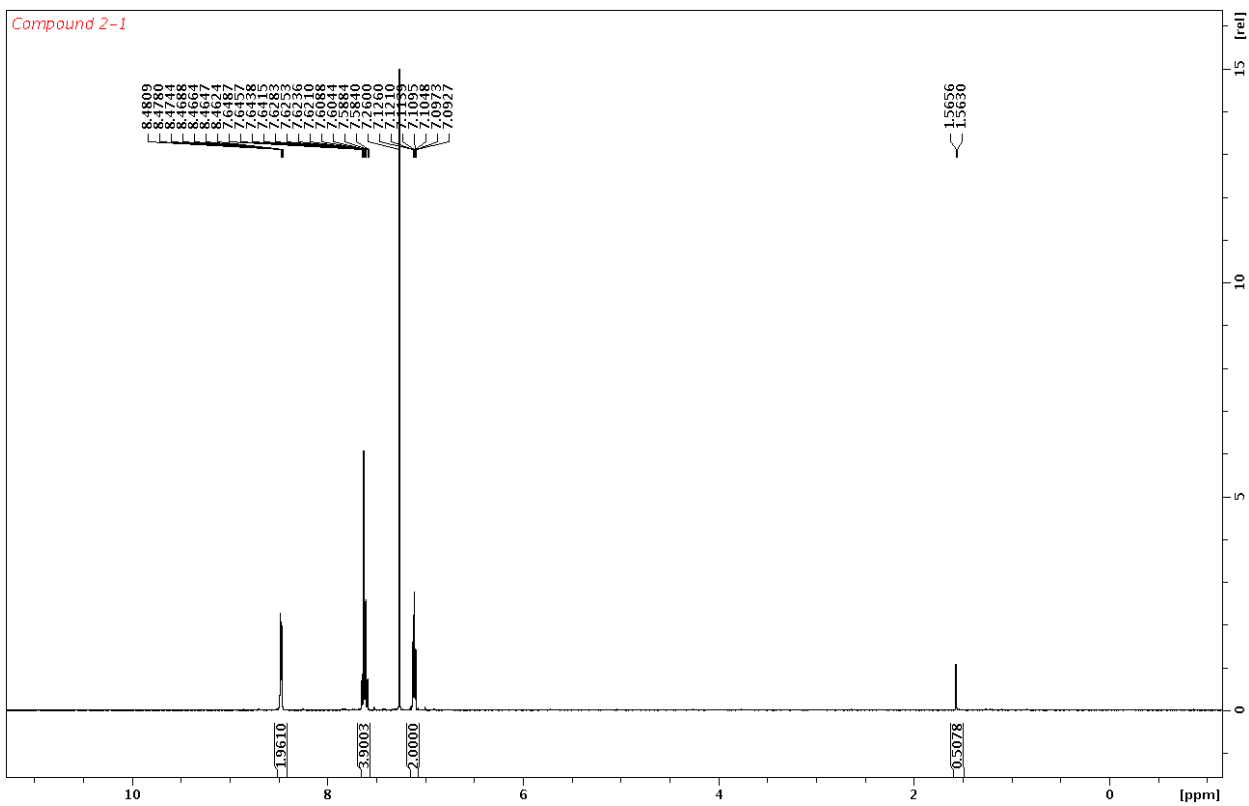


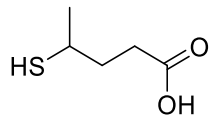


Appendix Chapter 2 NMR Spectra:

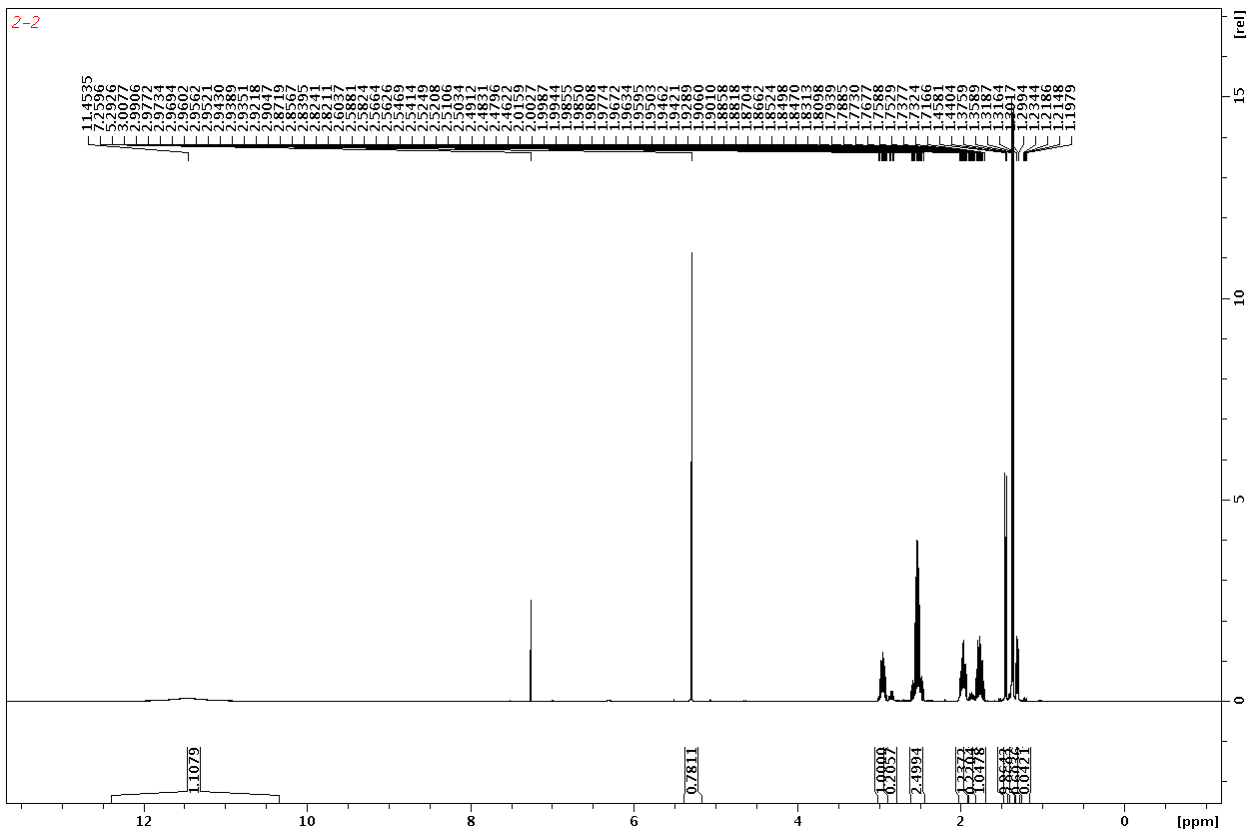


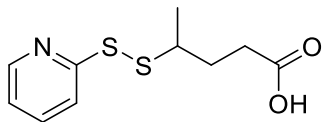
2-1



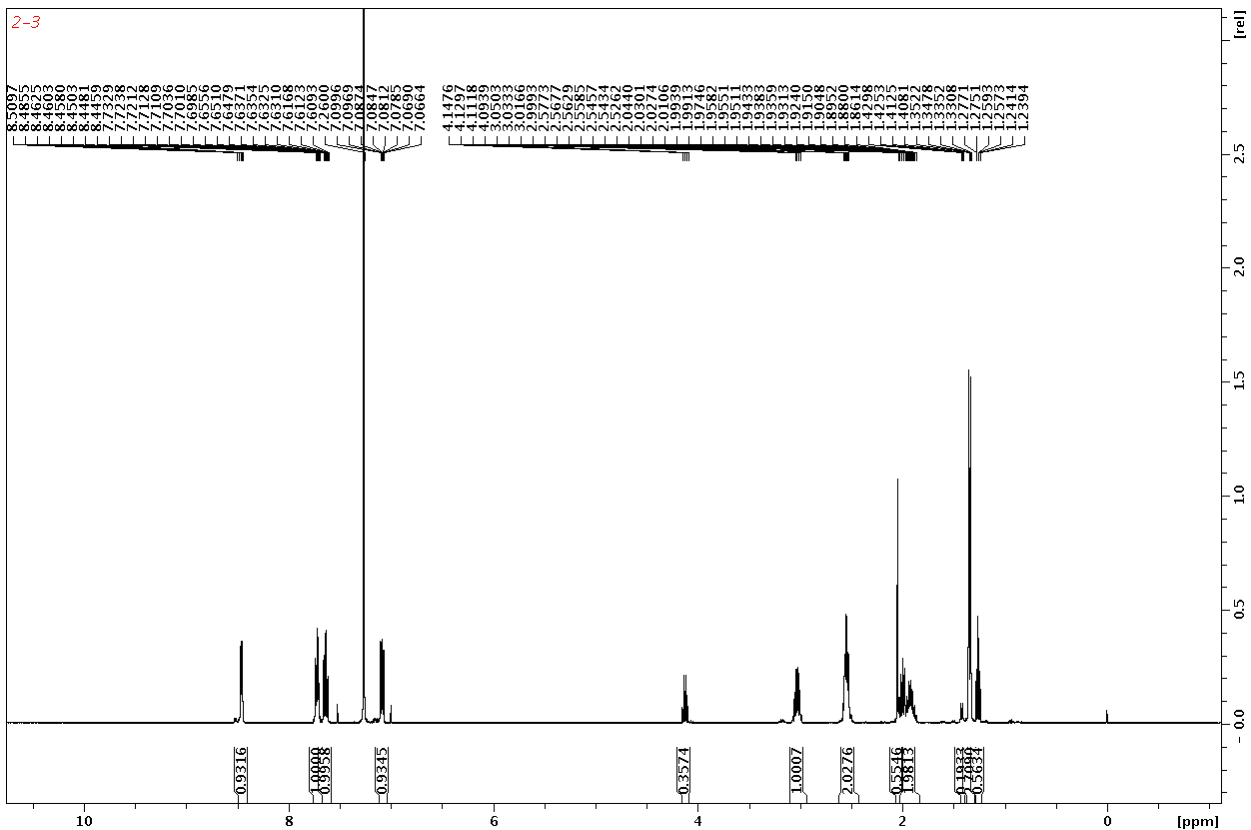


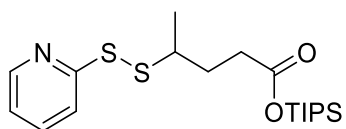
2-2



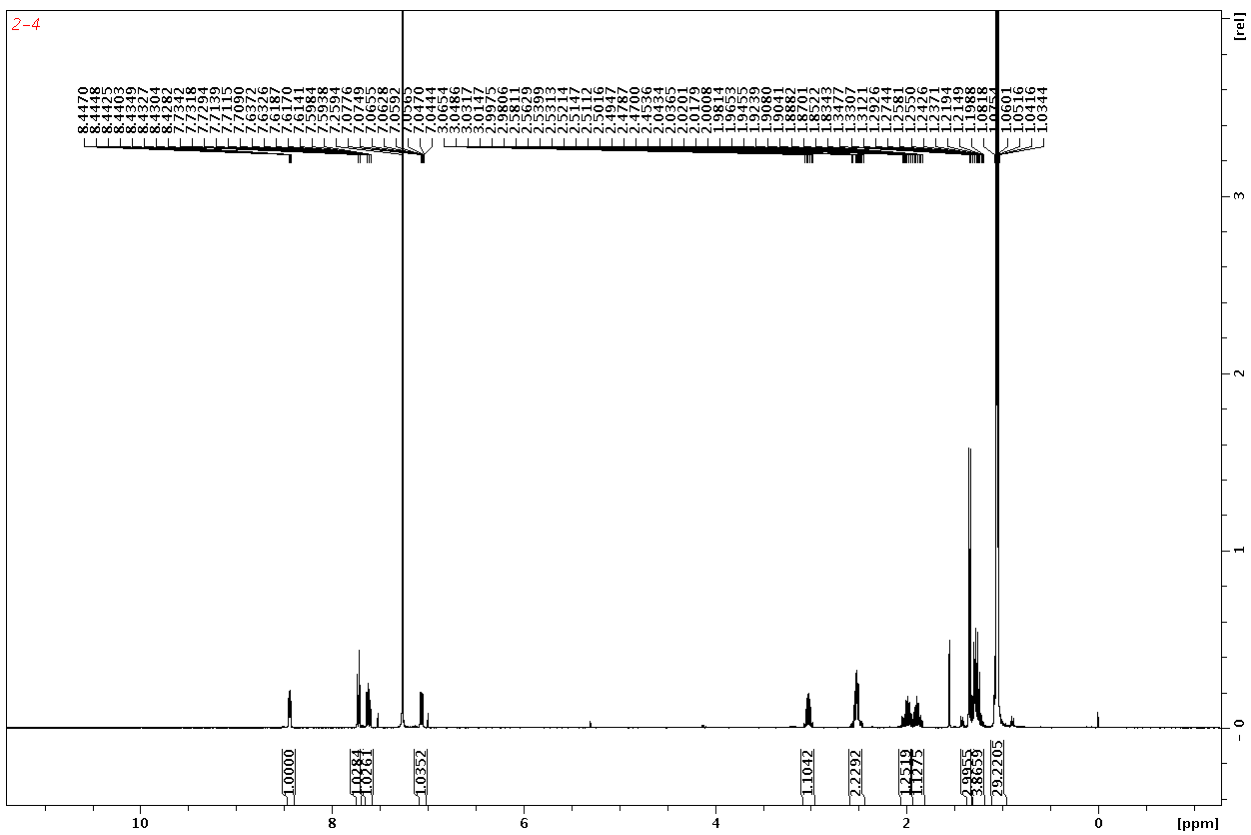


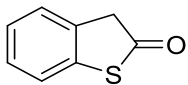
2-3





2-4

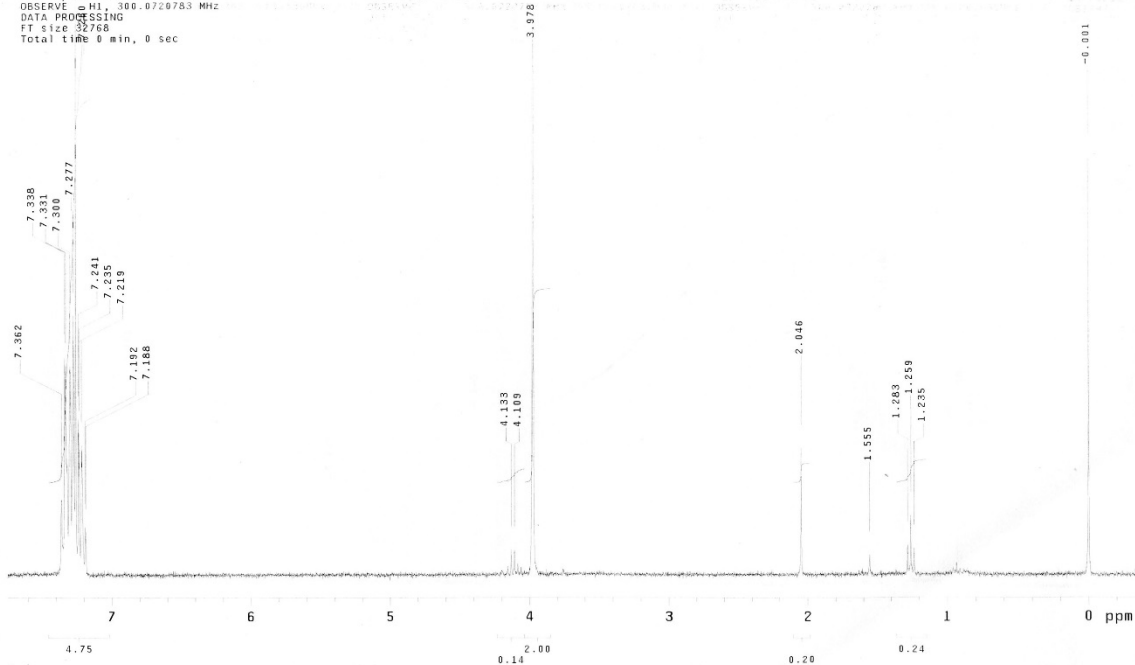
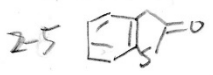


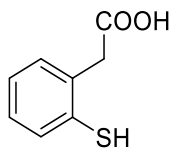


2-5

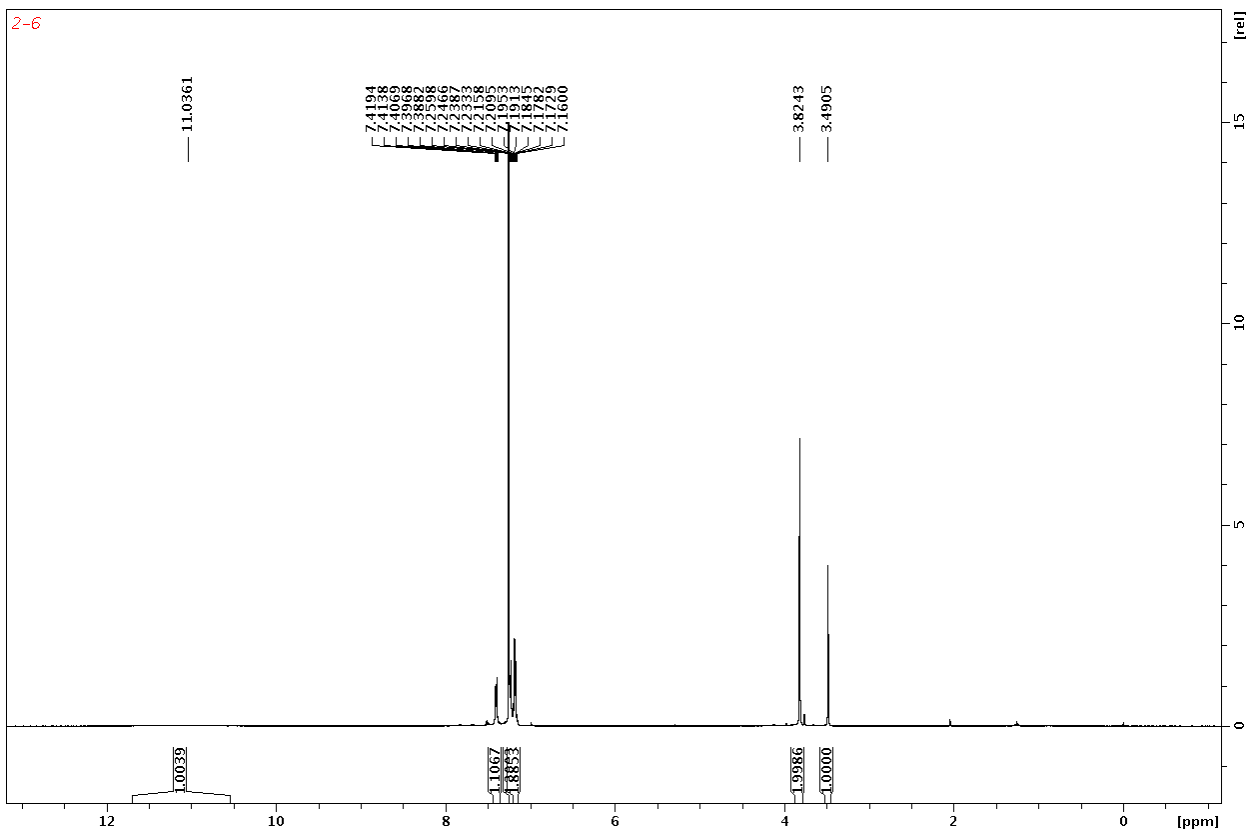
new experiment
 Pulse Sequence: zgpg30
 Solvent: CDCl3
 Temp: 25.0 C / 298.1 K
 GEMINI-500EB "gem2500"

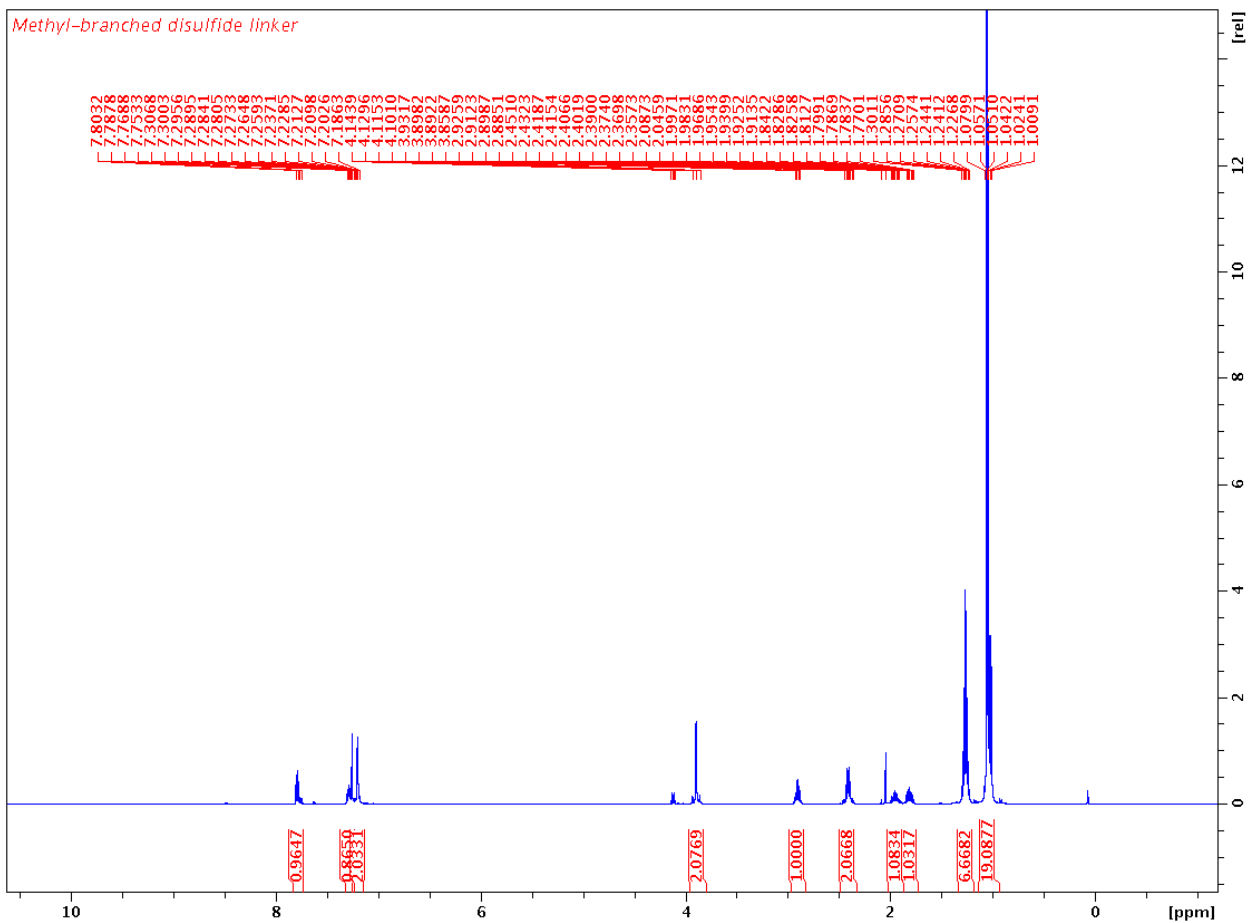
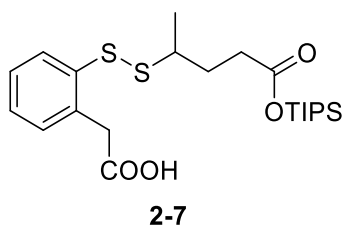
Relax. delay 1.000 sec
 Pulse 7.8 degrees
 Acq. time 1.998 sec
 Width 4500.5 Hz
 16 repetitions
 OBSERVE c H1, 300.0720783 MHz
 DATA PROCESSING
 FT size 32768
 Total time 0 min, 0 sec



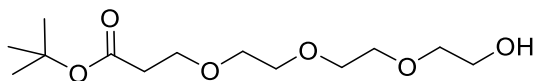


2-6

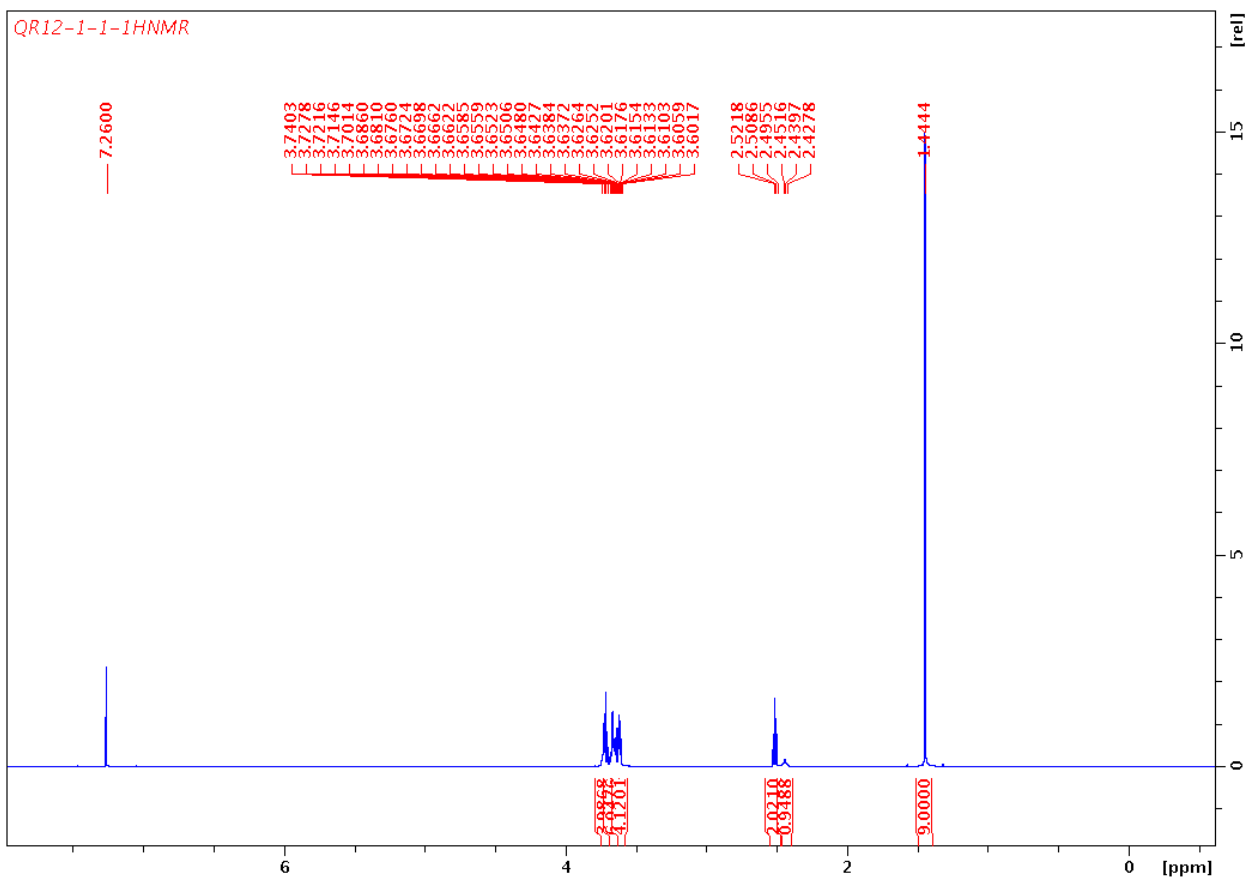


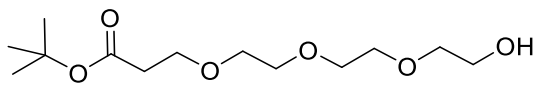


Appendix Chapter 3 NMR Spectra:

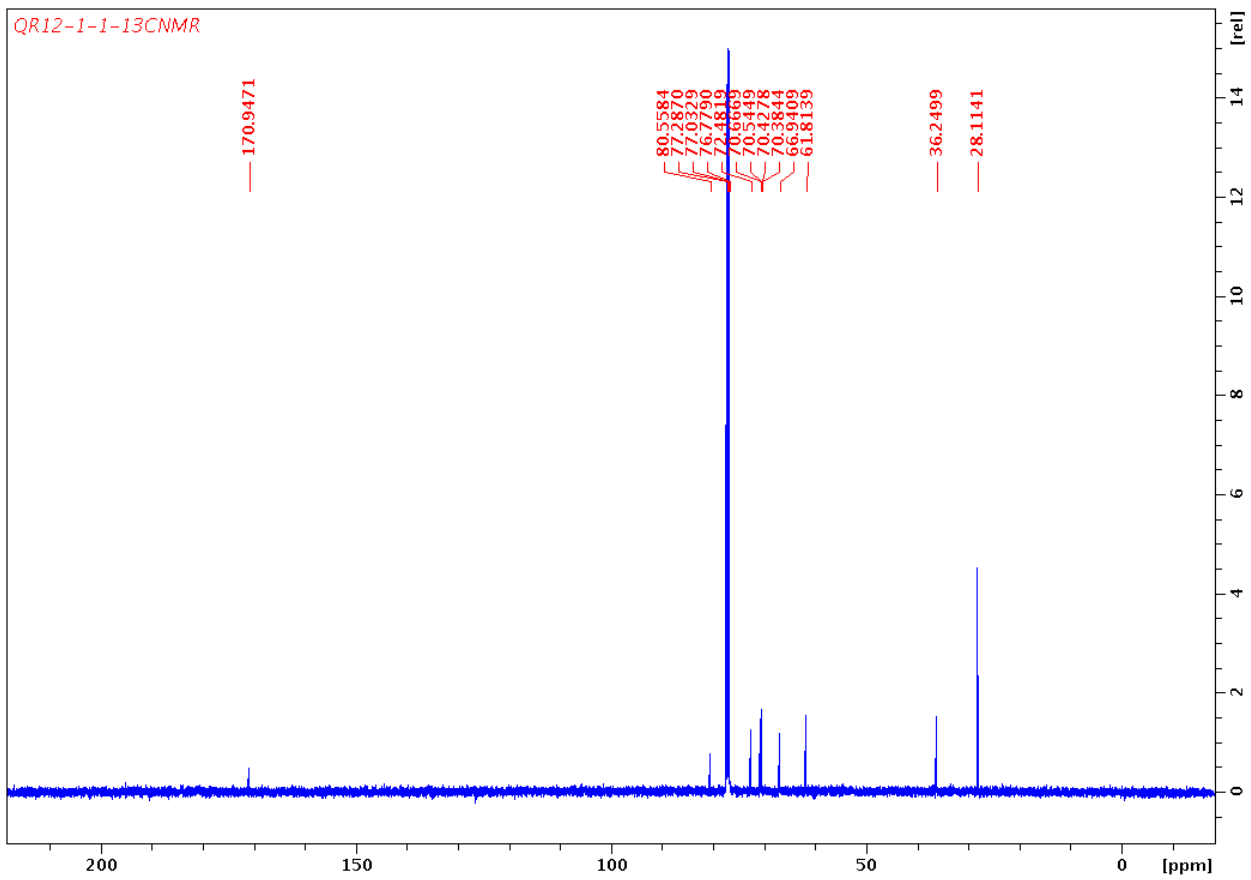


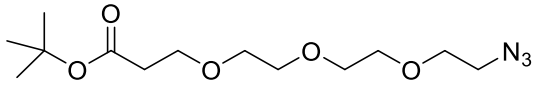
3-1



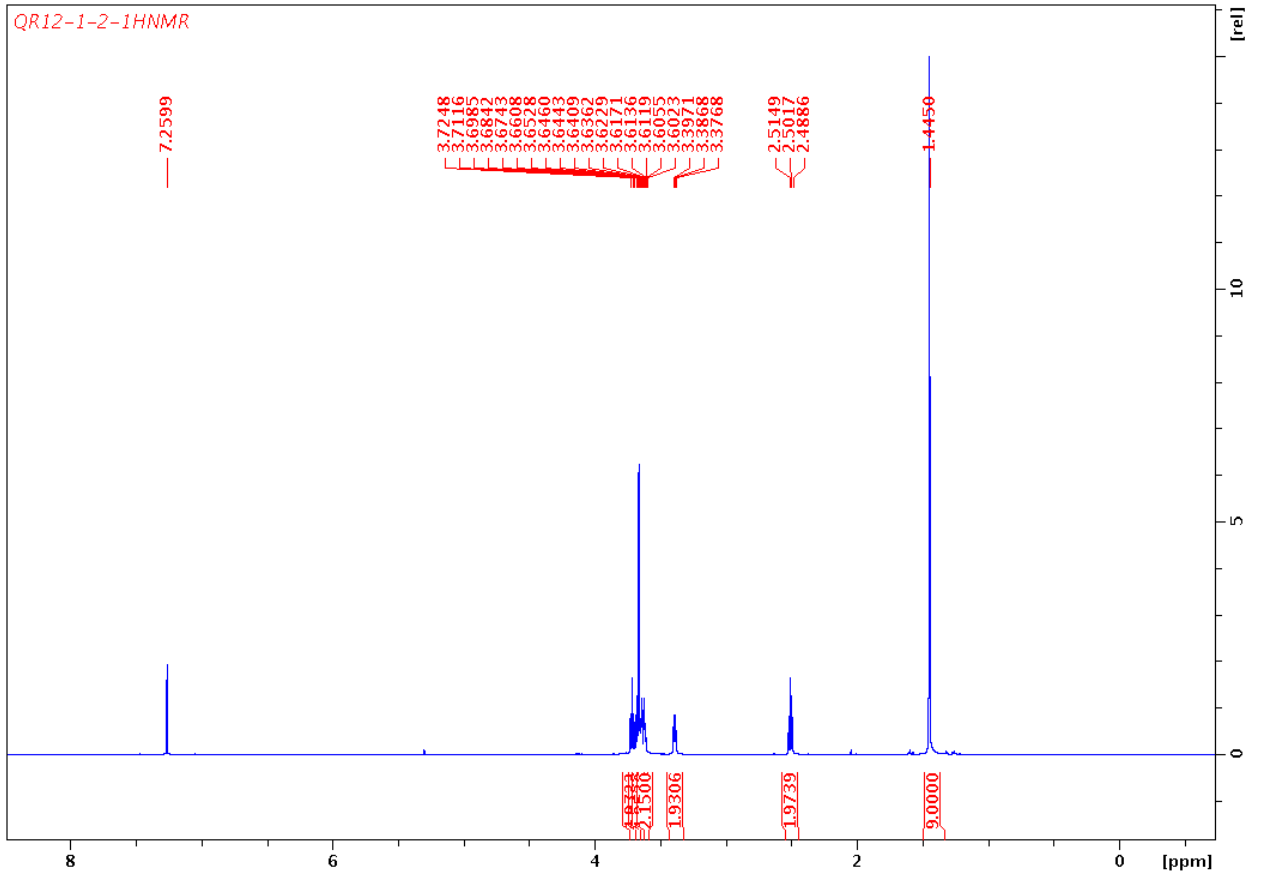


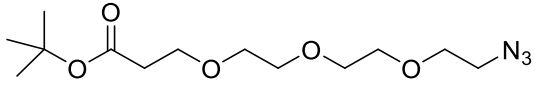
3-1



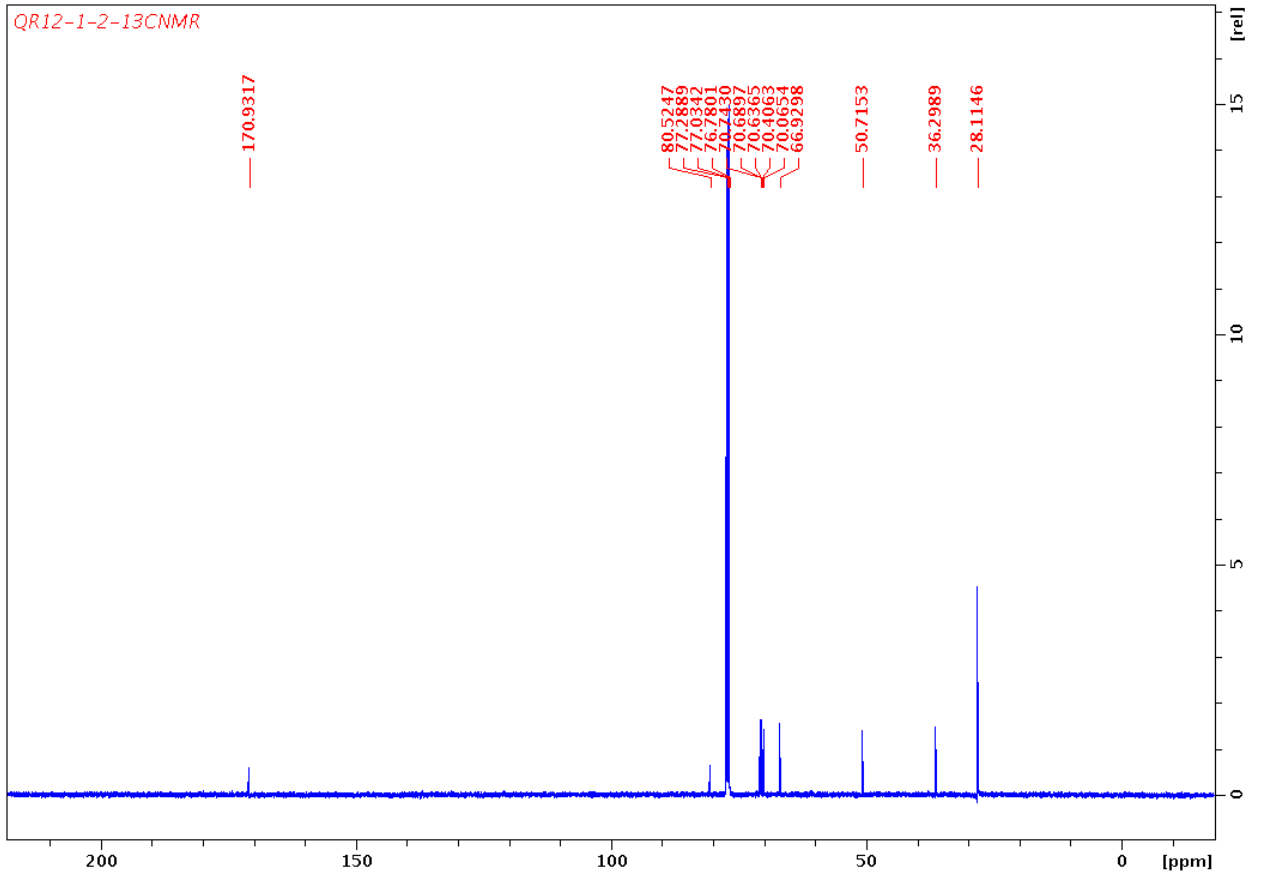


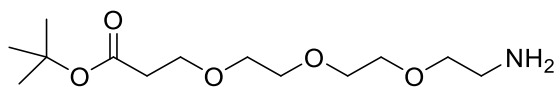
3-2



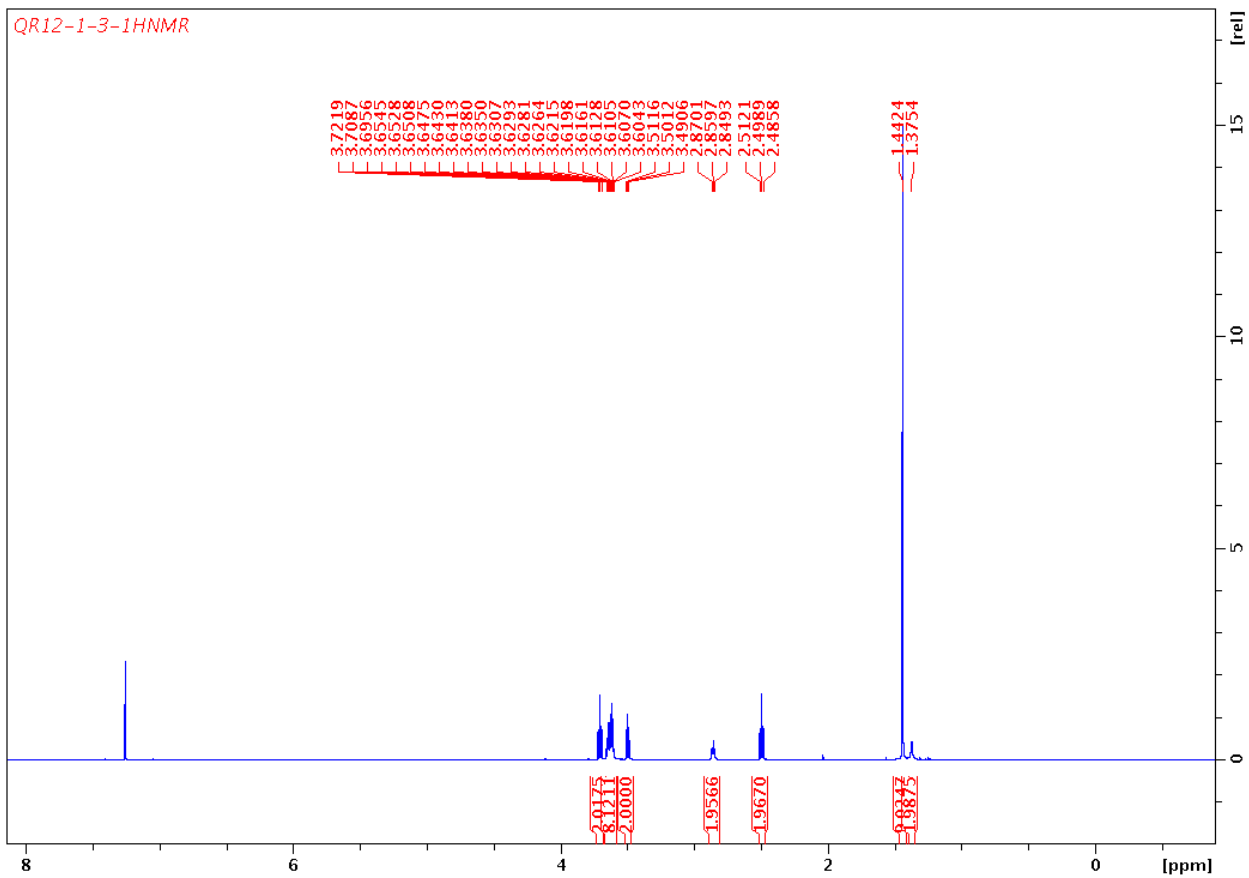


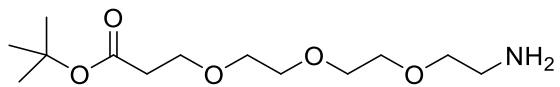
3-2



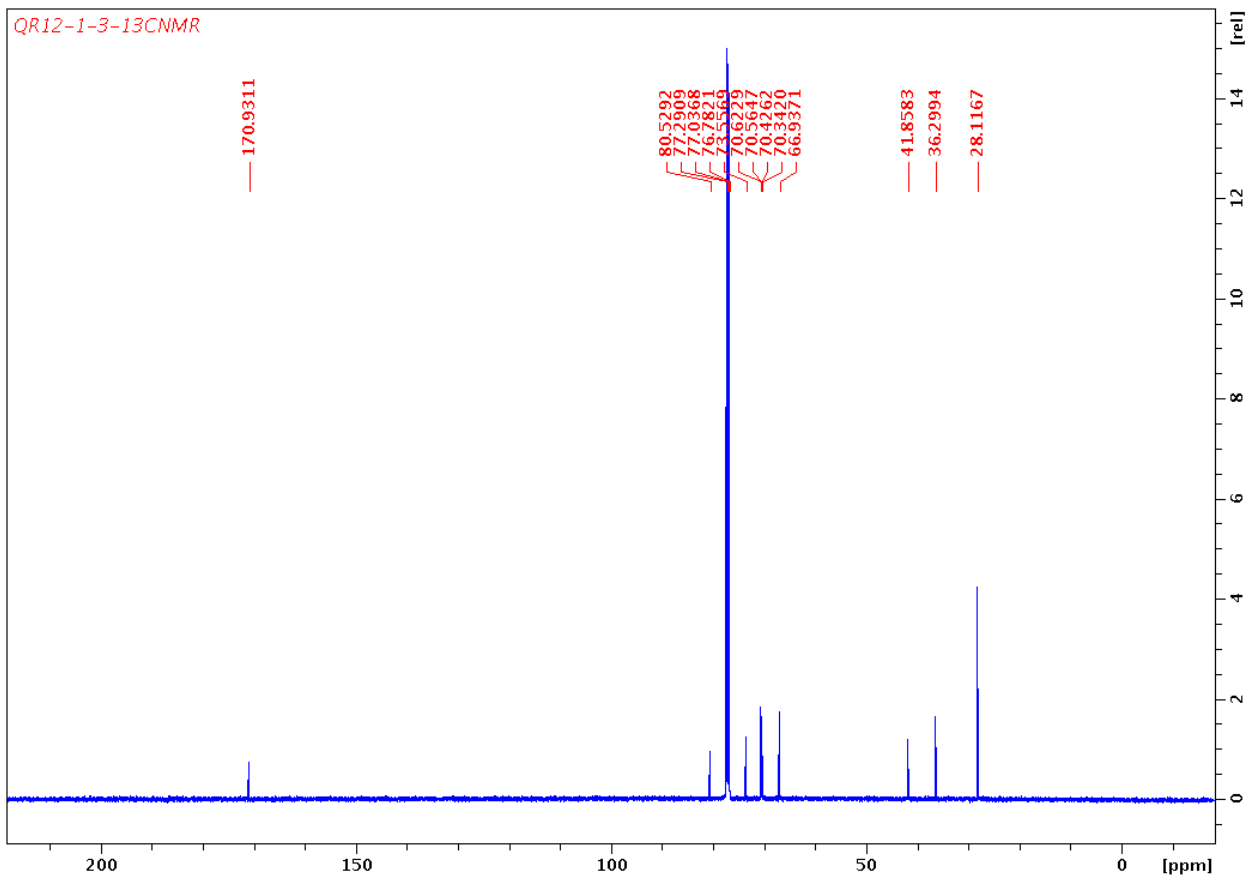


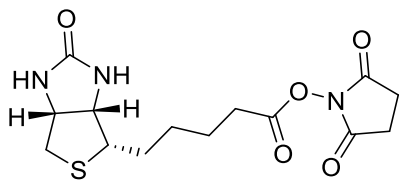
3-3



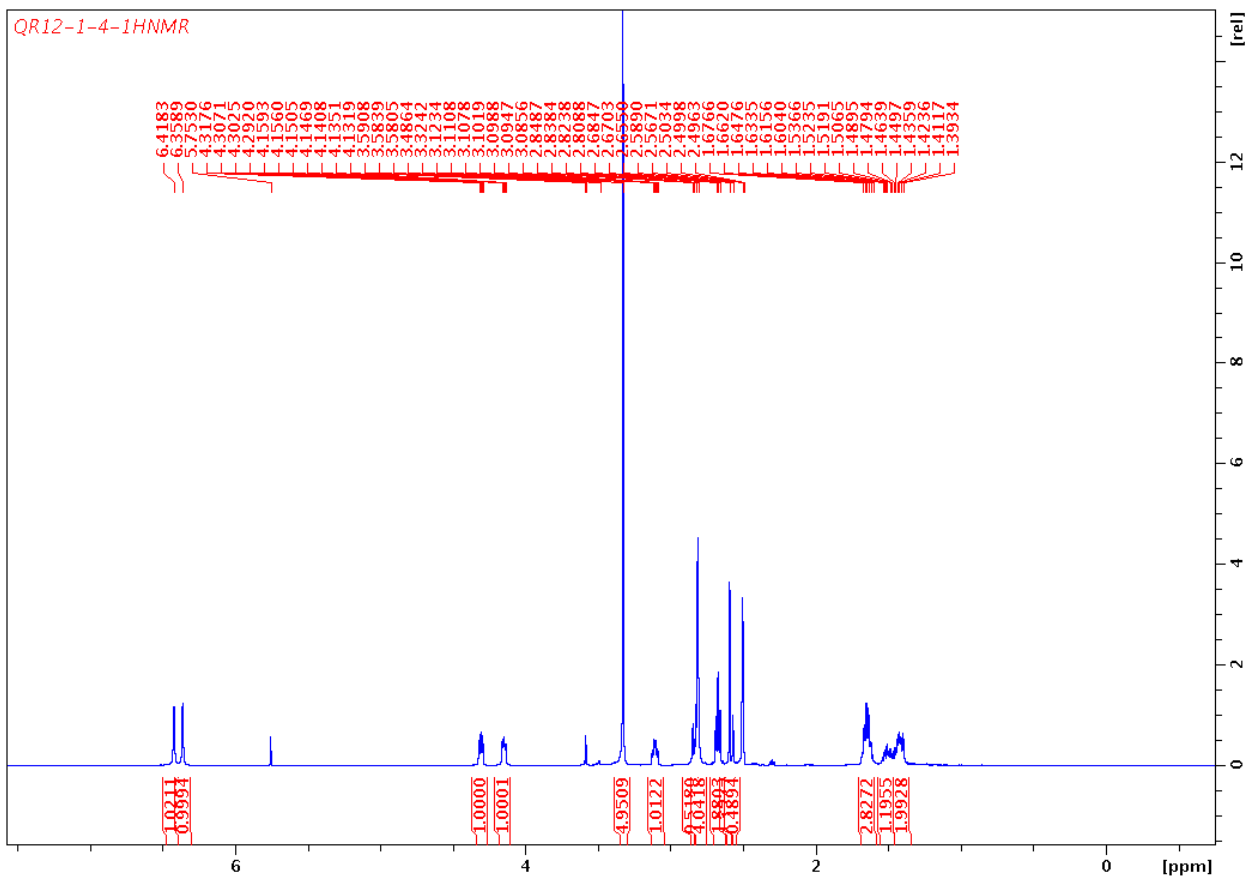


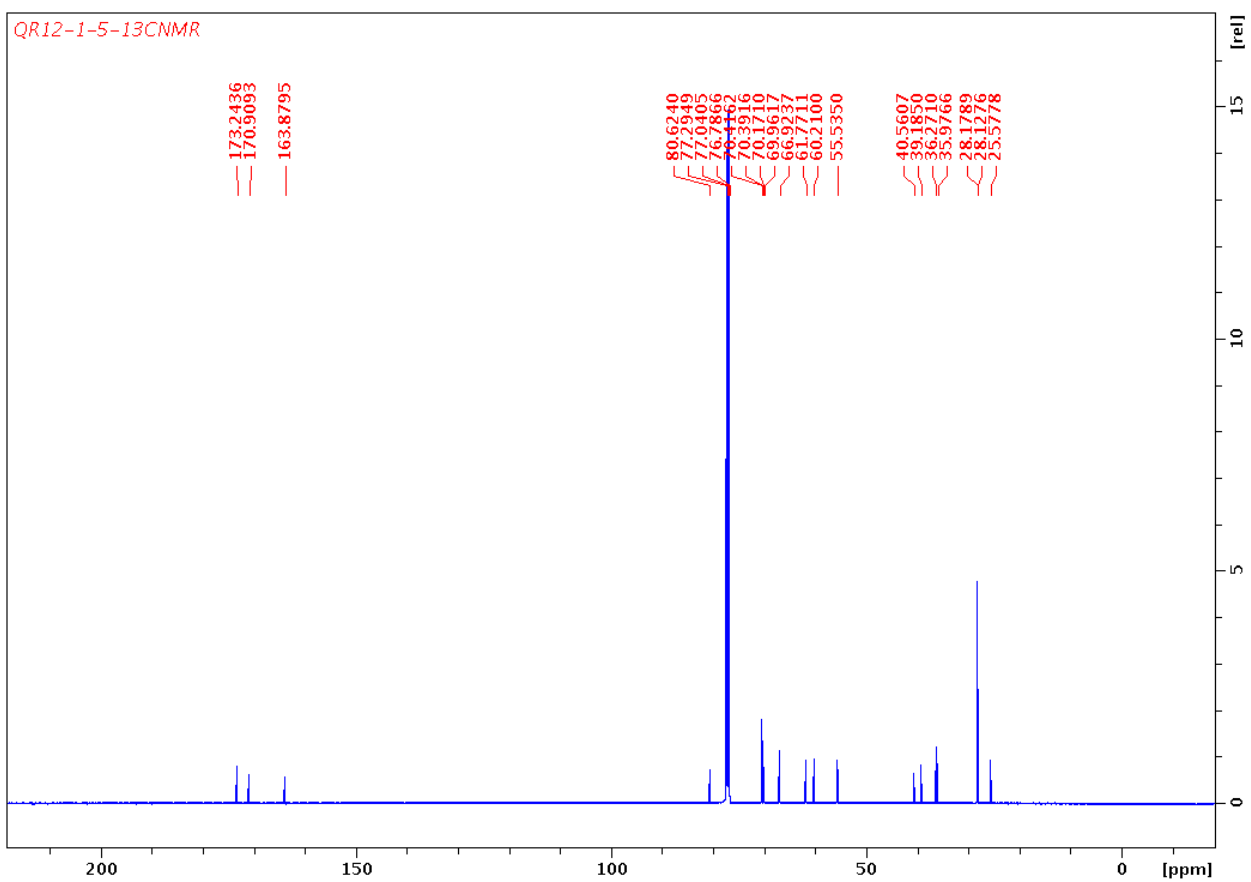
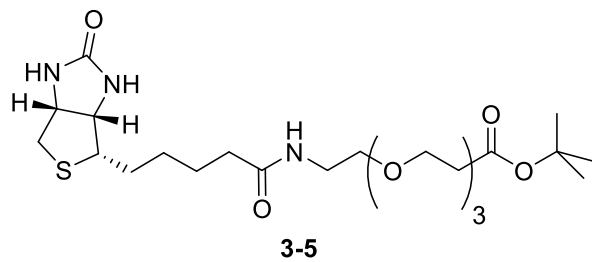
3-3

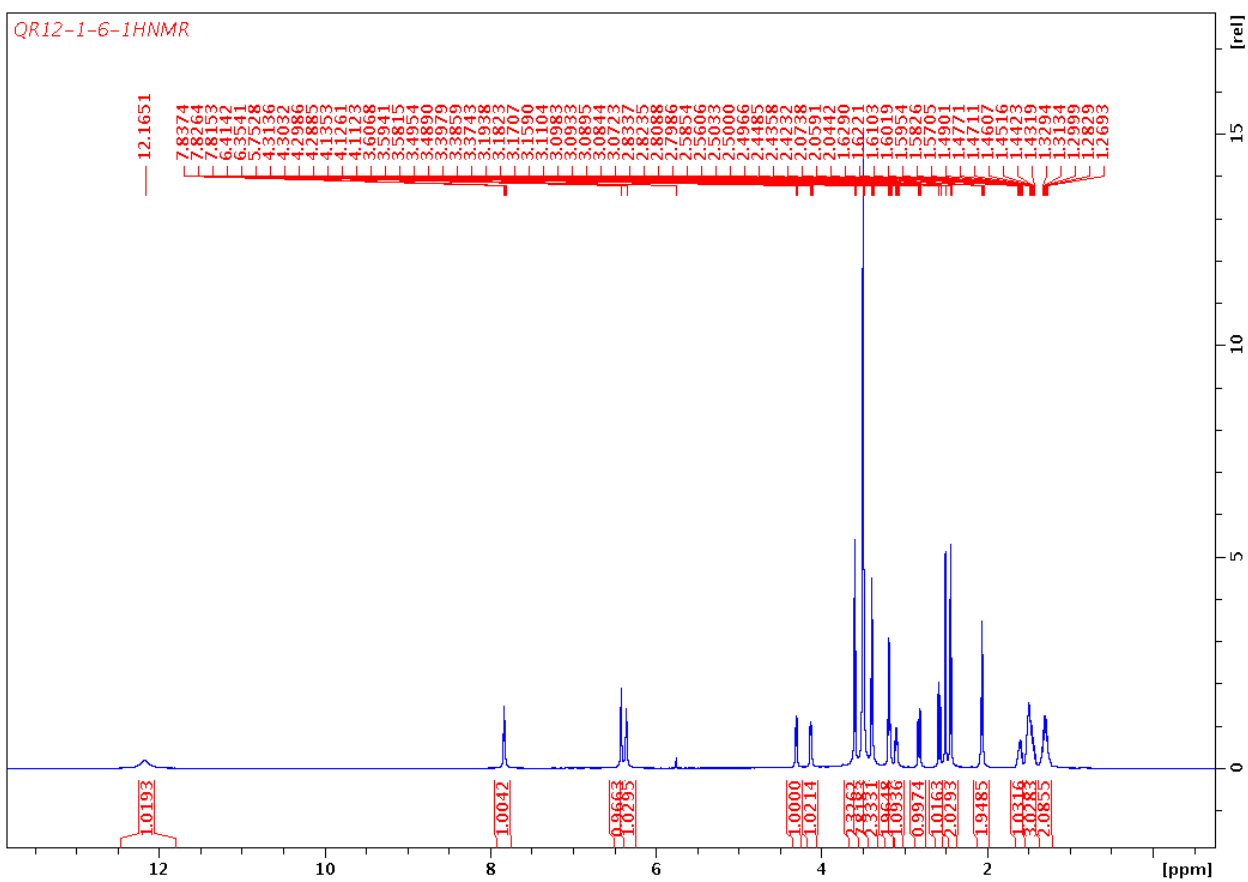
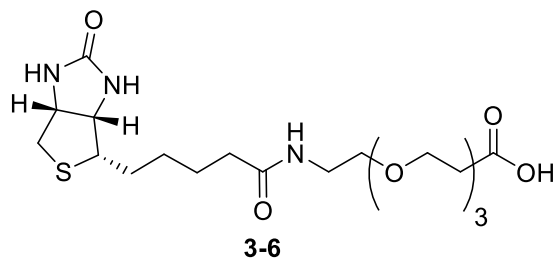


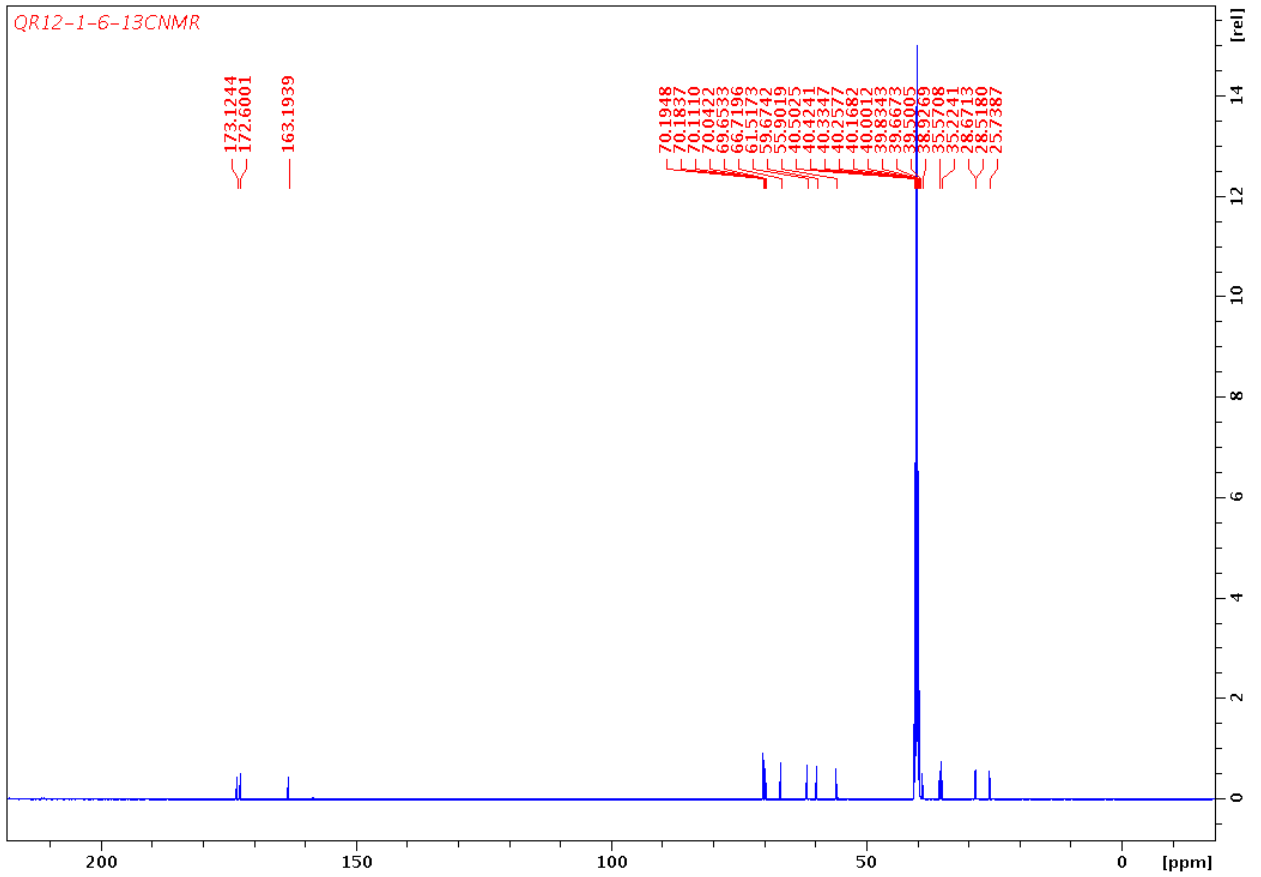
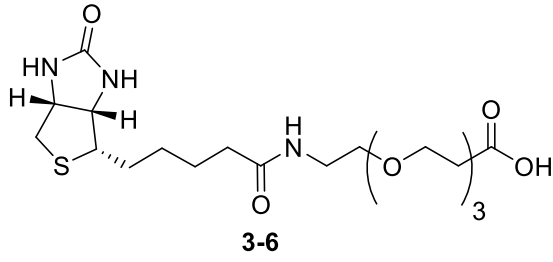


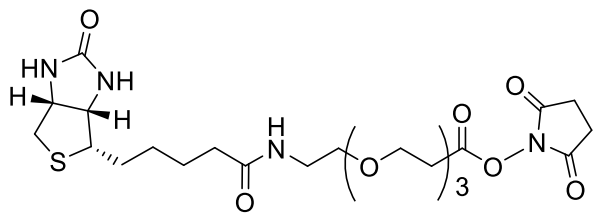
3-4



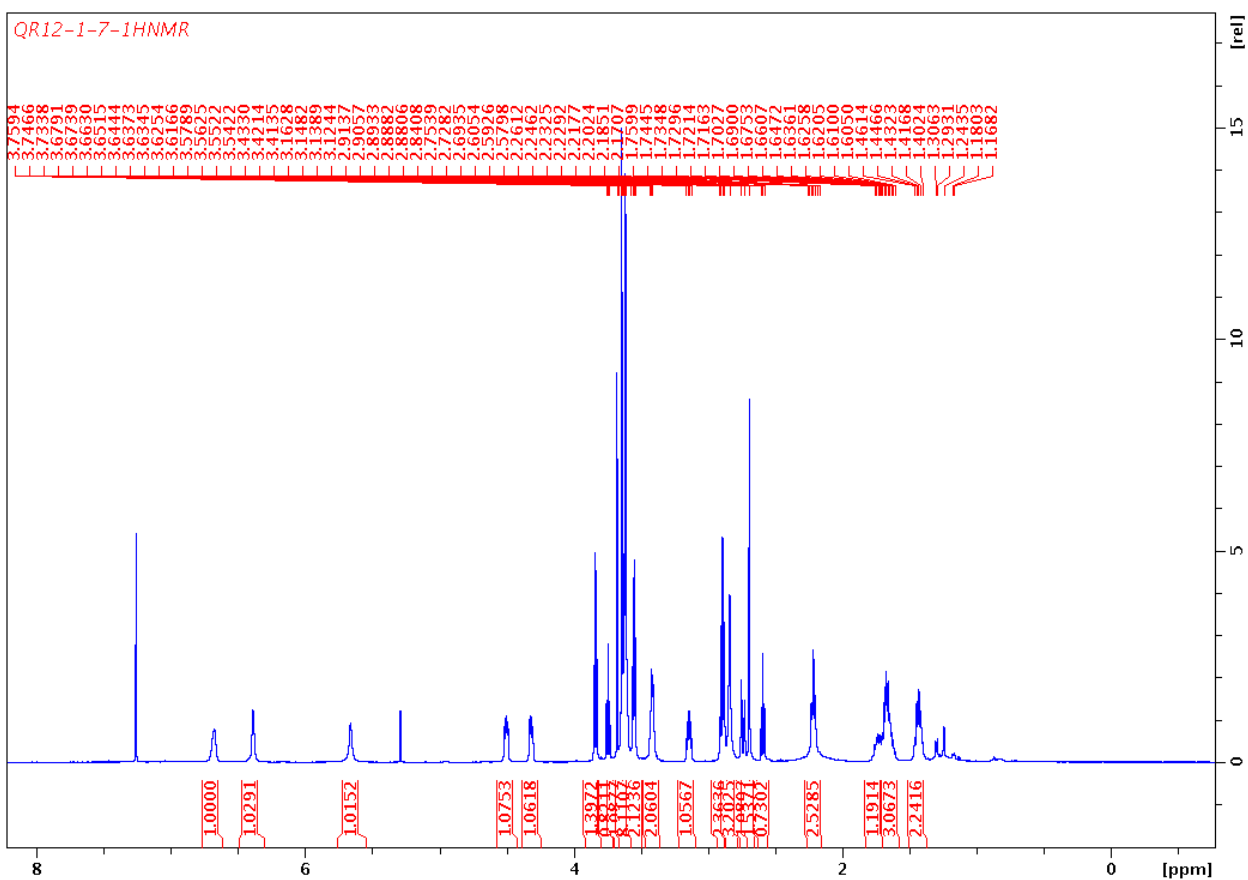


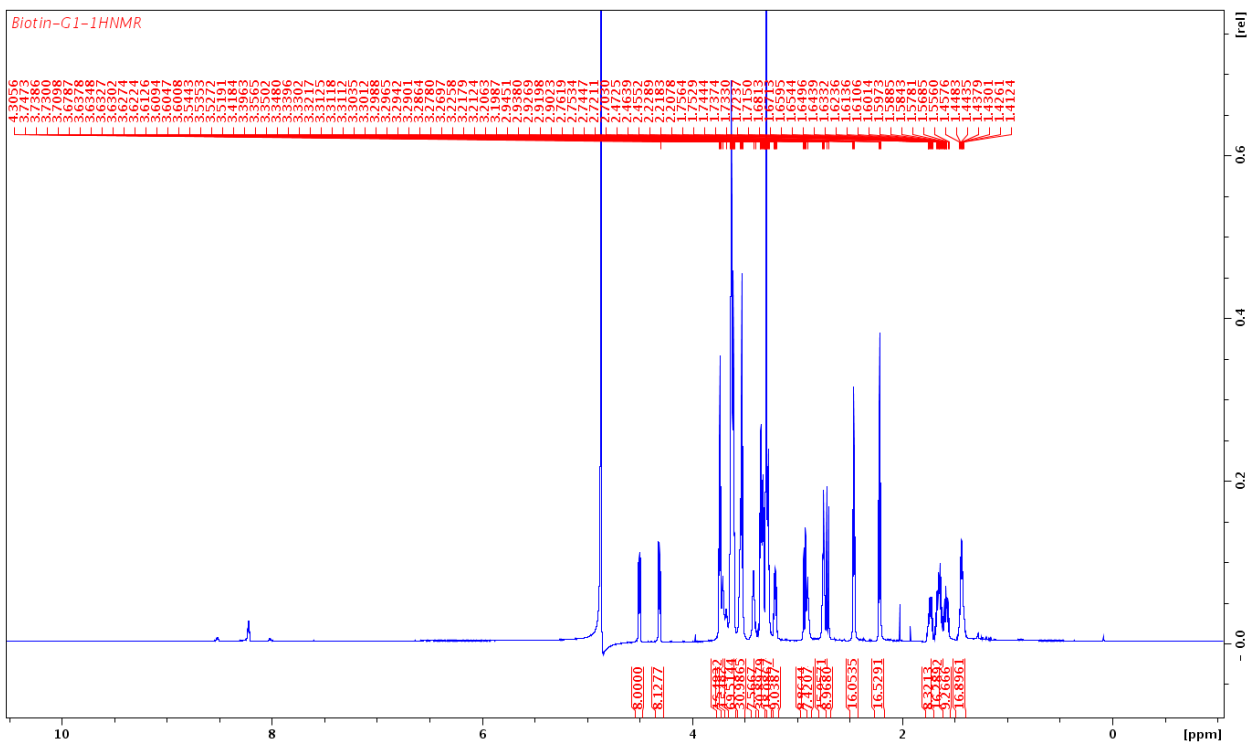
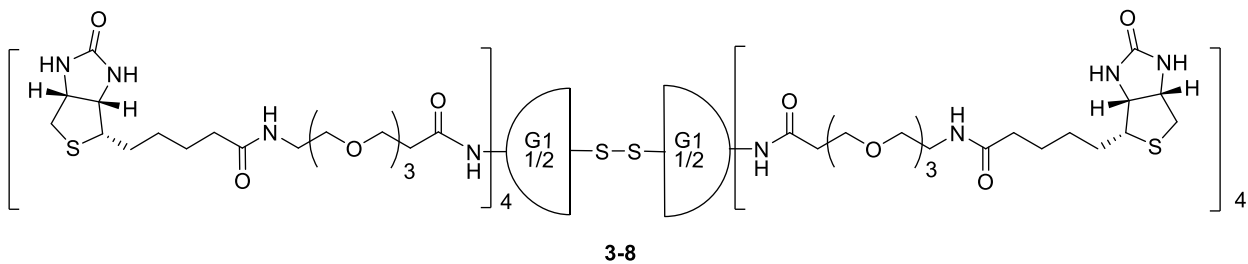


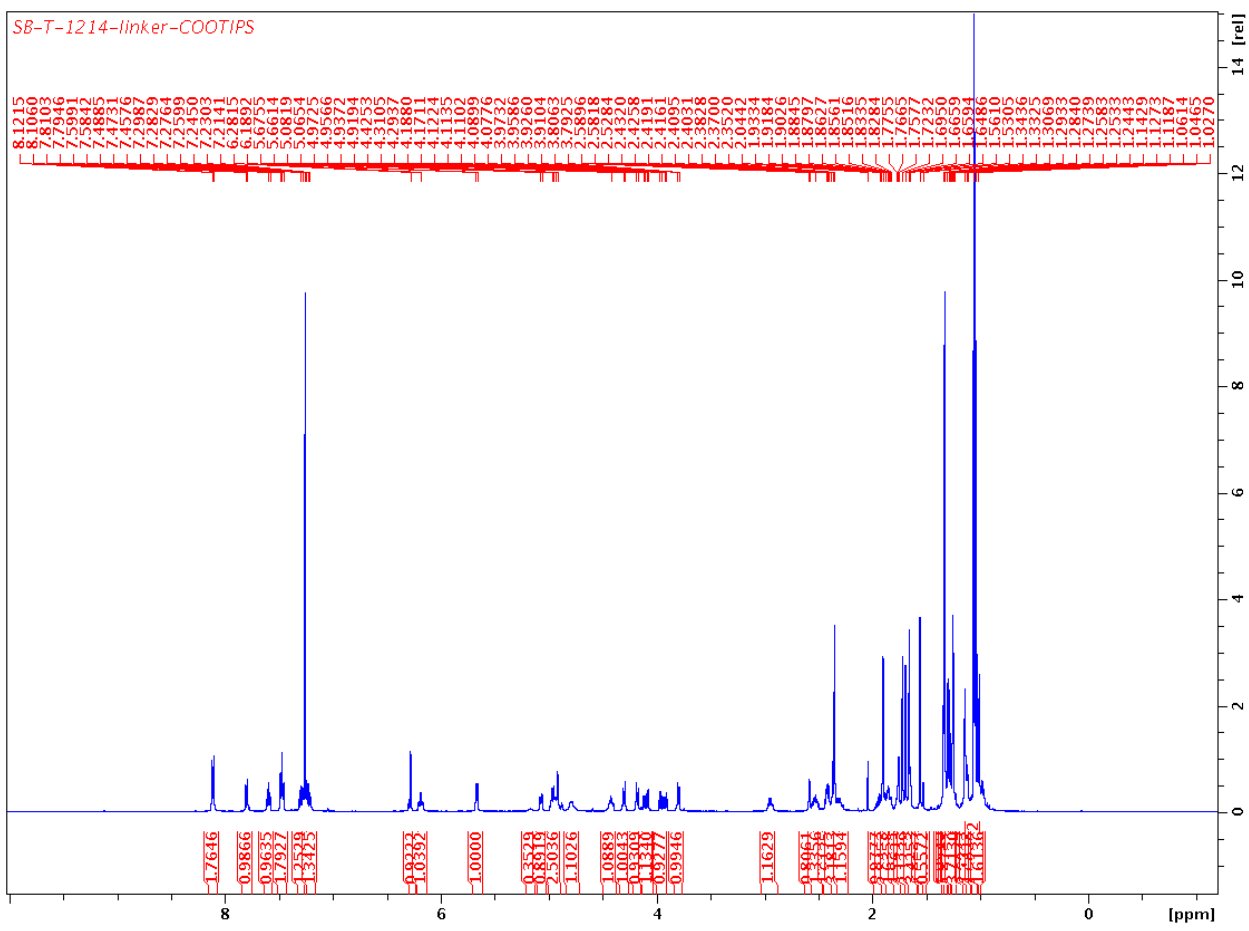
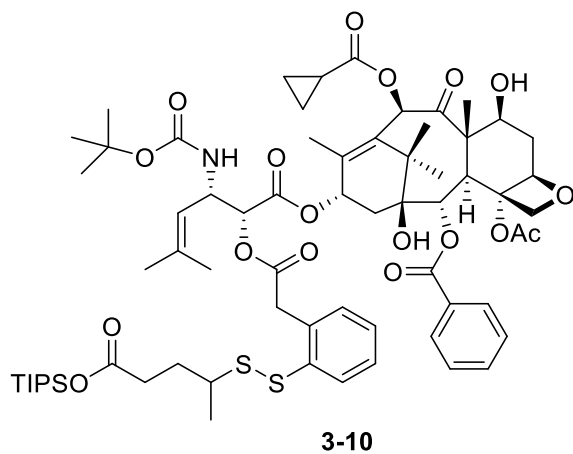


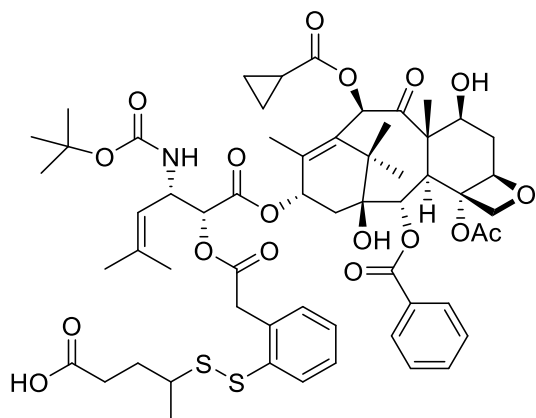


3-7

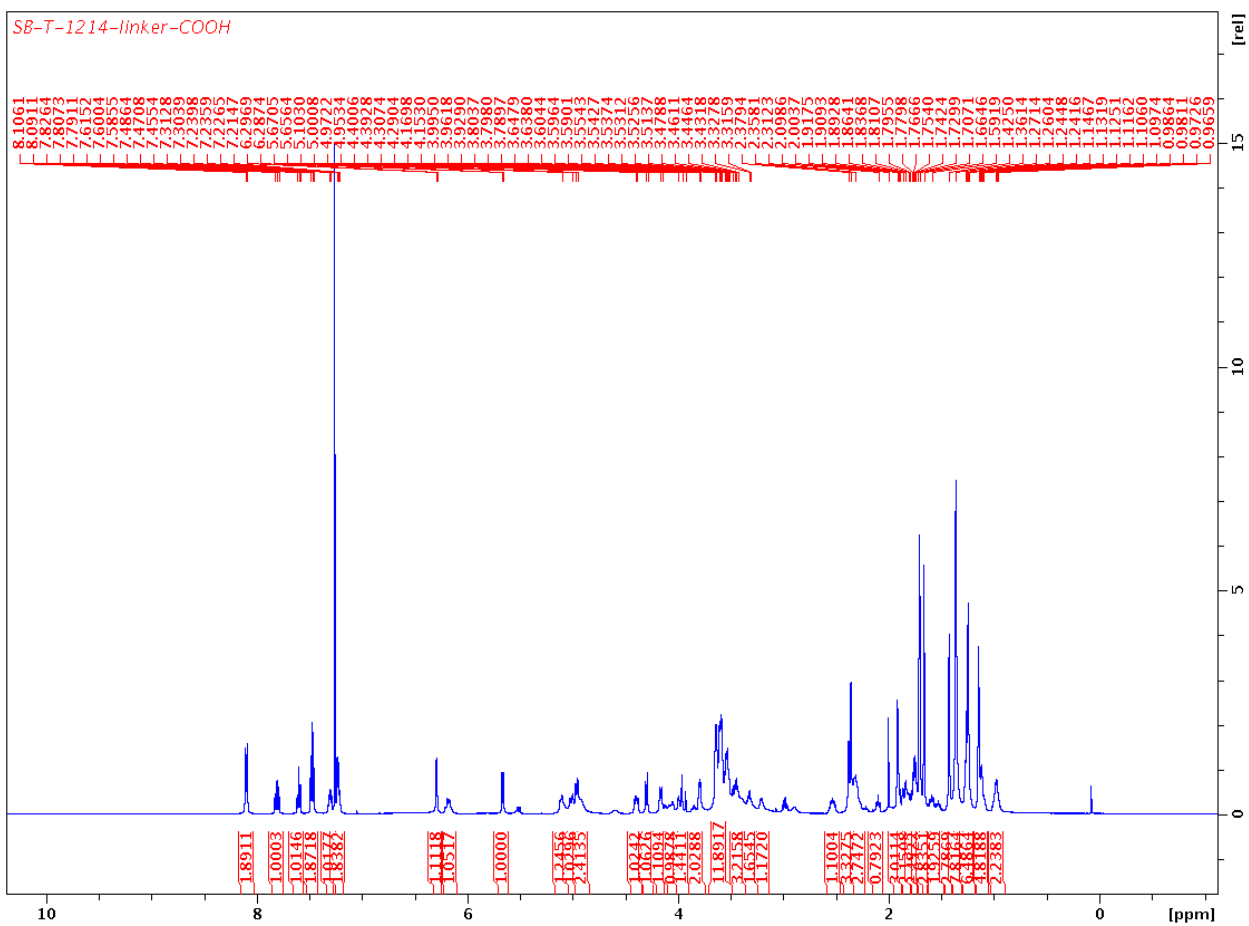


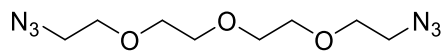






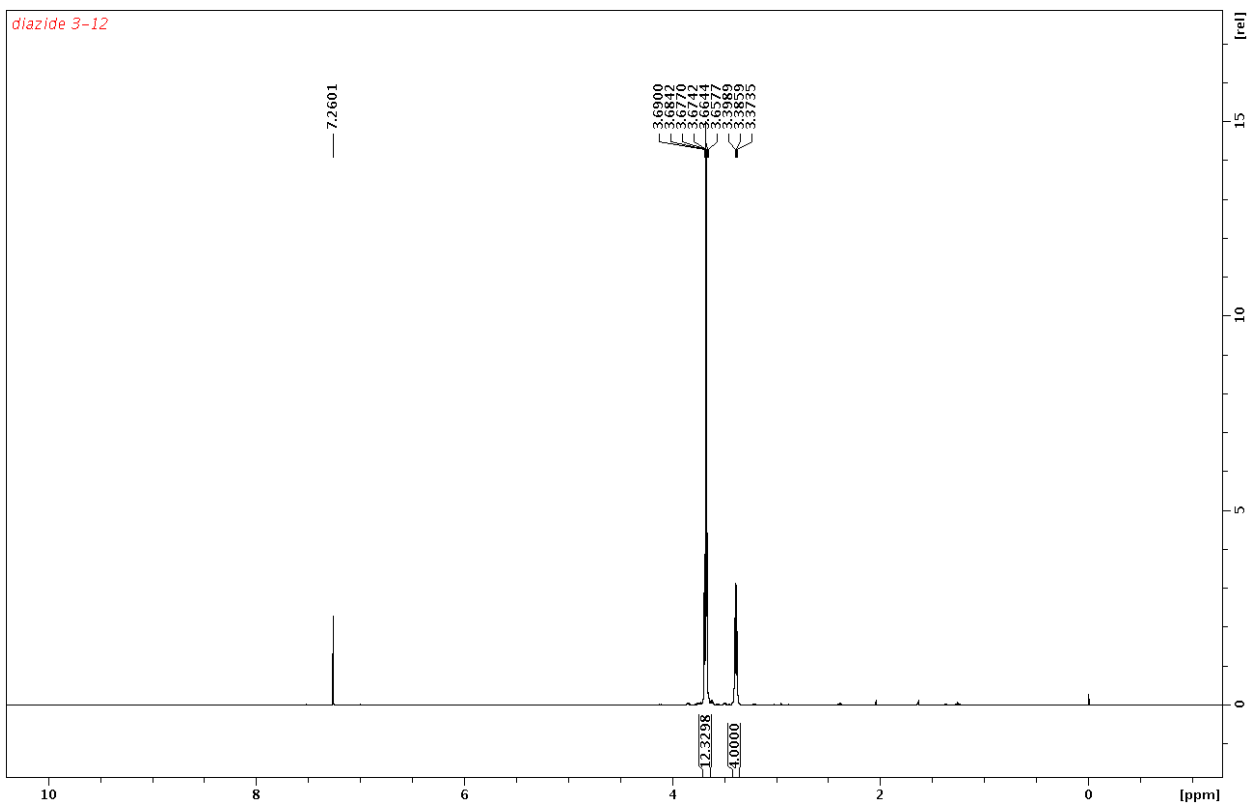
3-11

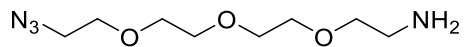




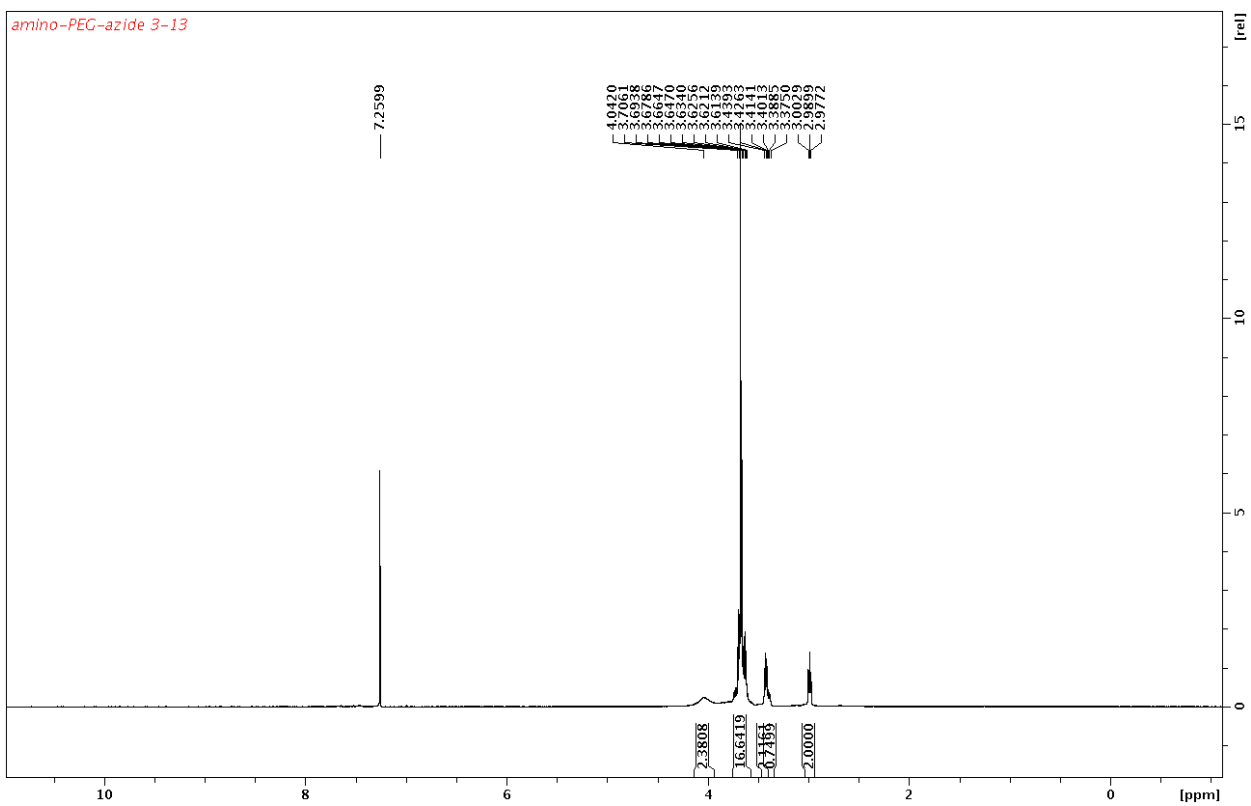
crude

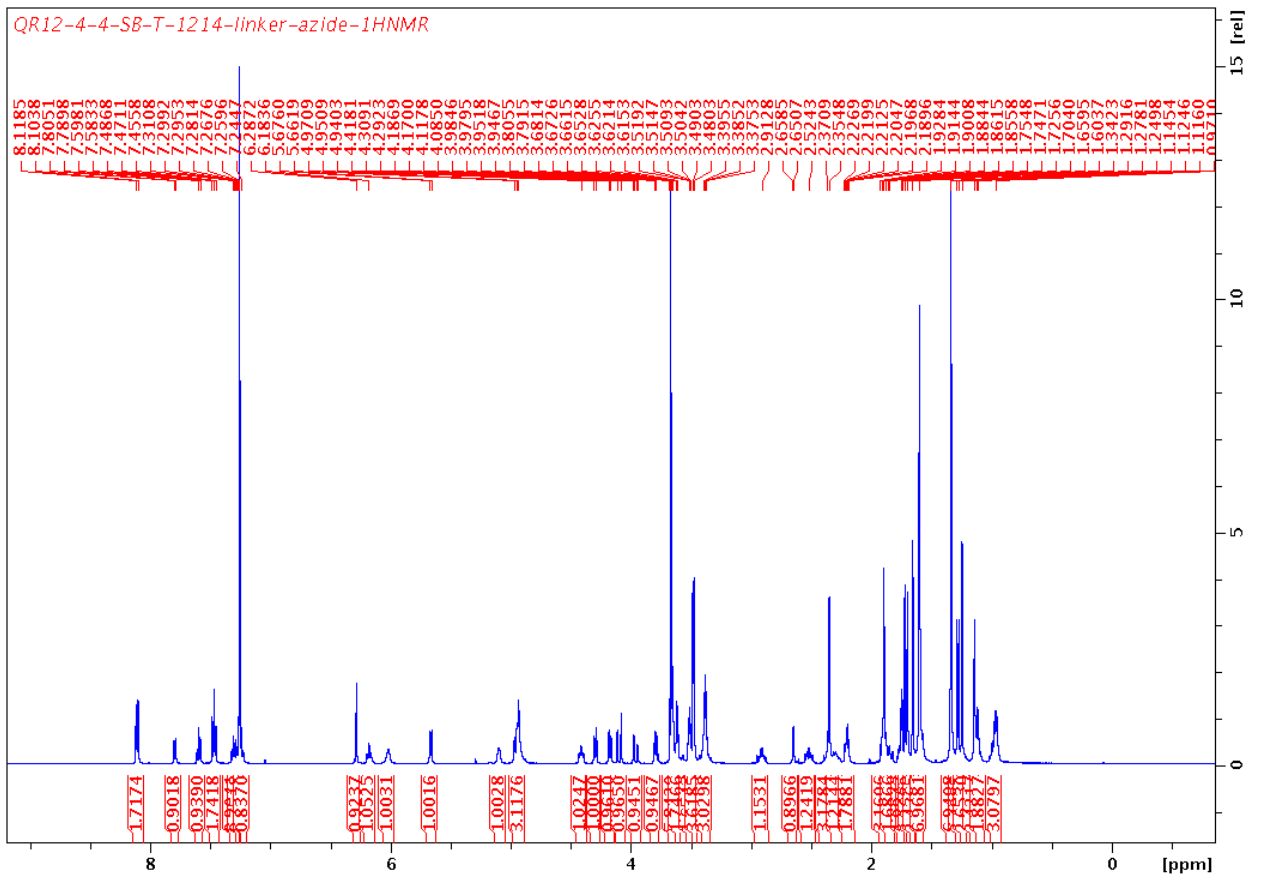
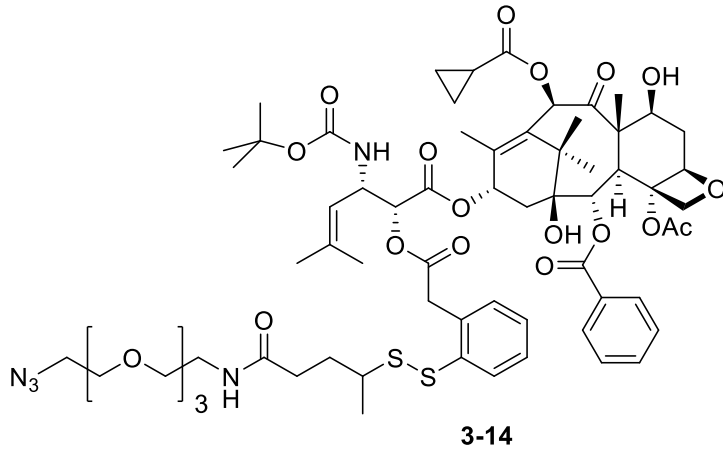
3-12

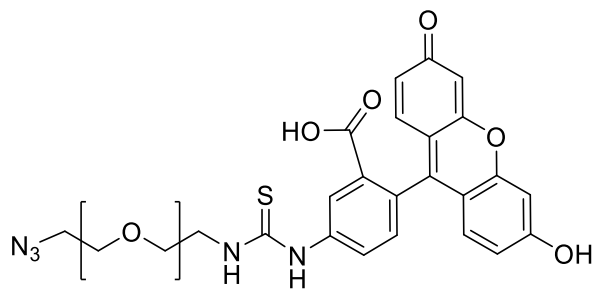




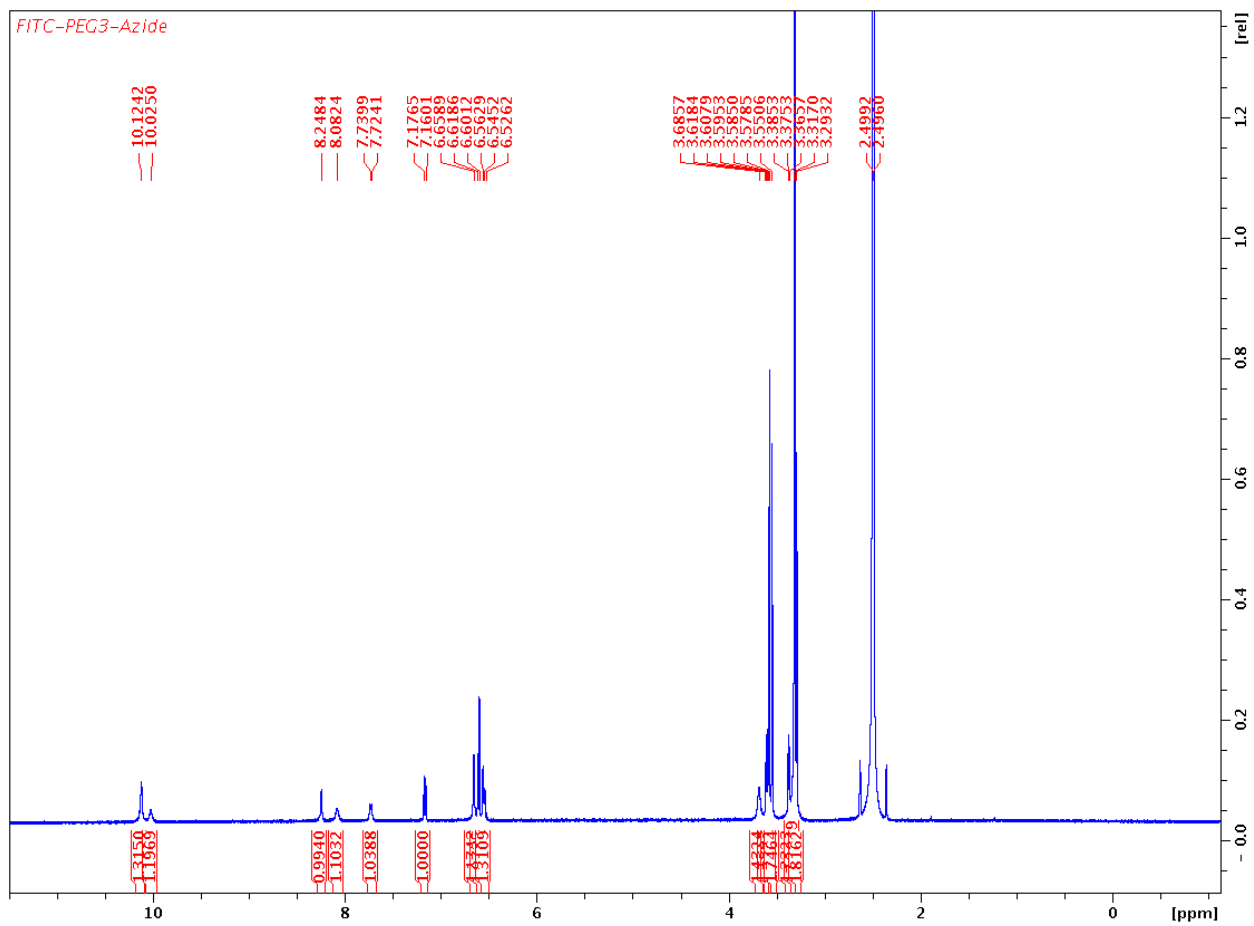
3-13

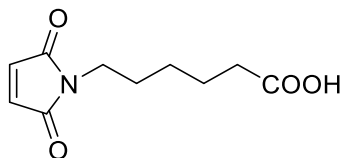




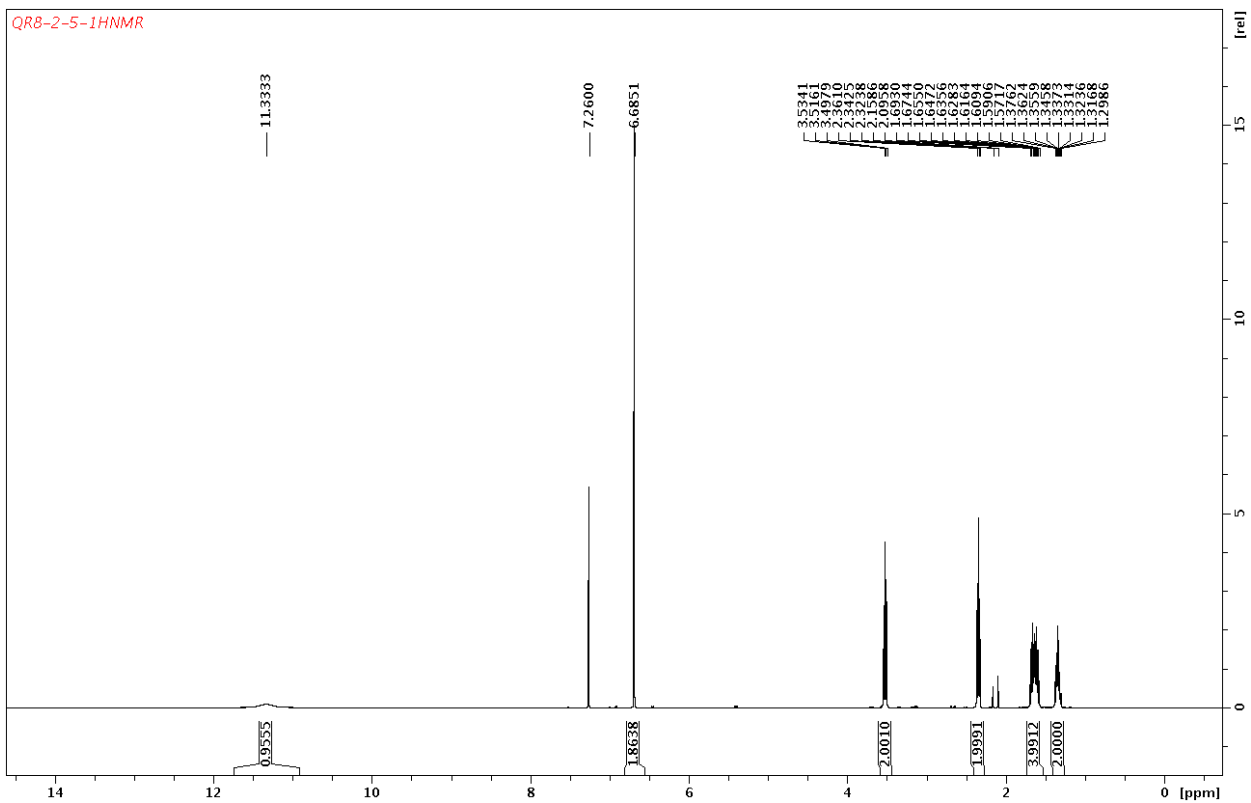


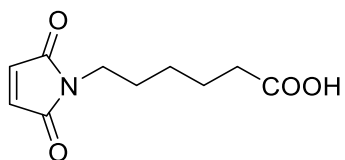
3-15



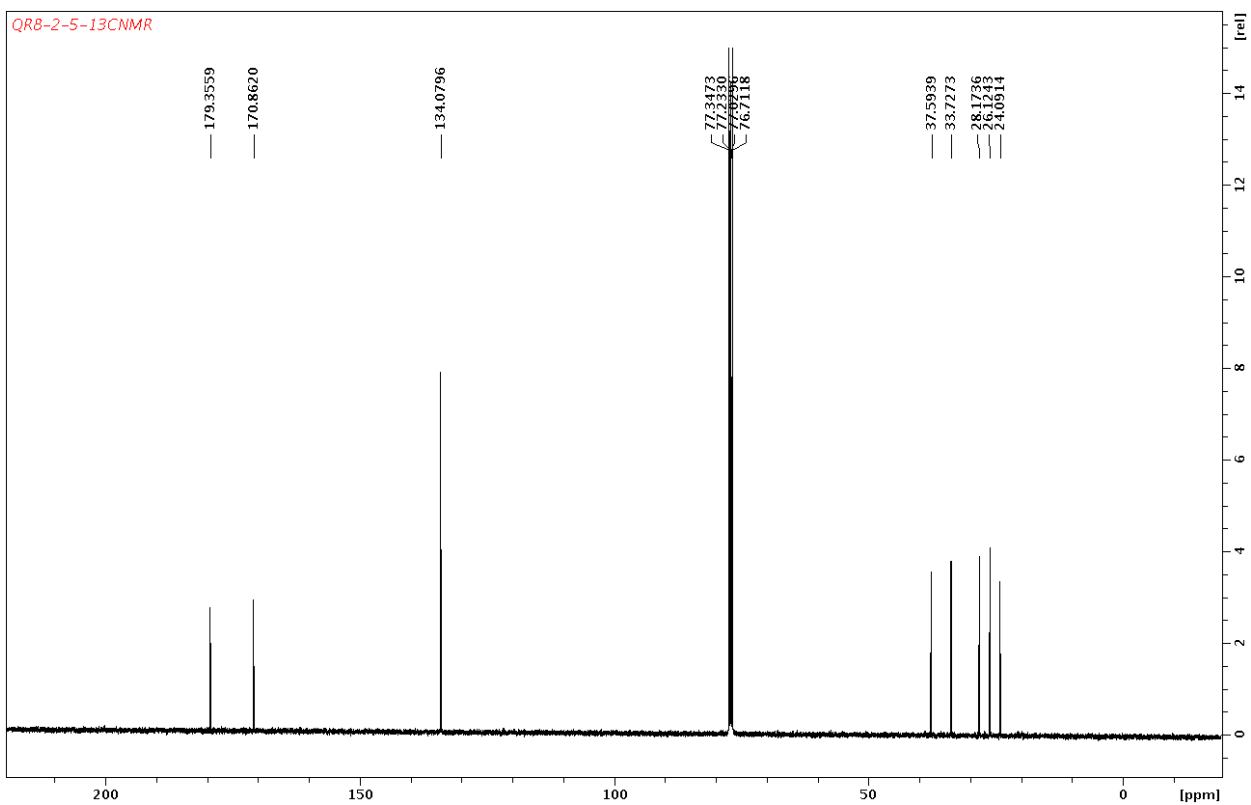


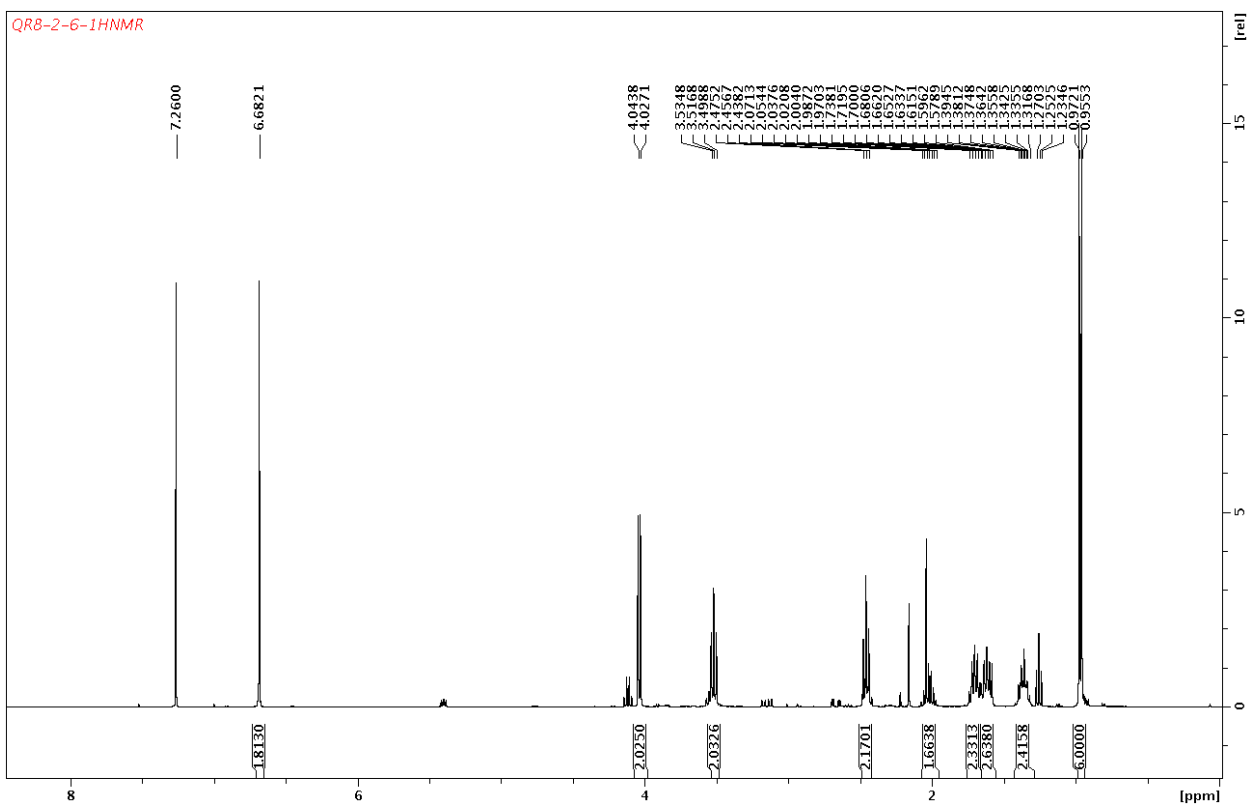
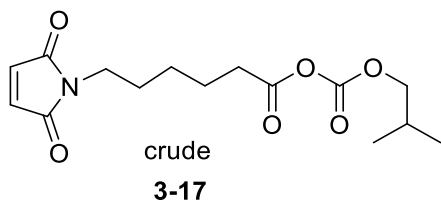
3-16

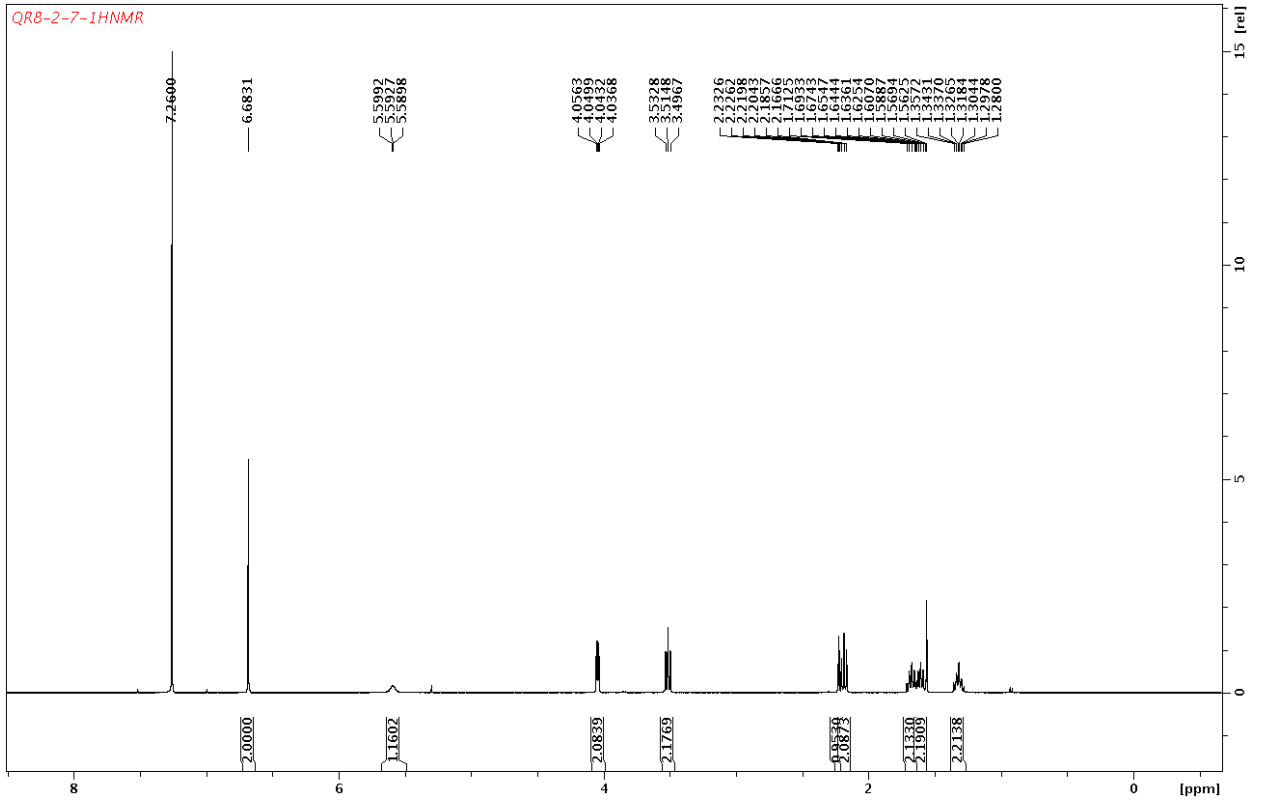
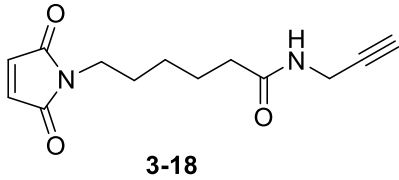


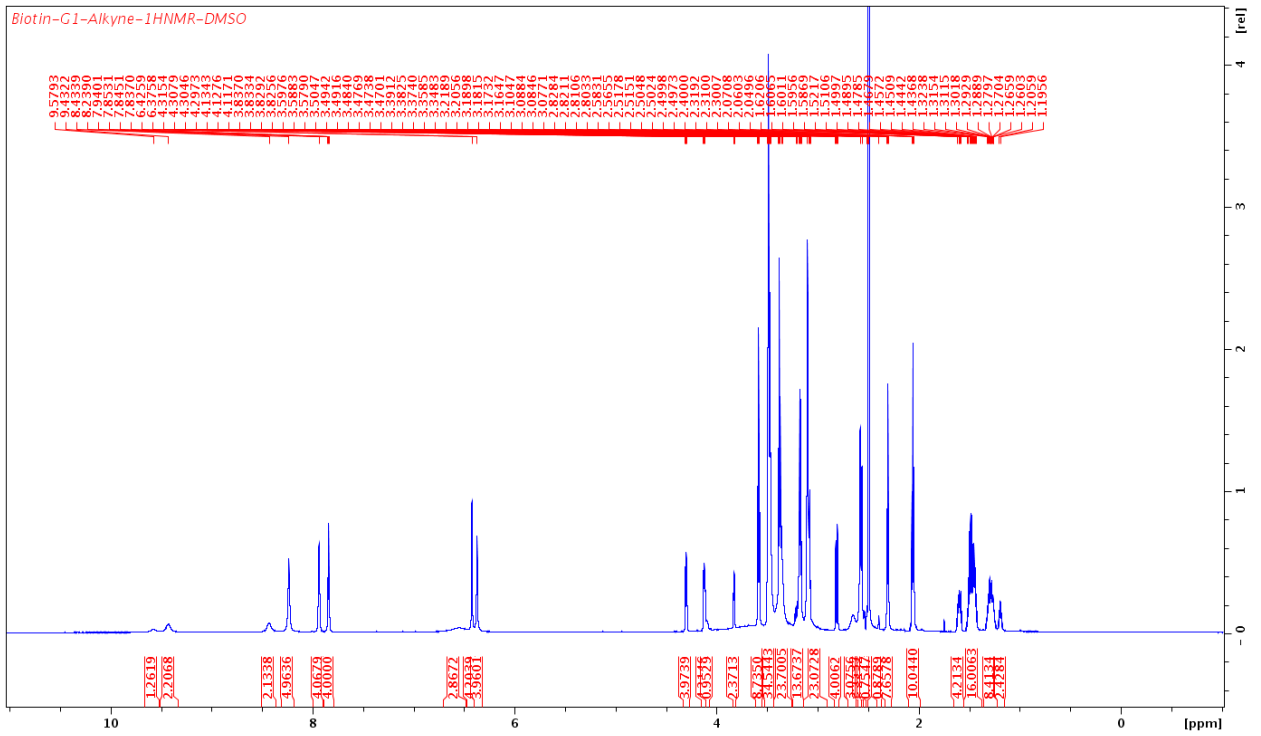
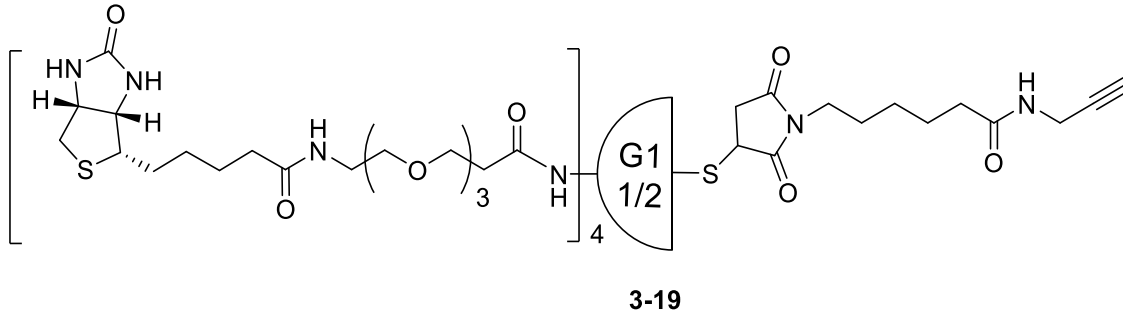


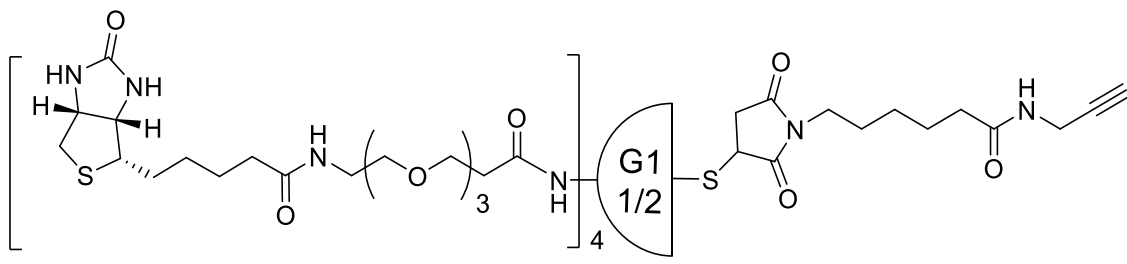
3-16



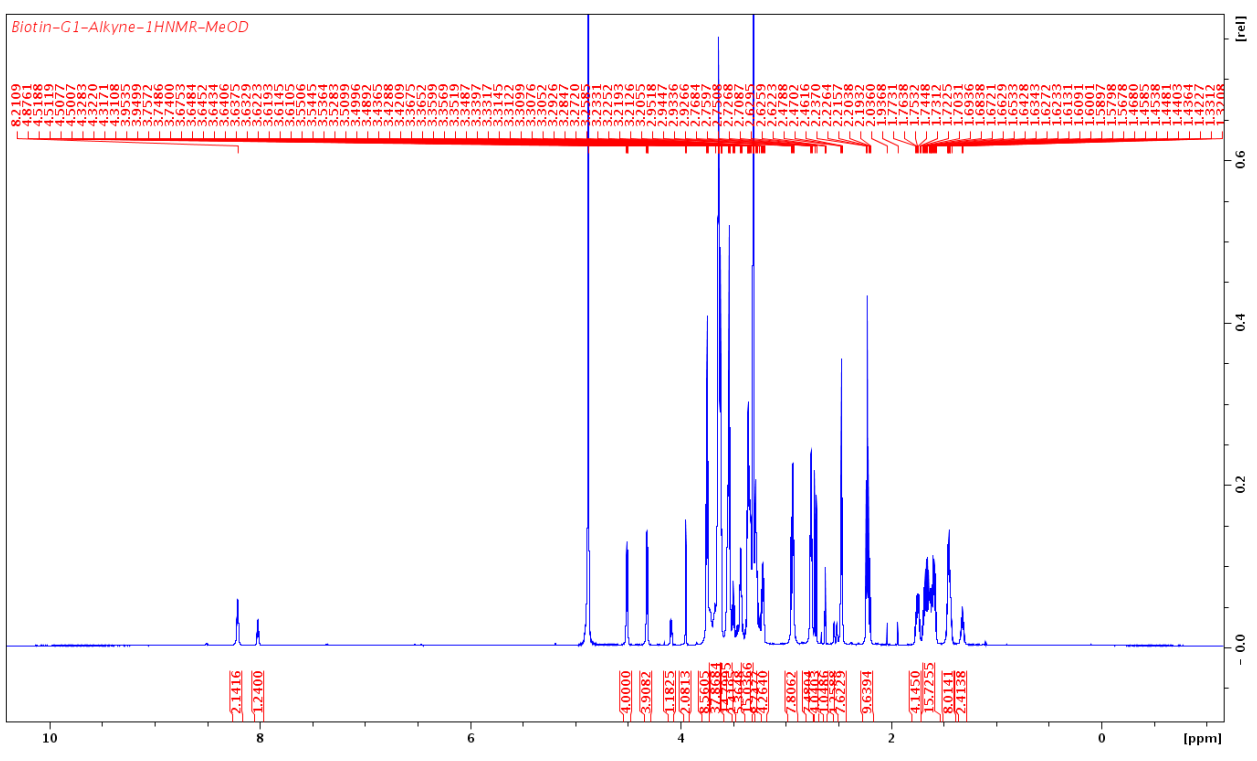


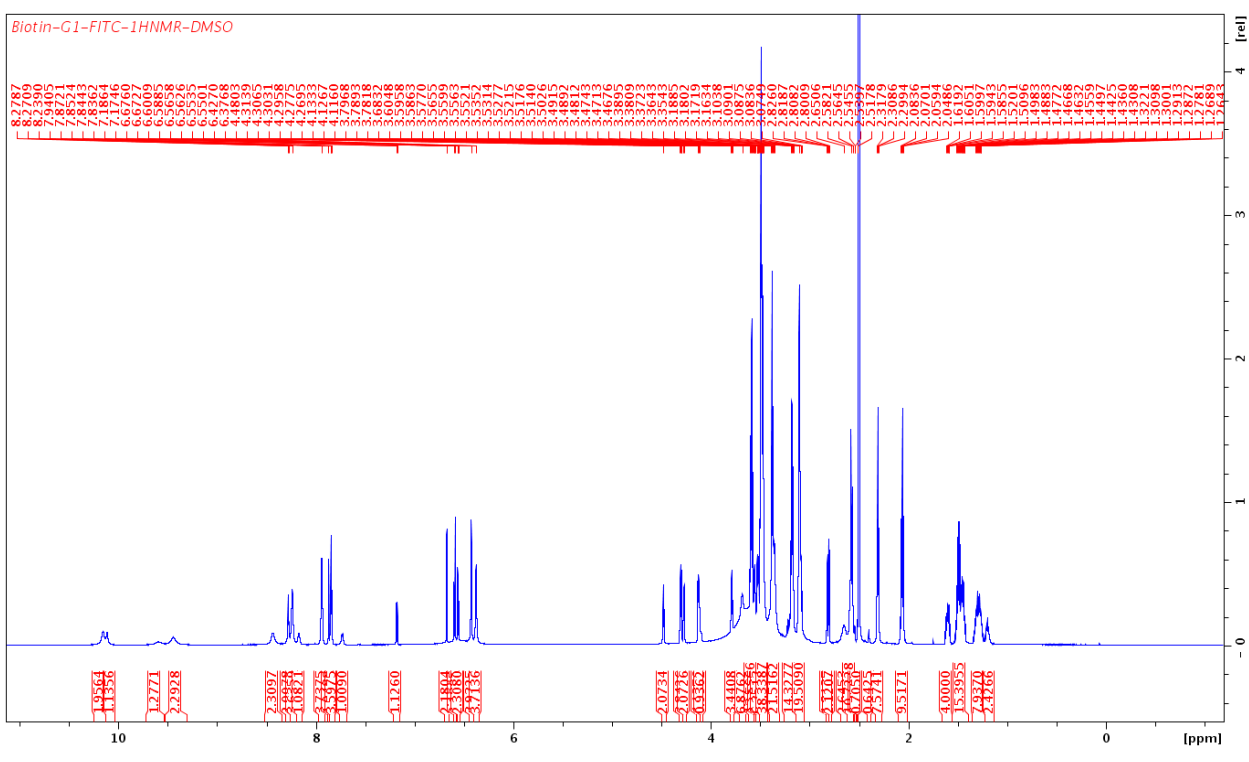
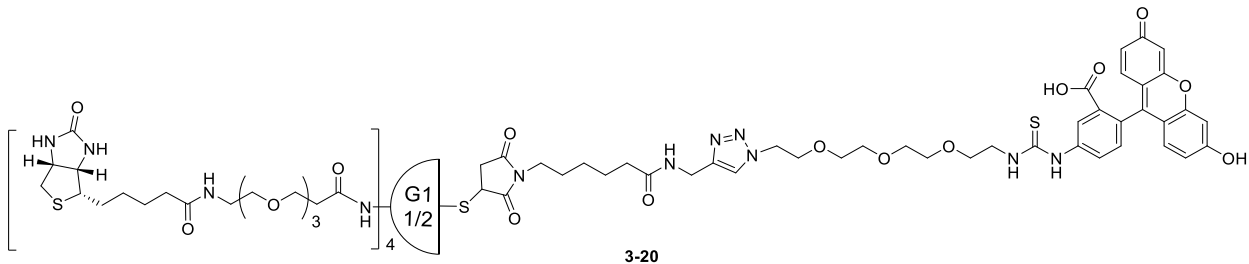


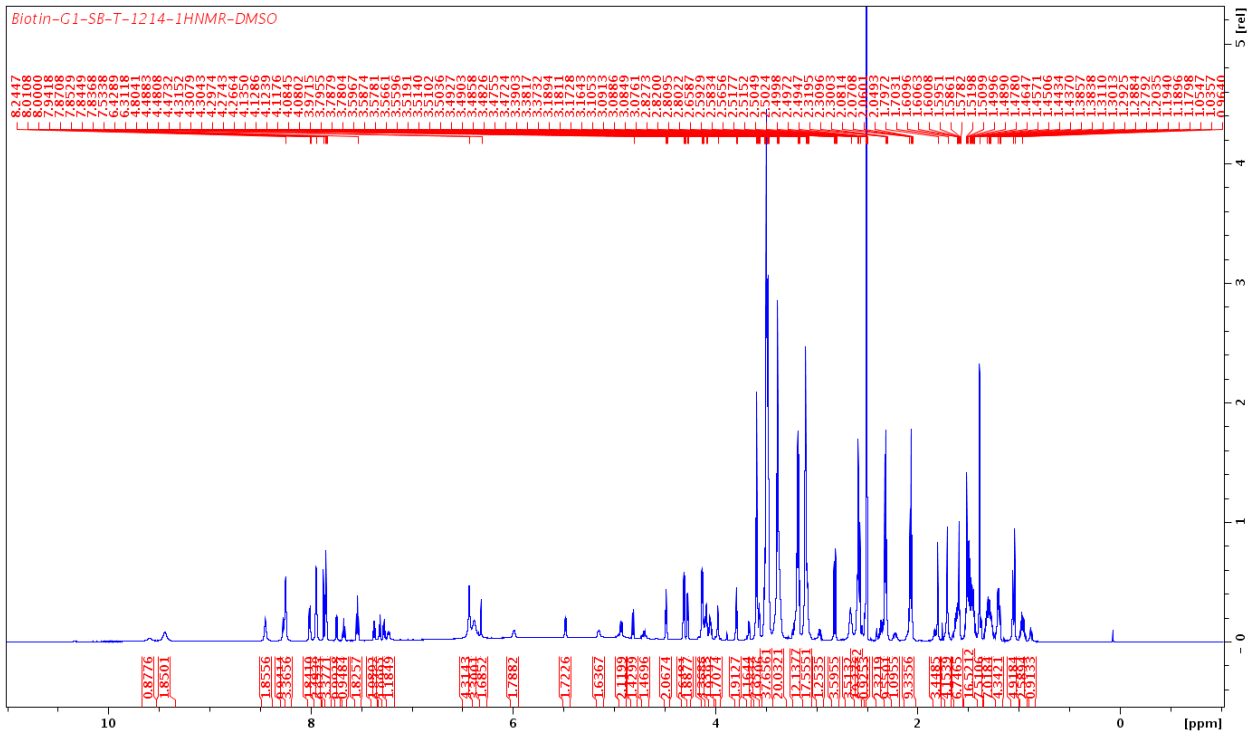
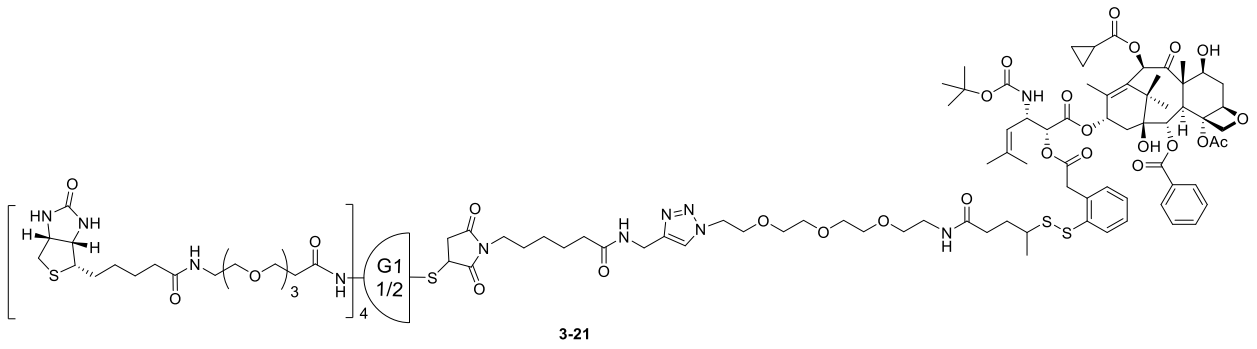


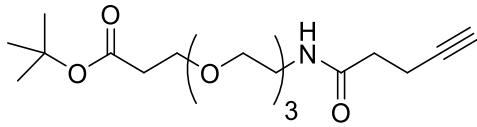


3-19

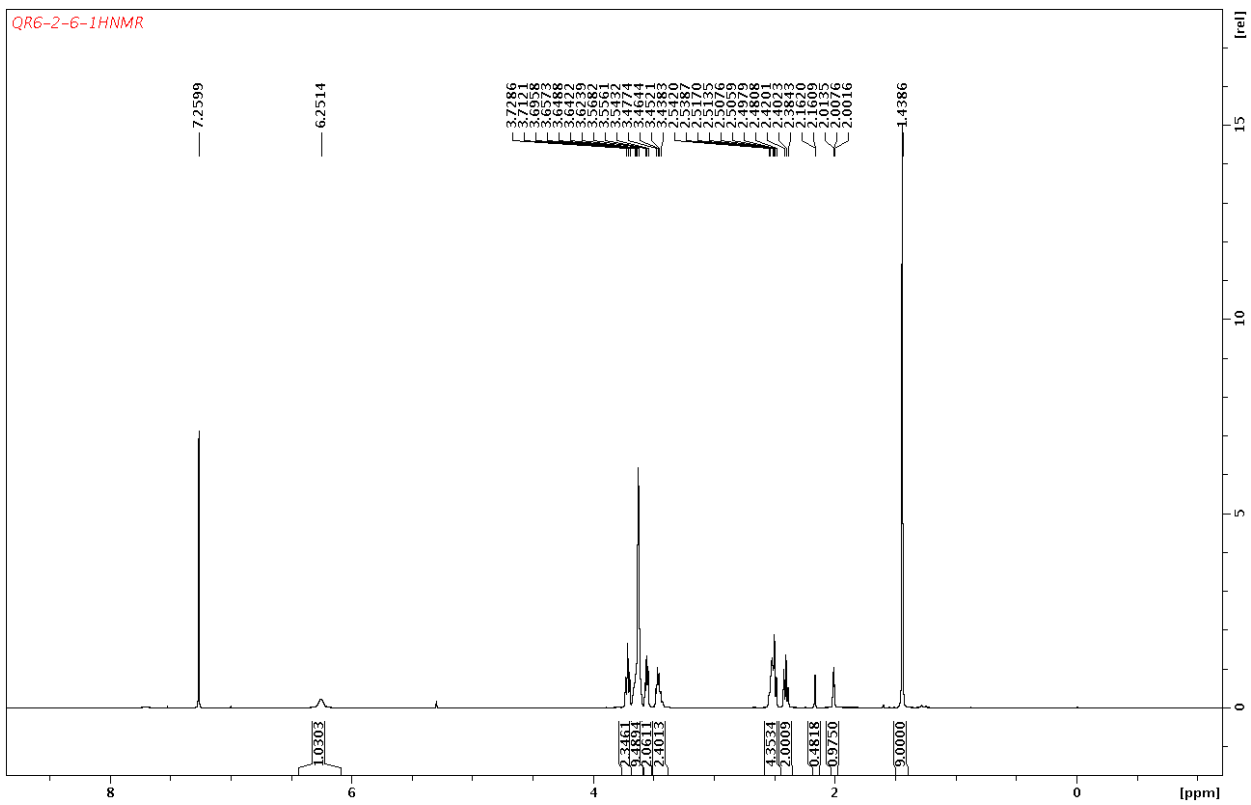


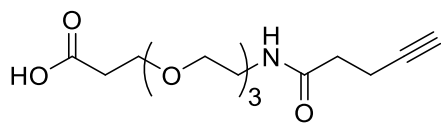




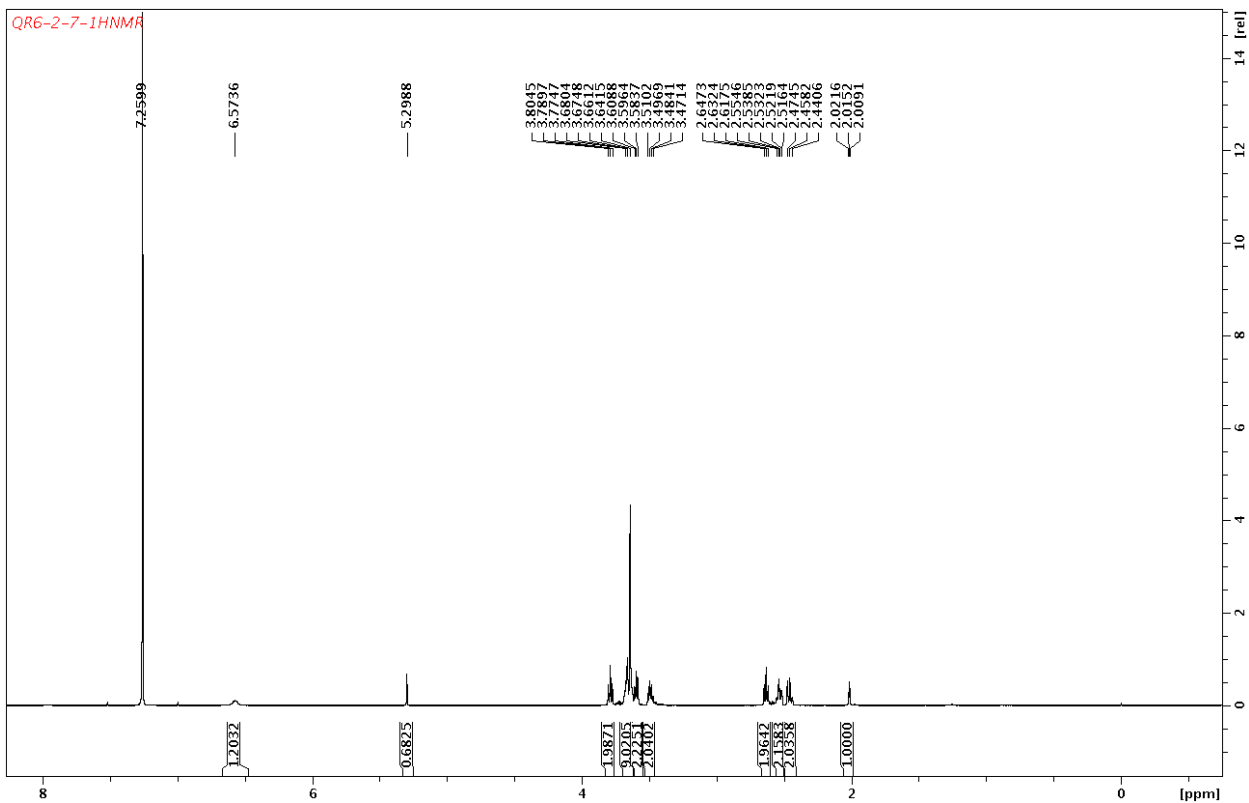


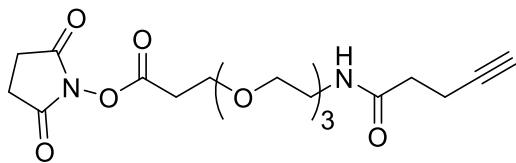
3-25



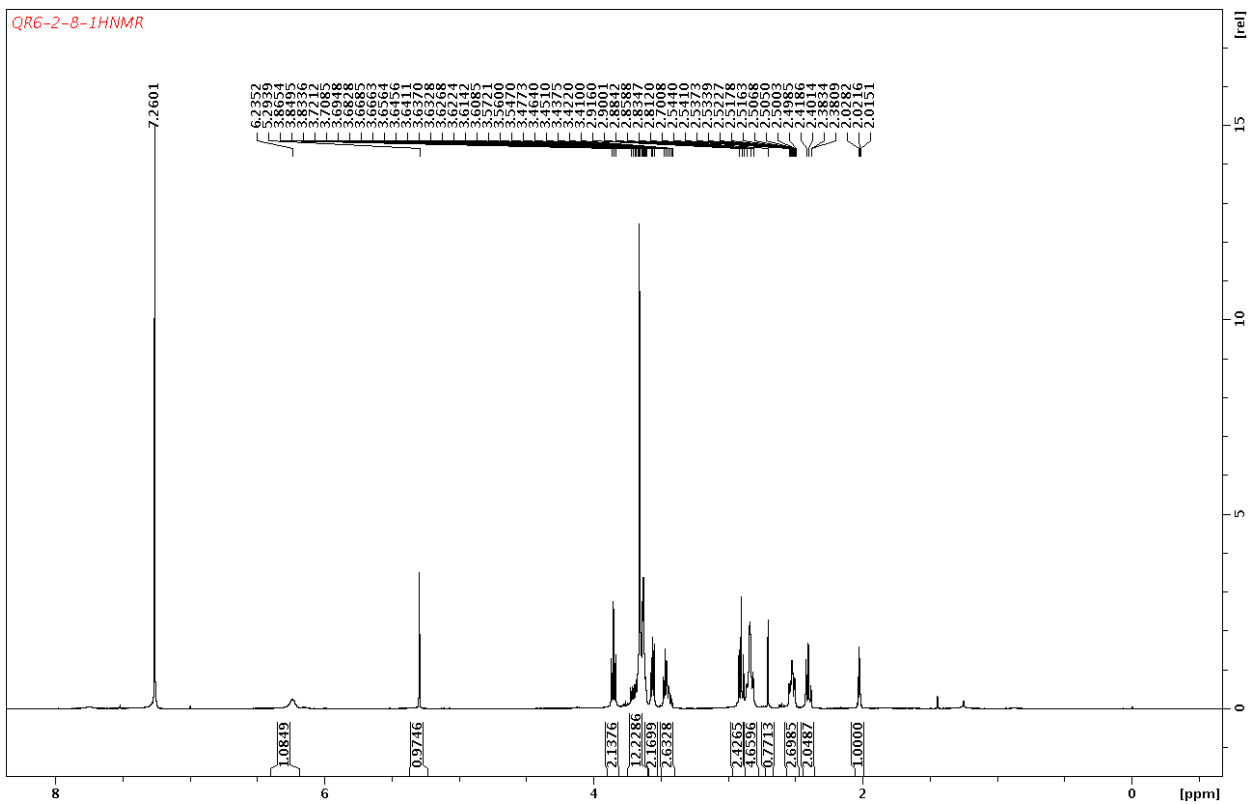


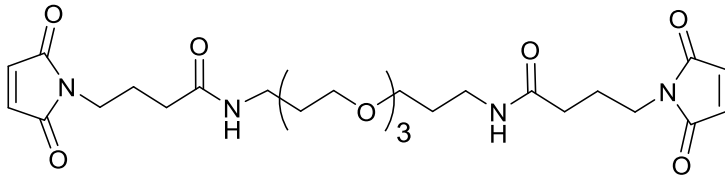
3-26



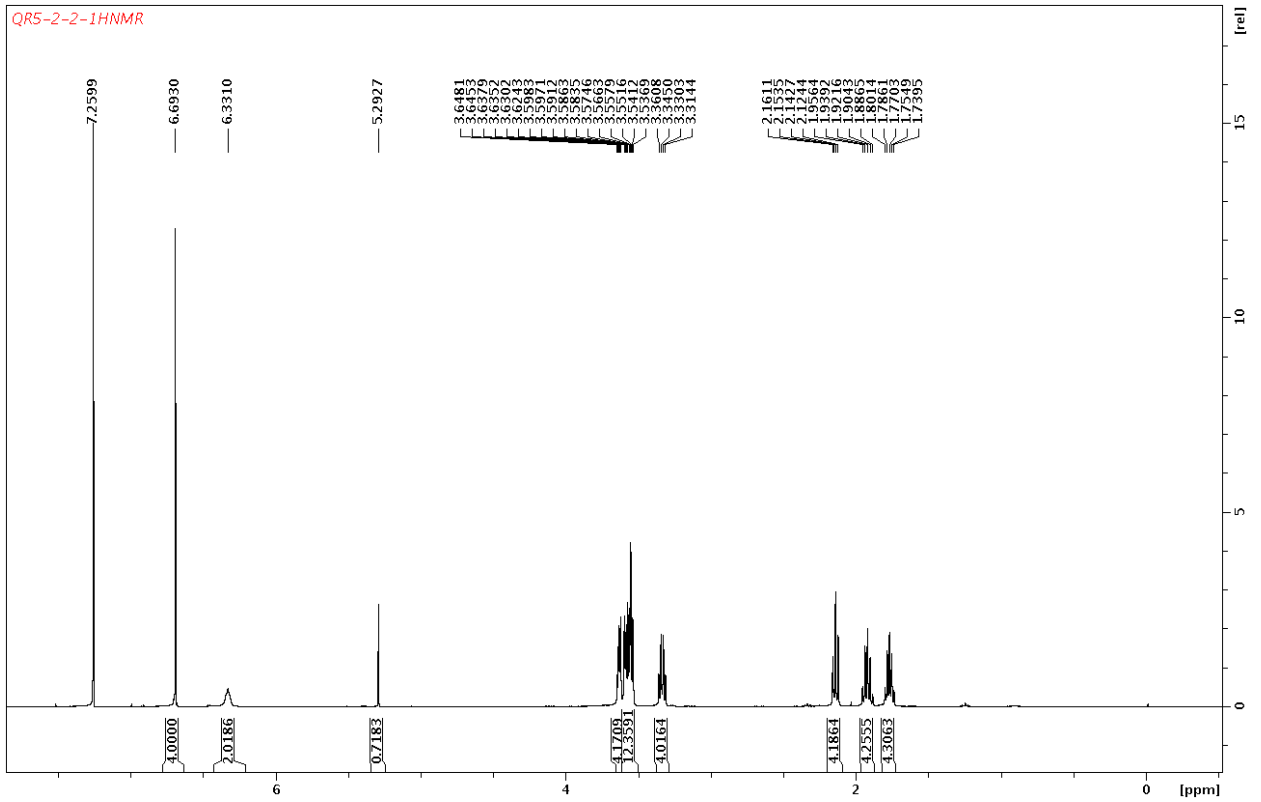


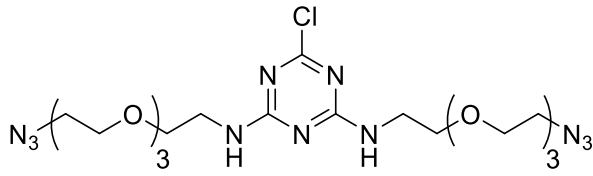
3-27



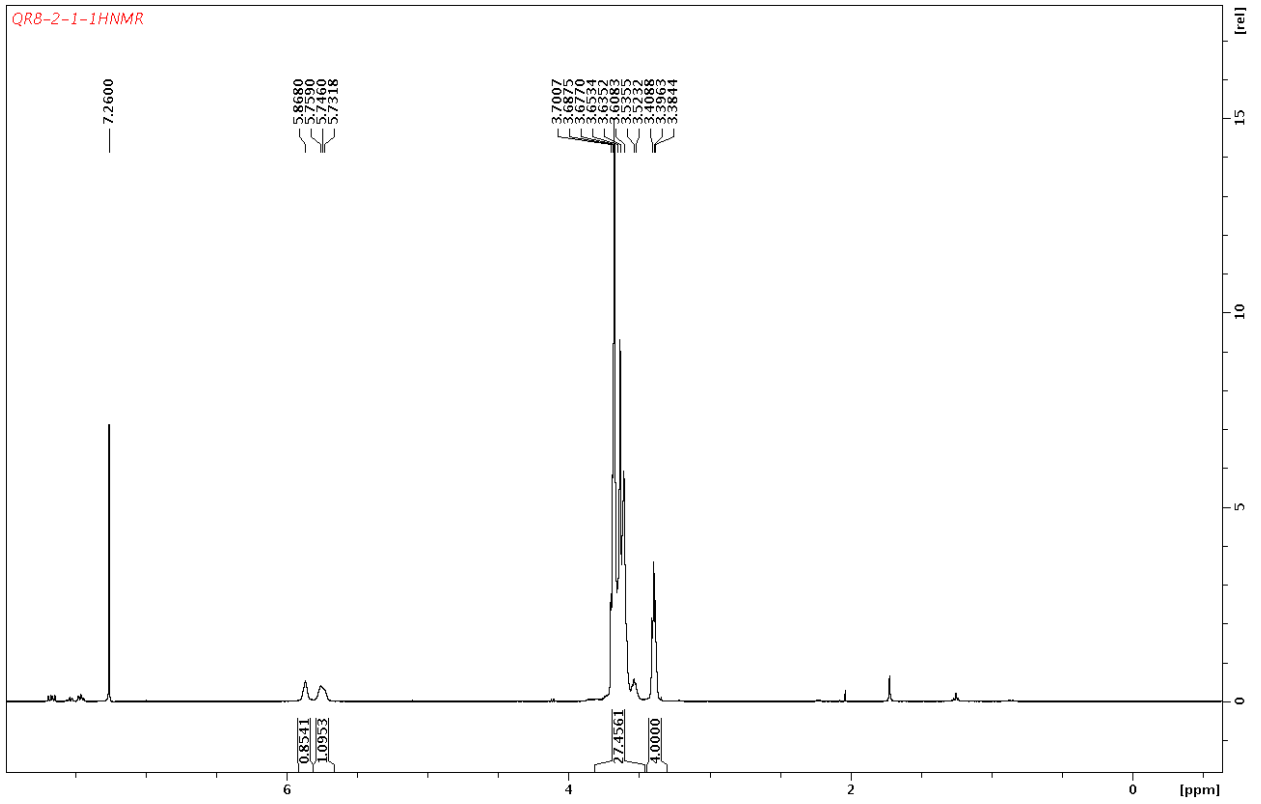


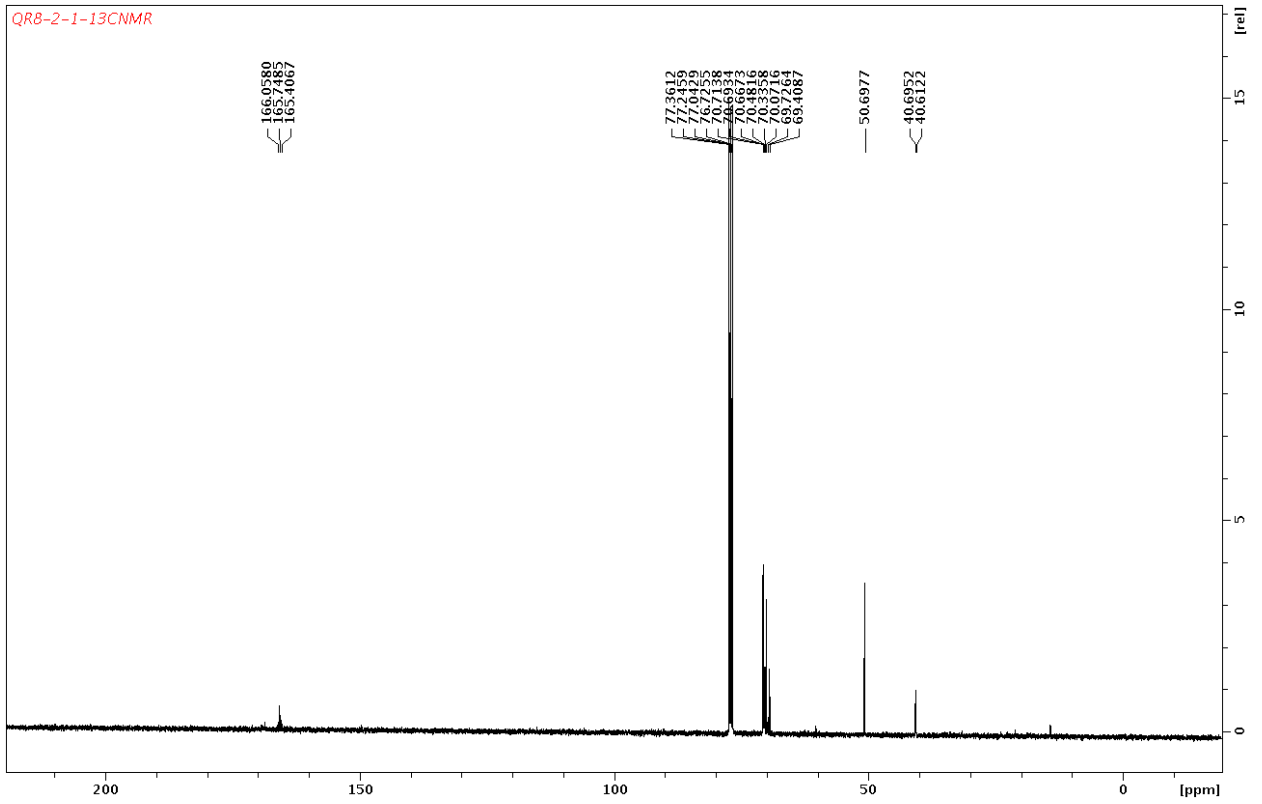
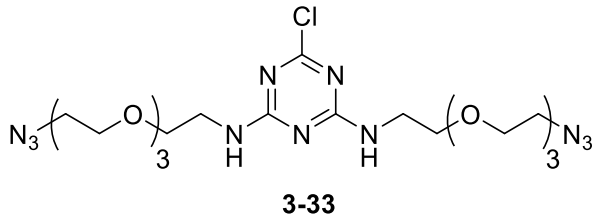
3-29

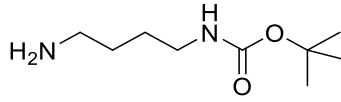




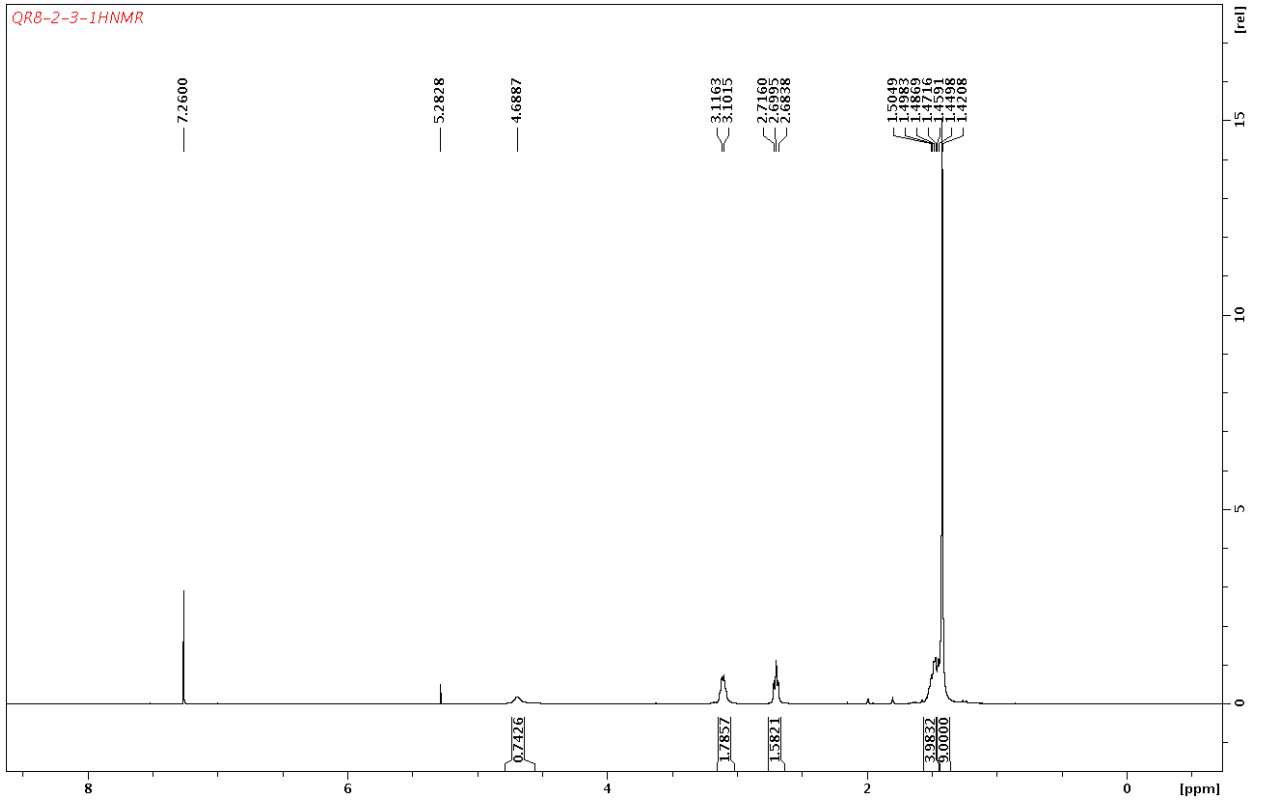
3-33

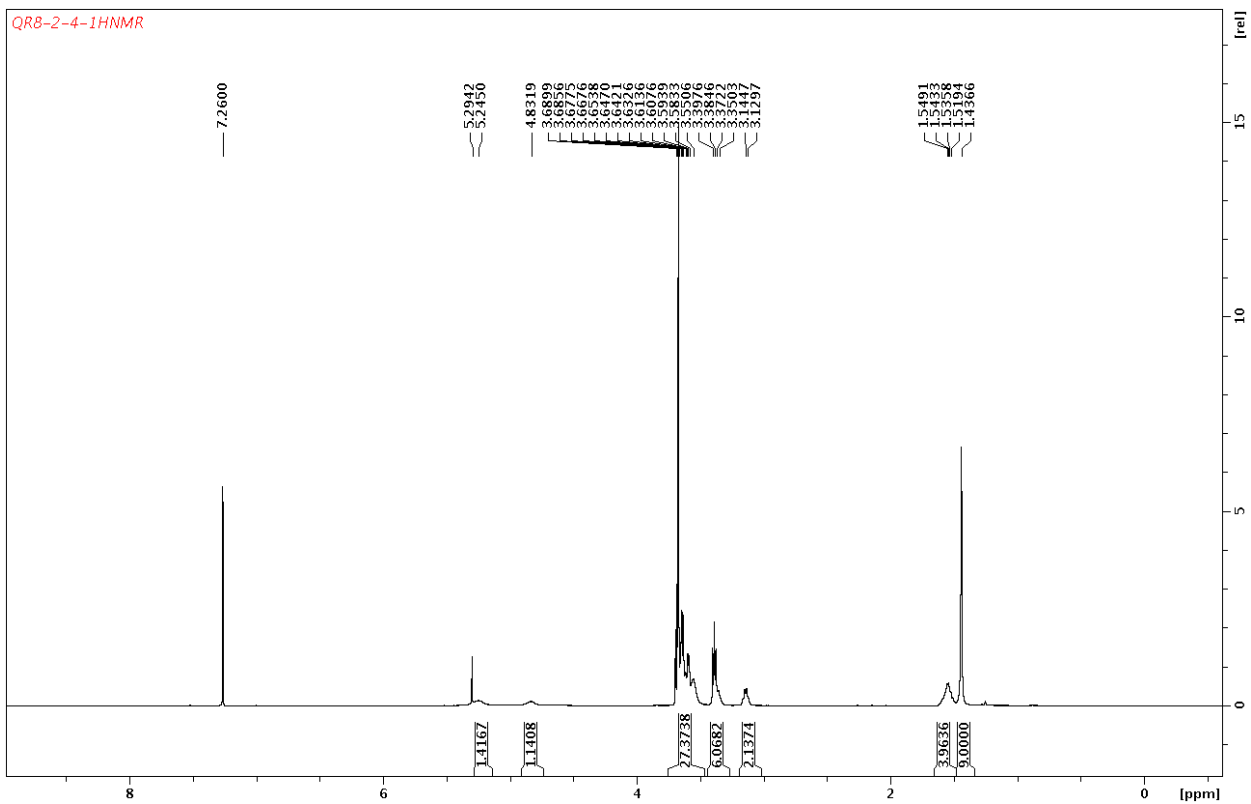
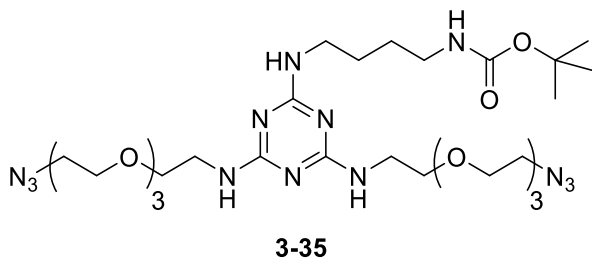


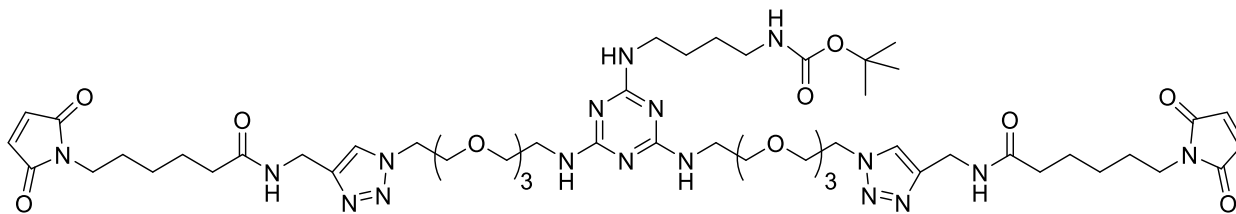




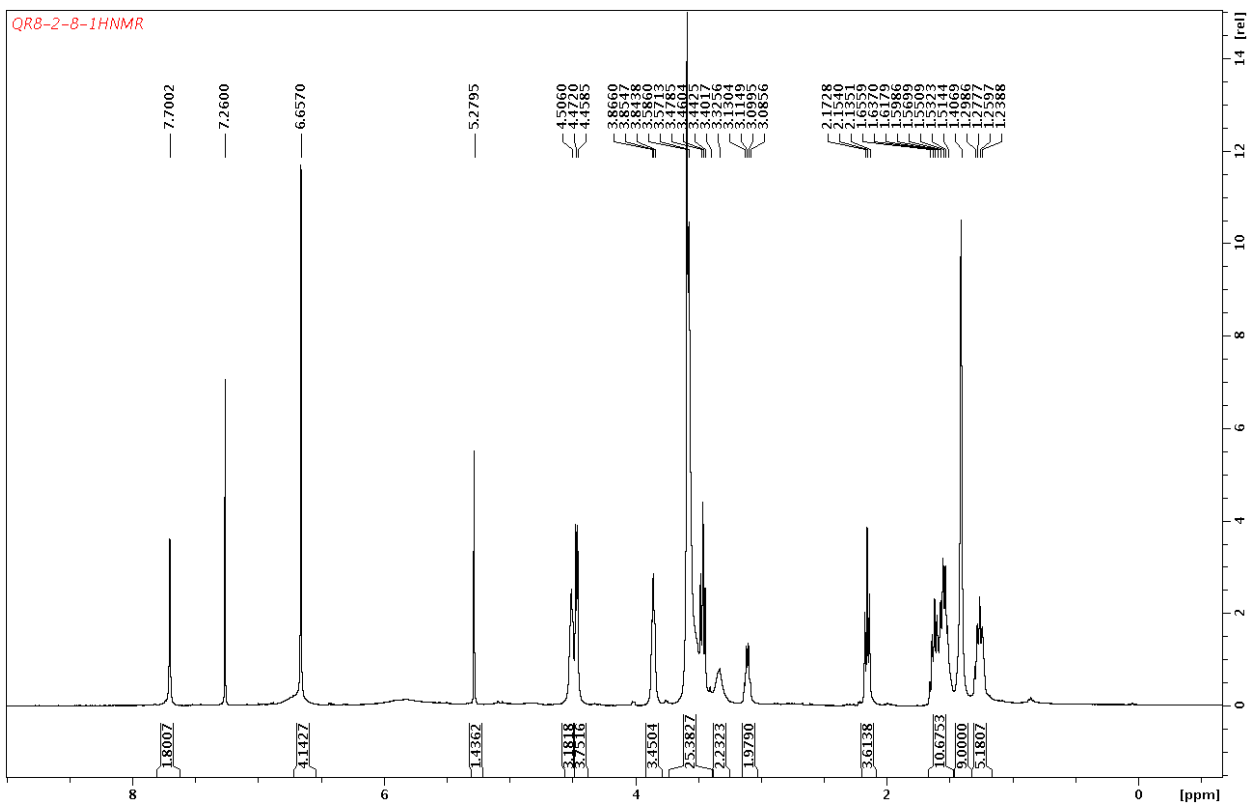
3-34

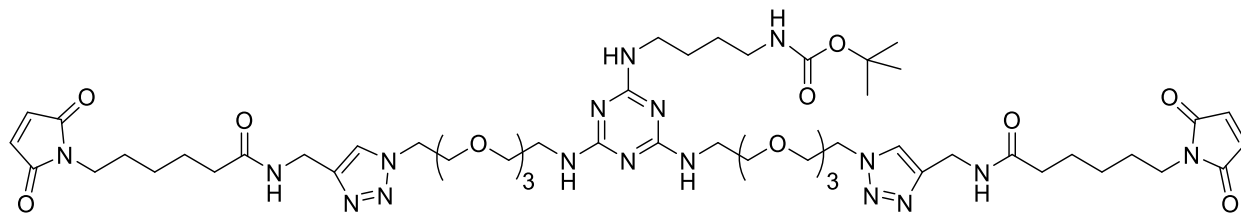




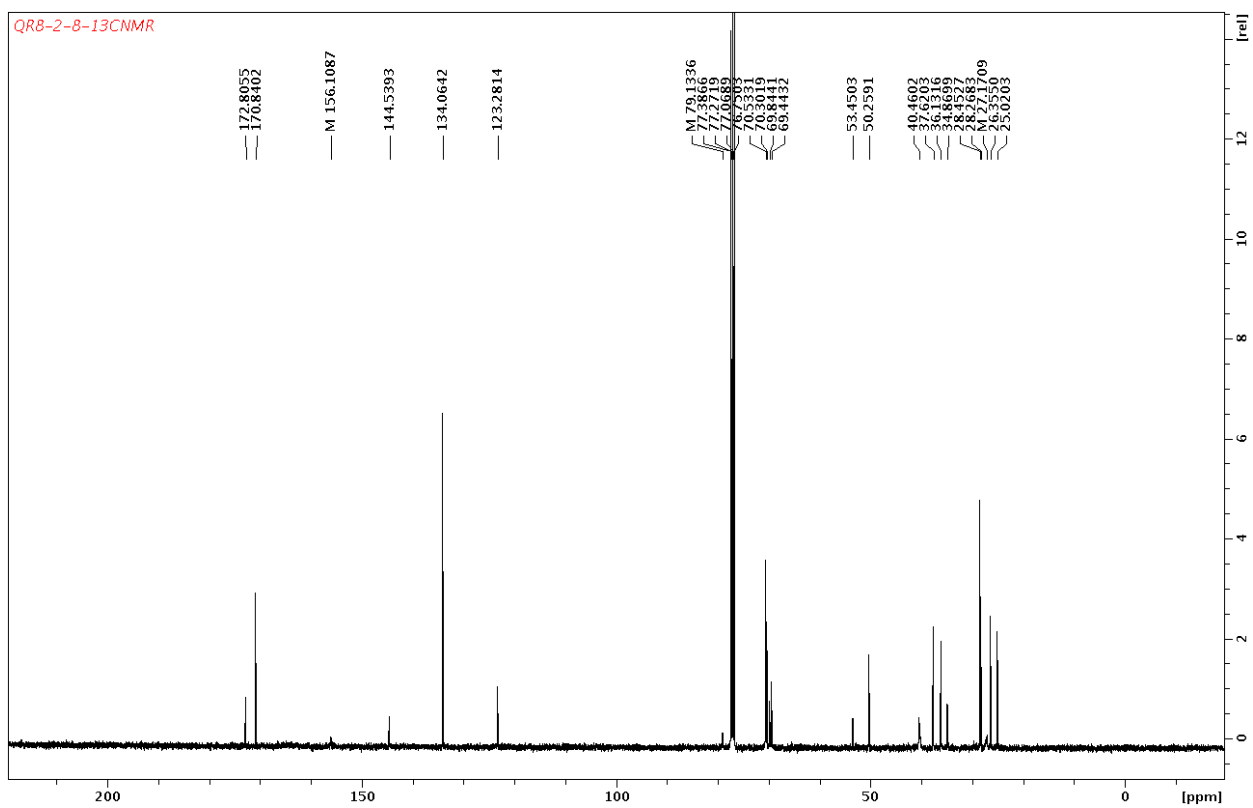


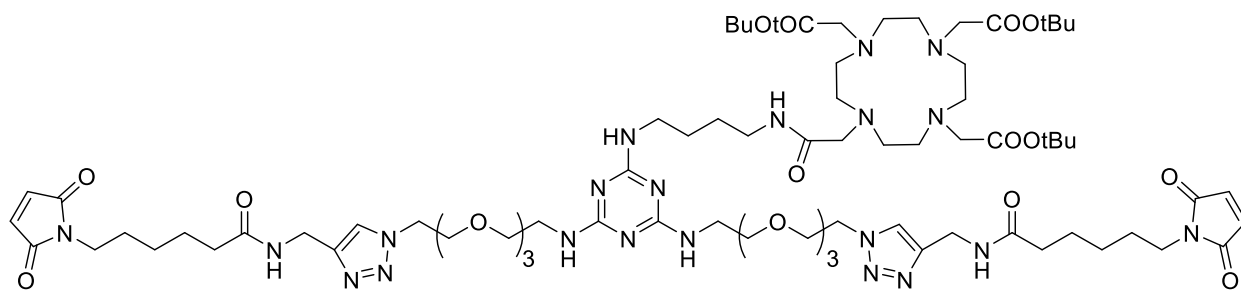
3-36



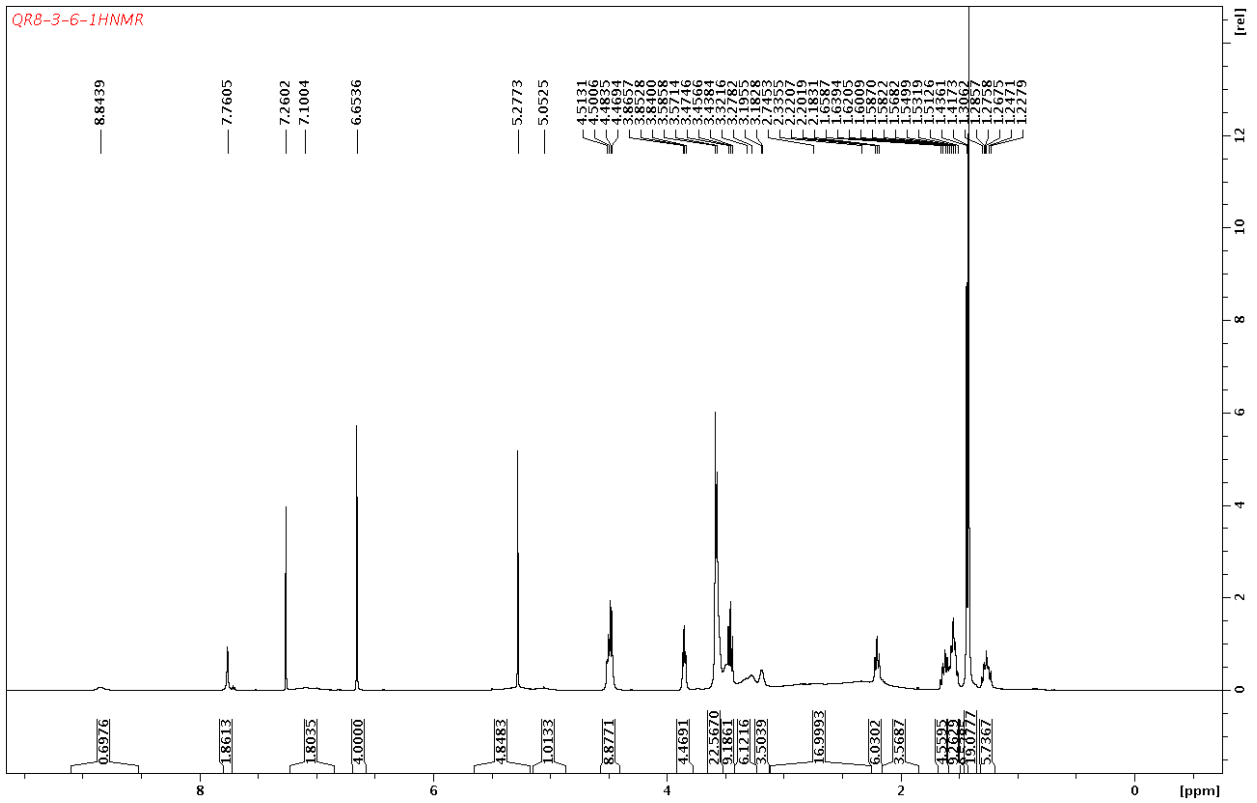


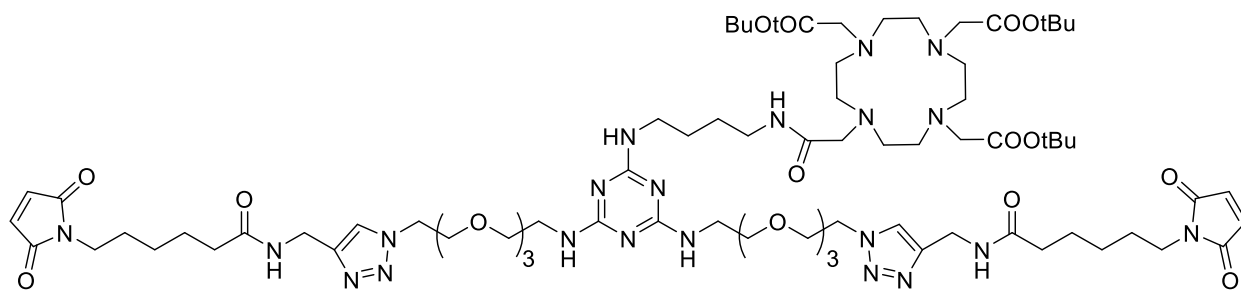
3-36



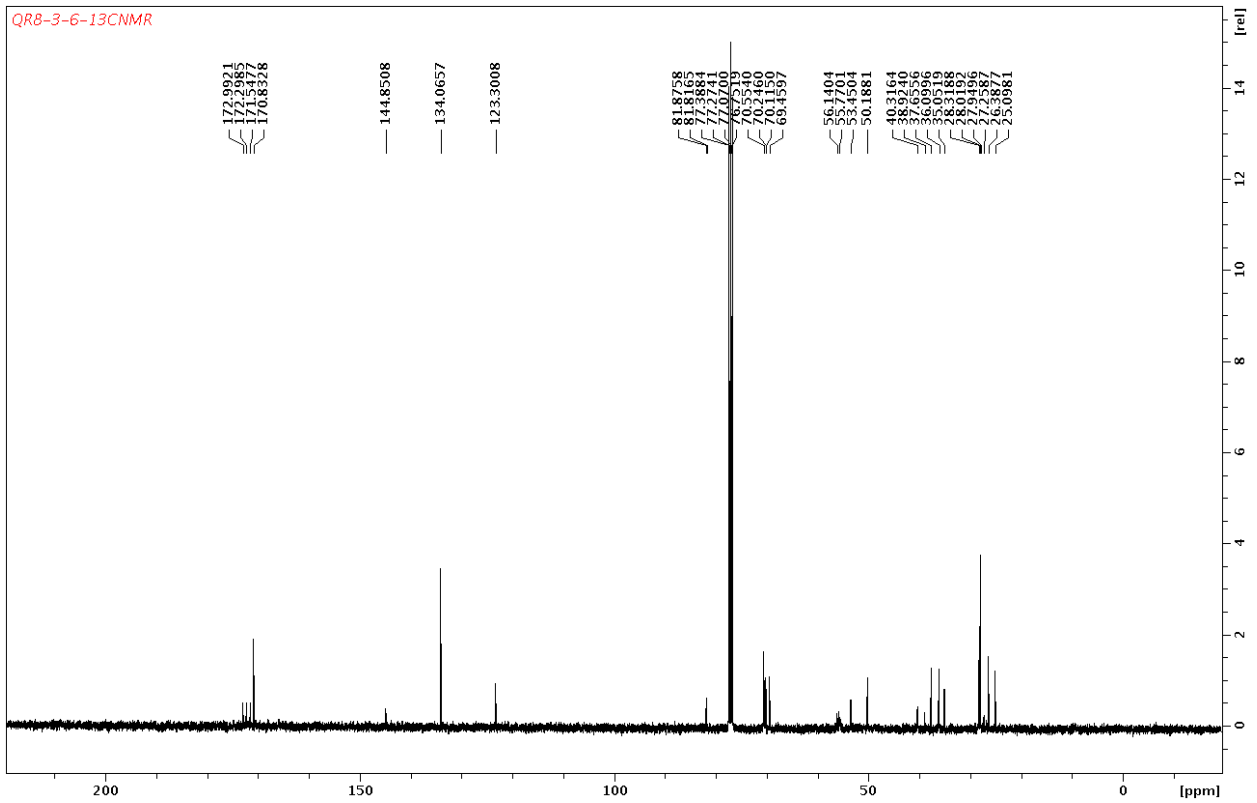


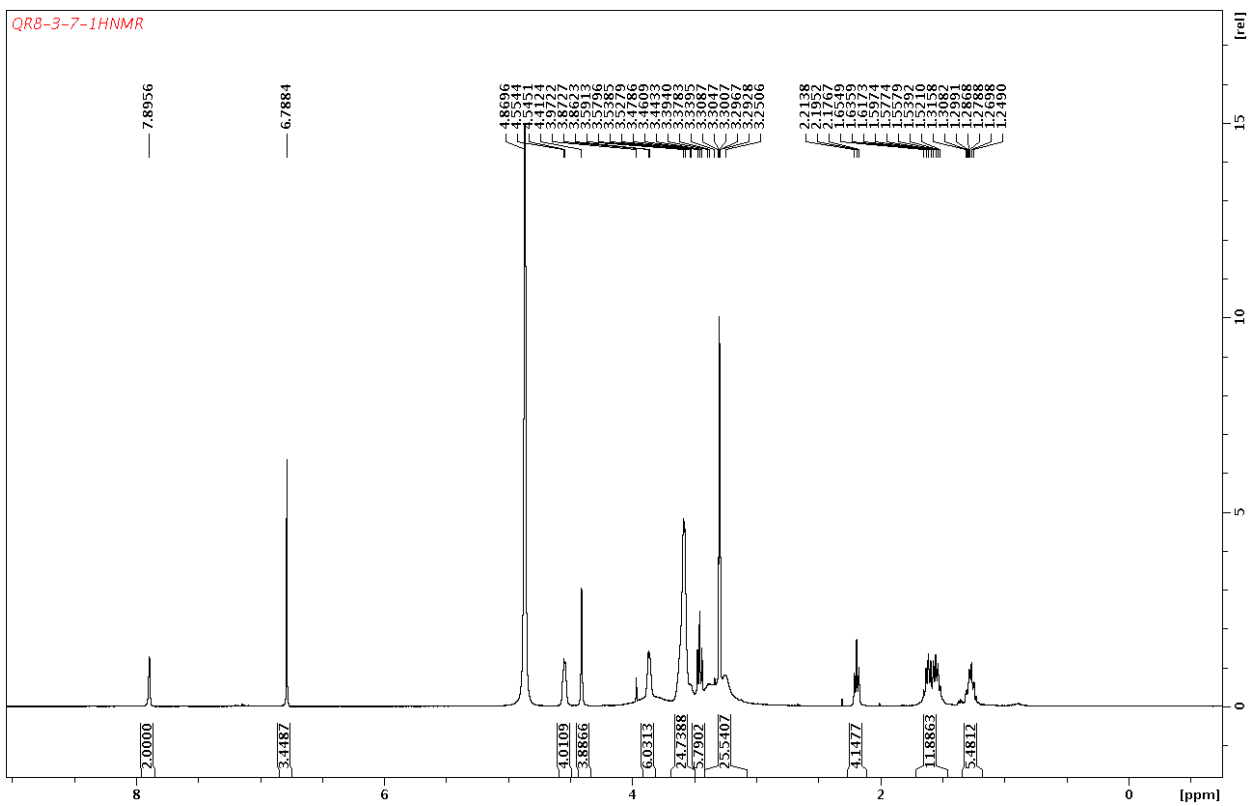
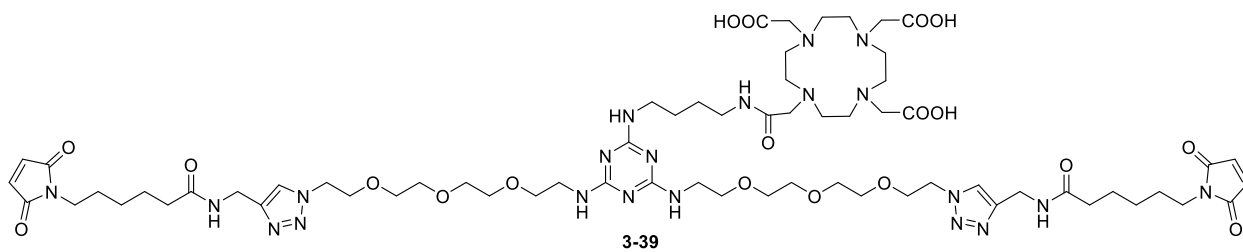
3-38

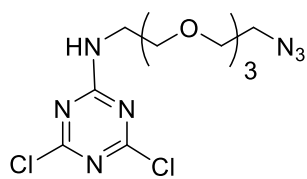




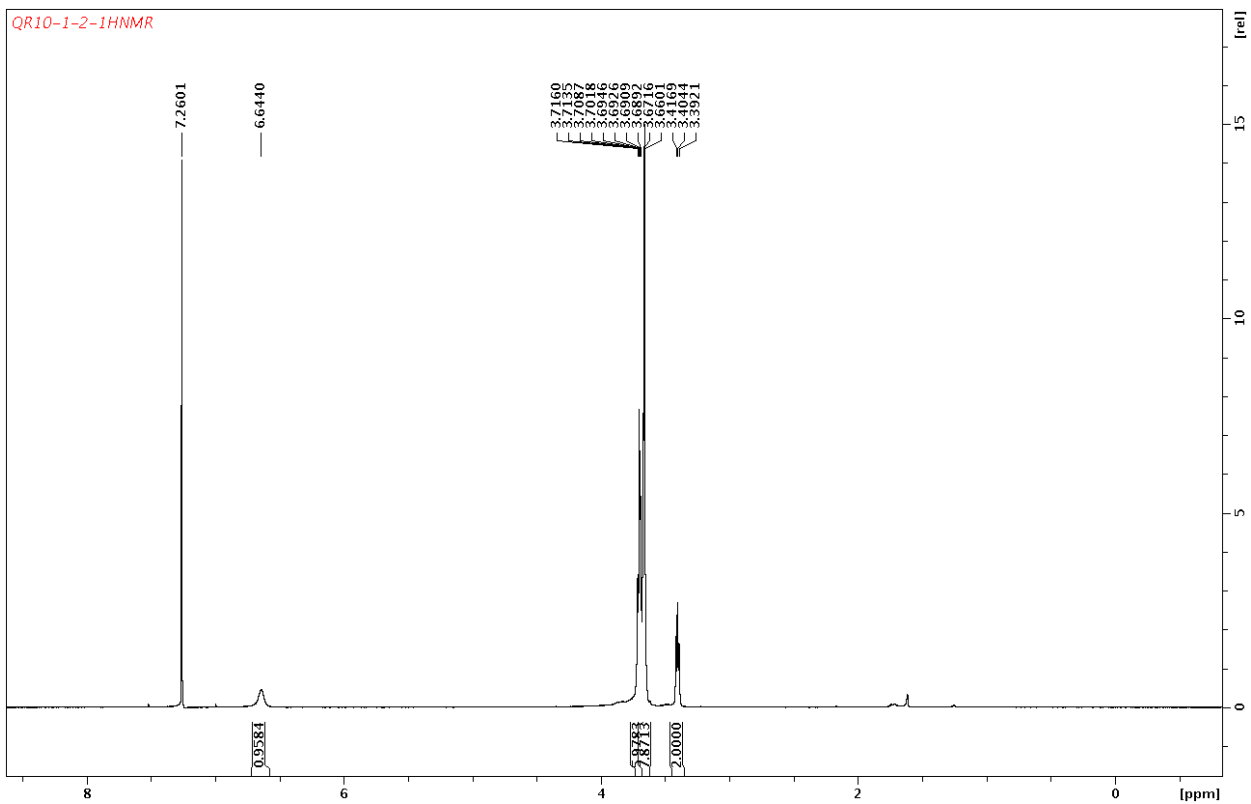
3-38

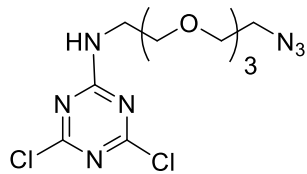




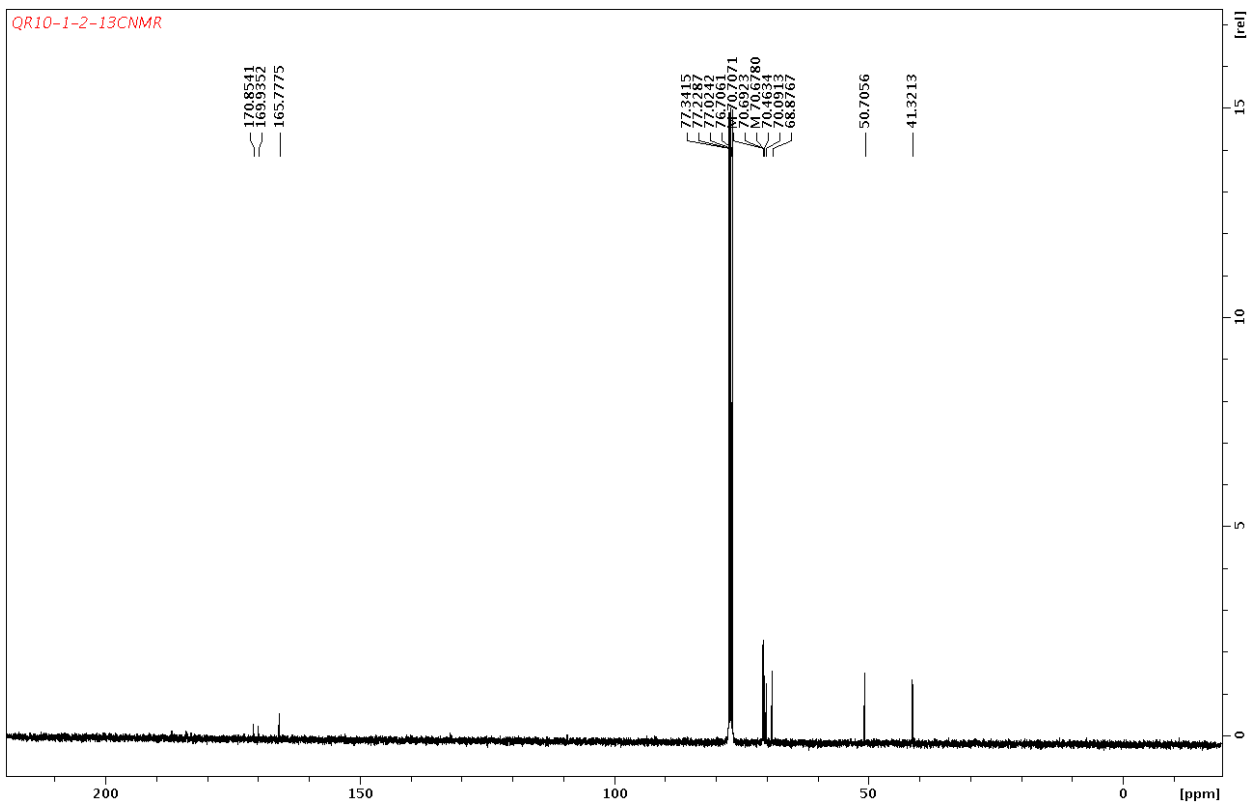


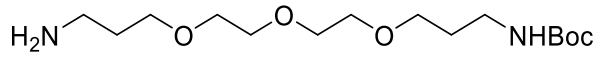
3-42



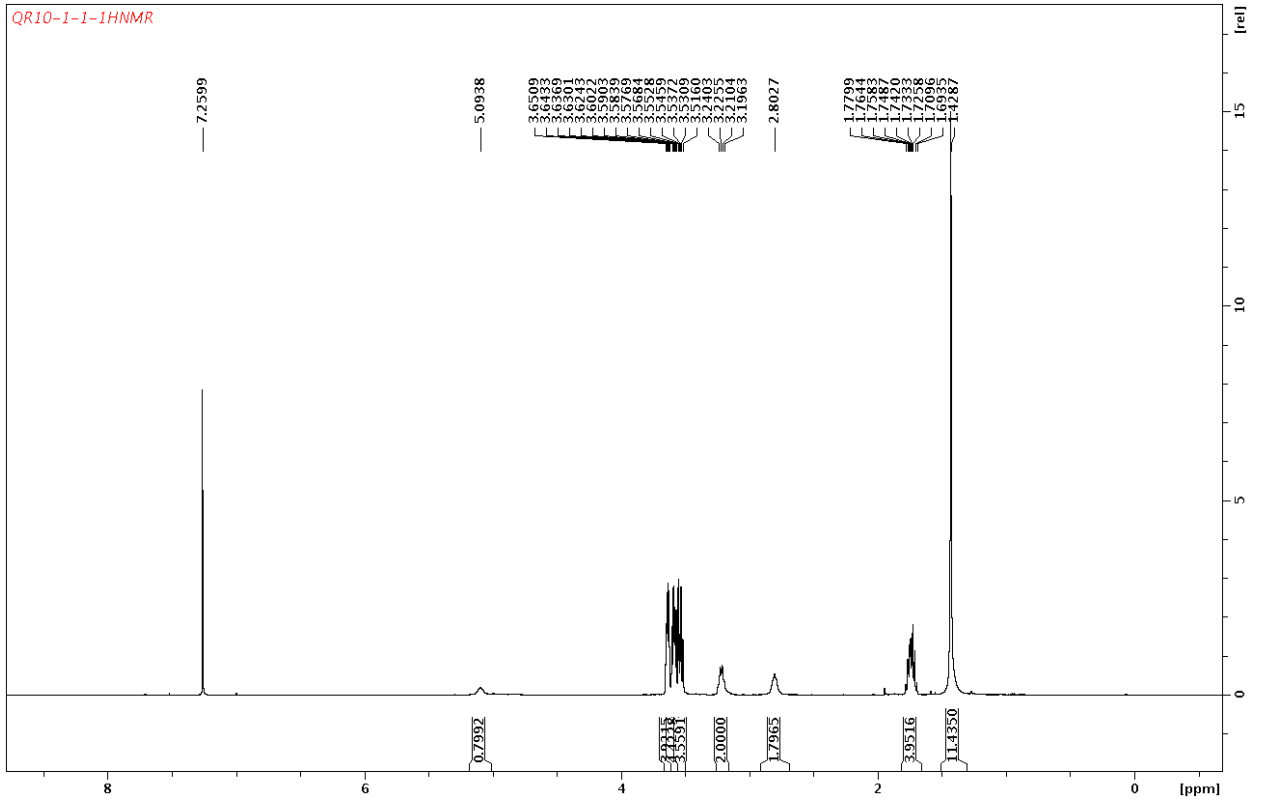


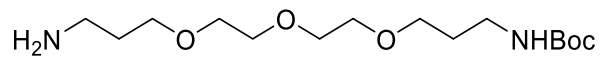
3-42



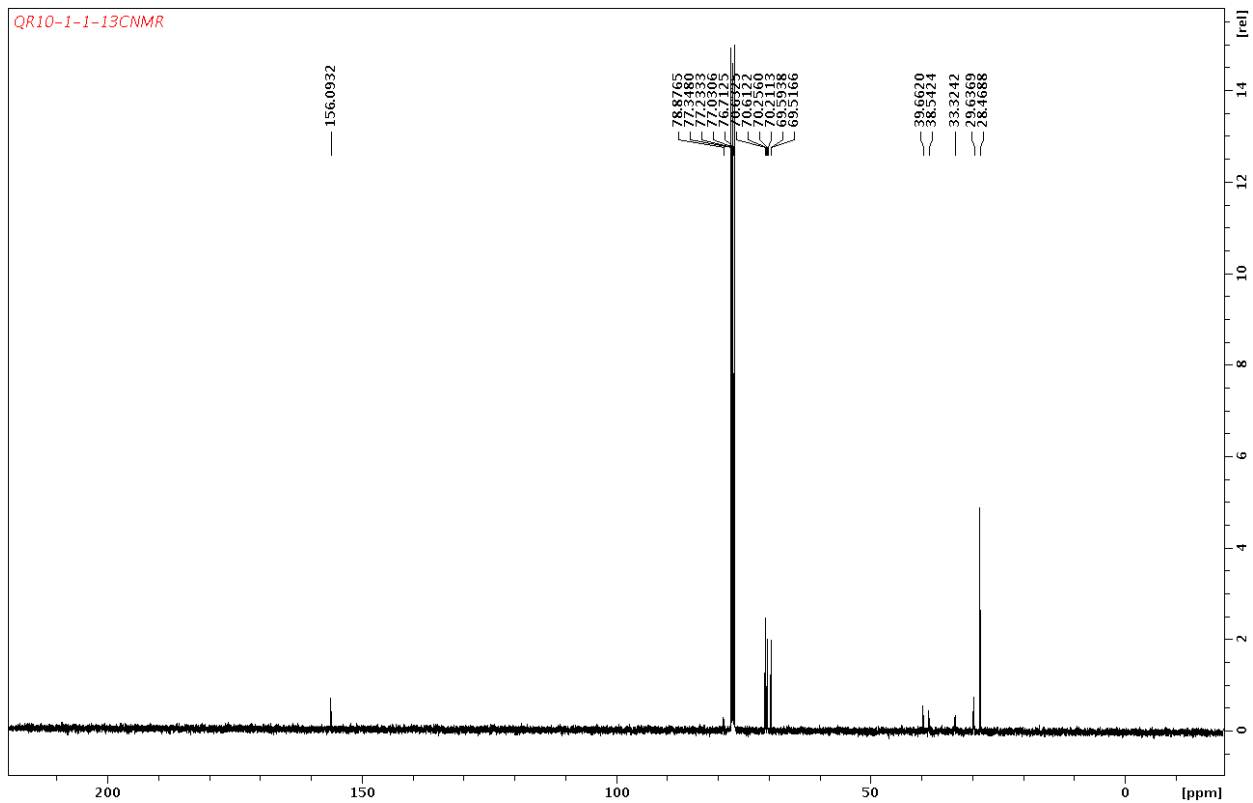


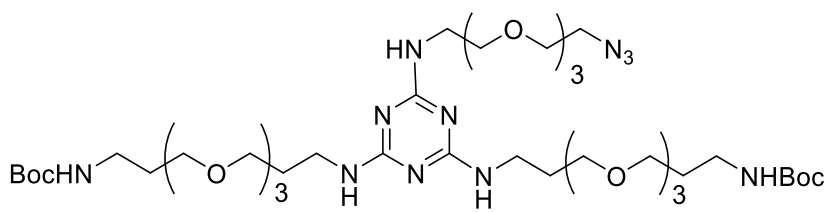
3-43



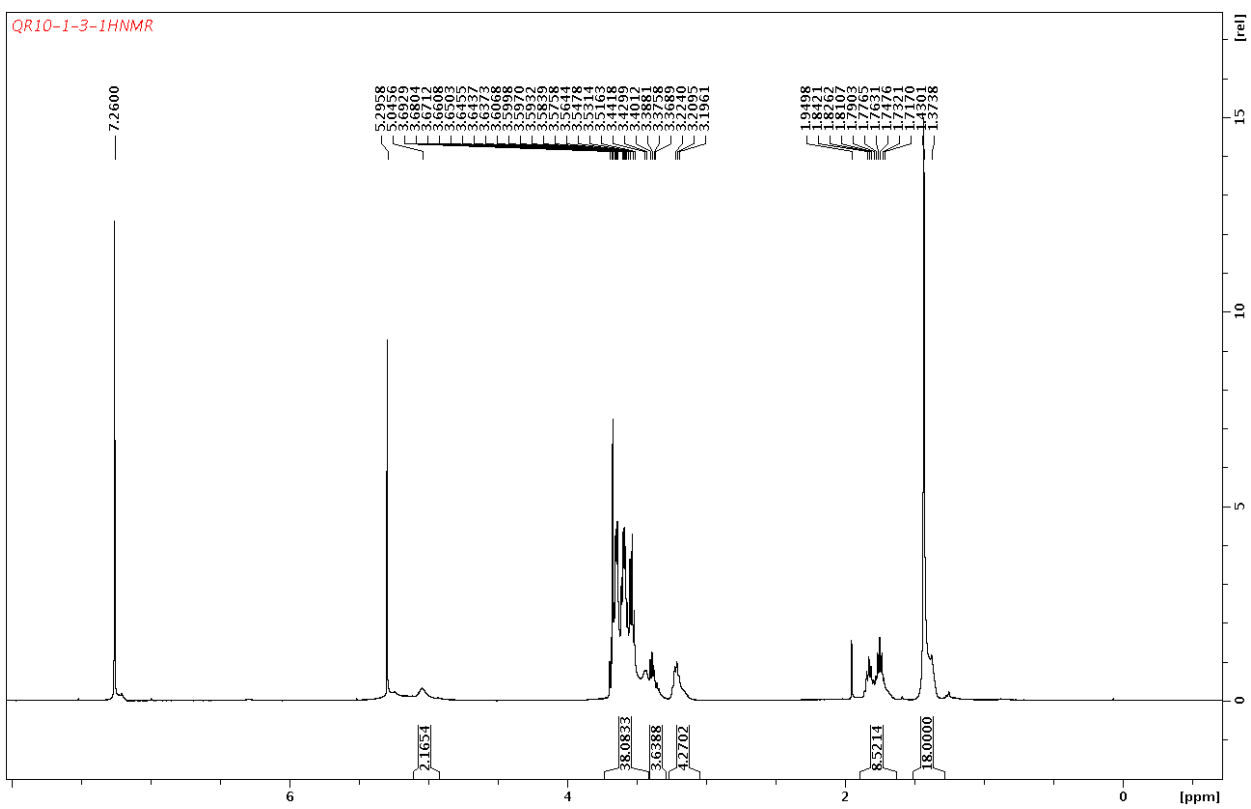


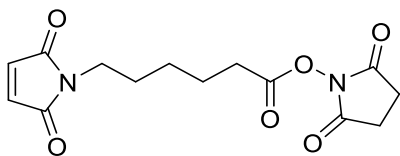
3-43



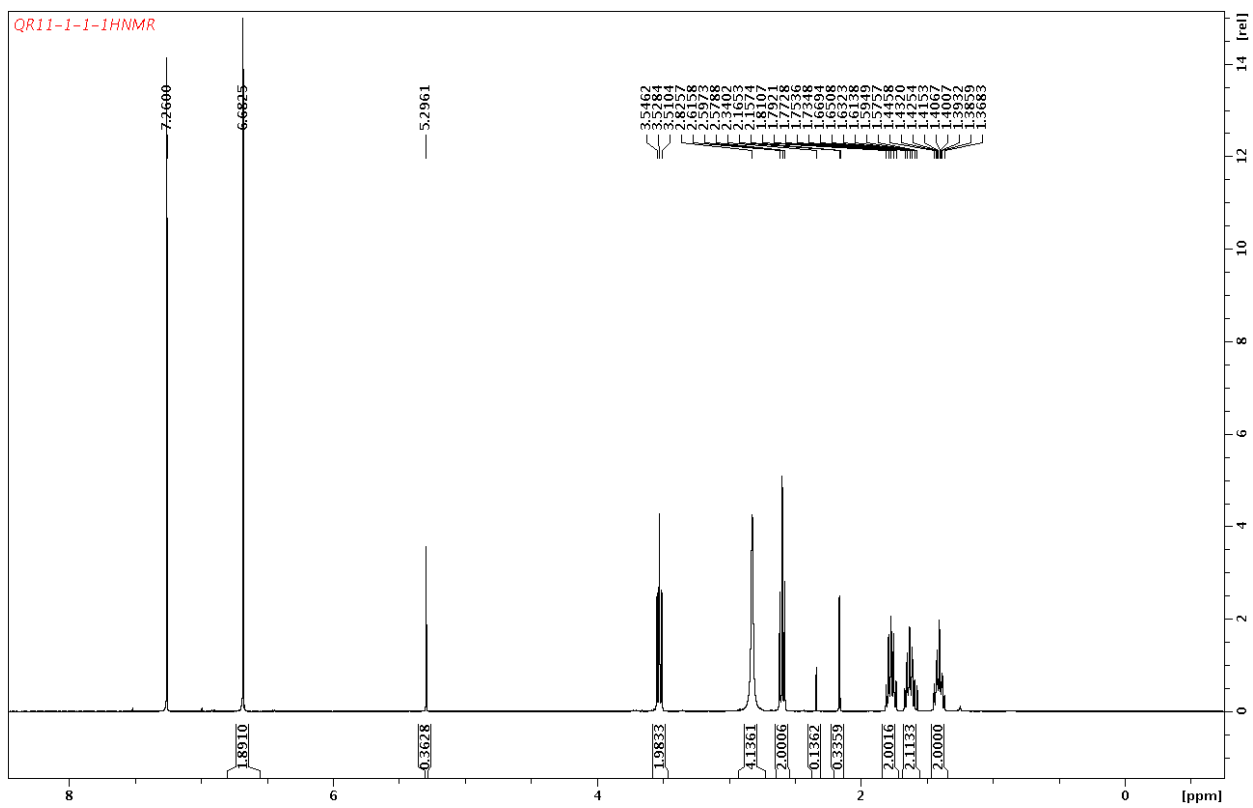


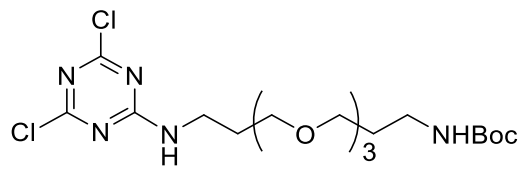
3-44



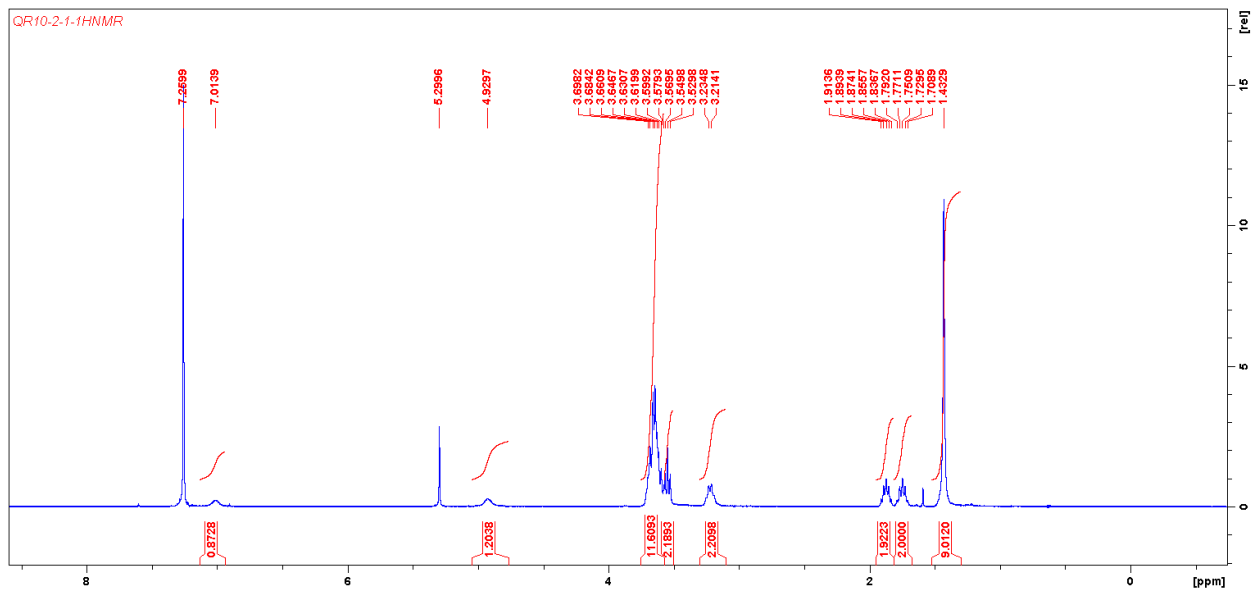


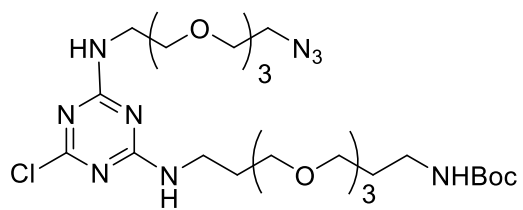
3-46



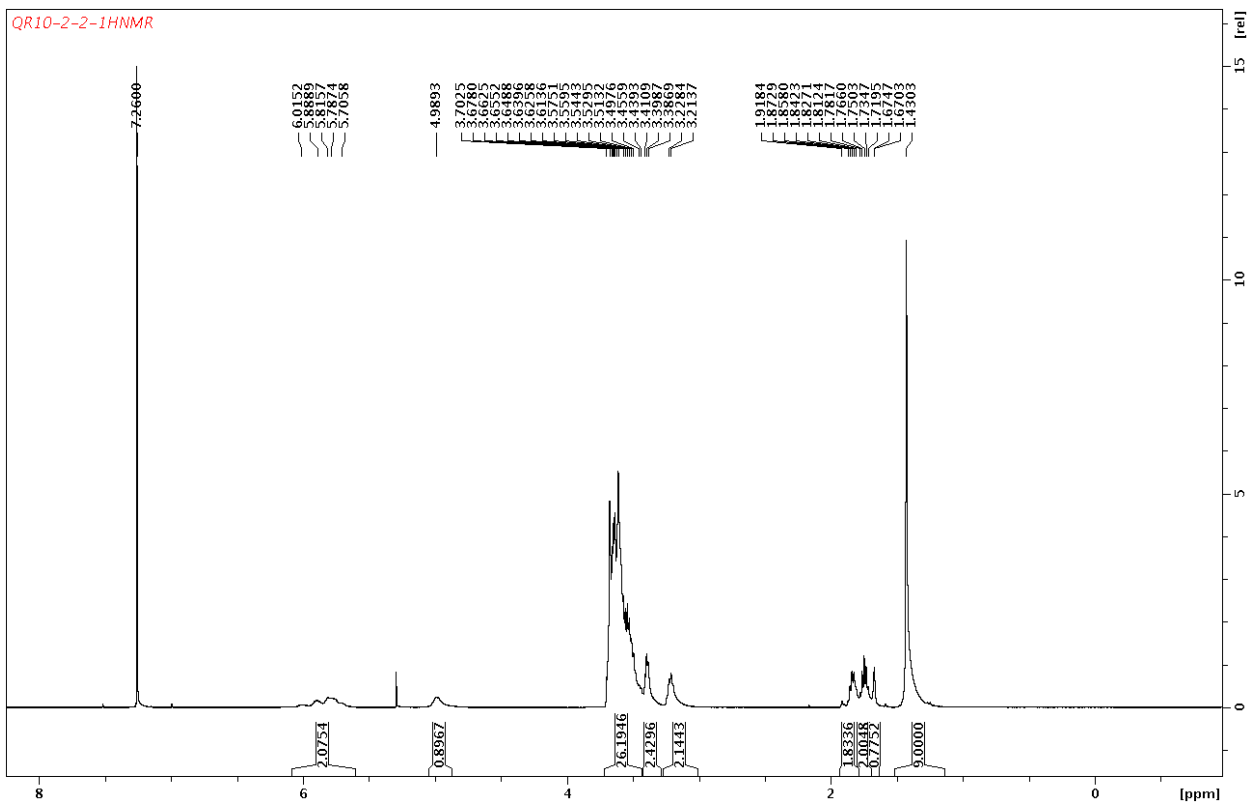


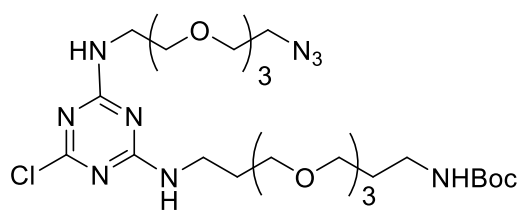
3-50



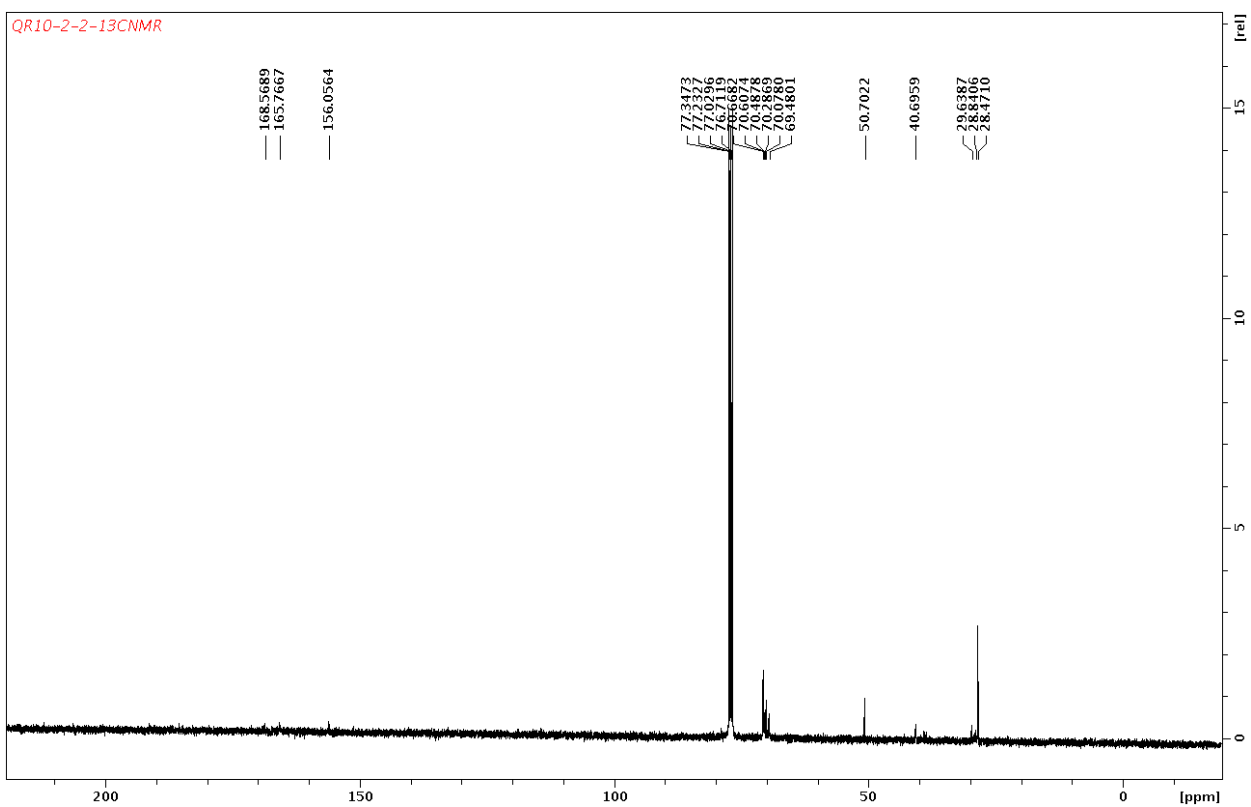


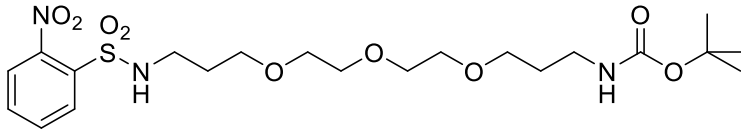
3-51



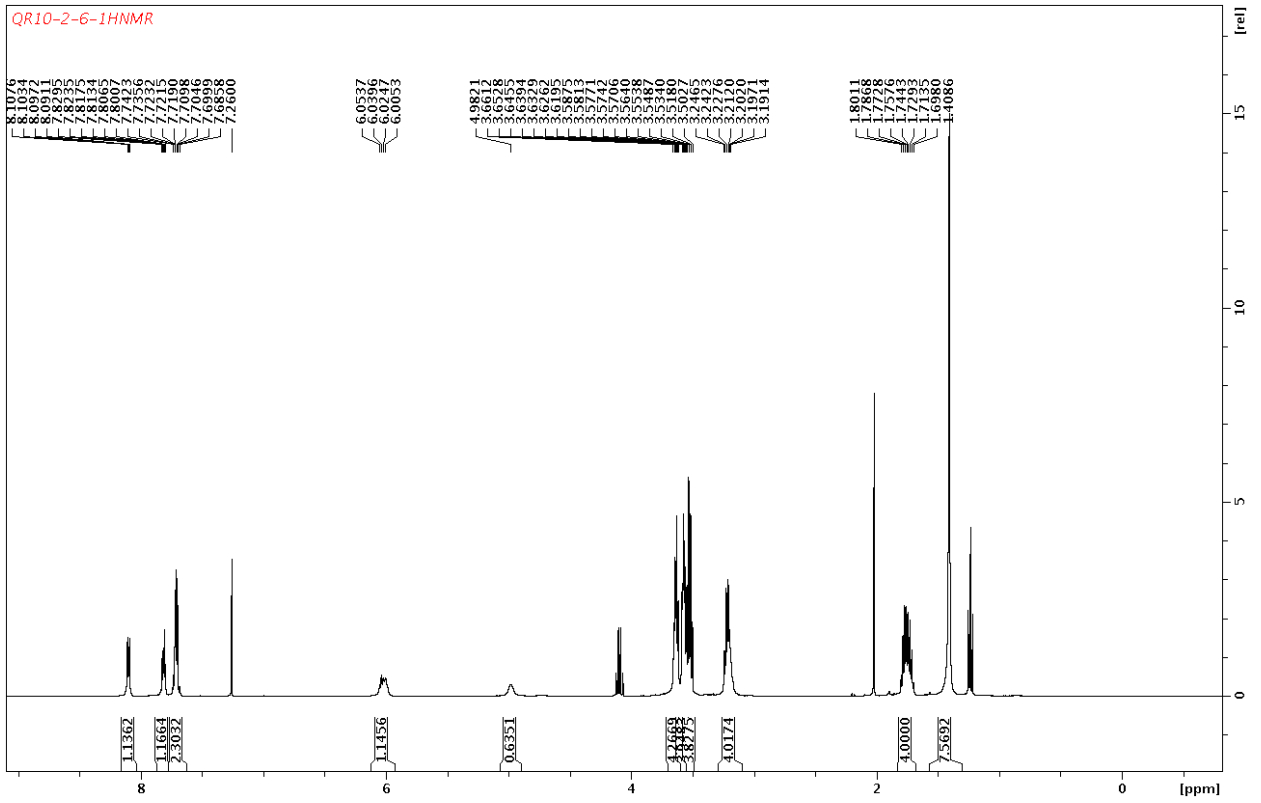


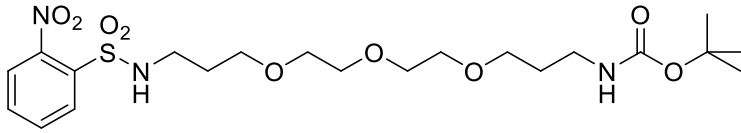
3-51



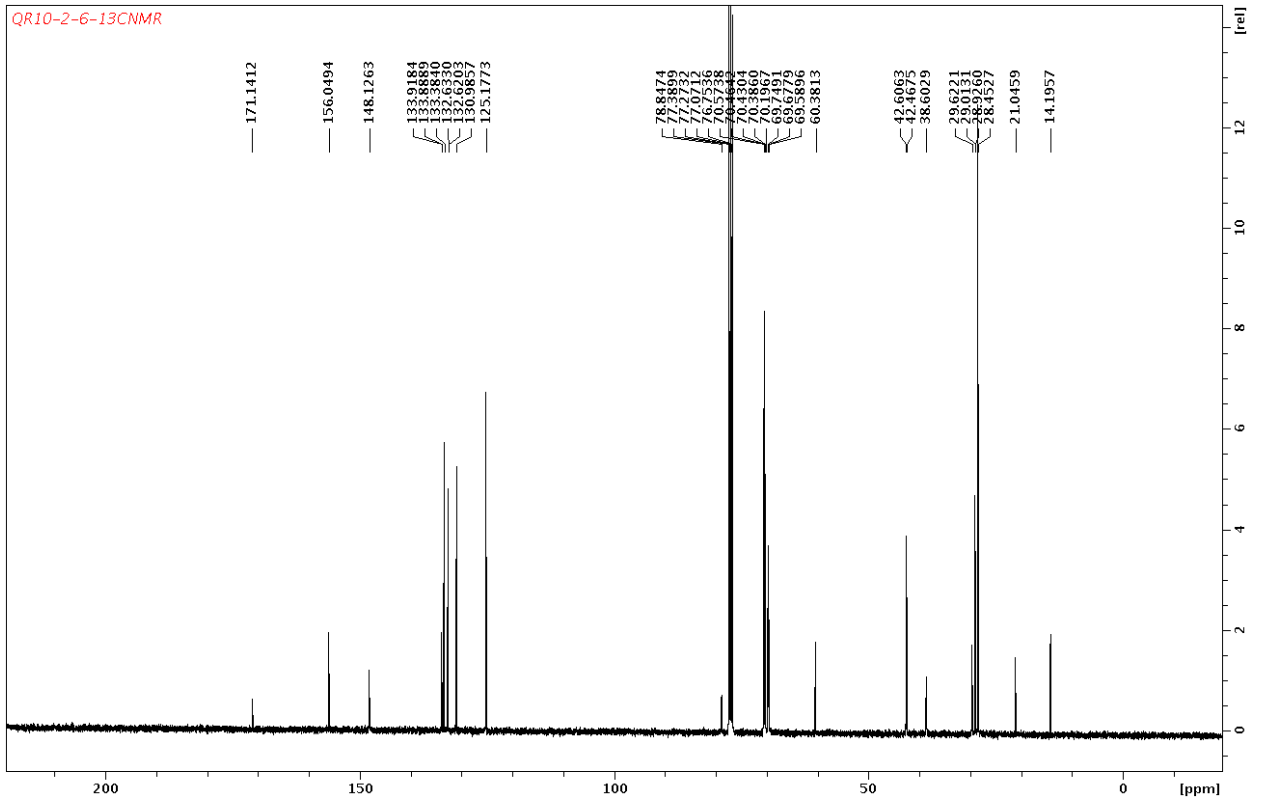


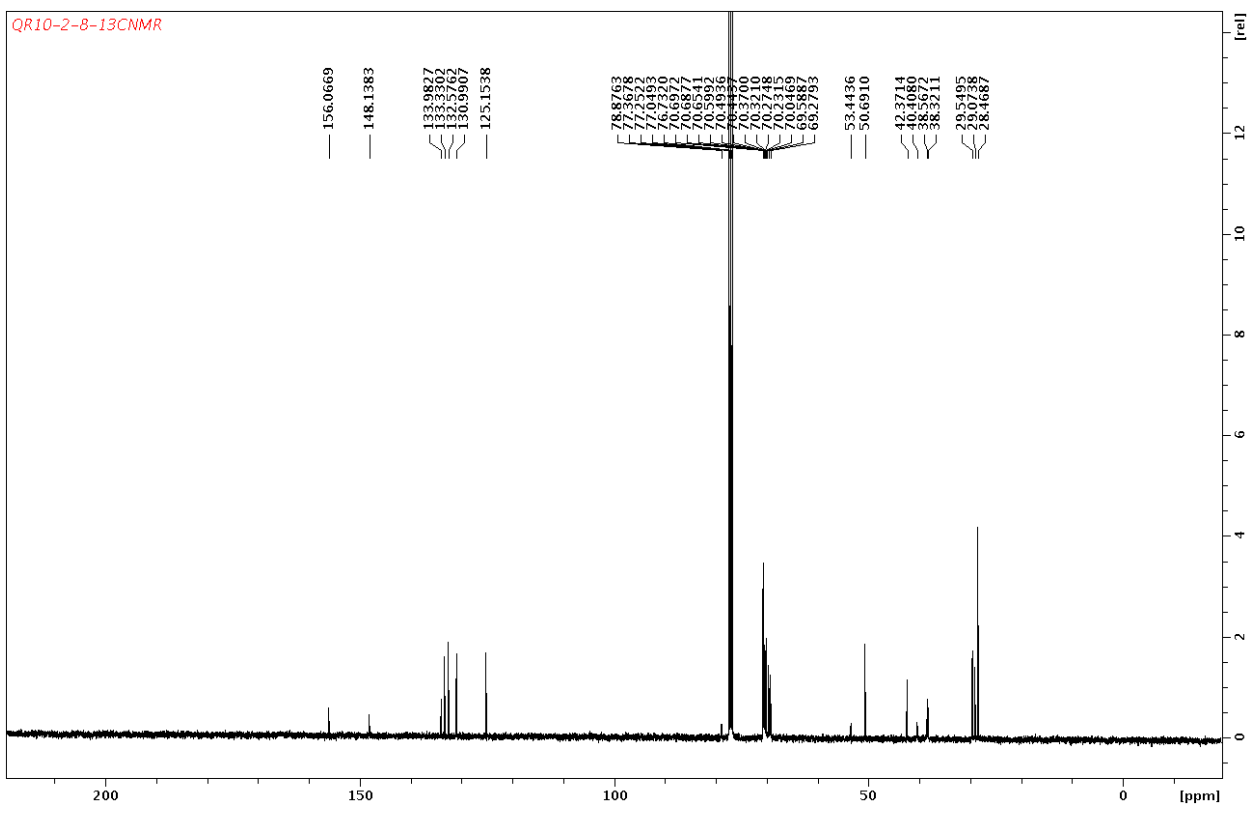
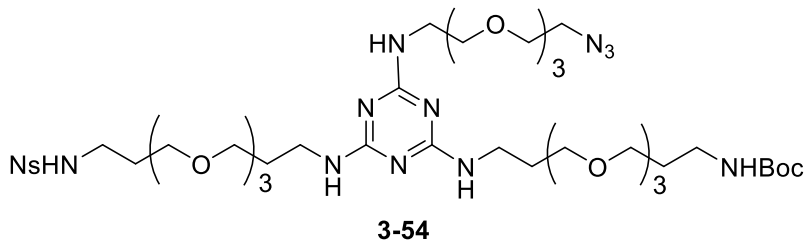
3-52

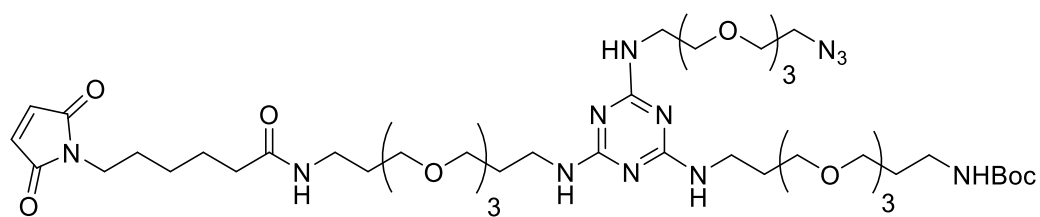




3-52







3-56

